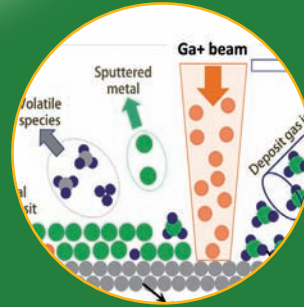
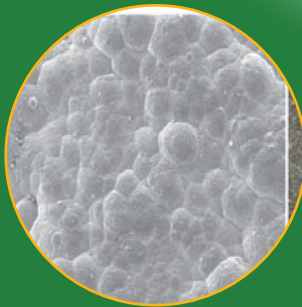
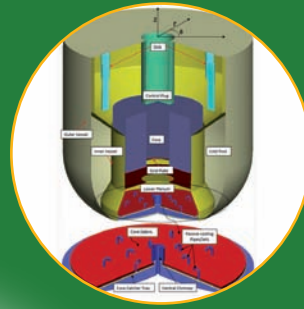
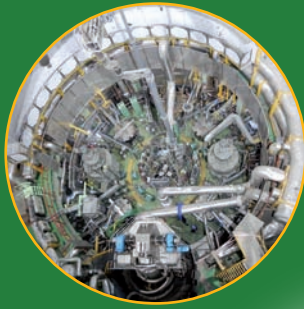




Indira Gandhi Centre for Atomic Research

Annual Report - 2019



सत्यमेव जयते

Government of India
Department of Atomic Energy
Indira Gandhi Centre for Atomic Research
Kalpakkam - 603 102

IGCAR

2019

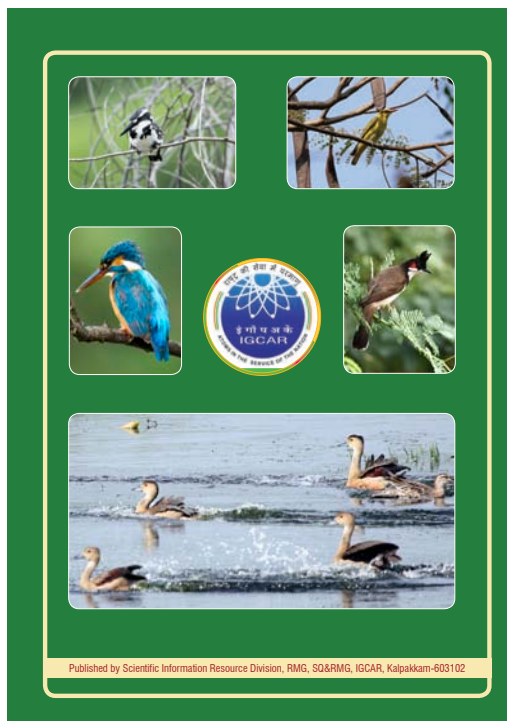
INDIRA GANDHI CENTRE FOR ATOMIC RESEARCH

ANNUAL REPORT

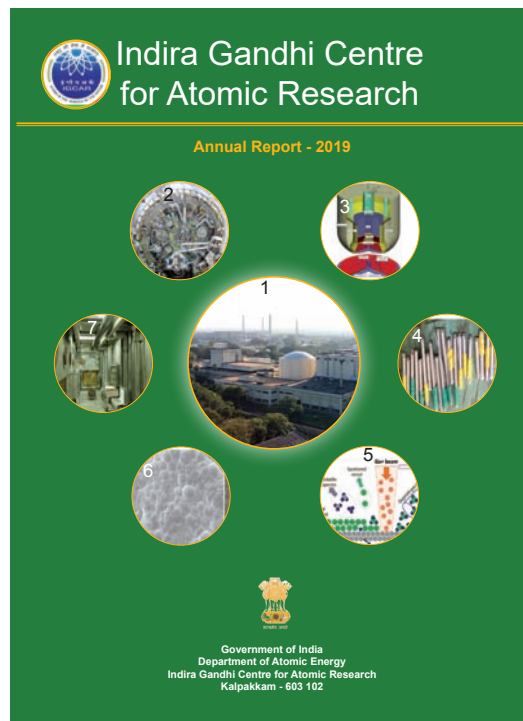


Government of India
Department of Atomic Energy
Indira Gandhi Centre for
Atomic Research
Kalpakkam 603 102

Back Cover



Front Cover



Front Cover

1. Fast Breeder Test Reactor
2. Top view of reactor assembly of PFBR
3. Full scale computational model with multi jet/pipe core catcher of SFR
4. Chopped pieces of FSA dummy fuel pins
5. Schematic of focused ion beam induced deposition of metallic layer by ion beam decomposition of organometallic precursor on the surface of a substrate
6. SEM of pyrolytic graphite coating on high density graphite
7. A view of in-cell crane inside lead cell containment box

Back Cover

Flora and Fauna at Kalpakkam

CONTENTS

Foreword	
Editorial	
I. Fast Breeder Test Reactor	1
II. Prototype Fast Breeder Reactor	15
III. R&D for Fast Breeder Reactors	43
IV. Fuel Cycle	65
V. Basic Research	85
VI. Directed Basic Research	121
VII. Infrastructure Facilities	142
VIII. Awards/Publications/News&Events/Organisation	173

Editorial Committee Members:

Dr. T. S. Lakshmi Narasimhan, Dr. N. V. Chandra Shekar, Dr. C. K. Mukhopadhyay, Dr. Vidya Sundararajan, Shri A. Suriyanarayanan, Dr. C. V. S. Brahmananda Rao, Dr. V. Subramanian, Ms. R. Preetha, Shri J. Kodandaraman, Shri G. Venkat Kishore, Shri S. Kishore, Dr. N. Desigan, Shri M. Rajendra Kumar, Ms. S. Rajeswari, Shri K. Ganesan, Shri K. Varathan and Shri G. Pentaiah

Address for Correspondence

Dr. T. S. Lakshmi Narasimhan
 Associate Director, Resource Management Group, SQRMG
 Indira Gandhi Centre for Atomic Research
 Kalpakkam - 603 102
 Phone : +91-44-2748 0301; Fax : +91-44-2748 0060;
 Email : tslak@igcar.gov.in; Website : www.igcar.gov.in

Mission of IGCAR

- *To conduct a broad based multidisciplinary programme of scientific research and advanced engineering development, directed towards the establishment of the technology of Sodium cooled Fast Breeder Reactors (FBR) and associated fuel cycle facilities in the country*
- *The development and applications of new and improved materials, techniques, equipment and systems for FBRs*
- *To pursue basic research to achieve breakthroughs in fast reactor technology*
- *To utilize the expertise in core and strategic sectors like materials development for Advanced Ultra Super Critical Technology, testing of pyro devices etc., beyond the accomplishment of mission oriented programmes*

Vision

To be a Global Leader in Sodium cooled Fast Breeder Reactor and associated Fuel Cycle Technologies

Foreword



It is my pleasure to share with you the Annual report of IGCAR for 2019. Indira Gandhi Centre for Atomic Research is focused on conducting multi-disciplinary scientific research and advanced engineering development directed towards the establishment of technology for sodium cooled fast breeder reactors and associated fuel cycle.

In the year 2019, the Fast Breeder Test Reactor (FBTR), the flagship experimental reactor of our Centre operated at 32 MWt during the 27th and 28th irradiation campaigns. The turbo generator synchronized to the Grid produced an electrical output of 7 MWe. The objective to be achieved further is operation at its rated power of 40 MWt with a core design of seventy Mark-I fuel sub-assemblies and necessary approvals for the same has been sought. Further, towards extending the life of Grid plate, replacement of axial shielding in fuel sub-assemblies with tungsten carbide has been recommended, A speeder gear automatic control system for FBTR turbine has been successfully installed and commissioned. As part of post-Fukushima retrofit, a supplementary control panel has been installed. A global sodium leak detection system for detecting sodium leaks from remote positions and seismic instrumentation have been successfully commissioned. The U-233 fueled Kalpakkam Mini (KAMINI) reactor continued to operate upto 30 kWt for neutron radiography of boron coated gamma compensated ion chambers, fission chambers from ECIL, PFBR neutron detector etc.,

IGCAR continued its technical support towards commissioning of Prototype Fast Breeder Reactor (PFBR). The onsite performance of secondary sodium pumps were carried out. A system for online condition monitoring of secondary sodium pumps & Annular Linear Induction pump (ALIP) has been commissioned. The high temperature testing and qualification of Dissimilar

Metal Weld Inspection Device (DISHA) vehicle were conducted successfully. Performance testing of modified transfer arm guide in sodium was carried out. The first batch of 42 fuel sub-assemblies for PFBR has been shifted to BHAVINI site.

For the future FBR's, plant dynamic studies towards the design of plant protection system has been carried out. Performance qualification of large diameter bearings was carried out. Studies on molten fuel coolant interaction in sodium using simulated CORIUM was conducted as part of severe accident research. Inflatable seals made of silicone have been developed indigenously. A genetic algorithm is implemented for optimization of control rod positioning in FBR core.

COmpact Reprocessing facility for Advanced fuels in Lead cells (CORAL) has achieved its designated mandate of reprocessing fourteen spent fuel sub-assemblies over forty eight campaigns. Eight more reprocessing campaigns have been completed at CORAL after relicensing by AERB. A new continuous precipitator for plutonium reconversion at CORAL has been commissioned. In the Demonstration Fuel Reprocessing Plant (DFRP), water runs have been completed and acid-solvent (TBP) run is in progress. The seismic qualification of integrated Glove box assembly in the plutonium reconversion lab has been completed.

The construction of Fast Reactor Fuel Cycle Facility (FRFCF) is in full swing with completion of cumulative concreting of about 4.0 lakh cubic metre. Gold rated Green building certificate has been received for the Training Centre. A single uninterrupted megapour of size 8200 cu.m. of temperature controlled concrete was successfully completed within 130 hours as against an estimated time of 145 hours. High density concrete was developed for Waste Tank Farm Roof slab of fuel reprocessing plants

Foreword

As part of development programs for use of metallic fuels for future fast reactors, 1000 kg LiCl-KCl eutectic salt was prepared and purified for the purpose of pyro chemical reprocessing. Also methods have been developed for the estimation of actinides in cadmium and eutectic salts. Process parameters and characterisation procedures were optimised for the preparation of metallic fuel by injection casting method.

A good number of new experimental facilities and processes have been commissioned which include: production of high density tungsten carbide pellets by spark plasma sintering; plasma nitriding of large FBR components; explosive welding technique for plugging degraded PFBR steam generator tubes; dissimilar metal welding of turbine rotor for Advanced Ultra Super Critical Coal fired thermal power plant; indigenous development of simulator platform for FBR's; development of technologies for manufacture of hard faced wear rings for FBR's.

On the electronics and instrumentation side, a prototype plutonium continuous air monitor has been developed. Further, design and development of temperature and radiation resistant MEM based pressure sensors and numerical protection relays have been completed. Touch screen based virtual control panel for nuclear plants were installed.

On the materials front, polymer based nanocomposites have been developed for diagnostic X-ray shielding as an alternate for lead shielding. A modified method for welding 304B4 stainless steel has been developed. A novel high performance nanophase modified fly ash concrete with inhibitors has shown promise for extending the life of concrete structures in nuclear installations. In the areas of basic research, SiO₂ based microcantilever

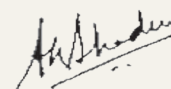
has been developed for relative humidity sensing. SQUID based TDEM system for sounding measurements have been developed and field testing has been successfully reported.

Online Nuclear Emergency Response system (ONERS) has been developed and upgraded for accurate weather prediction for Nuclear Power Plants.

IGCAR celebrated its foundation day for the first time on 30th April, 2019. It was this day in 1971 that Dr. Vikram Sarabhai, the then Chairman, Atomic Energy Commission approved the formation of Reactor Research Centre (RRC) by an executive order, which was later renamed as Indira Gandhi Centre for Atomic Research in 1985. As part of this, "Open House" was organised for the families of employees of IGCAR.

Twenty three young trainee scientific officers have successfully graduated from BARC Training School at IGCAR and placed in various units of the department. Twenty five Research Scholars have joined IGCAR to pursue their doctoral program under HBNI. I am happy that we continue to attract bright and young talents who will pursue research in basic areas and in cutting edge technologies in line with the mission of the Centre.

I appreciate the efforts of the editorial committee for compiling the IGC annual report. I will be happy to receive any comments and suggestions from the readers towards improving the contents of the report.



Dr. Arun Kumar Bhaduri

Director, IGCAR

Editorial

I am herewith presenting the IGC Annual Report - 2019 on behalf of the Editorial committee. The excellent progress made by the Centre have been amply reflected in the technical articles with an overall increase in performance in all the domains.

This year the report is divided into eight chapters, viz., FBTR, PFBR, R&D of FBRs, Fuel cycle, Basic Research, Directed Basic Research, infrastructure Facilities, and compilation of events, seminars, awards etc. and the articles have been grouped accordingly. The technical articles represent the important activities and developments of the Centre in several areas of Science, Engineering and technology.

Chapter I highlight the FBTR reaching a power level of 32 MWt, with grid delivering an output of 7 MWe. The steam generator system has been retrofitted with new baffle valves. Also the testing and qualification of FBTR CRDM Gripper Bellows have been carried out. The articles presented the motivation for taking FBTR to its full rated power level of 40 MWt and also the efforts to extend the life of the Reactor. The reactor has continued serving as test bed for irradiation of various engineering components and also as experimental facility for irradiation of various samples. The life extension efforts will thus be a welcome development as the reactor will continue to provide the facility for the development of various innovative design of materials and components for future reactors.

In Chapter II, the present status of commissioning of PFBR is presented. The articles highlight the technical and R&D contribution of the Centre towards this effort. Sodium Aerosol Detector which is used for leak detection in Annular Linear Induction Pump (ALIP) of PFBR Primary sodium purification Circuit in nitrogen environment has been successfully qualified. An Electromagnet based Cleaning Mechanism for Diverse Safety Rod Drive Mechanism (DSRDM) of PFBR has been successfully developed. Chapter III is on R&D in FBRs and highlights the Centre's efforts towards developing innovative and indigenous technology for the future reactors programs.

These include technology development of hard faced components, microprocessor based safety logic systems for reactor shutdown, qualification of sacrificial material for core catcher of SFR etc.

Fast Reactor Fuel Cycle Facility (FRFCF) under construction with the purpose of closing the fuel cycle is going on in full swing with good progress in the infrastructure and nuclear island areas. The status of the project along with developments required as part of construction is described in Chapter IV. Also the design and development of various components and chemical procedures towards the fuel reprocessing program have also been included here. Salient features pertaining to Demonstration Fuel Reprocessing Plant (DFRP) and its commissioning status are also brought out here.

Basic research in the areas of physical, chemical and engineering sciences have continued to flourish and the interesting work related to some of the areas at the forefront of basic research are reported in Chapter V. These include, fabrication of photosensitive nanodevice using focused ion beam; Enhanced piezoelectricity in nanostructured compounds; and thermal, magnetic, electrical and other material properties of some important compounds. These articles reflect the high quality R&D capabilities of the Centre. Chapter VI focuses on Directed Basic Research which showcases how the basic research in some of the areas have been directly applied to the mission of our Centre. These include development of newer materials and processes.

Chapter VII reflects the Centre's investment towards strengthening the infrastructure facility of the Centre. Also articles which describe the upgradation and augmentation of facilities are listed here. The last chapter (i.e.) Chapter VIII details the events, awards, meetings, honours, seminars etc., pertaining to our Centre. The national and international events conducted during the year have enabled interaction of experts with younger colleagues of the Centre and have added further vibrancy to the R&D environment prevailing in the Centre. The successful functioning of BARC training

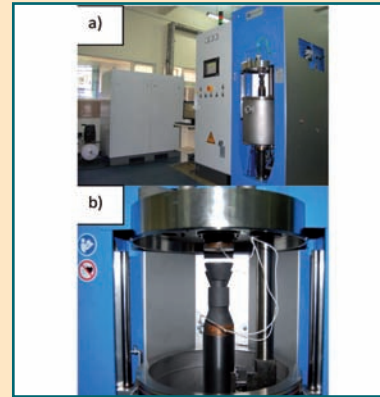
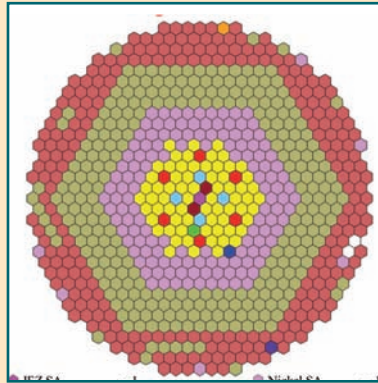
School at IGCAR and vital research contributions from HBNI scholars provide the required impetus for the academic component of the Centre.

The activities in various domains which have been brought out in a comprehensive way have made the task of bringing out the annual report enjoyable. We welcome and value suggestions and inputs from our readers which will be crucial for bringing improvements in the report. We thank the Group Directors for their support and authors from the different Groups for providing interesting articles reflecting their high quality R&D work. The committee sincerely thanks Dr. Arun Kumar Bhaduri, Director, IGCAR for his continued guidance, advice and constructive suggestions which enabled us to bring out such a comprehensive report. The committee also

thanks Dr. B. Venkatraman, Director, Safety, Quality and Resource Management Group and Electrical Services Group for the comprehensive support and suggestions rendered from time to time. I also thank all the members of the editorial committee for their sustained and dedicated efforts which has made possible to bring out the annual report.



(T. S. Lakshmi Narasimhan)
(On behalf of the Editorial Committee,
IGC Annual Report)



CHAPTER I

Fast Breeder Test Reactor

I.1 Studies towards Raising FBTR Power to 40 MWt

FBTR core is originally designed to operate at 40 MWt using MOX fuel with 30% PuO₂ and 70% UO₂ (85% enriched U). However, due to the non-availability of enriched uranium, mixed carbide fuel (Mark-1 (70% PuC+30%UC)) was chosen for the initial core. After first criticality in 1985, the initial core was operated with a maximum power of 10.6 MWt. Subsequent operations were made by adding many variants of carbide and oxide fuel sub-assemblies (FSAs) and increasing the operating Linear Heat Rate (LHR), based on the encouraging post-irradiation experiment results. The operated power in the 28th campaign is 32 MWt. This core had 58 FSAs; 49 Mark I, 1 Mark II and 8 MOX (44%PuO₂+56%UO₂). The objective to be achieved further is operating FBTR at its rated power of 40 MWt. To meet this objective, a core with 70 Mark-I FSAs has been designed (Figure 1).

Neutronics parameters for safety analysis

The main constraint in core design is respecting the minimum shutdown margin of 4200 pcm. It is achieved by using four numbers of B₄C (with 50% B-10 enrichment) poison SAs in the 2nd ring along with existing six control rod SAs (B-10 enrichment of 90 %) in the 4th ring.

Perturbation worths and kinetic parameters have been estimated for this core using ABBN-93 cross section library (2D analysis). The fuel slumping worth is estimated using a conservative 1/3rd slumping model. A maximum value of 1.12 \$/cm is obtained for the 4th channel. It is found that sodium void reactivity worth is

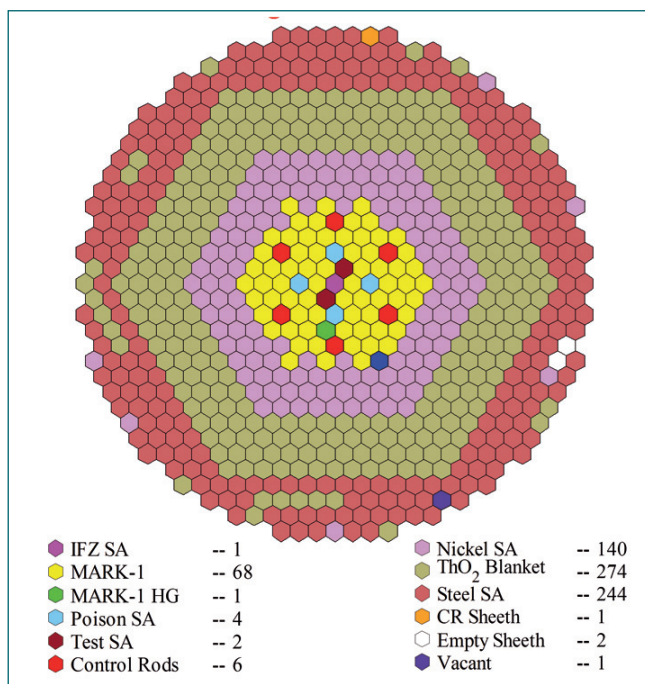


Fig. 1 Proposed 40MWt core configuration

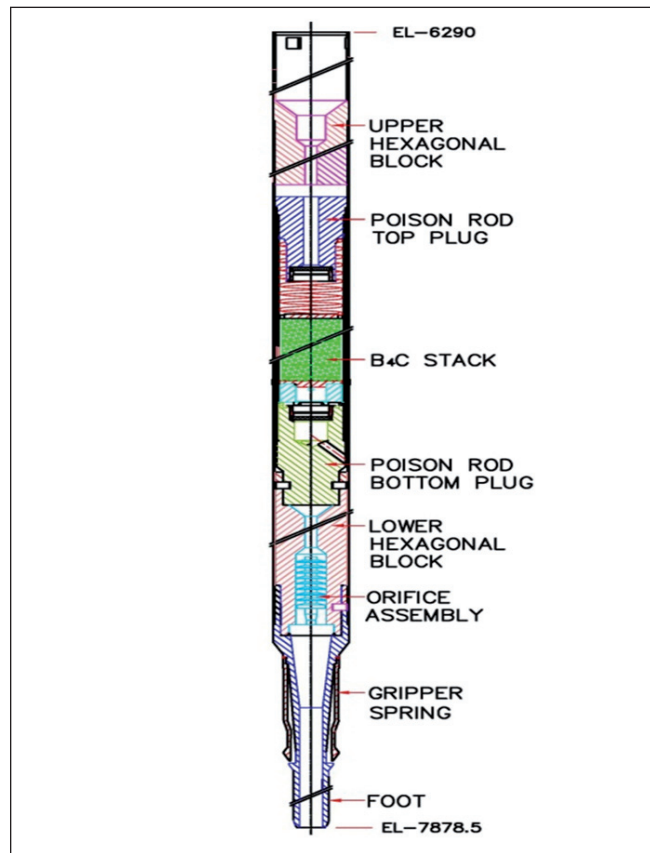


Fig. 2 FBTR Poison SA

-1035 pcm (-3.8 \$). The whole core voiding of steel and fuel reduce reactivity by -7 \$ and -219 \$ respectively. Doppler constant is found to be -47 pcm. The estimated effective delayed neutron fraction and prompt neutron lifetime are 271 pcm and 0.16 μs respectively. This data forms the major inputs for the safety analysis, plant dynamics analysis and severe accident analysis.

Poison SA design

Poison SA is designed with a maximum power of 35.73 kWt and peak LHR of 1140 W/cm. The designed flow through poison SA is 0.409 kg/s. The maximum clad mid-wall hotspot temperature and pellet centerline hotspot temperature for nominal power condition is 537.6°C and 2055.7°C respectively and this satisfies the respective DSL for nominal and 16% overpower conditions. The sodium temperature rise from inlet to outlet of the SA is 97.7°C, which satisfies thermal striping requirements. As the poison SA is to be loaded in fuel region, the foot is designed similar to that of fuel SA. The head of the SA is designed such that its handling is similar to that of a control rod assembly. To differentiate poison SA, during handling, poison SA length is designed to be shorter than the fuel SA. Details of a poison SA is schematically shown in Figure 2.

The required SA pressure drop of 278 kPa for the designed flow is realized by installing comb type labyrinths and orifice structure in the SA foot and also by suitable measures in upper and lower hexagonal blocks. The proposed flow restricting methods ensures that SA is free from cavitation even at 110% flow condition. The additional weight provided by top and bottom hexagonal blocks prevents lifting of SA even at 110% of sodium flow.

Shielding Studies

In this core, FSA boundary extends up to 24.14 cm in the radial direction (21.82 cm for 32 MWt core). So there is a reduction in the nickel reflector size. This is to be studied in terms of neutron and gamma flux, dose rates, heating, dpa and helium production. Calculations are performed using 2D transport code DORT in RZ geometry using multigroup cross section set IGC-S3. The core centre flux is $3.315E+15$ n/cm²/sec which is same as that of present 32 MWt core.

At the reactor vault exit location, there is a 50% increase in neutron flux and neutron dose level and 40% increase in gamma flux and gamma doses compared to the existing core. Similarly at top shield exit location, increase in neutron flux and neutron dose level is 20 % and that of gammas is 30 %.

During normal operation, cover gas activity increases up to 40 %. The increase in dpa in the centre of grid plate (GP) top region is 11% (6.3 dpa). The residual life of GP will come down from 8.14 full power year (fpy) to 7.25 fpy. For this time duration, dpa experienced by the core cover plate and reactor vessel are 0.3 and 0.02 respectively. The neutron spectra at GP centre is hard and the variation of dpa along GP in the radial direction is given in Figure 3. Also the variation of dpa is less than 15 % within 200 mm of GP in the radial direction where dpa experienced is maximum. The increase in helium production is 32 % in core cover plate. Detector flux increase in the detector pit location is 40 % ($1.0E+11$ n/cm²/s) and is favouring the operation. The total radiation heating at the beginning of reactor vault concrete is increasing from 7 to 10 W/m³. Since the biological shield cooling system is designed for 40 MWt, this increase could be accommodated. Since the rotating plug region temperature of FBTR is maintained below 130 °C, Wigner energy release from graphite due to the increase in total neutron flux from $4.82E+10$ to $6.40E+10$ n/cm²/s will not have significant effect.

The dose rate increase can be managed by restricted entry to different locations. Since the GP dpa is governing, FBTR is safe to operate for another 7.25 fpy at 40 MWt.

Analyses of unprotected transients

As a part of safety analysis, unprotected transients such

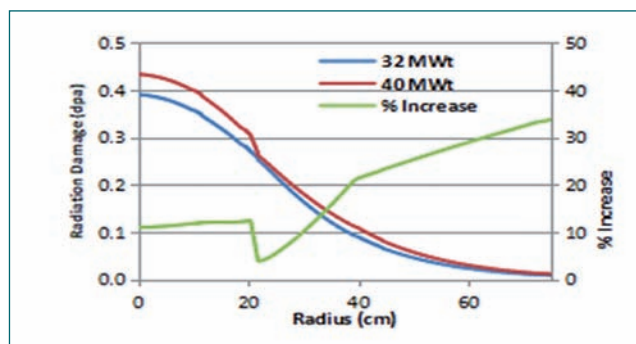


Fig. 3 Variation of dpa along grid plate

as Unprotected Loss Of Flow Accident (ULOCA) are analysed. It is carried out by dividing the sequence of events into three phases, viz., pre-disassembly phase, disassembly phase and mechanical energy release phase. In the pre-disassembly phase, the course of the accident is evaluated deterministically until the geometry of fuel pin or FSA is intact. The space dependent reactivity feedbacks from the fuel, clad and coolant are taken into account together with core radial expansion feedback. For computational purpose, the core is divided into seven radial channels and ten axial meshes. It is to be noted that the integral sodium void worth of this core is - 3.82 \$.

The PREDIS code was used to analyze the pre-disassembly phase and disassembly phase is analysed with VENUS II code. In all the analysis, latest equation of state, developed at IGCAR, was used in the disassembly phase. The initiating event for ULOCA is loss of power supply to primary pump and the ensuing flow coast down. A conservative flow halving time of 20 s (measured > 60 s) is considered. As the flow reduces, the coolant gets heated up, and sodium expansion and spacer pad expansion feedbacks together make the net reactivity negative. The reactor power falls below the decay heat level as shown in Figure 4. Giving credit to decay heat removal system, the transient does not lead to core disruptive accident.

Uncontrolled withdrawal of a control rod can lead to UTOPA. To simulate this, a continuous reactivity ramp of 6 pcm/s (peak differential worth of a single CR) is applied to the core. As there is continuous addition of external reactivity, the net reactivity in the system is positive throughout the transient and the power escalates from the initial value leading to fuel melting and slumping. The reactivity addition rate due to slumping at the end of pre disassembly phase is 27.6 \$/s. With peak fuel temperature crossing boiling point, pre disassembly phase is terminated and the calculation for disassembly phase starts.

For conservative assessment of the release of mechanical energy, a reactivity addition rate of 50 \$/s is considered as input to the disassembly phase. The

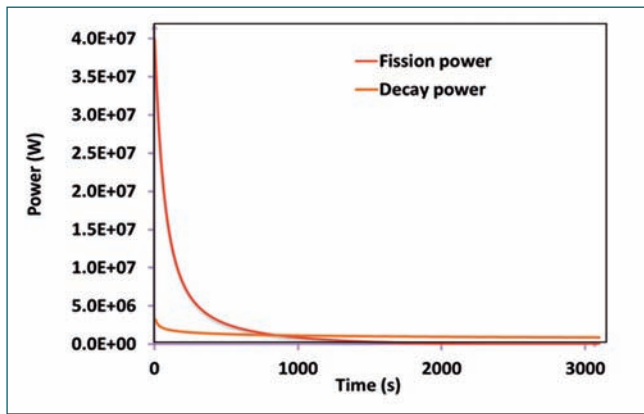


Fig. 4 Variation of reactor power under ULOF

estimated mechanical energy release under UTOPA is 6.9 kJ. Under ULOCA, the scenario considered is the breakage of coolant pipe and drain out of sodium. Hence, the transient is simulated by assuming a step reactivity addition of -3.82\$. The absence of heat removal causes fuel melting followed by slumping resulting in a large positive reactivity addition. Again, 50 \$/s reactivity addition rate is assumed in the disassembly phase. The maximum value of mechanical energy release is 11.94 MJ which is less than the design value (39 MJ) of mechanical energy release in FBTR under a severe accident. Hence, the present core is safe with respect to the above severe accidents considered.

Analysis of protected transients

In order to demonstrate the inherent safety characteristics and the capability of plant protection system with respect to various plant transients, analyses of various enveloping design basis events have been carried out using the plant dynamics code DYNAM. DYNAM is an in-house developed plant dynamics code validated against FBTR commissioning tests.

The code has models for simulation of neutronic power and thermal hydraulics of primary and secondary sodium circuits. All the enveloping events were analysed. It is seen that during these events, except ‘off-site power failure’, ‘station black out’ and ‘one control rod withdrawal’, the clad hotspot and fuel hotspot temperatures are limited below the design safety limits even without safety actions demonstrating the inherent safety characteristics of the plant. Moreover, safety of the plant is demonstrated with good margin under off-site power failure, station blackout and one control rod withdrawal events with reactor trip based on the second appearing parameter. During loss of feed water flow in one loop event, no parameters are available to initiate automatic trip of the reactor. Though there is no concern, an additional automatic trip parameter based on high reactor inlet temperature has been proposed to be added to the safety logic.

Another important event against which safety of the plant needs to be demonstrated is the single FSA blockage. This event is important due to the radiological consequences associated with it. For analysing this event, three dimensional CFD analysis of pool hydraulics in the region above core has been carried out. The main objective of the analysis is to estimate the detectable size of flow blockage in FSAs located at various locations in the core. This analysis is due to the introduction of poison subassemblies which may induce large temperature dilution (due to low heat generation in them) in the sodium outlet temperature measurement of nearby FSAs. Predicted temperature distribution for the case of a SA in fourth ring blocked is shown in Figure 5. It is seen that the detectable flow reduction in various rows of SAs varies between 9 % and 15 % which are much less than the permissible flow reduction of 44.5 %.

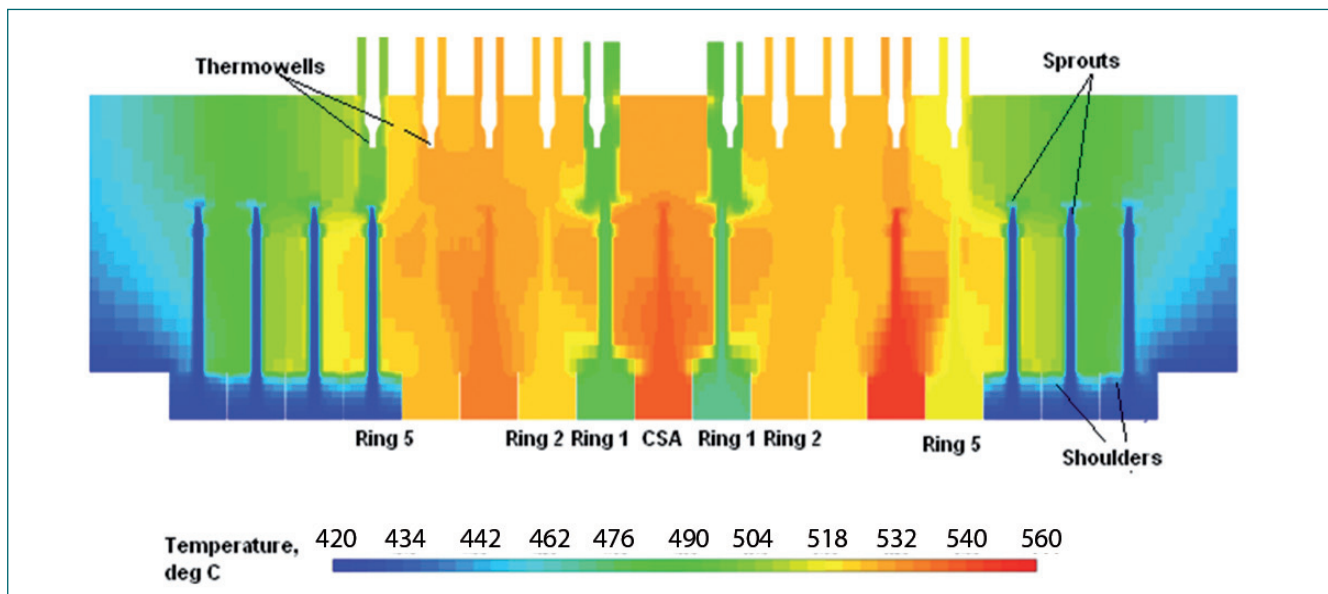


Fig. 5 Temperature distribution in pool when a SA in fourth ring is blocked

I.2 Installation and Commissioning of Speeder Gear Automatic Control System for FBTR Turbine

In FBTR, nuclear heat from the reactor core is transferred through primary and secondary sodium systems to steam generator to generate superheated steam at 125 bar and 480°C. The superheated steam is fed to 16.4 MWe Turbo Generator (TG) to generate electric power. The TG is synchronized to the grid to export the generated power. Earlier, the steam flow to the TG was being controlled manually using the speeder gear motor. Whenever the grid frequency varies, steam flow to the TG needs to be varied manually to maintain the power. Hence, steam flow to the turbine had to be adjusted manually by operating the speeder gear frequently. This is found to be an additional load on the operator.

In order to avoid manual operation and to ensure minimum steam flow through the bypass steam circuit for maintaining the required auxiliary header pressure and maximum steam flow to the turbine, it is proposed to have a Speeder gear auto Control for Turbine Flow (SCTF) for the turbine. In thermal reactors, drum type boilers are used and the Boiler Pressure Control (BPC) System controls the speeder gear of turbine for positioning turbine governor valves to enable turbine-follow-reactor type control. In FBTR, Steam Generator (SG) is of once through type and in the absence of a steam drum/ separator, this scheme could not be implemented. Hence, the new scheme is proposed.

The block diagram of SCTF system is shown in Figure 1. SCTF is a smart touch panel PC based computer system running on Linux based Ubuntu OS with multi function USB DAQ module connected to it. Application software

is developed in “C” language in Ubuntu environment. The SCTF system will function only on auto mode. The auto mode is effective only when Auto/Manual selector switch provided in CDcr 05 is selected on “Auto” and turbine lockout condition is in RESET condition. SCTF system scans the field inputs at every 10 second interval. Once the system is put on auto mode, the steam flow to the turbine at that instant is considered as the set point and SCTF system will maintain the flow within ± 0.5 T/h from the set point. At every scan, the system scans the steam flow and compares it with the set point and error is computed. When the error exceeds +0.5 T/h, “Un-Load” output will be ON for 0.37 s and will remain OFF for next 9.63 s. In the next scan, if the error still persists beyond +0.5 T/h, “Un-Load” output will be again turned ON for 0.37 s and OFF for 9.63 s. This pattern will continue until the error reaches within +0.5 T/h. This “Un-Load” output will actually reduce the steam flow to the turbine. Similarly when error is in the negative side, loading of the turbine takes place. At any point of time, if the error exceeds $\pm 10\%$ of set point or if “Turbine Lock out” is SET, the auto operation is made ineffective and an alarm “Speeder Gear Auto Operation Ineffective” is generated and “Auto ineffective” lamp will be ON. At this time, operator has to take the speeder gear control on manual mode and control the turbine flow manually. The system will accept new set point when the mode is again changed from manual to auto. A mimic as shown in Figure 2 has been developed to display the status of various parameters to the operator. The system has been commissioned successfully and was validated during 28th irradiation campaign.

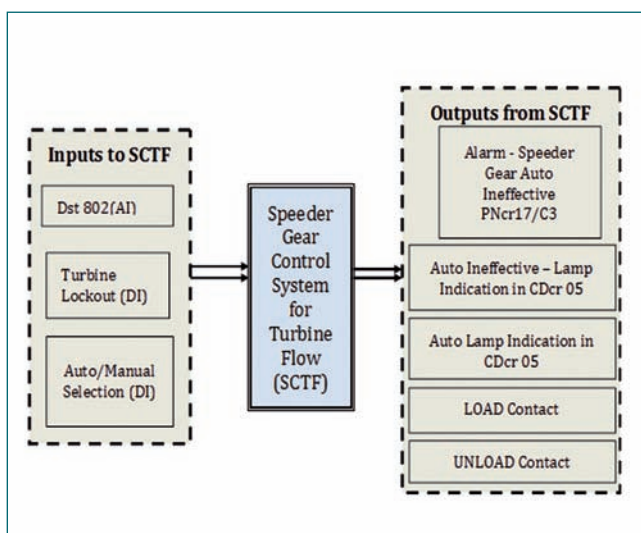


Fig. 1 Block Diagram of SCTF System

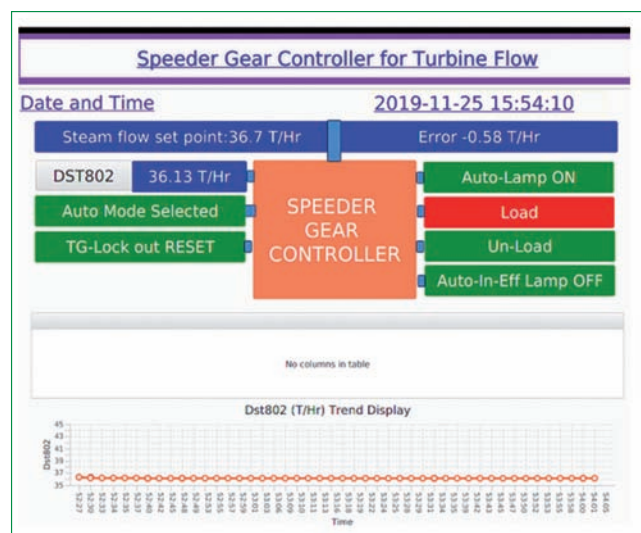


Fig. 2 Mimic: SCTF System

1.3 Commissioning of Global Sodium Leak Detection System in Secondary Sodium System of FBTR

The primary and secondary circuits of FBTR use large inventory of sodium as coolant. Leaks in sodium systems have extremely high hazardous potential due to reaction of liquid sodium with oxygen/water vapor in the air. Sodium reacts with air and catches fire. It is essential to detect sodium leaks at the incipient stage itself. Design provisions to contain the leak and leak detectors are provided to detect the leak before any potential risk to the plant and personnel. For detecting sodium leak in FBTR, wire type detectors are wound over sodium pipelines, spark plug type detectors for bellows sealed valves and double enveloped pipes, mutual inductance (MI) probes to detect failure of nickel tube in Steam Generator Leak Detection System (SGLDS) and Sodium Ionization Detector (SID) is used for detection of sodium leak in SG casing. All the sensors outside the SG casing are localized in nature. To provide diverse detection of sodium leak at the potentially susceptible leaky points, Global Sodium Leak Detection System (GSLDS) was installed and commissioned in the secondary sodium system of FBTR. The basic intent of GSLDS is to primarily detect sodium leak from remotely operated (motorized/pneumatic/hydraulic) valves in the secondary sodium system.

The GSLDS is divided into two independent loops (east GSLD and west GSLD). However, there is an inter connectability which gives freedom to divert the flow to other loop in case of any fault in one loop. This is effected by manually opening the valve. Figure 1 shows suction, discharge and branch off line along with sampling arrangement of GSLDS for both the secondary sodium loops. Ten sampling points each in east and west

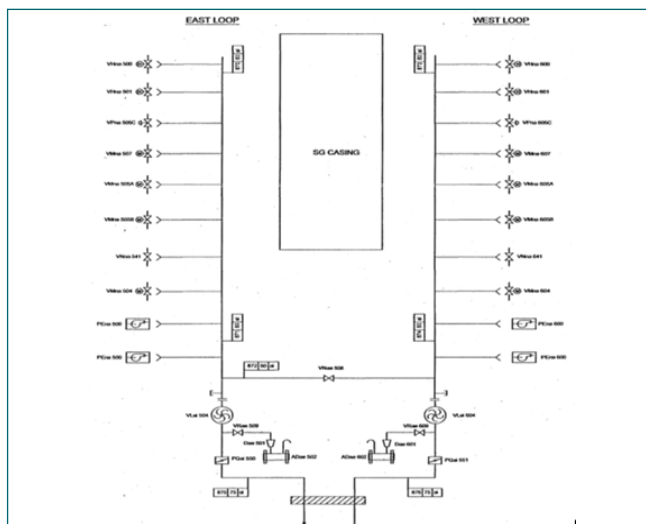


Fig. 1 Piping layout of global GSLDS



Fig. 2 Sensor and electronics of Global GSLDS

loop are provided to cover the potential leak points. A centrifugal blower with a capacity of 150 m³/h and static pressure of 8 inches of water column has been provided for each loop. The blower capacity is arrived based on pressure drop for the longest run of the pipe i.e. index run. Based on static pressure and flow, the motor power is arrived at 1 HP.

The detector chosen is SID. It works on the principle of preferential thermal ionization of sodium and this ion current is a measure of the leak. The criterion for choosing this sensor is that it can detect as low as 1 nanogram of sodium present in 1 cm³ of carrier gas. Hence a single detector can cater to many locations. The SID sensor has maximum sensitivity at sample flow of 1.2 to 1.5 lpm. The remaining blower outlet is being let out to atmosphere. The sensors along with rotameter were installed in the field with needle valves to precisely control the flow. The electronics was installed in the SGLDS cabin as shown in Figure 2. The response of both the units was checked by burning 1.5 g of sodium in the vicinity of the farthest sampling point. Performance of detectors is shown in Figure 3. Response of both the detectors is found to be satisfactory.

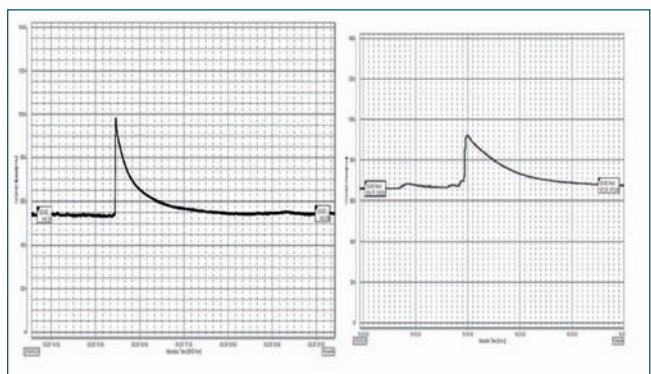


Fig. 3 Response of GSLDS by burning sodium

I.4 Commissioning of Supplementary Control Panel of FBTR

A Supplementary Control Panel (SCP) has been installed in FBTR as a part of Post-Fukushima retrofit as recommended by Safety Review Committee for Operating Plants (SARCOP) for relicensing of FBTR. SCP has safety functions like shutdown of the reactor and monitoring functions like safe shutdown state, decay heat removal for an extended period and monitoring and containment of radioactivity. SCP has been located in a suitable fireproof cabin in the southwest corner of the operating floor of Turbine Building.

The prototype SCP developed was subjected to all the qualification tests, viz. Environmental, Electromagnetic interference-electromagnetic compatibility and Seismic tests on the prototype panel, junction box and representative instrumentation and control (I&C) instruments as per the AERB guidelines.

After successful qualification of the prototype, industrial version of control panel and junction boxes (8 Nos.) was fabricated and installed in the field. Figure 1. shows the SCP installed in the cabin. All the I&C components were installed in the control panel and internal wiring from components to terminal blocks were carried out. Functional test was carried out on all the components installed in the control panel. Insulation resistance tests and voltage proof tests were also done on the control panel. Control panel was installed in the SCP cabin floor by grouting. Sensor signal cables like instrumentation cables, control cables and power cables (85 Nos.) were routed from field to control panel and terminated inside the panel. 8 No. of Junction Boxes (JB) have been installed in the field at various locations like Reactor Containment Building (RCB), Electronics room and Steam Generator building with proper anchoring as shown in Figure 2. All signals from the field sensors



Fig. 1 Supplementary control panel installed in cabin



Fig. 2 Junction box installed in the field

were terminated in JB's; the sensor signals are provided with signal conditioner modules (SCM) for conversion to current signals (4-20 mA) and transmitted to the control panel. Power supply (230Vac) is routed from control panel to JB's. Dual redundant DC regulated power supplies are installed inside the junction box for converting 230 Vac to 24 Vdc to power the SCMs installed in the JB's. Signal and power supply cables from RCB to control building are routed through specially fabricated cable penetration assemblies to maintain the leak tightness of RCB.

Wherever possible, dedicated sensors along with their processing electronics are provided viz. speed measurement of sodium pumps (primary and secondary), RCB D-zone pressure and temperature measurements, position indication (limit switches) for RCB isolation dampers and radiation monitors inside RCB D-zone.

Special support structures were fabricated for installation of magnetic speed sensors near the toothed wheel coupled to the primary and secondary sodium pump shafts. All the signals are simulated from the field and checked for their correctness in GUI and digital display provided in the control panel.

The SCP is also provided with access control, camera, hotline and redundant telephone lines. The "SCP fault" group alarm has been provided in main control room (MCR) which will annunciate on any of the conditions like power supply failure. SCP cabin temperature signals are monitored and displayed in MCR. Central Data Processing System (CDPS) acquires all the safety critical, safety related and non-safety signals, process and sends output to the plant. All the process signals of the plant are displayed in GUI of CDPS in MCR. The GUI of CDPS LAN is also extended to SCP cabin to display the signals. SCP has been installed and commissioned and its operation is found to be satisfactory.

I.5 Repair and Restoration of Steam Generator Module having Defective Thermal Baffle

Steam Generator (SG) of FBTR is an once through shell and tube type counter flow heat exchanger. The sodium flows in the shell side and water/steam in the tube side. Since the SG do not have tube sheets at both ends, thermal baffles are used at the entry and exit of tubes in the sodium inlet and outlet headers. There was a sodium leak from one of the thermal baffles. The leak was found to be from the Heat Affected Zone (HAZ) of the weld joint between the tube and the baffle. In-situ metallography of the affected portion indicated subsurface flaw in the material which has caused the failure. Considering the critical function of the thermal baffles which encounter hot sodium at 515°C, it was decided to replace all the thermal baffles with fresh ones. The defective steam generator was removed from the system and kept on a support structure in the Steam Generator building. After scooping out the leftover sodium from the sodium inlet and outlet headers, the headers were thoroughly cleaned with alcohol. The shell side was kept under inert conditions with argon after sufficient flushing. As replacement of the baffles in the SG sodium inlet header alone was not practically possible, it was decided to replace the entire sodium inlet header with prefabricated components. The procedure for baffle replacement and Quality Assurance Plan (QAP) were prepared and approval obtained for execution. The raw material (2.25Cr-1Mo) for sodium inlet header replacement was qualified by chemical analysis, mechanical testing and ultrasonic testing (UT) of the plates. New thermal baffles (7 No.) made of 9Cr-1Mo was machined for assembling in the steam generator. Procedure qualification and welder qualification for 9Cr-1Mo with 2.25Cr-1Mo dissimilar welding was carried out successfully. The water tubes and the thermal baffles



Fig. 1 Welded thermal baffles on header



Fig. 2 Inlet header long seam and circular joint fit up

were cut for removing the header. The longitudinal weld joint and circular weld joint of the sodium inlet header were cut and the header was removed as two halves. For fabricating the new sodium inlet header, the required 10 mm plates were machined out from 16 mm thick plates. The plate was formed for manufacture of 2 halves of sodium inlet header and heat treatment (normalizing and tempering) was carried out for the header halves. The top half header was drilled for assembling the thermal baffles. The two halves of the sodium inlet header were qualified by Liquid Penetrant Inspection (LPI). Suitable clamping was made to prevent distortion during welding of thermal baffles to the header half. After ensuring all dimensions, sequential welding of the thermal baffles with header was carried out. The inlet header halves were welded for longitudinal and circular seam to integrate with the steam generator. Suitable measures like clamping was carried out to prevent distortion. The welding of the tube to thermal baffle was made keeping the uniform clearance between them. All the weld joints were successfully qualified by LPI and UT. The restored SG is preserved and kept as a spare.



Fig. 3 Header with thermal baffles welded in-situ

I.6 Development of a Special Mock-up Steel Sub-Assembly for Irradiation of Seven Numbers of Test Fuel Pins in FBTR

Fast Breeder Test Reactor (FBTR) serves as an irradiation test facility for the development of improved and advanced versions of fuels for future Fast Breeder Reactors (FBRs). Some of the irradiation of test fuel pins carried out in FBTR are PFBR test fuel pins, metallic fuel pins of four different versions (U-6%Zr, 14.8 % enriched U -6% Zr, U-19%Pu-6%Zr & 19%EU-23%Pu-6%Zr), sphere-pac fuel pins (MOX), CHTR surrogate fuel materials with TRISO coating etc. Irradiation is carried out in FBTR using special steel sub-assembly (SA) having inner space of 22 mm bore diameter x 1200 mm length, and hence for irradiation of test fuel pins, capsules of dimensions up to 20 mm outer diameter can be used. With the above mentioned effective space, irradiation of three numbers of test fuel pins per capsule has been carried out.

Presently, there is a requirement for irradiation of a cluster of seven test fuel pins in FBTR. For this purpose, the space available for irradiation in the existing SA has been redesigned by enlarging the bore from 22 to 35 mm in the centre of SA. A modified version of the special steel subassembly with enlarged bore called "large bore mock-up steel sub-assembly" LBSA (Figure 1) has been designed and developed with a working space of $\varnothing 35\text{mm}$ x 1200 mm length. Due to this enlargement, a cluster of seven numbers of test fuel pins can be accommodated in the SA. The modified SA has an irradiation capsule consisting of an assembly of intermediate plugs, end plugs and seven numbers of dummy fuel pins without spacer wire. All the seven numbers of fuel pins are maintained at uniform pitch and are held in bores machined in the bottom and top most closing plugs, and covered by intermediate plugs of the capsule.

Flowering profile is machined on the inner side of the intermediate plugs to maintain flow of sufficient coolant



Fig. 1 View of components machined for LBSA



Fig. 2 View of end plugs, intermediate plugs, and arrangement of dummy pins in the capsule

around the outer fuel pins for effective transfer of heat (Figure 2). After irradiation, irradiation capsule can only be retrieved in hot cells after cutting open the sub-assembly with laser beam or through any other appropriate method. Subsequently, the test fuel pins can be retrieved from the irradiation capsule for post-irradiation examination.

Hydraulic test of the large bore mock-up SA was carried out in the water loop (Figure 3) of Hall-II. Since, kinematic viscosity of sodium at 670 K and water at 343 K are comparable, water is used as substitute test fluid. Pressure drops at different flow rates were determined and it was experimentally observed that the large bore SA did not lift from the locked hold down springs at 120% of nominal flow rate.



Fig. 3 View of water loop test section at Hall II for pressure drop and lifting force studies

I.7 Production of Tungsten Carbide (WC) Pellets by Spark Plasma Sintering (SPS) for FBTR Irradiation Experiments

In order to extend the life span of FBTR grid plate, attempts are being made to provide adequate axial shielding against fast neutron irradiation damage by introducing Tungsten Carbide (WC) shield subassemblies. Spark Plasma Sintering (SPS) technique is a novel powder metallurgy process which can be employed to produce high density sintered WC pellets. This process is adopted to produce pellets of WC, without making use of any sintering additives like Co or Ni, and these pellets are subjected to irradiation experiments upto about 1-2 dpa, in FBTR.

The SPS of Tungsten Carbide pellets were made using 200 g of WC powder fed in a 25T SPS facility, set up (Figure 1) in our Centre. The sintering process was carried out at 1750°C/14 kN employing a vacuum of 10^{-3} Pa.

The average microhardness of sintered pellets as measured on two different sized pellets with 200 g load was found to be 2217VHN. This compares well with typical values reported in the literature. The XRD results of the WC powder and SPS sintered pellets are shown in Figure 2. The XRD pattern shows diffraction peaks that are characteristic of phase-pure WC. Further

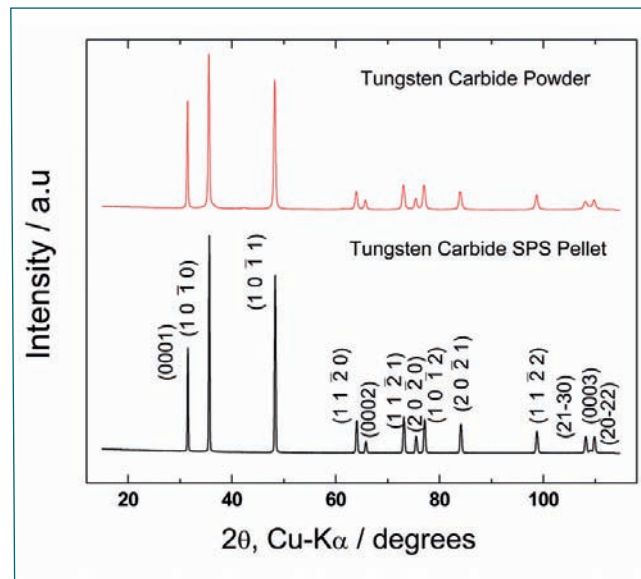


Fig. 2 XRD patterns of WC powder and the SPS processed pellet shown in comparison depicting that the phase purity remains even after SPS process

using SEM-EDX Spectrum it is confirmed that the pellet composition corresponds to pure WC phase.

Bulk production of tungsten carbide was made by processing 40 mm dia discs by SPS and subsequently EDM machining of the disc to generate pellets of required dimensions. The pellets so produced were also characterized for its thermal stability and thermophysical properties.

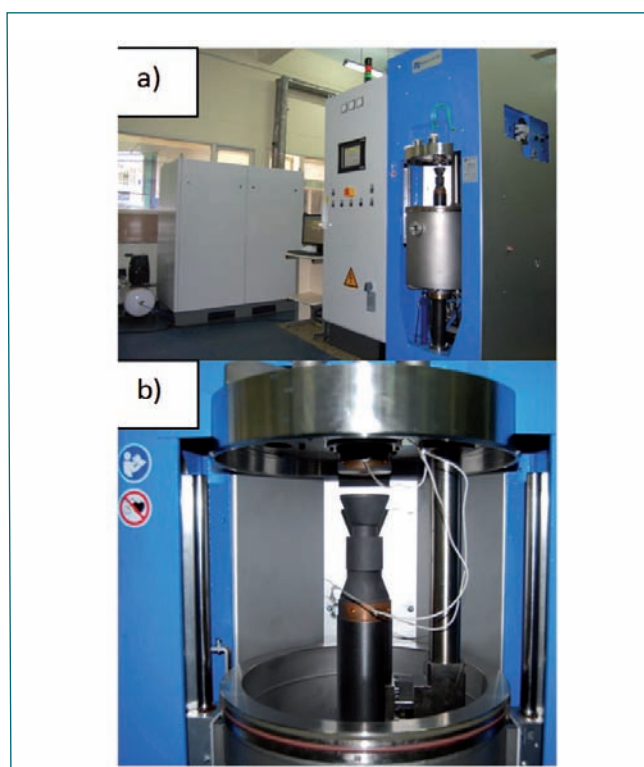


Fig. 1 (a) SPS facility at IGCAR; (b); sintering chamber shown in magnified view; arrow marks pellet location

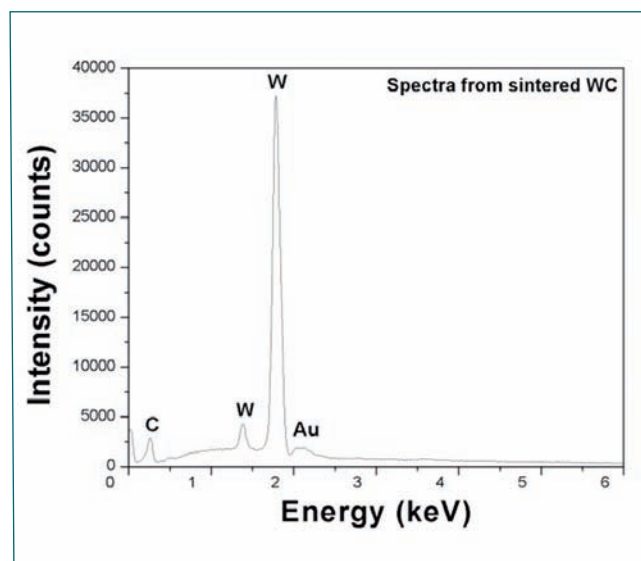


Fig. 3 Energy dispersive X-ray spectrum of SPS processed pellet showing distinct peaks of W and C.

I.8 Performance Assessment of FBTR Grid Plate Material Irradiated to 7 dpa

The grid plate of FBTR (Austenitic stainless steel SS 316) supporting the core subassemblies experiences temperatures in the range of 340 to 380 °C during reactor operation and has a cumulative neutron dose of ~2.2 dpa (displacement per atom). It is well known that neutron doses of 2-5 dpa accumulated over the years results in production of helium and can cause significant degradation in the mechanical properties of the steel. Irradiation induced loss in ductility of grid plate material is one of the factors considered for estimating the remaining life of FBTR.

The SS316 grid plate material irradiated in an earlier campaign in FBTR at 340°C up to 2.5 dpa indicated a residual ductility of above 20%. Towards assessing the strength and ductility changes of grid plate material subjected to neutron doses up to 7 dpa and facilitating life extension of FBTR, another accelerated irradiation experiment was conducted in FBTR. Sub size tensile (12.5 mm gauge length and 3.0 mm gauge width) and disc specimens fabricated from archival FBTR grid plate stainless steel of grade 316 were irradiated in an experimental capsule to a neutron dose of 2.30 to 6.75 dpa at 380°C.

The carrier assembly with capsule was received in hot cells and after cleaning with alcohol to remove residual sodium, the capsule was unlocked from carrier assembly and cut at pre-determined locations using a Nd-YAG Laser system to retrieve the specimens from the six compartments. Uniaxial

tensile tests were performed on tensile samples at 380°C which corresponds to the irradiation temperature. Tensile test results (Figure 1) show a progressive increase in yield strength (YS) and ultimate tensile strength (UTS) with increase in dpa. The YS at 6.75 dpa has increased by 2.9 times the unirradiated value, while UTS has increased by a factor of 1.33. With increasing dpa, the gap between yield strength and UTS narrowed down, indicating a reduced strain hardening capacity of the material, reflecting in loss in ductility as well (Figure 1). The uniform elongation of FBTR grid plate SS316 specimens subjected to 6.58 to 6.75 dpa, tested at 380°C was in the range of 12-15% and total elongation in the range of 16 to 19%.

The present results obtained by testing at 380°C, on comparison with earlier irradiation experiment carried out up to 2.5 dpa at 340°C, shows that higher irradiation temperatures (380°C) results in lower hardening and a higher residual ductility, consistent with the trends reported in the literature.

For the permanent core structure of fast reactors, a design limit for fast accumulated neutron dose is generally fixed to maintain a minimum of 10% fracture elongation. Factoring the higher rate of loss of ductility of grid plate during lower (340°C) operating temperature of FBTR in its initial irradiation campaigns, it is inferred that FBTR grid plate can be operated upto about 6.3 dpa based on the design limit of 10% ductility.

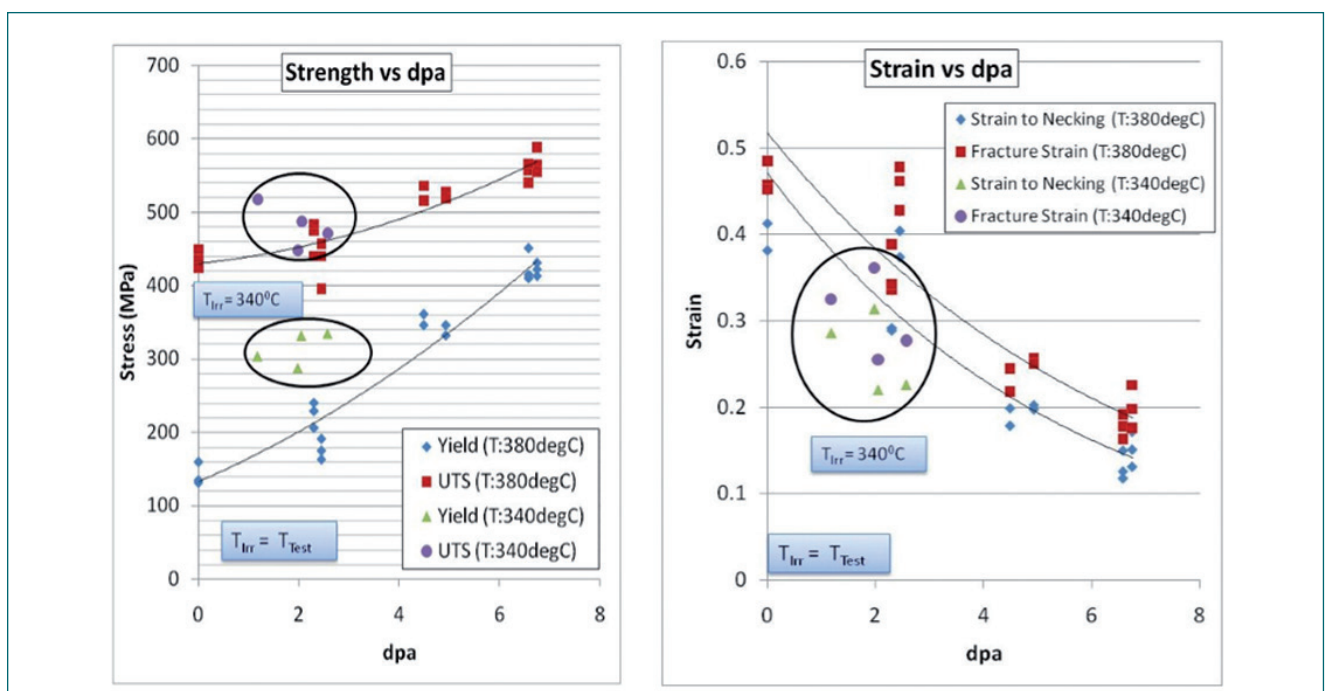


Fig. 1 Strength and ductility of SS316 with dpa

I.9 Testing and Qualification of FBTR CRDM Gripper Bellows

In Fast Breeder Test Reactor (FBTR), six numbers of Control Rod Drive Mechanisms (CRDM) are used for power regulation and safe shut down. Lower parts of the CRDMs are immersed in sodium. To prevent the entry of sodium in the annular spaces between the gripper control tube, translation tube, and outer sheath, welded disc bellows are used. The bellows which prevent the entry of sodium between translation and gripper control tube is called gripper bellows. The inner and outer diameters of the bellows are 36 and 49 mm respectively. The free length of the bellows is 131.5 mm, with a maximum stroke of 54 mm. The operating temperature of the bellows in FBTR is around 473K and during reactor operation, the bellows are immersed in sodium at 803K. Indigenous development of gripper bellows was initiated, and as part of the qualification process, one of the gripper bellows assembly was subjected to extensive testing. The bellows manufactured were AM350 material, which is precipitation hardened stainless steel.

Testing and qualification of the bellows was in accordance with the experimental stress analysis approach given in ASME section-III, Appendix-2. A test setup was designed for testing of the gripper bellows in sodium. The lower part of the test setup consists of an inner and outer tube. The top end of the gripper bellows was welded to the bottom flange of the outer tube while the lower end of the bellows was welded to the bottom flange of the inner tube. Sealing of cover gas between the tubes was carried out providing two radial O-rings at the top with inter-seal argon supply and a monitoring arrangement was provided to monitor leak tightness. A linear actuator was provided to facilitate the movement of the inner tube relative to the outer tube and produce the required compression of the gripper bellows by 54 mm. A control panel is provided for the up/down movement of the linear actuator. Pressure hold test of the bellows



Fig. 2 Sodium wetted lower part and bellows

was carried out by pressurizing the region between the bellows and the top O ring. The region was pressurized with Argon to 200 mbar (g), and it was found that there was no drop in pressure for 24 h.

The testing and qualification of the gripper bellows was carried out in three phases viz. testing in air, hot argon, and in sodium. Testing of the bellows in air was carried out for 20 cycles, and a pressure hold test was repeated after testing in air at room temperature and compared with the baseline data. The bellows were found to be leak tight. After testing in air, the test setup was assembled in test vessel-2 (TV-2) of large component test rig for high temperature testing in argon and sodium.

Testing in Argon was carried out at 423K for ten cycles, and the bellows were confirmed to be leak-tight after verification by pressure hold test. Subsequently, sodium was charged into TV-2 at 473 K and testing for two cycles at that temperature was carried out, which confirmed the smooth movement of the bellows for the required stroke of 54 mm. The bellows were then tested, in sodium, at 803K for 230 cycles. After 230 cycles, the bellows were subjected to hold time of 100 h followed by 10 more cycles of testing in sodium at 803 K. After the sodium testing, a pressure hold test at 200 mbar (g) was carried out for 24 h, and the leak tightness of the bellows was confirmed.



Fig. 1 Upper part of the test setup



Fig. 3 Gripper bellows after sodium cleaning

I.10 Novel Method for the Localisation of Gas Leaker Fuel Subassembly in Fast Breeder Reactor

In FBTR there are two types of diverse systems available for the detection of fuel pin clad failure. Delayed Neutron Detection (DND) system is installed in the primary sodium outlet lines. In case of a clad rupture, delayed neutron emitted by precursors such as ^{87}Br and ^{137}I will be detected. Another system is the Clad Rupture Detection (CRDAR) in reactor vessel cover gas (RVCG) circuit. During reactor operation, a mixture of argon and helium is used as RVCG and argon cover gas layer is provided for equipment like pumps, IHX and over flow tank. Gas sample from RVCG is continuously monitored by ion chambers for gross gamma activity, which will respond to increase in cover gas activity due to failed fuel pins. If the monitor reading is above the pre-set value then alarm annunciation is provided for prompt action. Both the systems are meant for detecting clad failure in the core. Another offline system commissioned for the determination of burn-up of suspected failed fuel sub-assemblies (FSAs) is the failed fuel localisation system from the ratio of ^{88}Kr or ^{87}Kr with ^{85}Kr in RVCG sample. Design provisions for sodium sampling from outlet of each FSA or dry sipping of gas samples from suspected FSAs are not available in FBTR. But, for the localisation of the failed fuel subassembly after its detection by the DND system, a detailed methodology is available.

In November 2018, an increase in cover gas activity was observed in CRD during reactor operation at 32 MWt; but the values were below the alarm threshold. Based on the monitor readings and estimated fission product noble gases (FPNG) activity in RVCG sample, the clad failure was confirmed. However, DND system did not show any increase in reading. The clad failure

in a FSA leading to release of only FPNGs is termed as gas leaker (GLFSA). Based on the design features in FBTR, it was decided to operate the reactor for a few hours after shuffling the suspected FSAs in the core and analyze the cover gas samples for the localisation of GLFSA. HPGe detector based gamma ray spectrometer was used for gas sample analysis. The specific activity of various radionuclides was calculated using the expression, $A_s = C_i f_i \epsilon_{d,i}^{gas}$ where A_s is the specific activity in sample 's' (Bq/cc), C is the net count rate at energy 'i' (cps), F is fraction of the transformations that yield a photon and $\epsilon_{d,i}^{gas}$ is the efficiency (Bq/cc/cps) for gas sample in 60 ml glass vial at a distance 'd' from the surface of the detector.

The specific activity of FPNGs in RVCG for reactor operation at 10 MWt to 25 MWt with GLFSA in core is shown in Figure 1. During normal reactor operation at 25 MWt, specific activity of ^{85}mKr shows an equilibrium trend after 4 h of continuous operation with a maximum baseline value (BV) of 48.7 Bq/cc. Similarly, ^{88}Kr and ^{87}Kr show an equilibrium trend after 2 h of operation with a maximum BV of 125 Bq/cc and 71.6 Bq/cc respectively. However, the specific activity of ^{135}Xe increases with time of operation with a maximum BV of 259 Bq/cc after 16 hours of operation. The specific activity of ^{85}mKr , ^{88}Kr and ^{87}Kr observed in the sample at 12 MWt with GLFSA in core is higher by a factor of 3 as compared to the activity observed during reactor operation for 16 hrs at 25 MWt. The specific activity of ^{87}Kr and ^{138}Xe at 12 MWt was 178 Bq/cc (BV: 71.6 Bq/cc) and 57 Bq/cc (BV: BDL) respectively. The estimated specific activity of krypton isotopes for reactor power at 20 MWt is 2280 Bq/cc (BV: 234 Bq/cc). Similarly, specific activity of xenon isotopes is 4680 Bq/cc (BV: 259 Bq/cc). Thus the presence of GLFSA in the core during short duration operation was confirmed.

It is observed that the presence of ^{133}mXe , ^{135}mXe and ^{85}Kr in RVCG samples are indicators of fuel pin clad failure. The specific activity of ^{133}Xe increases from a baseline value by three orders during clad failure incident at a reactor power 32 MWt. During the test operations for localisation of gas leaker fuel subassembly, the detection of ^{133}Xe , ^{138}Xe and ^{135}mXe in the RVCG samples indicates the presence of gas leaker in the core in the absence of DND counts. The measured specific activity of short lived ^{87}Kr with gas leaker fuel subassembly in core was found to be one order higher compared with baseline values during short operation.

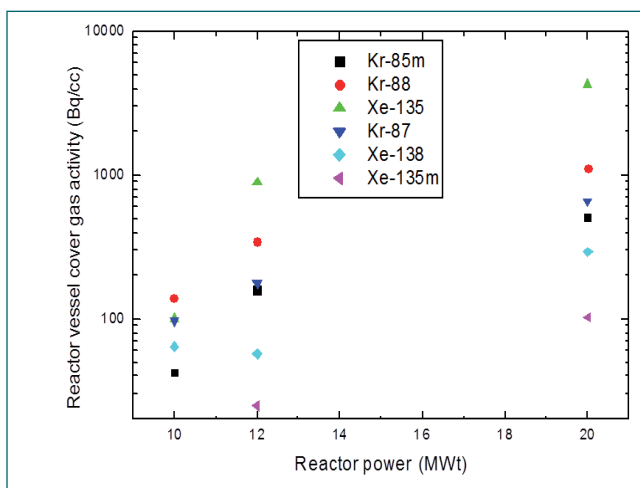


Fig. 1 Activity of FPNGs in RVCG obtained at various power levels with GLFSA in the core

I.11 Evaluation of Quality Control Parameters for ^{89}Sr Source Produced in FBTR

The radioisotope ^{89}Sr , a biological analogous of Ca, is a β^- emitter with a half-life of 50.57 days. Carrier free ^{89}Sr can be produced in a fast reactor via $^{89}\text{Y}(n,p)^{89}\text{Sr}$ with a required threshold energy of 720 keV. Sintered Yttria pellets were prepared and were irradiated in FBTR in SS irradiation capsule. The irradiated pellets were extracted from the irradiation capsule through laser cutting using the hot cell facilities. The irradiated yttria pellets of 25 g batch were dissolved in 9 M nitric acid under high pressure and temperature using a Ti container. The dissolver solution contained various radio-isotopic impurities such as the activated products of the target impurities, the clad material and the sintering aid ZnO along with the by-products ^{88}Y and ^{86}Rb . Purification of ^{89}Sr from the yttrium matrix of the dissolver solution was carried out by selectively removing Sr by solvent extraction using the Sr-Specific Crown Ether 4,4'(5') tert-butyl cyclo-hexano-18-Crown-6 (DtBuCH18C6).

The final Sr fraction was purified from undesirable anions and dissolved organic materials, made up to a known volume in the desired medium and quantified using various radiometric techniques. Various quality control (QC) measures such as appearance, pH, residual anion content, spectral identification, estimation of radioactive and non-radioactive impurities were carried out using various techniques. Biological quality control studies such as sterility and bacterial endotoxin were also carried out with the actual ^{89}Sr source and found to satisfy the required quality control criteria (Table 1) and in agreement with the Inter-laboratory comparison through BARC. The process of obtaining purified ^{89}Sr through six identical radiochemical reprocessing of irradiated yttria for the clearance by Radiopharmaceutical Committee (RPC) is also in progress. The number of doses at the end of the different irradiations varied between 5-275, where a single dose corresponds to 4 mCi of ^{89}Sr in 4 mL solution.

Table 1: QC parameters of ^{89}Sr source obtained from FBTR

Sl.No	Parameter	Recommended	Values obtained
1.	pH	4-7.5	6.0(\pm 0.1)
2.	Appearance	Colourless & clear solution	Colourless & clear solution
3.	Spectral Identification	$E_{\gamma}=909$ keV	$E_{\gamma}=909$ keV
4.	Radiochemical Purity	>90%	>90%
5.	Radionuclidic Purity		
	a. Other γ emitter impurities (%)	<0.4%	<0.4%
	b. Beta impurities ^{90}Sr , ^{32}P , ^{35}S	<0.2%	<0.2%
6.	Chemical Purity [wrt. Al, Fe &Pb]	<12 ppm	0.35 ppm
7.	Specific Activity [$A(^{89}\text{Sr})/\text{g}$ of Sr]	>80 mCi/g	>1500 Ci/g
8.	Sterility	YES	YES
9.	Bacterial Endotoxin Test	Negative	Negative



CHAPTER II

Prototype Fast Breeder Reactor

II.1 Commissioning Status of PFBR

Prototype Fast Breeder Reactor (PFBR) at Kalpakkam is a 500 MWe (1250 MWt) liquid sodium cooled, pool type fast reactor using mixed oxide of uranium and plutonium as fuel. The plant is located 500 m south of the existing Madras Atomic Power Station. After completion of construction, manufacture & erection of all the systems / components of PFBR, commissioning of the individual system and the integrated commissioning are in progress. Figure 1 shows the Westside view of PFBR. Figure 2 shows the Top view of Reactor Assembly. The major works that have been completed during the year 2019 are as follows:

Secondary sodium pumps (SSP) in both the loops were started once again after replacement of Pump Internal Assembly of SSP-2 and the speed was raised in steps. Required data collection was done & both the pumps were run continuously for about eight months and stable operation of secondary sodium loops was established. Subsequently, these pumps were shut down and the loops were completely drained as a preparatory step towards taking up the works on Large Rotatable Plug (LRP) bearing. During commissioning, LRP bearing which is used for positioning Transfer Arm (TA) over various fuel subassembly locations by its rotation, experienced slight deviation in its performance. It is planned to carry out minor remedial works on both LRP & Small Rotatable Plug (SRP) bearings.

Preheating system was shutdown to cool the main vessel and the main vessel is maintained in nitrogen atmosphere. Surface thermocouples and field instruments mounted over the rotatable plugs were disconnected and preserved. Thermal insulation and complementary shielding blocks provided over LRP, SRP, Control Plug and the associated cooling pipes have been removed. In parallel, preparations are underway for commissioning

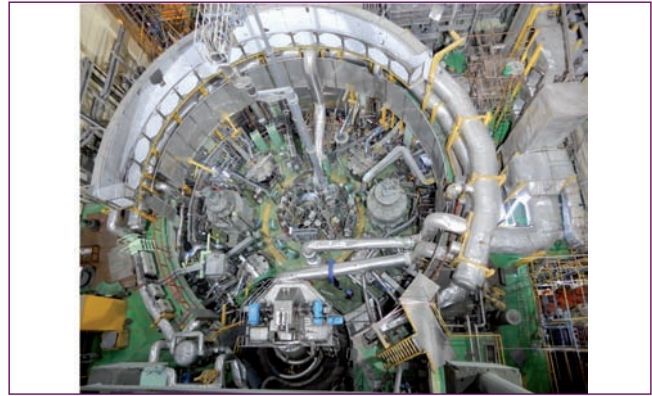


Fig. 2 Top view of reactor assembly

the primary sodium system.

With respect to fuel handling system, the modified gripper assembly of TA has undergone various tests at mock-up test station and was erected on pile and tested at preheated condition (150°C) of reactor assembly. All the systems for transporting Fuel Subassembly Cask from Interim Fuel Storage Building to Fuel Building was commissioned and elaborate mock up trials were conducted. Commissioning of the remaining fuel handling system is in progress in parallel.

Commissioning of three Nos. of 230 kV / 21 kV 200 MVA Generator Transformer from 230 kV Switchyard was completed successfully. All the tests and preparatory works for energisation of three numbers of Generator Transformer along with 35 MVA 21 kV / 6.9 kV Unit Auxiliary Transformer (UAT 1 & 2) were completed.

After completion of works on LRP & SRP bearings, pre-heating of reactor assembly & secondary sodium loops once again, the secondary sodium pumps will be operated in the loops towards commencement of sodium filling in Main Vessel. This will be followed by isothermal testing, fuel loading and first approach towards criticality.



Fig. 1 West side view of PFBR

II.2 Studies Associated with PFBR Commissioning

Analysis of On-site Performance of Secondary Sodium Pumps

Secondary Sodium Pump (SSP) circulates the sodium in Secondary Sodium Main Circuit (SSMC) of PFBR. The rated speed, head and flow rate of SSP are 900 rpm, 65 m/c and 12024 m³/h respectively. The performance of the pumps at various speeds is studied at site and compared against the performance test results at the manufacturer’s test facility.

Speed and flow rate of SSP is measured using toothed wheel with variable reluctance sensor and by-pass type permanent magnet flow meter respectively. Pump input power is estimated based on feedback current at Variable Frequency Drive (VFD). To assess the performance of SSP, its operating point in the respective SSMC has to be identified. The operating point of the pumps cannot be identified directly, as head developed by the pump is not measured. However, the same can be identified indirectly by intersection of pump performance curves and the flow rate measured by the flow meter. The pump performance curve is available at 900 rpm and the performance curves at reduced speeds are estimated using affinity laws ($H \propto N^2$ and $Q \propto N$).

To study the performance of the pumps, mean value of flow rate is considered, which remains fairly constant, as shown in Figure 1. The ratio of measured flow to nominal design flow at each speed, in both the SSPs are plotted in Figure 2. Study of long range flow rate data at 430 rpm indicated that, the ratio of measured flow to nominal design flow in SSP-1 and SSP-2 are ~102.7% and 95.9% respectively. The decrease in the ratio at lower speed was due to the minor deviation of pump characteristics from following affinity law at lower speed. Instrumentation for recording motor input power at VFD was introduced, to verify the difference in operating

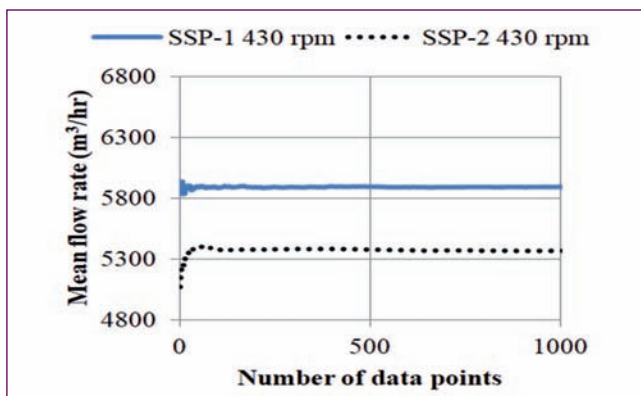


Fig. 1 Variation of mean flow with number of data points

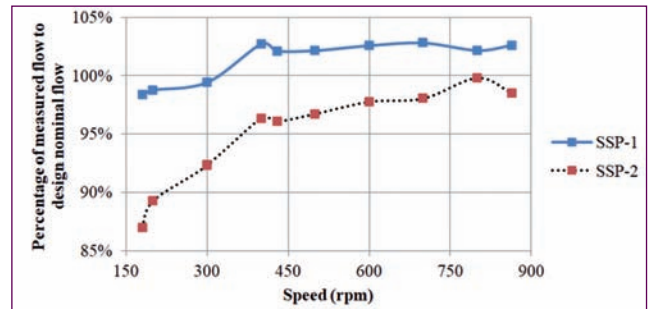


Fig. 2 Ratio of measured flow in SSP-1 and SSP-2 to nominal flow at various speed

point. The variation in measured motor input power of SSP-1 and SSP-2 were found to be negligible (within 1%). The difference in operating point of SSPs in SSMC-1 and SSMC-2 based on power consumption could not be established, as the power is nearly the same on either sides of design operating point. Thus, to identify distinction on the operating point, additional flow measurement possibilities are being studied. The vibration measured at top bearing housing and pump bowl (closer to hydrostatic bearing) was about 0.6 mm/s at 700 rpm, which is within the allowable limit of 2.5 mm/s. The maximum vibration measured at top bearing housing during 50 h endurance testing of SSP at manufacturer’s site is about 1.85 mm/s at 870 rpm.

The system characteristics of SSMC have been estimated analytically, for the cases with (i) all Steam Generators (SG) available and (ii) only 2 out of 4 SGs available. The flow rate estimated from the system characteristics compares well with the measurements at site as shown in Figure 3.

Qualification of Transfer Arm for High Temperature Nitrogen Environment

Transfer Arm (TA) is the in-vessel handling machine of PFBR with an offset of 572.5 mm. Gripper Assembly

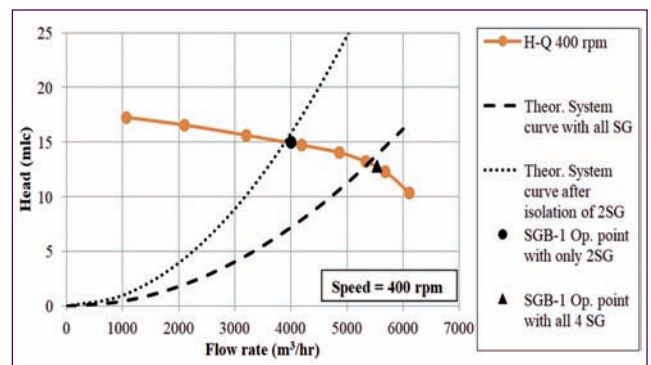


Fig. 3 Expected system curve after 2SG isolation and the operating point of SSP-1, after isolation of 2SG

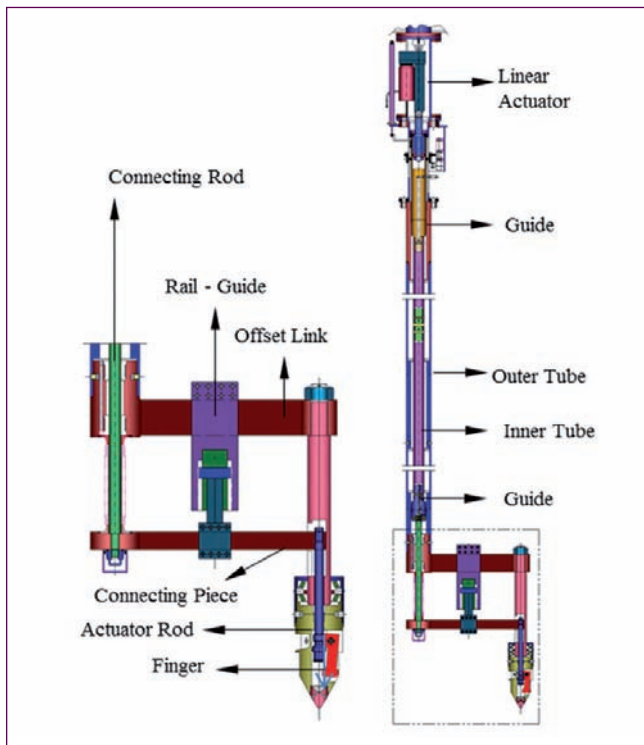


Fig. 4 Gripper assembly of transfer arm

(Figure 4) of TA is used for handling the core Subassembly (SA) during fuel handling and is made up of an outer tube assembly & concentric inner tube assembly. Gripper consists of three fingers housed in a finger holder connected to outer tube through central sleeve and offset link. Fingers grip the SA through positive action of downward movement of a profiled actuator rod which in turn is connected to inner tube through a connecting piece and connecting rod. A linear actuator drive connected to inner tube provides the required motion of actuator rod to obtain the required gripper finger positions. Rail & guide arrangement is provided between offset link and connecting piece to reduce lateral deflection and rotation of connecting rod thereby enabling the smooth movement of actuator rod.

Based on the feedback from commissioning trials and regulatory review, various modifications such as improved guide & rail, joint allowing rotational Degrees



Fig. 5 (a) Setup for qualification of improved guide & rail using robust transfer arm gripper at LCTR and (b) Setup for qualification of geometry modification of actuator rod

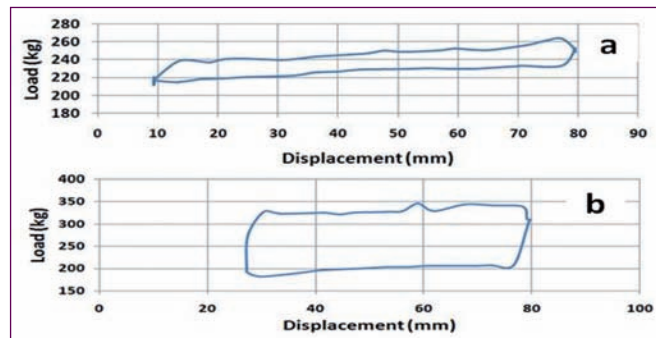


Fig. 6 Load vs displacement for inner tube movement (a) gripper in free condition (b) Gripper resting on SA condition

of Freedom (DOF) between actuator rod & connecting piece, inner tube load monitoring, reduced speed of inner tube movement, modified geometry of actuator rod and provision for on-pile calibration of finger (butt-stop feature) were carried out to improve the performance of gripper assembly.

Modifications in guide & rail were qualified for 6000 cycles in sodium at 200°C in a separate facility at LCTR (Figure 5a). Geometry modification in actuator rod was separately qualified for 600 cycles of operation using a separate test setup (Figure 5b). Subsequently, performance test of TA gripper assembly was carried out at room temperature for finger operation in free condition and gripper resting on subassembly respectively for 25 and 5 cycles.

Further the TA was erected on pile to qualify the gripper assembly at high temperature nitrogen environment. Requirement of re-calibration of fingers due to differential thermal expansion between inner and outer tube assembly was verified using butt-stop feature. 25 cycles of finger operation in free condition (Figure 6a) was carried out successfully. Revised angular position of SRP and TA were estimated to position TA over a specific SA to perform finger operation in resting on SA condition. Subsequently five cycles of finger operation (Figure 6b) was satisfactorily performed.

As a part of further qualification, raising and lowering of SA at three different locations were carried out thereby qualifying Transfer Arm for high temperature operation in nitrogen environment.

Scheme for filling primary sodium and subsequent temperature rise with associated purification

During the initial phase of commissioning of reactor, liquid sodium of nuclear grade (approx. 1100 tonnes) would be filled in the reactor vessel which contains core, heat exchangers, pumps etc. After filling sodium into reactor vessel, impurities (mainly oxygen and hydrogen) from fresh metal surface would migrate to pure sodium which shifts the freezing point of sodium to higher temperature. The migration of impurity from

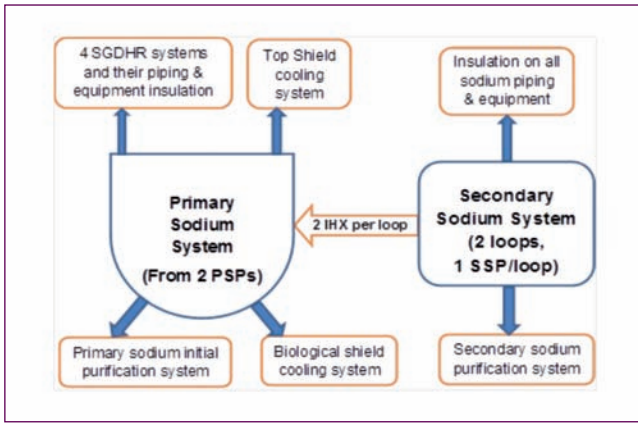


Fig. 7 Flow chart for various heat loss from primary, secondary and DHR systems

metal to sodium is a function of sodium temperature. The impurity is removed by online sodium purification system which works based on reduction of saturation solubility of sodium with decrease in temperature. Heating of sodium has to be carried out gradually in steps in order to avoid steep rise in solidification temperature of sodium which may plug the purification system and hinder its operation. Methodology for raising the temperature of sodium through viscous heating by running centrifugal sodium pumps considering various heat losses in reactor vessel and associated systems is evolved as shown in Figure 7. Time required to purify sodium at each stage of heating is predicted. The rate of heating of sodium is calculated from pumping power with respect to its rpm by using pump affinity law. Heat absorbed by sodium and structures including various components and heat losses through insulation are accounted as function of temperature. For sodium temperature up to 200 °C, heating is considered only by using secondary sodium pumps (SSP). Primary sodium pump is not allowed to start until required purity at 200 °C is achieved. After completion of purification at 200 °C, heat addition by

running primary sodium pumps (PSP) is also considered. Plugging temperature of oxygen and hydrogen are calculated by using Noden's equation (1) & Vissers equation (2) respectively as given below:

$$\log_{10}(C) = 6.2571 - \frac{2444.5}{T} \quad (1)$$

$$\log_{10}(C) = 6.067 - \frac{2880}{T} \quad (2)$$

- C - Concentration of oxygen/hydrogen (ppm)
- T - Temperature (Kelvin)

Time required to purify sodium is calculated by:

$$\log_e \left(\frac{C_s - C_e}{C_o - C_e} \right) = - \frac{\eta m t}{M} \quad (3)$$

C_o & C_s - Impurity concentration in sodium at initial time and at time t (hours) (in ppm)

C_e - Impurity concentration at the cold point temperature (in ppm)

- η - Efficiency of the cold trap
- m - Mass flow rate to cold trap (kg/h)
- M - Total sodium quantity to be purified (kg)
- t - Purification time (hours)

Two parametric cases have been studied viz. 50 and 75% flow rate for purification. It is found that 50% flow rate offers higher margin against plugging during initial purification period. Hence, the same is recommended for PFBR. It is estimated that the time required to start PSP is approximately 17.1 days from the day of starting of purification system and operation at 50% of rated flow. Time required to complete purification / achieve plugging temperature of <120 °C at sodium temperature of 450 °C is estimated as approx. 74.2 days. Evolution of sodium temperature and sodium purity indicated by the plugging temperature with time is depicted in Figure 8.

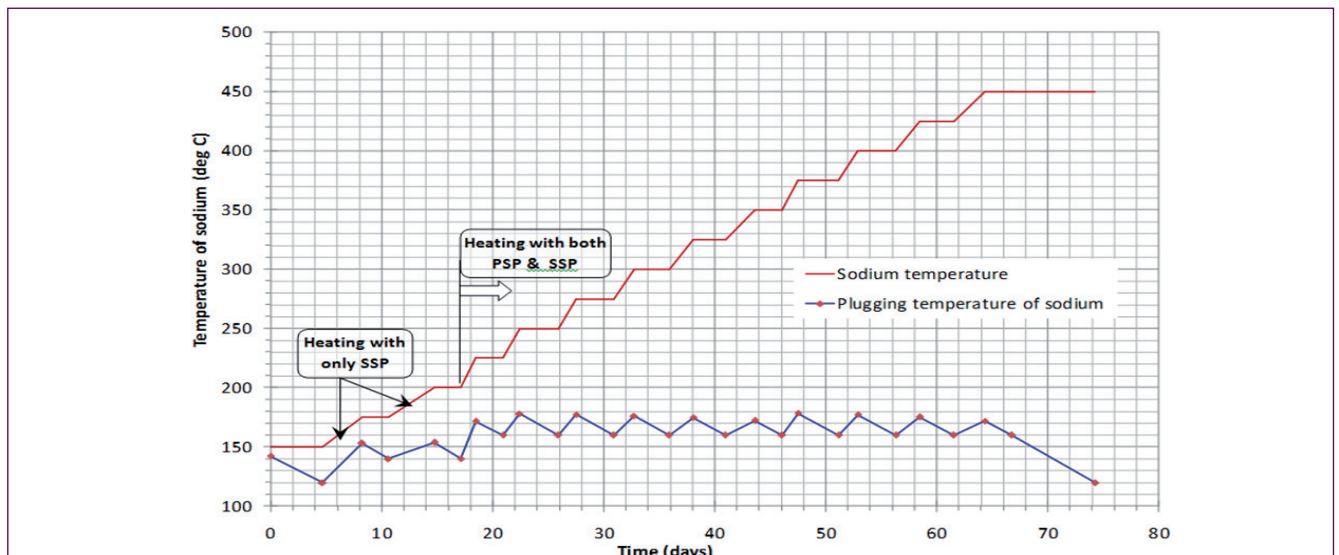


Fig. 8 Evolution of sodium temperature and plugging temperature with time

II.3 Design Optimization of Core Flow Monitoring Mechanism (CFMM)

Core Flow Monitoring Mechanism (CFMM) is the system used in PFBR to measure sodium flow rate through fresh reactor subassemblies (SA) and on few selected subassemblies during fuel handling campaign. The CFMM will be operated at reactor shut down condition, when sodium flow is reduced to 20% of the nominal flow rate through the core of the reactor. During flow measurement, CFMM is lowered and attached with the SA top. A portion of SA flow passes through CFMM and the balance flow exit through the safety holes provided at SA top. Eddy Current based flow sensor (ECFM sensor) positioned inside a guide tube is used as a sensor in CFMM for sodium flow measurement. It is found from earlier measurements in sodium that this ECFM sensor provides reliable output for a sodium velocity of 1 m/s and above around the sensor region. However, at present, sodium velocity across the ECFM sensor used to measure sodium flow rate through Blanket Subassembly (BSA) and Storage Subassembly (SSA) is in the range of 0.22 m/s to 0.56 m/s. Therefore, it was envisaged to modify the hydraulic design of the flow guide tube of this CFMM so as to increase the sodium velocity in the sensor region for obtaining reliable readings. The schematic of reference CFMM and modified CFMM designs to be used to measure sodium flow rate through BSA and SSA are shown in Figure 1 for comparison.

Towards the design optimization, various design

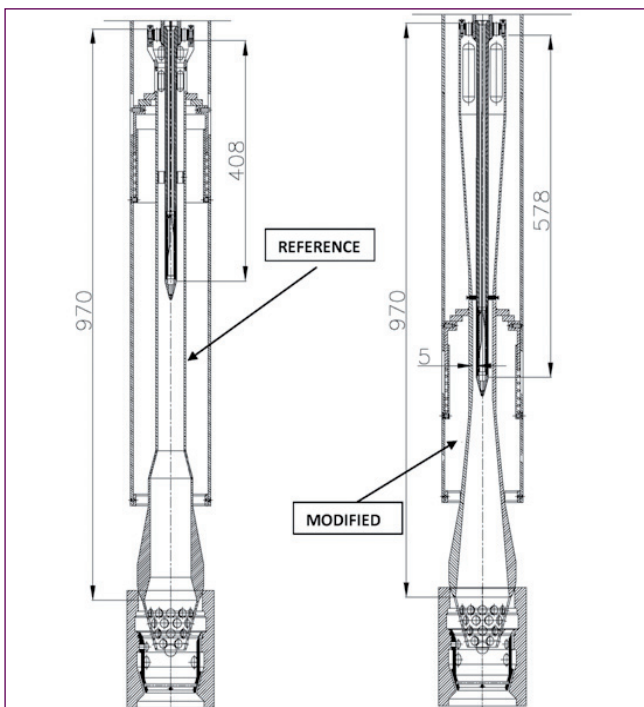


Fig. 1 Schematic of reference (a) and modified (b) CFMM -2 with SA top

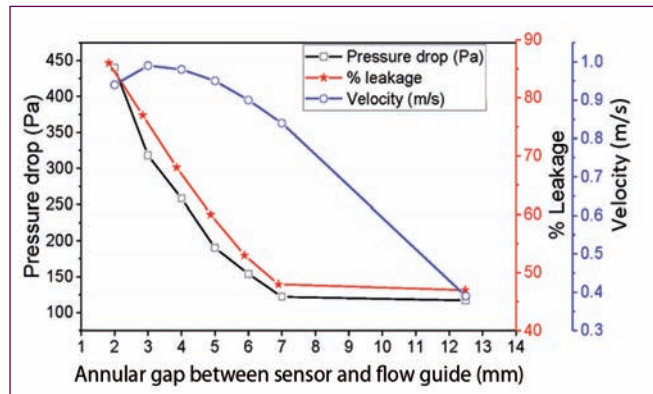


Fig. 2 Pressure drop, percentage leakage flow and velocity at sensor location vs annular gap

changes in lower part of CFMM have been studied using numerical tool to arrive an optimized design. The optimized design provides sufficient sodium flow velocity in the CFMM sensor region. Initially, the gap between sensor and flow guide has been reduced to increase the flow velocity. However this reduction in gap increases flow resistance through CFMM which in turn reduces flow through it and more flow can bypass the CFMM and exit through safety holes provided at SA top. Therefore, the geometry of CFMM flow guide is further optimized accordingly to compensate the additional flow resistance gained due to reduction in gap between sensor and the flow guide tube. This geometrical optimization of flow guide tube was carried out using iterative computational methods. Numerical analysis has been carried out for different annular gap between sensor and flow guide of CFMM. Variation in pressure drop, percentage leakage flow bypassing CFMM and velocity at the sensor location w.r.t gap between sensor and flow guide are shown in Figure 2.

The comparison of reference design and optimized design are tabulated in Table 1. It is can be seen that the sodium velocity in sensor location can be increased from 0.39 m/s to 0.95 m/s with optimized design. The same for storage subassembly is also increased from 0.23 m/s to 0.56 m/s.

Parameters (Zone -10, BSA)	Reference	Optimized
Gap between sensor and flow guide (mm)	12.5	5
Pressure drop (Pa)	117	190
Flow through CFMM	54%	40%
Average velocity across sensor (m/s)	0.4	0.95

II.4 Shielding Design of Various Storage Bays in Additional Spent Subassembly Storage Facility

It is proposed to build an Additional Spent Subassembly Storage Facility (ASSSF) within PFBR complex. Within this facility, different storage bays exist separately for storage of fresh fuel subassemblies(SAs) & spent core subassemblies (fuel, blanket, absorber, reflector, irradiated dummy and B₄C shielding subassemblies) discharged from PFBR. Spent fuel storage bay is a water pool storage bay, while all other storage bays are dry storage. The SAs are stored in triangular pitch with pitch distance of 32 cm. Shielding requirements for these storage bays are estimated using 3D transport code Monte Carlo n-Particle (MCNP.) Shield thickness is optimized to meet the design limit of 10 μSv/h on all sides of the storage bays. In all calculations, normal concrete with density of 2.4 g/cc is considered as shield material. Density loss (6%) due to ageing of concrete over a period of 40 years has been considered in all cases except for spent fuel storage bay. Due to this, concrete density falls from 2.4 g/cc to 2.256 g/cc. A safety factor of two has been considered in these estimations.

Fresh fuel storage bay

The fresh fuel storage bay in ASSSF contains two storage racks, where 232 fuel SAs are stored. Each fuel SA is kept inside a SS container of OD 21.9 cm and thickness 0.8 cm. The racks are 75 cm away from the concrete wall along the length and breadth side of the fuel bay. On the top, the roof lies 10 cm above SA head. Fresh fuel subassembly contains both neutron and gamma ray sources. Neutron sources come from spontaneous fission and (α,n) reaction. Major sources of gamma radiations are activation of actinides and fission product activity. For Neutron source strength estimation,

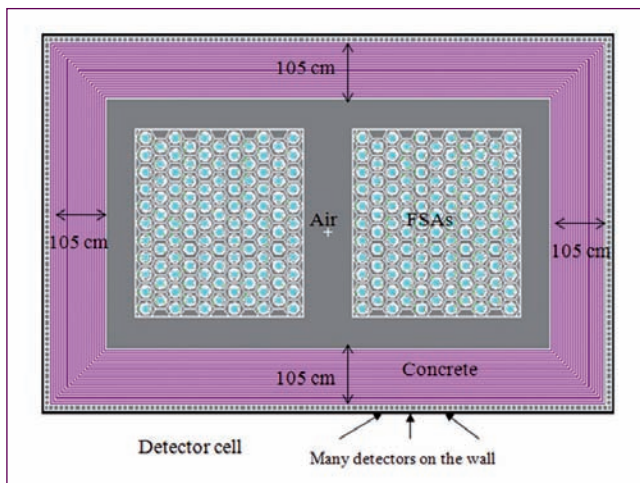


Fig. 1 Fresh fuel SA storage bay with shield - plan view (simulated by MCNP)

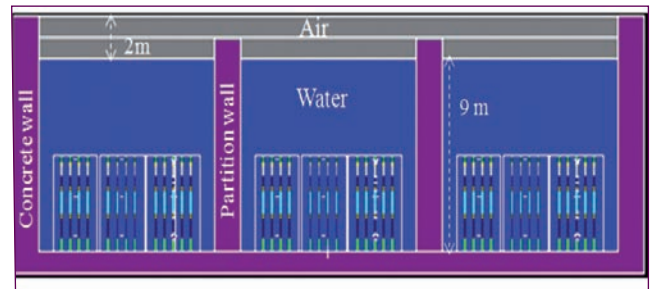


Fig. 2 Sectional view of the spent fuel storage bay (simulated using MCNP)

tenth cycle composition of core-2 fuel SA is considered conservatively. The neutron and gamma ray sources of outer core SA are 8.0E+06 n/s/SA and 2.10E+13 g/s/SA respectively.

Without shields, the estimated total dose rates along the length, breadth, bottom and top of the storage bay are 13 mSv/h, 12.4 mSv/h, 4.3 mSv/h and 4.8 mSv/h respectively. It is seen that the gamma dose is roughly four times more than that of neutron along the sides and 2.7 times more at the bottom and top of the storage bay. To meet the design criteria, 105 cm thick concrete is required on the sides and 90 cm thick concrete is required on the top and bottom of the storage bay as shown in Figure 1.

The k-eff of the fresh fuel storage bay in air and in water flooded condition are estimated as 0.51 and 0.60 respectively. Since the estimated k-eff under water flooded condition is less than the design limit of 0.95, the storage bay is safe.

Spent fuel Storage bay

The spent fuel storage bay (SFSB) in ASSSF is of dimension 4400 cm x 910 cm as shown in Figure 2. The storage capacity is 1005 sub-assemblies. There are three compartments, each of length 1100 cm. Subassemblies are kept in a storage rack with perforated guide plates of thickness 2 cm at the top and at different elevations to maintain the subassemblies in position, 335 fuel SAs are stored in each compartment. The partition wall provided between the compartments are of thickness 170 cm. Storage bay is filled with de-mineralized water up to a height of 450 cm above the subassemblies. Accessibility is required on top of the storage bay 200 cm above the water level at a height of 1100 cm. Though irradiated fuel and blanket subassemblies are stored in the storage bay, for calculation purpose all SAs are assumed as fuel SAs conservatively. Neutron source strength corresponds to tenth recycled FSA, and which has undergone 3 cycles of irradiation, 480 days in-vessel cooling and

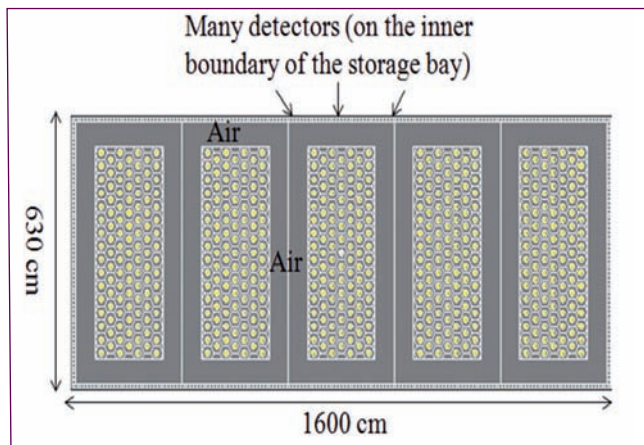


Fig. 3 Plan view of the replaceable SA storage bay without shield (simulated using MCNP)

240 days ex-vessel cooling. Neutron source strength is $1.14E+08$ n/s/SA. Gamma ray source strength from fission product activity and induced activity are $2.9E+15$ g/s/SA and $3.46E+14$ g/s/SA respectively.

Due to the presence of thick layer of water, the dose rate due to neutron is negligible. Gamma sources are the main contributor to dose rate outside the storage bay. Among activation gamma and fission product gamma, the contribution from fission product is more. To meet the design limit, 145 cm thick normal concrete is required for the side wall and floor of the spent fuel storage bay. Criticality analysis has been carried out conservatively assuming all 1005 subassemblies as core-2 fuel subassemblies. The estimated value of k-eff for spent fuel storage bay is 0.64.

Spent Replaceable Sub-Assembly Storage Bay

In Spent Replaceable Sub-Assembly Storage Bay (SRSSB) reflector subassemblies, inner B_4C subassemblies and long term exposed dummy SAs are stored. It is of dimension 1600 cm x 630 cm x 500 cm. There are 5 storage racks which are shown in Figure 3. The storage capacity is 545 SAs. Out of this, 138 locations are earmarked for reflector SAs, 375 locations are allocated for inner B_4C SAs, 6 locations are for dummy SAs and 26 extra locations still available. These SAs are stored bare after sodium cleaning.

Compared to reflector SA, the activity of inner B_4C is ~20 times less and the activity of dummy SA is ~100 times less. Since activity of reflector SA is more compared to other SAs, all the storage locations are assumed to be filled with reflector SAs conservatively. Induced activity of the reflector SA is the major source of radiation. The induced gamma source strength of the reflector SA is $4.83E+15$ g/s/SA.

The peak value of the dose rate along the length, breadth, bottom and top of the storage bay without shield are $3.46E+03$ Sv/h, $3.66E+03$ Sv/h, $1.23E+03$ Sv/h and

$1.75E+03$ Sv/h respectively. To meet the design limit, normal concrete of thickness 180, 170, 160 and 165 cm are required along the length, breadth, bottom and top of the storage bay respectively.

Spent Absorber Sub-Assembly Storage Bay

Four absorber SAs are discharged during each fuel handling campaign. Hence, to meet the storage requirement for 40 years of reactor life time, 243 storage locations are provided in the storage bay. It is of dimension 770 cm x 630 cm x 500 cm as shown in Figure 4. The SAs are canned in leak tight containers and stored in the bay. Container is a cylindrical structure of thickness 0.8 cm and height 497 cm and is made up of SS304L. While storing the absorber SA in the storage bay, top of the container will be closed by a shield plug made up of SS304L.

Induced activity of the absorber SA is the major source of radiation. Two years of irradiation and one day cooling is considered conservatively for source term estimation. Corresponding gamma source strength of the absorber SA is $6.71E+15$ g/s/SA.

The peak value of the dose rate along the length, breadth, bottom and top of the storage bay without shield are $8.83E+02$ Sv/h, $8.93E+02$ Sv/h, $8.02E+02$ Sv/h and $1.74E+03$ Sv/h respectively. To meet the design limit, normal concrete of thickness 155 cm, 145 and 150 cm are required for side wall, bottom and top of the storage bay respectively.

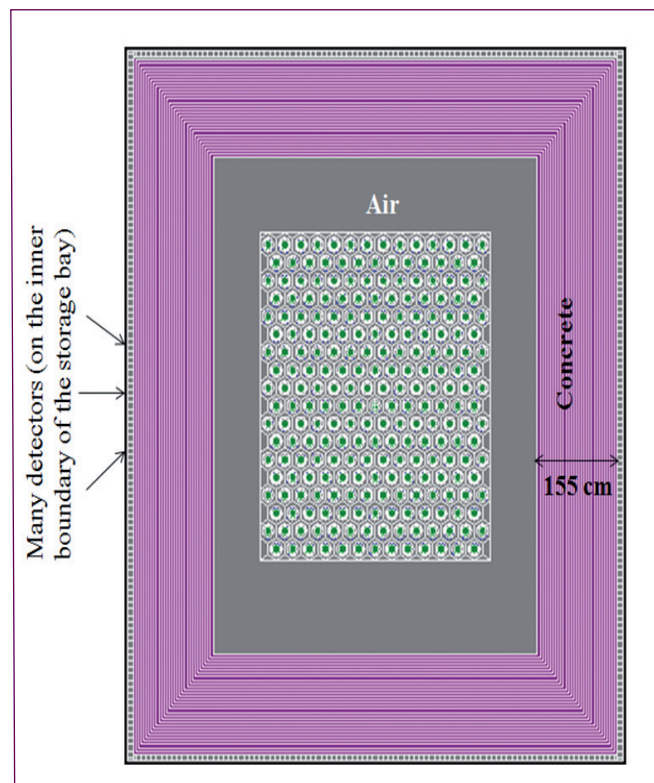


Fig. 4 Plan view of spent absorber subassembly storage bay with shield (simulated by MCNP)

II.5 Development of Explosive Welding Technique for Plugging of Degraded PFBR Steam Generator Tubes

PFBR Steam Generator (SG) will be periodically inspected using the indigenously designed and developed robotic device, PFBR SG Inspection System. During the inspection, if any one of the tube is found to have an unacceptable degradation then the corresponding tube has to be plugged on both ends to isolate the tube from service. The plugging of the SG tube is considered a cost-effective way compared to the total replacement of the SG unit. One of the methods of plugging of the SG tube is the explosive plugging technique. Figure 1 shows the schematic layout of the explosive plugging process using robotic devices. The advantage of the technique is that it is a solid state welding process and the bond can be made with little generation of heat at the weld interface and consequently there is no melting or heat affected zone formation at the weld interface. This particular advantage eliminates the process of post-weld heat treatment which is very difficult inside the SG headers.

The PFBR SG tubesheet hole diameter is 12.72 mm and in the explosive plugging process, a plug is placed inside the hole. The plug is a thin tube with spherical closure at one end and open at the other end. The explosive material is filled inside the plug and the explosive charge is detonated during the plugging process. The high pressure generated during the explosion concentrically expands the plug and make impact on the tubesheet surface at very high velocity causing a permanent

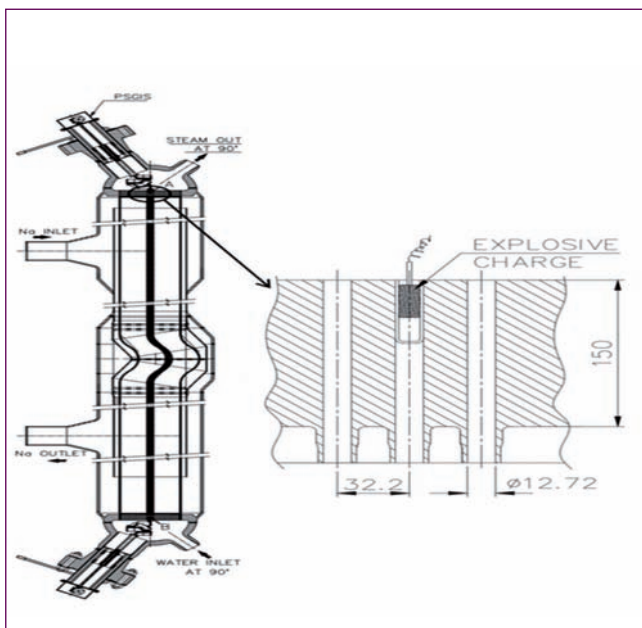


Fig. 1 Schematic layout of explosive plugging of PFBR SG tube

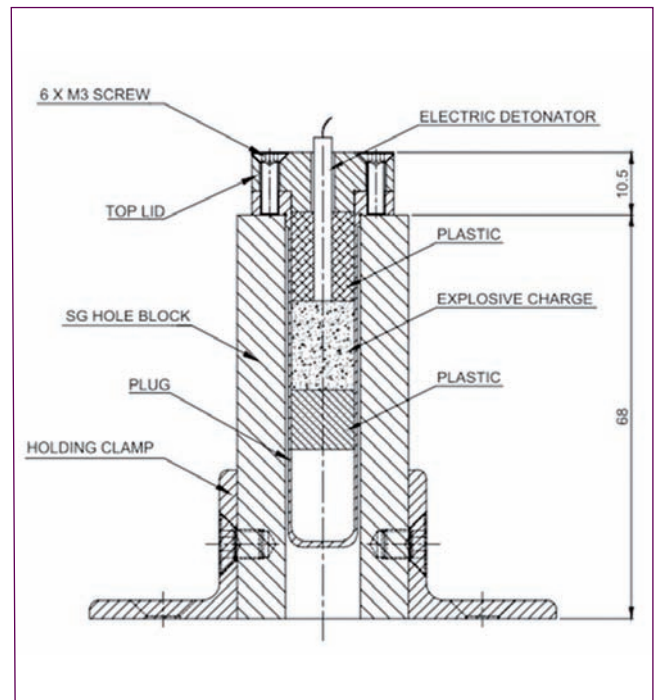


Fig. 2 Experimental setup of explosive plugging of SG tubes

joining/welding of the two mating surfaces. The plug is also made of Mod.9Cr1Mo material same as PFBR SG material to avoid dissimilar metal joint during the plugging process. Design of explosive plugging involves optimization of the process parameters such as the mass of the explosive, thickness of the plug, detonation velocity of the explosive, stand-off distance of the plug and oblique angle of impact. In the case of PFBR SG tube, the SG hole diameter is only 12.72 mm and with Mod.9Cr1Mo material having low ductility, the variation in the process parameters is very narrow and hence the optimization of the process parameters for a sound bonding of the material becomes very stringent.

The plugging of the SG tube using the explosive welding technique is being developed through a joint venture of Indira Gandhi Centre for Atomic Research, and Terminal Ballistics Research Laboratory (TBRL), DRDO, Chandigarh. The scientists from TBRL have developed a specific explosive suitable for plugging of PFBR SG tube dimension. To study the feasibility of the explosive plugging technique for the PFBR SG tubes, a set of experimental trials for different dimensions of the plug and different explosive strength were carried out. From the design of the plug based on operating conditions, the minimum required wall thickness of the plug was found to be 1.2 mm. To arrive at the optimum combination of the

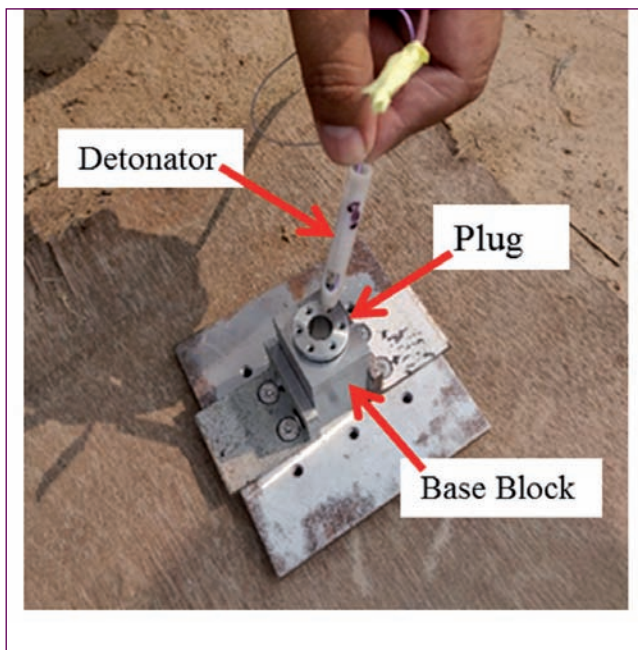


Fig. 3 Photograph of explosive welding setup for SG tubes

process parameters of the explosive welding technique, plugs of four different wall thickness and each with four different stand-off distance were chosen for carrying out the experiments. In the initial set of experiments, 0.5 mm wall thickness plugs with stand-off distance of 0.2, 0.3, 0.4 and 0.5 mm were fabricated in IGCAR and explosive welding trials were carried out at TBRL. As mentioned, specific explosive suitable for the SG tube dimension was prepared at TBRL with varying percentage of explosive content. The experiments were carried out for different combinations of stand-off distance and explosive content. The schematic experimental setup arrangement of the explosive welding technique for plugging of SG tubes is shown in Figure 2. The photograph showing the actual explosive welding setup at the TBRL site is shown in Figure 3. The explosive welding experiments were carried out at TBRL with proper protection procedures.

To qualify the explosive welded plug samples for the required strength and leak tightness, various non-destructive examinations, microstructural examinations and microhardness tests were carried out. Initially the helium leak test and radiography test were carried out on all the samples. From the radiography test, bonding at some regions along axial length of the plug could be observed in most of the samples. Subsequently, the explosive welded samples were longitudinally cut using wire-cut EDM process. The longitudinally cut samples were polished and the bond length of the samples were measured under the microscope. After the measurement of the bond length, the samples were etched and the

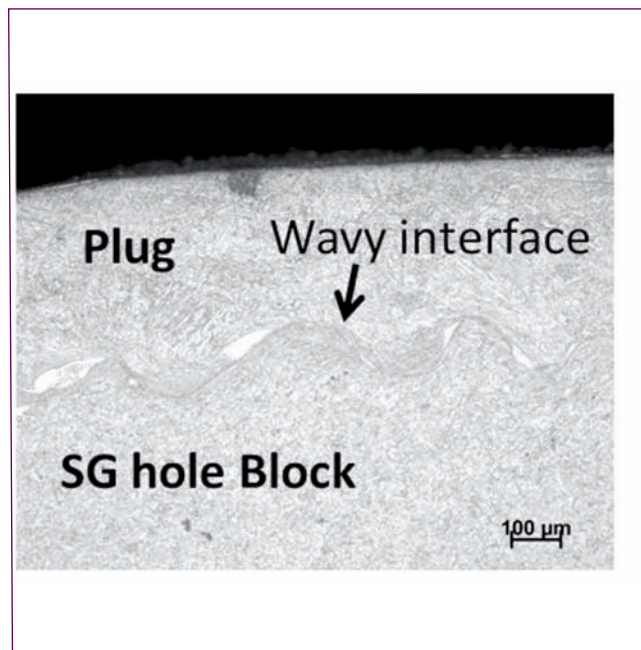


Fig. 4 Microstructure of the explosive weld interface

microstructure along the interface of the samples was examined. Figure 4 shows the microstructure observed at the explosive weld interface on one of the samples. This type of weld interface is termed as wavy interface and is considered as primary requirement for a sound weld joint in explosive welding technique. In a few samples, melt zones were found during the microstructural examination. The microstructural observations show that the average bond length of the explosive welded samples is nearly 5 mm. The microhardness tests were also carried out. The microhardness values were found to vary between 220 HV to 320 HV across the interface, and these variations are considered nominal for Mod.9Cr1Mo material in fusion weld joints after post-weld heat treatment.

With the experience of the examination of the first set of 20 plugs of 0.5 mm wall thickness, the design of the next set of plugs with 1.2 mm wall thickness was carried out and experimental trials are proposed. Based on the trials conducted so far, and the experience obtained in the explosive welding and also from the quality of the bonding generated, it is seen that the explosive welding is feasible for use in PFBR SG tube plugging. However, a qualification test setup is also being erected to validate the plug integrity by simulating the service conditions. Subsequent to the qualification of the explosive welding process for SG tube plugging, the robotic system is planned to be deployed to remotely carry out the explosive welding.

II.6 Development of Electromagnet Cleaning Mechanism for DSRDM of PFBR

The main function of electromagnet cleaning mechanism (EMCM) is to mechanically clean the butting face of electromagnet (EM) of DSRDM. In the literature, deposition of foreign particles on parting planes of sodium immersed EM & armature and consequent decrease in the EM lifting capacity has been reported. Parting planes of the effected EM are cleaned for restoring the EM lifting capacity. A mechanism to clean the parting plane of armature, called Armature cleaning mechanism, has been designed and its manufacturing is under progress.

Based on studies, the types of foreign particle depositions on EM parting plane are of two types, i.e., deposition of sticky layer or deposition of particles which are either impregnated or welded. To remove these depositions, the DSRDM needs to be decontaminated and dedicated cleaning of EM butting face is needed.

Various design options are considered to realise the functional requirements of the proposed EM cleaning mechanism. A simple design using standard linear actuators with in-built sensors along with rail guide arrangement is finalised. The use of standard items reduces the design and manufacturing requirements.

Cleaning of EM parting plane is to be done above DSRDM port within ADRM handling flask to reduce the time taken for handling. Therefore, EMCM is to be introduced between ARDM handling flask and airlock valve assembly of DSRDM port. Inert atmosphere is to be maintained in EMCM. After installing EMCM, the DSRDM is to be retracted. Then the cleaning tool is to be moved to touch the EM. Once EM is touched a force is applied, then the cleaning tool is to be reciprocated w.r.t. EM to perform the cleaning by rubbing action.

Manufacturing, assembly and shop floor testing of EMCM in air (Figure 1) is completed successfully. The test setup used to simulate EM bottom surface for developing appropriate cleaning surface is shown in Figure 2. Two polluted surfaces chosen for studies are (i) araldite deposited surface and (ii) SS chips embedded surface.



Fig. 1 EMCM in assembled condition

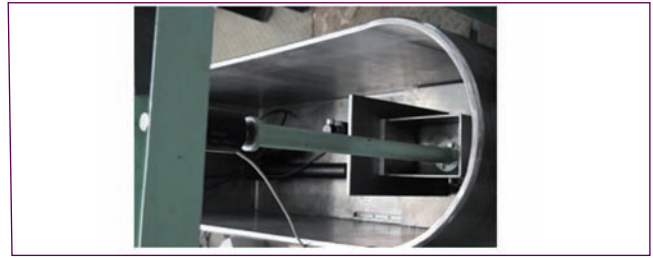


Fig. 2 EMCM with test setup

These polluted surfaces simulate various scenarios in reactor environment. Araldite deposition represents sodium oxide layer sticking on the surface and embedded chips represent foreign particle getting pressed between EM and armature during latching. Araldite deposited surface is made on SS plate while SS chips embedded surface is made on aluminium plate as shown in Figure 3.

Cleaning of the polluted surfaces is carried out with the emery paper of grade 180 and with wire brush fixed to the bottom of cleaning box of EMCM. While cleaning, a load of 50-70 kgf is applied. It is observed that the emery paper is capable of removing the SS chip partially while the removal of Araldite deposition is not possible. On the other hand, SS wire brush performed well with Araldite deposition, while it could only partially remove embedded chips on Aluminium surface. Surfaces cleaned are shown in Figure 4. Further testing with other cleaning tools, like grinding wheel and oil stone is under progress. A suitable surface cleaning procedure would be finalised after the testing. During testing, the operation of EMCM is found to be satisfactory.

The EMCM, designed for in-situ cleaning the parting plane of DSRDM, meets its functional requirements and development of suitable cleaning tool is under progress.

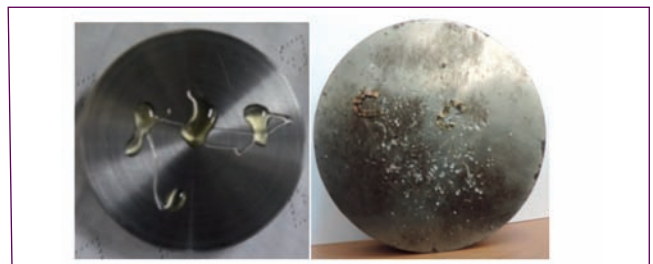


Fig. 3 Photograph of polluted surfaces



Fig. 4 Photograph of cleaned surfaces

II.7 Commissioning of System for Online Condition Monitoring of Secondary Sodium Pumps & ALIP

In PFBR an online condition monitoring system (CMS) for Secondary Sodium Pump (SSP) - 2 and Annular Linear Induction Pump (ALIP-1) in Secondary Sodium Main Circuit (SSMC-2) has been commissioned for periodic monitoring and recording of vibration data.

This system has 8 input channels for vibration sensors with a maximum sampling rate of 150 kHz. This system has three major functional units namely, field sensors, signal conditioning unit and base station. Field sensors (accelerometers) are the sensing elements in the system. In the current system, eight numbers of accelerometers (CLD type) are used to measure vibration. Five numbers of sensors are installed on SSP-2 and three numbers of sensors are installed on ALIP-1.

Signal conditioning unit is a data acquisition and monitoring system. Apart from signal conditioning and communication, it checks and controls measurements, processes and stores the measured data and triggers alarm. This unit being IP66 protected, it was mounted on a support structure on the SGB-2 side. The digitized vibration signal from the signal conditioning unit is routed to the base station control room using an ethernet cable. The monitoring, recording, displaying and storing of vibration data obtained from the sensors are carried out in the base station on a computer running with condition monitoring software. This software enables to setup all the measurement configurations according to the measurement requirements. It also manages periodic measurements and provides efficient and powerful analysis tools to obtain overall vibration trends, FFT spectra, water fall model, envelope filtering and many more modern measurement functions to diagnose machine problems efficiently.

SN	Sensor location	Overall velocity (mm/s)
1.	SSP-2 motor NDE bearing	1.42
2.	SSP-2 motor DE bearing	0.38
3.	SSP-2 pump DE bearing	0.42
4.	SSP-2 pump DE bearing	0.15
5.	SSP bowl handling lug	0.26
6.	ALIP-1 dish end	3.52
7.	ALIP-1 suction	1.52

The performance of the commissioned system was found to be satisfactory. Analysis has been carried out on the data recorded during commissioning run. The overall RMS value of vibration recorded in the unit is given in Table 1. Overall amplitude of vibration is observed to be within the acceptable limits in all the channels. In SSP-2 the maximum amplitude is observed in motor non-drive end where as in ALIP the maximum amplitude is observed in dish end which matches with earlier measurements done.

Apart from long term trending of vibration amplitude, the system is also capable of recording vibration time signal and frequency spectra at configured intervals. The system allows review and analysis of recorded signals at any instant of time. The stored spectra can be viewed as waterfall plot to identify the deviation in performance of the machine in the long run. Figure 1 shows a typical waterfall view of vibration spectra recorded from SSP-2 motor non-drive end. Implementation of similar system in SGB-1 of PFBR is also planned.

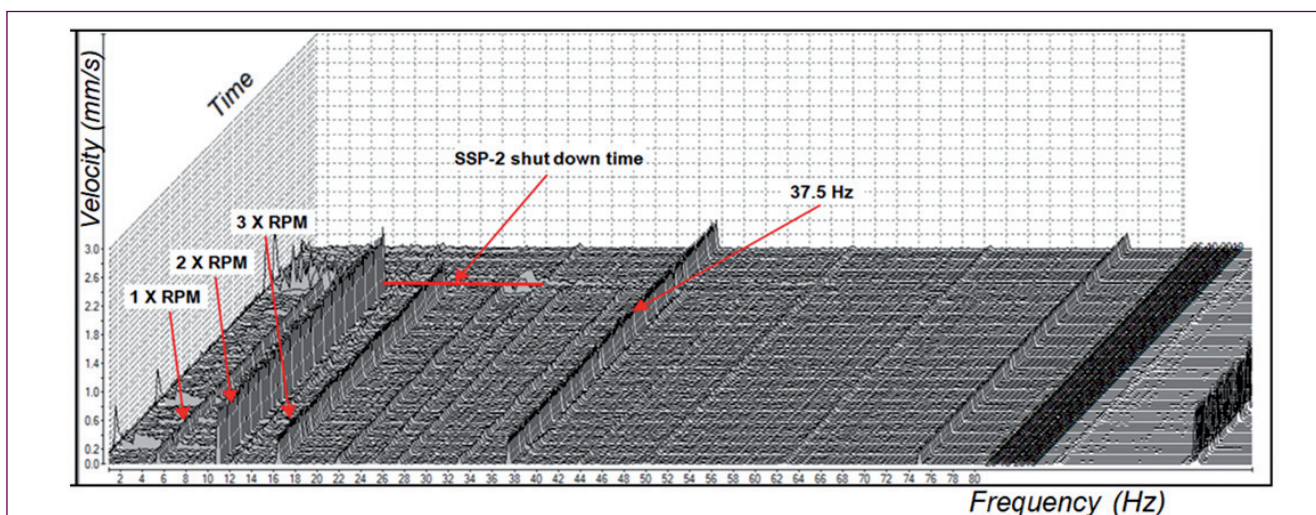


Fig. 1 Waterfall plot of SSP-2 motor – non-drive end (NDE)

II.8 Development of Permanent Magnet based Magnetic Particle Collector for Pre-commissioning of DSRDM

The second shutdown system of PFBR consists of three Diverse Safety Rod Drive mechanisms (DSRDM). Each mechanism consist of a diverse safety rod (DSR), which is held by an electromagnet (EM). The lifting capacity of DSRDM electromagnet is very sensitive to the gap between EM and armature of DSR. Any foreign particle between EM & DSR interface increases the nonmagnetic gap, hence reduces the capacity of EM to lift the DSR. It is essential to remove impurities including ferromagnetic particles from primary sodium during pre-commissioning stage of the reactor.

Magnetic particle collector (MPC) was designed & developed to collect the probable suspended magnetic particles from primary sodium of PFBR. MPC will operate at 200 °C under sodium environment. MPC consists of 68 blocks of Sm_2Co_{17} permanent magnets. Sm_2Co_{17} was chosen for this application due to its superior magnetic properties like high remanence, coercive force, high energy product, high Curie point & stability at the optimum operating temperature of 200 °C. Maximum operating temperature for Sm_2Co_{17} is 350 °C.

The design of magnetic module of MPC was based on the constraints in DSRDM location for its erection & removal. MPC needs to be inserted through two sleeves in control plug (support sleeve top & support sleeve bottom), jet breaker assembly & shroud tube. In its resting position, MPC will be inside the shroud tube. During PSP operation, flow in DSRDM location enters axially at the bottom of shroud tube and flows out to pool outside, through the radial holes drilled in shroud tube. The outer profile of magnet module was designed to suit the DSRDM opening. The support sleeve top of DSRDM is made up of carbon steel. If the permanent magnets in MPC are in the outer surface itself, then there is a possibility of magnets getting attached to support sleeve

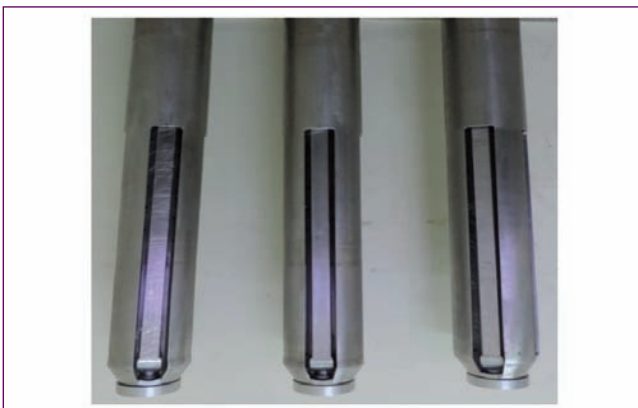


Fig. 1 Photograph of MPC

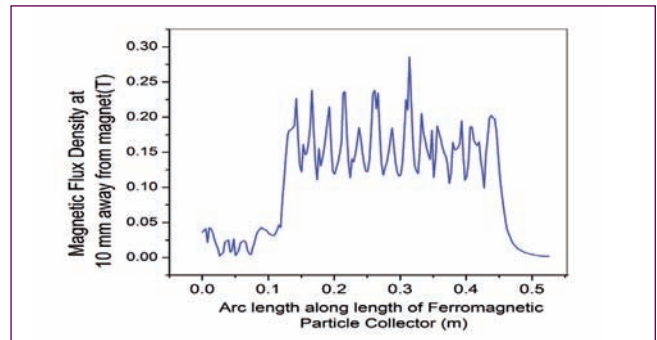


Fig. 2 Magnetic flux density along the length of MPC

and it can lead to difficulty in insertion & removal of MPC in the reactor. Hence it was decided to keep the magnets inside a housing and position the magnets sufficiently away from outer surface of the housing. Photograph of developed MPC is shown in Figure 1.

Three dimensional Finite Element (FE) analysis of MPC was carried out. Simulated magnetic flux density values along the length of MPC are shown in Figure 2. FE Analysis of MPC has shown that magnetic flux density values at 10 mm from magnet surface are more than 0.12 T. Surface plot of magnetic flux density produced by MPC is shown in Figure 3. DSRDM electromagnet was also modeled separately for the purpose of computing magnetic flux density values at different air gaps. It was seen from the analysis of DSRDM that at 1 mm distance, DSRDM produces maximum magnetic flux density of 0.075 T. Magnetic flux density values produced by MPC are higher than DSRDM values.

Four numbers of ferromagnetic particle collectors were manufactured. Magnetic flux density values were measured experimentally. Measured value of magnetic flux density at 10 mm from magnet surface is 0.13 T. Experimentally observed values match well with the results of FE analysis.

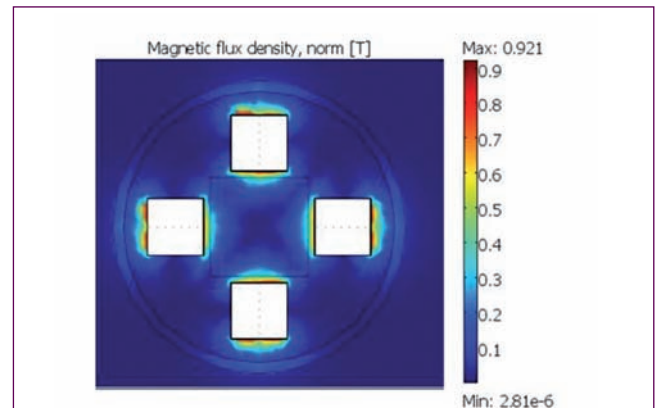


Fig. 3 Surface plot of magnetic flux density

II.9 Sodium Calibration of Mutual Inductance (MI) type Continuous and Discontinuous Level Probes for PFBR

MI type Continuous level probes and Discrete Level Probes (CLP and DLP) are used for monitoring sodium level in primary and secondary sodium circuits of PFBR. Four level probes (3 CLPs and 1 DLP) were received from PFBR for calibration, out of which three probes were spares and in one probe, mineral insulated cable was replaced. Thus sodium calibration is required for all the four probes.

The main aim of calibration of continuous level probe is to obtain the value of temperature compensating resistance, operating frequency and the value of secondary voltage with and without sodium at optimized frequency. The typical graph is shown in Figure 1. A view of Test Vessel (TV)-2 top flange of Large Component Test Rig (LCTR) is shown in Figure 2.

A Dipstick level of 11 meter long which was fabricated in-house shown in Figure 3. A chain pulley arrangement was provided for ease of operation.

Four level probes, were calibrated simultaneously with probes fully immersed in sodium. Flange was suitably modified with additional outer flange to mount on TV-2. At maximum temperature, the top flange temperature was around 150°C and hence a raised platform was provided in order to reduce the heat and to provide accessibility. Calibration setup in TV-2 is shown in Figure 4. To achieve cover gas space of 120 mm discrete and dipstick level probes were used. Fast dumping of sodium within 20 minutes was achieved for calibration of level probes.

All the for continuous level probe electronics, the secondary output for No Level (NL) and Full Level (FL) at maximum operating temperature was fed to the electronics and was configured for zero and span indications. For discrete level probe electronics, the sensor secondary outputs with sodium at maximum operating temperature and without sodium at minimum operating temperature were fed to the electronics and the threshold was set in the electronics for level indication.

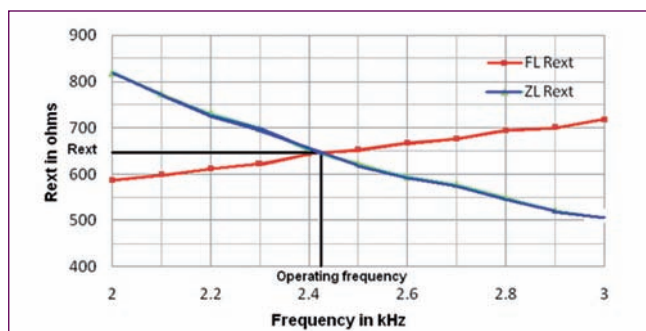


Fig. 1 Resistance vs frequency graph



Fig. 2 View of TV-2 top flange of LCTR

All the probes were successfully calibrated in sodium and sent to PFBR. Electronic chassis has to be calibrated in the field. Using in-house developed dipstick level probe, the level readings of calibrated probes were cross checked at various levels and error was found to be within $\pm 1.5\%$.

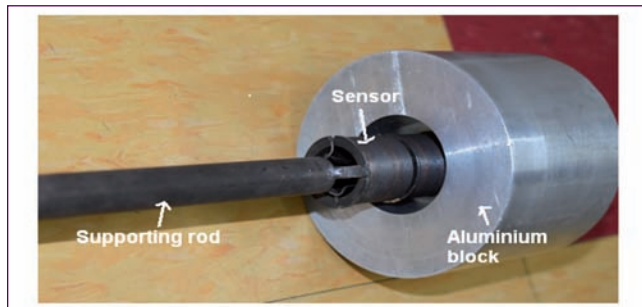


Fig. 3 Dipstick level probe test setup

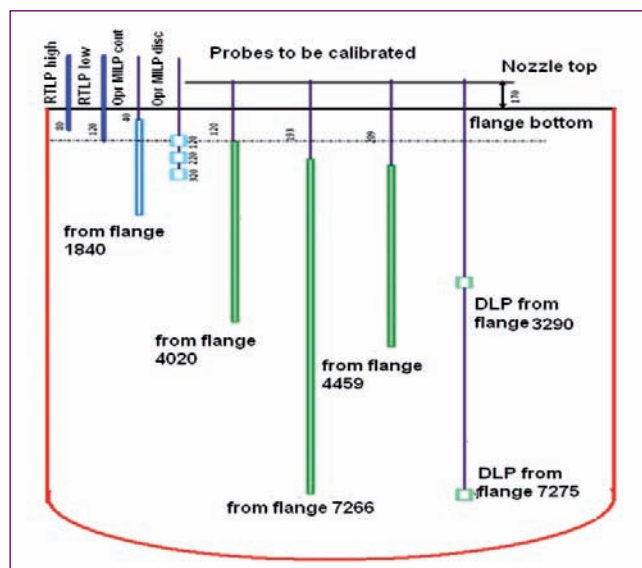


Fig. 4 Calibration setup in TV-2

II.10 Qualification of Sodium Aerosol Detector in Nitrogen Environment for Leak Detection in ALIP of PFBR Primary Sodium Purification Circuit

Primary Sodium Purification Circuit (PSPC) of PFBR is provided with an Annular Linear Induction Pump (ALIP) to circulate sodium. Figure 1 shows the cross sectional view of ALIP. Its sodium carrying pipe, which is insulated with ceramic material, is surrounded by the pump winding. In order to maintain the ALIP winding temperature within its design limits, a closed loop nitrogen gas cooling system is provided.

In case of a leak in the pipe, sodium interacts with the ceramic insulation and comes in contact with the flowing nitrogen gas. Sodium Aerosol Detector (SAD) is provided in a nitrogen sampling line at the downstream of ALIP in nitrogen circuit. SAD uses a heated filament to ionize sodium vapor or its aerosols in preference to the constituents of carrier gas. These positively charged sodium ions are then collected by a collector electrode to provide a measure of ion current which itself is an indication of sodium leak. Though SAD is a well proven global sodium leak detector, its performance in nitrogen environment is required to be demonstrated. Hence sodium leak is simulated with PFBR ALIP conditions and SAD performance was monitored. Before conducting the experiment, flow pattern of nitrogen in ALIP cooling duct and surface temperature of insulation were estimated by using CFD simulation.

Simulations were carried out for two cases viz., temperature of sodium at 400 °C, during normal operating conditions and temperature of sodium at 200 °C, during fuel handling condition. Velocity pattern in ALIP cross section is shown in Figure 2. Temperature profiles in ALIP cross section for a conservative case of sodium temperature as 200 °C is shown in Figure 3. Velocity pattern shows that maximum flow is bypassed through the gap between electrical winding and outer duct. But the flow over electrical winding is sufficient to keep the temperature limits. When the sodium temperature is at 400 °C, surface temperature of insulation provided on the outer surface of sodium

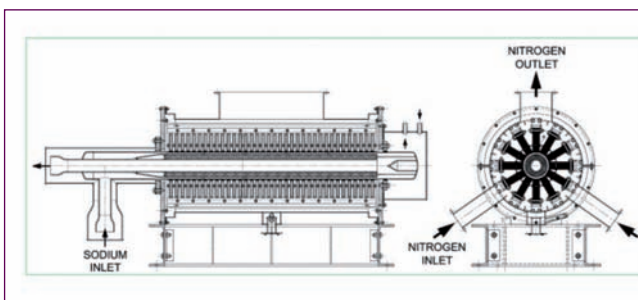


Fig. 1 Annular Linear Induction Pump

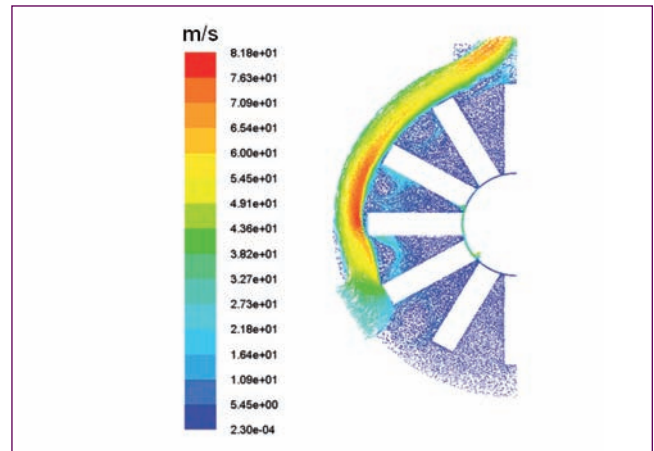


Fig. 2 Velocity pattern of nitrogen flow in ALIP

flowing duct varies from 79 °C to 336 °C and average temperature is 207 °C. When the sodium temperature is 200 °C, the surface temperature of insulation varies from 48 °C to 163 °C and average temperature is 105 °C. This indicates that if sodium leaks through the sodium flowing duct, it may interact with insulation at 48 °C. There is a probability of solidification of sodium on the duct surface and the aerosol formation will be minimum in this condition. Hence, the experimental studies were conducted at insulation temperature of 200 °C and 40 °C to simulate the expected condition. However, testing the performance of SAD when sodium interacts with insulation at 40 °C will be the most conservative case.

The schematic layout of the experimental setup simulating nitrogen gas sampling line of primary ALIP in PFBR is shown in Figure 4. The setup comprises of a cylindrical chamber of 75 liter capacity which is similar in volume of nitrogen duct in ALIP. A nitrogen supply system connected to the chamber provides continuous nitrogen flow to the chamber. A sodium holdup vessel

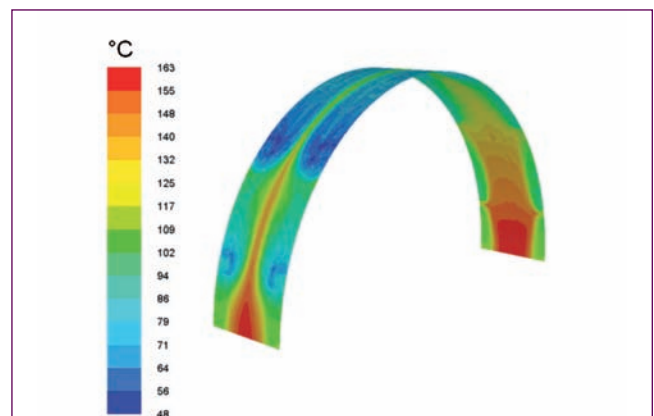


Fig. 3 Temperature of insulation surface when sodium at 200 °C

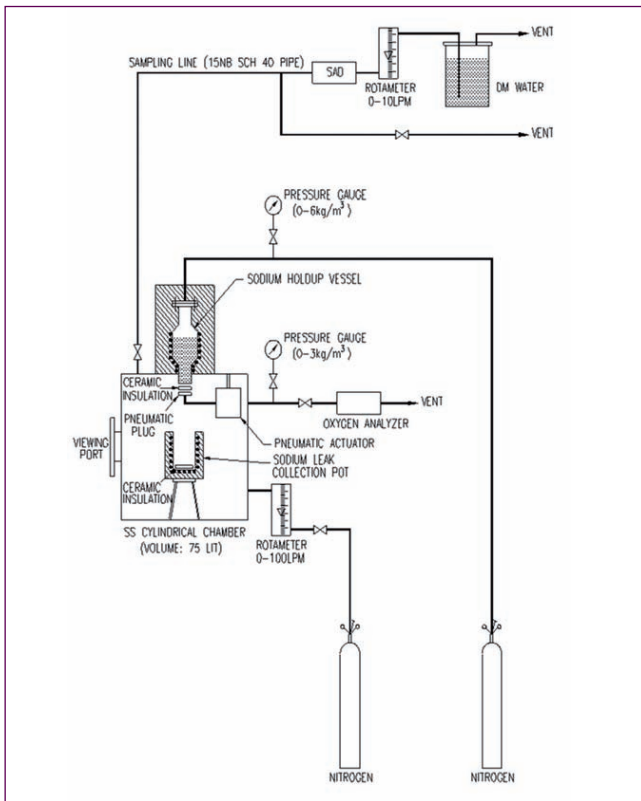


Fig. 4 Schematic layout of experimental setup

(SHV) provided with heaters and thermocouples was mounted on top of the chamber. The drain nozzle of SHV can be opened by remote operation of a valve to simulate sodium leak. Ceramic fiber material which is required in ALIP as insulation was kept at the nozzle of SHV to interact with sodium during leak. A sodium collection pot is provided beneath the SHV.

SAD sampling line was simulated as in PFBR layout. Out of 50 LPM main flow rate of nitrogen, 1 LPM was sampled through the SAD and rest was bypassed.

The experiments were conducted with 10 g of sodium and 2 g of insulation. The response of SAD to sodium aerosol generated during sodium leak was monitored using a data recorder. The nitrogen gas carrying sodium

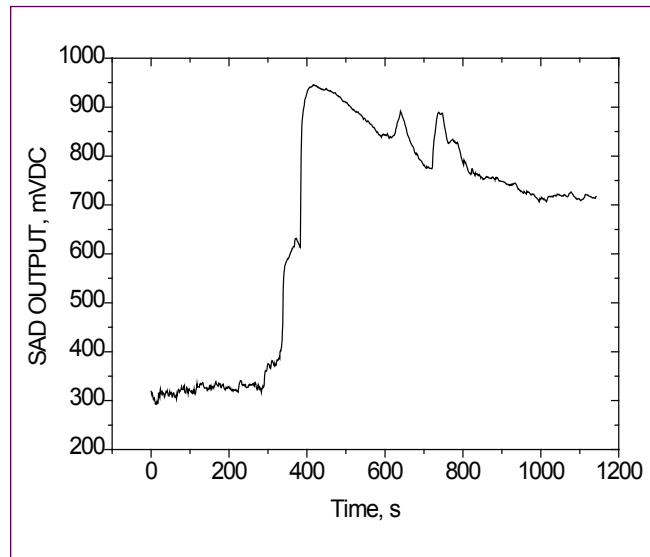


Fig. 5 Dropwise - Continuous

aerosols passing through the SAD was bubbled through DM water. DM water was analyzed for sodium using Atomic Absorption Spectrometer. The experiments were carried out for three different scenarios of sodium leak i.e. (i) Continuous drops of sodium leak from the SHV, (ii) Drops of sodium leak intermittently from the SHV and (iii) Sodium leak in the form of jet from the SHV. The results are shown in Figures 5 to 7 respectively. During discontinuous sodium leak, the intermittent release of sodium drops contributed to fluctuations in SAD response as shown in Figure 6. The response time of SAD during the experiments was found to be in the range of 40 to 128 seconds. The response time of SAD depends on duration of simulated leak.

It was observed that SAD produced a distinct and accountable increase in its output during all types of sodium leak simulated. These experiments show that Sodium Aerosol Detector can be used to detect sodium leak in ALIP duct. The detection time is much less than ASME SEC-XI DIV-3 stipulated value of 250 h for 100g/h sodium leak in inert environment.

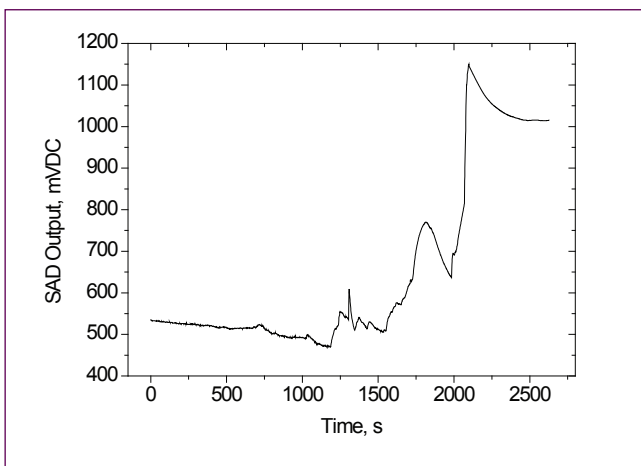


Fig. 6 Dropwise - discontinuous

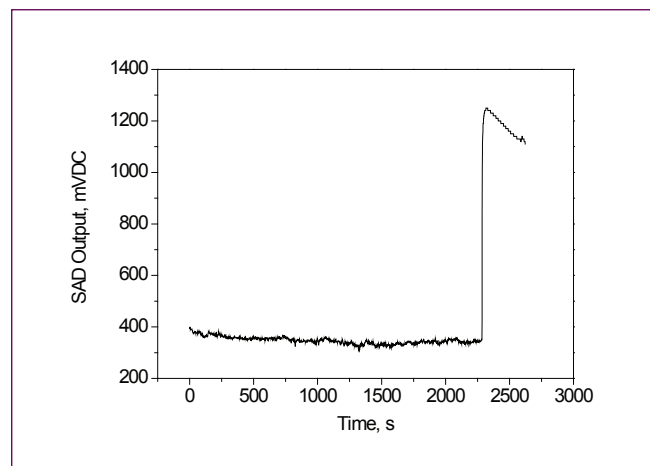


Fig. 7 Sodium leak in jet

II.11 High Temperature Testing and Qualification of Dissimilar Weld Inspection Vehicle (DISHA)

A Dissimilar Metal Weld Inspection Device (DISHA) has been developed, for carrying out periodic inspection of dissimilar metal weld between the roof-slab shell and main vessel of PFBR, above the anti-convection barrier (ACB). DISHA is a remotely controlled robotic vehicle to navigate in the interspace above ACB and to orient the Visual Examination (VE) camera, ultrasonic testing (UT) and Eddy Current Testing (ECT) transducers towards the weld zone for inspection. DISHA is designed to perform at a temperature of 120°C. DISHA is deployed by a cable take-up/release system (CTS), and moves around the roof slab on the ACB. Each campaign through an in-service-inspection (ISI) opening will cover a weld length of about 3.5 m on either side of the ISI opening. DISHA will be lowered through each of the six ISI openings onto the ACB for carrying out the inspection process.

After the room temperature trials, DISHA mock-up test facility at Site Assembly Shop (SAS), in BHAVINI was upgraded for conducting high temperature (HT) trials. The mock-up test facility replicates the ISI duct, ACB sector for one ISI opening of PFBR (Figure 1). A dissimilar weld calibration plate has been provided within the mock-up test facility for validating the UT of the weld.

In order to test and validate the intended functional requirements of DISHA for high temperature operation, detailed procedures were evolved and consolidated for the HT qualification trials. Prior to the commencement of elevated temperature tests, all critical components of DISHA like motors, limit switches, LEDs and camera modules were tested at 120 °C and integrated with DISHA. The preliminary high temperature testing of DISHA was conducted in three stages at 80, 100 and 120 °C, and each of the stages for a duration of 12 hours. Subsequent to the phased testing, the HT testing and qualification was



Fig. 2 Images acquired during high temperature trials of DISHA

conducted in the mock-up test facility, as per approved qualification procedure and check-list.

The mock-up test-facility was maintained at 120°C by controlled heating for HT qualification trials of DISHA. Instrumented air at 6.5 bar pressure was used for expanding / collapsing the wheels and for the actuation of UT module, and cooling of camera modules through a chiller. The inlet cooling air temperature to the camera modules was set at 10 °C to maintain a temperature of about 45 °C in all camera modules. DISHA was deployed from the operating platform using the CTS, through the ISI opening and duct of the mock-up test facility and rested on ACB, aided by the five navigation cameras. DISHA was operated for traversal over the ACB, across the opening to cover the complete 7.5 m sector of the mock-up test facility. During the movement of DISHA over the ACB, video from the visual examination module was continuously acquired, in the control panel digital video recorder.

Two UT successive auto-cycles were conducted on the calibration plate and UT data was acquired whenever DISHA approached the calibration plate during the traversal loops on the ACB. In the span of 24 hours, a total of 18 UT auto-scans were conducted on the calibration plate weld with a traversal of about 105 m on ACB. At the end of the 24 hours trial duration, DISHA was operated to reach the ISI duct location and retrieved through the ISI duct and opening back to the operating platform. DISHA was operated in manual and auto-mode by the operator during the HT trials. During the period of 24 hour trials, all the functional aspects of DISHA were checked and monitored continuously, along with temperature at various zones of HT mock-up facility.

The HT testing and qualification of DISHA vehicle were conducted successfully, and the functionality and performance of DISHA was demonstrated to meet the intended design requirements.

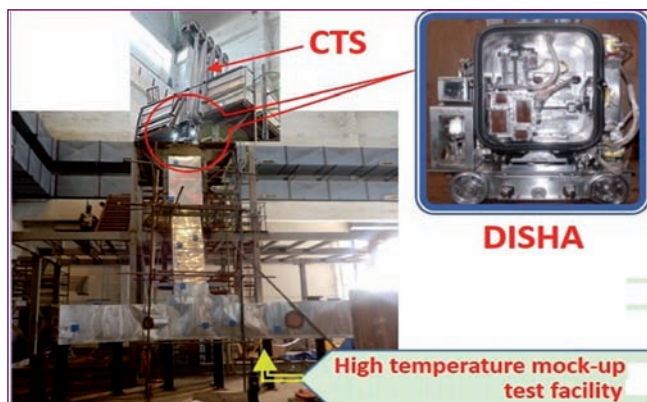


Fig. 1 High temperature trials of DISHA in mock-up test facility at BHAVINI

II.12 Qualification of PFBR PSP ECFM by Integrated Testing along with Electronics

In PFBR, eddy current flow meters (ECFMs) are used to measure the flow delivered by each primary sodium pump to monitor the pump performance and to obtain the flow through the core, thereby providing one of the SCRAM signals in any event of primary pipe rupture.

Each ECFM probe assembly consists of two eddy current flow sensors (ECFS) separated by a spacer tube, as shown in Figure 1. Each sensor has one primary and two secondary coils. Both the secondary coils are identical with respect to number of turns, dimensions and are equally spaced from the primary coil. Both the sensors are located in the same flow path.

The ECFM sensor is designed and developed in-house. All ECFM sensors required for PFBR (8 nos. including 4 nos. as spare) are manufactured in-house and are calibrated in 500 kW loop located in Hall-I. The sensor was qualified for high temperature operation up to 525°C (corresponding to safety grade decay heat removal system (SGDHR) condition) by testing in a dedicated test section in steam generator test facility (SGTF).

During the above tests, raw signals of the sensor coils are only measured and used for processing. For complete qualification of flow measurement system, which involves ECFS and its electronics, integrated testing of ECFM along with its electronics in ECFM test section of SGTF was carried out.

A spare probe, available with PFBR, along with its electronics and full length of the cable (50 m length, corresponding to PFBR length requirement) is used for the testing. Minor modifications were carried out in the test section in SGTF to meet the interface constraints of the spare probe.

Initially, trial studies were carried out to fine tune the various parameters of Look up table (LUT). These

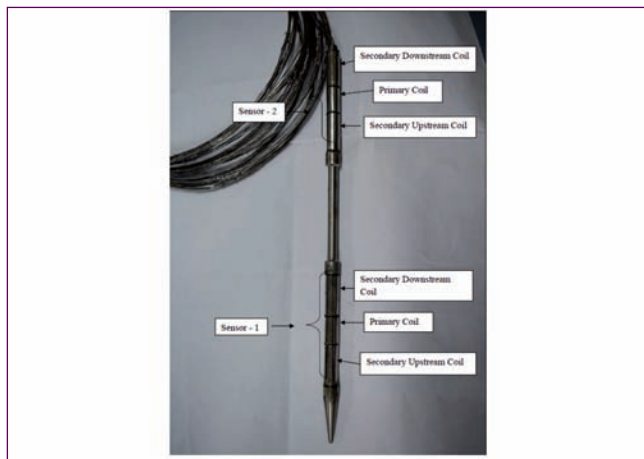


Fig. 1 ECFM probe assembly

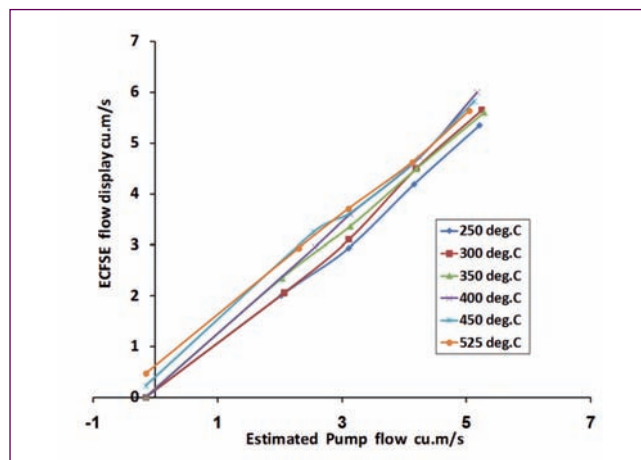


Fig. 2 Overall characteristics of ECFS

tables were used for converting the output voltages of ECFM into pump head and flow. After trial testing, all the calculated parameters were loaded in Eddy Current Flow Sensor Electronics (ECFSE) and comprehensive testing without disturbing the ECFSE was carried out.

During testing, the primary coil of the sensor was excited with sinusoidal current of magnitude 200 mA at a frequency of 400 Hz, which is the optimum frequency for the given sensors. The temperature was varied from 250°C to 525°C in steps of 50°C and the flow through the sensor was varied from static to 25 m³/hr in steps of 5 m³/hr.

For each test condition, AC outputs of individual secondary coil voltages were measured. Similarly, DC outputs of sensor 1 & sensor 2 i.e., ratio metric output (A-B /A+B), individual coil voltages (A & B), Delta H (Voltage and current), and Q (Voltage and current) were measured with multi-meter and delta H display and Q display in electronics were recorded.

The performance of the ECFM and the electronics was studied by a series of characteristics, namely sensor, electronics and overall characteristics. Figure 2 shows the overall characteristics of the sensor, wherein the actual flow measured by the ECFSE is drawn against estimated flow for different temperatures.

From the analysis of the results, it is inferred that the sensor accuracy is within $\pm 5\%$, with temperature compensation. It is found that the achieved level of accuracy is sufficient to meet the design requirement of providing SCRAM signal within the stipulated time after primary pipe rupture event.

The testing established the satisfactory operation of ECFM along with electronics, qualifying it for reactor operation.

II.13 Performance Testing of Modified Transfer Arm Guide in Sodium

Transfer arm (TA) is the in-vessel fuel handling machine of PFBR. An additional central guide arrangement was provided between the offset link and the connecting piece of the TA gripper for the centering of actuator rod during finger operation. The arrangement consists of a guide fixed to the connecting piece moving within two rails. The rails are V-shaped and rigidly fixed to offset link. The guide surfaces are colomony-5 coated, and guide surface geometry was made with double curvature to have a wider contact surface.

The performance testing, in sodium, of the central guide arrangement was done with a simulated reaction load on the central guide of TA gripper. In TA, the maximum horizontal reaction force of ~480N is developed between the central rail and guide when the gripper rests on subassembly (SA). This reactive force is simulated in sodium testing on the central guide of TA gripper by loading on the actuator side of connecting piece-end. Theoretical analysis showed that a load of 52kg at the connecting piece-end develops a reactive force of ~50kg in the rail-guide arrangement of TA gripper. Sodium testing was therefore carried out with this simulated load on the central guide.

The testing consisted of operating TA gripper between the two calibrated positions (fully closed position and open on SA) of finger operation. The number of cycles of testing was decided as per the guidelines of ASME Section-III, Appendix-2.

TA gripper test setup (Figure 1) consists of a pair of long tubes called Outer Tube (OT) (138 mm OD × 109.5 ID) and Inner Tube (IT) (60.3 mm OD × 46 mm ID). The length of OT & IT is approximately 3m, and IT is assembled inside the OT. The top end of the IT is connected to the linear actuator, through a load cell, which in turn is connected to the OT through its housing. The bottom end of the OT & IT are connected to the gripper assembly, and it consists of an offset arm (offset link) and connecting piece.

One test cycle consists of movement of IT assembly from finger fully closed to finger open on SA position and back to finger fully closed position. The IT assembly was operated at the rated speed of 5 mm/s for a total travel of 55 mm (finger close to finger open on SA position) using linear actuator through a VFD. All operations were carried out remotely through a relay-based control panel. Magnetostrictive sensor was provided for monitoring the continuous position of IT and reed switches in linear

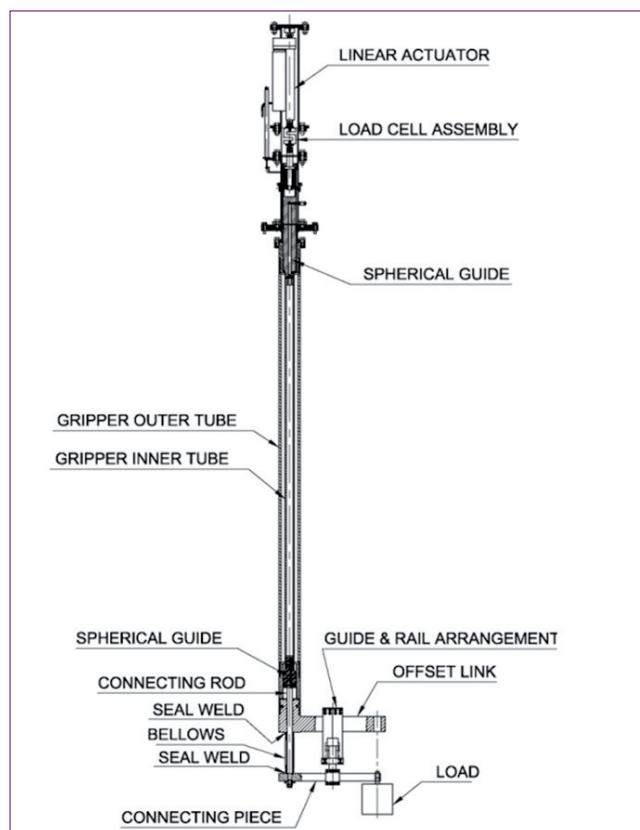


Fig. 1 Transfer Arm gripper assembly

actuator were used to stop the linear actuator movement at the end limits. Continuous position, load cell readings, and cycle count of IT assembly movement were recorded using a data logger.

In-sodium testing of TA gripper was carried out in Test Vessel-2 (TV-2) of LCTR. Before sodium testing, a series of tests were carried out in ambient condition and in hot argon at different temperatures viz. 373, 393 & 423 K. Then sodium was filled, and 6000 cycles of sodium testing at 473 K were carried out. During testing the space between the inner tube and the outer tube was filled with argon at 450 mbar (g) to check the healthiness of the bellows provided between IT & OT. The overall performance of the machine was satisfactory during testing, and all performance parameters were normal.

On completion of testing, the gripper test setup was taken out of TV-2, and investigations on the central guide contact surfaces were carried out after sodium cleaning. Slight rubbing marks were observed on the rail and guide contact surfaces. Hardness measurements of the same were confirmed to be within limits. Also, the healthiness of bellows between IT & OT of gripper assembly, after sodium testing, was confirmed by Helium Leak Test.

II.14 Natural Frequency Measurement of PSP, SSP and ALIP in Installed Condition

Natural frequency measurement of Primary Sodium Pump (PSP), Secondary Sodium Pump (SSP) and Annular Linear Induction Pumps (ALIP) in installed condition was carried out in PFBR as part of commissioning activity and design evaluation. Measurements were carried out by exciting the machines using electro-dynamic exciter and responses were measured using accelerometers.

Figure 1 shows the arrangement for exciting the PSP shaft with motor in decoupled condition. Natural frequency measurements were carried out initially with the weight of the rotating assembly supported on the top thrust bearing. Figure 2 shows a typical frequency response measured from PSP-1 shaft.

Later, the shaft lock nut is released and the weight of the rotating assembly is transferred to the top labyrinth. Natural frequency measurements were carried out in this condition. The measurements were repeated for PSP-2 also. The first lateral frequency of PSP-1 is 17.4 Hz and that of PSP-2 is 18 Hz. Although these values are expected to reduce marginally under sodium filled condition they were observed to be sufficiently away from the operating speed of 590 rpm (~10 Hz) thus ruling out resonance during operation. Further measurements are planned during motor coupling and after sodium filling. Measurements were carried out on SSP-2 shaft and bowl to determine its natural frequency. Figure 3 shows the test setup. Predominant frequency peaks are at 26.8 Hz for SSP shaft and 14.6 Hz for SSP bowl. Since bowl natural frequency falls within the SSP operating speed regime (3 Hz to 15 Hz), modification in bowl supports are taken up. The gap between the pump inlet piping and the guide

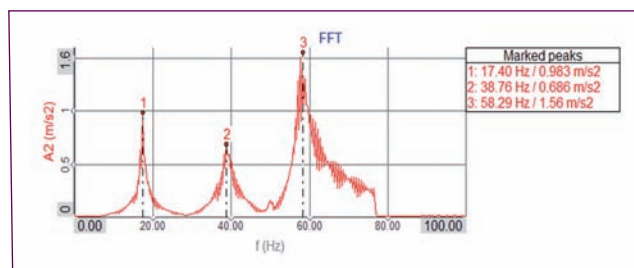


Fig. 2 Response spectra from PSP-1

was filled with shims (in x and z directions) to increase the pipe support stiffness and the bowl natural frequency is observed to be shifted from 14.6 Hz to 18.3 Hz. Later on, further modifications on piping supports were carried out and bowl natural frequency was shifted to ~ 24 Hz, which is well away from the operating regime.

ALIP is used in the secondary circuit for fill and drain purpose as well as to make up the sodium level during secondary circuit operation. Experimental determination of natural frequency was carried out on ALIPs (EMP Na 27001 and EMP Na 27002) located in secondary sodium circuit of Steam Generator Building-2 (SGB-2). Accelerometers were mounted on dished end, suction and discharge. Measurements are carried out in sodium filled condition as well as without sodium. The results are shown in Table 1.

SN	ALIP	Natural frequency (Hz)	
		with sodium	without sodium
1.	EMP Na 27001	18.3	18.6
2.	EMP Na 27002	23.5	23.8

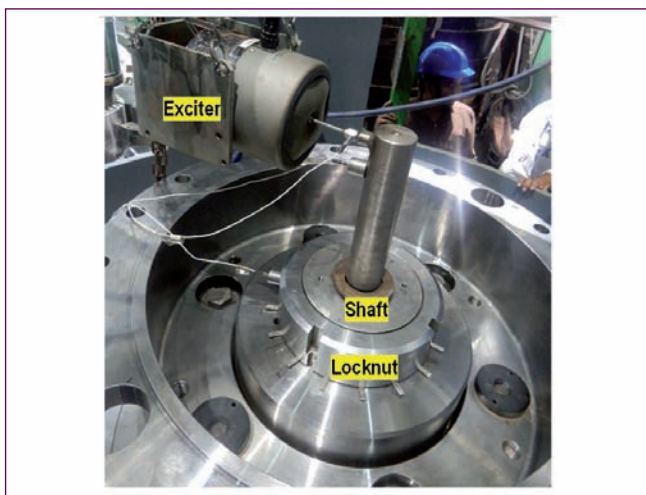


Fig. 1 Arrangement for PSP shaft excitation

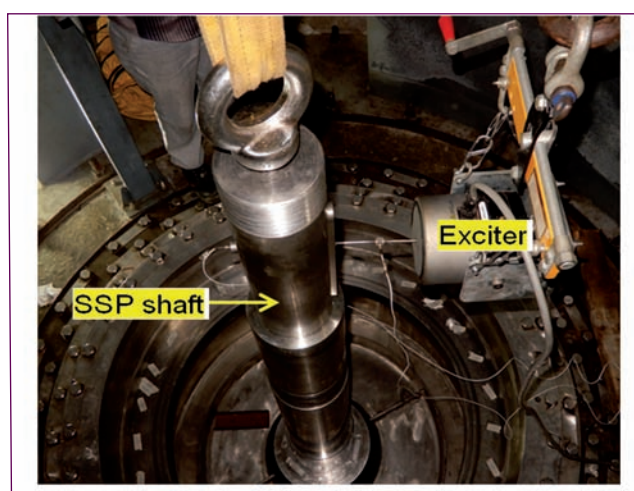


Fig. 3 SSP shaft excitation arrangement

II.15 Stability Analysis of Secondary Sodium Pump of PFBR

Secondary Sodium Pump (SSP) circulates the liquid sodium in secondary sodium main circuit of Prototype Fast Breeder Reactor. SSP, shown in Figure 1, is a long hollow drive shaft carried vertically in widely spaced journal bearings with in a cylindrical casing, and having the interspace between shaft and casing partially filled with molten sodium. The long shaft (5589 mm) of SSP carrying the impeller is mounted on a thrust bearing at the top. The shaft, at the bottom above the impeller is guided by a hydrostatic bearing (HSB), which is fed by pressurized sodium from the pump discharge. HSB is connected to the discharge casing, which in turn is connected to the outer casing via spherical header. Thus the shaft rotates freely within the shell. The spherical header is having two discharge nozzles and one suction nozzle. The outer casing as shown in Figure 1 is bolted to the floor at EL 37500. The suction nozzle connecting the suction piping is restrained at the bottom. The pump shaft is coupled to the drive motor shaft by means of a flexible coupling. The drive is an AC induction motor driven by variable speed, capable of running at any speed between 15 and 100 % of the nominal speed.

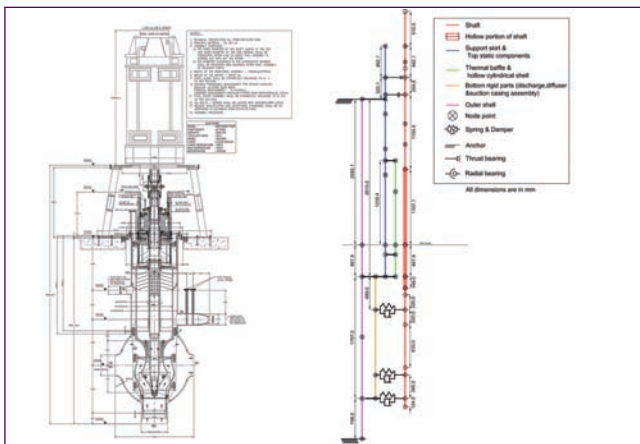


Fig. 1 (a) Schematic of SSP pump; (b) Finite element model of SSP

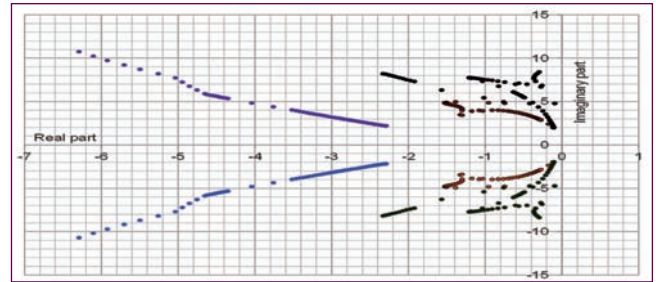


Fig. 3 Root locus plot for secondary sodium pump

Other than HSB, suction and discharge wear rings plays a key role on the stability of the pump. The pressure head of sodium, delivered by the pump itself, provides the required radial stiffness. Thus, the stiffness is a strong function of pump speed as shown in Figure 2.

Therefore, key aspects in SSP vibration are HSB stiffness values, which are determined by solving a set of strong non-linear fluid mechanics equations. Apart from this, effect of wear ring and gyroscopic effects need to be included in finite element formulation which is also a function of pump speed. The effect of sodium is considered as added mass on the shaft. Other than the mass effect, the damping effect of sodium is accounted by computing the equivalent damping coefficient based on literature survey. An in-house code DYDIN for the pump dynamics is developed in CAST3M. The network analysis of the HSB is solved using segregated CFD approach, where the system of equations is mapped on to a FEM mesh and solved for pressure. The stability analysis is done by numerically solving the dynamic equation for Eigen values in state space formulation using Implicitly Restarted Arnoldi Method

The root locus plot for the secondary pump is shown in Figure 3. The system is verified to be stable throughout the operating regime. It is also seen that as the RPM increases, the system is more stable due to increase in the damping in the system.

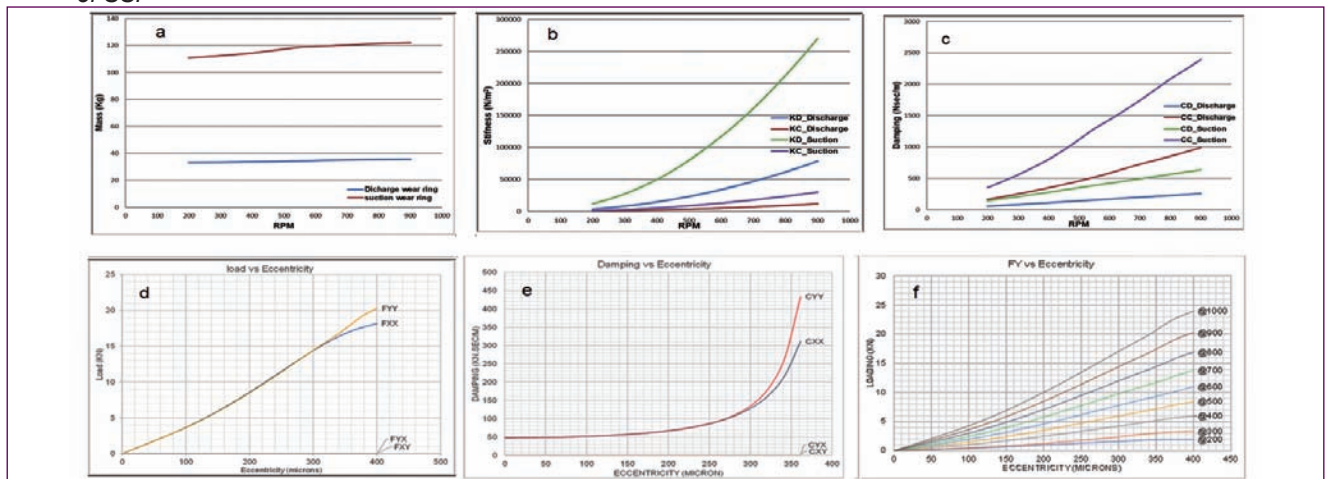


Fig. 2 Pump parameters: (a) mass of wear rings; (b)stiffness of wear rings; (c) damping of wear rings; (d) load characteristic of HSB; (e) damping in HSB;(f) load characteristic of HSB for various RPM

II.16 Pressure Transient Analyses in Secondary Sodium Piping of PFBR

During normal operating conditions, the coolant in sodium cooled Fast Reactors are circulated in the heat transport circuits by dedicated centrifugal mechanical pumps. Although coolant flows in these loops are intended to be steady, mild temporal fluctuations in the coolant flow rate are possible due to turbulence or by the transient vortices developed around combining / dividing junctions. Such conditions may arise inside the centrifugal pumps as well. This kind of flow variations are reported to have occurred in the US reactor Fast Flux Test Facility (FFTF). Static pressure peaking of about 48 kPa occurred at discharge location of secondary sodium pump in one loop. These pressure oscillations are envisaged to be associated with the flow fluctuations of up to 7 %. It is important to analyse the effect of such flow variations on plant safety as they are likely to be associated with development of dynamic forces on the pipelines of the circuit.

In the current study, a part of the secondary sodium circuit of PFBR from Surge Tank (ST) outlet to Secondary Sodium Pump (SSP) inlet has been modeled using general purpose system dynamics code **FLOWNEX**. The **FLOWNEX** model used in the study (half symmetry) is shown in Figure 1.

A steady state analysis is carried out first to estimate the pressure distribution in the circuit. Fixed pressure is specified at the ST outlet representing the constant cover gas pressure maintained in the ST. Mass flow rate is specified at the pump inlet. The predicted pressure distribution in the circuit for full power condition is shown in Figure 1. The pressure drops across various components of the circuit are in good agreement with the design values. Transient analysis is then carried out by considering sinusoidal flow oscillations of $\pm 10\%$

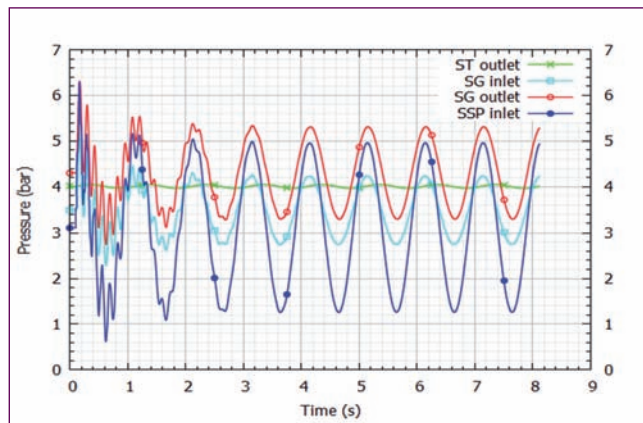


Fig. 2 Dynamic pressures developed in the circuit

and 1 Hz frequency. A maximum mesh length of 1 m and time step size of 0.25 ms is chosen (Maximum CFL number momentum = 0.99). The structural walls of all pipe segments are assumed to be rigid conservatively.

Evolution of pressure at few key locations in the circuit is shown in Figure 2 for full power conditions. It is observed that the frequencies of pressure oscillations are same as that of flow oscillations imposed (transient boundary condition). Maximum peak to peak pressure oscillation amplitude occurs at SSP inlet whose value is 3.67 bars in full power condition and 2.1 bars in 60 % power condition.

The forces on various pipe segments are also sinusoidal in nature. The mean values of oscillations of these forces are same as their steady state values. The frequency is same as that of flow oscillations imposed. The amplitude and phase shift of oscillation of these forces at various locations obtained from the simulation are subjected to structural investigation and found not to cause any significant structural damage.

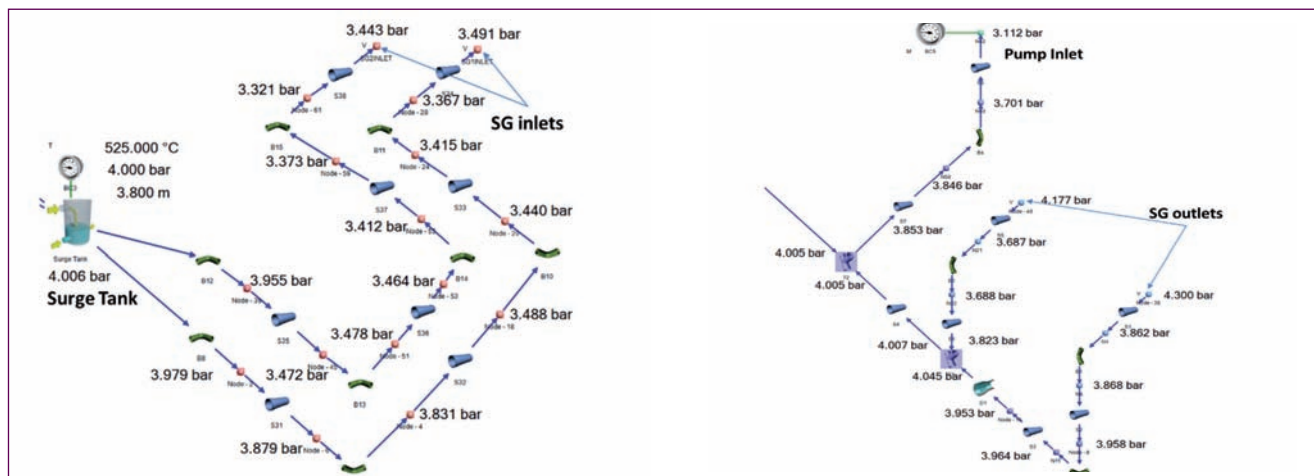


Fig. 1 Steady state pressure distribution in the circuit

II.17 Development of Sweep Frequency Remote Field Eddy Current Technique

Sweep Frequency Remote Field Eddy Current (SFRFEC) technique was developed for accurate and absolute measurement of thickness of PFBR steam generator (SG) tubes. RFEC is a low frequency eddy current technique which employs separate exciter and receive coils that are kept inside tube. The exciter coil is fed with a sinusoidal current which will produce eddy currents in the tube wall. The inductive component (quadrature) of impedance of the receiver coil is measured and used to correlate the presence of flaws and thickness reduction in the SG tubes. In SFRFEC technique, the excitation frequency is continuously changed for every fixed time period and the inductive component of the impedance at each frequency is measured. The inductive component of the impedance goes to zero for extreme values of frequency i.e. zero and infinity. This means that at some optimum frequency it is expected to attain a peak value. This peak frequency (F_p) is dependent on the thickness of the material following skin-effect theory. According to skin-effect the depth of penetration of eddy currents in a material is inversely related to the square root of the electrical conductivity, magnetic permeability and the excitation frequency. Thus, there exist a linear relationship between the square root of frequency and the thickness of the SG tubes. 2D axi-symmetric finite element model based studies were also carried out to understand the SFRFEC behaviour in modified 9Cr-1Mo ferritic steel tubes used for PFBR SG.

The SFRFEC instrument and probes (with exciter and receiver coils) were designed and developed in-house for experimental studies. It consists of a sine wave generator of variable frequency in the range of 100 - 5000 Hz. The receiver coil voltage was fed to a digital lock-in amplifier implemented through the LabVIEW software for quadrature measurement at each frequency. Ten cycles of sine wave of a particular frequency is generated and the same was used for measuring quadrature component with the LabVIEW based lock-in software. Analog input and output cards were used for sine wave generation and acquiring signals from



Fig. 1 Photograph of the in-house developed SFRFEC instrument with LabVIEW control software

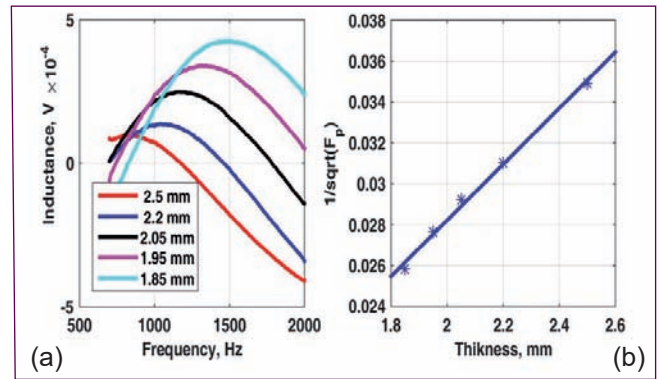


Fig. 2 (a) Variation of inductive component of the impedance of the RFEC probe with frequency, (b) Linear relationship between the square root of peak frequency (F_p) and thickness of the SG tubes

the receiver coil respectively. Additionally a 10 Watts power amplifier was used for amplifying the input sine wave for driving the excitation coil with a current of 100-200 mA. High dynamic (24-bit) range analog-to-digital converter was used for measuring small voltages from the receiver coil. All these add on cards were installed in a PXI chassis for integration and control. The control and data acquisition software was developed in LabVIEW environment. The software has the provision for choosing the range of frequencies to be swept and the interval in which individual frequencies are to be generated. A photograph of the in-house developed SFRFEC instrument is shown in Figure 1.

In order to study the performance of the SFRFEC instrument SG tubes having thicknesses of 2.5, 2.2, 2.05, 1.95 and 1.85 mm were fabricated (thickness extended over long range three times length of the probe). Figure 2a shows the variation of the inductive component of the SFRFEC probe for a frequency range 500-2000 Hz. As can be seen the inductive component peaks at different values for different thickness of the SG tube. Figure 2b shows variation of the square root of the peak frequency with thickness. A perfect linear relationship exist in Figure 2b with a correlation coefficient of 99%.

Experimental measurements were also performed on SG tubes having localized uniform wall thinning grooves of 3 mm and 5 mm width. The variations were found to be qualitatively similar to the one observed for the extended wall thinning, the difference being the slope and y intercept of the linear graph. Thus the sizing part involves characterizing the straight line itself. These studies demonstrate the fact that measurement of peak frequency enables accurate determination of the absolute thickness of SG tubes. Further developments are in progress to make an integrated RFEC probe for both flaw detection and thickness measurement.

II.18 Bubble Transportation Study inside PFBR Surge Tank using Water Model Experiment

Presence of argon bubbles in the secondary sodium circuit of SFR is a major concern which can cause various reactor operational problems. Argon bubbles can be from the locked up gas inside secondary sodium loop during filling or it can be due to continuous ingress of argon from sodium-argon interacting locations. These re-circulating bubbles get a chance to escape from the system to the cover gas through surge tank (ST) depending on the buoyancy and inertia forces acting on these bubbles inside ST. Therefore, if the gas bubble escape, probability through ST is sufficiently high, then over a period of time, the secondary sodium loop will be free from re-circulating gas bubbles until unless there is a constant ingress of gas from any other source. In order to quantify the escape probability of circulating gas volume in the secondary sodium circuit to the ST cover gas, experimental studies were carried out in a 5/8 scale geometrically similar water model of PFBR ST. The transportation of argon bubbles in sodium was simulated by injecting air bubbles to water through inlet lines of ST. Since the density difference between sodium and argon is nearly equal to that of water and air, the behavior of air-water mixture is similar to that of argon-sodium mixture. An arrangement for injection of measured quantity of air to both inlet lines of ST is provided in the facility. The quantity of air injected is measured using calorimetric air flow meters. Provisions are also made to measure the air volume released to the cover gas area of ST. The schematic of overall arrangement to quantify gas escaped to cover gas from ST is shown in Figure 1.

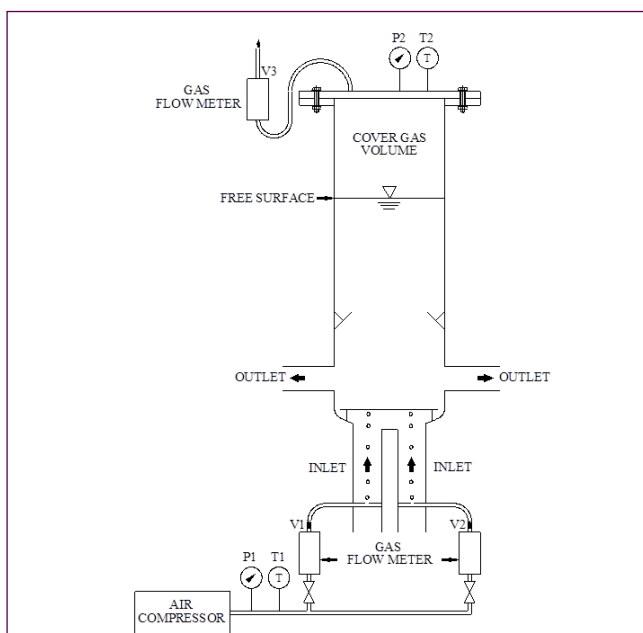


Fig. 1 The schematic of overall arrangement to quantify gas escaped to cover gas from surge tank

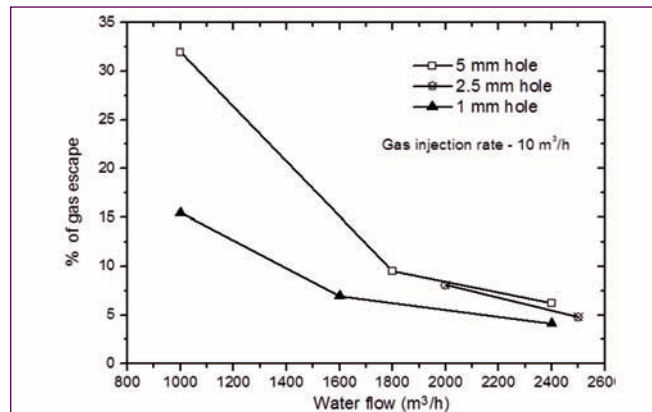


Fig. 2 Variation of bubble escape probability inside surge tank with water flow rate

From the experiments, it is found that for a constant rate of bubble injection to the ST, escape probability of bubbles reduces from 30% to 5% for an increase of water flow rate from 20% to 50% of nominal flow rate. When the water flow rate to the model is 50% of nominal flow rate and an air injection flow rate is 10 m³/h, 6% of the bubbles escape to the cover gas. When water flow rate to the ST increases, more bubbles are carried away by the flow to the outlets and the quantity of bubbles escaping to cover gas space reduces. It is also observed that, for a constant water flow rate to ST, more bubbles are escaped to the cover gas when the air injection rate to the inlets increases. The variation of bubble escape probability inside ST with (i) water flow rate and (ii) with air injection rate is depicted in Figure 2 and 3 respectively. By varying the hole size in the air injection nozzle, it is found that larger bubbles escape more to the cover gas. Lower sized bubbles are easily taken away by the water flow to the outlets. Also, a definite amount of gas escapes through surge tank to the cover gas in every pass depending upon the size distribution of the gas bubbles present in the flowing liquid.

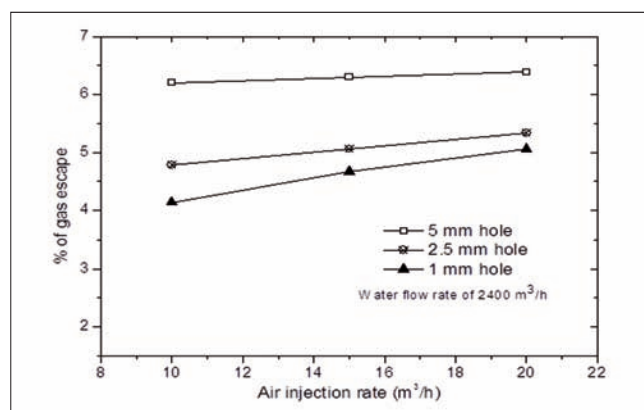


Fig. 3 Variation of bubble escape probability inside surge tank with air injection rate

II.19 Experimental Measurement of Leakage Flow Rate through DSR-Dashpot Interface in Water Facility

In PFBR, during SCRAM, electromagnets of Diverse Safety Rod (DSR) get de-energized to release the DSR for shutting down the reactor. DSR falls under gravity and is finally deposited on the dashpot. At shutdown condition, absorber rods (Boron Carbide) absorb energetic neutrons to bring down the neutron flux which results in heat generation within the absorber rods. To remove the heat generated, a minimum sodium coolant flow rate of 3 kg/s is required to pass through the mobile DSR. This flow rate through mobile DSR is 95% of the total flow rate (3.18 kg/s) which is passing through the DSR subassembly when it is deposited on dashpot. Therefore, only 5% of total flow shall leak through the DSR-dashpot interface. The schematic of flow paths during this condition is illustrated in Fig 1. It can be seen that there are two parallel flow paths: (i) Main flow through mobile DSR and (ii) Leakage flow through DSR-Dashpot interface. The flow between these two parallel paths is apportioned according to their relative hydraulic resistance.

The seat design of DSR-dashpot interface was simulated as in PFBR and an experimental study was conducted to validate this design. Accordingly, a simplified full scale water model of DSR-dashpot region was fabricated and experiments were carried out. The schematic of experimental test setup is shown in Figure 2.

The leakage measurement was carried out in the model considering the same apparent weight of DSR as in reactor, against a wide range of pressure drops across DSR-Dashpot interface. It was observed that the leakage flow is highly dependent on the positional alignment of the mobile DSR with respect to dashpot. Even a slight

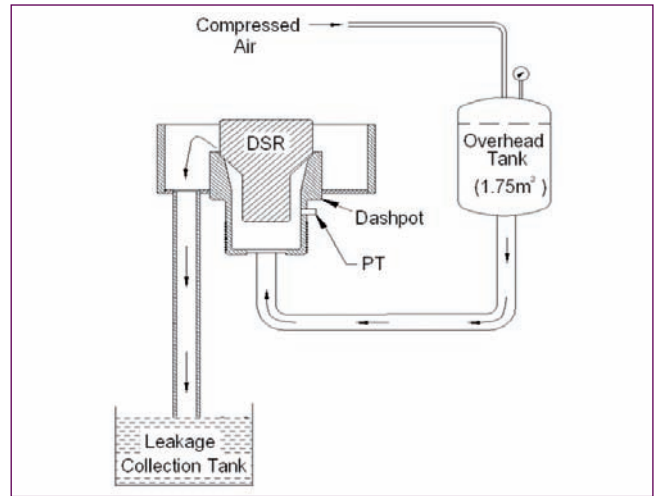


Fig. 2 Schematic of experimental test setup

change in the positional alignment alters the leakage flow considerably. Thus, DSR is positioned at different orientations and water leakage rate has been measured. All the experimental measurement data was transposed using appropriate similitude laws. The estimated sodium leakage rate against pressure drop across DSR-Dashpot interface in reactor is shown in Figure 3.

The variation in experimentally obtained leakage rate is high due to the high sensitivity of seat leakage with positional alignment. The estimated maximum sodium leakage rate through DSR-Dashpot interface including the prediction uncertainty is found to be 32.9 g/s which is around 1 % of the rated flow rate. However, the leakage value is much less than the maximum allowed value of 5%. Hence adequacy of hydraulic design of the interface is established.

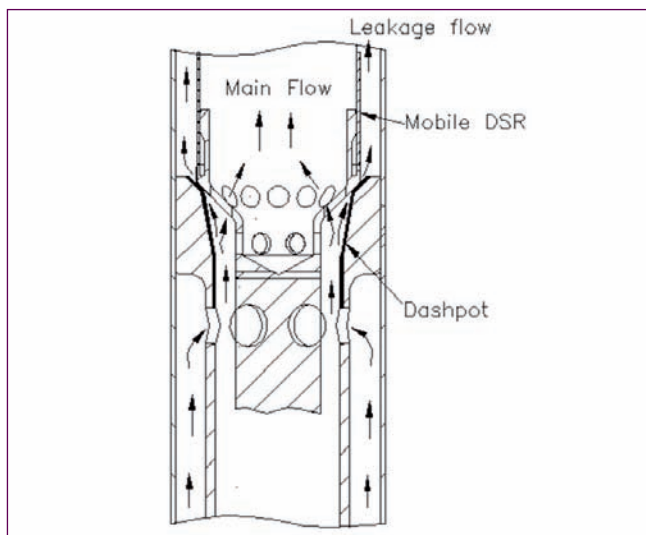


Fig. 1 Schematic of flow path in DSR-SA

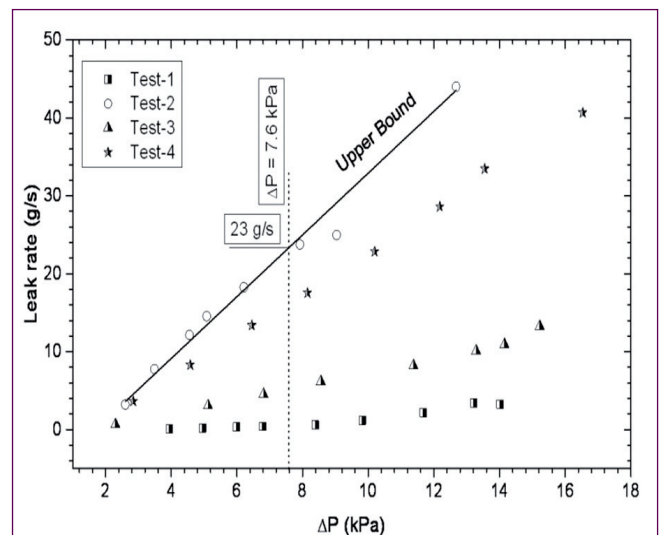


Fig. 3 Sodium leakage rate vs pressure drop

II.20 Quality Assurance and Testing during Procedure Qualification for Colmonoy Deposition on Stainless Steel Parts of Sodium Wetted Components of PFBR

Nickel based hard facing has been extensively used for PFBR sodium wetted systems, structures & components (SSC) where wear and tear at high temperature due to rotational/translational movement are of prime importance. Nickel based alloy colmonoy-5 has been chosen due to its excellent wear resistance properties at high temperature. Plasma Transferred Arc (PTA) process was selected for hard facing due to better dilution control and almost crack free weld deposition.

The Ni- based Cobalt free hard face powder RNi Cr-B (MOGUL N50P) as per PFBR specification (Table 1) has been used for Hard facing of PFBR parts like large size wear rings of secondary Sodium Pumps as shown in Figure 1 and Guide & Rail of transfer arm as shown in Figure 2. Typical Size of wear rings are 554 mm to 754 mm. The powder material for hard facing used is homogeneous with particle size of 45 to 125 µm.

Required thickness of Colmonoy weld deposit over SS 316L(N) base material shall be 150 to 200 microns as per Specification.

Hard facing: After thorough cleaning, qualification test coupon was mounted on PTA machine at 1G welding position. Then, the same was preheated to a range of 400-450°C by suitable electric coil heaters. Once the temperature of 450°C is attained, PTA machine was set to control the deposition parameters such as powder flow rate, welding current range (70-100 A), voltage (25-30 V) and travel speed (80-100 mm/min.). Weld deposition was carried out on base material surface in multi-pass layers from one end to other end until required thickness is achieved. After weld deposition, post-heating of test coupon was maintained at 400°C for 15 minutes with slow cooling under the cover of vermiculite powder to prevent any cracks. Subsequently, Post-weld heat treatment was carried out in a calibrated furnace at 850°C (max) with soaking period of 2.5 min./mm & rate of heating 100°C/hr (max). Subsequently, slow furnace cooling is effected to remove internal stresses developed during hard facing.

Quality Assurance: The following additional testing & qualifications performed in addition to ASME Section IX (Code for welding procedure & performance qualification)

as per PFBR specification. Before weld deposition on actual parts, a Production Test Coupon (PTC) was made simulating same shape, size of part, welding position, number of weld layers, minimum deposit thickness and Chemical composition test, Non-destructive testing & hardness measurements was carried out. Weld deposition on PTC representing guide & rail of transfer arm was carried out using Automatic PTA welding and performed all the above destructive & non-destructive tests. Based on successful test results of test coupon, procedure for hardfacing was approved.

Hard facing of actual parts were performed using qualified procedure. Inspection activities such as raw material identification of base material including Chemical analysis of Hard facing powder using X Ray fluorescence method, monitoring & controlling of welding parameters and interpass temperatures were carried out during welding. Visual and Dimensional Inspection and Liquid Penetrant testing using visible solvent removable method were performed.

Ultrasonic examination using pluse echo contact technique was carried out using reference block with dia 3.2 mm Flat Bottom Hole (FBH) & dia 2 mm Side Drilled Hole (SDH) to ensure soundness of the weld.

Test results reveals that dilution in the microhardness profile across hard facing is of the order of 0.5 mm from base metal and also variation in line hardness tests is within limits. Average surface hardness (10 data points) is found to be 50 HRC against the requirement of 45 to 50 HRC. With optimized welding parameters and better dilution control, undiluted weld deposition within 1.5 to 2 mm from base metal substrate after final machining is achieved. Stringent dimensional requirements with close tolerances such as radius, profile, surface finish within 0.4 µm, perpendicularity of 0.05 mm on transfer arm rails and concentricity of 0.06 mm on inner diameter of casing wear rings were achieved.



Fig. 1 Large size wear rings



Fig. 2 Guide-rail

Table 1 : The Chemical composition

Element/grade	RNi Cr-B as per PFBR (%)	Mogul N-50 Powder (%)
C	0.4 to 0.8	0.45
Cr	10.0 to 16.0	13
B	2.00 to 4.00	2.5
Si	3.0 to 5.0	3.4
Fe max.	7.00	4.5
Co Max.	0.25	0.05
Ni	Balance	Balance
Hardness(HRC)	45-50	49

II.21 Touch screen based Virtual Control Panel for Control Room Application in NPP

Modern control rooms and their Human Machine Interfaces (HMI) are designed, operated and maintained to match with human cognitive processing abilities and thus increase performance and reduce the likelihood of human errors. In order to improve the usability of manually operated devices, a touch screen based Virtual Control Panel (VCP), consisting of a high quality multi-touch screen units were installed & commissioned as shown in Figure 1.

Each of the vertical panel is assigned to a dedicated display station for Safety Class-1/2/3, NINS and Electrical Systems. Lower panel in each vertical is dedicated to control console whereas middle and top panels are earmarked for process display and alarm indication as shown in Figure 2. Initially, pre-developed plant GUIs were ported on to the VCP platform and simulation was completed. Virtual components in place of actual components like display meter, control knob, sliders, switches, etc. were developed using QTab widget classes and tested. This helped in validating the robustness and adequacy of control room components. The same facility has been utilized to test the Main Control Room (MCR) operation with the aid of PFBR full scope replica Operator Training Simulation i.e KALBR-SIM which is developed, tested and commissioned at IGCAR. KALBR-SIM integration with hardware panels has been replaced with the touch based soft screens. The MCR panels are segregated as annunciation, display & control screen to fill the vertical touch panel arrangement and soft screens are developed using GUI tool for all Control/console panels (Figure 3).

Socket management software has been introduced to populate the soft panels with the data obtained from simulation computer, fetch and communicate the control operations carried out on the soft panels and update the

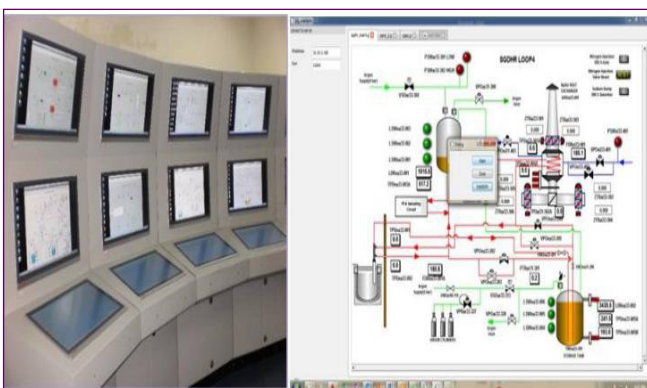


Fig. 1 Touch screen based virtual control panel and its application

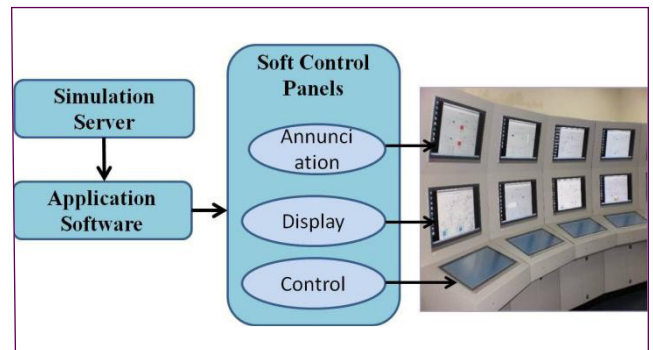


Fig. 2 Signal flow between simulation server and touch based control panel

plant variables in the simulation computer.

Integrated testing with simulator flow sheet has been carried out for different plant operating conditions to evaluate the performance of modern touch screen based control room as shown in Figure 4.

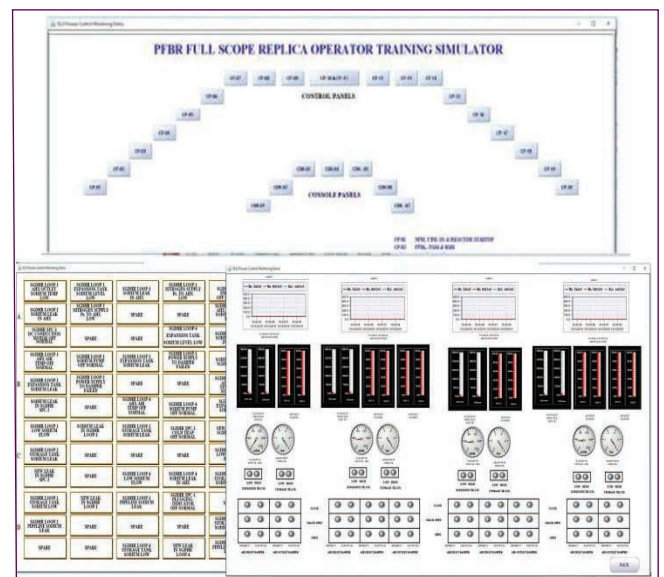


Fig. 3 Soft control panels with annunciation, display and control

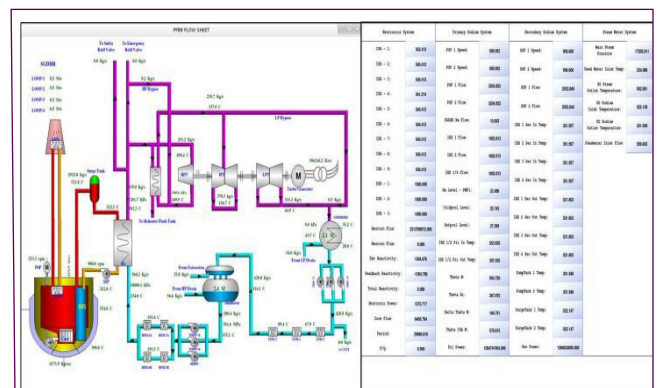


Fig. 4 Integrated testing with simulator flow sheet and result screen

II.22 Enhancement of Safety and Security Features of Computer Based I&C Systems of PFBR

Computer based I&C systems of PFBR include control nodes implemented using VME bus based computers, process computers and display stations (Figure 1). These systems are classified as Safety class 1, 2 or 3 based on the criticality of the functions they perform. They are subjected to multiple levels of review and audit by safety committees. Based on safety committee recommendations, safety and security of the embedded system software and Distributed Digital Control System (DDCS) software were enhanced by incorporating additional data integrity checks on memory as well as data packets for ensuring integrity of communication over the plant network. Additionally, Operating System (OS) hardening, VT100 terminal emulation with hardened OS for Core Temperature Monitoring Systems and implementation of network security were carried out.

For all control nodes that are part of the DDCS network of SC-1, SC2 and SC-3 classification, in order to improve robustness and security, the application software was modified to include the following additional integrity checks in addition to the existing self-diagnostic checks.

1. Cyclic Redundancy Checks (CRC) (using 32-bit CRC polynomial) to verify the integrity of program memory on power-on as well as periodically subsequently.
2. CRC check to verify the integrity of configuration data residing in the RAM every scan cycle.
3. Application level CRC checks on data and control packets sent / received from other DDCS components

In RTC-based Core Temperature Monitoring System which is an SC-1 system of PFBR, a VT100 terminal is required for local configuration of set points and other parameters. Due to the non-availability of VT100 terminals, a personal computer was used for emulating the VT100 terminal connected to Core Temperature Monitoring System through serial port. For this the computer was hardened by enabling only processes necessary for terminal emulation to run and disabling other processes.

RHEL OS running on display stations and process computers was hardened by configuring system and network components properly, removing unnecessary applications and services. As part of hardening while loading the OS only those base packages were selected which will be required for running the application software. While porting DDCS application into the OS only those runtime libraries of Qt are ported which are required for the application software. Finally all unnecessary services, users were removed and ports not to be used were blocked. Firewall was also configured to block unnecessary network traffic.

The architecture of the DDCS network implemented in PFBR was studied and a network layout diagram was made and compared for compliance with DDCS architecture. Various network hardening features including MAC-binding and blocking of HTTP access were configured and tested on the switches.

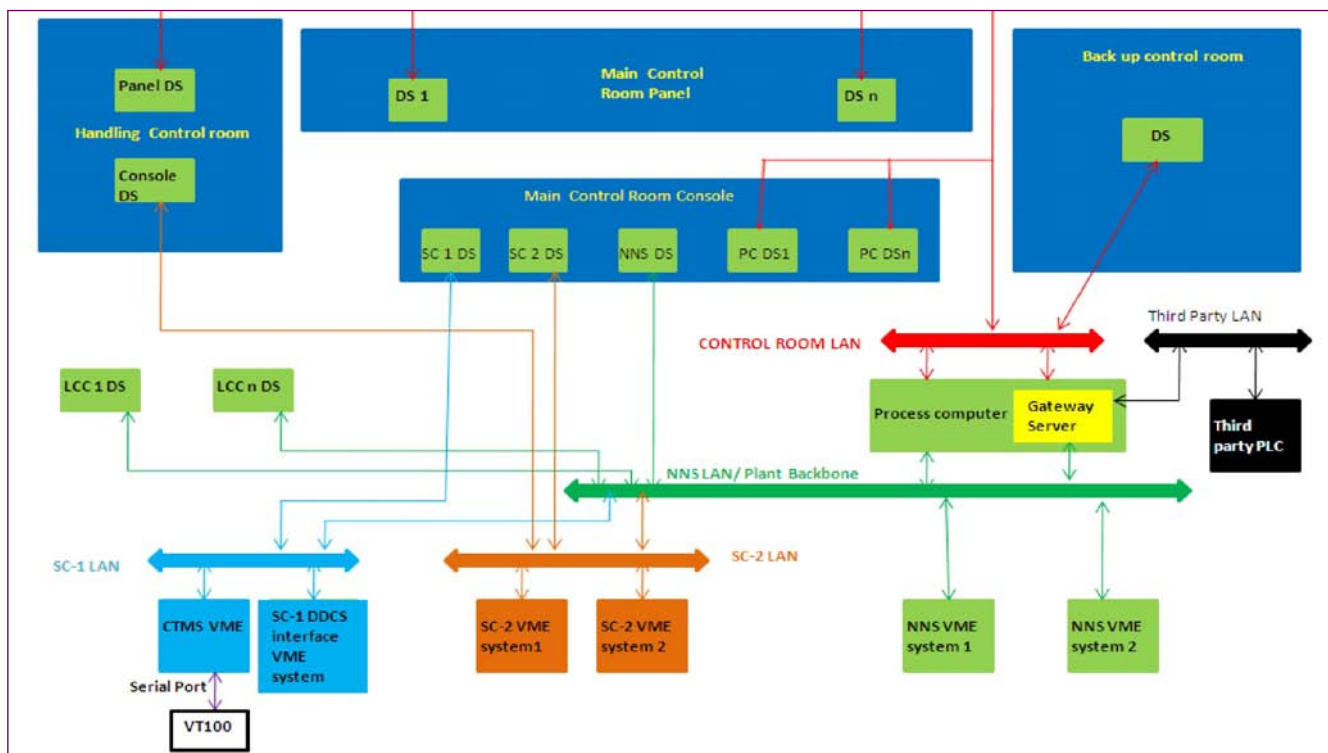
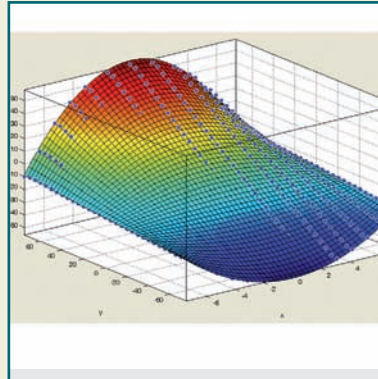
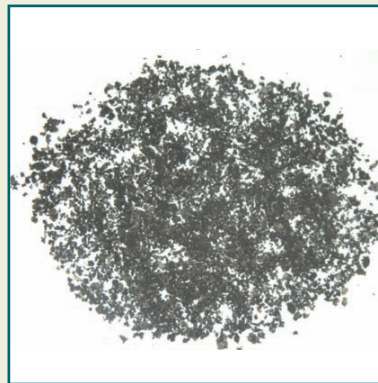
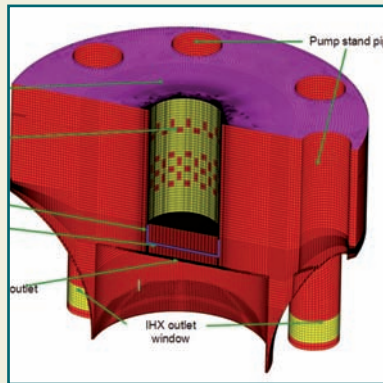


Fig. 1 Architecture of computer based I&C of PFBR



CHAPTER III

Research &
Development for FBRs

III.1 Steady State and Transient Pool Hydraulics for Future FBR

Future commercial fast reactors are envisaged to have twin-unit concept, with each unit generating 1500 MW of thermal power. The reactor vessel and coolant flow rate in the heat transport circuit are sized accordingly. It is essential to have the hydraulic design of reactor pools made in such a manner that the pool thermal hydraulic issues, viz., gas entrainment, thermal stratification, flow induced vibration of thin structures etc. are very well managed. Argon cover gas is maintained above the free surface of hot and cold sodium pools of primary sodium circuit. The free surface is turbulent in nature and the maximum free surface velocity is to be limited below 0.5 m/s to avoid the entrainment of argon. This can be achieved by providing a baffle attached to inner vessel. The axial location and width of baffle strongly influence the maximum free surface velocity and this needs to be optimised.

In this context, a 3D 180° sector model (Figure 1) of hot pool is developed using CFD software to carry out thermal hydraulic analysis. Parametric study with varying horizontal baffle width (100 mm to 900 mm) showed that minimum free surface velocity of 0.525 m/s is observed when the optimum baffle width is ~400 mm. The provision of vertical baffles on the inner vessel does not offer significant benefits in reducing the free surface velocity. However, providing two radial baffles of 400 mm width each at two different axial locations on the inner vessel, reduced the maximum free surface velocity to 0.44 m/s (Figure 2). Hence, this baffle configuration is recommended for FBR1&2.

Transient thermal loading on hot and cold pool components is one of the very important mechanical loading to be established for the thermo-mechanical design of reactor assembly components. Among the various design basis events that cause this loading,

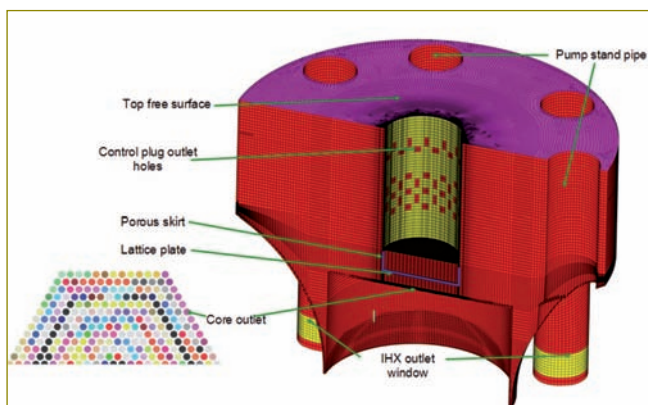


Fig. 1 Computational mesh of hot pool

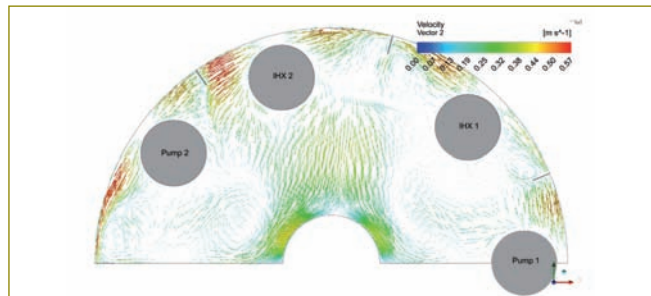


Fig. 2 Velocity vectors (m/s) of sodium at the free surface with the finalized horizontal and vertical antigas entrainment baffle

reactor SCRAM (due to cold shock) and trip of one secondary sodium pump (due to asymmetric thermal loading) are the main events governing the design of hot and cold pool components respectively.

Three dimensional transient analysis of flow and temperature evolution of sodium in hot pool of FBR1&2 have been carried out to predict the velocity and temperature distribution during SCRAM event. At the CP surface, the temperature contours (Figure 3) shows a stratification interface above holes in the CP shell and window of IHX-1. Stratification interfaces are also observed on the IV surface at time t=15 s which moves upwards with time.

At the IHX inlet window, a ΔT of 5 K is observed in the sodium stream entering it initially and the same increases to as high as 39 K during the transient.

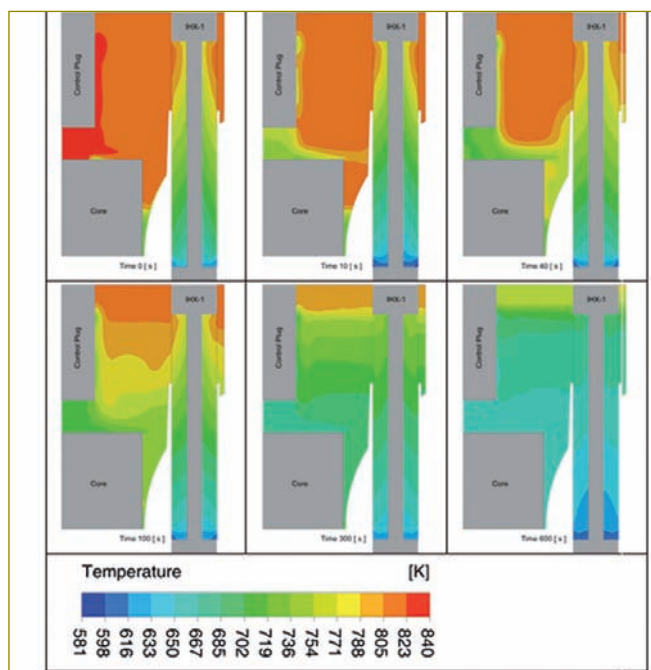


Fig. 3 Temperature contours (K) of sodium in the plane passing through IHX-1 at various instances

III.2 Plant Dynamics Studies Towards the Design of Plant Protection System of Future FBR

FBR-1&2 are commercial twin unit reactors in the second stage of Indian nuclear program which are being designed for a capacity of 600 MWe each. The safety of FBR-1&2, as for any other nuclear power plant, is evaluated by analyzing the plant response to various events affecting the safety of plant. This constitutes the plant dynamics studies.

DYANA-P is the in-house developed plant dynamics code for carrying out plant dynamics studies for PFBR. This code has been modified towards applying it for plant dynamic studies of FBR-1&2 and the modified code is designated as DYANA-P V2.0. The major modifications are for addressing the important design differences of FBR-1&2 from PFBR, viz., (i) the configuration of axial blanket in fuel subassemblies (lower axial blanket alone is present in FBR-1&2), (ii) the number of primary sodium pumps (two in PFBR whereas three in FBR-1&2) and (iii) the number of steam generator modules in each secondary sodium loop (four in PFBR whereas three in FBR-1&2).

Towards the safety analyses of FBR-1&2, nine enveloping events occurring both at full power conditions and plant operation with two out of three primary sodium pumps (2/3 PSP mode) in service have been analysed. To begin with, set of reference inputs related to Design Safety Limits (DSLs), list of SCRAM parameters and their threshold values, error in threshold settings, response time of safety instruments, flow halving time of sodium pumps, sympathetic safety action, drop behavior of absorber rods, hot spot factors etc. have been considered to be same as that established for PFBR design.

Some typical results from the simulation are shown in

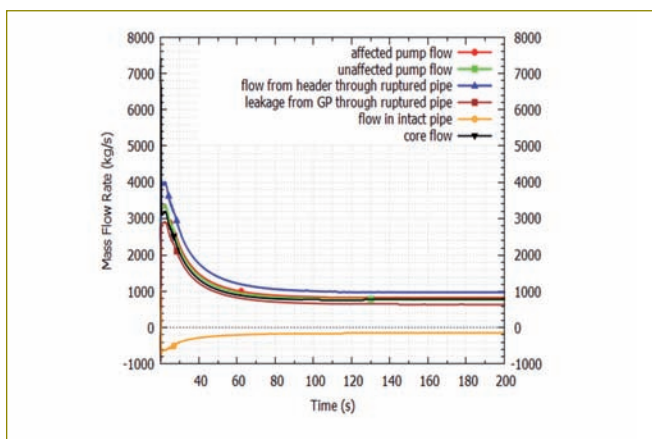


Fig. 1 Evolution of flow rates in the primary circuit during one primary pipe rupture at full power conditions

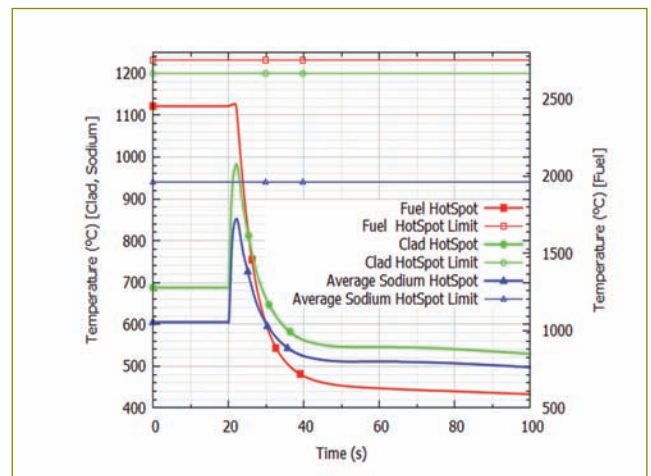


Fig. 2 Evolution of core hot spot temperatures during one primary pipe rupture at full power conditions

Figures 1 and 2. For all the events, SCRAM initiated based on the second appearing parameter is able to limit the consequences below the DSLs specified for the respective category of the event. Hence, safety of the reactor is ensured against the various enveloping events analysed. The SCRAM parameters available for various enveloping events are listed in Table 1. It is seen that for FBR1&2, the SCRAM parameters, viz., low primary pump speed (N_P) and low head developed by primary sodium pump (ΔH_P) (assessed to be essential for PFBR) can be omitted without compromising safety. This is due to the other parameters in the list being able to provide the required level of plant protection.

In order to design the instrumentation for measurement of various SCRAM parameters, the maximum permissible response time of various measurements needs to be specified. The permissible response time should be such that the consequences following various DBEs are limited within the respective category DSLs as per design criteria. With this objective, thermal hydraulic analysis of five enveloping DBEs (one control rod inadvertent withdrawal, one PSP trip, one PSP seizure, offsite power failure, primary pipe rupture) for which the consequences can exceed the respective category DSL has been carried out at full power and 2/3 PSP mode operating conditions.

It has been considered conservatively that the consequences of each event are to be limited within the DSLs of the category to which the event belongs with SCRAM by both 1st and 2nd SCRAM parameters except for one PSP seizure event at 2/3 PSP operating condition. For this event alone, the consequences are

considered to be limited below DSL for higher category with SCRAM by second parameter. This is in line with the safety criteria specified for the SCRAM parameters. A typical simulation result along with the approach followed for estimation of response time of an associated instrument is in shown in Figure 3. From the simulations, the permissible delay times for instruments (including trip logic delay and electromagnetic clutch release time of CSR & DSR) are worked out. The same worked out for critical instruments is given Table 2. The actual response time of SCRAM instruments established for PFBR are less than the permissible values established presently for FBR-1&2. The response times for other SCRAM parameters are not very critical from plant protection point of view. Therefore, they can be designed with a response time as low as practically possible in line with the design established for PFBR.

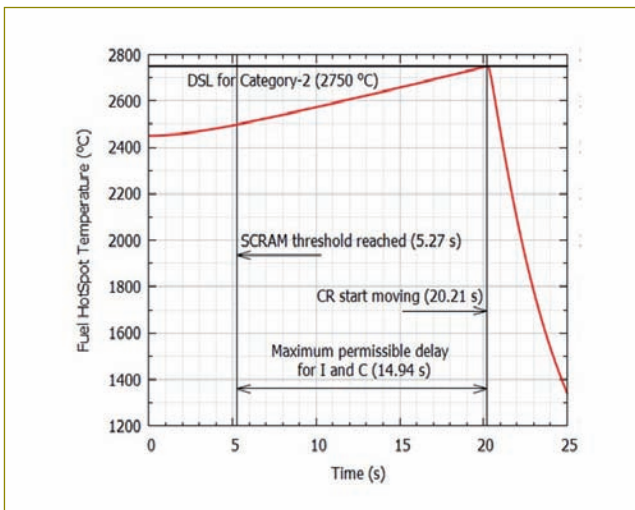


Fig. 3 Evolution of fuel hot spot temperature during one CSR withdrawal with SCRAM by shut down system-1 at full power conditions

Table 1: SCRAM Parameters Available for Various Enveloping DBEs

S I . No.	Enveloping DBE	SCRAM Parameters Available		
		SDS-1		SDS-2
		Full power cond.	2/3 PSP cond.	Both conditions
1	Inadvertent Withdrawal of One Control Rod	LinP, ρ , P/Q	LinP, ρ , P/Q	θ_{CSAM} , $\Delta\theta_{CSAM}$
2	One PSP trip	NP, P/Q, ΔH_P	NP, P/Q, ΔH_P	θ_{CSAM} , $\Delta\theta_{CSAM}$
3	One PSP seizure	NP, P/Q, $\Delta H_P, \rho$	NP, P/Q, ΔH_P	θ_{CSAM} , $\Delta\theta_{CSAM}$
4	Offsite Power Failure	NP, P/Q, $\Delta H_P, \rho$	NP, P/Q, ΔH_P	θ_{CSAM} , $\Delta\theta_{CSAM}$
5	One Primary Pipe Rupture	P/Q, $\Delta H_P, \rho$	P/Q, ρ , ΔH_P	θ_{CSAM} , $\Delta\theta_{CSAM}$
6	One Secondary Sodium Pump (SSP) trip	θ_{RI}	θ_{RI}	θ_{CSAM}
7	One SSP seizure	θ_{RI}	θ_{RI}	θ_{CSAM}
8	Loss of Feed water Flow to Steam Generator (SG) in Both Loops	θ_{RI} , ρ	θ_{RI} , ρ	θ_{CSAM}
9	Loss of Feed water Flow to SG in One Loop	θ_{RI}	θ_{RI} , ρ	θ_{CSAM}

Table 2: Permissible Delay Times for Critical Instruments

SCRAM parameter	Limiting Event	Limiting DSL	Allowable Time Delay	Actual time delay achieved in PFBR	Margin
ρ	One control rod withdrawal at full power	Fuel Hot Spot Temperature	14.94 s	4.3 s	10.64 s
P/Q	One PSP Seizure at 2/3 mode	Clad Hot Spot Temperature	1.36 s	1.1 s	0.26 s
θ_{CSAM}	Offsite power failure at full power	Clad Hot Spot Temperature	2.60 s	1.04 s	1.56 s

III.3 Design of a System to Localise Failed Fuel Pin at Dry Rupture Stage in FBR

The fuel pin failures are classified as dry rupture and wet rupture. A dry rupture event is accompanied by only emission of gaseous fission products mainly isotopes of Xe and Kr into sodium pool without fuel-coolant interaction. During wet rupture, sodium enters into fuel pin and interacts with fissile fuel. In PFBR, there is provision for detecting and localising fuel pin failure at wet rupture stage. Currently it is decided to localise failed fuel subassembly at dry rupture stage itself, so that it can be replaced with a fresh fuel subassembly, if required.

There are various identification methods available for a dry rupture detection which includes gas tagging, gas stripping, dry sipping, wet sipping, ultrasonic monitoring system, gas separation by centrifugal action etc. The gas stripping is found to be the best suitable option for PFBR.

The fission gases (isotopes of Xe & Kr) are γ emitters. The purpose of gas stripping system is to separate the fission gases from sodium and send to γ detectors placed outside the reactor. Xe and Kr will be present in the form of bubbles in sodium due to their very low solubility. The fission gas separation is achieved by purging fresh argon into sodium sample containing fission gas bubbles. When fresh argon come into contact with fission gas present in sodium, diffusion of these gases takes place. A sample of this gas is then sent to γ detectors. The presence of fission gases in the gas sample will be confirmed by γ detection, which confirms the dry rupture of fuel pin.

Wet rupture detection is done by selectively sampling sodium from each subassembly with the help of selector valve, DC conduction pump and associated sampling

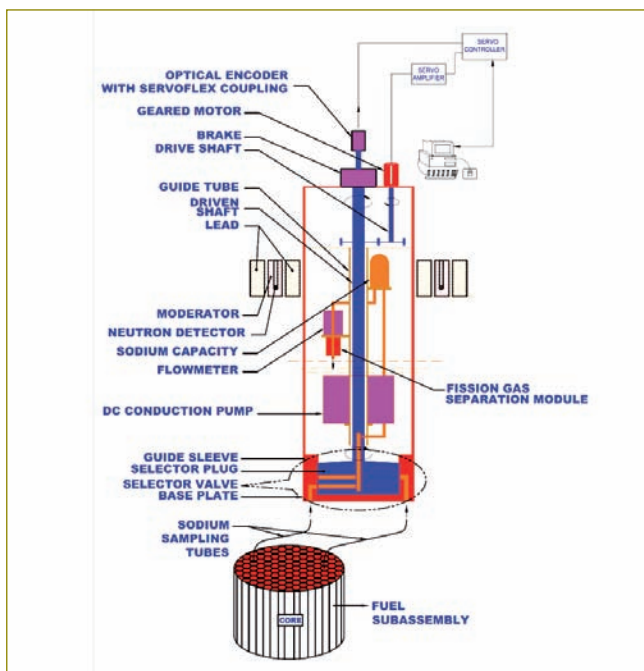


Fig. 1 Schematic of FFLM

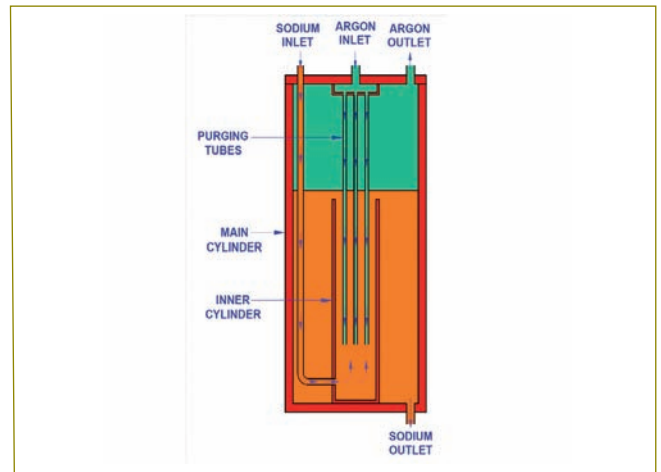


Fig. 2 Fission gas sparging module

tubes of FFLM and sending it to a capacity for delayed neutron detection.

A fission gas Sparging Module (FGSM) is designed and is to be retrofitted in FFLM for separating fission gas from sodium sample (Figure 1). Detail of FGSM is shown in Figure 2. It consists of two concentric cylinders. Sampled sodium enters into inner cylinder, from its bottom end. After filling the inner cylinder, sodium overflows and enters into main cylinder. A small opening is provided at the bottom of main cylinder through which sodium returns back to existing sodium line. Fresh Argon for fission gas stripping is supplied to a header, provided at the top and distributed in the inner cylinder through small tubes. FGSM is designed to provide maximum possible retention time for sodium in the capacity so as to increase the probability of interaction of stripping gas with fission gas bubbles. The purged gas along with fission gases get collected in the space above sodium free level. Gas samples will be taken from this space and supplied to gamma detectors through a tube connected to the top end of the capacity.

CFD analysis has been carried out to finalise the design of FGSM by optimising the flow characteristics of sodium and tube configuration for maximum sparging efficiency. CFD model and results of the selected tube configuration is given in Figure 3. The design is being validated by testing.

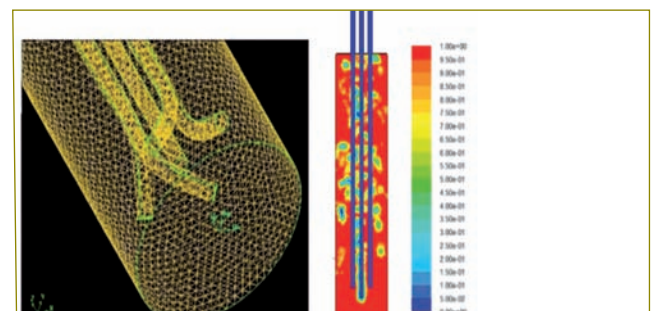


Fig. 3 CFD module for optimisation studies

III.4 Study on Translation Characteristics of DSRDM & DSR in Bowed DSR Subassembly

There are two independent, diverse and fast acting shutdown systems in PFBR. The Diverse Safety Rod (DSR) and its drive mechanism (DSRDM) forms the part of second shutdown system. Three DSR sub assembly along with DSR are mounted on third row of the grid plate. The DSRDMs are housed in Control Plug and are in line with DSR. Theoretically both DSR and DSRDM are in line. However, in the actual operating conditions,

there is misalignment between DSRDM and DSR subassembly due to various causes. Irradiation induced bowing of DSR subassemblies is one of the major causes. A study is carried out to confirm the adequacy of EM holding force requirement during translation of DSRDM and DSR inside bowed subassembly. A parametric study was also carried out taking 10% uncertainty in the governing factors. Finite element analysis at few crucial junctures during translation of DSRDM & DSR was carried out to estimate required EM holding force. Figure 1 shows the Schematic of DSRDM with Bowed DSR.

When DSRDM enters DSR subassembly, the misalignment has to be accommodated by bending of DSRDM & DSR subassembly. The DSR subassembly becomes fourth guide for mobile assembly. Upon further lowering of mobile assembly, the translation tube & EM travel inside the DSR subassembly. Finally EM enters the DSR head. The conical support of DSR in DSR subassembly acts as a pivot, DSR can rotate as a rigid body when load is applied at the top, until the clearance between piston and dashpot gets closed. Beyond that the misalignment has to be accommodated by bending

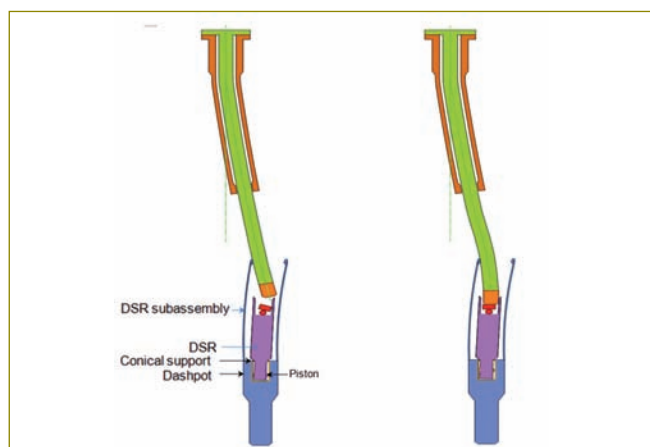


Fig. 1 Schematic of DSRDM & DSR before and after coupling

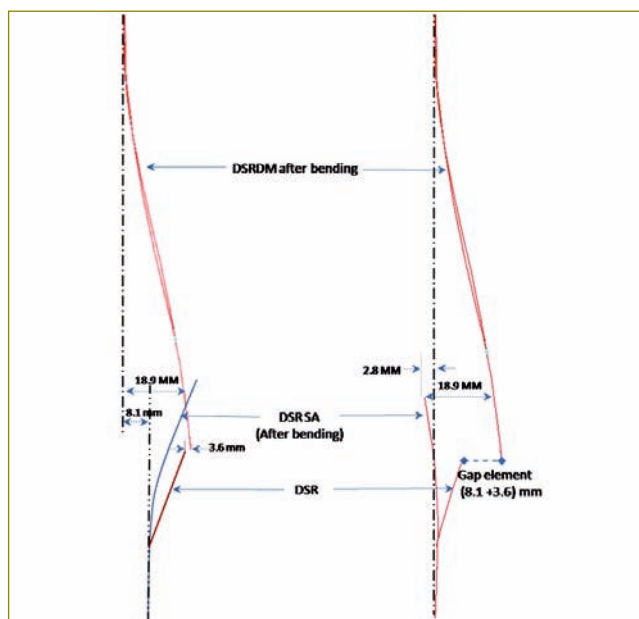


Fig. 2 Structural equivalent schematic of bowing analysis of DSR & DSRDM

of DSRDM and DSR. This is shown in Figure 1. Hence a reaction force is generated at EM –armature interface. The force at DSR top results in reactive forces at DSR – DSR subassembly interfaces and consequent frictional resistance results in higher EM holding force requirement for lifting DSR.

DSRDM, DSR subassembly & DSR were modeled as beam elements. The model was validated using experimentally measured stiffness values. In order to realistically simulate all the flexibilities and kinematics in the system, a structurally equivalent analysis methodology was worked out and EM holding force requirement was estimated. Figure 2 shows the structural equivalent schematic of DSRDM coupled with DSR in bowed subassembly. The estimation shows that the maximum lifting capacity is required at deposited condition of DSR and lifting capacity of EM with ~ 1A current is required to lift and translate the DSR in bowed subassembly A parametric study on DSRDM & DSR translation in bowed subassembly has been carried out to understand the effect of various parameters on the EM holding force requirement. The analysis shows that after accounting for 10 % uncertainty in all the factors, EM holding current of 1.2 A would be required to lift the DSR at 200°C. Hence it is concluded that the EM capacity is sufficient to lift the DSR in bowed subassembly.

III.5 Application of state-of-the-art Open Source Computer Codes OpenMC and NJOY-21 for FBR Core Neutronic Simulations

Monte Carlo (MC) based particle transport codes are well known for their application in Reactor Physics for solving problems in complicated geometries. Though there is a wide collection of MC based codes, with excellent capabilities, most of them are not licensed to all users. OpenMC, an open source MC based neutron transport code, is released in 2014, as a result of the work done by Computational Reactor Physics Group at MIT (Massachusetts Institute of Technology). The present version of this code has the capability to handle hexagonal geometry, and are found to be suited for FBR neutronics studies. In the meantime, NJOY-21, a nuclear data processing code is also released with an open source license. These two code systems have been installed at 400-node IVY high performance computing cluster in IGCAR with the objective of enhancing our FBR core neutronics simulation capabilities with the provision of using state-of-the-art nuclear data libraries along with a 3-D MC code with advanced features. The method of applying NJOY-21 and OpenMC code systems for FBR neutronics study is shown in Figure 1.

The first step involves the preparation of a continuous energy point cross section library for all important nuclides from ENDF-6 files in HDF5 format. The second step is providing the geometry and material information using separate '.xml' input files. The NJOY-21 and OpenMC system has been applied to studying core parameters of PFBR such as k_{eff} , sodium void worth and control rod worth. The results have shown excellent agreement with existing PFBR design estimations.

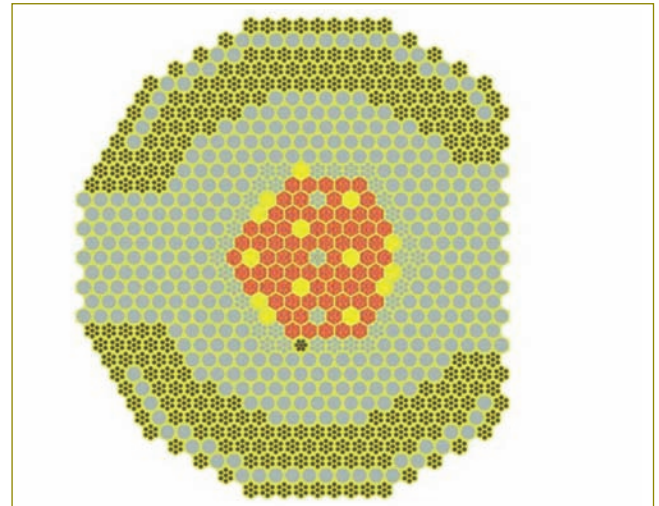


Fig. 2 Simulated CEFR core as a part of validation of OpenMC

This system is also used to simulate startup tests of Chinese Experimental Fast Reactor (CEFR) as part of an IAEA Coordinated Research Project (2018) in the “blind-phase” (Figure 2). Some of the experiments conducted during the first startup of CEFR, viz. fuel loading, first criticality, absorber rod worth measurement, reactivity coefficients measurement, foil activation (flux) measurements, were comprehensively analyzed. Analyses were done with ENDF/B VIII.0, JEFF 3.3, ROSFOND 2010, TENDL 2017, JENDL-4.0 and CENDL-3 data. OpenMC ‘blind’ predictions showed excellent agreement with the measured data. This exercise helped us to validate NJOY-21 and OpenMC system.

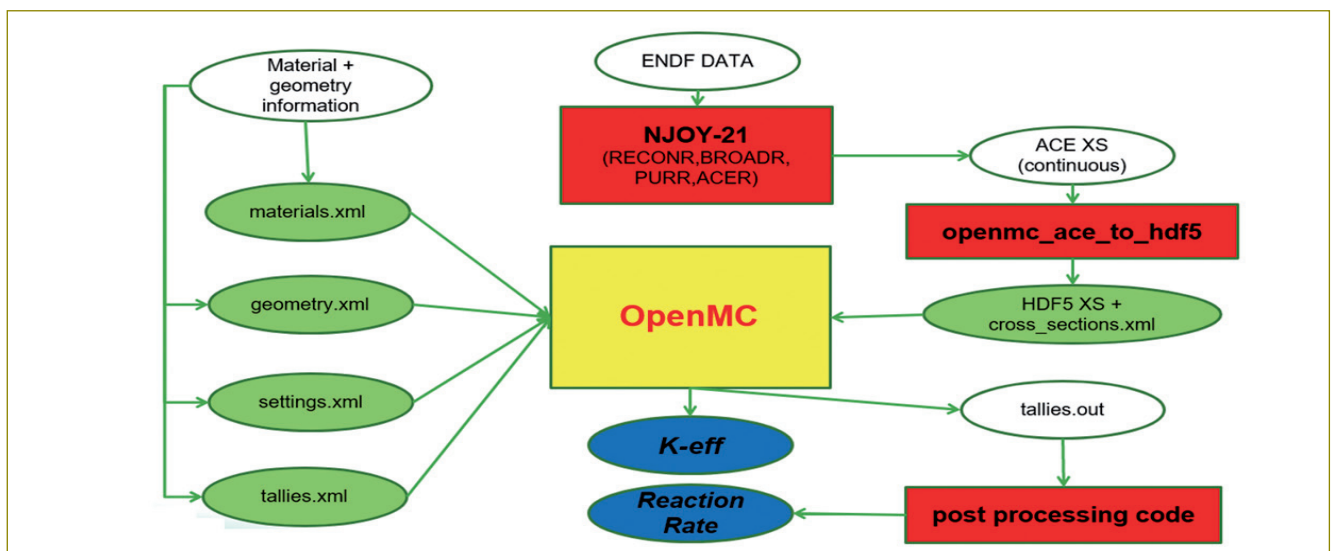


Fig. 1 Methodology of FBR neutronics simulation using NJOY-21 and OpenMC

III.6 Technology Development for Manufacture of Hardfaced Wear Rings for Sodium Pumps

Primary and Secondary Sodium Pumps circulates the liquid sodium in primary and secondary sodium main circuit of Fast Breeder Reactor. A typical Secondary Sodium Pump (SSP) comprises of three sub-assemblies namely, 1. Pump Outer Shell, 2. Inner static assembly and 3. Inner rotary assembly as shown in Figure 1.

Wear rings are provided between impeller and casing at suction as well as at delivery side as replaceable component in case of its wear & tear. The casing wear rings are static and impeller wear rings are rotary in nature. Even though the wear rings are not expected to have contact during pump operation, as a part of in-house technology development, work was undertaken to manufacture hard faced wear rings.

One set of wear rings has been manufactured using AISI 304 LN grade austenitic stainless steel as base metal and nickel based material as hard face coating, at Central Workshop, in accordance with the PFBR specifications.

The size of the wear rings chosen for hard facing is closer to the SSP of PFBR. The mating surfaces of suction side wear ring are $\varnothing 750H7 / \varnothing 748g6$ having 85 mm height and delivery side wear rings are $\varnothing 560H7 / \varnothing 558g6$ with a height of 60 mm. Manufacturing of wear rings involved cutting of 120 mm thick stainless steel slab to near net shape of wear rings using CNC abrasive water jet cutting machine, followed by pre-machining as shown in Figure 2a. It was preheated to 550°C and the same temperature was maintained throughout hard facing period (~ 4 hours) and post weld heat treatment was done at 750°C using innovative unique electrical resistance heating enclosure with job rotating facility (to facilitate the hard facing of curved outer / inner surfaces) as shown in Figure 2b). Proof machining of hard faced wear rings was carried out using coated tungsten carbide inserts and dimensional stabilization heat treatment was carried out at 500°C using induction heat treatment facility. The final machining was carried out using Cubic Boron Nitrate (CBN) inserts to achieve the specified surface finish.

The pre-machined wear rings were subjected to dimensional inspection, surface hardness measurements, liquid penetrant examination and ultrasonic examination before hard facing to ensure that the parent metal is free from defects. The same inspection techniques were used after proof machining to ensure the hard faced portion is free from crack and lack of bonding. The finished wear rings as shown in Figure 2c, were again subjected to dimensional inspection, ultrasonic testing, Hardness testing and surface finish measurements.

- Dimensional Tolerance: +/- 30 μm
- Coating Thickness : 1.9 to 2.2 mm
- Surface Finish: Better than 0.4 μm [Ra]
- Surface Hardness: 43 to 47 HR_C
- Variation in surface Hardness : less than 5 HR_C

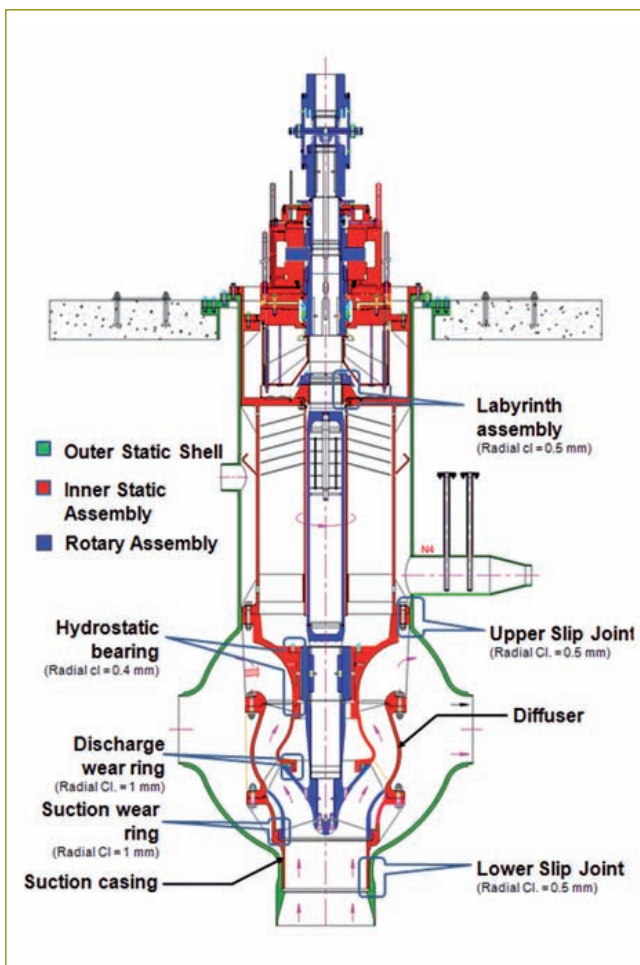


Fig. 1 Assembly segments of a typical SSP

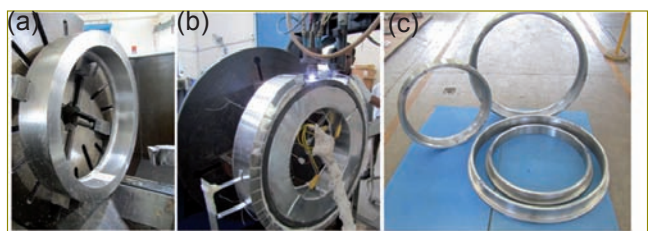


Fig. 2 (a) Pre machining, (b) Hard facing on PTA with electrical resistance heating enclosure and (c) Machined wear rings

III.7 Indigenous Development of Inflatable Seals in Silicone

In fast breeder reactors, to facilitate positioning of in-vessel fuel handling machine over desired fuel subassembly location, two rotatable plugs mounted over large diameter bearings are provided. The interface between the rotating and non-rotating members of the plugs forms boundary for primary radioactive argon cover gas and is sealed with a set of Inflatable Seals as a primary barrier. These are special type of seals, which should meet the operating conditions like high temperature of 100°C (max.), compatibility with sodium aerosols, resistant to gamma dose and long life. These conditions demand use of fluorocarbon or silicone as seal material. PFBR inflatable seals are imported seals and are made of silicone rubber. Hence, indigenous development of these seals in silicone is taken up.

Developmental activities were initiated with the objective of developing a test seal of $\phi 2\text{m}$ so that the same can be qualified in the test rig available at IGCAR before clearing for reactor application. Though the actual seal diameters are $\phi 6.3\text{m}$ & $\phi 4.2\text{m}$, the selection of reduced diameter of $\phi 2\text{m}$ for test seal is justified as matching the seal rubbing speed and inflation pressure are more important to simulate the seal operating conditions and further, a $\phi 2\text{m}$ with two joints is also quite big to simulate joint & length effect, if any. With the experience of previous seal development, a strategy was worked out to exploit the expertise available in rubber industries and a detailed technical specification was prepared.

The development was divided into two stages:

Stage -1:

Development of seal through extrusion/moulding, testing and manufacture of 4 m continuous length of seal.

Demonstration of end joining, meeting the splice strength and other visual quality.

Demonstrating inflation pressure and leak tightness using $\phi 0.5\text{m}$ seal in a Perspex rig (since no rotation



Fig. 1 Inflatable seal being extruded



Fig. 2 Seal being extruded

is planned, $\phi 0.5\text{m}$ is justified to meet the intended objectives).

Stage-2:

Five Nos. of 2 m diameter inflatable seals with Teflon coating over the sealing surfaces.

Process Flow:

Following process flow diagram was followed for the seal development:

Incoming Inspection of raw material → Batch mixing as per mixing ratio → Test slab and Button preparation → Test slab and Button inspection → Trial extrusion and inspection → Production seal extrusion → Nozzle built-up → End joining → Curing → PTFE coating and curing → Testing → Final inspection → Packing & despatch

Material:

Silicone base material, Elastosil ® R 401 / 70 S, which is a proprietary silicone compound from WACKER was mixed with FEF carbon and Dichloro Benzyl Peroxide in 100:1:7 proportion (by weight) to obtain the required rubber compound meeting the tensile properties as specified. Flat dumbbell shaped samples of 2 mm thick were used for checking the tensile properties.

Extrusion Trials:

Subsequent to finalization of material composition and

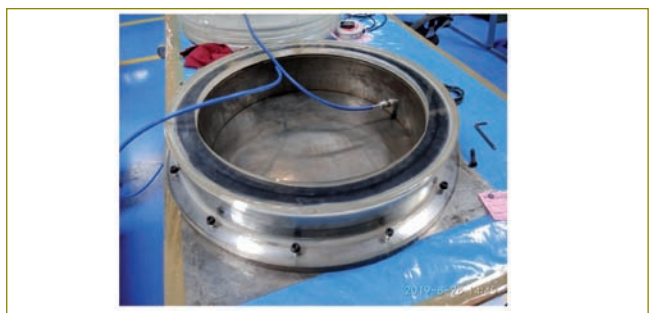


Fig. 3 Steel test rig with perspex shell for visual verification of inflation

achieving the specified mechanical properties, extrusion trial were taken-up to obtain a stable profile of inflatable seal. Extrusion was carried out using a screw feed type extruder (Figure 1). Since, the extruder was not fitted with a conveyor, seal was extruded continuously with normal feather touch support (Figure 2) and collected in the table with talc powder to avoid sticking. The inflation nozzle was integrated into the seals and the seal was joined using a proprietary silicone adhesive to obtain a $\phi 2m$ seal with single joint. Subsequently, the joined seal was cured in an Autoclave oven. The first trial seal was received at IGCAR for fitment trial in the available rig.

Based on the observation w.r.t. sharp edges at the base of the seal, the die was modified and new fitment seal was produced, which was checked and found to be meeting the requirements w.r.t. dimensions.

As-Achieved Mechanical Properties:

Flat dumbbell shaped specimens are extracted from the seal itself and tested for their properties. Further, heat ageing test on samples extracted from seal was carried out as per ASTM D573 after ageing the samples to 70 Hrs @ 250°C. Table-1 gives the achieved properties of samples extracted from seal under both aged and unaged conditions. The values are the average of 3 Nos. of samples tested. Based on the inputs from imported Silicone seal, a minimum tensile strength of 8 MPa was specified and it is seen that the achieved tensile strength meets the requirement. The changes in mechanical properties after ageing are found to be within the specified limits w.r.t. their unaged properties, as indicated.

Nozzle Fixing, End Joining & Teflon Coating:

The next major activity after the successful extrusion of seal was to fix the nozzle and achieve a perfect joint. Towards this, following procedures were drawn up:

Check the processed seal and check the length (6112 mm)



Fig. 4 Seal of $\phi 2m$ ready to despatch

and make a hole as per required size in the seal to insert the nozzle.

Insert the nozzle and apply the rubber solution over the nozzle area and allow it for ageing 30 min and keep inside the oven at 100°C for 1.5 hour.

Make sharp cut normal to the seal length & apply the proprietary silicone glue over the cut area.

Join the free ends to form a seal by providing overlap and allow to ageing for 2 hr at room temperature.

Apply a layer of Teflon coating over the profile as per the drawing and keep the seal for ageing for 15-20 min inside the oven for curing at 120°C.

The splice strength of the joined seal was demonstrated by extracting the dumbbell samples from the joint region and subjecting the same to tensile test. A splice strength of 7.54 MPa was achieved against a specified minimum base material tensile strength of 8MPa.

Demonstration of Inflation Pressure:

Further, to check for the inflation pressure and leak-tightness, a $\phi 0.5 m$ seal was prepared as similar to $\phi 2.0 m$ seal. A steel rig with Perspex outer shell was fabricated (Figure -3) and complete inflation of seal with an inflation gas pressure of ~30 kPa was demonstrated.

Extrusion of Supply Seal

Subsequent to successful extrusion trials and inflation pressure demonstration, clearance was given to industry to proceed with manufacture of 5 Nos. of $\phi 2m$ seals. Based on the clearance, Industry had completed the extrusion of these seals (Figure 4).

Examination:

Following examinations were carried out on extruded 5 Nos. of $\phi 2m$ dia. seals before their packing and dispatch.

- Visual examination of the surfaces for the presence of blisters, cracks, dents etc.
- Dimensional inspection.

The indigenous manufacture of inflatable seals in Silicone has been successfully demonstrated. Performance qualification of the seal in the test rig as well as verification of sodium aerosol compatibility of the seal material are planned in the next phase.

Table-1: Comparison of As-achieved mechanical Properties – Unaged and Aged			
S . No.	Parameter	Require-ment	O b s e r - vation
1	Hardness Shore A	70±5	71-72
2	Tensile Strength (Min) (MPa)	8 MPa	9.3
3	Elongation at Break (Min) %	175%	561
4	Tear Resistance TR (Min)	18 N/mm	26.07
5	Heat Ageing at 225°C for 70 Hours as per ASTM D573		
5.1	Hardness	±15	+2.0
5.2	Tensile Strength	±30%	+7.9%
5.3	Elongation @ Break	±50%	+22.13%
6	Compression Set Conditions @ 200°C for 22 Hours	50% (max)	29.43%

III.8 Performance Qualification of Large Diameter Bearing

Large diameter bearings ($\phi 4.6$ & $\phi 6.9$ m) are employed to enable rotation of rotatable plugs in fast breeder reactors to facilitate fuel handling. As an import substitute, a bearing measuring $\phi 4.6$ m was earlier designed and successfully developed indigenously. Towards validation of the bearing design, testing and qualification of the developed bearing under simulated reactor operating conditions was taken-up for its functionality & performance. In this context, an experimental facility for testing $\phi 4.6$ m bearing under simulated operating conditions such as load (230 tonnes), temperature (up to 100°C) and temperature difference (20°C) across the races etc. as expected in the reactor has been constructed, installed and commissioned.

Towards meeting the design intents of these bearings, following objectives were identified for the test rig

- To install an elevated temperature large diameter bearing test facility simulating operating conditions as in reactor.
- Study and compare the performance of bearing with two different balls configuration viz., only load balls and load + spacer balls.
- Test the performance of the bearing under 230 t dead load with eccentricity and at a temperature of 100°C with an axial ΔT of 20°C across the races.
- Check the bearing performance with circumferential temperature difference from 10°C – 30°C and support structure undulations as variable parameters.
- Test the bearing for its life & thus qualify the dynamic rating of bearing.
- Qualify the drive gear integrated with top race against fatigue failure.

Salient Features of Bearing Test Rig:

The cross section detail of the bearing test rig is shown in Figure 1. Following are the salient features of the test rig.

- The bearing qualification rig is a welded structure consisting of support structure and loading structure besides heater rings.

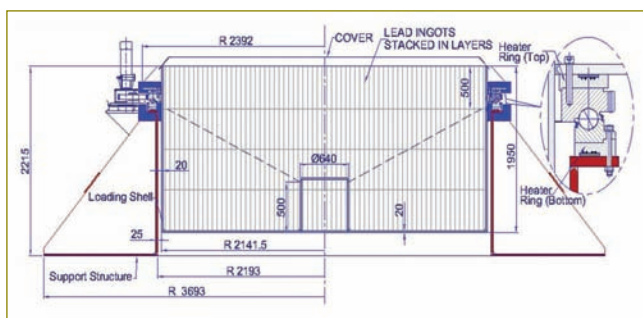


Fig. 1 Cross Section Details of Bearing Test Rig

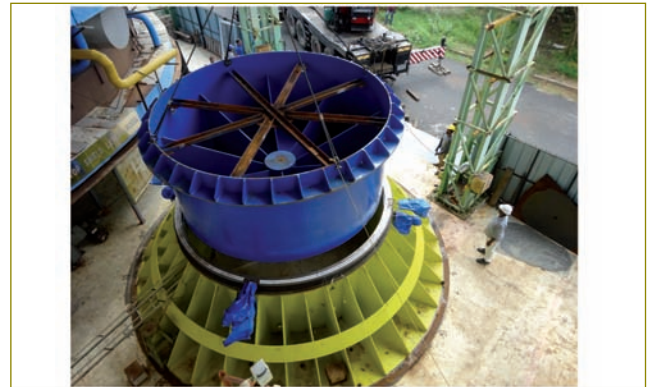


Fig. 2 Installation of Loading Structure

- Loading structure (Figure 2) consists of (i) cylindrical box structure wherein 230t of lead ingots has been placed and (ii) support flange arrangement, which transfers the load to the top ring of the bearing.
- The stiffness of the support flange is designed to match with that of top ring of SRP support arrangement in reactor so that the load transmission to bearing is simulated exactly.
- Support structure consists of support shell, bottom support plate and radial support stiffeners (36 Nos.).
- To facilitate heating of top and bottom races of bearing independently, ECR type heaters of $\phi 6$ mm were embedded within heating rings (top & bottom), which facilitates simulation of the temperatures across the bearing races as in reactor.
- 'K' type thermocouples were located and routed at various circumferential locations in heater rings as well as bearing to monitor/control the temperature.
- The design load of 230 t on bearing has been simulated using lead ingots, stacked in five layers with last two layers, partially to obtain a load eccentricity of 120 mm (Figure 3).

The functional tests i.e., to check for smooth rotation of the bearing were carried out at various stages of loading and the torque required to rotate the bearing was continuously



Fig. 3 Overall View of the Bearing Test Rig

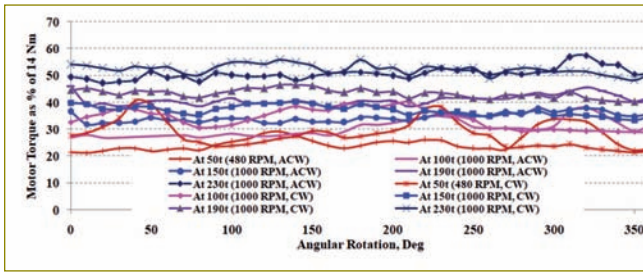


Fig. 4 Evolution of Torque with Load

monitored. Following sequence of tests was followed for testing:

- Checking the bearing rotation smoothness with:
 - * Bearing filled with only load balls (no spacer balls) under 50 t dead load
 - * Bearing filled with combination of load and spacer balls under 50 t dead load
- Comparing the performance of ball configurations and selecting the configuration for further testing.
- Continuing the testing of bearing with finalized ball configuration by increasing the loads from 50 to 100 t, 150 t, 190 t and 230 t in steps.

Based on the functional testing, following observations were made:

- With only load balls, the rotations were noisy with intermittent high torques at several locations.
- The rotation trials with load + spacer balls configuration were much smoother with torque variation within acceptable limits.
- The torque variations in both clockwise and anti-clockwise directions follow a typical pattern including the high points.
- The torque required to rotate the bearing steadily increases with the load (Figure 4). Further, the variation in torque values at higher loads is much less in comparison to lower loads.
- The measured change in torque w.r.t. load closely matches to the estimated value (Figure 5).

Performance tests

Subsequent to functional testing, performance assessment of the bearing was taken-up as part of design validation while keeping in view the requirement of addressing issues with LRP bearing rotation at PFBR. Towards this, following test matrix was prepared and followed.

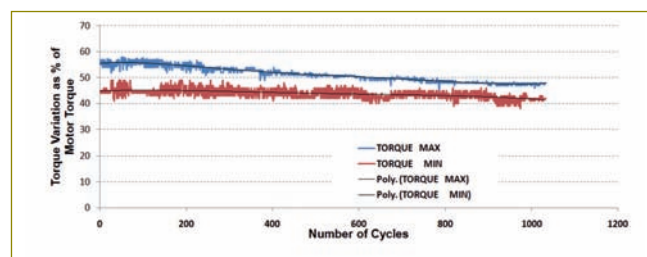


Fig. 6 Variation in Torque during Cyclic Testing @ Room Temperature

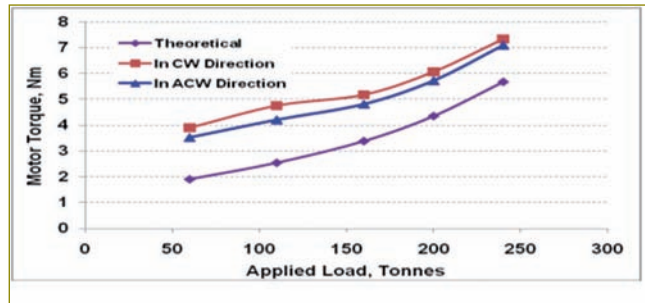


Fig. 5 Comparison of Estimated and Measured Torque

- Cyclic testing of bearing under the load for 1000 Cycles at room temperature.
- Cyclic testing of bearing under the load for 1000 Cycles with top race (TR) temperature of 80°C & bottom race (BR) temperature of 90°C, resulting in an axial gradient of 10°C while restricting the circumferential gradient to < 6°C.
- Cyclic testing of the bearing for 200 cycles with TR temperature of 80°C & BR temperature of 100°C, resulting in an axial gradient of 20°C.
- Cyclic testing with combination of axial ΔT (10 & 20°C) and circumferential ΔT (10, 20, 30 & 40°C) as part of parametric study to assess the bearing performance.

Based on the tests, following observations are made:

- 1000 cycles test of Bearing at both room temperature (Figure 6) and operating temperature of 90/70°C were smooth .
- Simulation of circumferential ΔT (up to 40°C) along with axial ΔT (10 °C) has not resulted in any significant change in torque (Figure 7 for a typical case).
- Rotation with TR temperature absolutely more than BR by 20°C (stress test) indicates a ~20% increase in torque associated with top race stop-start type motion at few locations → Possibility of raceways damage exist.
- General conclusion is irrespective of raceway mismatch either due to manufacture or temperature gradient, torque variation is marginal & no stalling is expected even though some raceway damage is expected.

The tests carried out on the bearing has given very useful data towards validation of indigenous design & development as well as insight into the LRP bearing issues to be addressed at PFBR site.

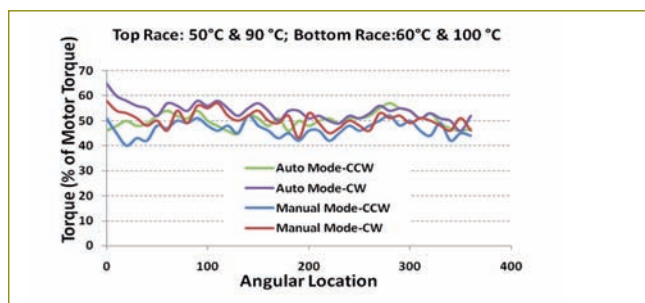


Fig. 7 Variation in Torque with Circ. ΔT

III.9 Development of Valve Position Monitoring System using Indigenous Processor based Remote Data Acquisition System for FBR

To monitor valve position status in the nuclear power plant, a remote data acquisition system is developed using indigenous processor Vikram1601. These remote data acquisition systems are geographically distributed across the plant to reduce cabling and avoid noise interference. The design philosophy of remote data acquisition system is based on single board computer architecture. These systems are placed in Local Control Centre and also in the field environment of the plant. In our effort towards indigenization of components used in I&C systems, utilizing the expertise available in other organizations, a Vikram1601 Processor based remote data acquisition system is developed for various reactor applications.

Vikram1601 is an indigenously developed microprocessor by VSSC, Trivandrum for acquisition of stage parameters of launch vehicles, processing and issuing of commands based on the inputs. Vikram1601 processor is shown in Figure 1. It is a 16 bit RISC architecture which supports external clock speed up to 80MHz. The set has 96 instructions including those for floating point arithmetic. This processor supports two addressing modes. In-circuit programmability and complex sequencing are also possible. Error handling is made simpler by tight synchronization with On-Board Computer (OBC).

In our application, this processor is designed to handle 8 digital input channels with forcing zero and forcing one diagnostic feature, one serial port communication and dual Ethernet ports for remote data communication apart from watchdog timer and external program/data memory as shown in the block diagram in Figure 2. The PCB fabrication and testing has been completed successfully as shown in Figure 3. Board level testing like on-board power supply, processor clock signals of

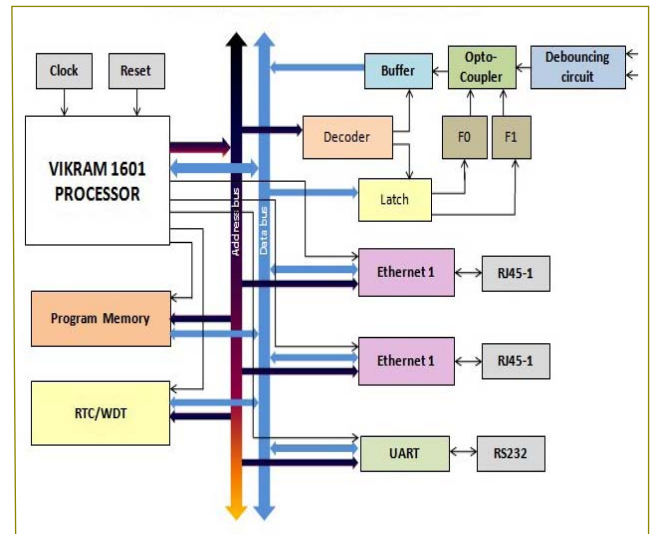


Fig. 2 Block diagram of remote data acquisition system

16Mhz, peripheral component ICs, reset signal and digital input signal have been completed.

The application program was written in assembly language for Vikram processor which was compiled using vasm.exe tool and linked using vlink.exe. The Hex code thus generated was ported on to EEPROM using Universal Programmer. The board utilizes memory mapped addressing scheme for connections of peripheral ICs. The board operates at 5Vdc power supply. The 1.8Vdc power supply required for the processor is derived from 5Vdc source. The testing of UART was performed by configuring with 4800 baud rate, no parity, 8 bit word length and with enabled FIFO. The processor could successfully write/read the data through serial port interfaced with a Qt based GUI running on the PC.



Fig. 1 Vikram1601 processor



Fig. 3 Fabricated PCB of remote data acquisition system

III.10 Development of Software Reliability Model and Assessment of HMI Software for Primary Main & Purification System of FBR

Computer based I&C systems are extensively used in NPP for safety critical and safety related applications. Hence reliability of computer based systems should be ensured. However, software component of computer based systems make them different from other electronic control (hardwired) systems which necessitates a different approach to prove the safety and reliability. The aim of the project is to develop software reliability model and reliability assessment for the Human Machine Interface software of primary sodium main & purification systems.

Software reliability estimation has been carried out using failure data obtained from testing and field failures. This data is generally time to failure data. Safety-critical and Safety-related software for various subsystems of a nuclear power plant, including the software for the instrumentation and control subsystem was developed systematically using a V model of development. A study was undertaken for the development process being followed for the software for the instrumentation and control subsystem.

Towards this, various available documents and interactive session were carried out with the software development team. After a careful analysis of the development process being followed, a gap analysis was done and some ways in which the development practices being followed are also suggested for further improvement.

The suggested models to the development practices resulted in improving the quality of the software being

developed and also helped in systematically capturing relevant data that can serve as the basis for reliability prediction and could serve as the necessary evidences required to support regulatory approval and safety certification.

Based on problem selection, data required and model formulations, following software reliability models are suggested:

- Error Seeding Models
- Failure Rate Models
- Nonhomogeneous Poisson Process (NHPP) Models
- Curve Fitting Models
- Time-series Models
- Input domain based Models

For generation of failure data, a simulation setup was made. Figure 1 shows the simulated test set-up. HME software has been established along with the underlying RHEL LINUX and Qt runtime environment. A primary sodium main system VME simulator has been developed to simulate the communication functionalities of the actual VME systems deployed in PFBR. Two instances of the VME simulator has been deployed with simulated switch over logic. The HMI software has been integrated with the dual VME simulators using dual redundant LAN. Various failure scenarios like one network failure, corruption of data during transit, failure of one VME system, dual LAN failure and dual VME system failure have been simulated. A database has been created to record the various failures. Failures reported were also recorded in Bugzilla software.

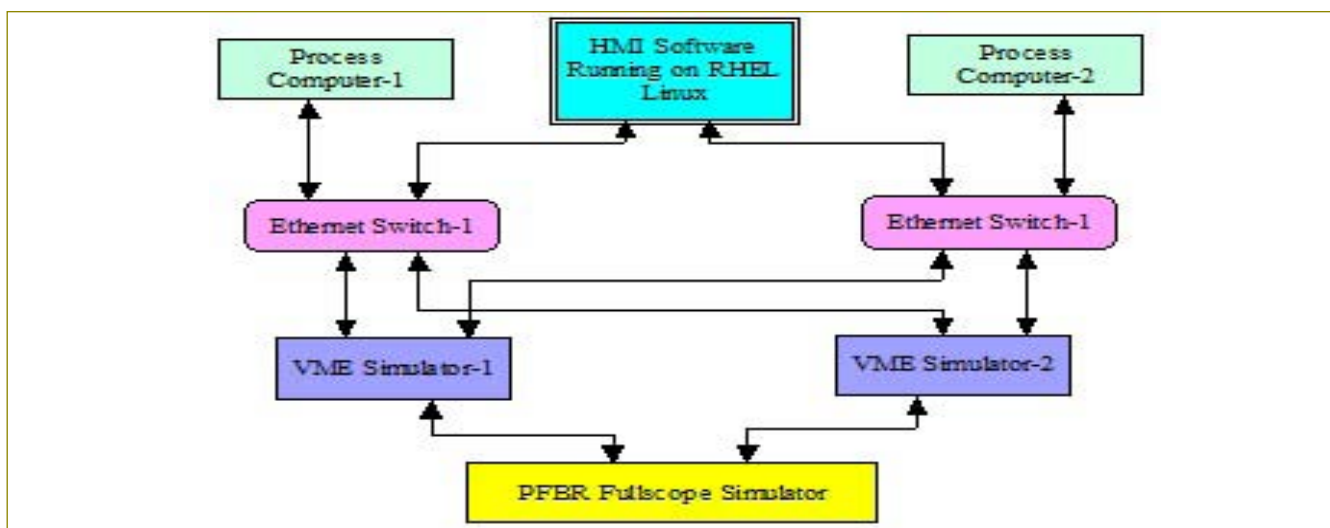


Fig. 1 A simulation set-up for generation of failure data

III.11 Microprocessor based Safety Logic System for Reactor Shutdown System of FBRs

Safety Logic System is a two out of three majority voting logic system, wherein if any two channels of a SCRAM parameter are out of its specified thresholds, generates trip signal. Since Programmable logic devices are used in both shutdown systems of PFBR, to reduce the common cause failure, a diverse Microprocessor based safety logic system is envisaged for Reactor Shutdown System of FBRs. Safety logic to reactor shutdown system is classified as safety critical system. So it has to satisfy the safety critical system design requirements like simple in design, redundancy, fail safeness, diversity, single failure criteria, isolation, independence and testability.

Safety Logic System receives triplicated SCRAM parameters and processes them in 2/3 voting logic. When any of the input SCRAM parameters passes the 2/3 voting logic, safety logic system will generate the SCRAM signal to the shutdown system.

Microprocessor based safety logic system is a software system. VME 32 Bus based Motorola 68020 Real Time Computer (RTC) System is used for the design of safety logic system. The RTC system consists of one CPU card, three digital input cards and one relay output card. The three digital input cards acquire the trip signals corresponding to the triple redundant channels A, B and C respectively. The software in the CPU card performs the 2 out of 3 logic for these A, B and C trip signals and generates the final trip output through relay output card. The diverse safety logic system shall be fault tolerant and the final logic output shall provide a failsafe output. Effective SCRAM output, all triplicated input parameters status, manual SCRAM output and diagnostic status shall be provided by the microprocessor based safety logic system.



Fig. 2 Test Setup

Software for safety logic system performs digital input scanning, performing 2 out of 3 logic and driving relay outputs. The software also continuously performs the diagnostic logic of the hardware.

Recovery block technique is implemented in the software of Safety Logic System to meet the fault tolerance requirement. Critical function is identified and diverse versions are implemented for this function. The error detection before executing any version of critical function is performed by acceptance test as shown in Figure 1. It first checks the validity of the results of version 1 and if result passes the test, version 1 will be executed. If it fails the acceptance test, the version 2 will be invoked and the result is checked again. If none of the versions is correct, it generates fail safe output and displays the error message. Testing is performed in VME32 based system by imposing suitable bugs in different methods and it is found that recovery block feature is driving the outputs successfully through alternate methods. Figure 2 shows the test setup of VME32 based Safety Logic System.

In future, diverse software versions using different programming languages in VME dual redundant configuration will be implemented.

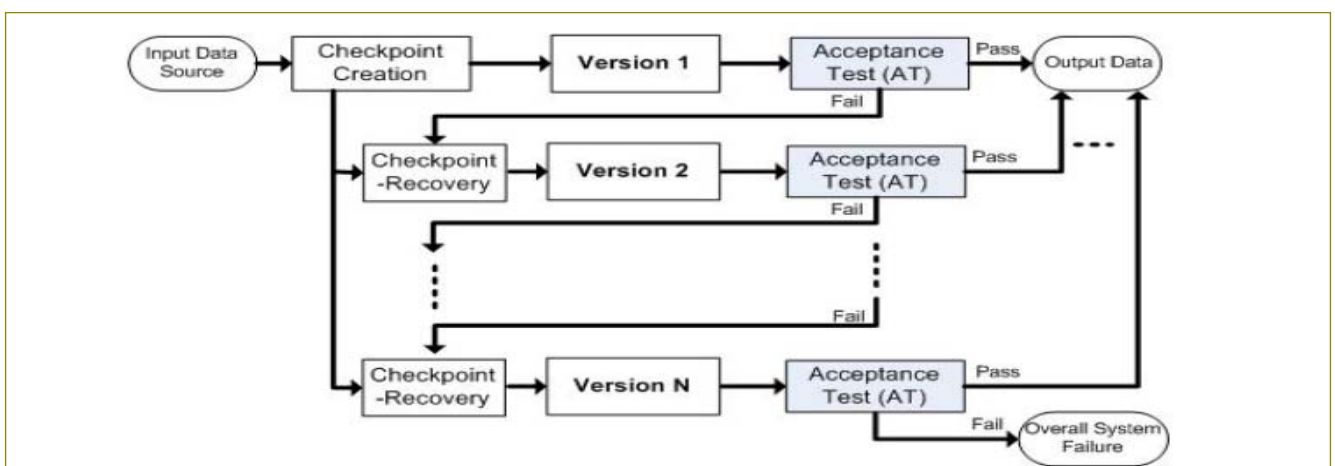


Fig. 1 Recovery Block Technique

III.12 Application of Genetic Algorithm for Optimization of Control Rods Positioning in a Fast Breeder Reactor Core

Genetic algorithm (GA) is a meta-heuristic optimization technique based on Darwin’s theory of biological evolution. A genetic algorithm is implemented for finding the optimal arrangement of 12 control rods within the active core of a fast breeder reactor, satisfying and optimizing operational and safety parameters. The core considered is similar to the core of 500 MWe PFBR. It is a multi-objective, multi constraint combinatorial optimization problem with a very large search space.

Objectives and Constraints

The reference core has 1758 sub-assemblies arranged in rings in a hexagonal lattice. The aim is to optimally place 12 control rods (9 CSRs and 3 DSRS) in any 2 rings within active core, with the following objectives & constraints:

1. Maximize Effective Reactivity Multiplication Factor
2. Maximize Total Control Rod Worth
3. Maximize Anti Shadowing Effect
4. Each group of rods should have a minimum worth to bring the reactor to shutdown independently. a) Total worth of CSRs > 9000 pcm b) Total worth of DSRS > 3500 pcm
5. Engineering considerations: a) 3 DSRS are to be arranged in a single ring with 120 degree symmetry. b) Any 2 control rods have to be at least 2 lattice pitches apart from each other.

Genetic Algorithm Procedure

The overall GA procedure for the problem is as follows:

- (i) Generate the initial population
- (ii) Evaluate the population, i.e., calculate fitness
- (iii) Select the parents and perform crossover and mutation to produce the next generation.
- (iv) Repeat steps (ii) and (iii) until the GA converges.

A reactor core simulation code called FARCOB is used

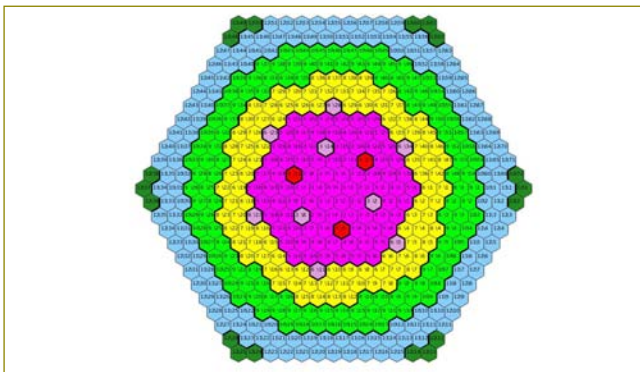


Fig. 1 Core configuration generated by GA

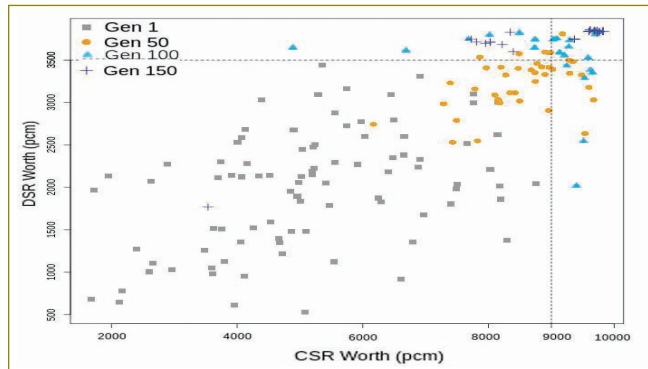


Fig. 2 Scatter plot of distribution of constraint values

to evaluate the fitness of chromosomes. An interface module converts the chromosome to an input file suitable for the code, and parses the output files.

GA Implementation Methodology

Encoding: An integer coding scheme is used to represent a chromosome, where 12 integers represent the positions of 12 control rods.

Crossover & Mutation: These are the genetic operations performed to produce offsprings belonging to the next generation. Both these operations are customized to consider the geometric positioning of the control rods in core. They act on the rings to which the control rods belong and their positions within the rings.

Fitness Calculation: Penalty function method is applied to convert the multi-objective optimization problem into a single objective form using a weighted sum approach. Constraints are handled by penalizing infeasible solutions.

Selection: Binary tournament selection is used for selecting offsprings for the next generation. Elitism is implemented, where a percentage of the best chromosomes are carried over to the next generation.

Parallelization: Evaluation of fitness with FARCOB is parallelized using master-slave approach.

GA was able to generate many feasible core configurations satisfying all constraints. A sample configuration is shown in Figure 1. Figure 2 shows a scatter plot of the constraints of the problem for 1st, 50th, 100th & 150th generations. Initially, all chromosomes are having infeasible constraint values. More chromosomes move towards the feasibility range in 50th & 100th generations. In 150th generation, most chromosomes are in feasible region. The results show that GA is capable of converging to optimal, feasible solutions by exploring the search space effectively.

III.13 Design of Hardware based Control and Safety Rod Drop Time and Electromagnet Response Time Measurement Module for FBRs

Fast Breeder Reactors (FBRs) are equipped with at least two independent and fast acting shutdown systems and intended to protect the reactor against neutronic, thermal, coolant flow and failed fuel incidents. One of the shutdown systems is provided with Control & Safety Rods (CSRs). CSRs are used for start-up, control and safety of the reactor. During reactor operation all the SCRAM parameters will be in healthy state and all the Electromagnet (EM) coils will be kept in energized state by passing suitable current. Whenever there is a demand for reactor shutdown, EM coils will be de-energized by stopping the flow of current and all the rods will fall under gravity into the reactor core. CSR drop time and EM response time are vital parameters and need to be measured during each SCRAM as part of the surveillance requirements of safety guides.

Currently, CSR drop time is measured using computer based system. EM response time is measured by physically connecting oscilloscope which is quite cumbersome. For future FBRs, to have a diverse scheme for drop time measurement and overcome the difficulties faced in EM response time measurement "Hardware based Drop Time and EM Response Time Measurement Module is being designed and developed". Context diagram of the CSR drop time and EM response time measurement module is provided in Figure 1. Block diagram is provided in Figure 2. CSR drop time includes Effective SCRAM signal generation time, free fall time and braking time. Free fall time is the time taken by the CSR to reach oil dashpot position from its current position on EM coil de-energisation based on the Effective SCRAM signal received from the Safety Logic system. Braking time is the time taken by the CSR to reach 0 mm position from the oil dashpot position. In

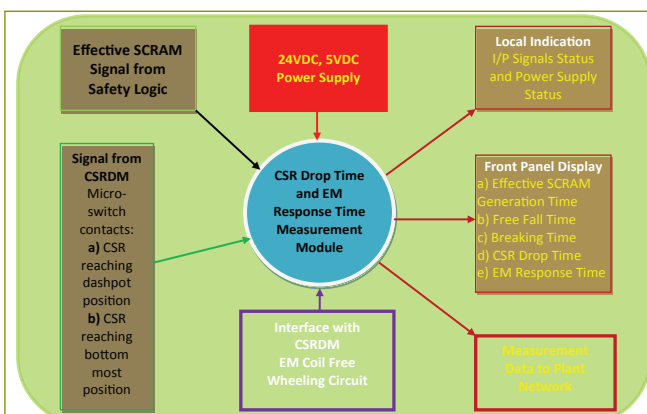


Fig. 1 CSR Drop Time and EM Response Time Measurement Module – Context Diagram

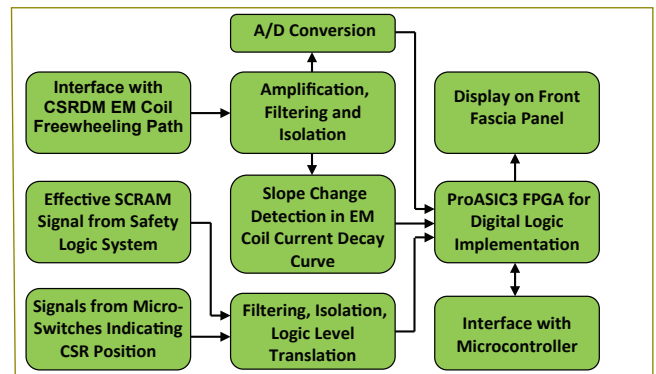


Fig. 2 CSR Drop Time and EM Response Time Measurement Module – Block Diagram

CSR drop time measurement, signals received from the microswitches located at discrete positions in CSRDM assemblies are used as the primary sensing element for the position of the CSR. EM response time is extracted from the current decay curve of the EM coil. A typical EM response time curve is shown in Figure 3. The time interval between the first and second peaks is the EM response time, as indicated in Figure 3.

Salient features of the design are as follows:

Measurement of EM Response Time and display in ms using slope change detection method on current decay curve.

Measurement of CSR Free Fall Time, Breaking Time and display in ms.

Computation of CSR Drop Time (which includes Free Fall Time, Breaking Time and Effective SCRAM signal generation time) and display in ms.

Compensation for the Effective SCRAM signal generation time.

Measurement accuracy: +/- 1 ms.

To ensure healthiness of the measurement module, extensive diagnostics is provided.

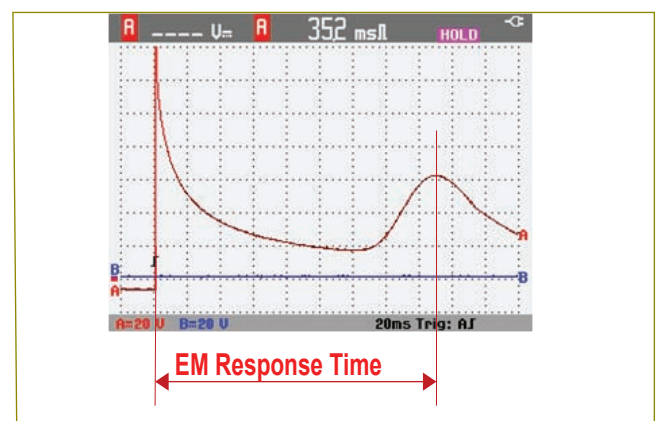


Fig. 3 Typical EM Coil Current Decay Curve - Under SCRAM Action

III.14 Investigation of Heat Transfer from Destroyed Core Debris using Multiple Passive Jets Type HSP

The natural convection plays a vital role in dissipation of decay heat generated from destroyed core. Such accidents may occur due to an imbalance in heat generated in core to the rate at which heat removed by coolant, even though various safety measures have been incorporated in reactor system to avoid the initiation of such low probable. However, as a defense-in-depth approach, the whole core melting scenario needs to be analysed in detail for robust and safe design of a reactor. After the core meltdown, metal-fuel-coolant interaction occurs and molten material fragments into fine particles called core debris. These debris may be the threat to integrity of Main Vessel (MV) once they come in contact with each other. A core collection tray called core catcher is placed in the lower plenum to avoid direct contact of these core debris with MV. The current core catcher design can easily accommodate the thermal load arising due to melting of seven sub-assemblies. For the robust design of future fast reactors, this capacity needs to be enhanced to take care the thermal load arising from whole core melt. Towards achieving this objective a 3-D analyses was carried out to explore the new concepts of core catcher.

First, the sensitivity of the different turbulent model was assessed. These results suggested the best turbulence model for such large 3-D domain, in term of fast convergence without compromising the superiority of results. It was found that k- ω SST model has a significant advantage over other RANS model in terms of solution time for large 3-D domain. Results of 2-D and 3-D numerical simulations were compared for similar boundary conditions. Multiple cooling pipes/jets concept was incorporated into full scale 3-D model [Figure 1].

Figure 2 depicts temperature evolution for 20 MW thermal load on 2-D and 3-D approximation. It can be seen that 2-D study over predicts the core debris

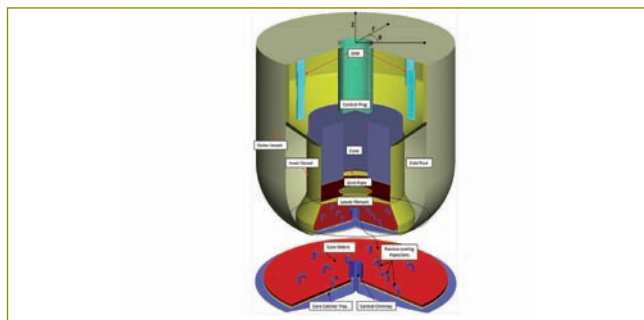


Fig. 1 Full scale computational model with multi jet/pipe core catcher

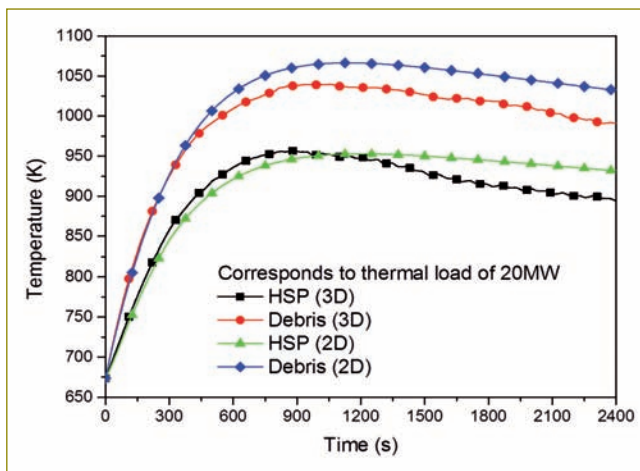


Fig. 2 Comparison for 2-D and 3-D CFD results

temperature approximately by about 40°C. This is because the turbulence in fluid is highly fluctuating and is a three-dimensional phenomena which may not be possible to capture all the flowing fluid features in 2-D domain. However, the temperature of solid body i.e. HSP's top surface does not have any significant temperature difference except the rate of cooling for HSP. Though the time for 3-D analysis is more as compared to 2-D simulation however, considering the importance of problem, it is suggested to carry out the numerical simulation on 3-D domain before finalizing the concept.

Figure 3 shows the temperature evolution in debris and over HSP. It is seen that passive jets enhance the coolability of HSP and debris bed. Due to the direct impingement of liquid sodium over debris which increases the turbulence and avoid the stagnation of liquid which in turn increases the rate of heat transfer. The temperature reduction of ~45°C is seen due to enhancement in coolability of HSP with proposed conceptual design of core collection tray. The new design also holds its benefits during the full-scale model analysis.

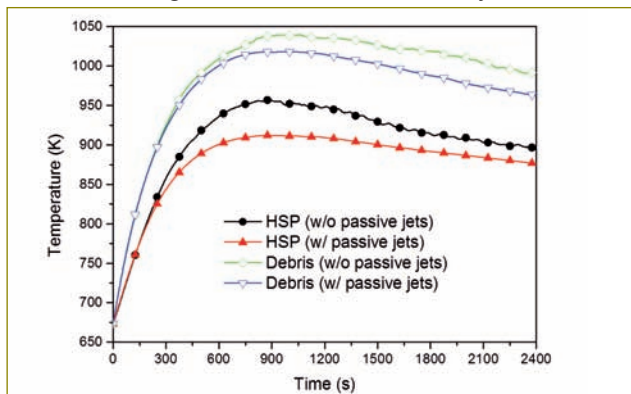


Fig. 3 Effect of passive cooling pipes in CC

III.15 Qualification of Sacrificial Material for Core Catcher of SFR

In Sodium cooled Fast Breeder Reactors, hypothetical whole core melt accident is being considered as design extension condition and consequently core catcher is provided for safe retention of corium under such severe accident. Large quantity of corium due to melting of whole core would form a thick bed after settling over core catcher. Thick corium beds have poor coolability resulting in dryout. Dried bed causes creep failure of core catcher. Prolonged insufficient cooling may cause re-melting of corium with separation of oxide fuel and structural material by stratification resulting in re-criticality and melt attack in the form of jet impingement over the core catcher.

Provision of a refractory sacrificial layer is being considered to protect the core catcher from creep failure or melt attack / instantaneous ablation during corium arrival. Due to its miscibility with molten oxide fuel, it can dilute the volumetric decay heat and also eliminate the risk of re-criticality. Long term compatibility with sodium in cold pool condition, resistance to thermal shock and neutron irradiation and high melting point are few of important requirements for the sacrificial material. High purity MgO with controlled porosities is considered as promising candidate for such application.

Commercially available sintered MgO bricks are used for thermal shock resistance testing. Chemical composition of the bricks is given in Table-1.

Cubical MgO bricks of size 75 mm were subjected to five cycles of thermal shocks by immersing in molten tin maintained at 900 °C. Thermal cycling was carried out between 400 °C and 900 °C. The MgO brick was heated to 400 °C in a furnace and then immersed in molten pool



Fig. 2 MgO bricks before and after thermal shock testing

of tin at 900 °C using a pneumatically operated plunger mechanism (Figure 1). After 30 minutes soaking at 900 °C, the brick was withdrawn and allowed to cool back to 400 °C and then cycles were repeated. Ultrasonic and compressive strength measurements of MgO bricks were carried out before and after exposure to molten tin to assess the structural integrity of the brick.

Thermal shock exposure caused visible surface cracks on MgO bricks (Figure 2). However, specimen remained structurally intact. The measured reduction in compressive strength (37 to 31 MPa) indicated that sintered MgO bricks can safely withstand thermal shocks caused by fragmented corium at a temperature upto boiling point of sodium. MgO bricks would have sufficient residual compressive strength to withstand corium weight.

Sodium compatibility testing of MgO bricks with 10% porosity had been carried out for a period of 1500 h at 400 °C (Figure 3).

Experimental results revealed that there is no significant penetration of sodium in MgO bricks. XRD analysis revealed that no chemical interaction occurred between MgO and sodium.

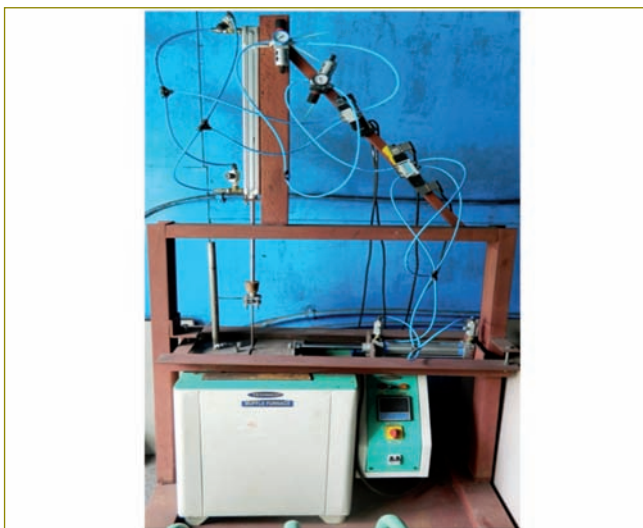


Fig. 1 Experimental Setup for thermal shock testing

Table 1. Chemical composition of MgO bricks				
Chemical Compound	MgO (Min.)	SiO ₂ (Min.)	CaO (Max.)	Al ₂ O ₃ (Max.)
Composition	90 %	4 %	2 %	1.7 %



Fig. 3 Setup for Sodium compatibility testing

III.16 Development of Indigenous Code CRaD to Estimate the Metrics of Primary Radiation Damage

It is well-known that the structural materials of nuclear reactors (facilities) undergo drastic changes in their physical and mechanical properties due to facing of intense radiation for a prolonged duration. Hence, it is vital to estimate the limits of the parameters of radiation damage while designing these systems. The primary radiation damage (PRD) (damage occurring within a few hundred picoseconds of radiation-matter interaction) is determined by estimating the four metrics: primary knock-on atom (PKA) spectra, displacements per atom (dpa), gas production and heating cross sections. These metrics along with their neutron spectra-integrated quantities for neutron-induced damage in the reactor structural materials have been determined using the recent basic ENDF-6 libraries with the help of a newly developed computer code, Computation of Radiation Damage (CRaD). The results on these metrics obtained from this code have been validated by comparing with other standard codes and databases.

The capabilities and different features of CRaD code are shown in Figure 1. The different parameters of PRD are determined using different parts of the code system. The code needs temperature-dependent basic point cross sections from a pre-processed ENDF-6 file as well as the other variables of neutron-nucleus interactions such as the energy and angular distributions of emitted particles and recoil nucleus from the raw ENDF-6 file.

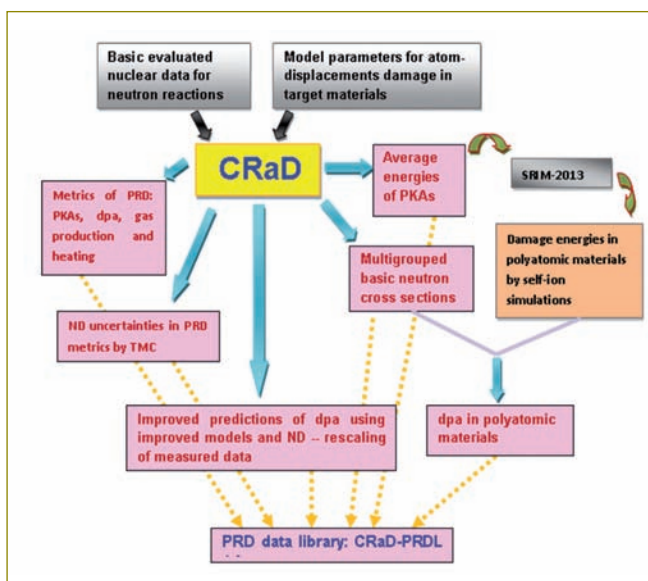


Fig. 1 Features of CRaD code

The dpa and heating cross sections are estimated in both point and multigrouped forms and the gas production cross sections are estimated in multigrouped form. The PKA spectra are estimated in matrix forms, where the dimensions of the matrix depend on the number of energy groups used for the incident neutrons and the recoil nucleus. Several options for energy group structures have been provided in-built with the code. The dpa cross sections based on both the NRT and arc-dpa models can be estimated with CRaD. In general, it is observed that the more realistic arc-dpa model predicts dpa values much less (about one-third) compared to the NRT model. Moreover, the arc-dpa model reproduces the observations made in realistic molecular dynamics and binary collision approximation simulations. Based on this, the measured parameters of damage like swelling, yield strength, etc. can be properly rescaled with the updated values of dpa.

The estimation of dpa in polyatomic materials is challenging when appropriate atomic potentials are not readily available. Towards finding a solution, a novel approach has been proposed with the help of CRaD. The average energies of PKA estimated from the PKA spectra can be used as self-ions in the SRIM-2013 code to compute dpa cross sections in polyatomic structural materials. The self-ion simulated values of dpa in SiC under different irradiation spectra, for instance, have been found to be promising and comparable with the standard data within the calculation uncertainties.

The use of different nuclear data libraries gives rise to spreads in the estimated values of the metrics which are due to the differences in the nuclear reaction variables in different libraries. The CRaD code has been used to quantify the nuclear data uncertainties in the damage metrics by following the Total Monte Carlo (TMC) methodology. In case of Fe subjected to different neutron spectra, the nuclear data uncertainties in the PKA energies, defect formation and dpa are found to be ~ 6-7%, in gas production ~ 16-56% and in heating ~ 9-29%. The energy-energy correlation matrices of dpa, heating and gas production cross sections have also been estimated. The databases of PRD metrics generated using the code have been compiled into a new library named as CRaD-PRDL 1.0 for future FBR applications.

III.17 Assembly and Functional Demonstration of Open Cathode Proton Exchange Membrane Fuel Cell Stack

Regeneration of secondary cold trap (RSCT) of RPFBR releases large quantity of H_2 and the process required to be carried out in the interval of every 5 years. Safe removal of hydrogen during the process is essential as it forms an explosive mixture in air when H_2 concentration exceeds 4%. Proton Exchange Membrane Fuel Cell (PEMFC) based Electrochemical Burner for hydrogen (ECBH) has been adopted for RSCT, which safely converts H_2 into water by producing current and heat. ECBH using commercial fuel cell stacks have been demonstrated for safe removal of H_2 during the simulation experiments of model secondary cold trap regeneration at SGTF/FRTG in three campaigns. Open cathode fuel cell stacks (OC-PEMFCs) have a design in which ambient air is used as oxidant as well as coolant by a cooling fan. Hence the design is very much suitable for field applications like RSCT.

In order to develop, Open Cathode-Proton Exchange Membrane Fuel Cell (OC-PEMFC) made in-house for RSCT; an eight cell stack with an active area of 70 cm^2 was developed. For the stack, grooved mono-polar plates (MPP), perforated sheet for cathode support (PSCS), plain sheet for MEA support (PSMS), silicon gaskets (SG) for H_2 gas sealing and carbon paper based anode flow field sheets (CAFS) were specially designed. MPP, PSCS and PSMS were fabricated using SS 304 and were coated with WC/C by arc evaporation method. The stack was designed to have a common inlet for fuel gas which will pass through all eight single cells in the stack. The gas flow design facilitates to distribute H_2 only to anodes. A DC cooling fan was fixed to the stack to suck ambient air to act as oxidant and coolant to the cathodes and the stacks respectively. The open cathode fuel cell stack assembled using aluminum end plates, copper current collectors along with the fabricated components assembled is shown in Figure 1.

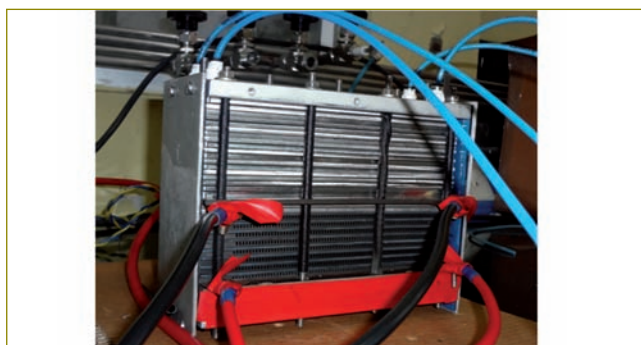


Fig. 1 Open cathode fuel cell stack using WC/C coated SS 304 mono-polar plates

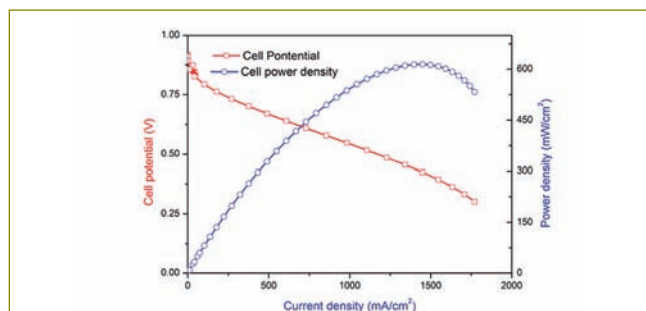


Fig. 2 Polarization curve of single cell for open cathode fuel cell stack

Electrodes for membrane electrode assembly (MEA) were prepared by brush coating of Pt/C on carbon paper with a loading of 0.5 mg/cm^2 for anode and 0.7 mg/cm^2 for cathode. Nafion 212R membrane was used as electrolyte after pre-treatment. MEAs were prepared by hot pressing the electrodes on both the sides of Nafion electrolyte at 120°C . Prior to assembly of the stack, the MEA was assembled as a single cell and tested for its performance by constant voltage polarization method which is shown in Figure 2. The single cell performance was satisfactory which rendered a maximum current density of 1.7 A/cm^2 with humidified gas streams. MEA was sealed with PSMS through the CAFS and SG. The assembled stack was studied for its performance by measuring the current and potential in constant voltage mode by purging H_2 on anode and turning on the coolant fan.

Electronic load bank was used to dissipate the power generated. The open circuit cell potential was observed to be 7.15 V.

The stack was tested in the ambient conditions without humidification and it produced peak current of 6.25 A at 3.1 V which is shown in Figure 3.

H_2 removal efficiency of the stack was found to be 84% at a flow rate of 200 SCCM of H_2 .

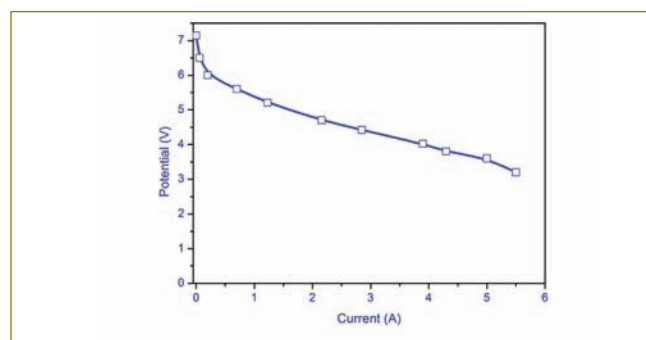


Fig. 3 Polarization curve of open cathode fuel cell stack

III.18 Studies on Molten Fuel Coolant Interaction in Sodium using Simulated CORIUM

As a part of severe accident research for Sodium Cooled Fast Reactors, Molten Fuel Coolant Interaction (MFCI) studies are being carried out with simulants. Following successful trials with simulated molten corium in water, experiments in sodium were conducted. The main objectives are to investigate fragmentation of simulated corium in sodium and to obtain particle size distribution of fragmented debris. Experiments were conducted by releasing molten mixture of alumina and steel generated by thermite reaction into sodium. A dedicated experimental setup has been designed, fabricated and erected at 'THEME' facility (Figure 1).

The experimental setup consists of a melt generation vessel, interaction vessel to hold sodium and test chamber for housing the interaction vessel. The melt generation vessel consists of a ceramic coated steel shell with conical bottom for melt release and an exhaust duct at the top for expelling the reaction gases. The bottom is connected to a fusible plug type release nozzle integrated to sodium interaction vessel by a gate valve as shown in Figure 1.

Three experiments were conducted with 100 g melt and 1 kg sodium maintained at $\sim 350^\circ\text{C}$ in inert test chamber. Thermite mixture was ignited remotely by electric triggering circuit and the generated melt at $\sim 2400^\circ\text{C}$ was released into sodium. The melt was observed to



Fig. 1 MFCI experimental setup

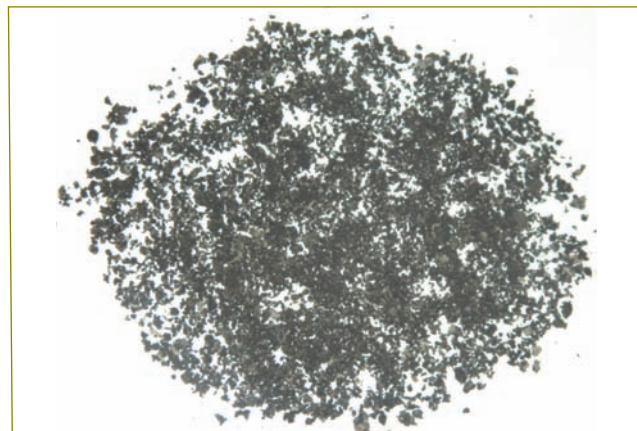


Fig. 2 Photograph of fragmented debris

get fragmented instantaneously upon contact in sodium. However, no energetic interaction was noticed. After the run, sodium interaction vessel was taken out and debris particles were retrieved after draining sodium through a wire mesh basket. The sticking sodium on the collected debris was removed by vacuum distillation. Particle size analysis indicated formation of very fine debris without any chunks, in all the runs. Photograph of fragmented debris is shown in Figure 2. The Mass Median Diameter of the debris was found to be about 0.2- 0.3 mm.

After successful completion of small scale runs, an experiment was carried out by releasing 1 kg of simulated melt into 4.5 kg of sodium at 200°C . After draining of sodium, the fragmented debris was cleaned by vacuum distillation. The fine debris was found to contain steel and ceramic particles. Among the steel debris, many elongated flake type of particles were observed indicating the fragmentation resulting from a stress solidification mechanism. The MMD of debris was found to be about 0.4 mm (Figure 3).

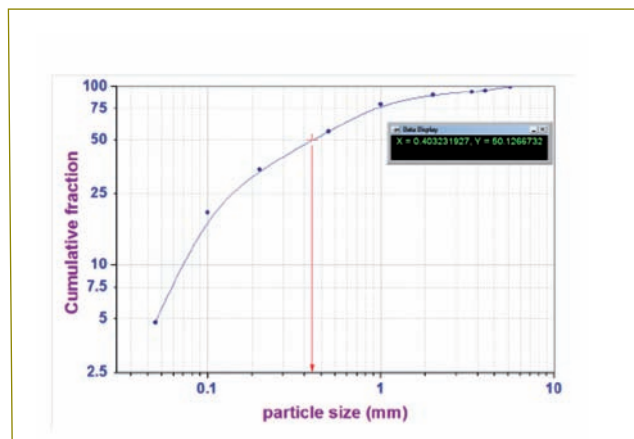
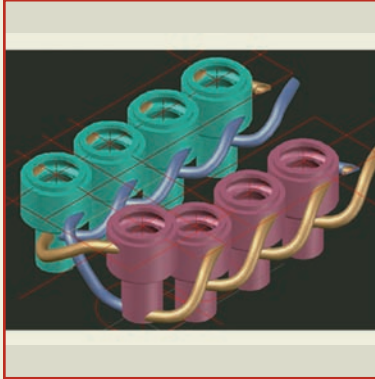
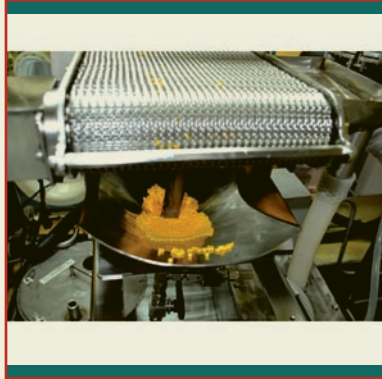


Fig. 3 Particle size distribution of fragmented debris



CHAPTER IV

Fuel Cycle

IV.1 Fast Reactor Fuel Cycle Facility- Current Status

Fast Reactor Fuel Cycle Facility (FRFCF) is being built with the objective of closing the fuel cycle and ensuring sustained fuel supply for Fast Breeder Reactors (FBRs) at Kalpakkam. FRFCF is a multi-unit mega project of DAE, coordinated by BARC, IGCAR & NFC and being executed by IGCAR. FRFCF, co-located along with PFBR, is an integrated facility housing five major plants in the nuclear island for carrying out reprocessing, fuel re-fabrication, assemblies and waste management. After obtaining all clearances, construction was commenced.

In the infrastructure area, civil construction of infrastructure, utilities & service buildings have been completed. Gold rated Green Building Certificate from Indian Green Building Council (IGBC) has been received for the training centre of FRFCF, the first Green building in DAE.

In the nuclear island, civil construction of the Core Sub-assembly Plant (CSP) building reached (+) 13.0 metre elevation (Figure 1a), Waste Management Plant (WMP) building reached (+) 6.0 metre elevation (Figure 1b), Fuel Fabrication Plant (FFP) & Reprocessed Uranium Oxide Plant (RUP) reached Finished Floor Level (FFL). One block of Fuel Reprocessing Plant (FRP) also reached FFL (Figure 1c).

Major pours involving placement of temperature controlled concrete have been undertaken to expeditiously complete civil construction. After mock-up studies, manufacture of heavy density (3600 kg/cubic metre) concrete has been commenced and first pour of heavy density concreting of 673 cubic metre for Waste Tank Farm slab of FRP Block-1 has been completed. Construction of RCC stack for FFP, RUP & CSP has been completed. Construction of Roof Slab of Plant Water Pump House upto FFL has been completed.

Cumulative concreting of about 4.0 lakh cubic metre has been completed in the nuclear plant buildings for structural members such as rafts, footings, columns and

tie beams with concurrent engineered soil back filling of 24 lakh cubic metre.

Procurement of first group of optical glass slabs required for fabrication of radiation shielding windows has been completed. Procurement & manufacturing of long-delivery equipment and components required for commissioning of various plants have been initiated. Large sized (over-dimensional consignment) waste tank farm storage tanks with 2 km piping inside have been manufactured and received at FRFCF site for erection in FRP. Review of design documents and drawings of evaporator and dissolver has been completed to initiate procurement.

Several equipment viz. master slave manipulators, lead bricks, annular tanks, ventilation system dampers, radiation shielding optical glass slabs, centrifugal fans, control room equipment, differential pressure transmitters, are being received at site in a phased manner. Installation & commissioning of Fire Detection & Alarm System and Plant Communication System in Infrastructure Buildings has been completed. Procurement actions have been initiated for area gamma & wide gamma monitors, criticality alarm systems, network switches and other I&C components.

High temperature sintering furnace and total gas analyzer for FFP have been received at site. Glove box integration of equipment for analytical certification laboratory of FFP has been initiated. Fuel pin passive gamma scanning system has been received and mock-up trials have been completed towards deployment.

A 30 metre tall chimney for exhaust of gases has been erected for Solid Waste Building of WMP and exhaust fans have been received at site. Electrical sub-station equipment of WMP have been received at site and erection & commissioning is initiated. Construction of low level liquid waste dilution facility of FRFCF has been completed. Manufacture of 200 ton capacity compactor for solid waste building has been completed.

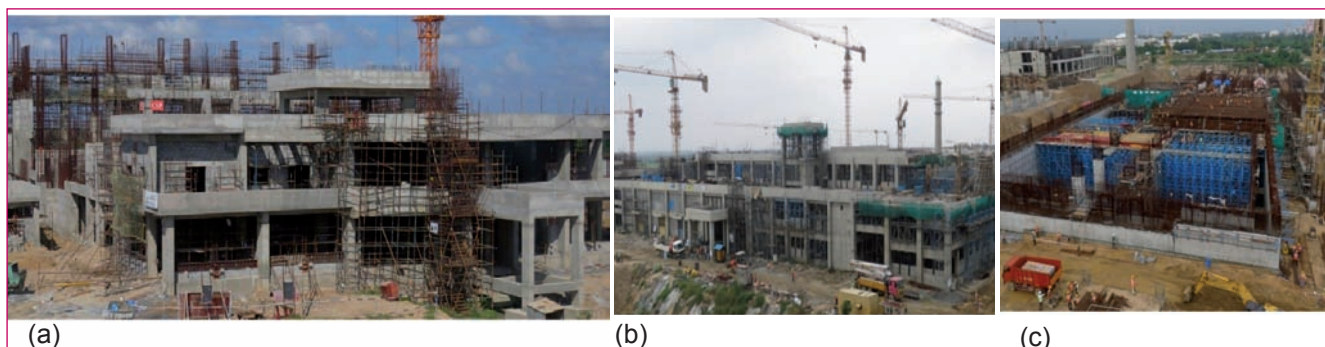


Fig. 1 (a) Core Sub-assembly Plant, (b) Waste Management Plant and (c) Fuel Reprocessing Plant

IV.2 Design, Fabrication and Transportation of Large Capacity High Level Liquid Waste Storage Tanks for FRP

Fuel Reprocessing Plant (FRP) of Fast Reactor Fuel Cycle Facility (FRFCF) will generate high level radioactive after concentrating the waste solutions resulting from the reprocessing of irradiated nuclear fuels by evaporation. Considerable volume of these wastes will be stored in large stainless steel (SS) storage tanks for a period of 6 years before discharging to Waste Management Plant (WMP).

In view of the highly corrosive and radioactive nature of the liquid wastes, the volume needed to be stored and the over-dimensional sizes of the tanks, design, material selection, fabrication, and transportation methodology are very important.

The tanks are of horizontal cylindrical with torispherically formed heads having an outside diameter of 4.7 m, an overall length of 13 m and weighing 67 tonnes. The internals of the tank includes 8 Nos. of cooling coils, 5 Nos. of baffle plates & 8 Nos. of ballast tanks. AISI 304L, conforming to the relevant ASTM product specifications with supplementary requirements like controlled parameters in chemical and physical properties, inclusion content, grain size, ultrasonic examination and IGC practice 'C', is used for construction of all the components of the tank. Manual and semi-automatic GTAW welding process is adopted with ER308L filler wires.

In order to minimize the fabrication time, a detailed study was carried out to decide the simultaneous fabrication of individual components and the assembling sequence. Accordingly, the individual shell courses baffle plates, ballast tanks, saddle supports, cooling coils and air spargers, dished ends with outlet piping, machining of nozzles, manholes and deep feed piping of all eight tanks were fabricated simultaneously. Sub-assemblies were fabricated before final assembly of the tanks, like assembly of individual shell courses to ensure obtaining the shell of required length, baffle plate to shell, saddle support to shell, ballast tank to shell, insertion & welding of cooling coil pipes, one dished end to shell, deep feed piping and manhole



Fig. 2 Cooling coils and ballast tank

to shell and closure dished end to shell. The shell (L=10.8 m) of the tank was fabricated by welding 7 Nos. of shell courses of length 1.5 m & 1 number of shell course of length 0.3 m with out-of-roundness & ovality of the fabricated shell meeting the requirements of ASME Sec-III Sub-section NC. Each of the five baffle plates were fabricated by welding 3 numbers of plate to obtain the required diameter of 4.7 m. 184 number of holes of diameter 92 mm were made by water jet cutting for the penetration of cooling coil pipes. The baffle plates were welded to the shell and the surface treatment of the entire tank was completed by rotating the shell on the support rollers & by spraying the acids by means of pumps in order to keep the tank surface wet. The saddle supports of the tank were fabricated separately and the shell after surface treatment were aligned on the saddle supports from the support rollers. The ballast tanks of diameter 406 mm with flat top head and bottom toriconical heads (solution annealed after forming) were fabricated, pneumatically tested and inserted through openings in the baffle plates (Figure 1). Cooling coils and ballast tank shown in Figure 2 and transportation of tank to FRFCF site shown in Figure 3.



Fig. 1 Fabrication of shells



Fig. 3 Transportation to FRFCF site

IV.3 Design and Development of Passive Gamma Scanning System

During the fabrication of nuclear fuel pins, fuel pellets of specific enrichment are loaded in clad tubes along with blanket pellets on either side and then, welded with an end plug. In order to avoid pellet mix-up a non-destructive technique is desired to ascertain whether appropriate pellets are stacked in the pin as per the design. As the fuel loaded pins are radioactive, the technique needs to be operated remotely, preferably with automation. This is also expected to help in meeting the production line requirements. For this purpose, a passive gamma scanning based system that utilizes the gamma radiation from the pellets has been designed and developed. The passive gamma scanning system consists of NaI detector assembly, multi-channel analyzer (MCA), data acquisition system and output module as typically shown Figure 1.

The system is designed to scan for gross gamma emission along the length of the fuel pin and to generate a graphical plot of gamma counts versus the length of pin. The scan graph output helps in confirmation of the fuel pellets of required enrichment at designated locations of the pin and also to identify any incidental case of cross mixing of fuel pellets in the axial blanket stack.

The counting window during scanning is equipped with a filter to discount Am-241 response, while measuring the gamma counts of Pu isotopes. This helps in differentiation between excess enrichment in fuel pellet and presence of Am-241 in the pellet. After fuel pellet loading, plug welding and decontamination, the fuel pin is passed through the scanning system to measure the gamma radiation emitted by the fuel pin.

The scan data, as typically shown in Figure 2 for two

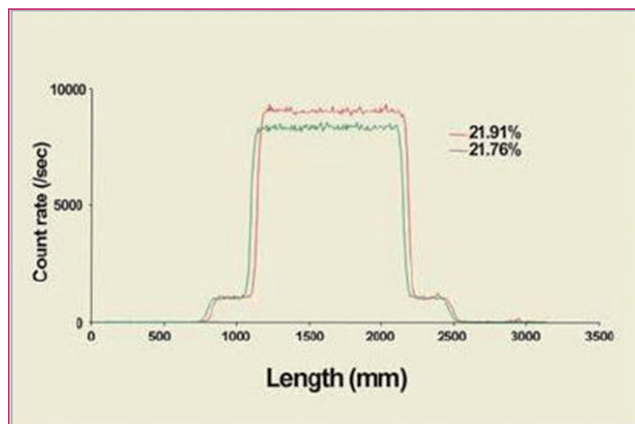


Fig. 2 Typical scan result

different cases, can be analyzed for selectively varying the energy window and the fuel pin length. After confirmation of the scan result with the required count data or reference data, the fuel pin is sent for spacer-wire wrapping.

The system is adaptive to remote operation and automation. The main system can be placed in a closed room and operated with a remote station, considerably reducing the radiation exposure to quality control personnel. The system can scan upto 8 pins (placed in a tray) in a sequential manner and display the results with suitable identification and labels. It requires about 2 hours to complete scan of one tray of 8 pins by the system.

The passive gamma scanning system was tested using dummy pins and a few mock trials with known gamma emitters were successfully completed. The system is ready for deployment in the fuel fabrication plant of FRFCF.



Fig. 1 Passive gamma scanning system

IV.4 Development of High Density Concrete for FRP Waste Tank Farm Roof Slab

High density concrete (HDC) of grade H30 using Hematite is required to be used for Waste Tank Farm roof slab in the fuel reprocessing plant (FRP) of Fast Reactor Fuel Cycle Facility (FRFCF). As there is no prior experience on high density concreting of radiation shielding zones in FRFCF, it is essential to demonstrate and gain confidence before taking up actual concreting, apart from obtaining clearance from regulators. In order to evaluate the constructability of beam of 2 metre depth along with 1.3 m thick high density concrete slab in a reinforcement-congested area having duct penetrations and compensatory shielding embedment, a mock-up study was carried out.

A full-scale model consisting of 1.3 metre thick slab along with 2 metre depth of beam was identified for carrying out the mock-up study (Figure 1). Foundation raft using N30 grade concrete with super structure consisting of columns and walls was constructed over an engineered backfilled soil area for the mock-up. Reinforcement for heavy density slab, duct penetration and compensatory shielding block (CSB) and EPs were placed as per the approved drawings. Subsequently, a duct of size 1.1 m x 0.6 m was erected and floor side CSB plates were erected and fastened as per the approved procedure. 100 mm diameter openings were provided in the top CSB plate to insert the needle vibrators to ensure compaction below top CSB.

The H30 mix designed with approved proportions was placed using concrete pump with a pipe line and boom placer. The height of fall was restricted to 1.5 metre for



Fig. 1 Full scale mockup slab



Fig. 2 Core samples drawn from mockup slab

preventing any segregation. Layer thickness of 300 mm was assumed and a needle vibrator with adequate length was used for achieving the required compaction. A number of pipe sleeves as grout nozzles were provided in and around the critical areas, where an obstruction to flow of concrete is expected like duct area of CSB & EP.

To qualify the mock-up concrete density in wet condition at the placement point and delivery point, conventional cube strength at the end of 7, 14 and 28 days, cylinder strength and split tensile strength were determined, water permeability test and ultrasonic pulse velocity (UPV) test were performed. In order to calibrate the UPV results, two heavy density concrete blocks of size 1.3 m x 0.6 m x 0.6 m, one with 50 mm thick plate on one side and another without plate to identify the effect of compensatory shielding plate, were casted and tested. Core samples, as shown in Figure 2, were drawn from the completed mock-up and compressive strength was tested at the end of 14 & 28 days. De-shuttering was done after 48 hours for beam & slab sides and curing was carried out for 14 days.

Post-concrete inspection indicated a satisfactory finishing of concrete surfaces and no defect / slurry loss was observed. The mock-up test was found to be satisfactory and no grout intake was observed. This mock-up study was also useful to prepare the methodology and to obtain regulatory clearances. Based on the experience from this mock-up study and following the same procedure high density concreting was successfully completed in Block -1 area of waste tank farm roof slab of fuel reprocessing plant of Fast Reactor Fuel Cycle Facility.

IV.5 Soil Structure Interaction Analysis of Safety Related UG Sump Supported on Engineered Backfilled Founding Medium

Fixed base analysis is acceptable for safety related structures supported on rock, where shear wave velocity is higher than 1100 m/s. But for the structures supported on engineered backfilled soil, shear wave velocity is of lower order and effect of variation in shear wave velocity of foundation medium needs to be analyzed. Based on ASCE 4-16, Soil Structure Interaction (SSI) analysis is required for such structures in order to arrive at super structure internal design forces.

In the present study, safety related Under-Ground (UG) structure of Low Level liquid Waste (LLLW) sump for FRFCF, resting on shallow engineered backfilled founding medium, is designed for site specific Operating Basis Earthquake Level (OBE), as indicated in Table 1. FE model of the UG sump generated is shown in Figure 1.

Field investigations were carried out at a similar engineered backfilled foundation medium in the infrastructure area of FRFCF and the same results were utilized to evaluate the parameters required for SSI studies of the LLLW sump. From geotechnical investigation data of engineered backfilled soil, a minimum Safe Bearing Capacity (SBC) that can be achieved is found to be 250 kN/m². Lower range of SBC is also considered accounting for the uncertainties involved in engineered backfilling operations. The range of shear wave velocity to be adopted for parametric study is indicated in Table 1.

SSI analysis has been carried out considering governing Load Cases & Load Combinations (LCOM) by estimating soil springs which are obtained from established safe bearing capacity relationship. Response Spectrum analysis has been performed for the range of soil springs, as indicated. Modal mass participation results are arrived. Base shear values for governing Load Combinations are calculated and further inter-story displacements are also calculated for varying shear modulus (G) values. Fundamental frequency from SSI modal analysis associated with each G value varies within 1% with respect

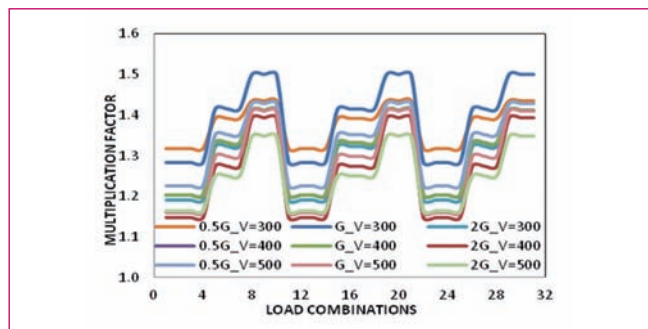


Fig. 2 Base Shear Ratio for various LCOM with fixed base

to fixed base analysis for the given UG sump structure. Higher mass participation occurs at lower frequency for lesser shear modulus, thus resulting in higher base shear and larger displacement. Variation of base shear with respect to fixed base analysis is represented in the form of Multiplication Factor for varying shear modulus as shown in Figure 2.

From the modal analysis results, it is observed that

1. At low frequency, more % of mass is participating in fixed base condition for all range of shear wave velocity in both horizontal directions.
2. Entire mass participate as in lower frequency range for the case of 0.5G. As shear wave velocity increases, % participation occurs at higher natural frequencies.
3. Fixed base analysis results give less base shear compared to that of SSI analysis results. Maximum base shear is at lower shear wave velocity.
4. The order of inter storey displacements are comparable. This may be attributable to the embedment effect of the sump. Maximum inter-storey displacement occurs at lower shear wave velocity.

Hence, for the safety structure of UG sump, supported on shallow foundation, shear wave velocity of foundation medium are required to be established by field and laboratory investigations and SSI analysis needs to be performed for a wider range of shear modulus. From the current study of SSI analysis for safety facility structure of UG sump, it is concluded that fixed base analysis may not be conservative.

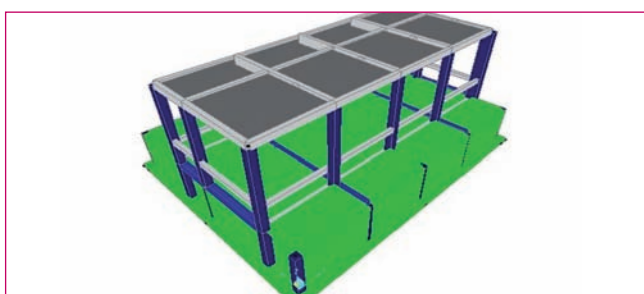


Fig. 1 FE Model of UG sump

Table 1: Parametric values for SSI Analysis

No	Parameter	Value
1	Maximum ground acceleration (OBE Level)	0.078 g
2	Shear wave velocity (Vs) for SBC 150 kN/m ²	300 m/s
3	Shear wave velocity (Vs) for SBC 200 kN/m ²	400 m/s
4	Shear wave velocity (Vs) for SBC 250 kN/m ²	500 m/s

IV.6 Commissioning of a Continuous Precipitator for Plutonium Reconversion at CORAL

The irradiated fuel discharged from FBTR is being reprocessed at the Compact Reprocessing of Advanced fuels in Lead shielded cells (CORAL). Plutonium is selectively precipitated as its tetravalent oxalate from the purified stripped product of the PUREX process and is calcined to get the plutonium oxide powder.

The throughput from the existing precipitator in the Plutonium reconversion laboratory (PuRCL) had to be enhanced as it could not be achieved by using the existing precipitator column in GB#1 of PuRCL, CORAL. This was mainly due to the vacuum aided mixing mode which hampers the continuous operation of the column. It was also found difficult to transfer the plutonium oxalate slurry. These factors restricted the use of this column during the reprocessing campaigns at CORAL. Hence, a new precipitator column with mechanical agitator was designed, fabricated, installed and commissioned to carry out this operation in semi-continuous mode so as to reduce the man-rem expenditure significantly. In addition, this would serve as a prototype equipment for similar operations to be carried out at DFRP and FRP, FRFCF. The new precipitator column (Figure 1) has been tested and qualified for erection in the glove box. The testing of this precipitator was carried out by mixing uranous nitrate (feed) and oxalic acid solutions (precipitant). In order to avoid loss of uranium, and to ensure quantitative precipitation of the latter, a known excess concentration oxalic acid, was maintained than the stoichiometric requirement. Feed solutions with different concentrations of uranium was mixed with



Fig. 2 Uranous oxalate precipitation

precipitant at different flow rates. The mixing of both these solutions was enabled by a mechanically operated stirrer. A picture showing precipitator column is presented in Figure 1 and the precipitator with uranous oxalate preceipitate is shown in Figure 2.

The precipitator column has been installed and commissioned. The performance of the column and efficiency of mixing was tested with actual plutonium stream (Figure 3) and were found to be satisfactory. The height of the mixing zone was so optimized as to ensure smooth and continuous precipitation of the desired quantity of plutonium oxalate. The performance of the precipitator column is found to be satisfactory and is put into operation from the 51st campaign of CORAL.

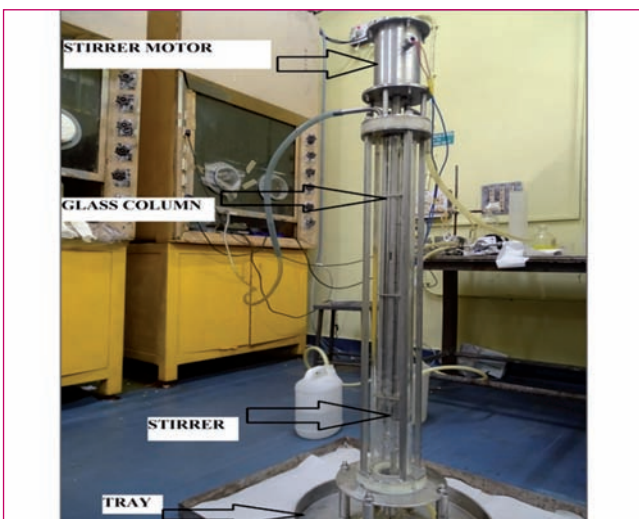


Fig. 1 New precipitator column for CORAL reconversion



Fig. 3 Plutonium oxalate precipitation in PuRC

IV.7 FBTR Spent Fuel Reprocessing Campaigns at CORAL

CORAL is the acronym for *COmpact Reprocessing of Advanced fuels in Lead cells* and is located in RpG. It houses equipments for reprocessing FBTR spent fuel. The primary objective of CORAL is to process the irradiated mixed carbide fuels with varying specific activities. This would provide valuable inputs for the evolution of the technology for FBR fuel reprocessing. By operating this facility the process parameters required for performance evaluation of the equipment as well as the validation of the plant design are being accomplished.

CORAL employs a PUREX process based aqueous technology suitably modified to handle Pu-rich irradiated fuels discharged from FBTR. Essentially it is a pilot facility dedicated to innovative research, design, development and deployment of closely guarded reprocessing technology required for higher capacity plants like DFRP for demonstration of recycling mixed-oxide FBR fuels and FRP of FRFCF.

Some critical equipment required specifically for FBR fuel reprocessing viz. fuel pin chopper, centrifuge for feed clarification and centrifugal extractors for handling high active feed solutions have been tested and validated with highly active Pu-rich solutions. Any amount of extensive testing on unirradiated materials would not reveal the operating problems; only under actual operating conditions, the designs can be improved to provide satisfactory operation.

This facility houses adequate intervention capabilities to incorporate design improvements and test the same under the actual operating conditions. With an array of small tanks and small process holdup, trials could be completed with small inventory of materials. Figure 1 shows a view of CORAL operating area.

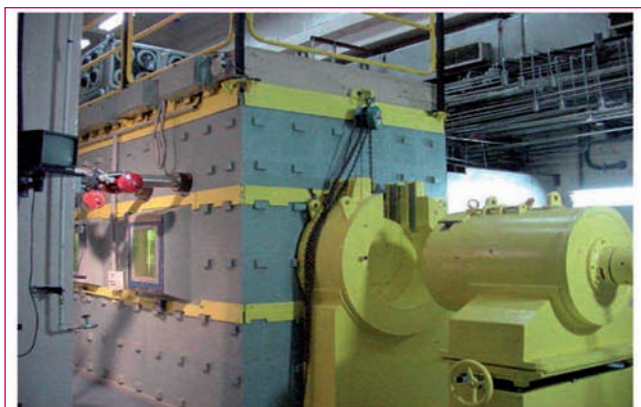


Fig. 1 A view of CORAL operating area

The major objectives realized from CORAL operations so far, are as follows:

1. Successful design, operation and improvisation of remote-handling tools for hot-cell operation
2. Indigenous design and development of centrifugal extractors in CORAL that led to their deployment in DFRP
3. Optimization of the process flow sheet for reprocessing of mixed carbide fuel in a single cycle operation
4. Indigenous design, development and deployment of centrifugal extractor drive-motors and their scale up for deployment in DFRP
5. Reprocessed Pu was refabricated into fuel and currently forms part of the driver fuel in FBTR. Closure of FBR fuel cycle has thus been demonstrated.

Under stage-wise clearance from AERB, it has successfully reprocessed the spent fuel from FBTR (low burn up, 25, 50, 100 and 155 GWd/t) since 2003 in campaign modes. Since 21st campaign, annual license for CORAL on regular basis was issued by AERB. It met its initial mandate of reprocessing of 14 FSAs of FBTR in Feb. 2017. After extensive deliberations, CORAL was relicensed by AERB for further operations for five more years from 2018.

Since January 2019, seven campaigns for reprocessing 155 GWd/t burnt FBTR fuel have been successfully completed meeting the product specifications and radiological safety norms. The eighth campaign is currently in progress.

The significant achievements after relicensing are the following;

Collective dose expenditure continues to show a decreasing trend, with the most recent 52nd campaign having the lowest dose expenditure among all the campaigns completed so far.

The plant continues to operate without any incidence of internal exposure to the personnel.

Waste generation and disposals were as per approved norms and all the discharges/disposal to waste management agency were within the limits stipulated by AERB.

IV.8 Salient Features pertaining to DFRP and its Commissioning

The Demonstration Fast Reactor fuel reprocessing Plant (DFRP) is advanced stage of commissioning. The commissioning of this plant involves Pre-operational checks and tests (Stage-I - Sub-system testing and commissioning), testing the systems with water and acid (Stage II), carrying out operation trials with acid and solvent (TBP) (Stage-III), testing with uranyl nitrate (cold feed run) (Stage-IV) and finally qualifying the system with radioactive feed, viz., hot run (Stage-V). As part of the Stage-I commissioning, physical verification of pipelines for proper connectivity, slope, continuity in process lines and proper erection of instruments were verified. Deficiencies were corrected and the systems tested. A typical view of tanks and equipment along with their associated piping inside the process cell is shown in Figure 1.

Eight utility systems, viz., (1) general use water system, (2) process cooling water (pcw) system, (3) fire water system, (4) chilled water system, (5) steam system, (6) compressed air system, (7) compressor and (8) DM water system were checked thoroughly and tested and put under operation.

In the stage –II, all process tanks and equipment were calibrated; functionality and performance were tested for all Transfer Airlift (TAL), Metering AirLift (MAL), Vacuum aided Airlift (VAL) and steam-jet transfers in Process Plant Facility (PPF) and the waste tank farm (WTF). All service headers, systems and lines were checked for their availability and functionality. In all cases instrument functionality and their responses were checked and also their communication with main control room was verified. All annunciation windows and functionality of the alarms were tested. The view of DFRP control room is shown in Figure 2.

Commissioning of the reconversion laboratory has been completed. A picture showing a view of the latter and that pertaining to the process control laboratory are shown in Figures 3 and 4, respectively.



Fig. 2 DFRP control room

All the process support systems were tested and their performance as per requirements have been verified. Due to the density of piping, the testing of all these systems and equipment were very challenging and warranted innovative techniques and procedures.

All the systems pertaining to air supply, off-gas and ventilation were tested for their functionality and performance. Leak testing of six alpha tight integrated large containment boxes and dissolver cell were completed and the stipulated leak tightness was achieved. The leak testing was rendered extremely difficult due to the large volume of the box and large number of penetrations. Limited access, low head room at some locations made these tests very challenging. For leak detection at inaccessible locations, an innovative method viz. smoke test with leak detection by the thermal imaging technique was used.

Commissioning of sampling systems based on both the Master Slave Manipulators (MSM) and Robot were completed with water as the test medium. Testing of pneumatic conveying system for sample bottle transfer between sampling/analytical cell to laboratory was completed. The MSM based sampling station and sample



Fig. 1 Typical view of tanks and equipment with piping inside process cell

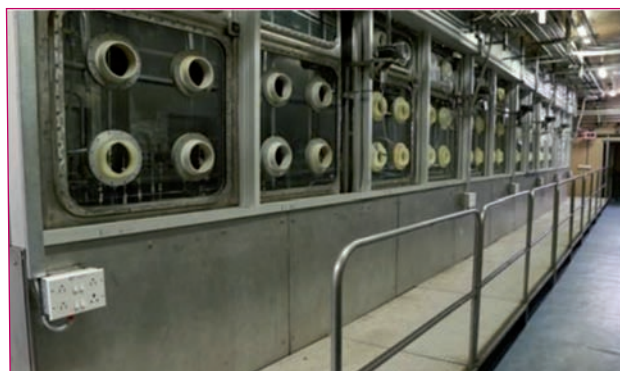


Fig. 3 Plutonium reconversion laboratory



Fig. 4 Process control laboratory



Fig. 5 MSM based sampling station



Fig. 6 Sampling handling robot inside cell

handling robot inside cell at installed condition is shown in Figures 5 and 6.

All the test reports pertaining to water runs were prepared in the required formats and submitted to AERB for obtaining clearance for the next stage of commissioning. After a detailed review of these reports by AERB, clearances were obtained for the next stage of commissioning viz., stage III [Acid-Solvent (TBP) run], and the same is currently in progress.

All the tanks and equipments, TAL, MAL, VAL and Steam-jet transfers were rinsed with acid for removal of corrosion products. Sampling systems were checked with nitric acid medium as per process requirement and performance has been found to be satisfactory.

It is planned to take up the cold feed run (Uranium run) shortly and towards this, further work is in progress.

IV.9 Design and Development of Multiple Pin Chopper Capable of Chopping both FSA and RSA Pins of PFBR for DFRP

A special, unique and a “first of its kind” shearing machine (chopper) has been designed to chop the fuel pins of the Radial blanket Subassemblies (RSA) and Fuel Subassemblies (FSA) of PFBR for use in DFRP. It is a vertical shearing machine with multi pin chopping (Figure 1). It has been designed modularly which facilitates easy replacement of those parts that are likely to undergo more wear and tear.



Fig. 1 RSA & FSA fuel pin chopping assembly

The major challenges faced in accomplishing this are listed below. The non-availability of information about a similar prototype necessitated an indigenous design. The design had to incorporate features for avoiding entanglement of the spacer wire while chopping. A suitable viewing system with components both optical and electronic that are resistant to radiation was needed. The design had to be optimized for remote operation and maintenance of this equipment in a highly acidic environment. Optimization of various features resulted in complex and intricate profile of critical components, which demanded special machining processes. Use of lengthy racks (approximate 3 m) necessitated splitting of these racks into two independent modules for carrying out milling operation.

After incorporating all the above task, the final equipment comprising the following was designed, viz., Magazine, Gripper block, Stationary block and Multiple Pin Cutter. Figure 2 shows the gripper, stationary block, cutting tool and guide plate assembly. The magazine was so designed as to hold 10 pins and had been optimized based on the limitations of size and weight of the magazine and cutting tool from a remote handling

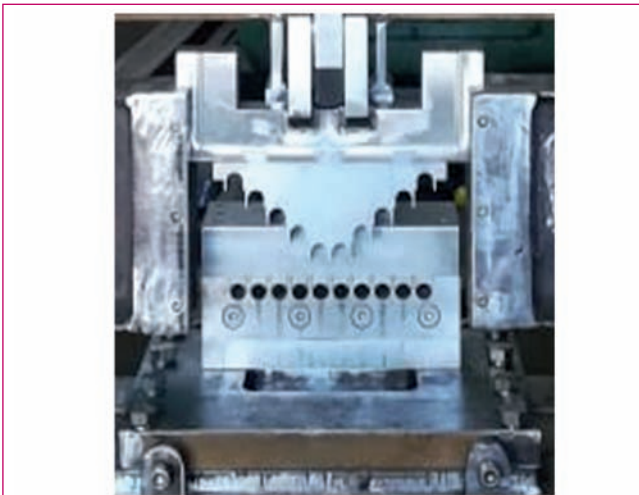


Fig. 2 Gripper, stationary block, cutting tool and guide plate assembly

perspective and the throughput requirements (Figure 3). Elongation of the pin after irradiation had also been taken into consideration while arriving at the length of the magazine.

In this machine the fuel pins are allowed to slide on a stationary block and are gripped by the gripper block with the help of a pneumatic cylinder such that a projected length of 32 mm of the pin is chopped by a multiple pin cutter.

The material of the cutting tool was chosen based on the prerequisites viz., hardness, toughness, corrosion resistance and wear resistance. A prototype of this chopper has been manufactured and mock up trials have been carried out to demonstrate feeding, gripping and shearing performance of this equipment.

In order to estimate the stresses on the cutting tool a Finite Element analysis had been carried out. Design



Fig. 3 Magazine assembly with chopper

life of the cutting tool had also been calculated based on the probable failure modes viz., blunting of the tool and high cycle fatigue. Based on the estimated shear force on the cutting tool (40 kN), and a maximum stress of 210 MPa (allowable: 1600 MPa), the life of this tool was estimated based on the fatigue to be greater than 10^6 cycles, and that due to blunting of the tool was found to be $\approx 10^5$ cycles.

The feeding, gripping and cutting mechanisms of the multi-pin chopper have been found to be satisfactory. The cutting tool performed well for aluminum rod, SS rods and dummy fuel pins with aluminum insert of PFBR pin (Figures 4 and 5). Dummy fuel pins along with spacer wire have been chopped and performance during chopping had been found to be satisfactory. Thus, the design has been validated. In addition, some more refinements are being incorporated in order to fabricate the actual chopper to be deployed in DFRP.



Fig. 4 Chopped pieces of RSA dummy fuel pins



Fig. 5 Chopped pieces of FSA dummy fuel pins

IV.10 Development of Laser Dismantling Machine for PFBR Subassemblies in Head End Facility of DFRP

Laser dismantling machine is a remotely operated computer controlled equipment for the dismantling of high burn-up FBTR and PFBR spent fuel subassemblies (FSA). This machine is capable of performing both the longitudinal and transverse cutting of stainless steel hexagonal sheaths using a laser torch assembly or a motorized slit-saw wheel for extraction of the fuel pin bundle. This machine comprises a fully automated as well as a motorized slit-saw for redundancy. Figures 1 and 2 show the 3D CAD model and the actual machine with a PFBR FSA loaded on it respectively. Pictures showing the FSA cut both longitudinally and transversely are given in Figure 3. This machine is constructed modularly in order to facilitate easy remote operation and maintenance. This machine could also carry out both length and temperature measurements on the subassemblies. It uses a touch trigger sensor assembly with radiation resistant linear scales on all axes in order to carry out dimensional measurements.

The data obtained from the touch trigger probe is then used for the reconstruction of a profile of the subassembly for further analysis of dimensional changes due to irradiation. Dimensional measurements of FSA could be carried out with an accuracy of 200 microns. A touch trigger sensor module mounted on the Y-stage carriage is used for the profilometry of these FSAs. Two horizontal styles are used to acquire surface points from various cross sections of the irradiated FSAs. A cylindrical calibration block shown in Figure 4 is used to verify the accuracy of the profilometric measurements made by this machine. This machine has been so designed as to operate in environments with radiation dose levels of the order of 10^4 Gy/hr.

The erection and commissioning of this “first of its kind” machine inside the hot cell proved to be very challenging due to its large size and weight (5 tons) and other stringent site prerequisites. This was carried out through the roof plug opening of 1m X 1m after detailed preparatory works, mock-up simulations and safety clearances. Each



Fig. 2 Laser dismantling machine

component was lifted to an elevation of 10.5 m by using an EOT crane and was vertically lowered into the hot cell through the roof plug opening, assembled and accurately positioned inside the cell. The machine was interfaced with power and control systems installed in the operating area by using nuclear grade cables laid through leak tight wall penetrations. A personal computer based graphic user interface (GUI) was incorporated in order to facilitate remote operation and data storage. As a redundant system to this interface a manually operable console was also installed.

After the successful erection of this machine inside the hot cell, functional test trials were performed on a dummy subassembly to check longitudinal and transverse cutting of hexagonal sheath, temperature and length measurements and profilometry.

Accuracy and repeatability of different stage motions were also checked. As part of the commissioning, profilometry of a calibration block was done and with the acquired data, a 3D CAD profile was reconstructed. This machine was successfully erected and commissioned inside the hot cells of head end facility (HEF) of DFRP.

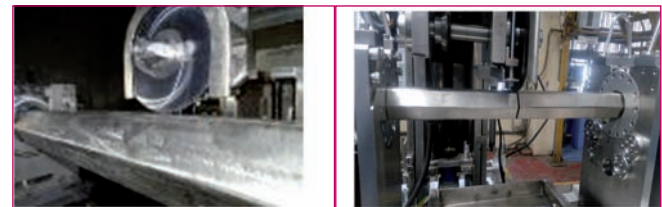


Fig. 3 Longitudinal and Transverse sections of the FSA.

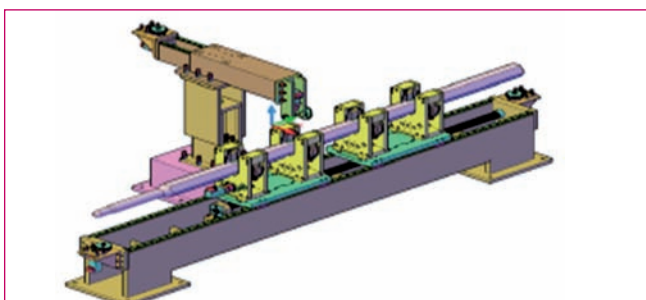


Fig. 1 3D CAD model of the Laser dismantling machine.

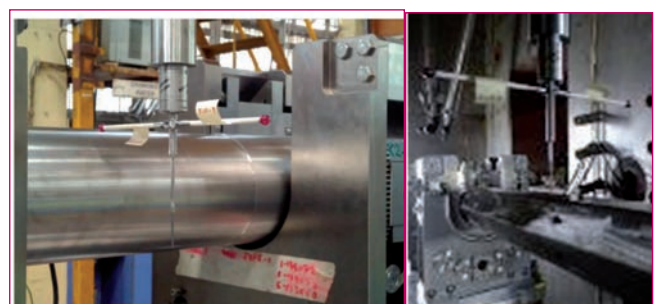


Fig. 4 Cylindrical block for profilometer calibration

IV.11 Design Modification in the Stationary Bowl of the Centrifugal Extractor for Reprocessing Applications

Annular centrifugal extractor (ACE) is most suitable for fast breeder nuclear reprocessing applications. It belongs to the class of stage-wise contactors and requires 16 to 20 stages in order to achieve good separation of uranium and plutonium from the spent nuclear fuel. However, this equipment required frequent maintenance due to high rotation speed, which is one of its limitations. In the Demonstration Fast Reactor Fuel Reprocessing Plant (DFRP), ACEs have been arranged in two rows to facilitate easy remote maintenance. Among these one of the rows have been located at an elevated position. This arrangement necessitates the use of inter-stage air-lift pumps to transfer liquid from the lower to the higher stages. A picture of these 20 stages comprising CE 40 mm bowl with inter-stage pump is shown in Figure 1.

In order to avoid the use of air-lift pumps that are prone to choke during solvent extraction operation, a new 8-stage 40 mm stationary bowl setup was developed suitable for use at DFRP which would enable for easy remote maintenance. Both a schematic as well as a photograph showing this 8 stage modified centrifugal extractor stationary bowl are shown Figures 2 and 3 respectively.

Flooding experiment was conducted in the 8-stage CE setup with 30% TBP and acidified water system. Result shows, it could be operated up to total throughput of 63 L/h



Fig. 1 20-Stage CE 40 mm bowl with inter-stage pump

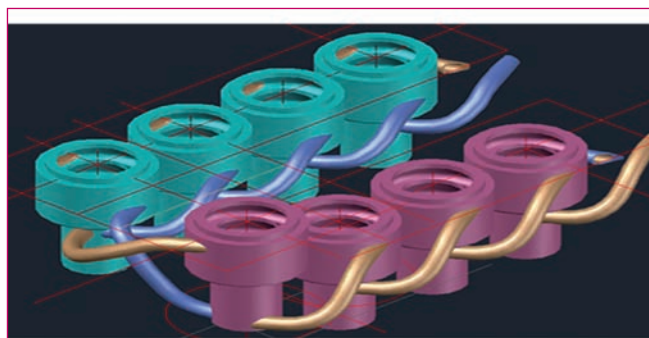


Fig. 2 Schematic view of pipe connections in modified CE stationary bowl (8 stages)

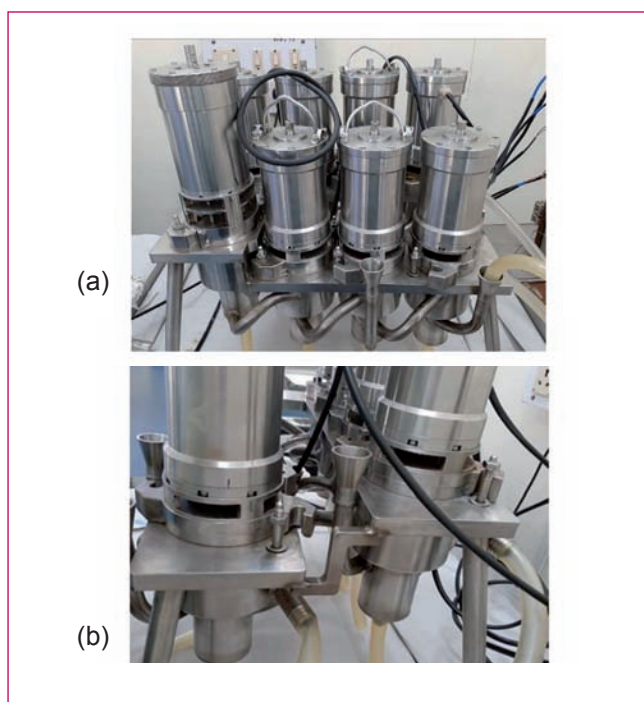


Fig. 3 Photograph showing the modified centrifugal extractor stationary bowl (a) front view and (b) side view

at aqueous to organic ratio (A/O) ratio of 1 at 3000 rpm.

In order to validate the proposed design, flooding experiments were conducted in a single stage CE (40 mm) at 3000 rpm over a wide range of A/O (flow rates) ratio varying from 0.1 to 10. The flooding throughput is shown in figure 4 and it is around 60 L/h at A/O ratio of 1.

Trials revealed that the operating throughput of the modified 8 stage CE setup is equivalent to that of a single stage setup and the proposed design modification is suitable for reprocessing application.

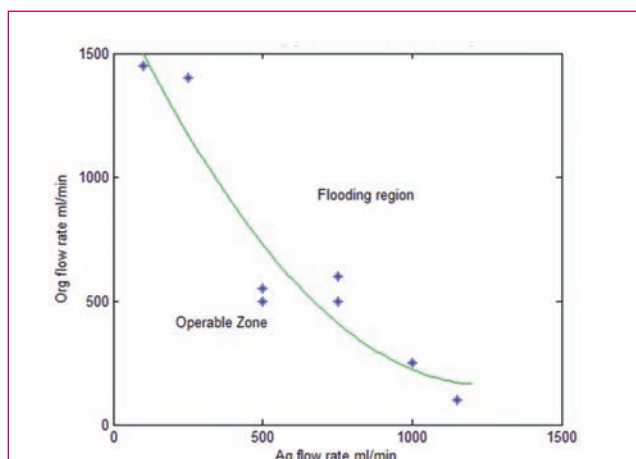


Fig. 4 Operating range of CE 40 mm bowl at 3000 rpm

IV.12 Seismic Qualification of Integrated Glove Box Train at DFRP

The plutonium re-conversion (PuRC) laboratory of Process Plant Facility (PPF) of the Demonstration Fast reactor fuel Reprocessing Plant (DFRP) receives the feed plutonium nitrate solution from the process plant and delivers the solid product i.e. plutonium oxide (PuO₂). PuRC lab includes glove boxes that are used for precipitation, filtration and calcination to form plutonium oxide. PuRC lab houses two trains of integrated double module glove boxes designated for specific operations that are interconnected linearly.

As per safety requirement, glove boxes with supporting structure at PuRC Lab had to be seismically qualified to ensure their safety during any seismic event.

Glove boxes, supporting structure, interconnecting ports and piping are constructed of SS 304L and the laminated glass panels are mounted on the glove boxes. Glass properties are attributed at the locations where the glass panels are mounted on the glove boxes. Glass panels are modeled for the purpose of applying pressure loads and contributes to the dead weight only. However, the stresses and deflections of the glass plates have not been considered for the glass panel as it is not being qualified based on this analysis.

The integrated PuRC glove boxes are categorized as safety class-2 components as per the safety classification of systems in Fuel Reprocessing Plant. Hence, the design and analysis have been performed in compliance with ASME Section-III, Subsection NC and the permissible stress limits as specified in Table 1.

Finite element (FE) analysis of the integrated glove boxes along with the supporting structure has been performed using general purpose FE package. All these glove boxes are connected through interconnecting ports in between them, along the length of the supporting structure. Two node beam elements have been used to model the supporting structure. Glove boxes have been modeled with four node structural shell element whereas mass elements along with rigid link elements were used for masses of the equipment inside the glove boxes (Figure 1).

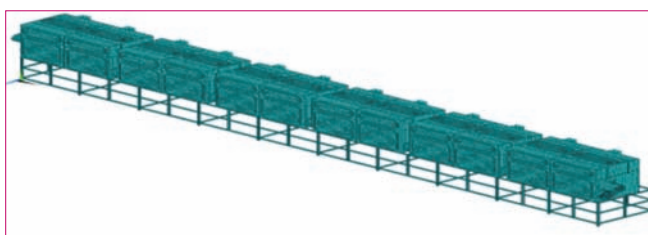


Fig. 1 FE Model of Pu-RC integrated glove box train

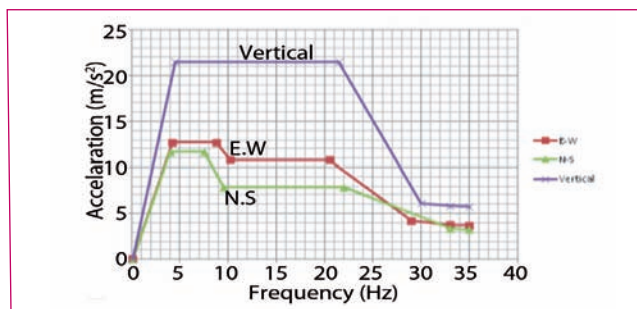


Fig. 2 FRS at +4.75 m elevation for 3% damping

Static structural analysis has been performed for the static load due to self-weight, weight of equipment inside the glove boxes and the pressure load. The total weight of the equipment inside the glove boxes is 3450 N. The glove boxes are subjected to a negative pressure of 25 and 75 mm water column under normal and abnormal conditions respectively.

Modal analysis of the system has been carried out in order to extract the natural frequencies, mode shapes and modal participation factor. Response spectrum method has been used for the seismic analysis. Spectral acceleration values corresponding to 3% damping at an elevation of +4.75 m for DFRP site have been used (Figure 2).

Values of the stresses Level D service limit at few

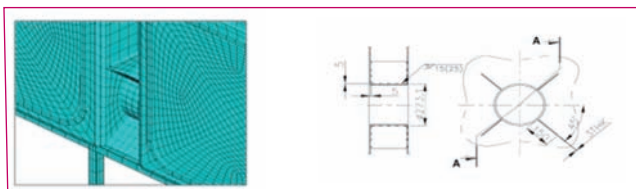


Fig. 3 Retro fitting of interconnecting port

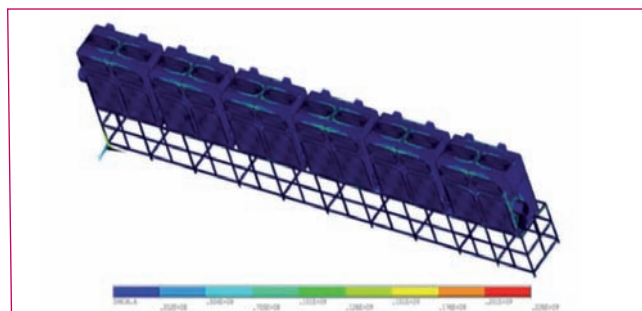


Fig. 4 Stress distribution plot of integrated glove boxes

Table 1: The permissible stress limits

Service Level	Stress Limit
Design Condition	$\sigma_m \leq 1.0 S$
Level A	$(\sigma_m \text{ or } \sigma_L) + \sigma_b \leq 1.5 S$
Level D	$\sigma_m \leq 2.0 S$ $(\sigma_m \text{ or } \sigma_L) + \sigma_b \leq 2.4 S$

locations exceeded the permissible stress limits. The observed maximum induced stress values were found to be located near the junctions of the interconnecting port of second last glove box and hence four numbers of ribs oriented at 90° apart, connecting the interconnecting port and end face of glove box are recommended as shown in Figure 3.

Post retrofitting, the FE analysis has been repeated, and it was found that the glove box train with supporting structure is seismically safe. Hence, with the recommendation of localized retrofitting of the interconnecting port, the integrated glove boxes of PuRC lab with supporting structure have been seismically qualified (Figure 4).

IV.13 Integration of Digital Process Instruments with Plant Control System for DFRP

In the Demonstration Fast Reactor Fuel Reprocessing Plant (DFRP), many different process parameters like pressure, level, density etc. are measured by using conventional 4-20mA differential pressure transmitters. The analog signal (420 mA) from each of these sensors is transmitted over dedicated cables from the field to RIO (remote input/output) drop near the Control Room. In order to overcome this difficulty we have resorted to Foundation Fieldbus (FF) technology in a small, non-safety loop and studied its characteristics. Our experience with this technology is briefly described below.

FF protocol is an all-digital, serial and two way communication protocol for field instruments. This has inherent advantages over the conventional 2 wire communication. These include significant reduction of field cabling with multidrop connection, control algorithm in field instruments i.e. Control In Field (CIF) feature, advanced device diagnosis, etc. Also all-digital communication has better accuracy over analog signal transmission. On a trial basis we have installed two field bus differential pressure transmitters and integrated the

FF field instruments and hardware with existing PLC & SCADA. The integration of these field instruments requires specific FF hardware & protocol converters like fieldbus trunk / segment, FF power supply, FF linking device (H1 to HSE converter).

The main challenge faced during the implementation of this technology was with the loading of proper DD (device description) files of the differential pressure transmitter in the FF linking device and configuring the linking device, version number mismatch and non availability of the files. Figure 1 shows the experimental test setup. The field devices and linking device (Figure 2) were configured with proprietary FF software. Further this hardware was interfaced with Schneider PLC and Vijeo Citect SCADA (Figure 3).

Process parameters could be viewed and configured using the FF software and a provision has also been made to configure through SCADA using MODBUS TCP/IP giving significant advantage as compared to the conventional 4-20mA wiring. This implementation has demonstrated that this protocol could be incorporated in the upcoming plants.

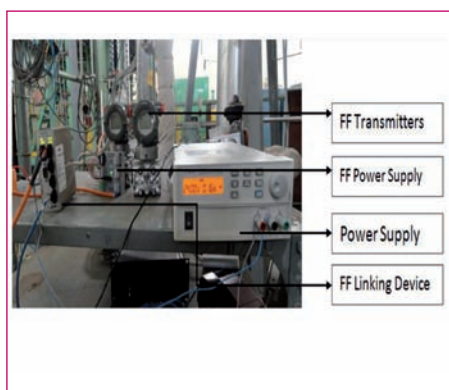


Fig. 1 Experimental Test Setup with Foundation Fieldbus Hardware

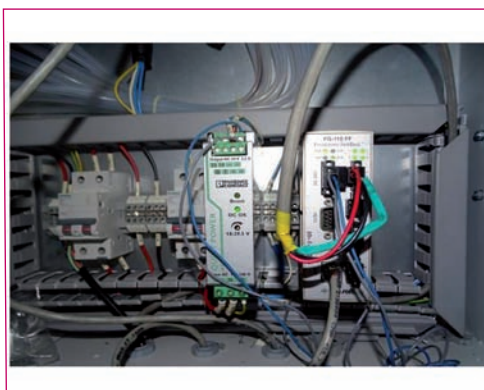


Fig. 2 FF linking device (H1 to HSE converter)

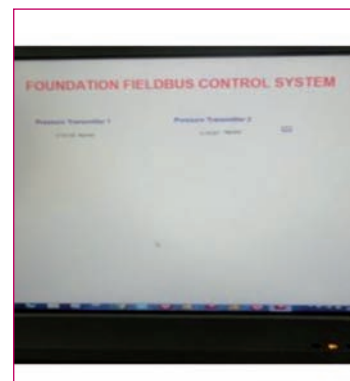


Fig. 3 SCADA Interface

IV.14 Preparation, Purification, Sampling and Transfer of 1 tonne of Eutectic Salt Electrolyte for Pyro Process R&D Facility

Pyro Process R&D Facility (PPRDF) is being set up in MC&MFCG to demonstrate important process steps of pyrochemical reprocessing. U alloy containing Zr and simulants for Pu and typical fission product elements will be used to simulate the spent metal fuel. The facility is designed to demonstrate main process steps for 10 kg of U alloy per batch scale.

Electrorefining is one of the main process steps. The electrolyte used in electrorefining is a eutectic mixture of LiCl(44.5 wt%)-KCl(55.5 wt%) salt. Approximately, 1 ton of this salt is required for initial campaigns of electrorefining in PPRDF. Commercially available LiCl and KCl cannot be directly used as it will contain significant amount of moisture, particularly after long storage at site. LiCl is highly hygroscopic and therefore all operations involving this salt have to be conducted in a dry atmosphere (< 50 ppm of moisture). For preparing the required quantity of salt, a Salt Handling & Purification System (SHPS) was installed and commissioned in PPRDF. Salt purification involves vacuum drying of solid salt to remove the unbound moisture followed by chlorination of molten salt to convert hydroxides to chlorides. SHPS consist of required subsystems/equipment for each stage of salt purification.

Mixing of salts in required proportions and vacuum drying the mixture, is carried out in a customized glove box (GB) with nitrogen atmosphere (Figure 1). GB is maintained at a positive pressure of +20 to +40 mm water column (G). A purification circuit comprising of blower, molecular sieves column, associated piping and instrumentation connected to GB helps to maintain moisture level below 50 ppm in N₂ atmosphere. Main equipment inside GB are mixer and vacuum oven designed to handle 50 kg (max) of mixed salt per batch. A cold trap is provided



Fig. 1 Glove Box for salt mixing & vacuum drying



Fig. 2 (a)Chlorination vessel inside fume hood (b)chlorine scrubbing system

between the oven and vacuum pump to prevent moisture entering the pump. 26 batches, each of 18 kg of LiCl & 22 kg of KCl (approximately), were mixed and vacuum dried at 250°C for 24 h. The dried salt powder was then transferred batch by batch to Chlorination Vessel (CV). In CV the salt mixture is melted and dry chlorine is bubbled through the melt. It is housed inside a fume hood (Figure 2a) connected to a scrubbing system (Figure 2b) through a blower. Dry chlorine is supplied from a chlorine tonner through a supply header. Any un-reacted chlorine from CV is scrubbed using sodium hydroxide solution in the scrubbing system. After chlorination, molten salt was transferred to storage vessel through a surface heated pipeline by pressure transfer method. Salt samples were taken before and after vacuum drying and after chlorination (Figure 3). The samples were analyzed for elemental impurities. The impurities were found to be within acceptable limits. Residual cathodic current densities were also determined and found to be acceptable. With round-the-clock shift operation for about five months, 1 ton of purified salt was prepared and stored in a vessel maintained with ultra high purity argon cover gas.



Fig. 3 Salt sample after chlorination

IV.15 Development of Non- Destructive Assay Methods for U, Pu and Am in Cd and LiCl-KCl Salts from Pyrochemical Reprocessing

U-Pu-Zr is a candidate material for the metallic fuel. During the pyrochemical reprocessing (molten-salt electrorefining) of metallic fuel using LiCl-KCl as eutectic melt operated at 773K temperature, U and (U, Pu & minor actinides) are electrodeposited at two different cathodes namely, solid steel and liquid cadmium cathode respectively (Figure 1). A non-destructive assay method for ^{239}Pu , ^{238}U and ^{241}Am in Cd matrix and LiCl-KCl salt samples was developed using gamma spectrometry by HPGe detector. The method was established using matrix and geometry matched gamma standards of ^{152}Eu and ^{241}Am for the assay of Pu, U and Am, respectively.

Alumina crucibles of 20 mm diameter, 30 mm height were taken and filled with ~50 g cadmium liquid. The Cd ingot obtained after cooling was sliced into multiple pieces of ~4 mm thickness each. Three gamma standards in Cd matrix were prepared using ^{152}Eu (Figure 2). In the first standard, a known amount of ^{152}Eu activity was spiked on each Cd slices as well as at the bottom of the alumina crucible and the slices were stacked inside the alumina crucible. The second and third standards were prepared by spiking the known amount of ^{152}Eu activity completely, at the bottom most and at the top most Cd slice respectively. The first standard was useful for analysis of uniformly distributed ^{239}Pu and ^{238}U inside the Cd matrix, whereas, the other two standards represent the lower and upper limits, for non-uniform distribution. Similarly, three gamma standards were also prepared using ^{241}Am spiked in Cd matrix. All these standards were positioned in a 50 mL polypropylene bottle and triply sealed in PVC bags as shown in Figure 2. Similarly, gamma standards were prepared in LiCl-KCl salt matrix by taking ~40 mg of salt into a 10 mL polypropylene vial and spiked with known amount of Pu. Similar standard was prepared with ^{241}Am . Both the standards were doubly sealed in PVC Bags.



Fig. 1 Typical liquid Cd cathodes used for molten salt electrorefining of U-Pu-Zr alloy

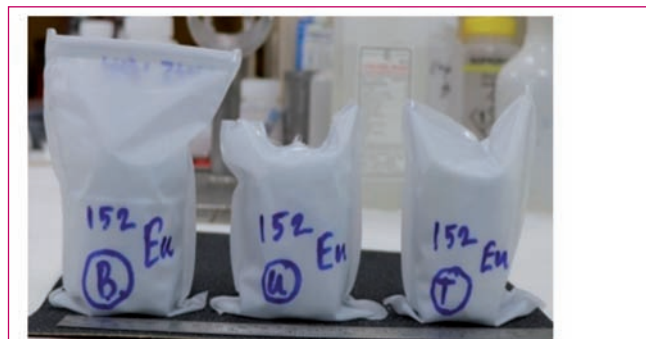


Fig. 2 ^{152}Eu reference standard in Cd cathode crucible (triple sealed)

All the samples and standards were assayed by gamma spectrometry in reproducible geometry. The amounts of Pu, Am and U present in Cd and LiCl-KCl salt matrices are presented in table 1 and 2, respectively in the case of uniform distribution. For non-uniform distribution of these elements in the Cd matrix, a range with lower and upper limits was also provided in brackets. The limits range was very close to the reported values of Pu and U, whereas the range was very broad for Am due to the large attenuation of 60 keV from ^{241}Am in the Cd matrix. Estimation of U in the LiCl-KCl salt sample would have been possible for the large size sample. Present study established a viable method to estimate ^{239}Pu , ^{241}Am and ^{238}U in Cd matrix as well as in LiCl-KCl salt matrices by non-destructive assay technique.

Table 1: Analysis of Cd matrix samples

Sample ID	^{239}Pu (mg/g)*	^{238}U (mg/g)*	^{241}Am (µg/g)*
P_Cd_1	9.4 (7.2-11.2)	14.4 (12.8-16)	11 (1.8 - 43.6)
P_Cd_2	17.3 (13.6-21.2)	38.2 (34-42.2)	5.2 (0.9 - 20.8)
P_Cd_3	13 (10-15.6)	27.8 (24.8-30.8)	9.2 (1.5-36.6)

(*Values obtained for the lower and upper limits are given in parenthesis, while the value represents that of uniformly distributed source for Cd matrix samples).

Table 2: Analysis of LiCl-KCl matrix samples

Sample ID	^{239}Pu (µg/g)	^{241}Am (ng/g)
Pyro_salt_1	21.2	114
Pyro_salt_2	24.3	130

IV.16 Calculation of DoHyA as the Solvent for the Pre-treatment of HLLW during Minor Actinides Partitioning

The U-Pu-Zr metallic alloy fuel contains 6-10 wt.% of zirconium. Aqueous reprocessing of the spent metallic fuel generates high-level liquid waste (HLLW) containing about 60% of the total zirconium present in the fuel. While the presence of zirconium in dissolver solution is not a big concern during the separation of uranium and plutonium during reprocessing, it poses several challenges in the subsequent trivalent actinide partitioning and Ln-An separation from HLLW, due to the complex co-ordination chemistry of Zr(IV) with the ligands employed for trivalent separation. In view of this, the extraction behavior of a trivalent representative ion, Nd(III), in the presence of Zr(IV) from nitric acid medium was studied in our laboratory using the candidate ligands proposed for trivalent actinide separation from HLLW, namely *N,N,N',N'*-tetraoctyldiglycolamide (TODGA), and *N,N*-di-octyl-2-hydroxyacetamide (DOHyA).

Studies have shown that the extraction of Zr(IV) in both TODGA and DOHyA phases was far higher than Nd(III), and the organic phase upon extraction of Zr(IV) undergoes either third phase formation or crud formation during loading. Figure 1 compares the average sizes of reverse micellar aggregates in TODGA and DOHyA extractants recorded after extraction of Zr(IV) and Nd(III) from 4 M nitric acid. Even though both these systems did not show any third phase during the extraction of Nd(III), the splitting of organic phase was observed in TODGA system during the extraction of Zr(IV) even in the presence of the best phase modifier namely, 1-octanol, due to the large size of aggregates as shown in Figure 1

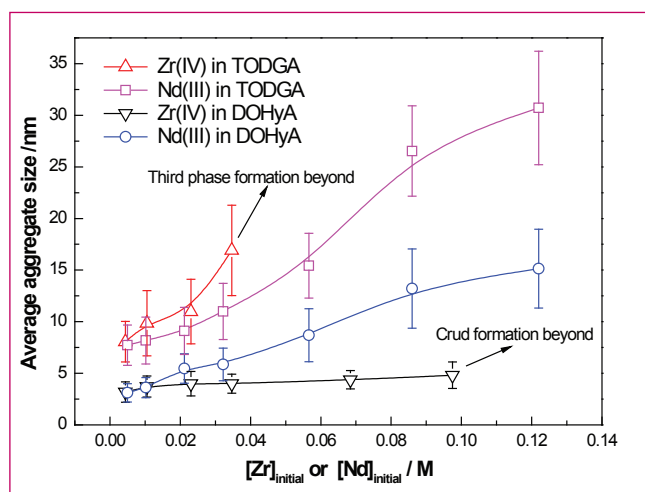


Fig. 1 Variation in the size of aggregates present in the organic phases obtained after the extraction of different concentrations of Nd(III) or Zr(IV) from nitric acid

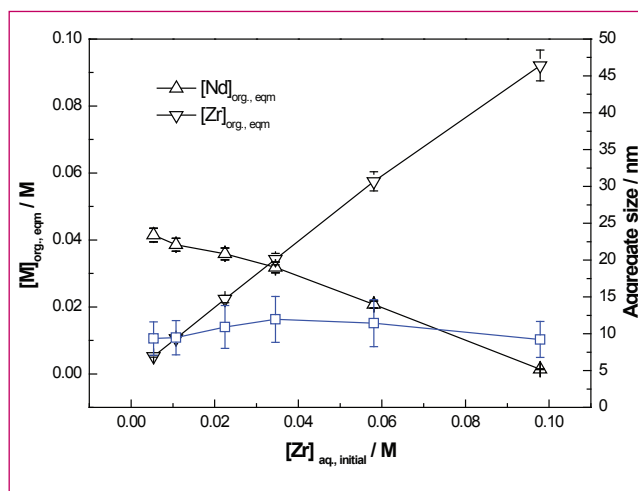


Fig. 2 Variation in the average aggregate size and concentration of Nd(III) and Zr(IV) in organic phase of DOHyA obtained after the extraction of Zr(IV) and Nd(III) from nitric acid studied as a function of Zr(IV) in aqueous phase

(Aqueous phase: Nd(III) or Zr(IV) in 4 M HNO₃. Organic phase: 0.4 M DOHyA in *n*-dodecane or 0.2 M TODGA in *n*-dodecane modified with 5 vol% 1-octanol).

In contrast, the DOHyA was found to be a better candidate for treatment of HLLW solutions containing higher amounts of Zr(IV). This extractant formed smaller aggregates during the extraction of both Nd(III) and Zr(IV). Crud formation was observed in this system only when the extraction of Zr(IV) exceeded the stoichiometric limits. Figure 2 shows the extraction of Zr(IV) and Nd(III) from a mixture of these two metal ions in 4 M nitric acid. Aqueous phase: 4 M nitric acid solution containing 0.044 M of Nd(III) and different concentrations (0.005 M to 0.1 M) of Zr(IV). Organic phase: 0.4 M DOHyA in *n*-dodecane. A gradual increase in the concentration of Zr(IV) in the presence of 0.04 M Nd(III) decreased the extraction of Nd(III) in organic phase. In all the cases, the extraction of Zr(IV) was quantitative, till the crud formation was observed beyond the stoichiometric loading of Zr(IV) (>0.1 M) in DOHyA. The results showed the preferential extraction of Zr(IV) in DOHyA in the presence of trivalent metal ions in HLLW, but the aggregation was not enhanced during the extraction of both metal ions, unlike that observed in TODGA systems.

Since the maximum concentration of Nd(III) and Zr(IV) present in HLLW arising from reprocessing of spent metallic fuel is expected to be 0.04 and 0.06 M respectively, the above results confirmed that the organic phase composed of 0.4 M DOHyA in *n*-DD can be recommended for the treatment of these HLLW solutions.

IV.17 Challenges in Setting up of Customized Glove Box Facility for Preparation of Minor Actinide Containing Microspheres by SOLGEL Route

A custom built glove box (Figure 1) is designed and fabricated for producing radioactive materials in the form of microspheres containing $\text{PuO}_2\text{-AmO}_2\text{-UO}_2$ through SOLGEL route. The glove box (2.5 Lx3.5 Wx1.25 H) accommodates various equipment for preparation of microspheres by gelation process. The following subsystems are housed inside the glove box,

1. Feed tank and Vibrator positioning system
2. Modular Gelation column
3. Micron mesh conveyor system
4. CCl_4 & NH_3 dispensing system

The raw material, SS-304L conforming to ASTM A240 and IGC Practice-AASTM A262 was used for construction of the glove box. The welders were qualified as per ASME Sec IX. Entire welding of glove box and its associated service lines were done using pulsed Gas tungsten arc welding (GTAW) process following sequential welding to control heat input and to avoid distortion / warpage on the shell and sealing frame. All the weld joints were subjected to visual examination and LPE for all passes. A comprehensive weld inspection report (WIR) was prepared as per quality assurance plan (QAP). The glove box was leak tested as per ASTM C852 and leak rate was found to be $<0.05\%$ of box volume per hour.

An insulated double walled feed tank of 1.0L capacity was designed, fabricated and positioned to maintain a uniform temperature of 5°C till the feed solution is expelled from vibrator nozzle.

A customised precise positioning system, sliding cum tilting system has been specially designed to position the feed tank and vibrator nozzle (Figure 2) to suit the modular glass column and to match the angle of impinge of feed solution jet at the hot silicon oil maintained at 90°C .



Fig. 1 Gelation glove box at SOLGEL facility



Fig. 2 Feed tank and vibrator positioning

The gelled microspheres from the glass column (Figure 3a) with hot silicon oil are separated effectively by endless SS mesh conveyor (Figure 3b) rotating at the desired speed. The microspheres are finally washed in the CCl_4 & NH_3 dispensing system and pumped to active waste collection tank.

The customized glove box with specialized equipment have been designed, fabricated and positioned. The special equipment like feed tank, vibrator nozzle, modular gel column and micron mesh conveyor system have been functionally tested.

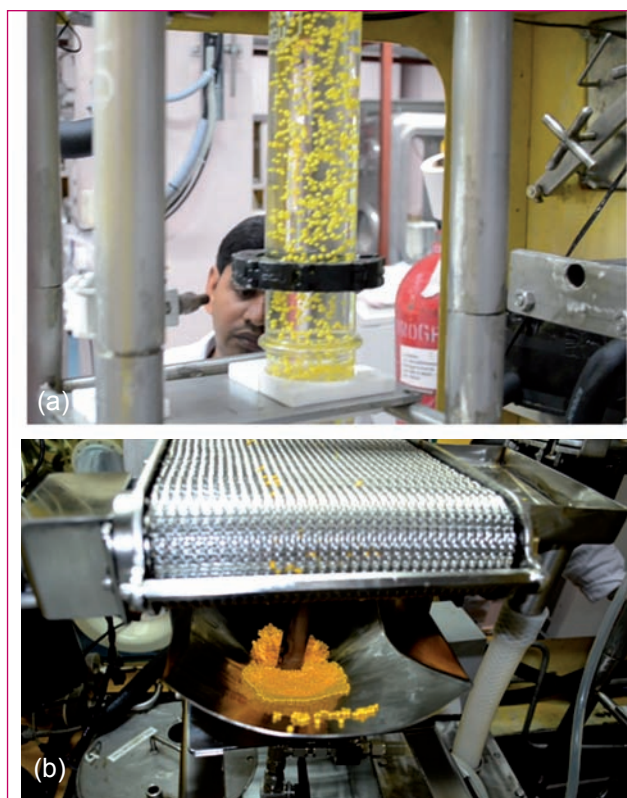


Fig. 3 (a) Modular glass gel column and (b) micron mesh conveyor system and UO_2 microspheres

IV.18 Indigenous Design & Development of Level Probe for Molten Salt Level Measurement for Upcoming Pyroprocessing Plants

Metallic fuels are planned to be introduced in the Indian Fast Breeder Reactor to exploit their high potential to breed fuel, high burn-up, and high heat transfer property to meet the escalating energy demand. To reprocess these spent fuel, pyrochemical methods based on the molten salt electro-refining process have been developed. In this method, high-temperature electrometallurgical processes are carried out at 500°C using molten LiCl-KCl eutectic salt as the electrolyte. Measuring the molten salt level in the electro refiner is essential to know the depth of the immersed electrodes. At present, there are no commercial-of-the-self (COTS) available in the market. To measure the molten salt level, a pulsating sensor based level probe and instrument has been developed in house. The development includes sensor design, fabrication of probe & instrument and testing.

Liquid level is sensed by sensitive monitoring of small shift in resistance of a vertically mounted resistive device, due to the change in liquid level. An assembly of twin SiC rods is the resistance assembly whose resistance changes on account of fractional variation in current, flowing between SiC rods due to change in level. This resistor is part of a timing circuit of a compact logic gate oscillator and, hence, shift in digital pulse frequency at the output of the oscillator is directly related to change in level. The level probe is constructed by using ferritic steel cylindrical tube and SiC/tungsten electrodes.

The sensor output is a train of rectangular transistor-transistor logic pulses; in which, the pulse frequency carries the information about the level of the molten salt. To measure the pulse frequency, a counter based

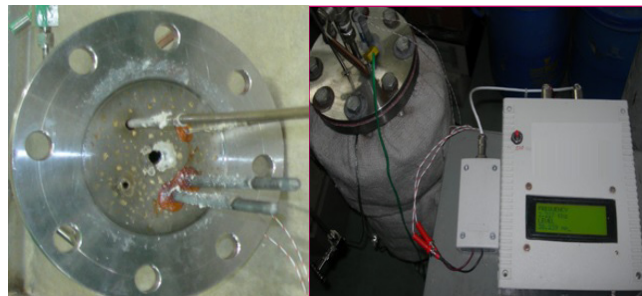


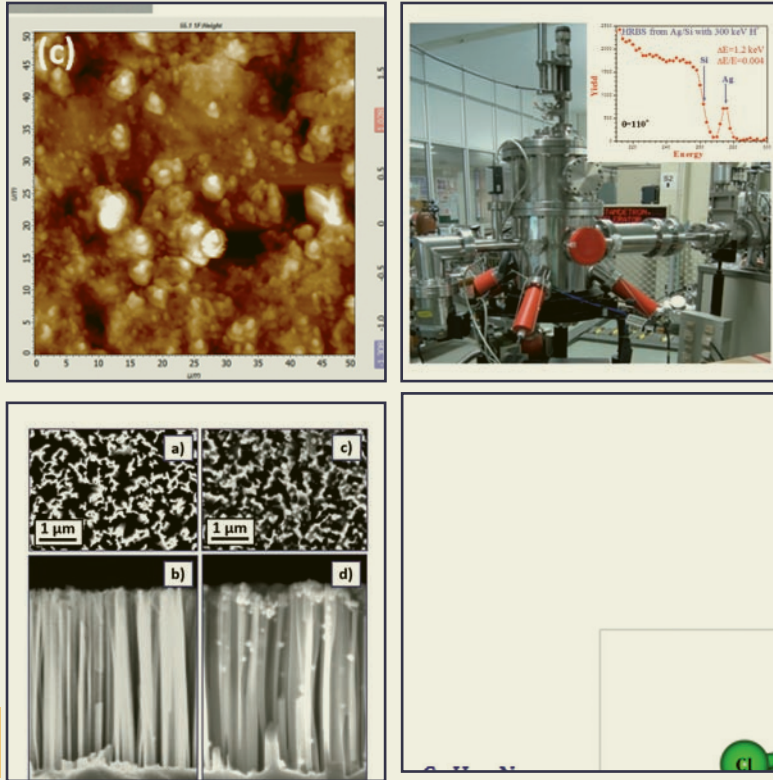
Fig. 1 (a) Level Probe with 30 cm range and (b) experimental Setup

data acquisition system is required. Towards this, a data acquisition system, based on a microcontroller is designed and fabricated in-house. This system mainly consists of opto-coupler, microcontroller, LCD display, RS-232 communication, and 5 V regulated power supply. Firmware is written in embedded C and compiled with mikro C cross compiler.

To test the in-house developed level probe along with instrumentation, an experimental setup is constructed in the laboratory as shown in Figure 1. A tank made up of ferritic steel with cylindrical shape is fabricated to hold the salt and a flange to hold the SiC rods. For testing purpose, hole is drilled on the flange to fill the LiCl and KCl salts, and a dip stick is used to cross check the level. Whenever salt is added, a minor change in the level of the molten salt (fraction of millimeter) causes a change in the resistance, which in turn results in large change in the pulse frequency. After successful testing of the level probe with SiC rods, large scale 1 m level probe has been fabricated. Figure 2 shows the 1 m level probe with instrument.



Fig. 2 Level Probe of 1 meter range with instrument



CHAPTER V

Basic Research

V.1 Development of Polymer based Nano-composites for Diagnostic X-ray Shielding

Nanomaterials are drawing great attention as an alternate to lead based radiation shielding material, as lead is a potent occupational toxin. In a quest to find lead-free diagnostic X-ray shielding material, we describe here the X-ray attenuation property of nanocomposites of silicone polymer containing Bi_2O_3 nanoparticles and graphene/MWCNT (multiwall carbon nanotube). The synergistic effect of graphene, MWCNT and polymer matrix of different densities on the diagnostic X-ray attenuation property of nanocomposites is studied here. The nanocomposite blocks are prepared using a simple solution casting method.

Figure 1 shows the percentage X-ray attenuation of neat silicone polymer (G1), G1 polymer containing only $\beta\text{-Bi}_2\text{O}_3$ nanoparticles (G1- Bi_2O_3), G1 polymer containing Bi_2O_3 nanoparticles and graphene nanoplatelets (G1- Bi_2O_3 -graphene) and G1 polymer containing Bi_2O_3 and MWCNT (G1- Bi_2O_3 -MWCNT). The X-ray attenuation property of G1 is found to decrease with an increase in X-ray photon energy. G1- Bi_2O_3 -Graphene nanocomposites are found to exhibit better attenuation than G1- Bi_2O_3 nanocomposites at higher photon energy (>56 keV). On the other hand, the attenuation property of G1- Bi_2O_3 -MWCNT nanocomposite is found to decrease with an increase in X-ray photon energy. The synergistic effect may be attributed to (i) a better dispersion of $\beta\text{-Bi}_2\text{O}_3$ nanoparticles in the presence of graphene and close packing of nanofillers normal to the direction of incoming X-rays; (ii) protection of polymer matrix from

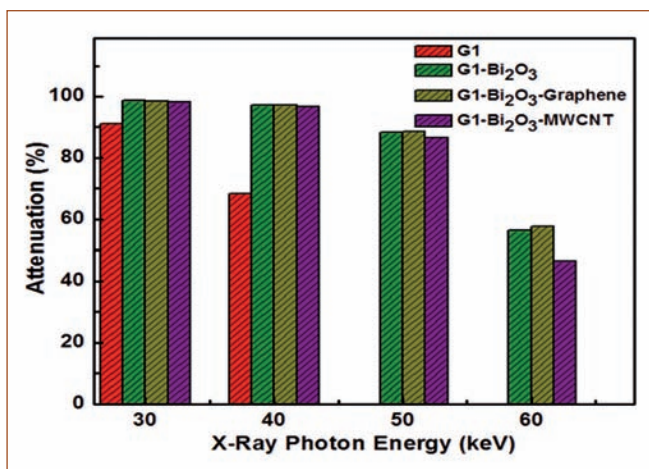


Fig. 1 Percentage X-ray attenuation of neat silicone polymer (G1), G1 polymer containing only $\beta\text{-Bi}_2\text{O}_3$ nanoparticles (G1- Bi_2O_3), G1 polymer containing Bi_2O_3 nanoparticles and graphene nanoplatelets (G1- Bi_2O_3 -graphene) and G1 polymer containing Bi_2O_3 and MWCNT (G1- Bi_2O_3 -MWCNT)

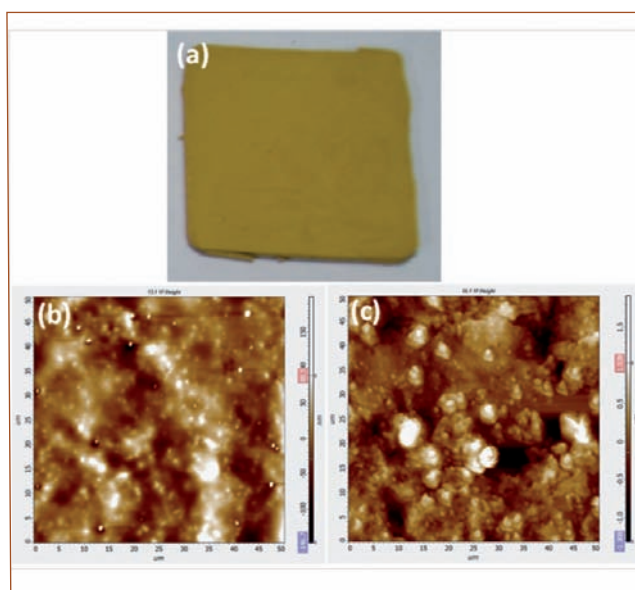


Fig. 2 Photograph and the AFM image of (b) top surface and (c) cleaved surface of nanocomposite containing $\beta\text{-Bi}_2\text{O}_3$ and graphene nanoplatelets

X-ray induced damages or (iii) due to a mechanism of X-ray attenuation in nano regime, which is yet to be understood, executed synergistically by $\beta\text{-Bi}_2\text{O}_3$ (heavy atom system) and graphene (material of light atoms) for X-rays of higher energy. Since the enhancement in attenuation by nanocomposite containing $\beta\text{-Bi}_2\text{O}_3$ and graphene is observed at a higher X-ray photon energy (greater than 56 keV), the synergistic effect is largely attributed to factors (ii) and (iii) discussed here. This is because a better dispersion and close packing of $\beta\text{-Bi}_2\text{O}_3$ nanoparticles in the presence of graphene should result in an enhancement in attenuation even for X-ray photons of lower energy. But as the enhancement is above 56 keV, factors (ii) and (iii) may be the influencing mechanism.

Figure 2 shows (a) the photograph and the atomic force microscopy (AFM) image of (b) top surface and (c) cleaved surface of nanocomposite containing $\beta\text{-Bi}_2\text{O}_3$ and graphene nanoplatelets. The nanocomposites are found to be flexible and macroscopically uniform. AFM image of the top and cleaved surface of nanocomposites containing $\beta\text{-Bi}_2\text{O}_3$ and graphene exhibits a surface roughness of 26 ± 1.4 nm and 272 ± 13 nm, respectively. Thus, G1- Bi_2O_3 -Graphene nanocomposite exhibits better attenuation than G1, G1- Bi_2O_3 and G1- Bi_2O_3 -MWCNT and are ideal candidates for the development of efficient radio-opaque fabric against diagnostic X-rays.

V.2 Fabrication of Photosensitive Nanodevice using Focused Ion Beam

Wide-band gap metal-oxide semiconductors, in the form of nanostructures, have been emerging as potential candidates for novel nanodevices in the past few decades due to their high surface to volume ratios compared to thin film or bulk form. Among them, Zinc Oxide (ZnO) nanorod (NR) is a promising candidate for electronic, optoelectronic and sensor devices owing to its wide band gap (3.37 eV at 300 K), n-type conduction and large exciton binding energy (60 meV). Due to ultraviolet (UV) and near-UV (defect/impurity-aided) sensitivity in ambient conditions, longer photo-carrier lifetime, shorter charge-carrier transit time, radiation hardness, high chemical stability and cost-effective synthesis methods, ZnO NRs are preferably considered for photodetector applications. ZnO NRs are also compatible with several other micro/nano-electronic devices, and hence expected to have demands in space research, warning systems, etc.

ZnO NR arrays/ensembles/networks based photodetectors have been fabricated and studied so far, where photodetection was the resultant of collective behavior of multiple NRs. However, knowledge on the contribution of a single nanorod (being the basic building block) is scarce and need to be studied to have a better understanding on the functionality. Such studies provide a knowledge on the influences of NR dimensions (often the size), morphology, microstructure and compositional variations (often doping) on the functional property.

Fabrication of nanodevice with a single NR is a critical work that requires a suitable nanofabrication technique.

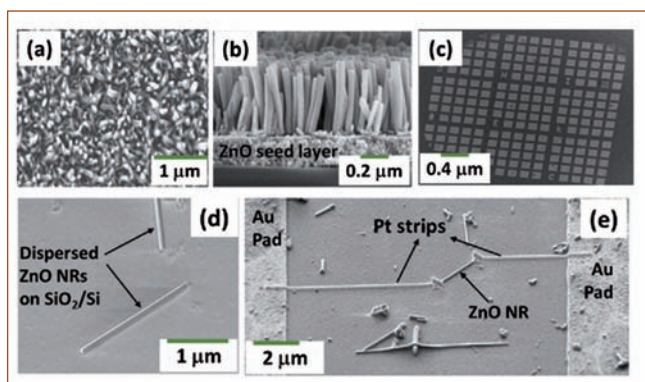


Fig. 1 SEM images showing top (a) and side (b) views of ZnO NRs grown on glass substrate with ZnO seed layer. (c) pattern of 200x200 μm Au pads on SiO_2/Si substrate, (d) dispersed ZnO NRs on SiO_2/Si substrate between Au pads, (e) ZnO NR electrically connected to Au pads at both ends by FIB-deposited Pt strips

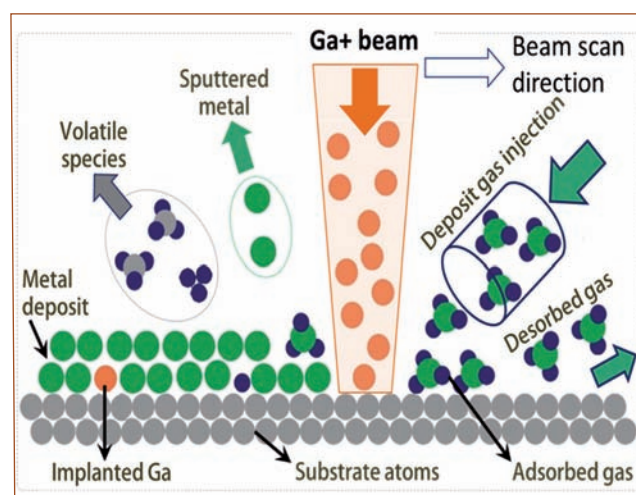


Fig. 2 Schematic of focused ion beam induced deposition of metallic layer by ion beam decomposition of organometallic precursor on the surface of a substrate

Among the various nanofabrication techniques with their advantages and constraints, Focused Ion Beam (FIB) system has been emerging as a powerful tool, in recent years. Gas injection system (GIS) attached to FIB system makes it more powerful as the nanofabrication could be performed at specific locations on the sample surface in a single-step without masks. In this article, fabrication of photosensitive nanodevice is demonstrated with a single ZnO NR using FIB system.

ZnO NRs were grown on a glass substrate by low temperature aqueous solution method after optimizing the morphology, defect and alignment. Top and side views of ZnO NRs on a glass substrate are shown in Figures 1a and 1b, respectively. The NRs were detached from the growth-substrate and dispersed onto a SiO_2 (300 nm thick insulating layer) coated Si substrate for device fabrication. Large number of Au electrode pads (200x200 μm in size, and 150 nm thick) were patterned on SiO_2/Si substrate before dispersing the NRs (Figure 1c). The substrate carrying the NRs and Au electrode pads was then loaded into FIB system for further processing of nanodevice fabrication. ZnO NRs with desired length and width were selected for device fabrication (see Figure 1d, NR at the middle of the image was selected). The procedure of deposition of metallic strips, those electrically connect the NR with Au pads as shown in Figure 1e, involves in decomposition of organometallic precursor molecules ($\text{C}_9\text{H}_{16}\text{Pt}$, in this case) by focused ion beam in a controlled way at nanoscale. When the gaseous precursor molecules

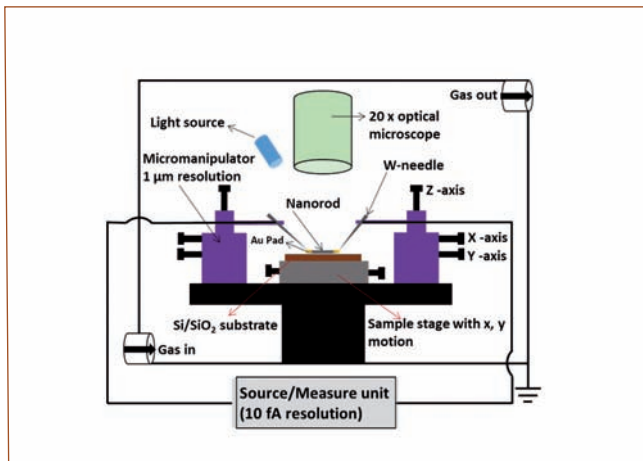


Fig. 3 Schematic of a home-built probe-station used for photo-detection experiments with a single ZnO NR based nanodevices

are sprayed over the substrate by a GIS nozzle (which is positioned <0.5 mm above the sample surface), they temporarily adsorb on the surface. Subsequent FIB scanning, on the area(s) where the molecules are adsorbed, leads to decomposition of the molecules into a volatile and nonvolatile parts. Nonvolatile part consisting metal (Pt in this case) and carbon paves a metallic strip on the surface, whereas volatile part is removed by vacuum pumping of the FIB system. The schematic illustration of this procedure is shown in Figure 2.

Electrical and photosensing experiments with the nanodevice were performed in a probestation placed in an electrostatic discharge safe environment. Such an environment was essential as the fabricated nanodevices were highly fragile to any spurious voltage/current spikes originate from the measurement setup or surroundings. A high precision source measure unit (SMU) with 10 fA resolution was used in a current-controlled mode for I/V measurements. Since ZnO NR resistivity was in the

order of Mega to Giga Ohms, 2-point probe method was adopted for IV measurement. Micro-positioners equipped with W probe needles (with 1 mm placement accuracy) were used to establish electrical contacts between SMU and Au pads. An optical microscope with 20X magnification was used for precise landing of the probes on the pads. Schematic of the probestation is shown in Figure 3. Nature of Pt-ZnO contact made by FIB was studied by IV measurements. Post-annealing treatments (in Ar atmosphere), if necessary, were carried-out in order to achieve Ohmic contacts between Pt and ZnO NR with lowest possible resistances. This was important as the performance of the device critically depends on the quality of the Ohmic contact. The device with low Ohmic contacts was tested further for light sensor application in the probestation using a 0.5 W white light LED source. Schematic of the experiment is shown in Figure 4a. A constant DC bias voltage of 1 to 2 V was applied between two ends of the NR and electrical current through the NR was measured. Dark (when light source is OFF) and photo-current (when light source is ON) for a certain period of time was measured and this was repeated for several times to examine the stability of ON and OFF states. Upon illumination, the current through the device increased significantly due to the creation of electron-hole pairs and their exited movements into the conduction and valance bands, respectively. It was found that the resistance of ON and OFF states was stable with a minor fluctuation. The resistance states were found to have a clear separation between them. The rise and decay time of the device was better than 1 second. In addition to the significant contrast in resistance and short response, low power consumption (a 1.5 V battery could be used) makes the nanodevice promising for light sensing applications at ambient conditions.

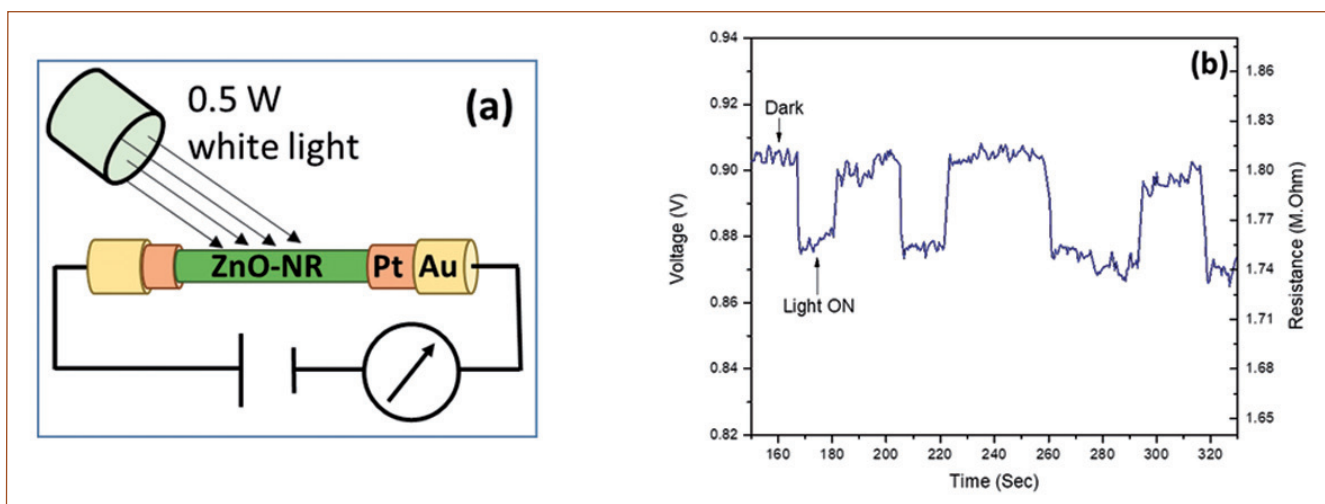


Fig. 4 (a) Schematic of a photosensing experiment with a single ZnO NR based nanodevice. (b) Variation of electrical resistance in a single ZnO nanorod based photo-sensor device upon the exposure of light

V.3 Fabrication of SiO₂ Microcantilever for Relative Humidity Sensing

Measuring relative humidity (RH) is of great importance in wide variety of applications, including climatology, agriculture, medical diagnosis, semiconductor industry, etc. In recent times, gravimetric sensors like quartz crystal microbalance, surface acoustic wave based devices and microcantilevers (MCs) have gained much attention for RH sensing owing to their superior characteristics like high sensitivity, fast response and recovery times in contrast to the conventional resistive and capacitive type humidity sensors. In order to enhance the RH sensitivity and selectivity, these sensors are usually coated with suitable moisture sensitive metal oxides, organic polymers or hybrid composite materials. However, presence of coating on these sensors introduces several undesired effects such as slow recovery time and hysteresis. Taking these aspects into consideration, in the present work we have shown that uncoated SiO₂ MCs can be effectively used for RH sensing with fast response time and low hysteresis.

SiO₂ MCs of various lengths (length = 50 to 330 μm, width = 37 μm and thickness = 1 μm) were fabricated using direct laser writer (DLW) and wet anisotropic chemical etching methods. After the successful MC pattern transfer using DLW on SiO₂/Si <100> wafer pieces, devices were released using 5% tetramethylammonium hydroxide water solution at 80 °C. Figure 1 shows a SEM image of a typical SiO₂ MC released in the present work. It may be noted, the sharp tip at the free end of the MC was introduced to avoid stiction during wet chemical release of these structures. RH sensing experiments were performed by measuring the shift in fundamental resonance frequency of these devices using nano vibration analyzer (NVA) at ambient conditions. MCs were excited using a piezo actuator and



Fig. 1 FESEM image of a typical SiO₂ MC fabricated using DLW and wet chemical etching methods

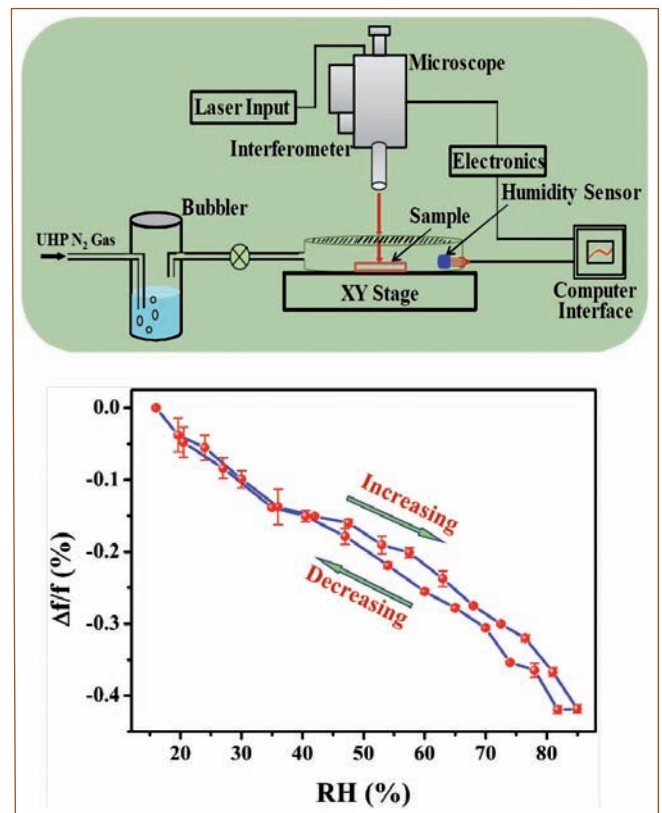


Fig. 2 (a) Schematic of the experimental setup used for measuring the RH sensitivity of microcantilevers using NVA. (b) The relative shift in the resonance frequency of a typical MC as a function of RH

were placed inside a RH controlled chamber, which in turn was placed on the XY stage of NVA (Figure 2a). RH inside the chamber was varied between 20 to 85 % using a bubbler setup and resonance spectrum was recorded at regular intervals. Figure 2(b) shows a typical response curve ($\Delta f/f$ % Vs RH) of a MC (Length = 210 μm) during one RH increase and decrease cycles. From this figure it is clear resonance frequency is decreasing with increasing RH and vice versa and is attributed to the adsorption and desorption of water molecules, respectively, on MC surface. It is also evident that hysteresis between increasing and decreasing curves is very low in these devices. This is attributed to the presence of silanol (–Si–OH) groups on the SiO₂ surface, which directly facilitates adsorption of water molecules through hydrogen bonding.

From Figure 2b, maximum RH sensitivity and resolution were estimated to be 1.3 Hz/%RH and < 1% RH, respectively, between 45 % and 80% RH. This indeed demonstrates that SiO₂ MCs can be effectively used as humidity sensors with a good sensitivity and resolution, without any functionalization.

V.4 Deep Reactive Ion Etching of Silicon Carbide for Microfabrication of MEMS Structures

Silicon Carbide (SiC) is an excellent material for developing MEMS sensors and actuators for high temperature and radiation environment, due to its unique material properties such as large band gap, high displacement energy and very low intrinsic carrier concentration. Despite its unique properties, SiC is a hard material and it is very difficult to etch for realizing the high aspect ratio microstructure. Towards the microfabrication of SiC microstructure, a process technology was developed using inductive coupled plasma deep reactive ion etching (ICP-RIE) method.

For creating the SiC diaphragm, SiC sample of resistivity 0.02-0.2 Ω.cm and thickness ~375 μm was used. It was cleaned with trichloroethylene and warm acetone. Later the SiC sample was rinsed with de-ionized (DI) water and boiled in hot and concentrated HNO₃ for 5 min. Thereafter, the sample was dipped into diluted HF to remove oxide and then rinsed with DI water. Finally, the sample was dried using nitrogen. In the next step, to reduce the thickness of SiC sample upto 180 μm, blanket etching of SiC was performed using ICP-RIE by varying the process parameters such as flow rates of SF₆ and O₂, pressure, ICP and RF power, temperature and time. To obtain higher etching rate and smooth surface morphology with an average roughness ~17 nm, flow rates of O₂ and SF₆ were 10 sccm and 50 sccm respectively were optimized. Tabel-1 indicates process parameter variation for achieving desired thickness and surface roughness.

To realize the SiC diaphragm (1.5 mm × 1.5 mm) with thickness ~ 75 μm, as shown in Figure 1, selective etching of the sample (~120 μm) was carried out from the backside. To perform the selective etching, thick Ni mask was selected for creating the high aspect ratio in the structure. In order to deposit thick Ni (high purity 99.9%) of ~8 μm on SiC sample at backside, pulsed electroplating method was adopted. Before electroplating, SiC sample was coated with Cr/Au

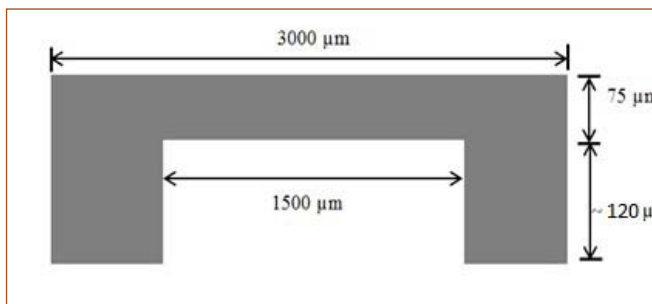


Fig. 1 Physical Dimension for SiC MEMS structure

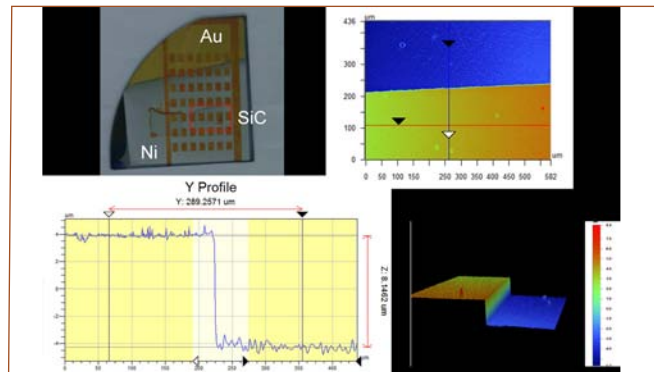


Fig. 2 Depth profile of electroplated Ni on SiC

(thickness ~ 20 nm/120 nm), followed by patterning of photoresist. Gold was used as seed layer for electroplating. Ni was electroplated using a Watt's bath recipe. Nickel sulphate, nickel chloride and boric acid were used as salts for the electroplating. A pulsed current with current density of 10⁻¹⁴ mA/cm² and pulse width of 4 ms with 40% duty cycle was passed through the electrolytic solution for 40 minutes to obtain a Ni layer of thickness 8 μm, as shown in Figure 2.

After Ni electroplating process, photoresist was removed using acetone. Subsequently, the layer of Cr/Au, not protected by nickel, was etched using metal etchant to create the SiC diaphragm. SiC was etched using RIE to obtain the desired size of depth as shown in Figure 3.

Table 1: Process parameter optimization details		
Sample # 1	Sample # 2	Sample # 3
O ₂ : 8 sccm	O ₂ : 10 sccm	O ₂ : 12 sccm
Thickness after etching ~174 μm	Thickness after etching ~195 μm	Thickness after etching ~177.5 μm
Etch rate ~ 0.60 μm/min	Etch rate ~ 0.52 μm/min	Etch rate ~ 0.58 μm/min
Average roughness ~ 42 nm	Average roughness ~ 17 nm	Average roughness ~ 47 nm

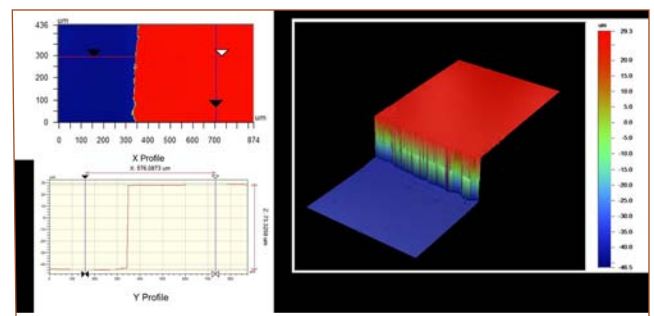


Fig. 3 Etched depth profile of SiC MEMS structure

V.5 MBE and HiRBS Facilities for Deposition and Analysis of Ultra-Thin Films

A programme on ion beam analysis of materials and radiation damage is being pursued using ion accelerators. Routinely materials characterization with Rutherford backscattering spectrometry (RBS) is carried out with surface barrier detector which has an energy resolution of 15 keV, corresponding to a depth resolution of 5 to 20 nm. Recently a High Resolution RBS detector (HiRBS) with an energy resolution of 1.6 at 400 keV, corresponding to a depth resolution of 2 to 3 Å and improved mass resolution is installed. It is a unique facility in India, the schematic of which is shown in Figure 1.

It consists of a Toroidal electrostatic energy analyzer (TEA), Microchannel plates (MCP) and a 1D-position sensitive detector. The detector is housed in a high vacuum scattering chamber system coupled to the 1.7 MV tandetron accelerator which is shown in Figure 2. The detector and data collection system are automated using LABVIEW software. The inset of Figure 2 shows a typical HiRBS spectrum taken from a silver ultra thin film of thickness 3 nm, deposited on H-passivated Si(100) substrate, using a recently installed Molecular Beam Epitaxy (MBE) system which is shown in Figure 3a.

The MBE system consists of a double walled UHV chamber with a base vacuum of 2×10^{-10} mbar, a UHV radial distribution chamber and high vacuum load lock chamber. The deposition system can be used for depositing a few Angstrom thick ultra thin metal and semiconductor films using three numbers of effusion cells and a 6 kW E-gun evaporator for thicker films. During growth, substrates can be heated upto 1200°C and also can be rotated upto 30 revolutions per minute for obtaining laterally uniform epitaxial growth. Thickness can be monitored *in-situ* using a quartz crystal thickness monitor. Crystallinity can be monitored in real time using

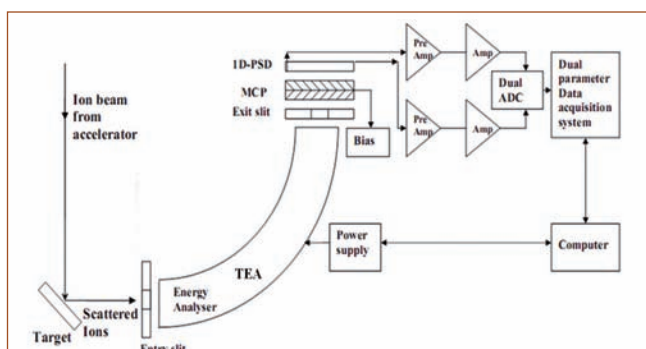


Fig. 1 Schematic of HiRBS set up

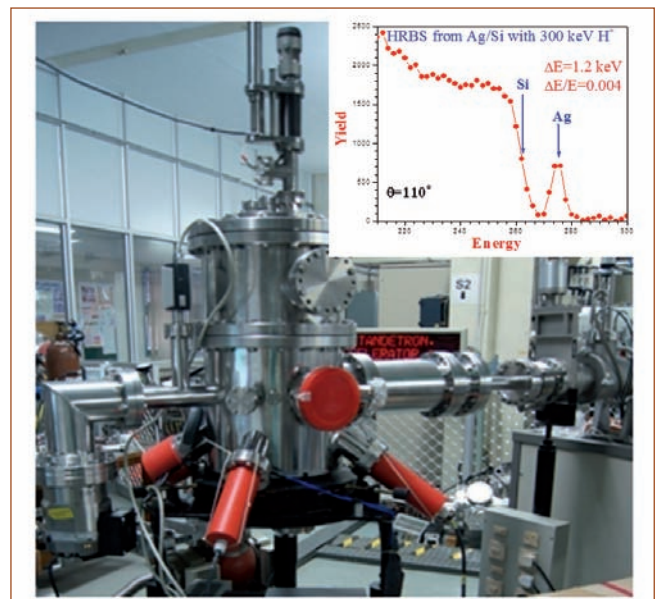


Fig. 2 HiRBS scattering chamber. HiRBS spectrum from Ag/H-Si(100) is in the inset

a 30 kV Reflection High Energy Electron Diffraction (RHEED). RHEED patterns obtained from H-passivated Si(100) and epitaxial silver islands grown on this substrate at 430°C are shown in Figure 3b.

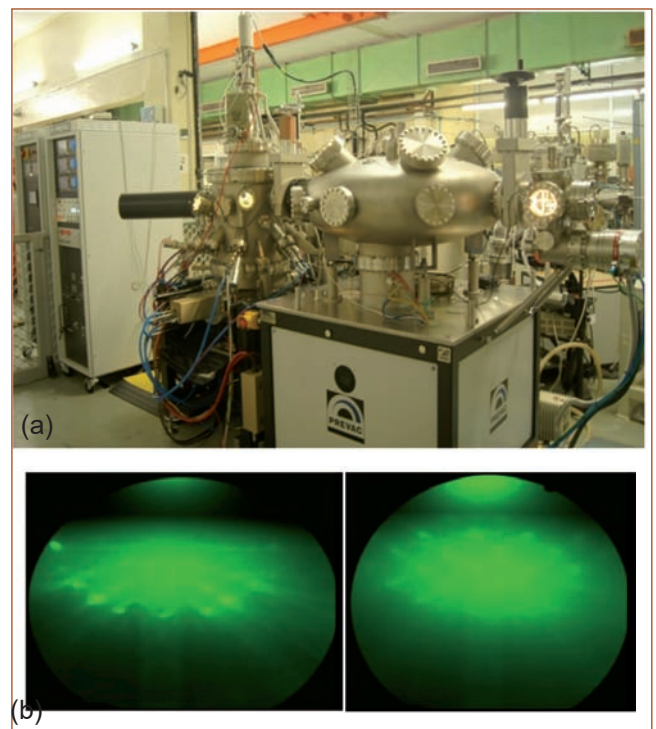


Fig. 3 (a) MBE system with deposition, radial distribution and load lock chambers are seen from left to right and (b) RHEED patterns from H-Si(100) (left) and Ag/H-Si(100) (right) reflect the 4-fold crystalline symmetry

V.6 Tuning of Charge Carrier Density by Deposition Pressure in Sb-doped Bi₂Se₃ Thin Films

Thin films of Sb-doped Bi₂Se₃ topological insulator with nominal composition Bi_{1.95}Sb_{0.05}Se₃ were grown in a pulsed laser deposition system at different deposition pressures of Ar (0.002 Pa vacuum, 4 Pa Ar, and 50 Pa Ar) and different substrate temperatures. Dynamic partial pressure of Ar maintained in the chamber during deposition suppresses Se escape, effectively regulating the stoichiometry. Energy dispersive X-ray spectroscopy studies reveal a significant over-stoichiometry of Bi in low pressure deposited films and a corresponding deficiency of Se. System tends to the expected stoichiometry for a deposition pressure of 50 Pa. Se vacancies being n-type charge donors, stoichiometry regulation in turn modulates the charge carrier density. With increase in deposition pressure, a striking three order decrease in carrier density has been recorded (Figure 1a) and with additional control through the substrate temperature a carrier density value as low as $2 \times 10^{18} \text{ cm}^{-3}$ has been observed. The over-stoichiometry of Bi in films deposited at low pressure results in the segregation of Bi, which is seen as the additional Raman band at 92 cm^{-1} in the 0.002 Pa deposited film which shifts to 97 cm^{-1} at higher pressure (Figure 1b). This band may correspond to A_{1g} mode of Bi-Bi bond.

The magneto-transport studies performed on the films reveal weak antilocalization (WAL) behavior (Figure 2a).

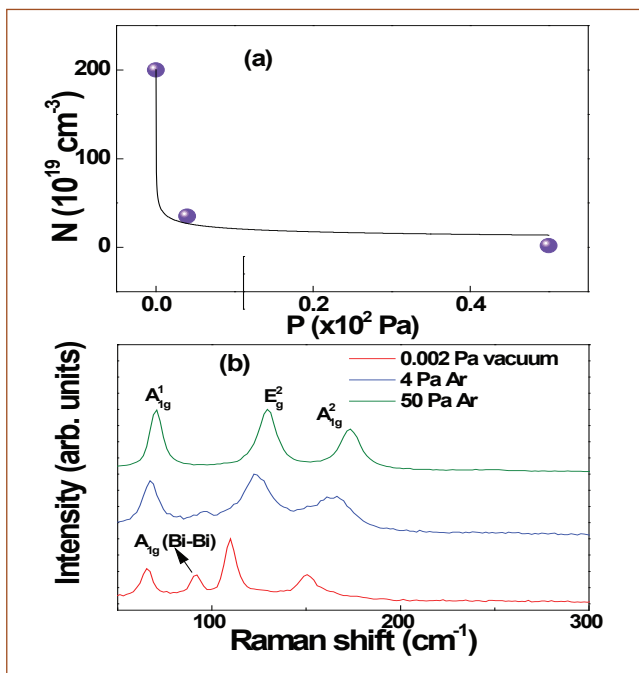


Fig. 1 (a) Carrier density as a function of deposition pressure. (b) Raman modes of the films deposited at different Ar pressures

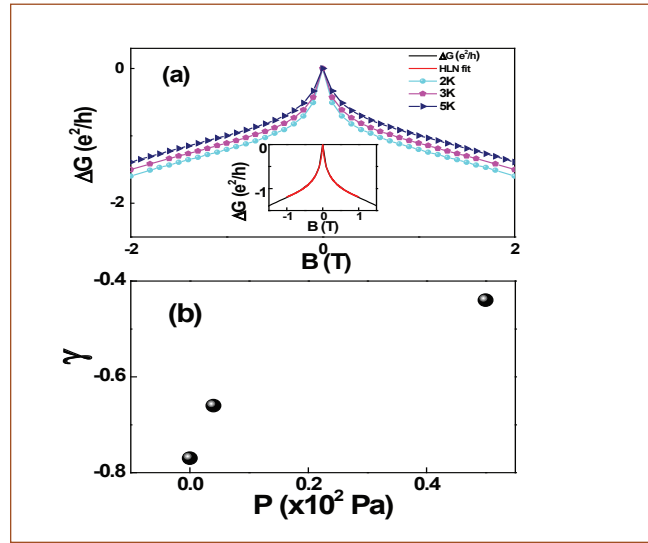


Fig. 2 (a) Magneto-conductance data of 50 Pa and 350°C deposited film at few representative temperatures. HLN fit of 2 K data in inset. (b) γ as a function of deposition pressure

On analyzing the WAL within the purview of the Hikami Larkin Nagaoka (HLN) Equation 1), we have been able to determine the influence of deposition pressure on properties like the de-phasing mechanism involved in the system, the number of effective transport channels and the coherence length (l_ϕ).

$$\Delta G(B) = -\alpha \times \frac{e^2}{2\pi^2\hbar} \times \left[\Psi \left(\left(\frac{\hbar}{4el_\phi^2 B} \right) + \frac{1}{2} \right) - \ln \left(\frac{\hbar}{4el_\phi^2 B} \right) \right] - \text{Eq. 1}$$

ψ is the digamma function, \hbar the reduced Planck's constant, e the electronic charge, and l_ϕ and α the parameters obtained through the fitting. Films deposited in 50 Pa Ar have been seen to possess an α with a value of -1, indicating the presence of two completely de-coupled channels involved in coherent charge transport. The coherence lengths are plotted as a function of temperature and the power law $l_\phi = T^\gamma$ fit yields the exponent γ which approaches -0.5 with increasing pressure (Figure 2b). γ is found to be -0.44 for the 50 Pa deposited film suggesting that the decoherence mechanism involved in the 50 Pa deposited system is solely electron-electron interaction based. The 50 Pa deposition pressure condition (at 350 °C substrate temperature) is also found to support the longest coherence length (223 nm) among the studied conditions.

V.7 Enhanced Piezoelectricity in Nanostructured Al_{1-x}Ga_xN

Piezoelectricity is the phenomenon of production of electrical potential in a crystal with the application of mechanical stress. Recently, piezoelectricity has attracted the scientific community because of its fruitful application in renewable energy production. Piezoresponse force microscopy (PFM), the versatile and efficient member of scanning probe microscopy (SPM) family, is the best choice for the identification and imaging of piezoelectric domains in the nanostructure with resolution down to tens of picometer. In the present study, we demonstrate the PFM imaging of the plasma-assisted molecular beam epitaxy (PA-MBE) Al_{0.97}Ga_{0.03}N nanorods oriented in different crystallographic directions (Figure 1). The polarities of the different planes of *m* and *c* are imaged at high resolution, and the value of piezoelectric coefficient (*d*₃₃) is calculated.

The topographic image of the Al_{0.97}Ga_{0.03}N nanorods collected over an area of 5×5 μm² area is depicted in Figure 2a. The nanorods are distributed all over the substrate with different size and orientations. Some of the nanorods are vertically oriented (marked as 1 in Figure 2a), and some are horizontally laying on the substrate (marked as 2 in Figure 2a). The corresponding phase image is shown in the Figure 2b. The zoomed topographic and corresponding phase images of the marked position 1 and 2 of the topographic image (Figure 2a) are depicted in Figures 2c, 2d and 2e, 2f, respectively. In the topographic image (Figure 2a) both the positions (position 1 and 2) appears to be bright with the height of ~80 and ~50 nm, respectively. In the case of the phase image (Figure 2b) the marked position 1 (Figure 2d) shows the dark contrast signifying the piezoelectric deformation in the probed direction. Moreover, the dark contrast implies that the applied field and the polarization direction are anti-parallel (**E**↑**P**) to each other. Whereas, the marked position 2 (Figure 2f) does not show any variation in the contrast as compared to the background, signifying no piezoresponse for the particular direction.

Al_{0.97}Ga_{0.03}N is a wurtzite crystal, belonging to the hexagonal family. Wurtzite crystal shows a spontaneous



Fig. 1 Micrograph of Al_{0.97}Ga_{0.03}N nanorods

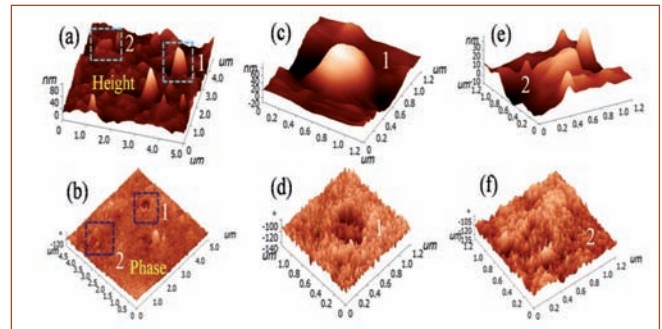


Fig. 2 (a) The topographic image of Al_{0.97}Ga_{0.03}N nanorods with (b) the corresponding phase image; (c) and (e) the zoomed region of the position 1 and 2 marked in dotted boxes with (d), (f) corresponding phase images

polarization along the *c*-axis and, the *c*-plane of the crystal is called a polar plane. However, *m*-plane oriented crystal does not show any spontaneous polarization and hence is called as a non-polar plane. Considering the above facts, one can expect piezoelectric deformation in the *c*-plane oriented crystals probed in a direction perpendicular to it. In the present study, the marked position 1 (Figures 2b and 2d) shows piezoelectric deformation implying that the crystal is aligned in the *c*-axis and the corresponding piezoresponse image signifies the polar nature of the *c*-plane. The absence of piezoelectric deformation in the marked position 2 (Figure 2) signifies that the corresponding plane is nonpolar in nature (*m*-plane).

Further to quantify the observed piezoresponse, the *d*₃₃ value was calculated. In the present study, the voltage applied across the nanorod of height *h*; generates an electric field *E*₃ along the *c*-axis, which elongates or contracts the nanorod by an amount Δ*h*. Then the piezoelectric coefficient *d*₃₃ is given as,

$$d_{33} = \Delta S_3 / E_3 \dots\dots\dots (1)$$

where *E*₃ = *V*/*h* and Δ*S*₃ = Δ*h*/*h* is the change of strain along the *c*-axis. Putting the values of *E*₃ and Δ*S*₃ in the equation (1), *d*₃₃ can be written as

$$d_{33} = \Delta h / V \dots\dots\dots (2)$$

The average value of the *d*₃₃ was calculated from the different nanorods and was found to be 9.0±1 pm/V. the *d*₃₃ value obtained in the present study is higher as compared to the reported values for AlN and GaN either in the form of thin film or bulk. Therefore, the high value of *d*₃₃ in Al_{0.97}Ga_{0.03}N nanorods, observed in the present study, may be pertaining to the nanostructure. The enhancement of piezoresponse can be attributed to the size of the crystal in the nanometer scale, due to the availability of free boundary for volume expansion or contraction with the applied voltage.

V.8 Pristine and Palladium Decorated Silicon Nanowalls for Hydrogen Sensing

The safe production, storage, transportation and utilization H₂ in the diverse field of applications demand development of low cost H₂ sensor with high sensitivity, fast response time, high selectivity and full reversibility. The present work reports H₂ sensing behaviour of silicon nanowalls (SiNWs) prepared by metal assisted chemical etching (MACE) as well as the palladium-decorated silicon nanowalls (Pd-SiNWs) using galvanic displacement deposition (GD) method. Since both processes are purely chemical without requiring any high cost vacuum equipment, the present study is useful for the production of low cost Si-based H₂ sensor. Figure 1 shows the scanning electron microscopic (SEM) images of the as-prepared/pristine (Figures 1a and 1b) and platinum decorated SiNWs (Figures 1c & d). Figure 2 shows the the sensor response ($S = ((R-R_0) / R_0) \times 100$), where R₀ and R are resistance before and after H₂ injection). S for Pd-SiNW increases continuously upto 200°C with a significant increase observed at 150°C. Figure 3 depicting the comparison of S between SiNWs and Pd-SiNWs for 200°C reveals the superior response behaviour of Pd-SiNWs. It is observed that SiNWs start sensing H₂ gas at 100°C whereas Pd-SiNWs starts at 50°C, along with increase in S with increase in H₂ concentration. It is also observed that S increases with temperature for SiNWs upto 150°C and then slightly decreases at 200°C, especially for higher concentration with a maximum response value < 1%. The superior sensing performance of Pd-SiNWs is ascribed to the combined effect of chemical and electronic sensitization caused by the Pd nanoparticles. The chemical sensitization, also known as spillover effect, is based on the fact that the Pd provide more active sites for H₂

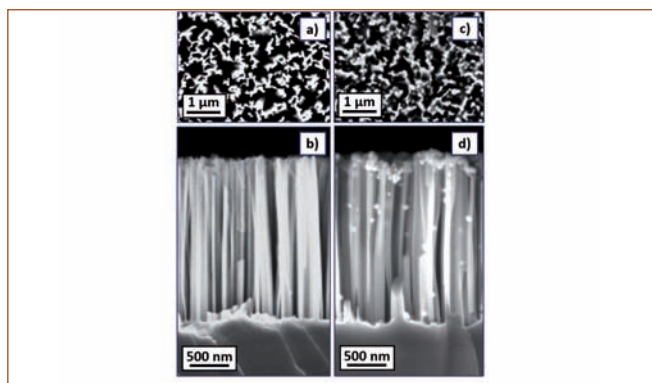


Fig. 1 SEM micrographs of Pristine and Pd decorated SiNWs: a)&b) Top and cross-section view of SiNWs respectively; c)&d) Top and cross-section view of Pd-SiNWs respectively

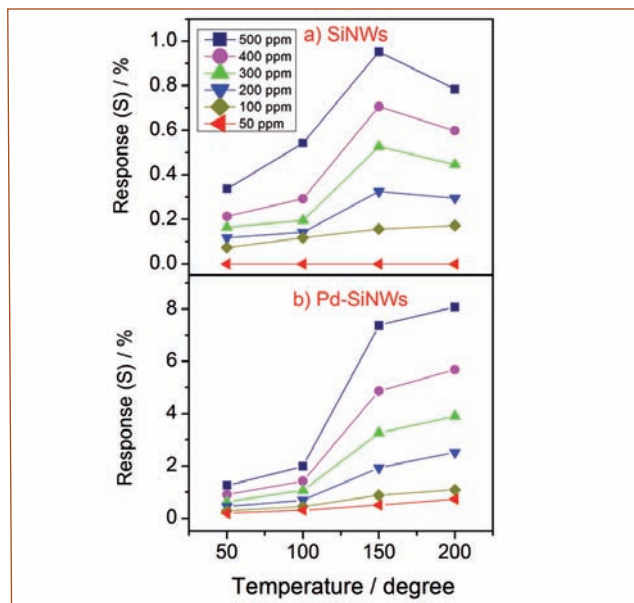


Fig. 2 Sensor response (S) versus temperature for SiNWs and Pd-SiNWs, at different H₂ gas concentrations

adsorption thereby increasing the resistance (more for p-type Si). The electronic sensitization is based on the fact that H₂ has high solubility and diffusivity in metallic Pd, as a result, after its dissociation on Pd surface, it diffuses rapidly through it and get adsorbed at the Pd-Si interface, where it induces a dipole layer reducing the work function of Pd. As a result, the ohmic junction between p-type SiNWs and Pd is changed to Schottky junction significantly increasing the resistance. This results in the higher sensing response of Pd-SiNWs. The above study highlights that MACE and GD can be used to fabricate low cost Si-based H₂ sensors.

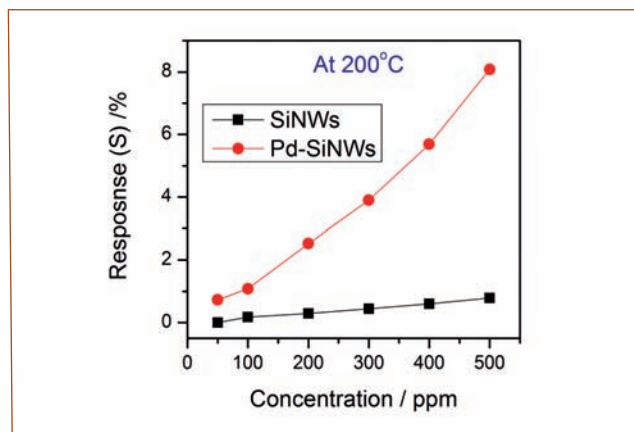


Fig. 3 Comparison of sensor response (S) versus H₂ gas concentration at 200°C

V.9 High-temperature Irradiation Damage Studies on INRAFM Steel Investigated using Positron Annihilation Spectroscopy

Indian Reduced Activation Ferritic/ Martensitic (INRAFM) steel has been developed in IGCAR as a core structural material for Indian Lead-Lithium Ceramic Breeder Test Blanket Module (LLCB-TBM) in International Thermonuclear Experimental Reactor (ITER), which is an international nuclear fusion reactor being built in France. The plasma-facing materials of a fusion reactor undergoes severe displacement damage due to 14 MeV fusion neutrons. Displacement damage of the order of 20-30 dpa/year is being associated with a large amount of hydrogen and helium of the order of 40-50 appm H/dpa and 10-15 appm He/dpa is introduced into the first-wall material made up of steel. The vacancies that are produced by displacement damage agglomerate to form larger voids. The presence of helium stabilizes the vacancies against vacancy-interstitial recombination and promotes the nucleation and growth of voids. This leads to void swelling and premature failure of the core structural materials.

Irradiation damage studies were performed on INRAFM steel at doses and temperatures relevant to fusion reactor first-wall. Ion beam irradiation has been employed to simulate the neutron-induced damage in the material. The samples were irradiated with 1.1 MeV Fe ions to a peak dose of 70 dpa with and without pre-injected helium ions. The irradiated samples were characterized by positron beam based Doppler broadening spectroscopy. In the first study (Figure 1), the samples were irradiated with 1.1 MeV Fe ions to a peak dose of 70 dpa at various temperatures to study the thermal stability of vacancy-type defects induced by irradiation. The samples were irradiated at

room temperature (RT), 473 K, 673 K and 773 K. All the irradiated samples show a higher S-parameter as compared to the unirradiated sample due to the presence of irradiation-induced vacancy-type defects. The RT irradiated sample shows a reduced S-parameter at the peak damage region due to the reduced concentration/size of vacancy-type defects due to injected-interstitial effect. As the irradiation temperature increases, the S-parameter decreases due to the reduction in vacancy concentration due to their migration towards sinks or recombination with interstitial. Complete defect recovery is observed at 673 K.

In the second study (Figure 2), the samples were pre-injected with helium ions having energies 50, 90 and 130 keV to get a uniform concentration of around 700 appm at the peak damage region. These samples were then irradiated with 1.1 MeV Fe ions to 70 dpa at different temperatures to study the growth of helium bubbles. He/dpa ratio was maintained at 10 appm/dpa. As the irradiation temperature increases, the S-parameter decreases till 673 K, due to the annealing of bare vacancies /vacancy clusters and the filling of helium to vacancies/vacancy clusters thereby increasing their He/vacancy ratio. Further increase in irradiation temperature increases the S-parameter at 773 K, which is due to the growth of helium bubbles. Hence it is concluded that, in the absence of pre-injected helium, all the vacancy-type defects are getting annealed out at 673 K, and no growth of empty voids occur. Whereas, the presence of pre-injected helium stabilizes vacancies and promote the growth of helium bubbles.

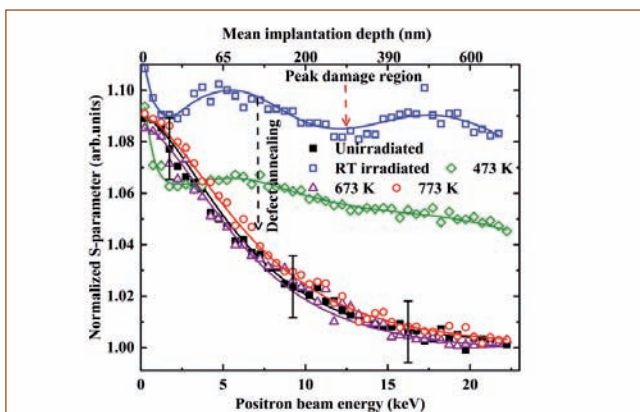


Fig. 1 Normalized S-parameter vs. positron beam energy plots of INRAFM samples implanted with 1.1 MeV Fe ions to a peak dose of 70 dpa at different temperatures

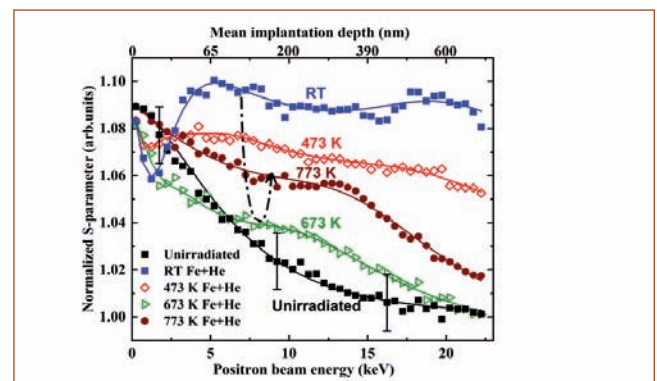


Fig. 2 Normalized S-parameter vs. positron beam energy plots of INRAFM samples implanted with 1.1 MeV Fe ions to a peak dose of 70 dpa at different temperatures with pre-injected helium at a He/dpa ratio of 10 appm/dpa.

V.10 Weldability of 304HCu Stainless Steel for AUSC Application

304HCu austenitic stainless steel is a candidate structural material chosen for boiler tube applications exposed to temperatures below 650°C in the proposed Advance Ultra Super Critical Power Plants. Fusion welding process is used to join this steel with the matching or nickel based filler wire. Hence, a systematic study was performed in order to understand the hot cracking susceptibility of this steel.

Hot cracking is a term that refers to cracking that occurs in the weld joint during welding. Varestraint test procedure is a method, which enables quantitative evaluation of susceptibility of materials to hot cracking. It is accomplished by applying an augmented bending strain to produce cracking during actual welding. After testing, crack lengths on the surface of tested specimens were measured using stereo microscope.

Hot-ductility tests were conducted in a “Gleeble”™ thermo mechanical simulator so that heating and cooling of the test specimen can be accurately programmed to reproduce the rapid temperature profile that occur during welding. To determine the hot ductility curve, first the Nil Strength Temperature (NST), at which strength is completely exhausted is determined. Nil Ductility Temperature (NDT) is defined as a temperature at which ductility of the steel is exhausted while heating. The temperature at which 5% ductility recovery is achieved is taken as Ductility Recovery Temperature (DRT). For NDT and DRT, tests were carried in stroke controlled mode. A stroke rate of 25 mm s⁻¹ was used during the determination of NDT and DRT so that the pulling is completed at the pre-determined test temperature. Reduction in area is measured from the initial and final diameters of the specimen. On cooling, tests were conducted at different temperatures below the NDT, after heating the specimen to NST.

Figure 1a shows the microstructure of NST tested specimen of SS 304HCu SS which reveals incipient melting at the boundary. Figure 1b shows Nb mapping obtained in SEM EDS. Photomicrograph of hot cracked

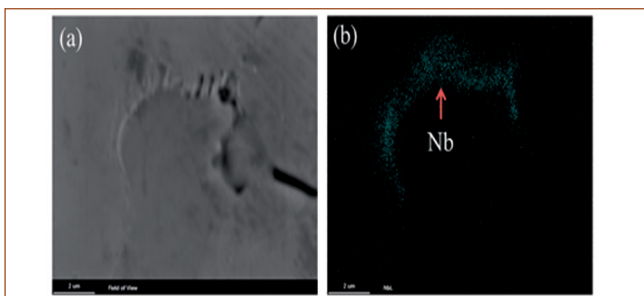


Fig. 1 (a) SE image of 304HCu SS base metal

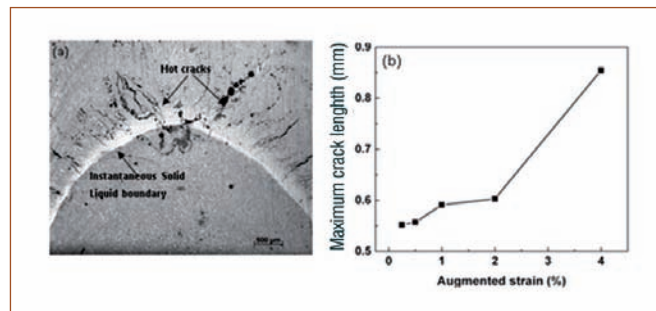


Fig. 2 (a) Macrostructure of varestraint tested specimen (b) Plot of maximum crack length vs % augmented strain

specimen is shown in Figure 2a. Numerous cracks are visible around the instantaneous solid-liquid interface as shown in the figure. Figure 2b shows a plot of maximum crack length (MCL) vs. % augmented strain measured from the hot crack tested specimens. The varestraint test results show that the threshold strain for cracking is 0.25 %. Threshold strain for cracking in 304SS is reported to be ~ 1% augmented strain determined using similar varestraint test conditions.

Reduction in area vs. test temperature obtained from the “Gleeble”™ tests is plotted in Figure 3 for *on heating* and *on cooling* conditions. NST for 304HCu SS is indicated in the same figure. Ductility decreases sharply from 87 % to 0 % with increasing temperature from 1270 to 1280°C which is a very narrow range. On the other hand, *on cooling*, ductility recovery starts at 1050°C. About 5 % ductility recovery occurs at 1027°C. Therefore, Nil Ductility Range (NDR) (NST – DRT) of the present steel is determined to be 257°C which is comparatively higher compared to other FCC materials. The high NDR observed in this steel indicates that constitutional liquation of precipitates increases in solidification range. It is known that alloys with higher NDR are more susceptible to hot cracking. Therefore, welding parameters have to be chosen carefully during fabrication.

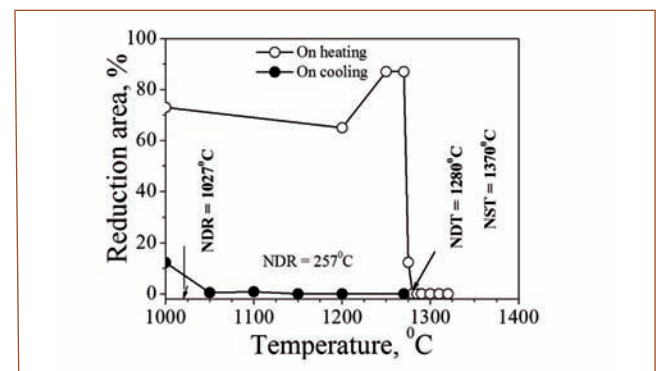


Fig. 3 Change in reduction area on heating and on cooling

V.11 A Novel Approach for Welding 304B4 SS using Standard Austenitic Consumables with Low Cracking Tendency

AISI 304B4 SS (Table 1) plates containing ~1.24 wt.% Boron (B) was chosen for fabrication of neutron shields for Intermediate Heat Exchangers (IHX) for the Indian Prototype Fast Breeder Reactor. The purpose of neutron shields is to reduce induced radioactivity in the secondary sodium which flows in to steam generator situated outside the reactor vessel. Though it is reported that borated stainless steels with B content in the range of 0.5-2 wt.% are immune to hot cracking, the most challenging task faced during fabrication of IHX was welding 10 and 28 mm thick 304B4 SS neutron shields around the shell in bottom portion of IHX. Welding consumable recommended for SS 304B4 is standard E309 as it solidifies in the primary ferritic mode. In the fabrication of neutron shields for IHX, though E309 welding consumable was chosen to weld AISI 304B4 - to minimize the risk of hot cracking - extensive cracks were observed especially in the thick section joints. Our preliminary study showed that severe cracking in weld joints produced using E309 could be due to base metal dilution in the weld metal. Base metal dilution can introduce B in fusion zone and its concentration can vary depending on the dilution ratio - being high close to the fusion boundary and less at the weld centre. Also, the hot cracking susceptibility study conducted on direct weld joints prepared using E309 welding consumables reveals the possibility of improving the hot cracking resistance of the weld joints by adopting a welding procedure with buttering.

The modified welding procedure adopted for welding SS 304B4 using standard E309 electrode is described schematically in Figure 1. In this welding procedure, the edge surfaces are to be first buttered with E309 SS welding consumable and the thickness of the buttered

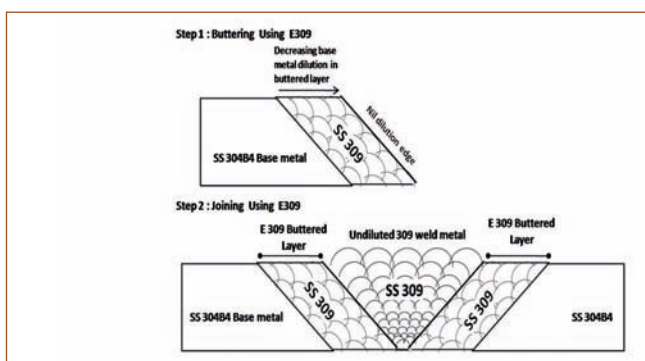


Fig. 1 Schematic representation of modified welding procedure adopted for welding 304B4 SS using E309 electrode

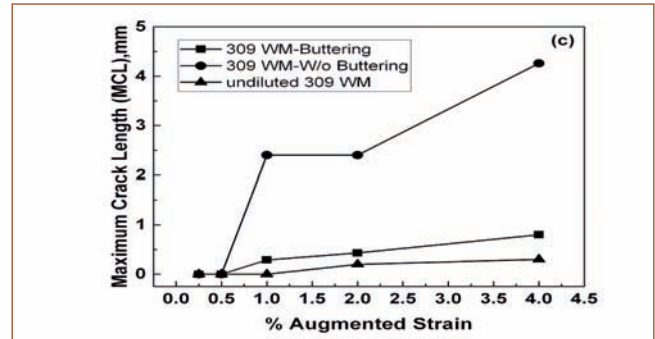


Fig. 2 Plot of Maximum Crack Length (MCL) vs % augmented strain of weld joints prepared using E309 with, without buttering and undiluted 309 weld metal

layer should be such that on the faces prepared after machining of the buttered layer, dilution from base metal should be negligible, per se 7 mm. Since there is no joining involved during buttering, residual stresses generated during buttering would be less. Though the weld metal microstructure could be susceptible, risk of cracking would be less. Further, during buttering, there is much better control of heat input and hence, dilution from base metal can also be minimized in the buttered layer. Subsequently, welding is carried out using the plates with edges prepared with buttered layers as shown in Figure 1. Now in the actual welding, only melting of the free surface of the welding, only melting of the free surface of the buttered layer, which is same as the fused E309 welding consumable, occurs. Hence, risk of cracking is expected to be reduced. In order to demonstrate this hypothesis, Vareststraint test specimens were prepared from the weld joints made as described above and susceptibility of the fusion zone in which melting and mixing of both buttered layer and welding consumable take place during actual joining, is evaluated.

A comparison of the crack length data shown in Figure 2 shows that MCL obtained for the weld joint prepared using modified welding procedure is lower than that for the direct joint, thus, indicating lower susceptibility of the buttered joint to cracking. This is attributed to the microstructure near the interface between the butter layer and the weld metal in the modified joint which is almost free of borides than that observed for similar zone in the direct joint between 304B4 plates using E309 consumable.

	C	Cr	Ni	Mn	B	Si	Fe
304B4	0.02	18.05	12.29	1.74	1.24	0.55	bal

V.12 Thermophysical Properties of Alpha (α) and Sigma (σ) Phases in Fe-Cr Alloy

Sigma (σ) phase is one of the detrimental intermetallic phases that forms in many structural steels after prolonged high temperature exposure, leading to significant degradation in toughness and other mechanical properties. In particular, the weldments of nuclear grade austenitic stainless steel are susceptible to sigma phase formation, during post weld heat treatment due to the decomposition of metastable δ -ferrite phase. σ phase has a complex tetragonal crystal structure with 30 atoms, distributed in five non equivalent lattice sites. The possibility of preferential and random site occupancy of constituent atoms makes the sigma phase non stoichiometric and which also enables modification by suitable alloying additions. Thus the physical properties of sigma phase can be tailored by alloying. In literature, only fewer studies are available on thermo-physical properties of sigma phase. No data could be found on thermal conductivity and thermal expansion behaviour of sigma phase in important Fe-Cr system. The present study addresses this gap partly for Fe₅₆Cr₄₄ alloy.

Buttons of Fe₅₆Cr₄₄ (at.%) alloys were arc melted, homogenized at 1373 K for 2 h, to obtain equilibrium α -ferrite phase. To synthesize the metastable σ -phase, the homogenized alloy was vacuum-, annealed at 973 K for 360 h, followed by water quenching. Microstructures of α -ferrite and σ -phases are shown in Figure 1. Average hardness values measured for the σ phase was 1100 HV0.1; and that of α -ferrite phase was 325 HV0.1 Analysis of high temperature phase stability using differential scanning calorimetry, for

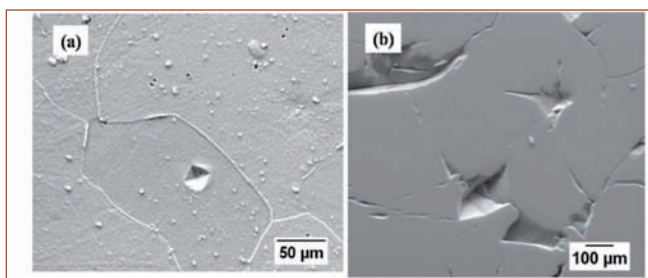


Fig. 1 Microstructure of (a) α -ferrite and (b) σ -phase

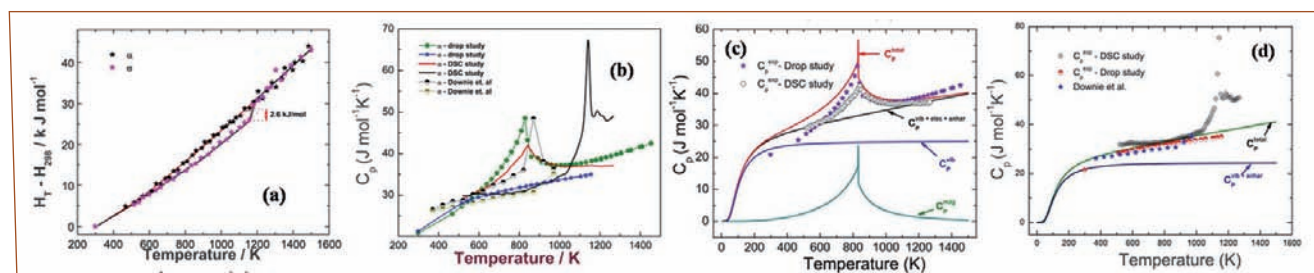


Fig. 2 Measured (a) enthalpy and (b) specific heat for α -ferrite and σ phases. Comparison of measured and estimated specific heat for (c) α -ferrite and (d) σ -phases

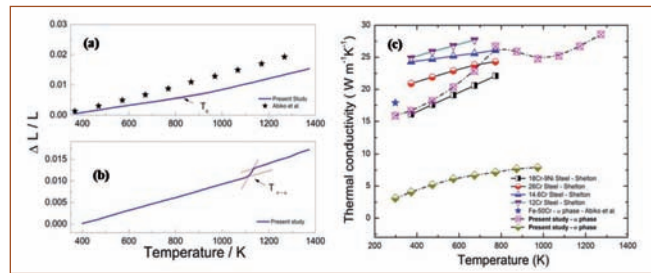


Fig. 3 Measured thermal expansion for (a) α and (b) σ phases; (c) Comparison of thermal conductivity obtained in the present study with literature data

showed a magnetic transformation of the α phase at 831 K, followed by $\sigma \rightarrow \alpha$ structural transformation at 1120 K. The transformation enthalpy for $\sigma \rightarrow \alpha$ change is found to be 2.6 ± 0.2 kJ mole⁻¹. Enthalpy increment ($H_T - H_{298}$) and specific heat capacity were determined for both σ and α phases by inverse drop calorimetry. The results are shown in Figure 2a and 2b respectively. Figure 2b shows a comparison of the specific heat for both the phases obtained in the present work with relevant literature information. To determine different contributions to the total specific heat, Debye Gruneisen quasi-harmonic modelling was adopted and the results obtained for α and σ phases are shown in Figure 2c and 2d respectively. Bulk Thermal expansion was measured using thermo mechanical analyzer and results are shown in Figures 3a and 3b respectively. Room temperature thermal expansion coefficient for α and σ phases are 7.4×10^{-6} K⁻¹ and 15.1×10^{-6} K⁻¹ respectively. Thermal expansion coefficient for σ is significantly higher than that of α phase. Thermal diffusivity for α and σ phases was measured using laser flash thermal diffusivity analyzer. Room temperatures values are found to be, 0.0484 and 0.011 cm²/s respectively for α and σ phases. Room temperature thermal conductivity for σ was much lower (3.1 Wm⁻¹K⁻¹) than that of α phase (16.22 Wm⁻¹K⁻¹) (Figure 3c). From the present study, it emerges that formation of σ phase will have adverse effect on the heat transport properties of structural steels, especially their weldments.

V.13 Characterising the Influence of Cold Work on Precipitation Kinetics in 304HCu Steel using Electrical Conductivity and Hardness Measurements

304HCu is an 18Cr-9Ni type heat resistant austenitic stainless steel with 3 wt.% copper addition for improving its high temperature strength. The 304HCu steel exhibits excellent creep rupture strength due to precipitation of coherent Cu-rich phase as well as dispersion strengthening due to fine precipitate particles of NbCrN, Nb(C, N) and $M_{23}C_6$ formed during thermal aging. This steel is considered for use as boiler tubes in Advanced Ultra Super Critical (AUSC) thermal power plants due to its excellent mechanical properties. During fabrication of boiler tubes cold working/straining occurs which influences the microstructure as well as the precipitation behaviour on ageing. This study is focused on the kinetics of precipitation during thermal ageing of 304HCu steel under the influence of prior cold working (CW) using electrical conductivity and hardness measurements.

The chemical composition of 304HCu steel used in this study is Fe-18Cr-9Ni-0.5Nb-3Cu-0.1C. The 304HCu steel specimens were solution annealed (SA) at 1050 °C for half an hour followed by water quenching. The solution annealed samples were cold worked to 10% (SA+10CW) and 20% (SA+20CW) reduction in thickness at ambient temperature. Samples with these three initial conditions were isothermally aged at 650 °C for 0.25, 0.5, 1, 3, 5, 22 and 100 hours durations and the change in hardness and electrical conductivity were studied.

The change in hardness and electrical conductivity of SA, SA+10% and SA+20% cold worked samples on isothermal ageing are shown in Figures 1 and 2

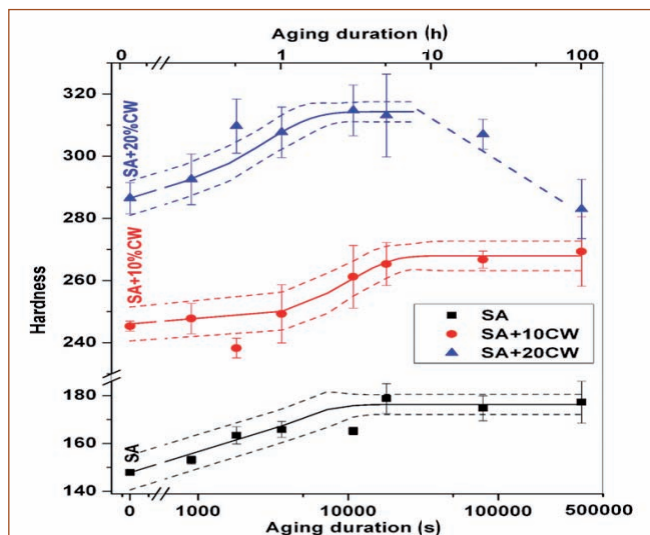


Fig. 1 The variation of hardness for SA, SA+10% and SA+20% CW 304HCu steel samples with aging

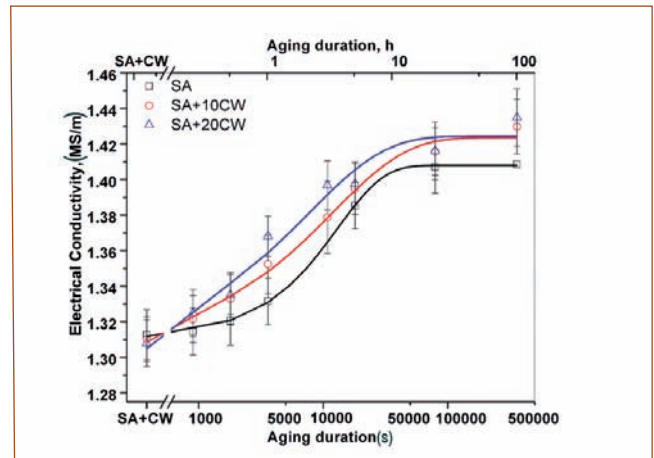


Fig. 2 The variation of electrical conductivity of solution annealed followed by cold worked samples with respect to aging duration

respectively. On initial cold work while the hardness increases due to deformation induced dislocations, no significant change is seen in electrical conductivity. However, conductivity increases on thermal ageing due to precipitation of different phases and shows saturation whereas hardness saturates and decreases after 10 h in 20% prior CW sample due to annihilation of dislocations. To study the kinetics of precipitation under different prior CW conditions, the Johnson–Mehl–Avrami (JMA) equation (Equation 1) is fitted (shown as solid line in figures) to the changes in hardness and conductivity during ageing.

$$f = 1 - \exp(-(kt)^n) \quad (1)$$

The reaction rate k and Avrami exponent n obtained from JMA fit are shown in Table 1. The higher reaction rate for 20% prior cold worked sample shows accelerated precipitation behaviour as compared to solution annealed sample. The observed change in precipitation kinetics due to deformation is analyzed to evaluate an equivalent change in activation energy which is attributed to an equivalent of increase in aging temperature.

Table 1: The reaction rate k and Avrami exponent n obtained from JMA fit				
CW (%)	JMA fit to hardness		JMA fit to conductivity	
	Reaction rate (k , s ⁻¹)	Avrami Exponent (n)	Reaction rate (k , s ⁻¹)	Avrami Exponent (n)
0	3.13×10^{-4}	1.16 ± 0.27	7.66×10^{-5}	1.17 ± 0.05
10	1.12×10^{-4}	1.25 ± 0.27	8.42×10^{-5}	0.72 ± 0.10
20	3.70×10^{-4}	1.28 ± 0.15	1.33×10^{-4}	0.70 ± 0.17

V.14 Experimental and Computational Exploration of Pnicogen Bonding

The study of non-covalent interactions plays a pivotal role in understanding the properties of the molecules in chemical and biological systems. Scientific curiosity went beyond the search of non-covalent interactions including chalcogen, triel, tetral and pnicogen bonding other than conventional hydrogen bonding. Of these, pnicogen bonding, that involves pnicogen atoms i.e. N, P, As, Sb and Bi as the interacting Lewis acid moiety assumes importance among experimentalists in bringing forth the concept with the evidence using varieties of spectroscopic techniques. Since its discovery, the amount of theoretical reports was substantial on pnicogen bonding but with the limited experimental proofs. Thus, there exists a huge gap between theory and experiment and hence a genuine bridging between the two is therefore indispensable.

The specific terminology of ‘phosphorus bonding’ in place of pnicogen bonding was coined, in order to emphasize the interactions centered on phosphorus. Of the phosphorus centric molecules, phosphorus trichloride (PCl_3) can be considered as a perfect paradigmatic model to explore pnicogen (phosphorus) bonding as the central phosphorus atom is highly electropositive due to the electron withdrawing effect of chlorine atoms. To explore the pnicogen (phosphorus) bonding interactions therefore, matrix isolation infrared spectroscopy in combination with the *ab initio* quantum chemical computational methodology were utilized in our laboratory.

To establish phosphorus bonding with PCl_3 prototype, a large number of Lewis bases (H_2O , CH_3OH , C_6H_6 , $\text{C}_5\text{H}_5\text{N}$ and $\text{C}_4\text{H}_5\text{N}$) were independently co-deposited with PCl_3 at 12 K with large excess of matrix gas (Ar or

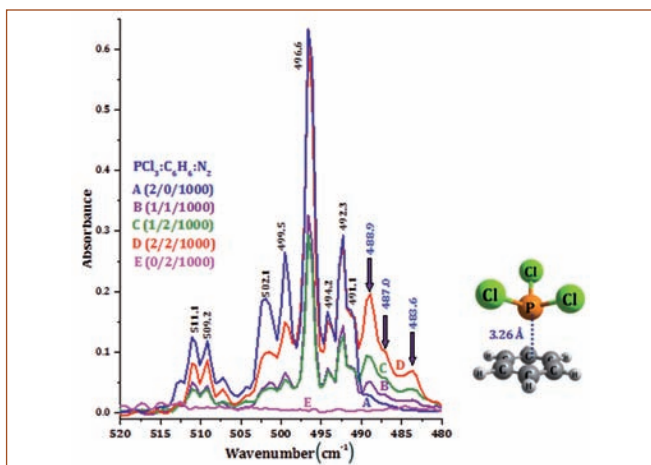


Fig. 1 Matrix isolation infrared spectra for varying concentrations of $\text{PCl}_3:\text{C}_6\text{H}_6:\text{N}_2$

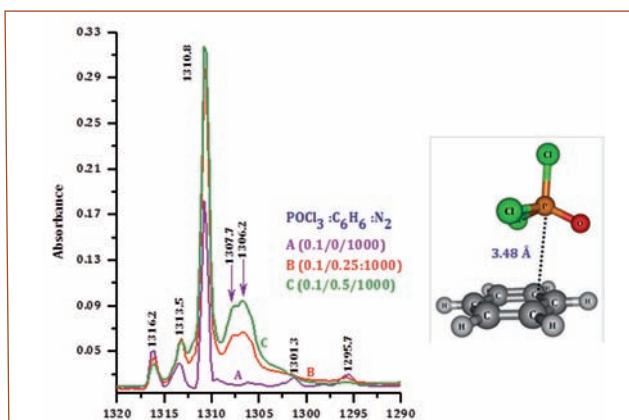


Fig. 2 Matrix isolation infrared spectra for varying concentrations of $\text{POCl}_3:\text{C}_6\text{H}_6:\text{N}_2$

N_2). As a consequence of annealing the matrix followed by diffusion of the precursors, the heterodimers were generated at low temperatures. These heterodimers were probed using infrared spectroscopy and their structures were characterized with *ab initio* computational methodology. Typical Matrix isolation infrared spectra for varying concentrations of PCl_3 and C_6H_6 precursors are shown in Figure 1. The spectral features that were discerned at 488.9, 487.0 and 483.6 cm^{-1} (P-Cl stretching region of PCl_3) are due to $\text{PCl}_3\text{-C}_6\text{H}_6$ heterodimer stabilized through phosphorus bonding. Using Atoms in Molecules (AIM) and Natural Bond Orbital (NBO) analyses, the existence of phosphorus bonding in these systems were confirmed.

In addition to PCl_3 , where phosphorus atom exists in its trivalent state, the phosphorus bonding can also be envisaged in POCl_3 , where phosphorus is present in the pentavalent state. Consequently, matrix isolation experiments were performed on POCl_3 dimer, $\text{POCl}_3\text{-H}_2\text{O}$, $\text{POCl}_3\text{-C}_2\text{H}_2$, $\text{POCl}_3\text{-C}_2\text{H}_4$ and $\text{PCl}_3\text{-C}_6\text{H}_6$ systems and as a result, unambiguous evidence on pentavalent phosphorus bonding was established. Typical Matrix isolation infrared spectra for varying concentrations of POCl_3 and C_6H_6 precursors are shown in Figure 2. The spectral features that were discerned at 1307.7, and 1306.2 cm^{-1} (P=O stretching region of POCl_3) are due to $\text{POCl}_3\text{-C}_6\text{H}_6$ heterodimer stabilized through pentavalent phosphorus bonding.

A comparison of trivalent phosphorous bonding with conventional interactions revealed that phosphorus bonding is stronger than any other weak interactions. Conversely, in presence of strong hydrogen bonding partner, pentavalent phosphorous bonding operates co-operatively.

V.15 Suppression of Spin Wave Excitations in BiFeO₃ through Aliovalent Substitution

BiFeO₃ has a rhombohedral crystal structure, with space group R3c. It exhibits atomic translation along pseudo cubic $\langle 111 \rangle_{pc}$ direction and anti-phase tilting of nearby FeO₆ octahedra due to the stereochemical activity of lone pair of electrons of Bi³⁺ ion. This effect leads to ferroelectric ordering with spontaneous polarization along $\langle 111 \rangle_{pc}$. On the other hand, a microscopic model describes magnetic interactions in BiFeO₃, which includes nearest and next-nearest neighbor superexchange (SE) interactions, *Dzyaloshinskii-Moriya (DM) interactions and single-ion anisotropy (SIA)*. These interactions lead to a spiral cycloidal spin structure (with a periodicity of 62 nm). However, the presence of cycloid hinders the macroscopic magnetization and linear magnetoelectric (ME) effect. To improve the magnetic and ME properties in BiFeO₃, its cycloidal spin structure needs to be suppressed. This can be achieved through doping, induced strain in the thin film, by applying hydrostatic pressure or magnetic field.

BiFeO₃ (BFO), Bi_{0.9}Ba_{0.1}FeO_{2.95} (BBFO), Bi_{0.9}Ba_{0.05}Ca_{0.05}FeO_{2.95} (BBCFO) and Bi_{0.9}Ca_{0.1}FeO_{2.95} (BCFO) samples were synthesized by sol-gel route and characterized by XRD technique. Near-normal incidence reflectivities of the samples in the far-infrared region were obtained using Bruker Vertex 80V FTIR spectrometer, with gold mirror as reference.

The measured reflectivity, $R(\omega)$, spectra of the pristine and doped BiFeO₃ samples at room temperature recorded in the frequency range from 50 to 650 cm⁻¹ are shown in Figure 1. These $R(\omega)$ spectra were fitted

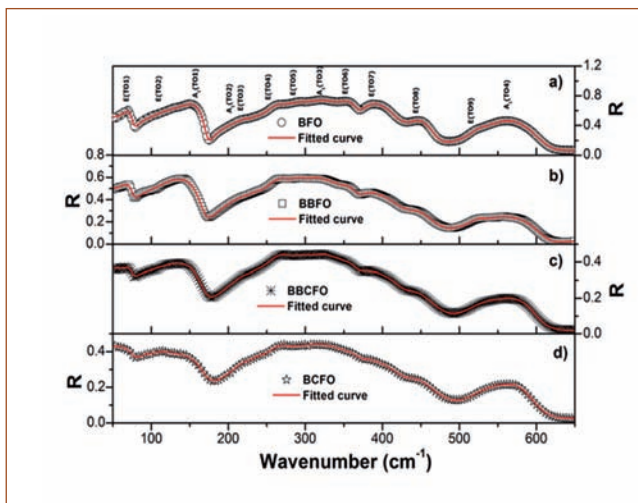


Fig. 1 Reflectance spectra of the pristine and doped BFO samples

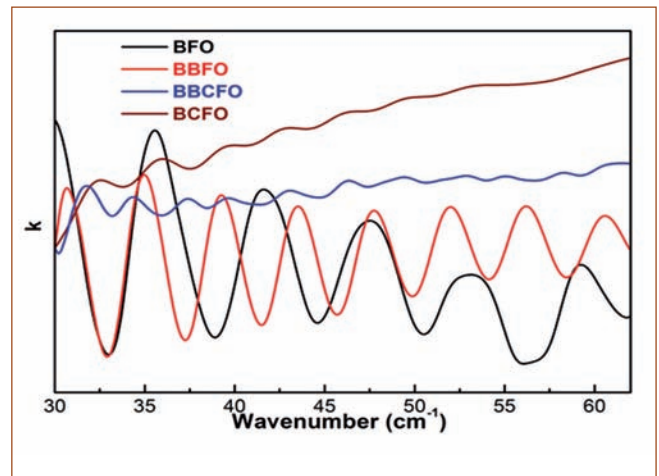


Fig. 2 k -spectra of spin excitations in the pristine and doped BFO samples

satisfactorily with all the 13 ($9E+4A_1$) expected IR-active phonon modes using the four-parameter model.

Doping of Ca at the Bi site is found to affect the Bi-related modes the most, which harden by about 4% compared to the pristine sample. Since we also observe a decrease in the unit cell volume with increasing Ca content from the XRD data of these samples, the hardening of Bi-related modes points to an increased chemical pressure on doping.

The low energy spin wave excitations (SWEs) of the samples are observed clearly in the k -spectra, as illustrated in Figure 2. The SWEs of the BFO sample show a series of magnetic excitations. The SWEs are substantially modified in the co-doped and Ca-doped samples while only a moderate change is seen for BBFO. The Ca doping in BiFeO₃ almost completely suppresses the SWEs. This is due to an increased anharmonicity in the spin cycloid, which, in turn, can be attributed to an increase in single-ion anisotropy upon doping. The SWE modes of all the samples were also index generated separately for the cyclons and the extra cyclons. The cyclon energy for all the samples was found to be $5.8 \pm 0.2 \text{ cm}^{-1}$, which is close to the theoretical value of 5.3 cm^{-1} . The largest energy separation between the cyclons and the extra-cyclons was observed for BCFO, which also showed the maximum suppression of the SWEs.

In summary, suppression of spin-wave excitations in BiFeO₃ was noticed through aliovalent doping of Ca and Ba at the Bi site. The chemical pressure induced modifications of the SWEs has been explained by an enhanced SIA contribution in the doped samples.

V.16 Magnetic Properties of Double Perovskites, A_2ZnMnO_6 (A: Sr/Y)

Double perovskites with chemical formula, $A_2BB'O_6$ (A: alkaline earth/ rare-earth; B, B': two different transition metals) have attracted researchers attention owing to their magnetic, electric properties combined with dielectric properties. Relative ionic sizes and oxidation states of B and B' decide the arrangement of cations resulting in ordered structures. Room Temperature (RT) half metallicity was discovered in an ordered double perovskite, Sr_2FeMoO_6 . Materials that display half metallic character are basically semiconductors with 100% spin polarization near the Fermi Level. These materials play a key role in technological applications such as magnetic sensors, computer memory etc. Electronic structure calculations based on density functional theory predict manganese based Sr_2ZnMnO_6 (SZMO) compound to be half metallic ferrimagnetic. In an exploration to find materials showing half metallic properties around RT, investigations on SZMO and Y_2ZnMnO_6 (YZMO) were undertaken.

Polycrystalline materials of $(Sr/Y)_2ZnMnO_6$ were synthesized using ceramic route. Raman spectra at RT were recorded with 514.5 nm. Magnetization measurements in Zero Field Cooled (ZFC) and Field Cooled (FC) modes were carried out at 100 Oe and 1 Tesla from 5-350 K. $M(H)$ curves were obtained from -7 to +7T at various temperatures.

X-ray powder diffraction patterns showed that the major phase crystallizes in a monoclinic structure. A large number of bands observed in Raman spectra of both materials in the low wave number region (Figure 1) may be an indication of monoclinic structure. Moreover, the strong Raman band at $\sim 670\text{ cm}^{-1}$ can be associated with $P2_1/n$ symmetry. While low wave number vibrations are ascribed to coupled $(Zn/Mn)O_6$ tilting vibrations and Sr-O stretching, two modes at ~ 530 and $\sim 650\text{ cm}^{-1}$ are ascribed to stretching and antistretching modes of $(Zn/Mn)O_6$ octahedra. These modes are activated by the monoclinic distortions and are more sensitive to ionic radius at A site.

Dependence of $\chi(T)$ (Figure 2a) indicates that SZMO may contain both the ordered and disordered phases. But, $\chi_{ZFC}(T)$ data of YZMO (Figure 2c) measured at 100 Oe showed a peak while $\chi_{FCW}(T)$ with a slope change continues to increase as the temperature is reduced. Both $\chi_{ZFC}(T)$ and $\chi_{FCW}(T)$ curves of both samples measured at 1 T merge into a single curve (Figures 2b and 2d). Experimental values of effective

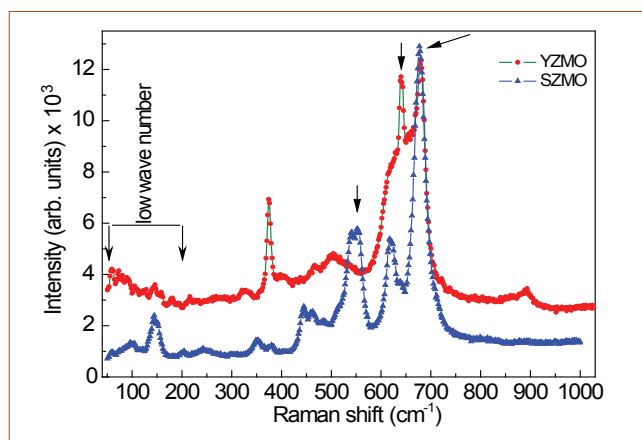


Fig. 1 Raman spectra of SZMO and YZMO

magnetic moments (μ_{eff}) for SZMO and YZMO found from Curie-Weiss fit are 3.99 and 4.36 μ_B , higher than the theoretical values 1.73 and 3.87 μ_B .

The high value of μ_{eff} (expt.) for SZMO corroborates mixture of ordered and disordered crystalline phases. However, MH loop of SZMO at 5K showed no tendency for saturation with a small magnetic moment, 0.106 $\mu_B/\text{f.u.}$ at 7 T with a negligible coercive field while MH loop of YZMO at 5K has a coercive field of 480 Oe with a moment of 1.3 μ_B at 7 T (Figure 2d inset). Such a low value of magnetic moment per formula unit may be ascribed to half metallic property of SZMO. With non-magnetic ground states, Sr and Zn ions have negligible contribution to magnetization and magnetization arises from the magnetic Mn ions only.

In conclusion, of the two new double perovskite materials, SZMO showed half metallic nature unlike YZMO.

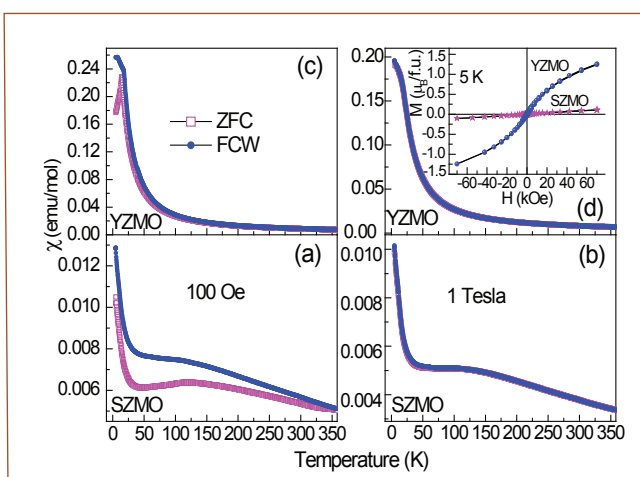


Fig. 2 Magnetization as a function of temperature and applied magnetic field for SZMO & YZMO

V.17 Imaging Dislocation Core in Bulk Nanocrystalline CP-Ti using Geometrical Phase Analysis of Aberration Corrected HRTEM Image

Defect analysis through electron microscope in the atomic scale always poses a challenge and excitement to microscopists. Deviation from the exit wave vector coupled with the complex nature of the single atom potential at the defect core makes defect imaging very challenging in an electron microscope. In the recent past, development of the spherical image aberration corrected TEM and the quantitative high-resolution analysis, have enabled the microscopists to more frequently address the issue of imaging the defect cores. In the present work, an attempt has been made to image the dislocation core in a bulk nanocrystalline CP-Ti through mapping of localized strain (lattice distortion). This has been done by means of interpretation of direct contrast of high-resolution aberration corrected TEM images. The technique is intriguing since the atom column contrast is governed by several parameters viz., thickness, defocus and drift apart from localized strain. Multislice image simulation has been systematically used to understand the nature of the image contrast and in turn the defect analysis in this system. The understanding of the defect in this system will help to assess the system for its in-service behavior.

This nanocrystalline (nc) Ti has been developed by means of cryo-rolling of coarse grained bulk CP-Ti by means of cryo-rolling by imparting heavy true strains of

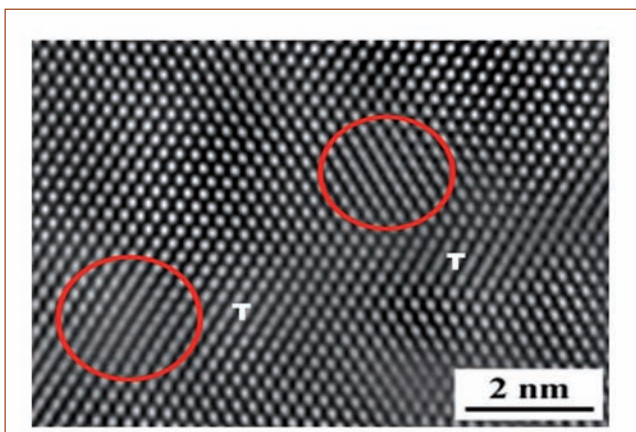


Fig. 1 Image aberration corrected phase contrast micrograph from bulk nanocrystalline CP-Ti

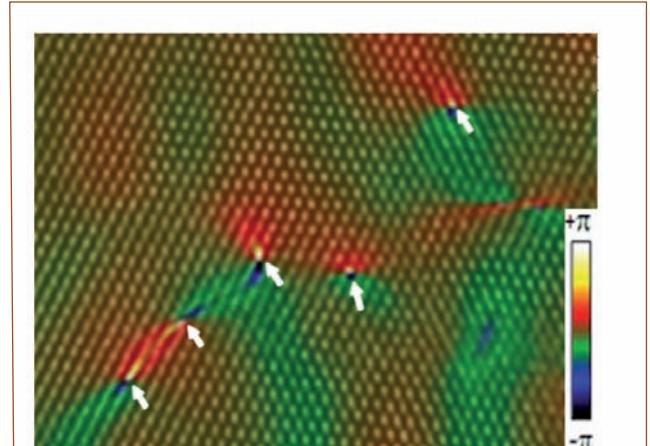


Fig. 2 GPA map superimposed over the phase contrast image. The dislocations cores are marked in the figure

the order of 2-3. An in-depth analysis of the nc-Ti through geometrical phase analysis (GPA) provides an indication about the severity of plastic deformation of CP-Ti and subsequent grain fragmentation.

Figure 1 shows aberration corrected phase contrast micrograph from severely cryo-rolled Ti, showing atomic arrangement in the system. The deformed planes are encircled and the dislocation cores are marked in the micrograph. A careful observation also reveals occurrence of dislocations.

Figure 2, on the other hand, shows the corresponding GPA map superimposed on the aberration corrected phase contrast image. The strain is colour coded as follows: black represents a compressive strain of π and white represents a tensile strain of $-\pi$. The superimposed micrograph clearly reveals that a dislocation core (marked in the image) is always associated with a sharp change from the tensile to the compressive nature of strain. The nearby strain field is generated because of the dislocation field corresponding to the dislocation core. Moreover, from the superimposed micrograph it can also be seen that the core of the tensile and the compressive component co-exists over a distance of about two atomic spacing which is consistent with the concept of the sinusoidal nature of the lattice strain.

V.18 Effective Utilization of Defect Modulated Photoluminescence in SnO₂ Quantum Dots for Selective Detection of Ammonia at RT

The obvious advantage of optical-based sensing like low temperature and contactless operations urges a need for material with good optical response. Various degrees of freedom during optical sensing like measurements of wavelength, frequency, degree of polarizability further add to its merits for application. In the above context, SnO₂ a direct and wide band gap (3.6 eV in room temperature) n-type semiconductor is a potential candidate. Notably, in the field of electrical based (resistive and capacitive) gas sensors, SnO₂ enjoyed a large prevalence, due to its chemical stability and donor level defects close to the conduction band. In spite of forbidden band to band transition, intrinsic defects like tin interstitial and oxygen vacancies, dominate in nano-structured SnO₂ and it helps in tailoring the optical properties to a large extent. Thus, defect induced photoluminescence (PL) makes this material viable for many optical applications. Importantly, these defects may not participate in chemisorptions based sensing process but become available exclusively as optical probe. Hence the current work focuses to utilize oxygen vacancies in SnO₂ to develop PL based optical sensor for ammonia. SnO₂ quantum dot (QD) providing large surface to volume ratio with maximum area for exposures to an analyte was used.

QD of SnO₂ was synthesized in solution by addition of ammonium hydroxide (NH₄OH) to stannic chloride (SnCl₄). Rutile tetragonal structure of SnO₂ QDs was verified using the X-ray diffraction as shown in Figure 1a. The crystallite size measured by high resolution transmission electron microscope Figure (1b) was found to be 2.4 ± 0.1 nm. PL spectra were acquired using 325 nm (He-Cd laser) as the excitation source at room temperature. A broad peak was observed around 2 eV for the PL collected from the QDs (Figure 1c). This peak was convoluted with the constituent peaks centered at 1.84, 1.96, 2.11, 2.28 and 2.43 eV. The first three transitions arise due to bridging oxygen vacancies (V_B) and later two transitions are due to in-plane oxygen vacancies

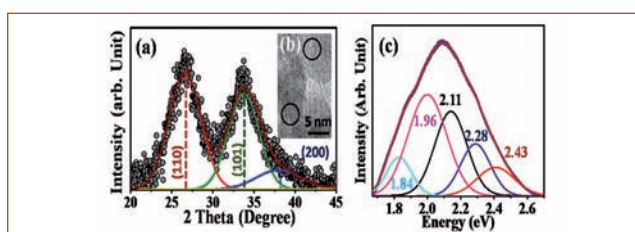


Fig. 1 (a) XRD (b) HRTEM and (c) Convoluted PL spectra collected from SnO₂ QDs

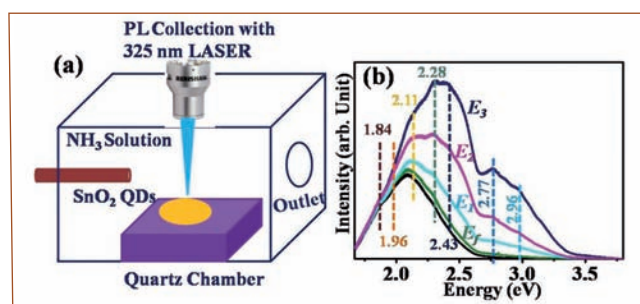


Fig. 2 (a) Schematic of sensing chamber (b) Variation in PL spectra of SnO₂ QDs in presence of NH₃

(V_I). Earlier reports show evidence that V_I and V_B create shallow and deep donor levels, respectively. In-order to perform PL based gas sensing measurement, a quartz chamber was used. To mimic the real life situation the experiment was conducted at room temperature under atmospheric pressure. The detailed schematic diagram of PL based contactless gas sensing set up is shown in Figure 2 a. Different volumes of NH₄OH (10-30 μ L) were put inside the chamber for the target NH₃ gas.

In the presence of NH₃, PL was recorded from SnO₂ QDs using 325 nm LASER and is depicted in Figure 2(b). Variation of NH₃ concentrations showed change in intensity of PL spectra. They are designated as E₁ (10 μ L) E₂ (20 μ L) and E₃ (30 μ L). Air was passed through the chamber to get rid of exposed NH₃ to understand the recovery process at RT. After that PL spectrum was collected and referred as E_f in Figure 2b. In the presence of NH₃, drastic variation was observed in PL peaks (Figure 2b). An increase in the intensity was observed for the peaks related to V_I (2.28 and 2.43 eV) on gradual increment in NH₃ concentration and the difference after exposure from baseline was considered to be sensor response. It is to be noted that peaks at 1.84, 1.96 and 2.11 eV remain unaffected with NH₃ exposures.

The underlying mechanism was explained considering the acid-base interaction. Presence of Sn⁴⁺ on the QDs SnO₂ surfaces acts as lewis acid and interacts with NH₃ which is a lewis base because of lone pair of electron in nitrogen. Reduction of particle size ensures a very large surface and hence an abundant amount of acidic site. After the adsorption of NH₃ on the SnO₂ surface electron redistribution happens and increases the probability of radiative transition by recombination of e-h pairs and allows enhancement of PL intensities of 2.28 and 2.43 eV at RT. PL as a probe for contactless sensing of NH₃ is important aspect for technological application of toxic gas detection and industrial safety.

V.19 Experimental and Computational Determination of Thermal Expansion of Energetic Material TEX

The secondary explosive TEX ($C_6H_6N_4O_8$) is a molecular solid, and it is the second-most dense nitramine with a density of 1.985 g/cm^3 . It is friction insensitive, has low impact and shock sensitivities, high velocity of detonation (8500 m/s) and a large critical diameter, making it an attractive explosive filler for insensitive munitions. One of the important properties of explosives is the volume thermal expansion coefficient (α_v) that plays a significant role in applications like modeling the response of energetic material to external stimuli. Anisotropic thermal expansion in explosive crystals causes internal stress and when the effect of this stress is larger than the cohesive energy micro cracks will appear in the crystal. These internal micro voids can induce hot spots and increase the sensitivity of the energetic materials.

We have carried out temperature dependent x-ray diffraction (XRD) measurements on TEX up to 150°C and obtained the volume thermal expansion coefficient α_v and its anisotropy. We have also calculated α_v using Gruneisen formalism from the pressure dependence of the phonon frequencies in TEX using density functional theory (DFT) calculations. About 15 mg of TEX powder was mounted on a tantalum strip that was resistively heated and the sample temperature was monitored with a thermocouple spot welded to the rear of the strip. All measurements were carried out in a vacuum of $\sim 10^{-5}$ Torr.

To obtain the phonon modes of solid TEX using first principles calculations, geometry optimization of the crystal structure was carried out with CASTEP code in the Materials Studio Version 6.0 (Accelrys) package using norm-conserving pseudo potentials and a plane wave expansion of the wave functions. Phonon mode frequencies were also calculated at 1 GPa and 2 GPa using CASTEP.

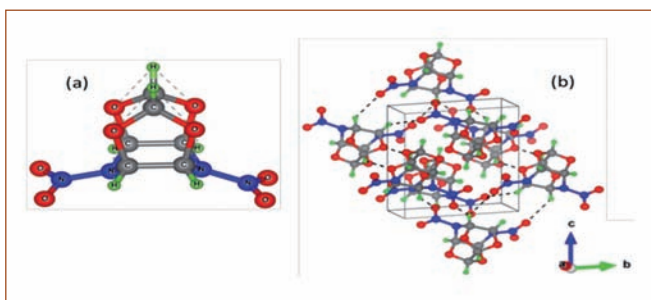


Fig. 1 (a) Molecular structure and (b) Crystal structure of TEX. Molecules are linked by C-H \cdots O hydrogen bonds nearly along a and b directions

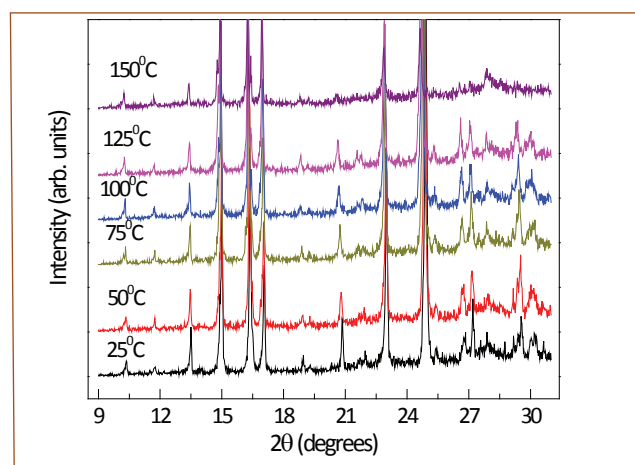


Fig. 2 XRD patterns of TEX at different temperatures

The molecular and crystal structures of TEX are shown in Figure 1. At ambient conditions TEX crystallizes in a triclinic structure (space group P) with two formula units per unit cell. Rietveld refined XRD pattern of TEX at ambient conditions recorded with a STOE diffractometer is shown in Figure 2. The refined lattice parameters are $a=6.849 \text{ \AA}$, $b=7.644 \text{ \AA}$, $c=8.829 \text{ \AA}$, $\alpha=82.5^\circ$, $\beta=75.0^\circ$, $\gamma=79.5^\circ$ and volume $V=437.2 \text{ \AA}^3$. The calculated density at ambient conditions is $\rho=1.991 \text{ g/cm}^3$.

XRD patterns of TEX during the heating cycle from 25 to 150°C were recorded in steps of 25°C . The patterns show normal shift of Bragg peaks to lower 2θ angles as the temperature is increased, indicating an increase in inter-planar spacing due to thermal expansion (Figure 2).

The crystal structure is fitted to triclinic with space group $P\bar{1}$ at all temperatures. Le-Bail fitting of XRD patterns is carried out to obtain the lattice parameters ($a = 6.850 \text{ \AA}$, $b = 7.665 \text{ \AA}$, $c = 8.826 \text{ \AA}$, $\alpha = 82.38^\circ$, $\beta = 75.0^\circ$, and $\gamma = 79.30^\circ$ at 25°C) as a function of temperature. The lattice parameters obtained at 25°C with PANalytical X'Pert Pro MPD and STOE X-ray diffractometer are in reasonable agreement with each other. Over the temperature range $25\text{--}150^\circ\text{C}$, lattice parameter a increases by 0.6%, b by 0.3%, c by 1.3% and the volume by 2.1%. They increase anisotropically with temperature, i.e., the expansion is different in different directions ($\alpha_a = 4.4 \times 10^{-5}$, $\alpha_b = 3.2 \times 10^{-5}$ and $\alpha_c = 9.7 \times 10^{-5} \text{ K}^{-1}$) (Figure 3).

Coefficient of linear thermal expansion and its anisotropy depend on the chemical structure of the molecule, packing structure in the crystal lattice and the chain configuration. In the crystal lattice TEX molecules are linked by C-H \cdots O hydrogen bonds nearly along a and

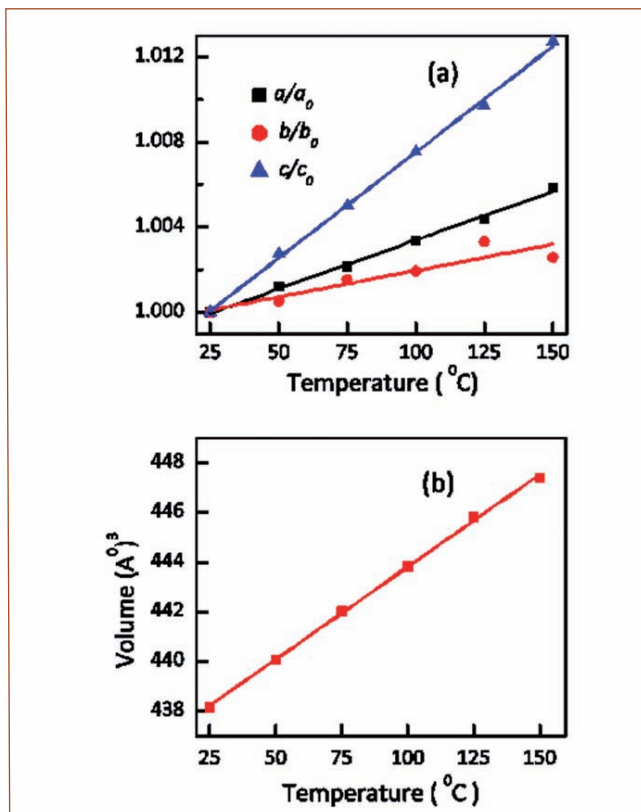


Fig. 3 (a) Lattice parameters increase anisotropically with temperature; (b) Volume increases linearly with temperature; straight line represents linear fit to the data points

b directions (Figure 1b). Van der Waals interaction along the c direction (nearly perpendicular to hydrogen bonds) makes the crystal softer in this direction. The directions of strong and weak hydrogen bonds in the crystal structure can be correlated to thermal expansion anisotropy. Dispersion in hydrogen bond length has been reported for TEX crystal (variation being in the range 2.49–2.559 \AA), and this difference can be related to the difference in α_a and α_b . Volume thermal expansion coefficient α_v was calculated using a linear least squares fit of V vs. T , where V is the volume of a unit cell of TEX at 25 °C. $\alpha_v = (1/V)(dV/dT)_P = 17.4 \times 10^{-5} \text{ K}^{-1}$. This is in good agreement the $\alpha_v = 11.3 \times 10^{-5} \text{ K}^{-1}$ obtained from the reported volumes of TEX at $-173 \text{ }^\circ\text{C}$ (428.8 \AA^3) and $-73 \text{ }^\circ\text{C}$ (433.64 \AA^3). The latter value of $11.3 \times 10^{-5} \text{ K}^{-1}$ is slightly lower compared to the one obtained by us since α_v is expected to reduce at low temperatures following the behaviour of specific heat.

Volume thermal expansion coefficient is defined as,

$$\alpha_v = \frac{\gamma_{av} C_v}{V_m B}, \text{ where } \gamma_{av}$$

is the average Gruneisen parameter, C_v the specific heat at constant volume, B the bulk modulus and V_m is the molar volume. For TEX crystal $V_m = 130.6 \text{ cm}^3/\text{mol}$. The specific heat at constant volume can be calculated by the formula

$$C_v = \frac{1}{2} \sum p_i C_i,$$

where p_i is the degeneracy, i.e., number of phonons or branches of frequency ω_i in the phonon dispersion curves, and C_i is the specific heat contribution from a single mode of frequency ω_i . The factor 1/2 in the above equation takes into account the fact that the triclinic unit cell contains two formula units of TEX molecule. $C_i = R[x_i^2 \exp(x_i)]/[\exp(x_i)-1]^2$, where $x_i = \hbar\omega_i/k_B T$, R is the gas constant and k_B is the Boltzmann constant. We computed the phonon frequencies of geometry optimized TEX crystal using CASTEP module in Material Studio 6. The C_v calculated using 141 optic modes of TEX crystal is 213 J/mol K.

In order to calculate α_v one needs to evaluate γ_{av} defined as

$$\gamma_{av} = \frac{\frac{1}{2} \sum p_i C_i \gamma_i}{C_v}.$$

The mode Gruneisen parameter is defined as

$$\gamma_i = - \frac{\partial \ln \omega_i}{\partial \ln V} = \frac{B}{\omega_i} \frac{\partial \omega_i}{\partial P}$$

where ω_i is the frequency of the i^{th} mode, B is the bulk modulus, P is the pressure, and V is the volume. Bulk modulus of TEX, $B = 14.9 \text{ GPa}$ has been reported by us earlier. Phonon frequency calculations were done at 0, 1, and 2 GPa using CASTEP codes. Mode Gruneisen parameters for all optic modes were calculated by obtaining the $d\omega_i/dP$ from these data. The average Gruneisen parameter $\gamma_{av} = 0.56$. The volume thermal expansion coefficient calculated using this Gruneisen formalism is $\alpha_v = 6.1 \times 10^{-5} \text{ K}^{-1}$. This value is somewhat lower compared to the $\alpha_v = 17.4 \times 10^{-5}$ measured from high temperature x-ray diffraction. This could be because in this calculation we have neglected the contributions from acoustic modes.

TEX shows anisotropic compressibility in which the lattice parameter c is more compressible (10%) than a (7.7%) and b (4.1%). The most compressible c direction is nearly normal to the hydrogen bonds. It is seen that this c direction is also the one showing the highest thermal expansion, $\alpha_c = 9.7 \times 10^{-5} \text{ K}^{-1}$. Thermal expansion coefficients in the a and b directions are also consistent with the compressibility in the respective directions, indicating the underlying atomic level connection between these two properties.

To summarize, the thermal expansion coefficient of TEX from x-ray powder diffraction studies in the temperature range 25–150 °C, and also from first principles calculations of phonon frequencies as a function of pressure using Gruneisen formalism is obtained. The volume thermal expansion coefficient $17.4 \times 10^{-5} \text{ K}^{-1}$ is comparable to that of a related material, CL-20 ($\alpha_v = 13.5 \times 10^{-5} \text{ K}^{-1}$).

V.20 Compressibility and Thermal Expansion Study of δ -UZr₂ at Elevated Pressure and Temperature

U-Pu-Zr alloy is a candidate fuel material for the metallic fuel based fast reactors. The U-Zr binary phase diagram shows the existence of only δ phase in the homogeneity range 64.2-78.2 at%Zr. This phase forms on cooling below 908 K from the high-temperature bcc U-Zr solid solution. High-temperature (HT) gamma phase transforms to δ phase by ω phase transformation mechanism where alternate (111) planes of gamma phase collapse and form A1B₂ type (C32) hexagonal crystal structure, which is related to the ω structure. The fascinating properties of δ -UZr₂ such as better mechanical properties of ω phase, similarity in the structural phase transition with Zr at high temperature, and a series of structural phase transitions in A1B₂ type UX₂ (X=transition metal) compounds make this study relevant and interesting.

δ -UZr₂ was prepared using the arc-melting technique. High Pressure (HP) X-Ray Diffraction (XRD) studies on δ -UZr₂ were carried out up to 20 GPa at BL-12 Indus-2, RRCAT. HP-XRD patterns indicate the structural stability of the parent δ -UZr₂ phase up to 20 GPa. The pressure-volume data fitted with 3rd order Birch Murnaghan equation of state results in the bulk modulus and its pressure derivative to be 108.3 GPa and 5.0, respectively. An anomaly in the lattice compression is observed at \sim 10 GPa. Up to 10 GPa the c/a ratio is found to decrease slowly, after which the reduction rate increases sharply (Figure 1). The same trend of variation has also been seen in the c/a ratio estimated from Density Functional Theory (DFT) calculation.

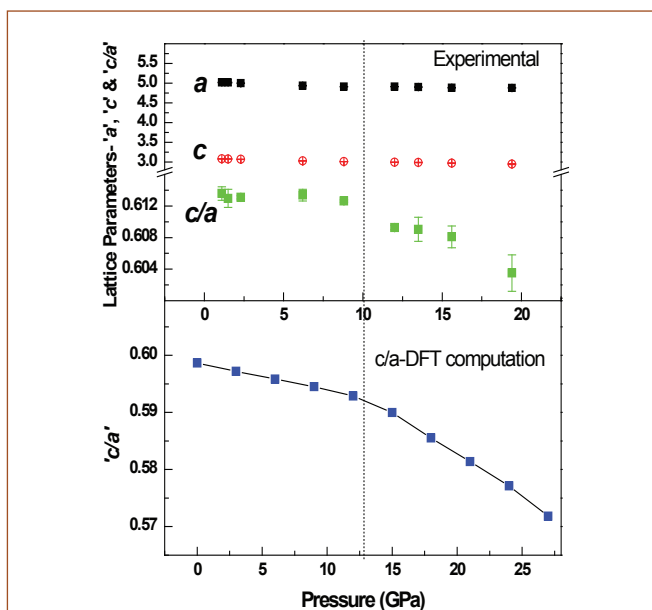


Fig. 1 Variation of a , c and c/a variation with pressure, the bottom curve shows computed c/a ratio

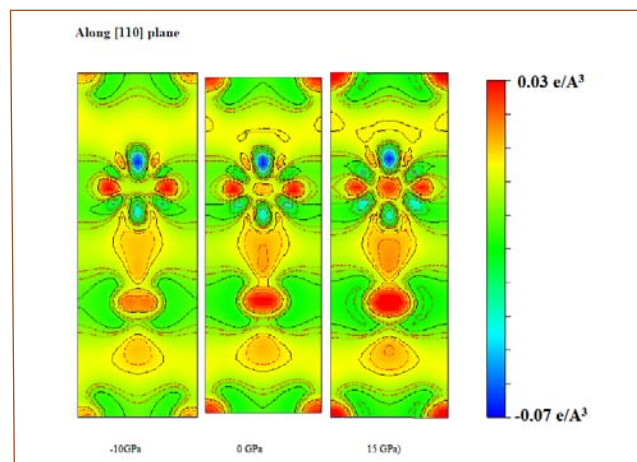


Fig. 2 Difference Charge density along (110) plane (linear scale)

Variations in the rate of change in c/a with pressure can be understood from the bonding nature between the U & Zr atoms at (1/3, 2/3, 1/2) and (2/3, 1/3, 1/2) positions. Difference charge density calculated along (110) plane (Figure 2) indicates metallic bonding between corner Zr-Zr bonds and partial covalent bonding between U(1/3,2/3,1/2)-Zr(2/3,1/3,1/2). At higher pressures, the charge concentration increases between U-Zr atoms indicating the strengthening of partial U-Zr covalent bond which leads to resistance in compression along 'a' axis at higher pressures. These changes in lattice parameter 'a', reflects in the c/a ratio. Thus U-Zr bond along the a-axis dictates the high pressure behavior of the compound. DFT computation also reveals the localization of charge density across the lattice which may lead to a drop in the metallization of the material.

In-situ HP-HT XRD studies were also carried out using a novel custom-designed combination of membrane Diamond Anvil Cell coupled to a high flux micro-focus X-ray machine. The study shows that the compounds remains stable in δ phase up to 6 GPa and 673 K. The fitting of the pressure-volume data at high temperature results in the bulk moduli of the materials to be 104.8 GPa and 101.6 GPa at 373 K and 473 K, respectively. A drop in the bulk modulus, observed at high temperature, signifies softening of the material. Apart from the compressibility study, thermal expansion behavior of the material has also been studied. The thermal expansion coefficients have been estimated as a function of pressure and found to be $4.6 \times 10^{-5} \text{ K}^{-1}$, $3.7 \times 10^{-5} \text{ K}^{-1}$, $2.7 \times 10^{-5} \text{ K}^{-1}$ at 1.2 GPa, 4.8 GPa and 6.6 GPa, respectively, in the temperature range 300 K - 473 K. A decrease in the thermal expansion coefficient as a function of pressure is expected because applied pressure places constraints for the thermal expansion of the lattice.

V.21 Actinide-Phosphonate Complexation: Experimental and Theoretical Approach

Organophosphorous extractants show high complexation abilities towards actinide elements and shows selectivity for the actinides during their separation from a mixture of elements e.g. dissolver solution of a spent nuclear fuel. The extraction ability of organophosphorus extractants depends on the basicity of the phosphoryl oxygen and follows the order: phosphine oxides [$R_3P=O$] > phosphinates [$R_2(RO)P=O$] > phosphonates [$R(RO)_2P=O$] > phosphates [$(RO)_3P=O$]. Phosphonates show higher extraction of actinides than phosphates. However, phosphonates do not complex actinides too strongly (as is the case of phosphinates and phosphine oxides) hence enabling the recovery of actinides from the complex. H-phosphonates in particular shows interesting extraction ability as it extracts metal ions via two different extraction modes. To study this behavior Diamyl-H-phosphonate (DAHP), Di-sec-amyl-H-phosphonate (DsAHP) and Diisooamyl-H-Phosphonate (Figure 1) were synthesised, characterised and evaluated for their physico-chemical properties of viscosity, density and aqueous solubility. Solvent extraction behaviour of these extractants were studied as a function of nitric acid concentration (0.01-8M) with uranyl nitrate. The extraction behaviour shows cation-exchange mechanism via an enol tautomer at low acidities of less than 1 M and through a solvation

mechanism at higher acidities (Figure 2). To understand this behaviour theoretical investigations were carried out on the structures and complexation abilities of DAHP, DsAHP and DiAHP with uranyl nitrate through DFT calculations. ORCA 3.0.3 electronic structure program was used to optimize the geometries and compute the binding free energies. The geometries were optimized within the framework of DFT by employing the BP86 functional in conjunction with the all electron def2-SV(P) basis set. Optimizations have been carried out by incorporating dispersion correction (DFT-D3BJ). All the geometries have been verified as minima by computing their harmonic vibration frequencies using the NUMFREQ module. The theoretical calculations predicted an unexpectedly higher stability for the uranyl-DsAHP complex compared to the compositionally analogous uranyl-DAHP complex. The interactions leading to the stabilisation of the uranyl complex with the branched isomer have been observed. The $UO_2(NO_3)_2 \cdot 2DsAHP$ complex is more stable as compared to both $UO_2(NO_3)_2 \cdot 2DAHP$ and $UO_2(NO_3)_2 \cdot 2DiAHP$ complexes, which is due to the presence of shorter $CH \cdots O$ hydrogen bonds in the $UO_2(NO_3)_2 \cdot 2DsAHP$ complex. Among other factors, relative strength of the weak H bonding dictates the relative stability of these complexes.

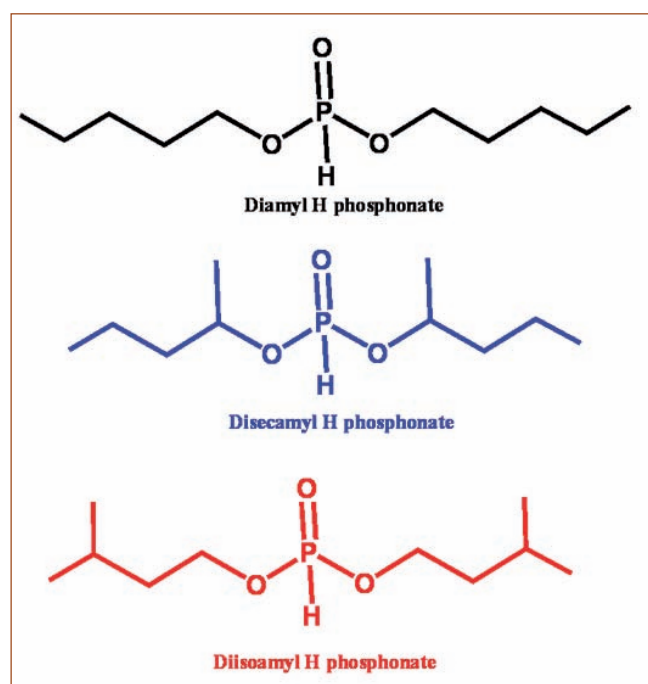


Fig. 1 Structures of the H-phosphonates

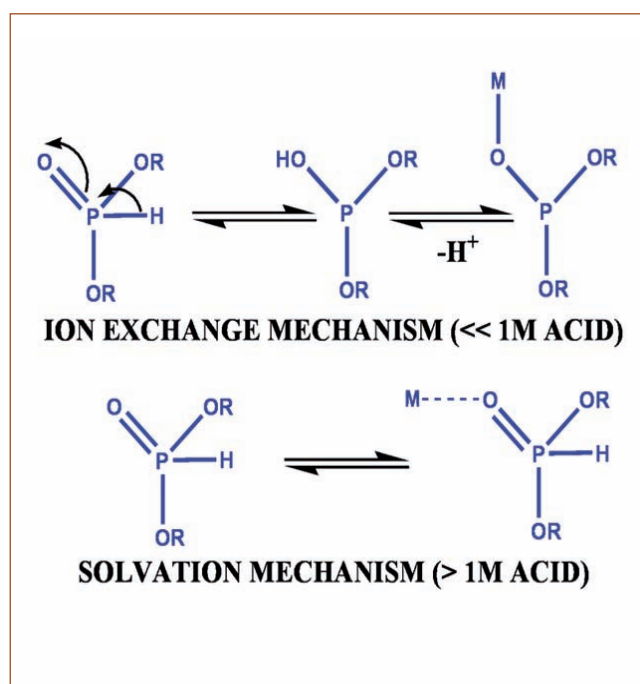


Fig. 2 Ion-exchange and solvation mechanism of H-phosphonates extracting metal ions in different pH

V.22 Solubility of Ligands in Supercritical Carbon Dioxide Medium and its Application to Extraction of Metal Ions

In recent years, supercritical carbon dioxide (SCCO₂) has attracted attention as a green solvent, allowing the replacement of toxic organic solvents in various chemical processes. Supercritical fluid extraction (SFE) (uses SCCO₂ as a solvent) offers several advantages over conventional extraction techniques. SFE based methods have higher mass transfer rate and provide solvent-free products and reduction/elimination of liquid waste generation. The development of an SFE method for the recovery of metal ions involves: (a) identification of specific ligands based on nature of matrix; (b) measurement of solubility of ligands of interest in SCCO₂ medium and optimization of experimental conditions; (c) use of SCCO₂ containing ligand for recovery of metal ions from different matrices. Therefore, measurement of solubility of ligands in SCCO₂ media is the foremost step in designing a SFE process.

The solubilities of various ligands such as trialkyl phosphates, dialkylalkyl phosphonates, H-phosphonates, N,N-dialkylamides and quarternary ammonium based ionic liquids in SCCO₂ medium were measured as a function of temperature and pressure; the same was successfully applied for the development of SFE methods for the recovery of actinides from different matrices. Recently, solubility of 2,6-pyridinedicarboxylic acid (PDCA) in SCCO₂ medium was determined to assess its ability to extract/recover heavy metals from different matrices. The solubility measurements were carried out at 313-333 K with pressure ranging from 10-20 MPa using a dynamic flow method (Figure 1). The solubility of PDCA in SCCO₂ medium was found to be low, ranged from 1.3×10^{-6} to 1.1×10^{-5} mole/mole in the investigated region. To enhance the solubility, alcohol was used as a co-solvent and the solubility behavior was studied in

SCCO₂ + methanol medium (1, 4 and 10 mol% methanol) at 313 & 323 K with pressure varying from 10-20 MPa. The highest solubility of PDCA in SCCO₂ + methanol mixture is 2.5×10^{-4} mole/mole at 313 K and 20 MPa with a methanol composition of 10 mol%. The study indicated that higher solubilities can be achieved by fine-tuning the composition of SCCO₂ + methanol phase. The solubility of PDCA increases with the pressure and retrograde solubility is observed with the temperature, where the solubility decreases with temperature.

As experimental determination of solubility of PDCA is a tedious and time-consuming process, experimental solubility data were modeled for better understanding SFE process and prediction of the solubility at different temperatures and pressures with minimum experimental work. The solubility of PDCA in neat SCCO₂ was correlated using different semi-empirical equation such as Chrastil, Mendez-Teja and Bartle models. The solubility of PDCA in SCCO₂ + methanol phase was correlated using different semi-empirical/empirical models.

Subsequently, SCCO₂ containing PDCA was employed for extraction of heavy metals (Pb(II), Cd(II) and Ni(II)) from aqueous medium and sand matrix. SCCO₂ + methanol (10 mol%) + PDCA mixture was continuously allowed to pass through the matrix containing heavy metals. The extracted heavy metals were collected and the quantification of heavy metal ions was carried out using high-pressure liquid chromatography and ion chromatography. These experiments resulted in an extraction efficiency of 80% for all heavy metals. These studies have indicated that, PDCA can be employed as a ligand for the recovery of heavy metal ions from different environments with minimum generation of liquid waste. Future endeavor includes the extraction of actinides from different matrices.

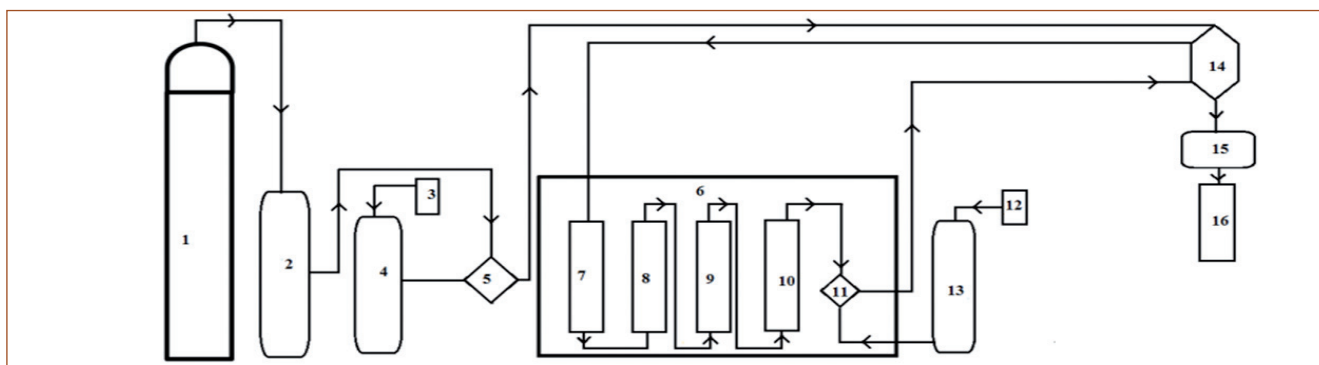


Fig. 1 Schematic of dynamic flow apparatus for solubility measurements. (1) CO₂ cylinder; (2) CO₂ pump; (3) methanol reservoir; (4) methanol pump; (5) T-joint; (6) oven; (7) heat-exchanger (8), (9) & (10) high pressure equilibrium cells; (11) T-joint; (12) methanol reservoir; (13) methanol pump for washing; (14) six-way valve; (15) back pressure regulator; (16) collection vessel

V.23 Development of an Iodine Trap using Ag Modified Zeolite-13X

Release of gaseous radionuclide, especially Iodine, is of a great concern during nuclear accidents from the health point of view. At present, activated charcoal is used in nuclear reactors to trap the radioactive iodine. Present work describes studies on the development of iodine trap using chemically modified Zeolite-13X.

Method of preparation of Ag-modified zeolite with a higher Ag content i.e. ~ 25% was standardized for trapping iodine with a higher capacity. The optimization of the procedure involved three steps, i.e. 1) Equilibration of the Zeolite with 100 mg/mL silver nitrate solution 2) Washing it with water to get Ag substituted zeolite-13X and 3) Soaking of Ag-substituted zeolite-13X in 500 mg/mL of silver nitrate solution to get Ag nitrate loaded zeolite-13X. The Ag nitrate loaded zeolite was heated to 400° C in flowing argon to decompose the silver nitrate to metallic silver. After heating, it was treated with ascorbic acid to get Ag modified zeolite-13X for iodine trap studies. The reduction of silver nitrate to metallic silver was confirmed by the XRD analysis. Ag-modified zeolite-13X could not be dissolved completely by open acid digestion. Therefore, microwave dissolution procedure using the mixture of HF, HNO₃, boric acid and hydrogen peroxide was established to dissolve the Ag modified zeolite. The concentration of the resultant Ag was found to be around 23%.

The experimental setup of I₂ trap is shown in Figure 1. Iodine granules were taken in a glass bubbler and zeolite was taken in the glass tube, fitted into a heater assembly (Figure 2) and heated at 150°C. Argon gas at a flow rate of 60 mL/min was introduced into the bubbler for carrying iodine and the outlet of the modified tube was bubbled through 0.01M NaOH solution to collect the iodine as iodide. Peristaltic pump was provided to remove the sodium hydroxide solution from the bubbler for analysis.

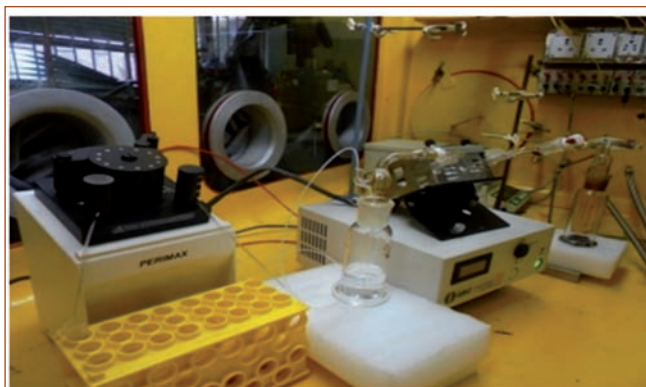


Fig. 1 Experimental set-up of I₂ trap



Fig. 2 Modified tube with Zeolite

The iodide in NaOH solution was determined by ICP-OES with appropriate dilution. The same peristaltic pump was also used for pumping the equal volume of fresh 0.01M NaOH solution to the bubbler solution so as to maintain the same volume of sodium hydroxide solution for collecting the un-trapped iodine

Efficiency of iodine capture was calculated by using the following formula i.e.

$$\text{Efficiency(\%)} = [(I_{2(WO)} - I_{2(W)}) / I_{2(WO)}] * 100$$

Where, I_{2(WO)} = I₂ collected in NaOH without Zeolite & I_{2(W)} = I₂ collected in NaOH with zeolite

Iodine trap capacity was calculated by passing known concentration of I₂ in argon through 1g of Ag modified zeolite in the iodine trap setup i.e. Glass "V" tube (Figure 3) and calculating the time, to reach the saturation limit of I₂ in zeolite. Trap capacity of Ag loaded zeolite for iodine was calculated from starting time until saturation in the solution. In the present work, efficiency study was carried out for 20 g of Ag modified zeolite with the simple modification in loading tube (Figure 2) and was found to be ~100%. Iodine Trap capacity of the Ag modified zeolite having 23% Ag was found to be around 280 mg/g which is in good agreement to the literature value of 280-330 mg/g.



Fig. 3 Glass "V" Tube for capacity study

V.24 Investigation of $\text{Th}^{4+}|\text{Th}$ Redox Couple at Tungsten and Cadmium Electrodes in LiCl-KCl Eutectic Melt using Impedance Spectroscopy

Electrochemistry of thorium in molten salts has been studied using various electrochemical transient techniques such as cyclic voltammetry, chronopotentiometry, square-wave voltammetry etc. in LiCl-KCl eutectic melt. Electrochemical properties such as number of electrons exchanged during reduction (n), charge transfer coefficient (α), diffusion coefficient (D), and standard electrode potential (E°) of $\text{Th}^{4+}|\text{Th}$ couple were estimated. Cyclic voltammogram of $\text{Th}^{4+}|\text{Th}$ couple recorded at inert W electrode is shown in Figure 1.

Electrochemical impedance spectroscopy (EIS) study also was employed to study the redox behaviour of thorium at different working electrodes such as inert W, liquid Cd and Th in LiCl-KCl eutectic melt.

Complex impedance spectra were recorded in the temperature range 698-798 K at specific applied potentials at inert tungsten, liquid cadmium and metallic thorium electrodes using a perturbation amplitude of 10 mV in the frequency range 10 Hz-10 kHz. Complex impedance data were also validated by Kramers-Kronig transforms. Recorded complex impedance spectra were then analysed by equivalent circuit as shown in Figure 2. Impedance data recorded at inert W electrode is shown in the form of Nyquist plot shown in Figure 3a, where a flattened semi-circle is observed at higher frequency region that suggests a very fast charge transfer process and a linear region at lower frequency region attributed to diffusional impedance. Nyquist plot for reduction of Th^{4+} at liquid Cd electrode in Figure 3b shows similar behaviour as observed at inert W electrode. Nyquist plots recorded for anodic dissolution of Th are characterized by a very prominent semicircle at higher frequencies and a comparatively smaller linear region at lower

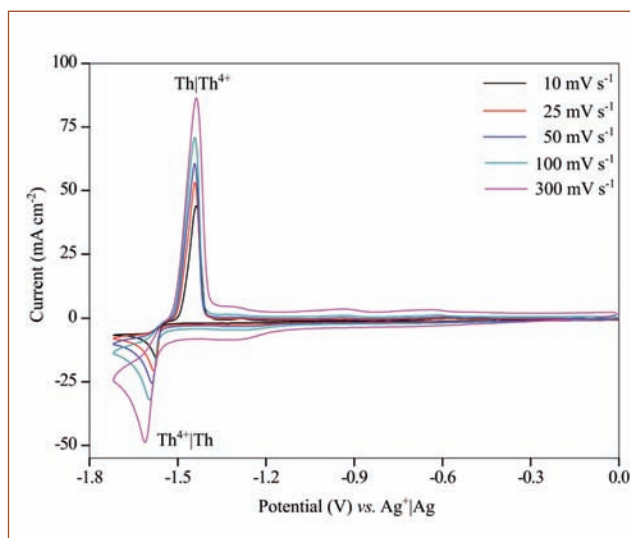


Fig. 1 Cyclic voltammogram of LiCl-KC-ThCl₄ electrolyte recorded at inert W electrode at 773 K

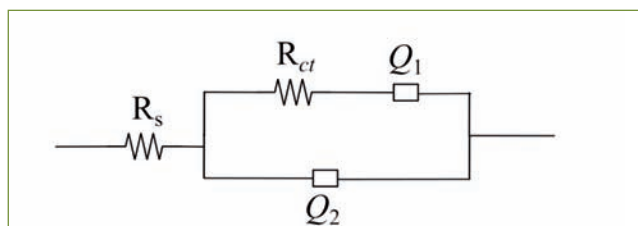


Fig. 2 Equivalent circuit used for fitting complex impedance recorded at inert W, liq. Cd and Th electrodes

frequencies as shown in Figure 3c.

Heterogeneous rate constant k_s was estimated for cathodic and anodic reactions and temperature dependence of k_s was studied. $\text{Th}^{4+}|\text{Th}$ couple was found to be quasi-reversible using Matsuda-Ayabe criteria.

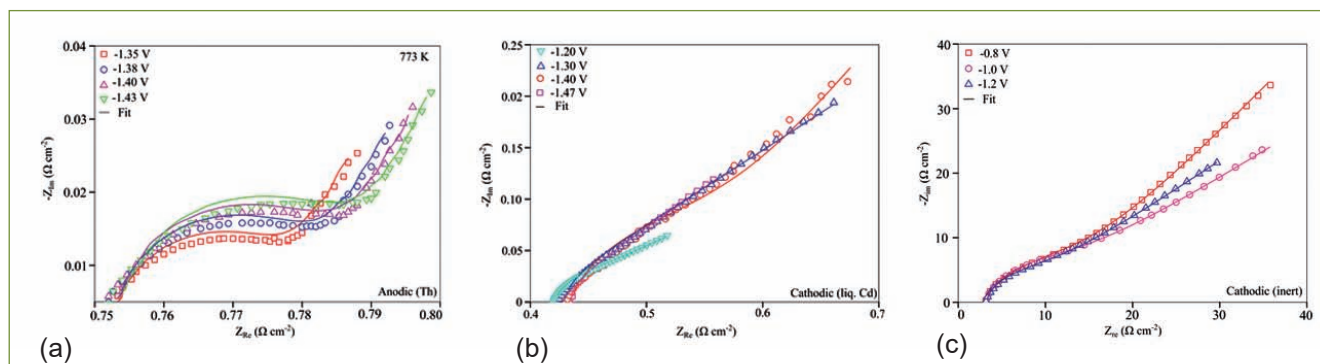


Fig. 3 Nyquist plots of ThCl_4 at (a) inert W, (b) liquid Cd and (c) Th electrodes in LiCl-KCl eutectic. Concentration of ThCl_4 : $1.02 \times 10^{-4} \text{ mol cm}^{-3}$, $T=773 \text{ K}$

V.25 Knudsen Effusion Mass Spectrometric Studies on U-Al System: Thermodynamic Properties over (UAl₂+UAl₃) Biphasic Region

Thermodynamic properties of U-Al alloys are of interest in nuclear technology since these alloys are used as fuel in research reactors. The samples with compositions 28 and 30 at.% U and pertaining to the two-phase region (UAl₂+UAl₃) were used for the vaporisation experiments. These alloy samples were prepared by arc melting. The as-prepared samples were wrapped in cleaned tantalum sheets and sealed under vacuum in quartz tube at a residual pressure of 10⁻⁵ Torr under an atmosphere of argon. The samples were heated, initially at 950K for 50 h and then at 1100K for two weeks. The annealed samples were stored inside an argon atmosphere glove box in which the oxygen and moisture levels were maintained at values less than 10 ppm.

Vaporisation studies on these samples were carried out by using an indigenously built Knudsen effusion mass spectrometer. The samples were contained in Knudsen cell made of zirconia with a lid at the top with a knife edged orifice of 0.5 mm diameter and this was placed inside a tantalum outer cup and lid. The samples were heated by electron bombardment furnace. The temperature of the sample was measured by using a chromel-alumel thermocouple inserted through the bottom of the outer tantalum cup. The vapour effusing out of the cell were ionised by electron impact ionisation. The ions produced were mass analysed by a quadrupole mass filter and detected by a secondary electron multiplier operating in pulse counting mode.

Knudsen effusion mass spectrometric studies over (UAl₂+UAl₃) biphasic region were carried out in the

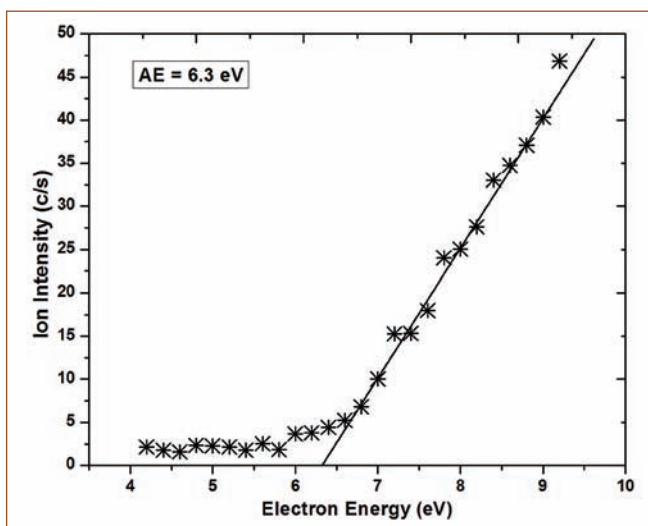


Fig. 1 Typical ionisation efficiency curve for ²⁷Al⁺ over (UAl₂+UAl₃) biphasic region

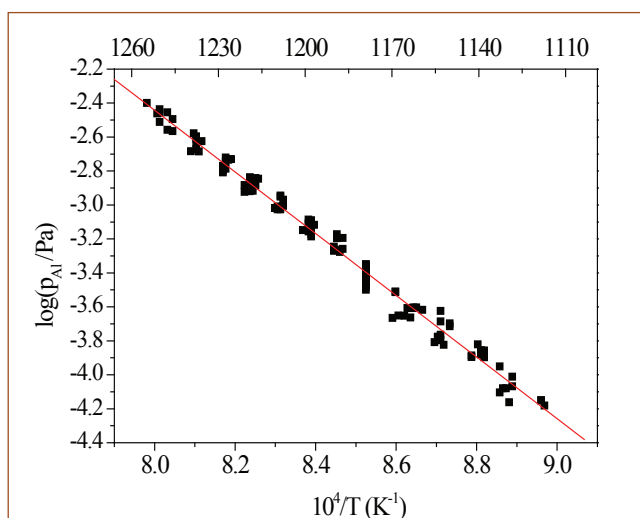


Fig. 2 Combined plot of $\log(p_{Al(g)}/Pa)$ Vs $1/T (K^{-1})$ over UAl₂(s) + UAl₃(s) biphasic mixture

temperature range of 1115–1253 K. The vaporisation reaction was found to be incongruent and Al(g) was the neutral species (Figure 1) in the vapour in equilibrium with the condensed phase. The temperature dependence of the partial pressure was derived (Figure 2) as $\log(p_{Al}/Pa) = (-18215 \pm 157)/T + (12.12 \pm 0.13)$. From the values of the partial pressures, the enthalpy of the reaction UAl₃(s) = UAl₂(s) + Al(g) at 298.15 K was deduced by applying the second and third law methods. The enthalpy (Table 1) and Gibbs energy of formation of UAl₃ were derived from the above data and were found to be $\Delta_f H^\circ_{298.15} = -112.1 \pm 12.8 \text{ kJ mol}^{-1}$ and $\Delta_f G^\circ_T (\pm 3.4) = -158.8 + 0.0591 T \text{ (kJ mol}^{-1})$. Vaporisation study on this system had been carried out for the first time.

Table 1: Comparison of the enthalpies of formation (kJ mol ⁻¹)			
Compound	$\Delta_f H^\circ_{298.15}$	Method	Reference
UAl ₃ w.r.t α -U and solid Al	-112.1 ± 12.8	KEMS	Present study
	-108.4 ± 8.4	Solution and adiabatic calorimetry	Chiotti and Kateley
	-105.4 ± 9.2	Solution and adiabatic calorimetry	Ivanov et al.
	-117.6	Estimation	Kassner et al.
	-118.1 ± 8.2	High temperature calorimeter	Nagarajan et al.
	-104.6	Compilation	Barin

V.26 TDEM Sounding Measurements in the Field with SQUID based TDEM System

Electromagnetic techniques are widely used in geophysical exploration applications and the response of these techniques is directly related to the surface and sub-surface properties of the earth, in particular electrical resistivity. The popular and widely used technique is a Time Domain Electro-Magnetic (TDEM) technique, in which the magnetic field in the form of transients is applied to the ground to induce eddy currents. In response, the decay of the eddy currents and its associated secondary magnetic field is sensed by the suitable sensor. Since the transient consists of a continuum of frequencies, it is easier to detect conductive targets both at surface as well as at greater depth with a single transient excitation. Conventionally, air core induction coils whose output voltage is proportional to the rate of change of magnetic field ($V \propto \partial B / \partial t$) are used to sense the decay of the secondary magnetic field for TDEM measurements. The other one which entered into this field in recent years and directly measures the magnetic field ($V \propto B$) is the SQUID. As part of the SQUID's system development program, a SQUID based TDEM system for geophysical applications has been developed and tested at laboratory level. The SQUID based TDEM system comprises of a transmitter to drive a current in the form of trapezoidal pulses through the transmitter loop with the help of external batteries, transmitter controller to set and control the waveform parameters in the transmitter, transmitter loop (size and shape as desired by the user) and fast data acquisition system to record the response of the SQUID.

After the tests at laboratory level, the system has been used in the field for the TDEM central loop sounding measurements at Tumullapalle, Kadapa (dt.), Andhra



Fig. 1 Photograph of the experimental site along with the coordinates of the 400 m x 400 m transmitter loop and the experimental setup.

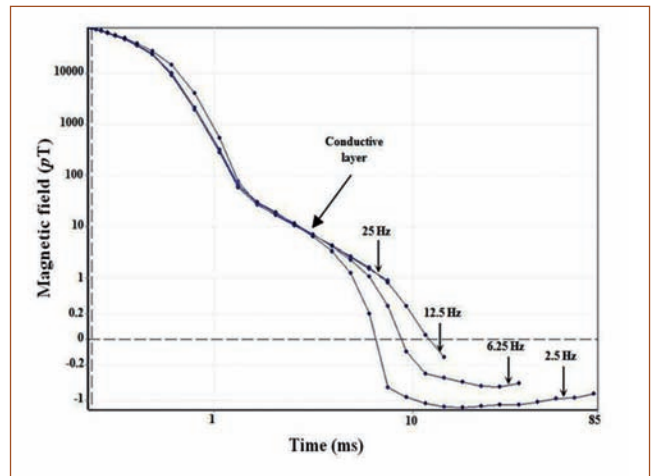


Fig. 2 The decay of the secondary magnetic field recorded by the SQUID with different base frequencies for the 400 m x 400 m transmitter loop with applied current of 27 A

Pradesh. This place was chosen based on prior information regarding the lithological structure of the region. In this region, the upper layer consists of a thick (250 - 300 m) highly resistive subsurface layer of dolostone / limestone followed by a thin (20-25 m) conductive layer of shale. Below the shale, a resistive layer of uraniferous dolostone is known to be present. In this work, current of 27 A in the form of trapezoidal pulses with base frequency of 2.5 Hz has been passed through a transmitter loop with size of 400 m x 400 m. The central loop soundings were also performed with different base frequencies of 6.25 Hz, 12.5 Hz and 25 Hz. Here, the cryostat containing the SQUID probe has been partially buried in the ground in order to arrest the wind generated mechanical vibrations. The photograph of the experimental site along with the coordinates of the 400 m square transmitter loop and the experimental setup has been shown in Figure 1. The decay of the secondary magnetic field recorded by the SQUID sensor with different base frequencies for the transmitter loop size of 400 m x 400 m is shown in Figure 2. Figure 2 shows the upper weathered zone followed by a highly resistive layer (dolostone) visible at early times. Further, the decay slows down showing the presence of conductive layer (shale) followed by another resistive layer. The central loop sounding measurements have also been carried out with an induction coil sensor as receiver in the same location for comparison. The use of SQUID as a receiver in TDEM central loop sounding measurements shows better depth resolution of the conducting target as compared to the conventional induction coil as a receiver.

V.27 Standardization of Protocol for Carbon-14 Measurements through Bubbler Mechanism in Air Samples

Carbon-14 is a pure beta emitter ($E_{\max} = 156 \text{ keV}$) with a half-life of 5730 years. ^{14}C is formed naturally by cosmic neutron interaction with atmospheric nitrogen $^{14}\text{N} (n, p)^{14}\text{C}$. In nuclear reactors, ^{14}C is produced in the fuel, core structural materials and in the moderator by neutron reactions with oxygen, nitrogen and Carbon. Measurement of the ^{14}C in the atmospheric air is carried out by sampling different forms of carbon. Sampling of the air can be carried out either by active or by passive methods. In the active air sampling technique, atmospheric air is pulled through a pump and passed through a trap but in passive air sampling it does not require the pump, sample can be collected by exposing the sample absorbers to air. In this study, sampling of CO_2 in the atmospheric air was carried out by using 2N NaOH solution by active sampling method, absorption capacity of CO_2 in 2N NaOH solution, recovery of CO_2 and then the measurement of ^{14}C from the recovered CO_2 by liquid scintillation counter using CO_2 absorption method are discussed.

Experimental set-up for sampling of atmospheric air is as shown in the Figure 1. The system contains a pump (12 V DC), flow controller, and two bubblers containing the 200 ml of 2N NaOH solutions. Atmospheric air is pulled through bubblers at the flow rate of 400 ml/min for 8 days. After completion of sampling, the carbon absorbed in the solution is precipitated as barium



Fig. 1 Experimental set up for active sampling

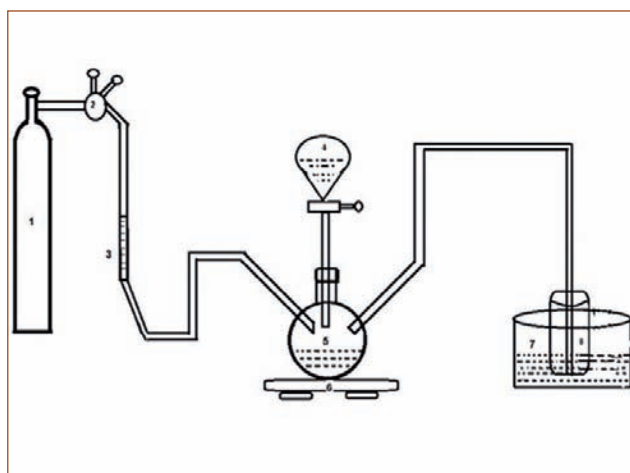


Fig. 2 Experimental set-up for CO_2 absorption method

carbonate by addition of barium chloride and then used in the CO_2 absorption method as shown in Figure 2 for ^{14}C measurements.

The sampling period is designed based on the typical concentrations of CO_2 in the atmosphere air and minimum amount of carbon required for LSC measurements to meet the detection limits of ^{14}C activities. The average global atmosphere air concentrations of CO_2 is 400 ppmv, sampling of air is carried at the rate of 0.4 LPM and minimum amount of CO_2 required for saturation of 10:10 mL absorption mixture (CS/PE) in CO_2 absorption method is 2.35 g of CO_2 . From these parameters, the minimum number of days required for sampling is calculated as per Equation 1 and it was found that a minimum of 5.03 days sampling is required. But in the CO_2 absorption method all the CO_2 released may not get absorbed in the absorption mixture, so sampling period was fixed as 8 days where an average 3.68 g of CO_2 is sampled.

$$\text{Sampling time (days)} = A / (B \cdot C \cdot D \cdot 1440) \quad [1]$$

A= amount of CO_2 required (2.35 g)

B= Density of CO_2 (2 g/L)

C=Flow rate= 0.4 LPM

D= Concentration of CO_2 in the air (400 ppmv)

Measurement of amount of Carbon absorbed

Atmospheric air is sampled at five different times. Amount of CO_2 absorbed in the 2N NaOH solutions is measured using Total inorganic carbon (TIC) analyzer and the

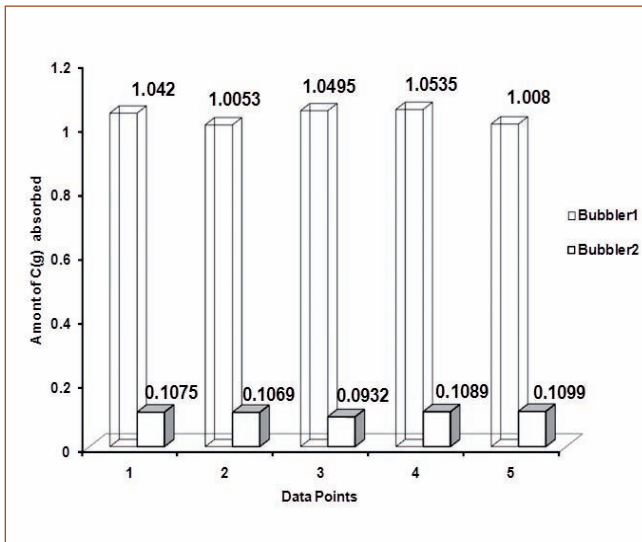


Fig. 3 Variation of absorption capacities of two bubblers

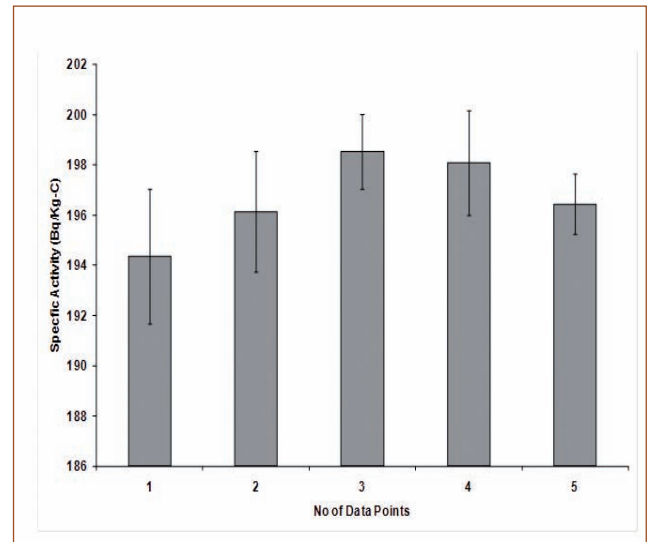


Fig. 4 Variation of measured ¹⁴C specific activities in air

measured carbon levels are given in the Table 1. An average of 1.13±0.02 g of carbon is absorbed in both the bubblers. Comparison of absorption amounts in two bubblers is shown in Figure 3 and it is found that 90.74% of the total is trapped in first bubbler and the remaining 9.26% is absorbed in the second bubbler.

The absorbed CO₂ in the NaOH solution is recovered as barium carbonate by addition of barium chloride. Percentage of Recovery is calculated as per Equation 3 are given in Table 2. It is found that an average recovery percentage is of 97%.

Theoretical or expected weight is estimated as follows

$$\frac{\text{amount of carbon absorbed (g)} * \text{mlo. weight of CO}(= 44\text{g})}{\text{Mocelular weight of Carbon}(= 12\text{g})} \quad [2]$$

$$\text{Recovery} = \frac{\text{weightt of Final precipitate}}{\text{Expected Weight}} \quad [3]$$

The precipitated barium carbonate is re-dissolved by using hydrochloric acid (HCl) solution to generate ¹⁴CO₂. The released ¹⁴CO₂ is absorbed into 10 ml

each of Carbo-Sorb (CS) and Permaflour (PE) mixture and then measured for ¹⁴C activity using the liquid scintillation counter for 200 minutes. The variation in the measured specific activities of ¹⁴C is shown in Figure 4 and the average measured ¹⁴C specific activity value is 197.01±3.15 Bq/kg-C. The activity concentrations of the ¹⁴C (Bq/ m³) in air is estimated using the Equation 4 are given in Table 1 and it was found that an average ¹⁴C concentration is 45.23±21 Bq/m³

$$C_s = A_s * C \quad [4]$$

Where A is the specific activity in the air (Bq/m³),

C is the total concentration in the sampled air (g (C)/ m³).

An indigenous sampling Set is made and used for the sampling of ¹⁴C in the air. An average of 1.13±0.02 g of carbon is absorbed in both the bubblers for the 8 days sampling period. Recovery of CO₂ as barium carbonate is found to be 97%. The measured average ¹⁴C specific activity value is 197.01±3.15 Bq/kg-C, and the corresponding concentration of ¹⁴C (Bq/m³) in air is found to be 45.23±21 Bq/m³.

S. No	Collected Volume (L)	Mass of carbon absorbed (g)	Activity Concentration (Bq/m ³)
1	4608	1.149	47.50±1.72
2	4608	1.112	45.47±1.87
3	4608	1.142	46.50±1.79
4	4608	1.162	46.14±1.85
5	4608	1.117	45.65±1.67

S. No	Mass of Barium Carbonate (g)		Recovery
	Theoretical	Actual	
1	19.16	18.63	97.2
2	18.54	18.04	97.3
3	19.05	18.46	96.9
4	19.37	18.88	97.5
5	18.63	17.81	95.5

V.28 Enhancement in Field Induced Heating Efficiency under in-situ Orientation of Superparamagnetic Iron Oxide Nanoparticles in Dispersion

In recent times, magnetic fluid hyperthermia (MFH) using superparamagnetic (SPM) Fe_3O_4 nanoparticles (MNP) have attracted widespread research interests due to its applications in cancer therapy owing to the bio-compatibility of Fe_3O_4 and possibility of field induced distal guidance. When subjected to a radiofrequency alternating magnetic field (RFAMF), SPM MNPs undergo Neel-Brown relaxation, where magneto-thermal conversion of energy occurs during randomization of magnetic moments on field withdrawal and whole scale rotation of the MNPs, respectively. This leads to an increase in fluid/tissue temperature, thereby rendering therapeutic benefits. However, an increased medium viscosity in tissue-like environment leads to the abrogation of Brownian relaxation, that reduces the heating efficiency (expressed in terms of specific absorption rate: SAR), which is undesirable for practical applications. Strict guidelines on allowable values of RFAMF amplitude and frequency makes enhancing SAR non-trivial, under such a scenario. With this objective, $\sim 62\%$ enhancement in SAR is demonstrated for an aqueous ferrofluid containing SPM MNPs, upon *in situ* orientation under a static bias field (H_{DC}), applied parallel to the RFAMF. Further, dynamic hysteresis loop simulations were performed, under SPM conditions to verify the experimental results.

Experiments were performed on phosphate coated SPM Fe_3O_4 MNPs of average size $\sim 7.9 \pm 0.6$ nm (Figure 1a). The zeta potential, saturation magnetization, blocking temperature and effective anisotropy energy density were ~ -31 mV, 52 emu/g, 86 K and 124.15 kJ/m³, respectively. MFH studies were carried out on ferrofluids with varying sample concentrations (3-6 wt. %), at a fixed frequency of 126 kHz and under varying

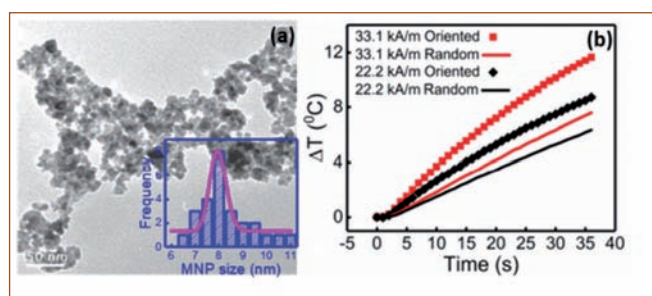


Fig. 1 (a) Transmission electron microscopy image of the SPM MNPs. (Inset) Size distribution. (b) Temperature rise curves for the random and oriented ferrofluids for two different RFAMF amplitudes

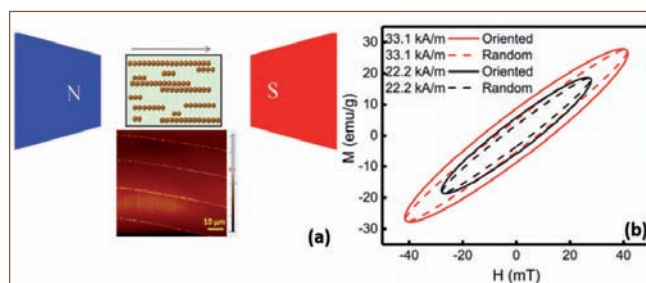


Fig. 2 (a) Schematic of HDC induced chain formation along with the atomic force microscopy images showing the chains. (b) Simulated dynamic hysteresis loops for the oriented and random SPM MNPs for two different RFAMF amplitudes

RFAMF amplitudes ($H_{\text{max}} \sim 33.1$ kAm⁻¹). Figure 1b shows the typical temperature rise curves ($\Delta T = T - 28$ °C) for the random and oriented ferrofluids with MNP concentration of 6 wt. %, during field induced heating under two different RFAMF amplitudes. It can be seen from Figure 1b that H_{DC} induced orientational ordering resulted in higher rates of temperature rise, which was attributed to the enhancement of effective anisotropy energy density along the chain axis.

Under the influence of an external DC bias field, the dispersed MNPs undergo a disorder-to-order transition and form linear chain-like structures due to head-on aggregation along the direction of H_{DC} (schematically shown in Figure 2a). Formation of such linear chain-like structures was experimentally confirmed from atomic force microscopy studies (Figure 2a). Such linear arrangement resulted in an enhancement in effective anisotropy energy density due to nearest neighbour interactions, which was theoretically estimated using flexible chain model. Further, the heating efficiency for the oriented and random samples was estimated from the dynamic hysteresis loop simulations. Figure 2b shows the simulated dynamic hysteresis loops for the random and oriented samples under two different RFAMF amplitudes, where it was observed that the loop areas (heating efficiency proportional to loop area) were higher for the oriented samples. Experimental results indicated $\sim 62\%$ enhancement in SAR, which was found to be in agreement with the theoretical values. The observed SAR enhancement offers possibilities of reducing the exposure time during therapy and provides further impetus towards the realization of MFH as an effective therapeutic procedure.

V.29 FISH Translocation Dose Response Curve for Γ -Rays and Determination of Role of NHEJ Pathway Factors in Translocation Formation using NU1025/NU7026 Inhibitors

In biodosimetry, FISH (Fluorescent In-Situ Hybridization) - translocation assay is the method of choice for retrospective dose estimation of past radiation exposures and for post exposure follow-up studies due to relatively higher stability of translocations compared to other aberration types such as dicentric¹. To have retrospective biodosimetry capability it is essential for a biodosimetry lab to establish its own FISH-translocation dose response curve for the radiation quality of interest. In this regard a FISH-translocation dose response curve for Cs-137 γ -rays (0.1Gy/min dose rate) was established in biodosimetry facility by irradiating peripheral blood samples obtained from a consented male volunteer. Blood samples exposed to 9 different doses (0.1, 0.25, 0.5, 0.75, 1, 2, 3, 4 & 5Gy) were subjected to standard FISH-Translocation assay using 3 color FISH painting probes (XCP Probe Mix, Metasystem) for 3 different Chromosomes viz. #1 (red), #2 (green) and #4 (red and green) (Figure 1).

Based on the translocation aberration frequencies scored from the blood samples FISH-translocation dose response curve was constructed using CABAS software and the equation obtained was $Y = 0.096D^2 \pm (0.009) + 0.025D \pm (0.019) + 0.005 \pm (0.004)$ where Y – translocation /cell and D- Dose in Gy (Figure 2). Thus the retrospective biodosimetry capability has been established in IGCAR for personnel monitoring and follow up studies.

Normally radiation induced chromosomal translocations are formed due to improper repair of DNA double strand breaks (DSB) caused by radiation exposure of cell.

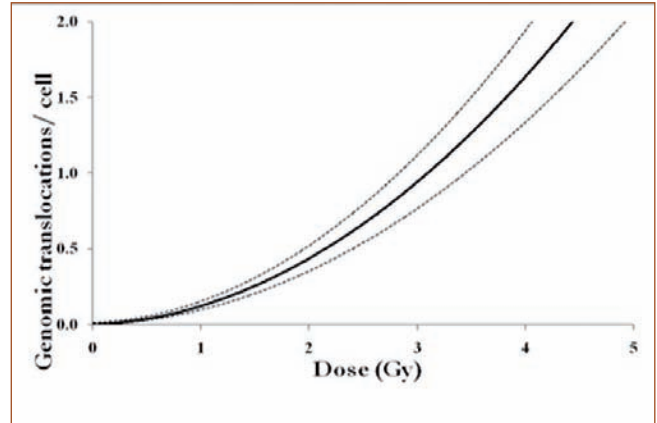


Fig. 2 Dose response curve of translocation frequency irradiated with ^{137}Cs (0.1Gy/min) γ rays

Basically two major repair pathways are involved in this repair process i.e. HR (Homologous Recombination) and NHEJ (Non-Homologous End Joining) pathways.

Although translocations are the most common contributors for their role in malignancies, the exact molecular mechanism is still not known completely. Ku70- Ku80 complex of cNHEJ pathway (Non-Homologous End Joining) compete with Poly [ADP-Ribose] Polymerase 1 (PARP1) of aNHEJ pathway for attachment at the break site.

Objectives

1. To construct a dose response curve for chromosomal translocation induced by ^{137}Cs γ rays for retrospective biodosimetry application
2. To understand the molecular mechanism of chromosomal translocation on exposure to gamma

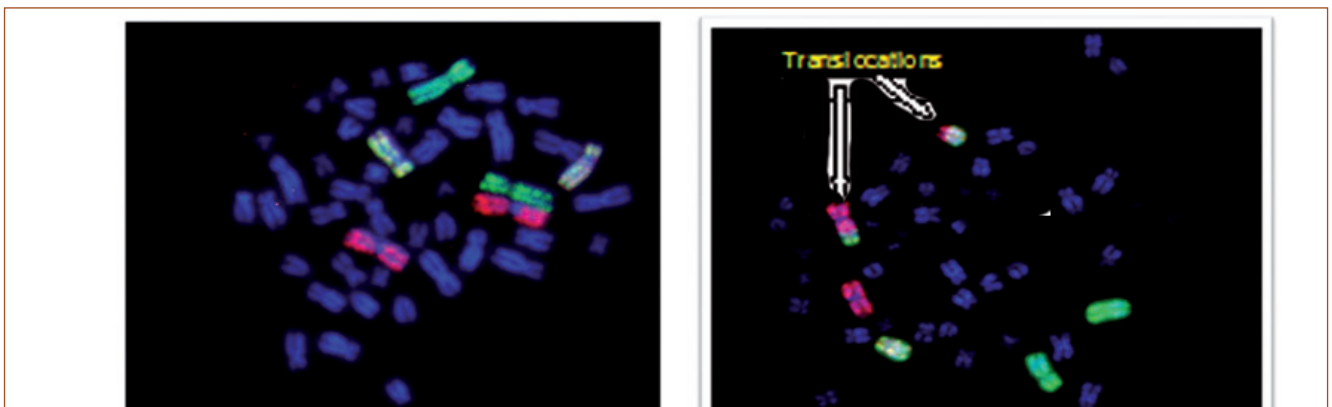


Fig. 1 Normal and irradiated cells (with chromosomal translocation) obtained by painting chromosome 1 (red), 2 (green) and 4 (red+green) with a genome coverage of 22.71%

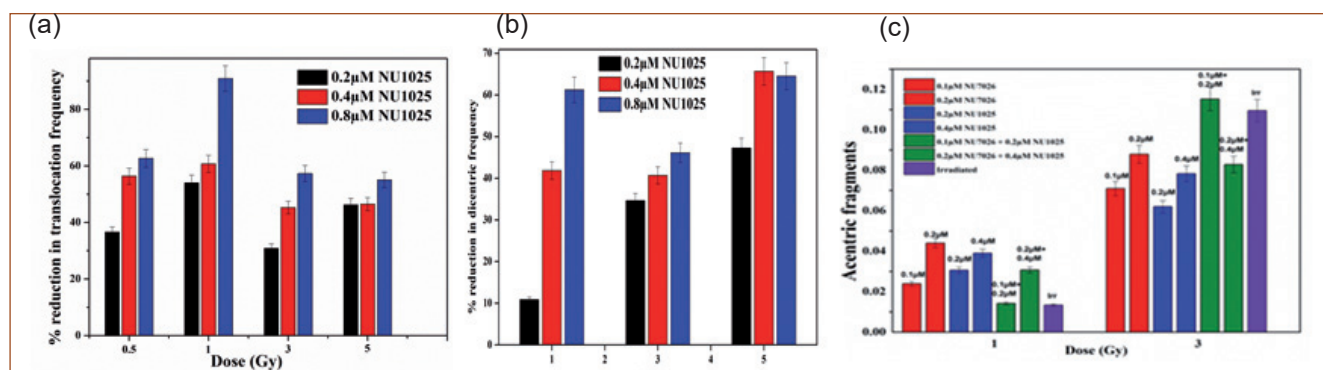


Fig. 3 (a) Translocations, (b) dicentrics, and (c) acentric fragments were scored from cells (unirradiated and irradiated) incubated with and without NHEJ pathway inhibitors

radiation through modulation of translocation frequency by inhibition of both the canonical and alternate NHEJ pathways.

FISH-translocation dose response curve for Cs-137 γ -rays (0.1Gy/min dose rate) was But till now the details of molecular mechanism behind radiation induced translocations is not known completely due to multitude of triggers present in cell for activating these repair pathways e.g. cell cycle phase, common regulatory factors, sub pathways within main pathways etc.

Past studies have clearly established that NHEJ is the main pathway responsible for radiation induced translocation formation in cells. Further NHEJ has two sub pathways i.e. canonical (cNHEJ) and alternate (aNHEJ) which are competing with each other for DNA DSB break sites. The DNA repair initiating factors of cNHEJ i.e. Ku70-Ku80 complex compete with Poly [ADP-Ribose] Polymerase 1 (PARP1) of aNHEJ for attachment at DNA break site.

In perspective of this NHEJ pathway inhibitors (NU7026 for cNHEJ and NU1025 for aNHEJ) were used along with

FISH probes for chromosome 1, 2 and 4 to understand the mechanism behind γ -radiation induced chromosomal translocation formation.

Translocations, dicentrics, and acentric fragments were scored from cells (unirradiated and irradiated) incubated with and without NHEJ pathway inhibitors exposed were scored and percent changes in their frequencies were calculated (Figures 3a to 3c) . Analysis of results revealed that

- i. aNHEJ is a major pathway in the formation of translocation and PARP1 enhances the translocation frequency on induction of DSB
- ii. cNHEJ play a minor role in the repair of DSBs
- iii. The possibility of crosstalk between aNHEJ and cNHEJ in radiation induced translocation formation
- iv. Although aNHEJ is the key pathway in translocation formation reduction in dicentric frequency in presence of PARP1 implies that cNHEJ is the active pathway in dicentric formation.

V.30 An Account of Plankton Diversity in the Coastal Waters of Kalpakkam during the Last Decade

Coastal biodiversity study of Kalpakkam is of great importance due to the existing and upcoming nuclear facilities. Among different biodiversity components of this coastal water, a study on diversity of phytoplankton and zooplankton is presented here. Phytoplankton, the microscopic plant components of aquatic system constitutes the most vital component of the biological community as primary producers. In marine ecosystem, about 95% of the total primary production through photosynthesis is contributed by the phytoplankters, which is also about 40% of the

global productivity. The primary production is transferred to the next higher levels in the marine food chain by zooplankton, which is considered as the secondary producer as well as primary & secondary consumers. It accounts for about one tenth of the total marine biomass. Therefore, for assessing the fisheries yield, it is important to have knowledge on phytoplankton and zooplankton abundance and their variability. In addition, the plankton assemblages are often used as the indicators of water quality including pollution. The plankton flora comprises the group of diatoms, dinoflagellates, cyanobacteria,

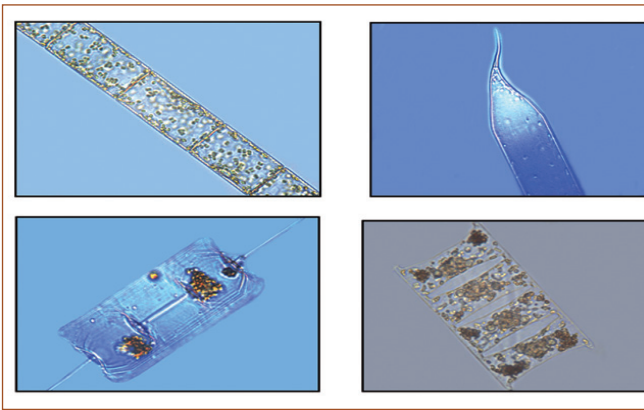


Fig. 1 Photographs of phytoplankton (a) *Leptocylindrus danicus* (b) *Pseudosolenia calcar-avis* (c) *Ditylum brightwelli* (d) *Hemiaulus membranacea*

silicoflagellate, coccolithophores etc, however, diatoms dominate the phytoplankton assemblage. Zooplankton comprises protozoans, annelids, mollusks, arthropods, chaetognaths, echinoderms etc.

The study revealed presence of ~400 species of phytoplankton over a period of 10 years. Photographs of some of the frequently available phytoplankton and zooplankton species are given in Figures 1 & 2. Well pronounced fluctuation in phytoplankton density was observed during the course of present study with a minimum and maximum density of 1.01×10^5 cells L^{-1} and 7.04×10^5 cells L^{-1} respectively (Figure 3). Heavy phytoplankton proliferation was observed during post monsoon (pom), summer and pre-monsoon (prm) period, which might be due to relatively stable as well as optimal conditions of salinity, temperature, light and nutrient levels and upwelling & vertical mixing that occurs during pre-monsoon (August – September). However, prevalence of relatively high concentration of

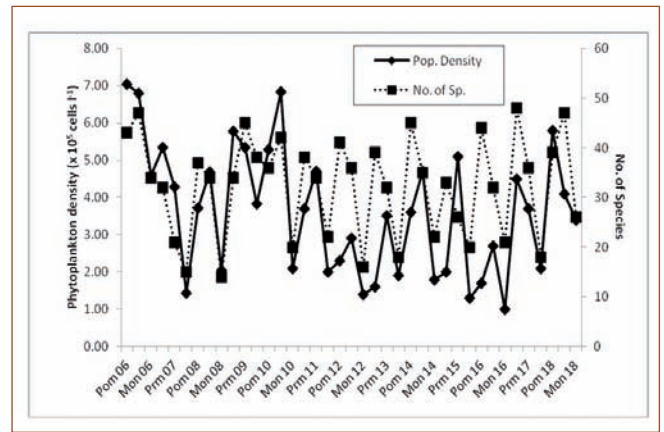


Fig. 3 Population density and diversity of phytoplankton assemblage

nutrients (phosphate, nitrate, silicate) during monsoon months could not support the growth and proliferation of phytoplankton. During this period low salinity, low light penetration, high turbidity and low temperature inhibited phytoplankton growth in spite of abundant availability of nutrients.

Zooplankton study is first of its kind from this location. Results showed copepods such as *Canthocalanus pauper*, *Acrocalanus gibber*, *Paracalanus parvus*, *Pseudodiaptomous serricaudatus* and *Oithona rigida* were the very dominant forms, which contributed 40-75% to the total zooplankton population throughout the study period. Among copepods, *Oithona* sp. and *Euterpina acutifrons* were abundant during monsoon period as ovigerous females. Moreover, mon period was also found favorable for meroplankton population. The trend in zooplankton abundance/ density was found in tune with phytoplankton (Figure 4).

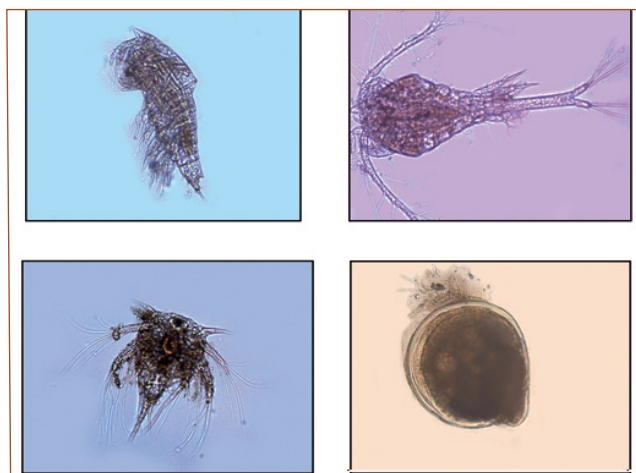


Fig. 2 Photographs of zooplankton (a) *Clytemnestra scutellata*, (b) *Oithona hebes*, (c) *Barnacle nauplius* and (d) *Bivalve larva*

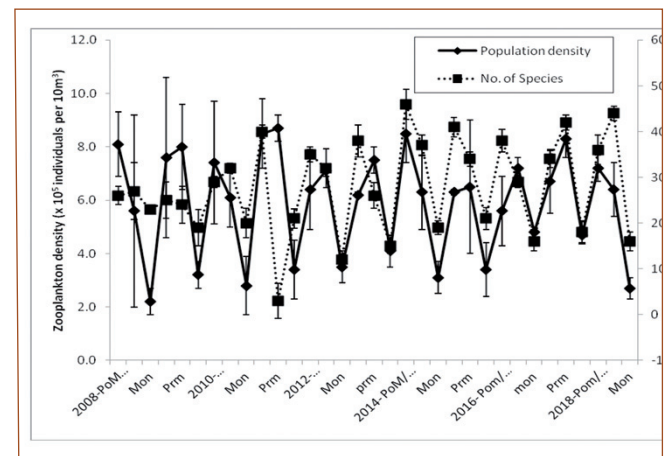


Fig. 4 Population density and diversity of zooplankton assemblage

V.31 Ergonomics for the Management of Work-related Musculoskeletal Disorders

The human musculoskeletal system comprises the muscles, bones of the skeleton, cartilage, joints, nerves, blood vessels, the spine and connective tissues such as tendons and ligaments. Musculoskeletal disorders (MSDs) are the injuries caused to the human musculoskeletal system due to ergonomically deficient working conditions. These injuries develop gradually over weeks, months or years. The occupational risk factors include prolonged exposure to excessive force, repetitive movements, static and awkward posture, contact stress, excessive vibration, quick motions etc. The most common MSDs are the tendon disorder, carpal tunnel syndrome and back injury. Prolonged repetitive activities, forceful exertion, awkward and static postures, and contact stress causes tendon disorders. The carpal tunnel syndrome is caused by compression of the median nerve due to repetitive motion and forceful manual task. Tingling, pain, loss of strength, and sometimes permanent loss of sensation and partial paralysis occurs in the hands and wrist. Back injuries involve strained muscles, ligaments and tendons. More serious injuries are associated with the spinal disc. Prolonged activities, repetitive motions, working in static posture are major contributors to back injuries. According to U.S. Department of Labor-Occupational Safety & Health Administration (OSHA), MSDs is a serious workplace health hazard, expensive in terms of treatment and incurs indirect costs from increased employee absenteeism. The solution lay with good ergonomic work practices. Ergonomics is an applied science, concerned with designing and arranging the work place for safe and efficient working.

The proliferation of computer applications worldwide has escalated computer-related MSDs to 25 %. Prolonged computer operations is associated with static postures, repetitive wrist movement, awkward wrist, back and neck

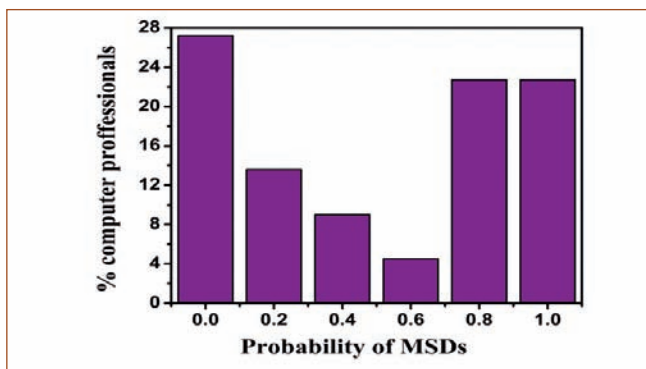


Fig. 1 Probability of developing MSDs among 22 extensive computer users

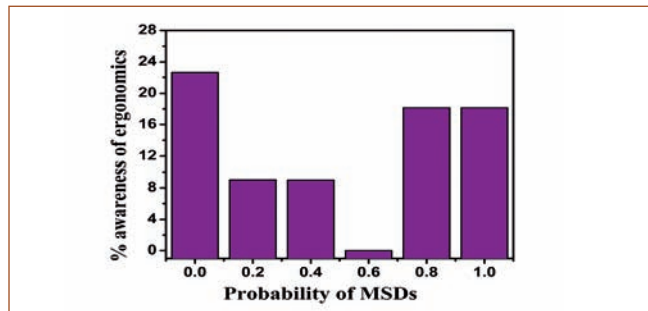
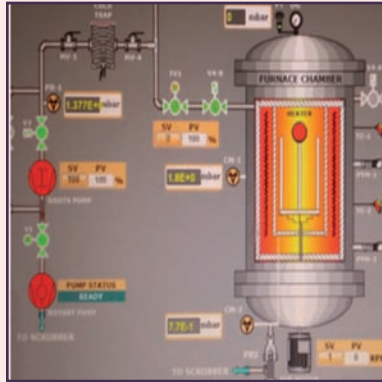


Fig. 2 Awareness of ergonomics & probability of MSDs

postures that culminate in carpal tunnel syndrome, back injury and neck pain.

As a part of initiating an ergonomic programme, a case study was conducted by carrying out survey among extensive users of computers in computer division/IGCAR to investigate the prevalence of MSDs and their awareness of ergonomics. Symptoms considered include tingling, numbness in the fingers, and pain in the wrist / neck / back. The probability of developing MSDs was arrived from the ratio of number of symptoms shown to that of the total number of symptoms considered. The plot (Figure 1) of probability of developing MSDs and the percentage of professionals with these probabilities indicated that 45.4 % exhibited highest, 27.2 % showed least and, the rest showed moderate to low probability of developing MSDs. Despite awareness of ergonomics, symptoms of susceptibility to MSDs (Figure 2) yet prevailed. Hence, it is imperative to educate employees about work-related MSDs and to implement ergonomic work programmes.

Following ergonomic standards is a preventive measure to reduce work-related MSDs. The first fundamental ergonomic principle is to maintain neutral posture, where the body and joints are aligned while sitting or standing. This minimizes the stress applied to the muscles, tendons, nerves and bones. Prolonged forceful exertion requires contraction forces by the muscles, causing tendon irritation, constriction of blood vessels and nerves in the area. Eliminating excessive force reduces the risk of MSDs. Continuous working in static position causes fatigue. It is necessary to break and stretch to improve muscle co-ordination. Many work tasks are repetitive in nature. High repetition rates for the same movement, like using a keyboard or mouse for 4h/day increases susceptibility to MSDs. One way to circumvent is to take stretch breaks in between, while also performing simple exercises. Ergonomically designed computer workstations and following computer ergonomics is necessary to combat computer related MSDs.



CHAPTER VI

Directed Basic
Research

VI.1 Development of High Performance Green Nuclear Concrete through Nanophase Modification and Inhibitor Addition for Seawater Applications

The structural stability and durability of concrete structures especially those in contact with seawater is of extreme importance for extending the life span of nuclear installations over 60 years, to reduce the cost per unit power production. In this direction, an attempt was made to fabricate a novel high performance green concrete designated as CFNI with optimal composition of 40 wt.% fly ash, 2 wt.% nano-TiO₂ and nano-CaCO₃ in 1:1 ratio, 2 wt.% sodium nitrite based corrosion inhibitor and 56% Ordinary Portland Cement for seawater applications. The newly fabricated CFNI was well characterized to ascertain the enhancement in strength, durability, antibacterial and reinforcement corrosion resistance properties and improved microstructural characteristics as compared to conventional concrete (CC). The synergy, if any, between the three additives in enhancing the properties of concrete was also investigated by comparing with only fly ash (FA); and FA and nanoparticles supplemented concrete designated as CF and CFN, respectively.

Figure 1 shows the improvement in the early age strength of CFNI at par with CC and reduction in 7 day strength of CF. Thus the serious shortfall of reduction in early age strength associated with FA addition was overcome in CFNI. A tenfold reduction in the depth of water penetration (Figure 2) was shown by CFNI in comparison to CC confirming the presence of an highly impermeable cover which resist ingress of corrosive ions and help in extending service life of the structure. Mercury ion porosimetry analysis (Figure 3) showed highest amount of gel pores at nanoscale (~10nm) which confirmed the synergistic effect of additives in refining the pore structure of concrete, resulting in enhanced impermeability and strength characteristics of CFNI.

CFNI specimens showed a very significant decrease of 70.66% in the Rapid Chloride Penetration Test value

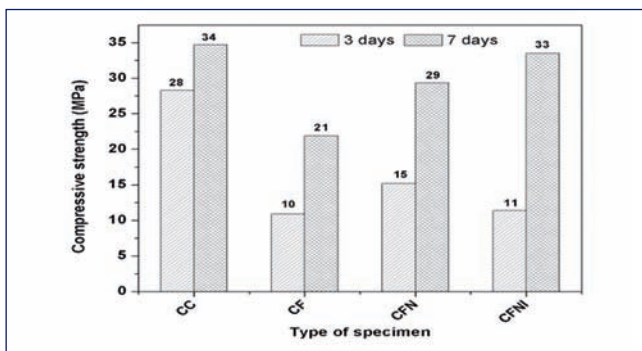


Fig. 1 Early age compressive strength development of specimens after 3 and 7 days of curing

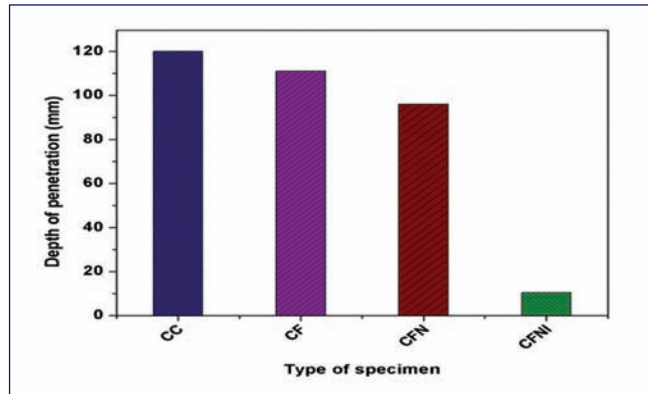


Fig. 2 Comparison of depth of penetration observed in water permeability test for 18 days cured concrete specimens

as compared to CC specimens, indicating its improved chloride ion permeability resistance. Exposure studies of these specimens in Kalpakkam coastal waters showed lesser biomass attachment (0.155g/100 cm²), four order lesser total bacterial density, least biofilm thickness (28.93 ± 0.02 μm) in CFNI as compared to CC evidencing excellent biofouling resistance. Thermogravimetric analysis of 28 day cured specimens showed that weight loss due to dehydration of C-S-H was more on CFNI specimens which indicated the presence of highest amount of the most desirable hydration product C-S-H gel in these specimens.

The weight loss due to decomposition of CaCO₃ was least for CFNI indicating lesser carbonation. Electrochemical evaluation of corrosion behavior of embedded steel bar in new concrete by impressed voltage technique showed maximum time to cracking and minimum anodic current confirming excellent corrosion resistance.

This novel high performance green concrete developed by incorporating fly ash, nanoparticles and corrosion inhibiting admixture into conventional M45 grade concrete exhibited enhanced biodeterioration and reinforcement corrosion resistance in seawater environments.

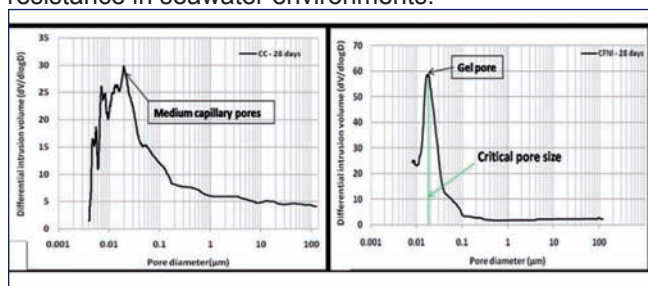


Fig. 3 Pore structure of CC and CFNI specimens after 28 days of curing

VI.3 Evaluation of Durability of Plasma Sprayed Alumina Coating on Inconel 600 collars for Fast Reactor Neutron Detector Application

Alumina coating with high electrical resistivity on Inconel 600 collars is preferred for the high temperature fission chamber (HTFC) neutron detectors of prototype fast breeder reactor. In order to evaluate the feasibility and durability of such coating for the above application, plasma sprayed alumina coating is done over Inconel 600 collars for HTFC neutron detectors with an intermediate Ni-50Cr bond coat deposited by HVOF technique. The alumina coated Inconel 600 collars were subjected to 100 thermal cycles at 570°C in argon atmosphere as per the specifications at ECIL to evaluate its durability. Thermal cycling studies were conducted initially by heating to 570°C for 100 h followed by thermal cycling as per the requirement of 0.2 cps/nv HTFC detectors. The thermal cycle consists of heating to 570°C in 10 h, cooling from 570 to 400°C in 1200 s and then cooling to 200°C in 5 h. Finally, the samples were subjected to 100 h of heating at 570°C. After 33 cycles, insulation resistance (IR), measured at ECIL at room temperature, was found to be $\sim 1 \times 10^{10} \Omega$ at 400 V DC. After 100 cycles, IR values (measured at RDG at room temperature and 600 V DC) were 5.2×10^{10} and $1.62 \times 10^{11} \Omega$, respectively for the small and big collars. After completing 100 thermal cycles, visual examination of Inconel 600 collars was carried out. It is found that the ceramic coating is intact without any flaking/peeling off in the top and bottom portions as shown in Figure 1a and 1b, respectively. After

exposure to 100 thermal cycles, SEM examination was carried out on alumina coated Inconel 600 collar (small). No major cracks were observed on the surface and the surface appeared relatively dense (Figure 2a). At higher magnification, micro cracks were observed as shown in Figure 2b, which are typically found in plasma sprayed alumina.

Thermal cycling studies were carried out on alumina coated samples with NiCrAlY and Ni-50Cr bond coat by heating to 650°C, holding for 1 h and then forced air cooling to room temperature in 15 min. No major change in weight loss/gain or spallation was observed after 100 thermal cycles. XRD analysis showed $\gamma \text{Al}_2\text{O}_3$ in the as-coated samples, while after thermal cycling, presence of minor $\alpha \text{Al}_2\text{O}_3$ phase was observed. SEM examination of alumina top coat with Ni-50Cr and NiCrAlY bond coats did not show any significant difference after thermal cycling experiments. This could be due to insufficient oxide formation over Ni-50Cr and NiCrAlY bond coats after thermal cycling experiments that caused microcracks.

Though thermal cycling experiments could not reveal any difference between the two bond coats in 100 thermal cycles, higher oxidation of Ni-50Cr bond coat with bulky oxide formation could result in premature spallation. These results suggest that NiCrAlY bond coat is better than Ni-50Cr bond coat.

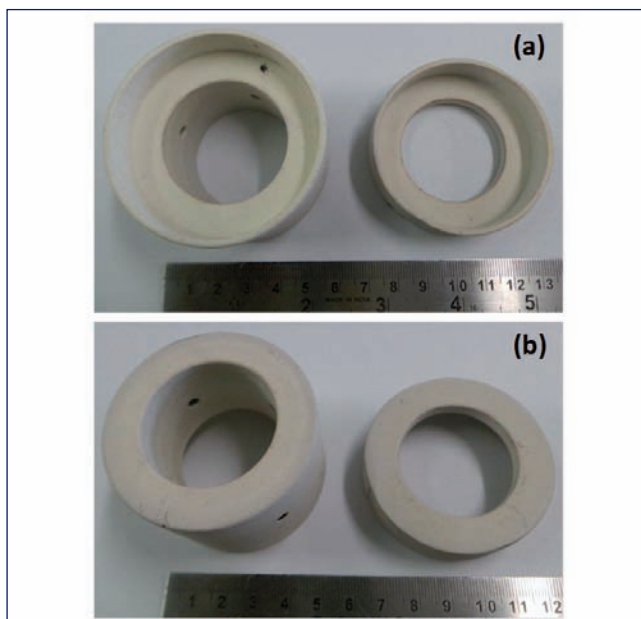


Fig. 1 Photograph of plasma sprayed alumina coated Inconel 600 collars after 100 thermal cycles at ECIL (a) bottom view and (b) top view

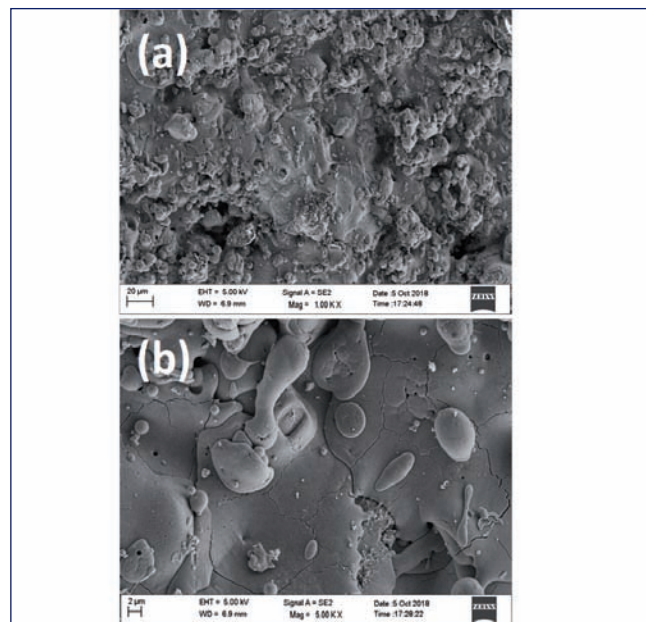


Fig. 2 Surface morphology of plasma sprayed alumina coated Inconel 600 collar (small) (a) 1000x and (b) 5000x

VI.4 Plasma Nitriding of Large FBR Components

Several engineering components of Fast Breeder Reactors (FBRs) during their service will experience one-to-one physical contact in the presence of flowing fluid media like liquid Sodium or gaseous Argon. Such tribologically vulnerable parts, if not adequately taken care of by design, would lead to failures. Hence, there is always a need to improve the combined wear-corrosion-erosion resistance of such components by employing suitable surface modification strategy like hard facing. Though hard facing of FBR components by Ni-based Colmonoy coatings is a widely preferred choice, it becomes prudent in the case of some components, to develop alternate strategy, such as Plasma Nitriding (PN), to take care of intricate component geometry coupled to minimal distortion and avoiding post deposition machining possibility. The present report brings out the results of plasma nitriding of the mockup casing ring of PFBR secondary sodium pump. The material of the ring is annealed 316L stainless steel and the dimensions are: outer diameter is 558.5 mm; inner diameter is 529 mm; and thickness 14 mm (referred to as thicker section). The ring also has a step on one side (referred as thinner section; Figure 1).

The PN process involves: (i) stress relieving the component (ii) hard chrome plating to required thickness and (iii) final plasma nitriding. Plasma nitriding of SS316L casing ring has been carried out as per recommended procedures. At every stage, a representative test sample was also processed so that comprehensive characterisation of the complete process could be realized. X-ray diffraction analysis of plasma nitrided sample at 520°C, exhibited the presence of γ -austenite phase and various chromium nitride precipitates, as



Fig. 1 Plasma nitrided casing ring and test specimen

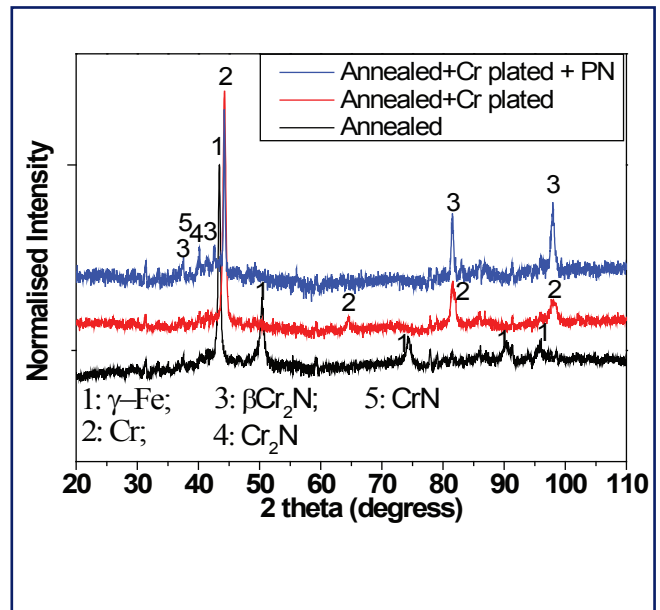


Fig. 2 XRD pattern of Stress relieved (SR); Stress relieved and chrome plated (CP); Stress relieved, Cr plated and plasma nitrided 316L coupons

shown in Figure 2. The hardness profiles of the Cr-plated and nitrided test specimens showed (Figure 3) that hardness value of the plasma nitrided layer on 316L SS ring is about ~ 800 VHN, which is about four times higher as compared to that of annealed stainless steel (220 VHN). The case depth is found to be around 100 microns in the case of thicker section and is around 55 microns. The dimensional stability of post-nitrided component has been audited and virtually no deviation from prescribed design has been observed. This indicates that Plasma Nitriding as a hardening method does not introduce any gross distortion to the component and can be adopted for large FBR components as well.

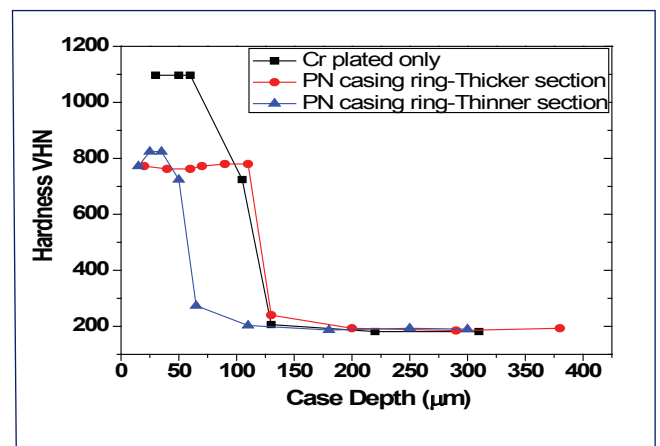


Fig. 3 Hardness Profile of hard chrome plated sample; thicker section of nitrided ring and thinner Section of nitrided ring

VI.5 Controlling Texture in 18Cr ODS Steel through a Combination of Thermo-Mechanical Processing Steps

Consolidation of oxide dispersion strengthened (ODS) 18Cr ferritic steel (Fe-18Cr-2W-0.25Ti-0.1C-0.35Y₂O₃) powder by hot extrusion results in high density material with fine grained microstructure with enhanced mechanical properties. However, unidirectional processing of hot extruded rod results in columnar grains of high aspect ratio (upto ~35), which increases with further axial deformation during pilgering. Although recrystallized grains enhance high temperature strength of the tube in hoop direction, there are difficulties in achieving a stable fine equiaxed grain structure by various intermediate heat treatments. This is due to the lack of high temperature $\gamma \rightarrow \alpha$ phase transformation. It is well known that the stored energy in deformed alloys can be exploited to obtain equiaxed grains by recrystallization process, despite the extreme directionality of initial microstructure. Accordingly, suitable thermo-mechanical treatments were identified to reduce anisotropy during unidirectional cold rolling of hot extruded 18Cr ODS ferritic steel. This was achieved by heavy rolling (50% reduction) of the extruded rod in multiple steps followed by heat treatments; unlike gradual reduction of thickness and intermediate annealing in the case of pilgering process.

As seen in Figure 1, strong α -fibre texture resulted after extrusion. Cold rolling (50%) along ED (Extrusion Direction) retained the directional microstructure; but with ultra-fine banded structure (width < 0.5 μm) parallel to ED. Differential Scanning Calorimetry (DSC) analysis of the rolled steel established the occurrence of two significant events during heating, namely recovery and recrystallization, which were found to be strongly influenced by heating rate. Distinct recovery and recrystallization domains were thus identified at around 1350 K and 1420 K, respectively, using a low heating rate of 7 K $\cdot\text{min}^{-1}$. The resultant microstructure showed very coarse elongated grains interspersed with regions of ultrafine (<1 μm) equiaxed grains, due to incomplete recovery. It was conjectured that higher incubation period in the recovery domain preceding recrystallization step, could result in finer grains, owing to reduction in stored energy.

Based on above observations, the hot extruded steel that was cold rolled to 50% along ED was subjected to two step heat treatment: – 1st iteration involved recovery at (1350 K/2 h) followed by recrystallization (1420 K/ 0.5 h). This steel with the recrystallised microstructure, but still

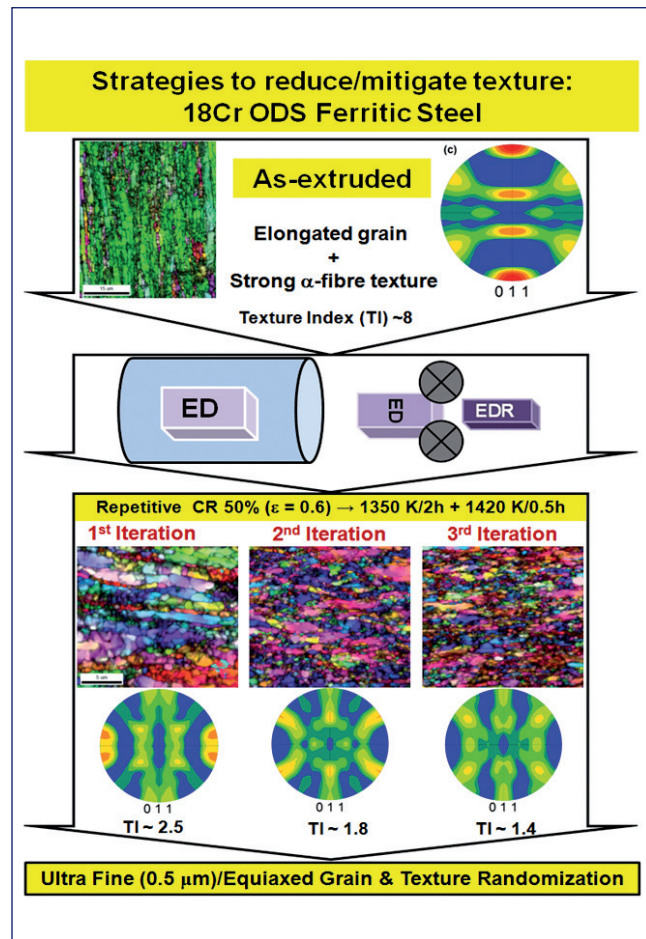


Fig. 1 Schematic of process flow chart to maximise the fraction of ultrafine equiaxed grains through repeated deformation and two step heat treatments and achieve texture randomization

possessing a banded structure, was again subjected to another 50% cold rolling along ED followed once again by the above two step heat treatment (2nd iteration) and repeated the steps again (3rd iteration).

EBSD crystal orientation map superposed with IQ map of the deformed steel after the above processing (Figure 1) showed ultrafine (average size ~ 0.5 μm) equiaxed grains. This is attributed to the fragmentation of elongated grains during cold rolling and nucleation of fine grains during the two step heat treatment. Respective (011) pole figures show a highly random texture in all cases. A gradual increase in hardness during above iterations has also been noticed, suggesting an increase in dislocation density. Above studies clearly established a viable methodology for mitigating the texture issue in 18Cr ODS steel.

VI.6 Measurement & Modeling of Thermodynamic Properties of Ni₅₁Fe₃₆Co₁₃ Alloy - Magnetic Switch Material for DSRDM

Ni₅₁Fe₃₆Co₁₃ (Wt.%) ferromagnetic alloy was developed indigenously to be used as the sensor material in temperature sensitive magnetic switch in the diverse safety rod drive mechanism (DSRDM) in future FBRs. Alloy of this composition was chosen because of its favorable Curie transition (T_C) temperature. However thermodynamic properties of this ferromagnetic alloy will be significantly affected by the magnetic transition posing serious challenges during high temperature fabrication and application. Therefore, prior knowledge on high temperature phase stability and thermodynamic properties is highly essential for the design and fabrication of the magnetic switch. In this regard, the present study deals with the investigation on phase stability as well as the measurement and modelling of the thermodynamic properties for Ni₅₁Fe₃₆Co₁₃ alloy from RT to 1273 K.

The alloy was prepared by induction melting followed by investment casting. Subsequently it was annealed at 1273 K for 1 h in Ar-ambience, before specimen preparation for other experiments. X-Ray diffraction analysis indicated a FCC structure for the alloy with lattice parameter of 0.364 ± 0.02 nm at RT (Figure 1). Phase stability investigations using DSC confirmed the alloy to be single phase, up to 1073 K except for a ferromagnetic to paramagnetic Curie transition at $T_C = 898$ K. The temperature dependent enthalpy increment and thermal dilation were measured using drop calorimetry and push rod dilatometry respectively

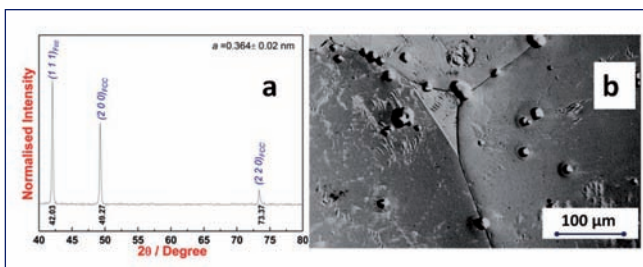


Fig. 1 (a) XRD profile and (b) microstructure for Ni₅₁Fe₃₆Co₁₃ alloy

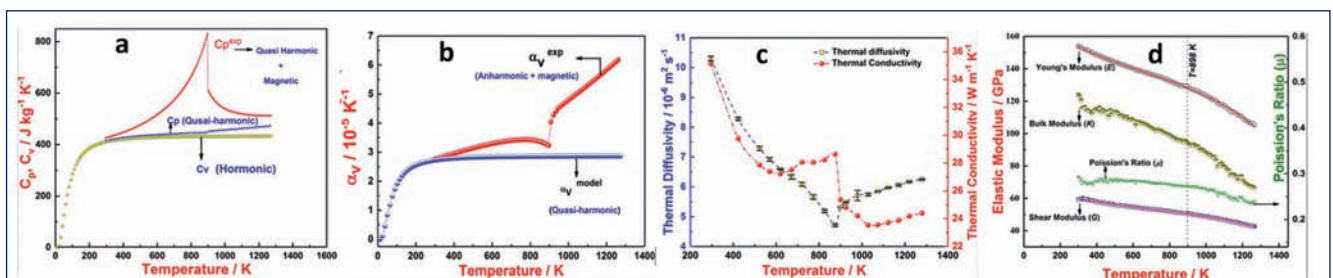


Fig. 2 Measured and model estimated (a) Heat capacity (b) Volume thermal expansivity (c) Thermal diffusivity and conductivity and (d) elastic Moduli and Poisson's ratio for Ni₅₁Fe₃₆Co₁₃ alloy

and the corresponding isobaric specific heat and thermal expansion were estimated. Temperature dependent density values were also obtained from the measured thermal expansion. Young's (E), Shear (G) and Bulk Modulus (K) as well as Poisson's ratio (μ) were determined using impulse excitation technique. Thermal diffusivity (λ) was measured using laser flash technique from which thermal conductivity (k) was estimated.

Figure 2 shows the measured thermodynamic properties for Ni₅₁Fe₃₆Co₁₃ alloy from room temperature up to 1273 K. It is interesting to note that the magnetic contribution to the heat capacity and thermal expansion have been treated separately in this study using the CALPHAD thermodynamic approach for a qualitative analysis of magneto-caloric and magneto-volume effect in the alloy. The heat capacity and thermal expansion were estimated using Debye-Grüneisen quasi harmonic approach from 0 to 1273 K. It has been observed that magnetic contribution plays a dominant role in deciding the high temperature thermodynamic properties. The measured values of thermodynamic properties of this alloy are listed in Table 1.

Table 1: The measured values of thermodynamic properties of the alloy

Temp/K	C_p / J kg ⁻¹ K ⁻¹	α / 10 ⁻⁶ x K ⁻¹	k / W m ⁻¹ K ⁻¹	E / GPa
298	427	0.92	35.10	154
373	442	0.97	31.35	150
473	468	1.03	28.41	146
573	505	1.08	27.32	142
673	556	1.12	27.47	139
773	636	1.14	28.18	134
873	781	1.10	28.67	131
973	547	1.55	24.30	128
1073	521	1.72	23.55	123
1173	512	1.90	23.85	116
1273	511	2.07	24.34	112

VI.7 Optimization of Process Parameters and Characterization of Injection Cast Uranium Zirconium (U- 6wt.%Zr) Alloy

The U-Pu-Zr ternary alloy is one of the candidate fuel for the future metal fuel fast reactors. U-6wt.%Zr binary alloy will be used as blanket slug for the sodium bonded metal fuel pins. An engineering scale facility for the optimization of process parameters for preparation of alloy fuel by injection casting method was established in MC&MFCG (Figure 1a). The 1.0 kg capacity injection casting system was qualified for its functionality by casting nickel slugs. Later the system was installed and commissioned inside a glove box to handle radioactive materials. Various process parameters viz. power of the induction heater, heating rate, purity of the glove box, vacuum inside the casting chamber, temperature of melting / casting, dwell time for molten alloy, casting pressure and time of casting were optimized in various campaigns to arrive at defect free U-Zr slugs.

Quartz tubes coated (inner surface) with yttria are used as mould for injection casting (Figure 1b). The process for coating inner surface of the quartz tube was developed and standardized. The in house coated quartz tubes were used for casting of U-Zr slug. Graphite crucible is used as container material for molten alloy. To avoid contamination of alloy with carbon these crucibles were also coated with yttria.

Casting of U-Zr slugs involved the following procedure: Blank experiments with yttria coated graphite crucible, i.e. without charge. Uranium metal was cleaned to remove oxide coating. The procedure to clean uranium metal was standardized. A photo of uranium metal before

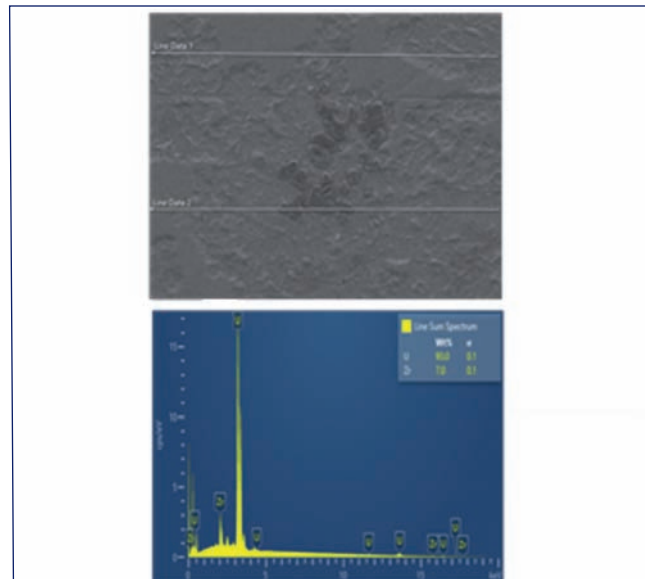


Fig. 2 SEM image with EDAX spectrum

and after cleaning is shown in Figure 1c and zirconium sponges were used as received (Figure 1d). Accurately weighed quantities of uranium and zirconium were taken in the coated graphite crucible and loaded in the injection casting chamber. To achieve the homogeneous mixing, melting was carried out at 1723 K. After completion of first melting, the molten alloy was cooled (Figure 1e), inverted and re-melted at the same temperature. Quartz moulds were lowered in the melt, the system was pressurized at 0.25 bar with UHP argon gas and slugs were cast. The cast U-6 wt.%Zr slug is shown in Figure 1f.

Physical and chemical characterization of the U-6 wt.%Zr slug was carried out to qualify the slugs. The dimensions and the weight of the slugs are given in the Table 1. The desired density of the slug was achieved in this process. The slug was also characterized for its chemical composition and phase studies. Scanning electron microscopic image of the slug sample is presented in Figure 2. The desired chemical composition, phase and microstructure were achieved for the cast alloy.

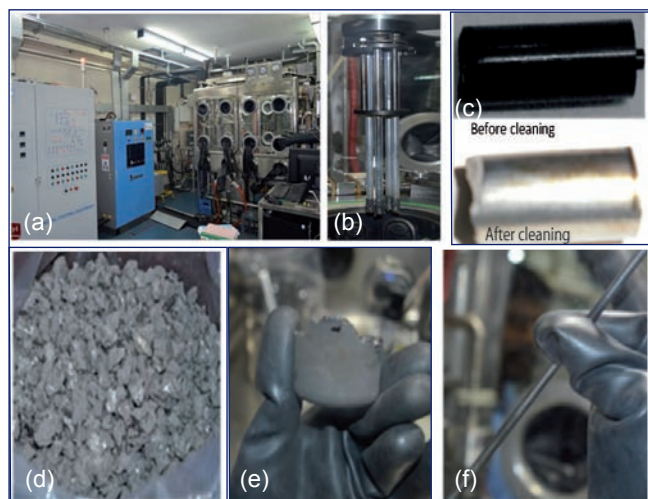


Fig. 1 (a) Facility for injection casting of alloy, (b) mould holder with cast UZr alloy, (c) U metal before and after cleaning, (d) zirconium metal, (e) U-Zr alloy ingot and (f) U-Zr Blanket slug after injection casting

Table 1: Characteristics of the injection cast slug				
Slug no.	Weight (g)	Length (mm)	Dia. (mm)	Density (g/cc)
1	76.1	242	4.86	16.95
2	78.9	245	4.93	16.87
3	76.3	244	4.94	15.61
4	76.4	243	4.85	17.01

VI.8 Generation of Creep-Fatigue Interaction Diagram for Modified 9Cr- 1Mo Steel

Creep-fatigue interaction (CFI) is an important aspect for high temperature design of steam generator components in fast breeder reactors. These components are often subjected to cyclic thermal stresses as a result of temperature gradients across thick sections that occur due to startups, shutdowns and transients of power plant. This results in high temperature low cycle fatigue (LCF). In addition, steady state operation of the plant at elevated temperatures introduces creep damage, resulting in a complex interaction between creep and fatigue, within the LCF regime.

Modified 9Cr-1Mo steel is a candidate material for the steam generator applications. RCC-MR design code and ASME section III, subsection NH present different CFI diagrams for this steel. Both the codes recommend bi-linear CFI diagram for the alloy. However, the damage lines intersect at different points viz., (0.3, 0.3) and (0.1, 0.01) in RCC-MR and ASME section-III respectively as shown in Figure 1. A project was therefore initiated to generate the CFI diagram for the above steel. Towards this, CFI tests were performed on two chemical variants of modified 9Cr-1Mo steel (steel-1 & steel-2) at two temperatures (773 and 823 K) and three strain amplitudes (± 0.4 , ± 0.6 and $\pm 0.8\%$). Peak tensile and compressive strain holds with durations in the range 1 to 60 min. were employed for the tests which were conducted at a constant strain rate of $3 \times 10^{-3} s^{-1}$. The steel exhibited a continuous cyclic softening that culminated in a near-saturation regime before the final failure, as presented in Figure 2. Hold time generally resulted in higher cyclic stress response (CSR) compared to continuous cycling as seen from the above figure. Besides, compressive hold resulted in a higher CSR compared to tensile hold. It was observed that the fatigue life decreases in presence of hold time. Further, the compressive hold was found to be more deleterious compared to the hold in the tensile peak strain.

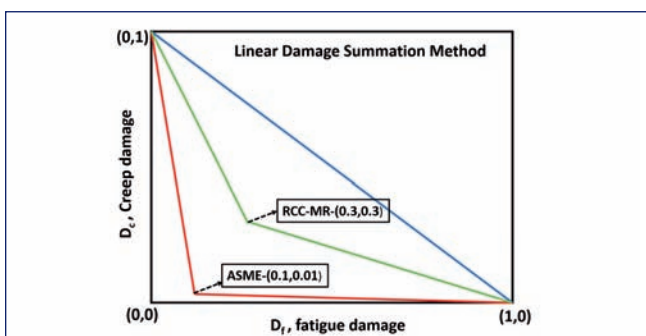


Fig. 1 Creep-Fatigue Interaction diagram for modified 9Cr-1Mo steel

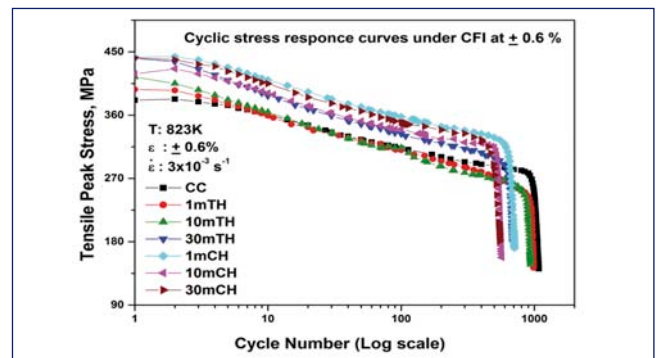


Fig. 2 Cyclic stress response curves for modified 9Cr-1Mo steel-1 under creep-fatigue interaction

Linear Damage Summation Method was used in the present study to generate CFI diagram. In this method, life fraction as fatigue damage and time fraction as creep damage are summed up to unity and the failure criterion is expressed by the below equation:

$$\frac{n_f}{N_f} + \frac{t}{t_r} = 1$$

where N_f , n_f , t_r , t represent fatigue life without hold, fatigue life with hold, creep rupture time and the cumulative hold time in n_f number of cycles respectively. Calculation of cycle fraction (n_f/N_f) in the above equation is straight forward. However, calculation of creep damage (t/t_r) needs to be addressed. It should be noted that the creep damage does not appear in the material immediately upon the initiation of stress relaxation due to the occurrence of high strain rates. Stress values corresponding to a typical 'transition strain rate' (of the order of 10^{-5} to $10^{-7} s^{-1}$) marking a shift of the damage from the matrix to the grain boundary owing to creep deformation during the stress relaxation was used to obtain the t_r values from the RCC-MR creep design data. It was observed that the CFI damage is closer to the ASME recommendation of (0.1, 0.01) as shown in Figure 3.

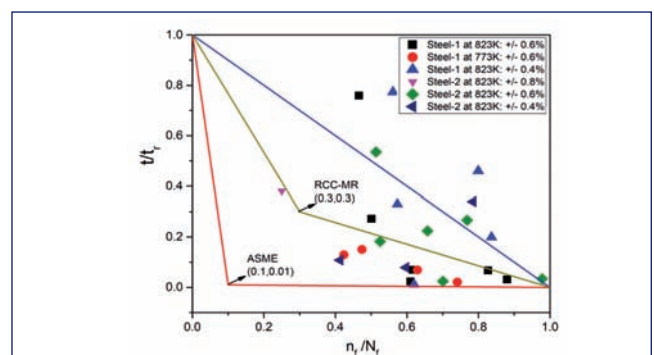


Fig. 3 Creep-fatigue interaction diagram for modified 9Cr-1Mo steel and comparison with the RCC-MR and ASME diagrams

VI.9 Corrosion Behavior of Pyrolytic Graphite in UCl_3 -LiCl-KCl Molten Salt by Electrochemical Techniques

Carbon-based materials like graphite and its various forms are being proposed as the candidate materials for process containers in pyrochemical reprocessing of spent metallic fuels of future FBR's. The pyroreprocessing has various unit of operations like salt purification, electrorefining, cathode processing and fuel casting. The processes uses molten LiCl-KCl salt along with UCl_3 and various metals like U, Pu and Zr at high temperatures ranging between 500 to 1500°C. Especially in electrorefining process, LiCl-KCl molten salt with 5 to 6 wt. % UCl_3 is used as the electrolyte in the temperature range of 500 – 600 °C under ultra-high pure argon atmosphere. Hence, the material for process vessels for salt purification and electrorefining process should exhibit high corrosion resistance in molten LiCl-KCl salt under Cl_2 gas and molten LiCl-KCl- UCl_3 salt, respectively. Electrochemical transient techniques are rapid and promising compared to the conventional weight loss measurements for corrosion monitoring of materials. In the present work, the electrochemical behavior of pyrolytic graphite (PyG) is studied in molten LiCl-KCl with 5-6 wt. % UCl_3 salt at 600°C under argon atmosphere. The open circuit potential (OCP) of PyG specimen was measured against Pt quasi-reference electrode (QRE) for a total duration of 200 h. The OCP versus time data as shown in Figure 1 that indicated the initial decrease followed by stabilization at around 60 h of duration, further no change in OCP was observed, which suggests the less corrosion of PyG in molten salt.

The linear polarization resistance (LPR) measurements (Figure 2) were carried out by scanning the potential of the PyG specimen over the potential range ± 10 mV from the OCP. There is little change in slope of the LPR curves observed with duration of exposure and also the change in E_{corr} (1.6 mV at 10 h to -3.9 mV at 200 h)

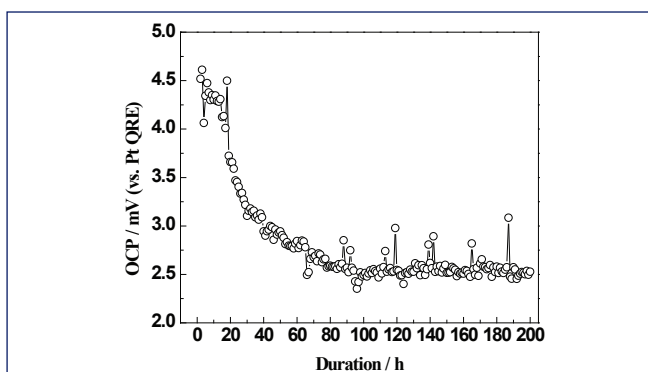


Fig. 1 OCP versus duration of exposure of PyG to UCl_3 -LiCl-KCl molten salt

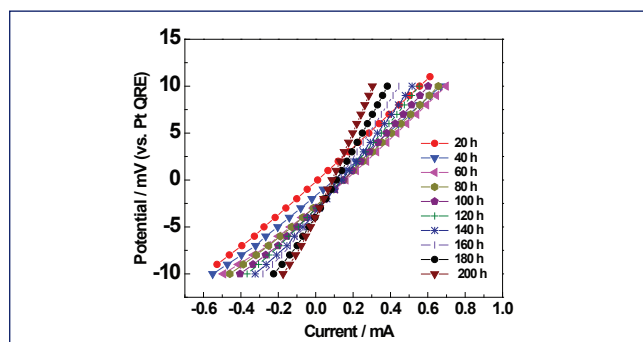


Fig. 2 LPR curves at different time intervals for PyG exposed to UCl_3 -LiCl-KCl molten salt

and R_{ct} (22.33 Ω at 10 h to 45.66 Ω at 200 h) is less indicating that insignificant corrosion of the PyG in molten salt at 600°C. The electrochemical impedance (EIS) measurements were recorded at different frequencies ranging from 10 kHz to 0.1 Hz with voltage amplitude of ± 0.01 V (Figure 3).

The Nyquist plots showed one semi-circle at higher frequencies (Figure 3 inset) and a straight line at 45° angle in the lower frequencies region. Indicating that the PyG electrode undergoes activation polarization resulting in charge transfer resistance (R_{ct}) and Warburg impedance (W) due to the diffusion of U^{3+} ions in the molten salt. There is no weight loss observed even after 200 h exposure. The surface analysis of 200 h tested PyG sample showed similar behavior as fresh as-received PyG. Since there was no weight loss or gain, it was considered that PyG acted as an inert electrode in molten salt.

In summary, PyG is highly inert and showed excellent corrosion resistance to molten salt. Hence, it shows a potential material as pre-standing material or coating on graphite for salt purification and electrorefining processes in pyrochemical reprocessing application.

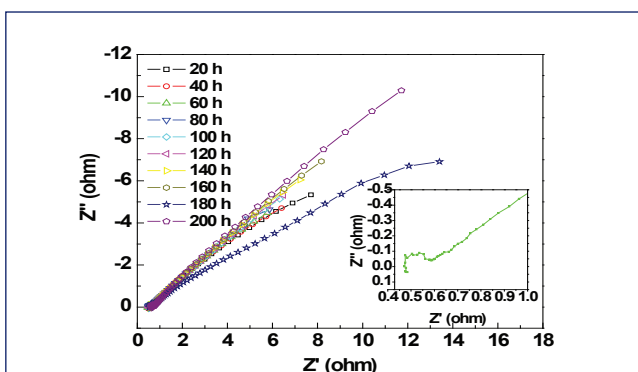


Fig. 3 Nyquist plots of PyG exposed to molten UCl_3 -LiCl-KCl salt

VI.10 Porting and Development of Integrated Simulator Development Platform on x64 hardware

An operator training simulator was developed to impart comprehensive training to PFBR plant operators. The tool/platform used for the development of the simulator is TICSS which runs only on the Tru64 UNIX OS installed on DEC ALPHA hardware. TICSS is an Integrated Development Environment (IDE) equipped with all the necessary features required for operator training and assessment. It is a collection of various subset of tools that aid in the overall development of simulator. The TICSS software stack on ALPHA hardware is shown in Figure 1. The graphics library available in the tool is a proprietary third party product, only the binary version of library and the executables for Tru64 Unix are available. As ALPHA hardware is becoming obsolete the maintenance of the server hardware becomes difficult. Hence in order to overcome the obsolescence of ALPHA hardware, porting of TICSS to x64 based architecture was carried out.

TICSS provides three key modules used in the simulator development namely Promodeller for process modeling, COSLOG and Logic display for development and debugging of plant logics and vdraw for soft control panel development. Few other components like the messaging and data sharing services, logger for saving/loading the state of simulator, and simulator database services form the core of the IDE. All the source codes of these modules along with simulator runtime environment were ported into x64 hardware platform with Linux operating system (CentOS). The interface libraries required to assist these modules on Linux platform were developed. To replace the functionality of proprietary graphics library in the tool, GUIs for instructor, TICSS process model debugger developed with GTK and COSLOG editor is ported using the Cairo graphics libraries. The functionality of soft panel development module is implemented using Genlogic tools. The built-in modules of Genlogic tool were customized and new widgets were developed to emulate the functionality of analog and digital meters, switches, push buttons

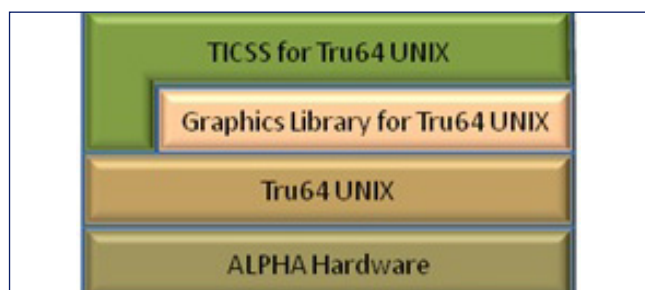


Fig. 1 TICSS software stack on ALPHA Hardware

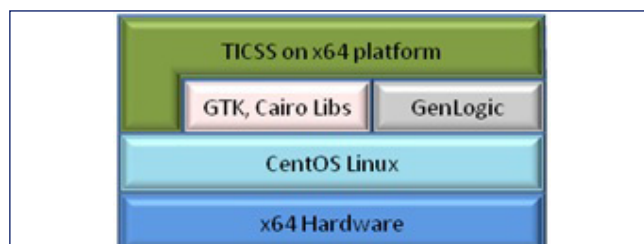


Fig. 2 TICSS after Porting to x64 platform

etc. An interface program is developed to parse, debug and include the developed soft panels into simulator environment. The soft panels for main control room and handling control room of PFBR were developed using Genlogic tool and integrated with simulator. The external modules and database of existing PFBR operator training simulator which contains the configuration of all verified and validated PFBR process and logic components were imported in to runtime environment. The TICSS software stack on x64 hardware is shown in Figure 2.

The functionality testing of all the modules in the ported TICSS tool like instructor, executive, logger etc. was carried out. The simulator is tested for its real time performance in steady and transient states. The hardware panels were tested in integration with the ported simulator on x64 platform. The ported tool is subjected to 24 hours burn-in test to ensure the stability of the tool for an extended period of time. The performance of benchmark transients simulated in PFBR operator training simulator is evaluated and performance was found to be satisfactory. The screenshot of PFBR process flow sheet under x64 platform is shown in Figure 3.

A procedure was developed and tested to simplify the process of porting any existing version of simulator based on TICSS which runs on ALPHA hardware to CentOS running on x64 platform.

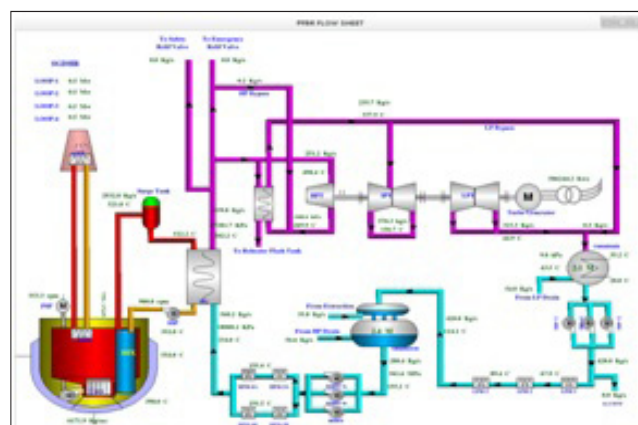


Fig. 3 Screenshot of PFBR process flow sheet with parameters from simulator running on x64 platform

VI.11 Feasibility of Preparation of Metallic U from Pyroprocess Laboratory Waste Solutions using Direct Oxide Electro-Deoxidation Route

Pyrochemical reprocessing of spent metal fuels involves several batch operations pertaining to separation, consolidation, purification, spent salt treatment carried out at high temperatures. During laboratory scale pyroprocessing experiments carried out over the last five years on uranium and uranium based alloys, LiCl-KCl eutectic melt was usually sampled from the melt for estimation of U by traditional Davies and Gray method. Several hundreds of such salt solutions containing U were collected and stored during this period in the pyroprocessing laboratory and it was therefore necessary to develop a flow sheet to recover uranium from the waste analytical solutions for converting it to metallic form for further use in electrorefining experiments. It was felt that aqueous laboratory waste could be treated in the conventional way for precipitating uranium as ammonium di-uranate (ADU) and electroreduce it to metallic uranium by molten salt based Direct Oxide Electrochemical Reduction (DOER) route. This process in laboratory scale was demonstrated by initially precipitating uranium as ADU from about 10 L of nitrate form of laboratory analytical waste. ADU was then analyzed for various impurities such as Fe, Cr, Ni, Cu, Zn, Ag and Cd using AAS. Total U in ADU was also estimated using Davies and Gray method. The precipitated product was then taken in 70 g batches and calcined at 800°C and pelletized. Finally the uranium oxide pellets were reduced under Ar-4 wt.% H₂ atmosphere at 1600°C to prepare sintered UO₂. Flow-sheet for preparing sintered UO₂ pellets from ADU is shown in Figure 1.

These pellets were subsequently loaded in 30 g batches in cathode basket in a high temperature electrolyser

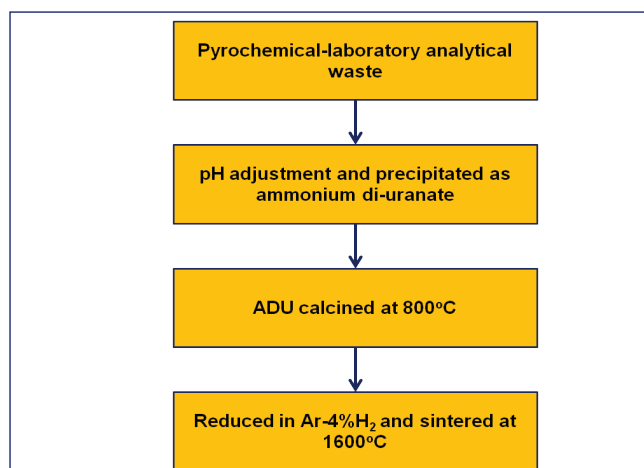


Fig. 1 Flow-sheet for recovery of U from laboratory salt waste recovered as ADU

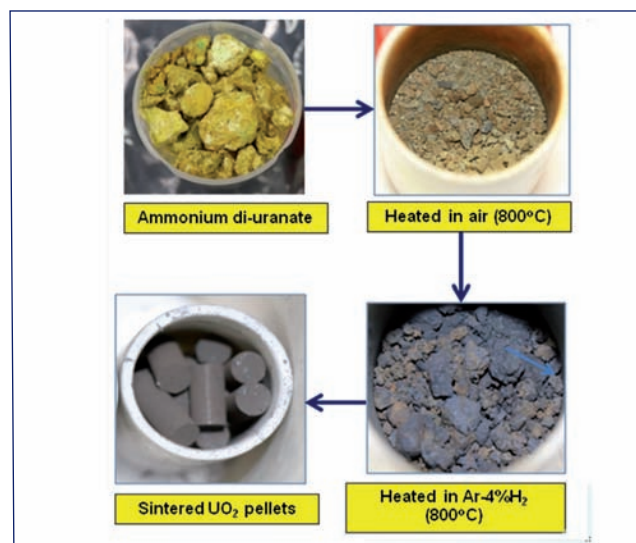


Fig. 2 Pictures of various products obtained at various stages during the preparation of sintered UO₂ pellets

vessel containing 450 g of LiCl-1wt.%Li₂O melt operated at 650°C with Pt as anode. Figure 2 shows various products obtained at various stages during the preparation of sintered UO₂ pellets.

Prior to the electro-reduction experiments, cyclic voltammetry was carried out to determine the Li⁺|Li cathodic onset potential and onset potential of chlorine evolution at 650°C thereby establishing the purity of the melt. Ni|NiO was used as reference electrode. Electroreduction was carried out at constant current (5 A) mode for 8 h. The reduced product after electrolysis was distilled under vacuum at 900°C for removing the adhered LiCl salt (about 20 - 30 wt%). Few pellets after distillation were further arc-melted and from the metallic luster of the consolidated product, near complete reduction with extent of reduction of >95% was confirmed (Figure 3). Thus, the proposed method for the recovery of uranium as U metal from pyrochemical laboratory analytical waste is confirmed.

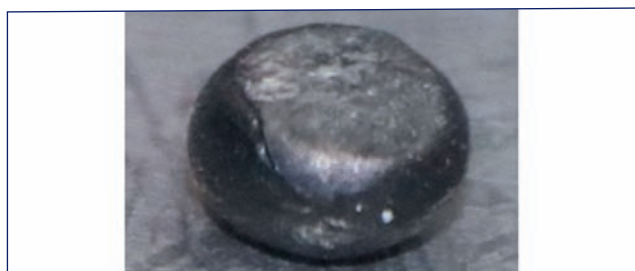


Fig. 3 Electro-reduced U metal after distillation of salt and arc-melting

VI.12 Studies on the Separation of Uranium in Presence of Rare Earths (Yttrium And Cerium) and Re-Oxidation of Uranium from Cadmium Alloy

Pyrochemical reprocessing based on the molten salt electrorefining is best suited for reprocessing spent metallic fuels. This is a high temperature process and the separation is based on the differences in the stabilities of the chlorides of fuel elements and the fission products. LiCl-KCl eutectic loaded with small percentage of actinide chlorides is used as an electrolyte in the process. The alkali, alkaline earth and rare earth fission products get converted to their respective chlorides (being more stable) and accumulate in the salt phase during electrorefining. The noble metal chlorides being the least stable, their fission products do not convert to their chlorides and they get retained in the anode basket as metals. The actinide chlorides being intermediate stable, they can be converted to their chlorides and electro transported to cathode. Two types of cathodes were used: only uranium deposits when a solid mandrel is used as a cathode; and uranium, plutonium and minor actinides gets co-deposited when liquid cadmium is used as cathode.

As mentioned, alkali, alkaline earth and rare earth chlorides gets accumulated and their concentration builds up in the electrolyte during electrorefining. Rare earths get deposited along with actinides and contaminate the product. Hence, rare earths need to be removed from the salt phase so that purified salt can be reused. Since the electrolyte has actinide chlorides also in the salt phase, actinides have to be removed from the salt phase before the removal of rare earths. Actinides from the salt phase are removed by Actinide Draw Down Process (ADDP) into Cd metal phase. The actinides from the Cd metal phase were again oxidized back to salt phase and the salt is reused. As a part of

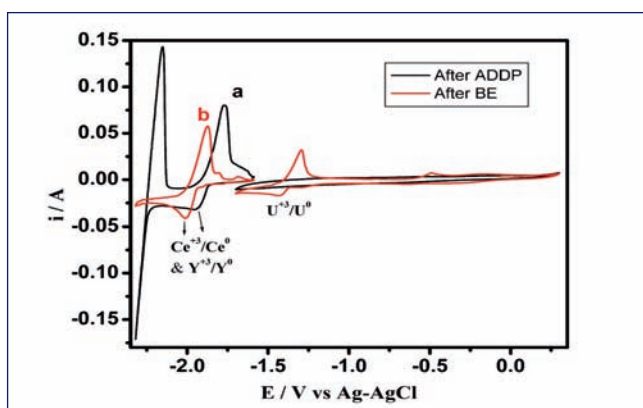


Fig. 1 Cyclic voltammograms of salt (a) after ADDP and (b) after back extraction

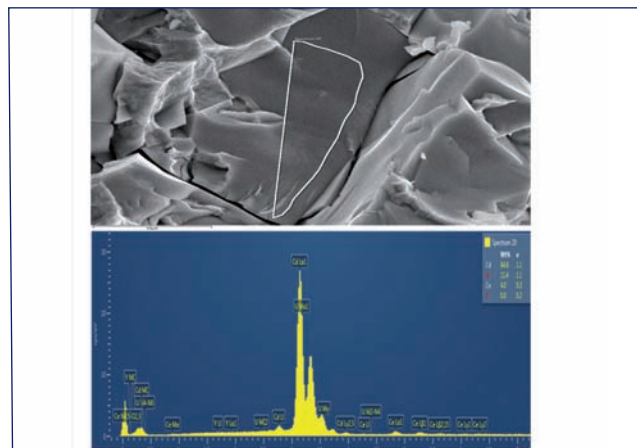


Fig. 2 SEM-EDX analysis of Cd phase after ADDP

the studies, the separation of the U from salt phase in presence of rare earths in LiCl-KCl eutectic melt have been carried out in our laboratory. In continuation of the ADDP work, studies on the separation of U from LiCl-KCl-UCl₃-CeCl₃-YCl₃ and reoxidation of U from Cd metal have been taken up.

Experiments were carried out by taking 0.9wt.% to 3.45wt.% of U in the form of UCl₃ and similar percentage of Ce and Y together in the form of their trichlorides in LiCl-KCl. The U was separated/drawn down into Cd metal phase by equilibrating with Li-Cd alloy. Li-Cd alloy required for the experiments was prepared in our laboratory.

UCl₃ was loaded into the salt by equilibrating U metal with CdCl₂ at 773K. Commercially available high pure CeCl₃ and YCl₃ were used in the studies. Experiments were carried out in the temperature range of 773 to 800K in inert atmosphere glove box. U from the Cd phase was oxidized back into the salt phase by equilibrating with CdCl₂ in LiCl-KCl melt at 773K.

U in the salt was analysed by Davis & Grey potentiometry, U in Cd and Ce and Y in the salt and the Cd phase were analysed by Inductively Coupled Plasma Optical Emission Spectroscopy (ICPOES). The U was separated from the salt phase and significant percentage of Ce and Y also got extracted. About 68% of U was back extracted from Cd phase to salt phase.

Figure 1 Shows the cyclic voltammograms of the salt phase after ADDP and back extraction experiments. Figure 2 shows the SEM-EDX analysis of Cd phase after ADDP confirming the presence of U with small percentage of Ce.

VI.13 Numerical Modeling of Anodic Dissolution Process of Spent Metal Fuel in Molten Salt Electrorefiner for Pyroprocessing

In pyrochemical reprocessing or pyroprocessing, actinides from chopped spent metal fuel pins loaded in a steel anode basket are electrochemically dissolved in molten salt during electrorefining operation. The composition of the metal fuel is basically U-Zr or U-Pu-Zr. Zr is added to keep the melting point of the fuels sufficiently high and to prevent fuel clad chemical interaction. Since Zr has a high standard redox potential next to that of U, it is inevitable that some part of Zr dissolves with the actinides in molten salt as U in the fuel is dissolved by the anodic dissolution. In pyroprocessing, dissolution of Zr from anode is to be prevented during electrorefining operation since it will increase the operating temperature at cathode processing step. It will also have negative influence on the decontamination against noble metal FPs. Zr will also increase difficulty in actinide recovery and decrease the processing rate of the electrorefiner throughout in long term. So the detailed investigation on the relation between the operation condition of electrorefining and the anode behaviour are thus of great importance, and development of proper numerical model of anodic dissolution process will be an indispensable tool for the design of the electrorefining process for pyroprocessing.

In this regard a numerical model for simulating anodic dissolution process is developed. The model is based on two-layer diffusion model where outer diffusion layer developed due to bulk flow and mass transfer phenomena remain same but inner porous diffusion layer formed due to undissolved Zr changes with the actinides and Zr dissolution, as shown in Figure 1.

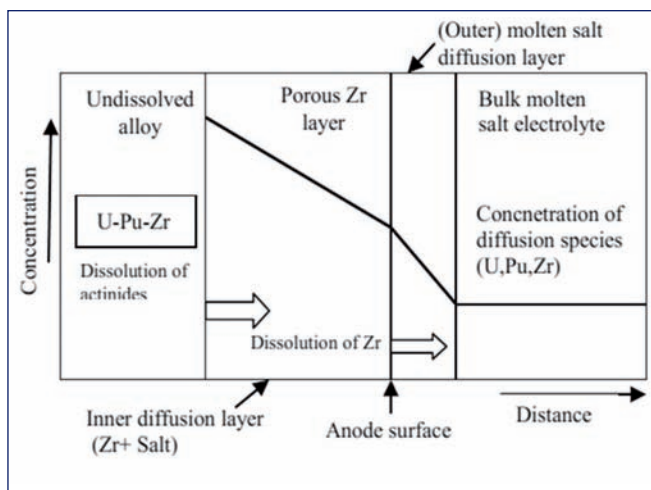


Fig. 1 Schematic view of anode dissolution model

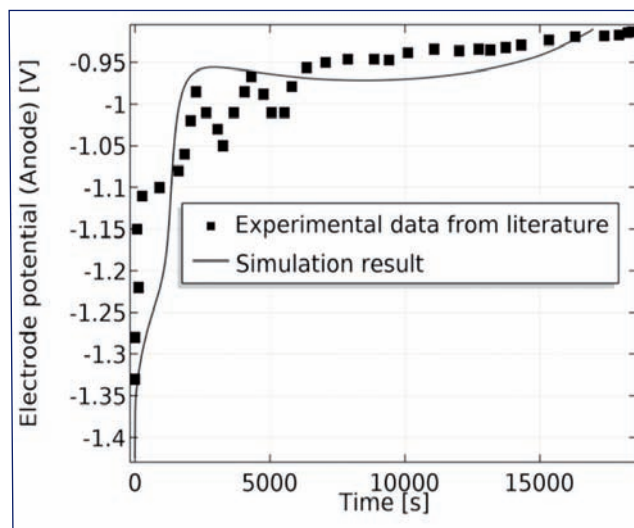


Fig. 2 Change in anode potential during electrorefining test (literature data) and predicted using anode dissolution model

The numerical modeling of anodic dissolution process is developed in commercially available COMSOL multiphysics software platform. The simulation results from numerical model are validated with experimental results given in literature. Figure 2 shows the simulation and literature data for variation in the anode potential with time. The electrode potential predicted by the model showed better agreement with literature data. Figure 3 shows the simulation results for dissolution of U, Pu and Zr from anode with time. Simulation results show that Zr and actinides dissolution are affected by the multiple diffusion layer formation.

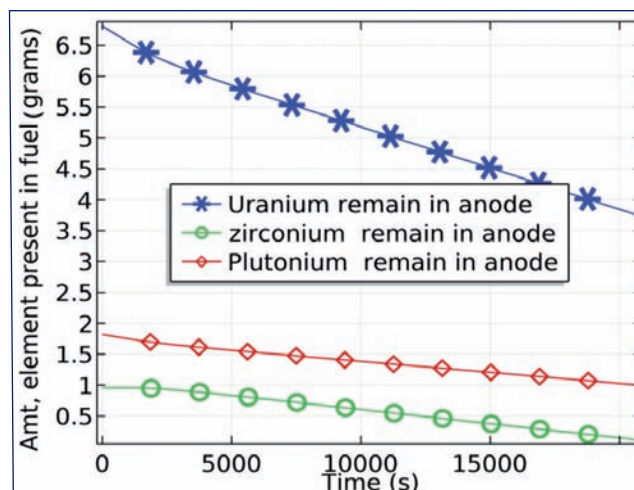


Fig. 3 Change in amount of U, Pu & Zr in anode with time

VI.14 Quality Assurance and NDE during Fabrication of Geometrically Safe Annular Tanks for Nuclear Reprocessing Applications

Annular tanks are the distinct types of critically safe tanks used in reprocessing plants for storing process liquid with high concentration of fissile material. Annular tanks construction is by cold rolling of two shells of different diameters assembled concentrically forming the required annular gap of 60 mm. The annular space of the tank is closed with flat heads at the top & bottom ends. Process liquid is stored inside the annular space and various size of nozzles are welded to the top and bottom flat heads for liquid transfer and process data acquisition. Since annular tank is used for handling liquid with high concentration of fissile material, the fabrication of annular tank is very critical and annular space has to be maintained within a close dimensional tolerance to avoid critical mass of fissile material. Hence, these annular tanks must be precisely fabricated to minimize the distortion during welding of support pad plates to outer shell, Nozzles to flat heads etc. Austenitic Stainless Steel 304 L has been used as material of construction for annular tank and its components due to its inherent corrosion resistance in acidic environment and also ease of fabricability. The outer and inner shell diameters are 1506 mm and 1362 mm(OD) respectively with annular gap of 60 mm and overall height of 2512 mm of a typical annular tank as shown in Figure 1. The inner and outer shells are connected by top and bottom flanges where deep feed nozzles are located on a particular PCD for processing the aqueous solution. The deep nozzles are supported by spacer rings in the annular gap to maintain the consistent gap.

Fabricability and inspectability are the two important areas need to be addressed for such critical tanks. In fact, the deep nozzles and air sparger bends are positioned between the annular gap. Once the top and bottom flanges welding are completed, many nozzles and supports between annular gap become nearly inaccessible for Non Destructive Evaluation (NDE). Hence during the fabrication stage, rigorous Quality



Fig. 1 Typical Annular Tank

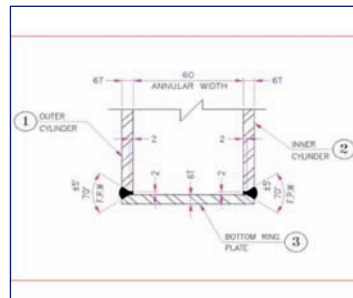


Fig. 2 Corner weld joint



Fig. 3 UT of Corner weld

Assurance (QA) practices coupled with fabrication sequence have been formulated and implemented so that all the weld joints became accessible for NDE as per approved procedure. Various surface NDE methods such as Visual examination, Liquid Penetrant examination and volumetric NDE methods such as Radiographic examination, Leak testing, Ultrasonic examination are employed to achieve the desired quality during fabrication of Annular tanks. Ultrasonic testing of corner weld joints (Joint between inner & outer shells with both top & bottom flanges) as shown in Figure 2 is a real challenge as geometry related discontinuities may also be misconstrued as root side planar defects. To surmount this issue, every indication beyond 20% FSH in UT at root side as shown in Figure 3 has been ascertained for its presence by means of boroscopic inspection through the annular gap. To control distortion during welding in annular tanks, different techniques are implemented such as (a) Providing copper sinks with water jackets for increasing cooling rate, (b) External constraint fixture as shown in Figure 4, (c) Welding sequencing such as skip and back step welding and (d) Use of pulsed GTAW. Pull through gauge (Go-No Go gauge) has been put in place to quantify the annular gap through the length to check the adequacy. A well thought, documented and proven quality assurance practices coupled with manufacturing sequence been put in place to meet design intent.

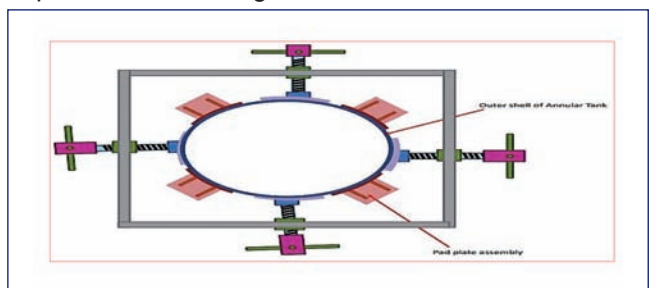


Fig. 4 Fixture for Distortion control

VI.15 Studies on Morphological Properties of Sodium, Fission Product, Structural Material and Mixed Aerosols towards Fast Reactor Safety

In the event of Core Disruptive Accident (CDA) condition in Sodium cooled Fast Reactor, the environmental source term is determined by the activity released from the Reactor Containment Building which in-turn depend on the concentration of radioactive aerosols that remain suspended in the containment. Various models are used to predict the time evolution of aerosol concentration and the critical input parameters required are aerosol morphological properties such as size, shape and density. Codes used for modeling concentration decay inside the containment generally assume the particles to be spherical (unity shape factor) and dense particulates (i.e particle density equals to bulk material density). During CDA conditions, RCB will be bottled-up with the mixture of sodium, fuel, fission product and structural material aerosols. The fuel, fission product and structural material aerosols are generated by vaporization and condensation process with sizes in sub-micron range. Sodium aerosols are generated by combustion process with sizes in micron range ($d_0 \sim 0.95 \mu\text{m}$ depending on prevailing RH%). Further, the size of sodium combustion aerosols increases with time due to coagulation and hygroscopic growth and the other aerosols undergo coagulation with sodium aerosols. Also the sodium aerosols undergo chemical changes with time by reaction with moisture and CO_2 present in ambient environment. All these processes combined together may lead to fractal and porous nature of particles with particle density deviating from the material density and these properties may change with time. Hence experimental studies are carried out at Aerosol Test Facility (ATF) to determine the morphological properties viz. particle diameters, particle density (ρ_p), effective density (ρ_e), shape factor (χ) of sodium, fission product (CeO_2 and SrO_2), structural steel (D9) and mixed aerosols (sodium + fission products). In this study, the required parameters of aerosols are obtained by measurements based on impaction, optical scattering, aerosol charging and electrical mobility based techniques. Parallel sampling

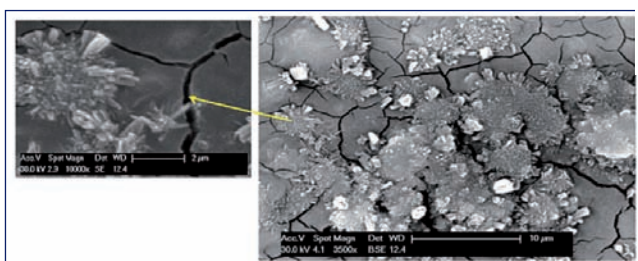


Fig. 1 SEM image of sodium aerosol

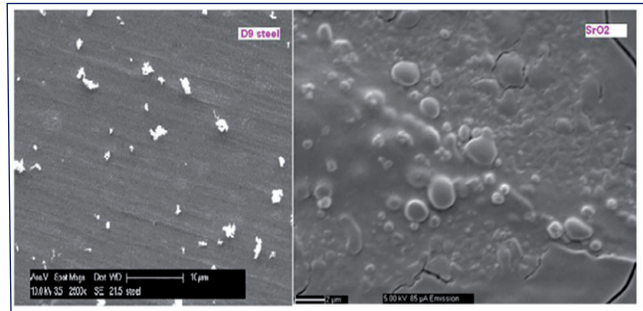


Fig. 2 SEM image of D9 steel (left) and SrO_2 aerosol

by coupling QCM-MASTERSIZER and ELPI-SMPS with both real time and off-line monitoring techniques were used to determine morphological properties.

Particle dynamic equations for the agglomerated aerosols that are porous and non-spherical aerosols were corrected through the relation given below.

$$d_{eq} = \alpha^{1/3} d = \left(\frac{\rho_p}{\chi \rho_m} \right)^{1/3} d \quad \text{--- (1)}$$

'd' is the actual diameter of the agglomerate 'd_{eq}' is the equivalent diameter measured by the instrument and 'α' is the correction factor due to the reduction in density of particle from that of material density due to agglomeration. In this study, particle density, porosity (p) and shape factors are computed from the equations given below,

$$\rho_p = \left(\frac{MMAD}{MMD} \right)^2 \chi \frac{C(MMAD)}{C(MMD)} \quad \text{.... (2)}$$

$$P = 1 - \frac{\rho_p}{\rho_m} \quad \text{..... (3)}$$

$$\chi = \left(\frac{d_{ve}}{MMD} \right)^2 \frac{C(d_{ve})}{C(MMD)} \quad \text{.... (4)}$$

Here MMAD is derived from QCM; MMD and d_{ve} are measured from MASTERSIZER. $C_c(d)$ is the Cunningham slip correction factor corresponding to the selected diameter. ρ_e is the effective density of aerosol which includes the effect of both particle density and shape factor, which is widely used for non-spherical and porous particles.

$$\rho_e = \frac{\rho_p}{\chi} = \left(\frac{CMAD}{CMMD} \right)^2 * \frac{C_c(CMAD)}{C_c(CMMD)} \quad \text{.... (5)}$$

Here CMMD and CMAD are measured by SMPS and ELPI respectively. Aerosols are generated and suspended inside the chamber of 1 m³ during the experiments. MASTERSIZER measures the particles in both air and liquid suspension. The values of MMD for sodium aerosols are measured in air medium by

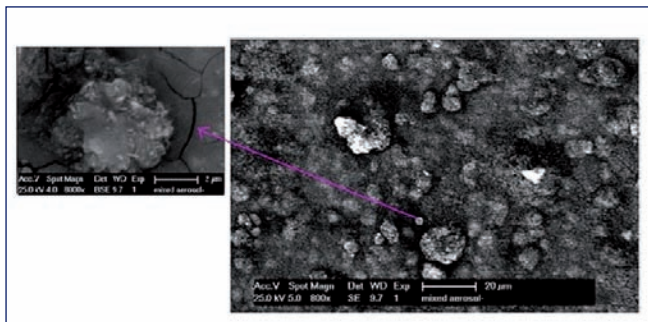


Fig. 3 SEM image of mixed aerosol

real-time analysis, while, the offline analysis is adopted for CeO₂, SrO₂ and mixed aerosols by drawing into the water medium (for SrO₂ and CeO₂) and liquid paraffin medium (for mixed SrO₂+CeO₂+sodium).

The Aluminum foils are placed at the bottom of the chamber in each experiment. The settled down aerosols on the foil are analyzed by SEM-EDAX.

Morphological properties derived from the measured parameters for various types of aerosols are given in Tables 1 and 2. The corresponding SEM images of aerosols is given in Figures 1,2 and 3.

ρ_p values obtained from QCM-MASTERSIZER technique are compared with the ρ_e values determined by SMPS-ELPI technique for the sub-micrometer aerosols' case.

Table 1: The derived parameters of sodium combustion aerosol using QCM-MASTERSIZER technique

Initial RH%	Measured Parameters			Derived parameters			T (min)
	d_v (μm)	MMAD (μm)	MMD (μm)	ρ_p (g/cc)	P (%)	X	
75 % (2 g/ m ³)	1.82	2.51	1.8	1.9	25	1.02	1
	1.95	2.48	1.92	1.64	35	1.03	4
	2.12	2.7	2.0	1.79	30	1.12	8
	2.46	3	2.4	1.54	39	1.05	15
	2.62	3.2	2.6	1.5	41	1.01	24
	Average				1.67		1.05
55 % (2 g/ m ³)	1.45	1.65	1.42	1.33	48	1.04	1
	1.54	1.67	1.48	1.26	50	1.08	3
	1.63	1.81	1.58	1.30	49	1.06	6
	1.68	2.05	1.63	1.55	39	1.06	11
	1.73	2.25	1.71	1.69	33	1.02	20
	Average				1.43		1.05
30 % (2 g/ m ³)	1.35	1.4	1.3	1.15	55	1.07	2
	1.41	1.52	1.33	1.29	49	1.12	21
	1.55	1.65	1.5	1.2	53	1.06	29
	1.56	1.68	1.52	1.21	52	1.05	41
	1.62	1.69	1.58	1.14	53	1.05	54
	Average				1.22		1.10

Table 2: Effective densities of aerosols measured using SMPI-ELPI technique at 50% RH

Type of Aerosol	Average density ρ_e (g/cc)
D9 steel	3.34
CeO ₂	4.23
SrO ₂	3.16

In the case of sodium aerosols, the average particle densities and the standard uncertainties arrived at 75%, 55% and 30% RH are 1.67 ± 0.41 , 1.43 ± 0.36 and 1.2 ± 0.31 respectively. Individual particle densities showed slightly increasing trend from 1.14 ± 0.14 to 1.90 ± 0.23 g/cc with the increase of humidity. The chemical behaviour is the dominant cause for the increasing density with higher humidity. Sodium aerosols are mostly spherical (individual shape factors varied from 1.01 ± 0.06 to 1.12 ± 0.06) for RH of 55% and 75%. This is due to colloidal nature of aerosol at the time of formation $t = 0$ (higher amount of hydroxide content) and particles are hygroscopic at higher humidity levels. The aerosols are slightly distorted towards cylindrical at 30%RH (individual shape factors varied from 1.05 ± 0.06 to 1.12 ± 0.06). This is due to solid nature of particles made of lesser content of hydroxide than carbonate.

For D9 Steel aerosols ρ_p and ρ_e are 3.92 ± 0.58 g/cc and 3.34 ± 0.69 g/cc respectively. The particle shape is found to be chain like structures ($\chi = 1.12 \pm 0.16$). For CeO₂ aerosols, ρ_p and ρ_e are 4.27 ± 0.54 and 4.23 ± 0.88 g/cc respectively. CeO₂ aerosols found to be spherical ($\chi = 1.00 \pm 0.14$). In case of SrO₂ aerosols, ρ_p and ρ_e are 3.57 ± 0.48 and 3.16 ± 0.57 g/cc respectively. SrO₂ aerosols are found to be nearly spherical ($\chi = 1.08 \pm 0.15$). In case of mixed aerosols ρ_p is around 2.0 ± 0.3 g/cc which is lesser than 2.57 g/cc (weighted mean based on aerosol concentration of sodium, CeO₂ and SrO₂ with perfect spherical approximation). The mixed aerosol particle shape is found to be deviated from spherical ($\chi = 1.13 \pm 0.16$ to 1.22 ± 0.17). It showed cluster aggregates i.e. bonded CeO₂ - SrO₂ aerosol with Sodium. All the three sub-micrometer aerosols have densities much less than material densities and varied in terms of packing fraction. The study shows that the particle densities of all the aerosols tested are found to deviate from that of material. They change with progress of time and tend to attain saturation value. The key parameters used for the estimation of depletion of sodium as well as mixed aerosols concentrations inside the containment building have necessarily to be redefined, so that realistic estimation of environmental source term may be obtained.

VI.16 Defect Detection and Quantification of Cracks using Active Thermography in 550 NB Pipe Elbow Model

Fail-safe design criteria such as Leak-Before-Break (LBB) based on fracture mechanics concepts requires the demonstration of integrity of the piping components. LBB design ensures that the crack grows through the thickness leading to detectable leakage and demonstrates that the crack will stabilise under the maximum loading conditions between the successive inspections. This study was carried out on fatigue cracks on pipe elbow at SML. This investigation was carried out on 550 NB AISI 304 pipe elbow with 15 mm thickness and 90° pipe bend for PFBR Secondary Sodium Circuits. The pipe was maintained under constant amplitude sinusoidal cyclic loading (0 – 130000 cycles). To detect the natural cracks and to quantify them, Lock in Thermography, an advanced NDE technique was carried out.

It is a well known fact that temperature and its distribution is one of a prime factor, which manifests on the state of components and plants in service. The magnitude and distribution of the temperature is a pure indicator of departure from normal/acceptance criteria. All the bodies above absolute zero emit electromagnetic radiation. At ambient and above, these radiations fall in the IR region (0.75 μm to 1000 μm) of the electromagnetic spectrum. With the help of IR detectors, these radiations can be converted into electrical signals. Advanced instrumentation parts, takes control of these electrical signals to be converted into a display image, which represents the complete surface temperature mapping on the object. With suitable calibration, it is possible to get the temperature of any point on the surface of the object. This non destructive test method is referred to as IR imaging, Thermography or Thermal Imaging. The unique advantages of this method include i) non contact nature ii) real time capability iii) ability to provide full fledged image iv) applicability on engineering components. Thermography is based on the principle that flaws or defects present on the surface or beneath exhibit different thermal radiation signature from its surroundings. This can be caused due to heat sources present within body or it can be induced artificially through external means. Generally, two techniques are adopted for carrying out Thermographic investigation i) Passive



Fig. 1 Experimental setup

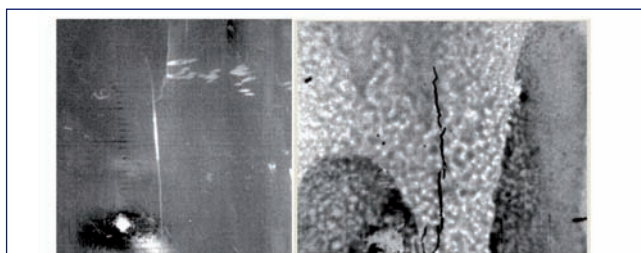


Fig. 2 Thermal Image of notch and natural crack

and ii) Active. Passive technique involves recording the natural heat distribution on the surface of an object. The technique is said to be active when external stimulus is used to disturb the thermal equilibrium of the inspecting component

Lock in Thermography is an advanced NDE imaging technique used for characterization of materials. This technique is better suitable for detection and quantification of surface and sub surface defects. It uses periodic sinusoidal thermal excitation in order to derive information on reflected thermal wave phase and magnitude from the object. By modulating the frequency the defect depth can be detected.

Experimentation was carried out using Cedip Silver 420 thermal imaging system (Figure 1). It is a focal plane array based IR camera with thermal sensitivity of 25 mK and maximum frame rate of 50 Hz. The detector used was Indium Antimonide with spectral sensitivity in the range of 3 to 5 μm. Acquisition of the thermal images of the sample was carried out using the ALTAIR software.

A notch initially measured to be 22.5 mm long and 2.00 mm depth was created on pipe. Due to cyclic loading, crack growth observed at the notch tips were also detected (Figure 2). For quantification, sizing of defects, the pixels in thermogram were calibrated for known length in the thermal image and subsequently the pixel value for the unknown feature was derived. The estimated crack length was validated with visual examination measurements. In order to obtain defect depth information, Thermal diffusion length (μ) which is the distance at which the thermal wave attenuates to 67% of its original strength was measured, is the function of defect depth. Thermal waves attenuate as they travel through material. Thermal diffusion length is given by following equation.

$$\mu = \sqrt{\frac{2k}{\omega\rho c}}$$

where, μ = Thermal diffusion length
 k= Thermal conductivity
 ω =angular frequency
 ρ =density of material
 c=heat capacity

	Notch Crack	Natural Crack
Length	100.85 mm	154.77 mm
Depth	11.39 mm	12.74 mm

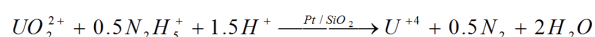
Length of the upper crack and branched crack of the notch is 20.16 and 36.8 mm respectively. Length of the crack

from the bottom of the notch is 43.89 mm. Apart from the crack at the notch region, a natural crack was observed at the opposite side to the notch. The natural crack has been labeled as top middle and bottom cracks with lengths of 103.2, 18.36 and 33.21 mm respectively. Depth of the natural crack and crack at notch region are quantified to be 12.74 and 11.39 mm respectively (Table 1). Lock-in thermography could successfully quantify the cracks.

VI.17 Catalytic reduction of U(VI) with Hydrazine using Pt/SiO₂ Catalyst in Nitric Acid Medium

In nuclear fuel reprocessing plant, hydrazine stabilized U(IV) is used as the reducing agent for the partitioning of U and Pu. This U(IV) is produced by electrochemical reduction of U(VI) using Pt / titanium electrodes with hydrazine nitrate as a stabilizing / holding agent. Some limitations of this method include poor kinetics, less efficiency (50-60%) and the need for frequent maintenance of the electrodes.

In the present study, an alternative chemical method developed in-house for the reduction of U(VI) using hydrazine as reducing agent over Pt/SiO₂ catalyst is described. The influence of some of the process parameters viz., mixing speed, catalyst loading, acidity, concentration of hydrazine and uranium, and temperature on the kinetics of catalytic reduction of U(VI) have been investigated. A kinetic model based on the Langmuir Hinshelwood (L-H) mechanism, had been found to best fit the experimental data. These experiments were performed in a batch SS reactor. The reduction could be described by the following equation.



The best fit for the experimental data was chosen on the premise that one among the three elementary steps of this reduction process, viz., adsorption of the reactants, surface reaction between adsorbed molecules and

desorption of products, is the rate-controlling step.

The values of intrinsic rate parameter, adsorption equilibrium constants for model equations were determined by nonlinear regression analysis. Calculations were performed by using MATLAB. The model equation considering the reaction of adsorbed reactants viz., uranium, nitric acid and hydrazine on the catalyst surface is

$$r_A = \frac{kK_A^2K_BK_C^3C_A^2C_B^3C_C^3}{(1 + K_A C_A + K_B C_B + K_C C_C)^6}$$

Where k represents rate constant (kmol.kg⁻¹.s⁻¹), K_A, K_B and K_C represent adsorption equilibrium constants (m³.kmol⁻¹), C_A, C_B and C_C represents the concentrations of U(VI), nitric acid and hydrazine (kmol.m⁻³) respectively.

Figures 1 and 2 show comparisons between experimental results and the model estimates, for a typical case wherein the agreement was found to be reasonably good.

Based on the observations presented above, it is reasonable to conclude that the surface reaction between adsorbed reactants uranium, hydrazine and nitric acid on the surface of the catalyst explains the catalytic reduction of U(VI). Based on the Arrhenius plot for the reaction, the apparent activation energy of the reaction was estimated to be 74.5 kJ/mol, suggesting a chemical reaction-controlled process.

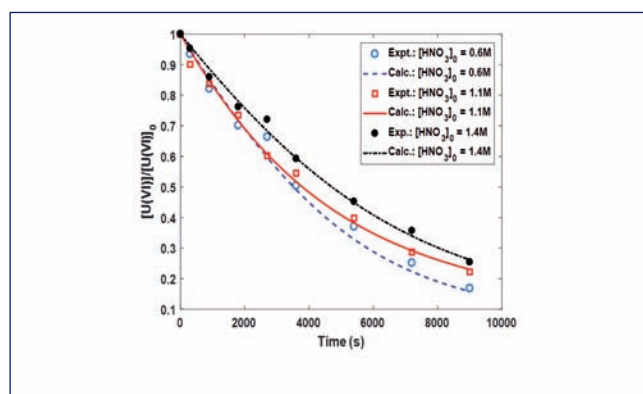


Fig. 1 Comparison between experimental and calculated concentration profiles of uranium

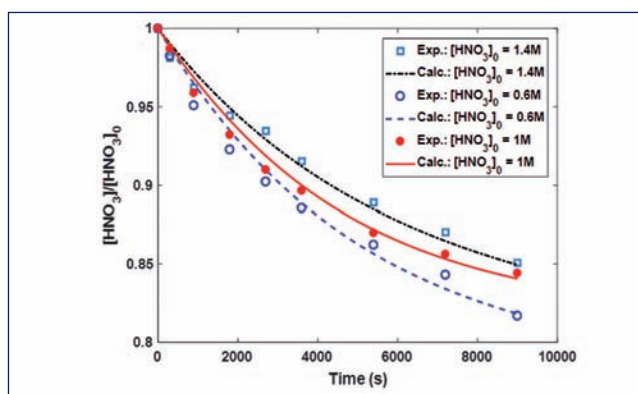


Fig. 2 Comparison between experimental and calculated concentration profiles of nitric acid

VI.18 Modeling and Experimental Studies on the Dissolution behavior of Simulated MOX Pellets in Nitric Acid Medium

Plutonium rich mixed oxide (MOX) is used as a fuel in commercial Fast Breeder Reactors (FBR). Among all the operations carried out during the reprocessing of spent FBR fuel by PUREX process, dissolution is one of the most critical processes. Carrying out dissolution in a continuous mode would help improve safety and render the process economical. Data on the kinetics of dissolution of (U, Pu) mixed oxide (MOX) fuel pellets in nitric acid are required for designing a continuous dissolution system for the reprocessing of FBR spent fuel by PUREX process.

In view of the above, systematic investigations were carried out on the solid solutions of (U, Ce) simulated MOX pellets in nitric acid, with Cerium (Ce) as the nonradioactive surrogate for Pu. Ce has been chosen owing to the following; (i) comparable ionic radii of Ce^{4+} and Pu^{4+} ions, (ii) similar thermal and material properties of the solid solutions of $(U,Ce)O_2$ and $(U,Pu)O_2$, (iii) similar thermodynamic properties of both CeO_2 and PuO_2 , and (iv) similar leaching behavior of both these oxides from immobilized matrices. The analogous solid state and electrochemical properties of these two oxides further ascertain the deployment of Ce as an appropriate surrogate for Pu. Four different (U, Ce) O_2 solid solutions with 15, 22, 28 and 35 atom % of Ce (in the metal fraction) were fabricated by the citrate gel combustion route and employed in this investigation (Figure 1). The effects of initial concentration of nitric acid, composition of the pellet, rate of mixing and temperature have been studied under typical PUREX process conditions.

The apparent activation energy of the reaction under the experimental conditions was found to be about

26 kJ/mol/K. The effects of different influencing parameters on the rate of dissolution were investigated systematically. The dissolution profile of all these pellets under all conditions were found to exhibit a 'S' shape. This is possibly due to the auto catalytic role of nitrous acid produced in-situ during dissolution.

The Ce content in the MOX pellet was found to be inversely proportional to the rate of the reaction. The composition of the NO_x gases liberated during the composition of the NO_x gas evolved during the reaction was analyzed by scrubbing the off gas in NaOH scrubbers and measuring the sodium nitrate and nitrite ions by ion chromatography. These data would be very useful in understanding the reaction mechanism.

Under the given experimental conditions, the intensity of mixing was found to have a retarding effect on the kinetics of dissolution up to 600 rpm. Beyond this it almost remained constant. This is probably due to the dispersion of the nitrous acid produced at the pellet-solution interface from there to the bulk of the reaction mixture. Hence its availability at the interface, the reaction zone, is reduced which in turn diminishes its accelerating effect on the rate of the reaction. Hence, all the subsequent kinetic experiments were conducted at a constant rate of mixing of 600 rpm as the rate parameters determined under these conditions would be intrinsic in nature and would be devoid of diffusional control.

The experimental and analytical methodology developed during these studies will be extended, with appropriate modification wherever required, to understand the dissolution behavior of Pu rich MOX fuel dissolution in nitric acid in the future.

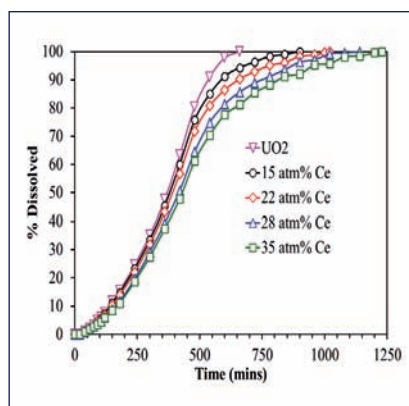


Fig. 1 Effect of Ce content on the dissolution behavior of (U, Ce) MOX pellets in nitric acid medium

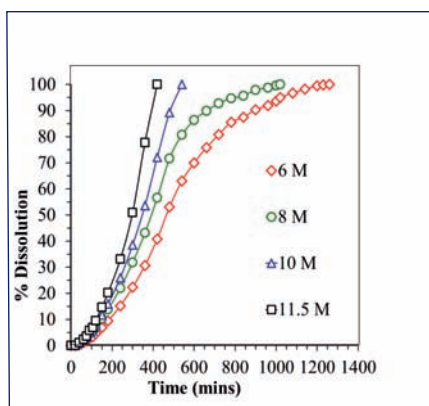


Fig. 2 Effect of initial concentration of nitric acid on the dissolution of $(U_{0.78}Ce_{0.22})O_2$ MOX pellets

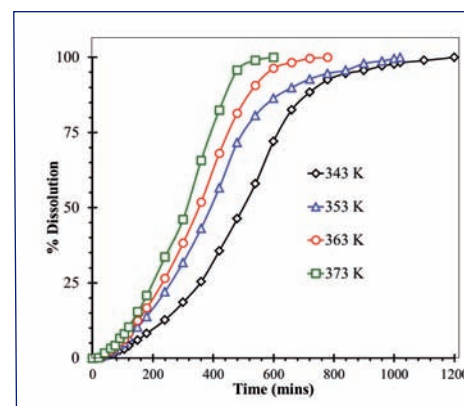
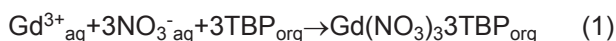


Fig. 3 Effect of temperature on the dissolution of simulated $(U_{0.78}Ce_{0.22})O_2$ MOX pellets

VI.19 Solvent Extraction Studies to Evaluate Gadolinium as a Soluble Neutron Poison in FBR Spent Fuel Reprocessing

Special consideration is required for the design of FBR spent fuel reprocessing plant with respect to nuclear criticality safety. This is particularly important for fast reactor fuel reprocessing due to the higher fissile material content in the process streams. In order to overcome this by design, addition of a soluble neutron poison was found to be more effective. Because of its high thermal neutron absorption cross section and its chemical compatibility with the PUREX process, Gadolinium (Gd) qualifies as a suitable candidate. As the recycled fuel specification has a very stringent upper limit for neutron poison impurities, it is essential to investigate the solvent extraction behavior of Gd under typical Purex conditions prevalent during FBR spent fuel reprocessing. In this context solvent extraction investigations were carried out by using a constant area stirred Lewis Cell. In all these experiments, mixing was carried out for 30 minutes which was sufficient for the equilibrium to be established. Subsequently, the mixture was allowed to settle for about 5 minutes for the phase separation.

The extraction behaviour of Gd(III) in TBP-HNO₃ system is very similar to that of the trivalent lanthanides and the overall chemical reaction could be represented by the following set of equation:



The apparent equilibrium constant pertaining to this reaction (Equation 1) could be represented as:

$$K_{\text{Gd}} = \frac{[\text{Gd}(\text{NO}_3)_3 \cdot 3\text{TBP}]}{[\text{Gd}^{3+}][\text{NO}_3^-]^3[\text{TBP}_f]^3} \quad (2)$$

The expression for the distribution coefficient of Gd (D_{Gd}) is given in Equation 3

$$D_{\text{Gd}} = \frac{[\text{Gd}(\text{NO}_3)_3 \cdot 3\text{TBP}]}{[\text{Gd}^{3+}]} \quad (3) \quad K_{\text{Gd}} = \frac{D_{\text{Gd}}}{[\text{NO}_3^-]^3[\text{TBP}_f]^3} \quad (4)$$

Extraction of Gd from its solutions of different concentrations (1-5 g/L) from 3.5 M nitric acid into an organic medium containing 10, 20 and 30 volume % TBP in *n*-DD was studied. The results are presented in Figure 1. It is evident from the latter that the D_{Gd}

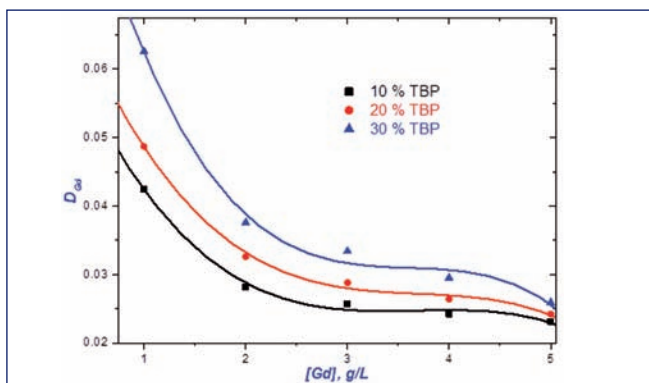


Fig. 1 Variation of D_{Gd} as a function of Gd

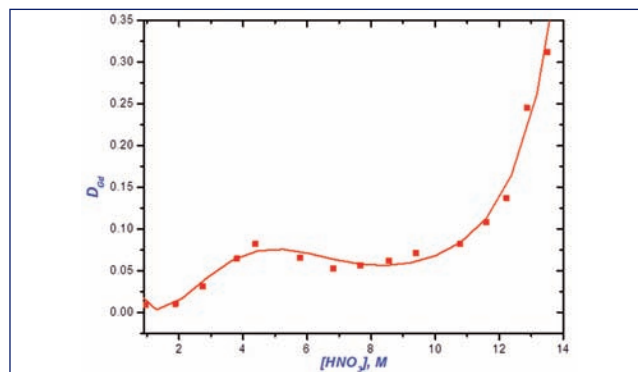


Fig. 2 Variation of D_{Gd} as a function of nitric acid

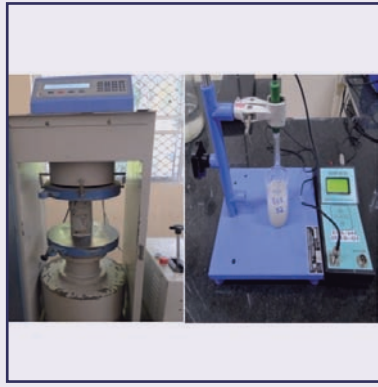
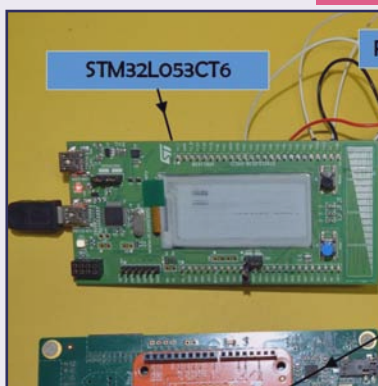
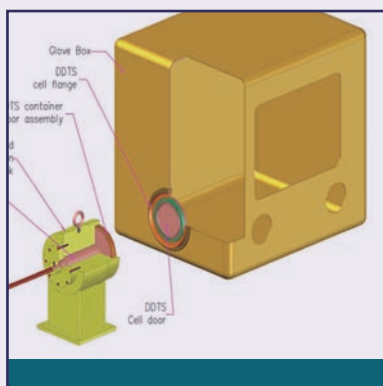
decreases with an increase in the concentration of Gd at a given concentration of TBP. It increases with the concentration of TBP for a given concentration of Gd.

The concentrations of Gd were arrived at based on the consideration of criticality safety. These values were rather low as compared to the concentration of the actinides in the process streams. Hence, the typical Gd concentration in a process stream would be far below the limits of its saturation in the organic stream. Hence, as predicted by Equation 3 the value of D_{Gd} decreases with an increase in the concentration of Gd.

The dependence of the extraction of Gd in nitric acid into an organic stream containing 1.1 M TBP in *n*-DD on varying concentrations of nitric acid (1-13.5 M) has been investigated. These results indicate that the D_{Gd} increases marginally with the concentration of nitric acid up to 4.5 M, and then drops slightly in the region 4-8 M and once again increases with nitric acid concentration as shown in Figure 2.

As the typical acidity employed in FBR fuel reprocessing streams would be about 4-6 M, the results assure better decontamination of Gd(III) as its D_{Gd} value is quite low in this region. The increase in D_{Gd} beyond 8 M clearly shows that there is a change in extraction mechanism. It is surmised that this increase may be due to the formation of some extractable higher charged complex formed between Gd(III) and nitrate ions.

The distribution behavior of Gd(III) in TBP in the presence U(VI) was studied which indicates the feasibility of Gd decontamination under typical PUREX process conditions. The value of D_{Gd} is very low (0.025) when the organic phase is 100% saturated with uranium. The U(VI)-TBP complex which is more soluble in the organic phase than its Gd(III) counterpart, is getting stabilized more in the TBP phase than the Gd(III)-TBP complex. Hence Gd(III) is not extracted in the presence of U. Thus it could be concluded confidently that Gd decontamination during FBR fuel reprocessing is highly feasible.



CHAPTER VII

Infrastructure Facilities

VII.1 Development of a Horizontal Transfer System for Alpha-Tight Transfer of Irradiated Fuel for Micro-Analytical Characterization

A facility is being set up for the post irradiation examination (PIE) of metallic and mixed carbide fuel pin sections using Scanning Electron Microscope (SEM). Typical SEM specimens of 5.1 mm in diameter and 1 mm in thickness were used in the facility. These specimens are prepared in the leak-tight shielded environment of hot cell #6. Since plutonium is α -emitter, these specimens have to be transferred from the hot cell to the examination chamber of SEM in leak-tight manner.

A glove box interfaced with SEM is used for the leak-tight transfer of specimens to SEM. The glove box has a cell flange-door assembly of a standard 270 mm diameter α -tight double door transfer system (DDTS) fixed on its wall. There is a 750 mm long tunnel connecting glove box and SEM specimen chamber. A VAT valve is provided in the tunnel for the leak-proof isolation of the environments of SEM and glove box. Necessary tools and tackles are provided inside the glove box for the transfer of specimens between the SEM chamber and glove box.

The typical SEM specimen moulds have 25 mm diameter and 20 mm height. The specimens prepared in hot cell # 6 are transferred to hot cell#5, through the inter-cell transfer port between them. There, the moulds will be locked inside leak-tight Shielded Specimen Holders (SSH) made of tungsten or stainless steel. SSH provides a minimum of 20 mm tungsten/stainless steel shielding all around for the specimen. Tungsten SSH is used during examinations of high activity irradiated fuel sections. There is a cell flange-door assembly of a standard 270 mm diameter α -tight DDTS fixed on the

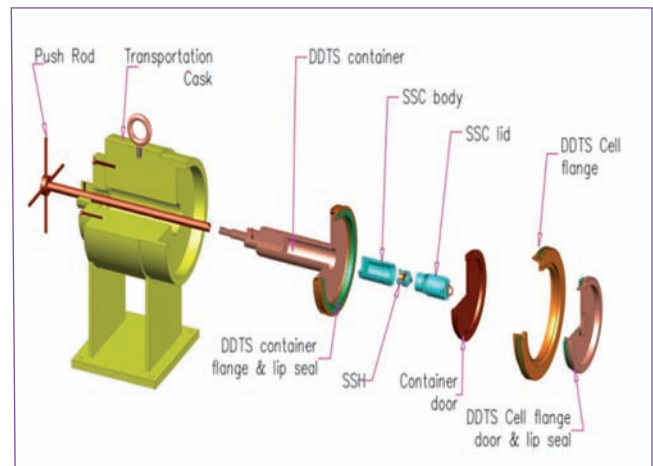


Fig. 2 Details of HTS internals

stainless steel rear sealing door of the hot cell#5.

Development of new Horizontal Transfer System

A customized Horizontal transfer system (HTS) has been developed for the α -tight transfer of SSH from hot cell#5 to the SEM glove box. The system consists of a mild steel shielded transportation cask, DDTS container, stainless steel cassette (SSC), push rod, and trolley. The HTS arrangement is shown in Figure 1.

The shielded transportation cask is 443 mm long and outer diameter is 390 mm. It has a cylindrical inner cavity of diameter 89.5 mm and length 295 mm to accommodate the stainless steel cassette. It is made of mild steel and weighs approximately 300 kgf. An eyebolt is provided for the handling of the transportation cask. It offers radiation shielding of 180 mm thick steel in the radial direction.

The DDTS container substitutes the basket-container assembly in the standard HTS arrangements. It uses the container side flange-door assembly of the standard 270 mm diameter α -tight DDTS. It weighs approximately 20 kgf and offers 120 mm thick steel axial shielding in the rear side. There is a 295 mm long, ϕ 90 mm diameter cavity inside to accommodate the SSC.

The SSC has a 60 mm long inner cavity of diameter ϕ 50 mm to receive SSH. It is made up of stainless steel and weighs around 4 kgf. The stainless steel lid of SSC is 120 mm thick and weighs 2 kgf. This lid offers 120 mm thick steel axial shielding in the front side. Details of HTS components are shown in Figure 2. The dimensions of the transportation cask and internals are chosen such that when one curie 2 MeV γ -rays emitting specimen is

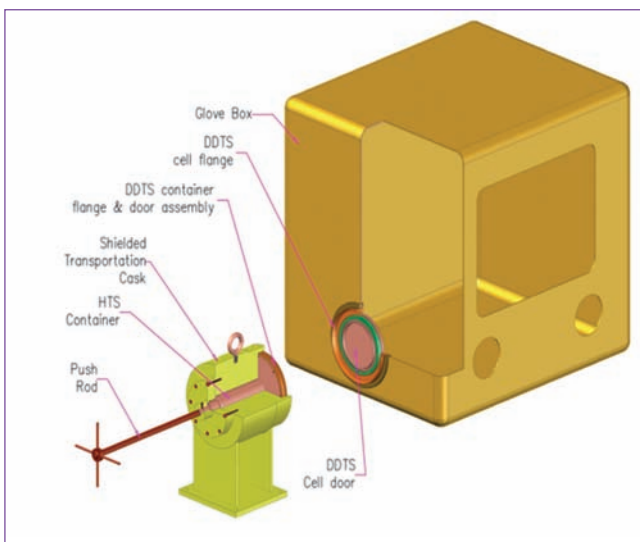


Fig. 1 3D model of general arrangement of HTS

inside the cask its surface dose is less than 200 mr/hr.

Push rod is used to lock/unlock the DDTS container with/from DDTS cell flange provided in the hot cell #5 rear sealing door/ GA6 glove box, and to pull/ push the DDTS container in/out the transportation cask. Trolley is used to align the axis of the transportation cask with the axes of DDTS cell flange fixed in the rear door/ glove box. Trolley also helps in the shifting of the transportation cask from lower isolation area (LIA) to GA6 and vice versa.

Horizontal Transfer System Validation

After bringing the transportation cask to LIA, it was matched with the DDTS cell flange provided in the hot cell #5 rear sealing door. Subsequently from the operating area, using master-slave manipulator (MSM), the cell flange and the container flange of DDTS are locked together, the doors of the flanges are locked, and the DDTS door assembly is opened to the hot cell. The SSC is then taken into the hot cell and SSH is loaded in it. Using MSM, after placing the SSH inside the HTS container, the DDTS door assembly is put back and the doors were locked with the respective flanges. Figure 3 shows the operation trials of HTS at LIA.

Subsequently, from LIA using push rod, the HTS container was detached from the DDTS cell flange; and the DDTS container is pulled inside the transportation cask and locked with it. The trolley with transportation cask is then moved to GA6. The axes transportation cask and glove box DDTS cell flange are aligned and the DDTS container is locked with the cell flange. Using gloves, manually the doors of HTS container and cell flange are locked; and the door assembly is opened. The



Fig. 3 HTS operation at LIA

SSC is then taken into the glove box and opened to take out the SSH. A photograph taken during operation trials of HTS at GA6 glove box is shown in Figure 4.

Extensive trials were carried out to validate the new α -tight double door transfer system. The performance of the system was found satisfactory during these trials; and it is approved for the leak-tight transfer of irradiated material specimens between hot cell facilities. It is decided to use the same system for the transfer of specimens and cut pieces of irradiated fuel/structural materials from RML phase-I hot cells to the new proposed facilities in RML phase-II such as Shielded facility for micro-structural characterization (SFMAC) of fuel and structural materials, and Mechanical property evaluation cells (MPEC).



Fig. 4 HTS operation trials at room no.GA6

VII.2 Development of an In-cell Crane for Lead Cell

A lead cell is being erected at IGCAR for the post irradiation examinations of irradiated metallic fuels. Specimens and cut sections of fuel/structural materials to be examined are transferred from the concrete hot cells to the lead cell through the inter cell transfer port between them. There are equipment for specimen preparation, metallography, measurement of density and hardness, etc., inside the lead cell. A 500 N capacity remotely operable and maintainable in-cell crane has been developed and installed in the containment box of lead cell for handling of heavy components/ instruments/ equipment inside.

The lead cell consists of a stainless steel containment box mounted on a support structure, surrounded by 0.25m thick lead walls in the front and lateral sides, 1.2m thick high density concrete wall in the rear side, and 0.3m thick mild steel roof. The size of containment box is 5.2m x 1.2m x 1.4m [L x B x H].

The lead cell has four numbers of radiation shielding glass windows- two in the front wall and one each in the side walls. There are two articulated manipulators (AM) of type A-11 above each of the glass windows. The lifting capacity of AM-11 is 45N.

In the original design of RML hot cell facility, there were

two lead cells. Each of these cells have predefined objectives; and addition of new PIE equipment or techniques in the future were not envisaged. Therefore, the equipment provided inside the cell have fixed positions. Hence in-cell crane was not provided in the lead cell for lifting and relocating of equipment inside.

To enhance operationality and for the efficient utilization of available space, recently, it was decided to convert the two lead cells into a single cell by removing the partition wall between them in the containment box. This modification has released ample floor space for the installation of new equipment for now and in future. Remote installation of new equipment/repair of existing equipment in future, in an operating lead cell require/involve remote handling of heavy equipment/ components weighing more than 45N. This has necessitated the development and installation of a crane inside the lead cell.

The in-cell crane has three motions: long travel (LT), cross travel (CT) and hoist. The crane has lead screw driven linear stages for LT motion and CT motion, and a winch for hoisting. Major structural material used for the fabrication of the crane is radiation and corrosion resistant AISI 304/304L. Only those materials which can withstand an absorbed dose of 10^7 rads of 1MeV γ -ray radiation or above are used for the construction of the crane.

The crane LT stage is bolted to the three numbers of L-shaped brackets welded to the roof and rear side inner wall of the containment box. The CT stage is bolted to the LT carriage and the hoist assembly is attached to the CT carriage. A stepper motor is provided for the LT movement. The motion from stepper motor is transmitted to the LT stage lead screw via bearing mounted shafts, spur gears, bevel gears and universal couplings. The LT motion of the crane is 3980 mm. Also there is a hand wheel for operating the stage manually using AM-11. A partially floating type nut is used in the LT carriage to accommodate the self-weight sagging of the lead screw. The CT operation of the crane is done manually using AM-11 by operating the hand wheel provided in the CT stage body. Shafts mounted on ball bearings, bevel gears are used to transmit motion from hand wheel to the CT stage lead screw. The CT motion of the crane is 600 mm. A hand wheel is provided on the CT stage body to operate the hoist using AM-11. The rotational motion

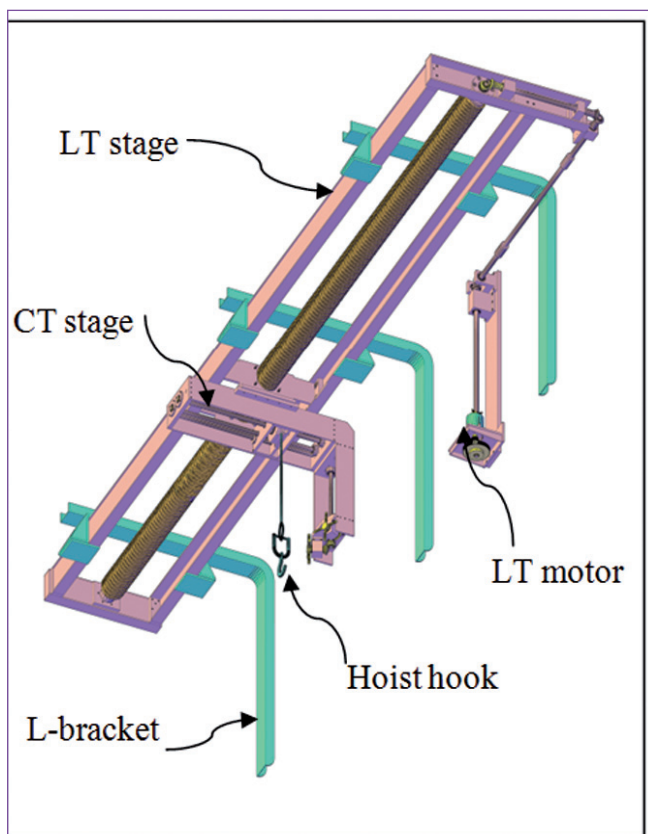


Fig. 1 3D model of in-cell crane

given to hand wheel is transmitted to hoist pulley via ball bearing mounted shafts, spline nut & shaft, worm & wheel arrangement, and bevel gears. The worm & wheel assembly in the drive train imparts self-locking feature to the crane. The clear lift of hoist is 250 mm.

The location of existing ventilation ducts, filter banks and electrical /pneumatic connectors, manipulator reach, visibility etc., presented many challenges during the design of the crane. Innovative design concepts were adopted to overcome the obstacles such as interference of components during crane operation, lack of visibility, inadequate manipulator reach, etc.

The main constraint to be addressed during design was that, the crane has to be installed in a completely built lead cell without dismantling it. To meet this, it was decided to size the crane components such that they can be taken inside the cell utilizing the existing material transfer ports. The available ports for material transfer are: a 0.635 m x 0.83 m man entry port on the containment box rear wall, a 360 mm circular port on the floor, and eight nos. of 170 mm diameter AM ports on the front and side walls. The first two ports can allow only the components up to a maximum length of 1.1 m, whereas the third 170 mm diameter AM port can allow components up to 5.0 m long. The length of the components of LT stage, such as lead screw and linear guides are approximately 4.2 m. They can be taken inside only through the AM ports. Therefore the lateral dimensions of these components were restricted such that they can pass through the AM port. High factor of safety was used in the design of the crane components, as the fixing location of the crane inside the containment

box is not falling in the remotely accessible area for maintenance/repair works using AM-11.

Numerous technical difficulties were faced in the fabrication/machining of long precision components such as 100 mm diameter 4.20 m long ACME thread lead screw from 8 mm thick AISI 304 stainless steel pipe, and 4.20 m long, 6 mm thick, 60 mm x 140 mm (B x H) C-shaped linear guides.

The crane uses a remotely replaceable motor provided inside the lead cell for the operation of the LT stage, i.e. no drive shaft penetrates through the containment box walls. This eliminates the need for a glove box attached to the lead cell for motor changing as needed in many of the similar in-cell crane designs.

Limited space availability for men and material movement, and lack of material handling equipment inside the containment box posed additional challenges during installation of the crane. Specially made fixtures were used inside the containment box for tackling the problems related to the handling of components.

An in-cell crane for a completely built lead cell has been developed, and its installation inside lead cell containment box and testing has been carried out. The whole exercise has given invaluable experience to the designers/engineers in the development of compact remotely operated material handling equipment for confined space applications. Several new concepts were employed in the design of the crane components such as hoist assembly, partially floating LT carriage drive nut, remotely replaceable LT stage motor assembly, etc.



Fig. 2 A view of in-cell crane inside lead cell containment box

VII.3 Design, Development, Integration and Testing of Compact Indigenous Plutonium in Air Monitor

The prompt detection of Plutonium (Pu) in air is a critical requirement to protect operating personnel from inhalation hazards at reprocessing plants and fabrication facilities handling Pu in powder form. Spectrometry based Pu continuous air monitors (PuCAM) are used continuously to monitor the volumetric activity of airborne Pu particulates in the working environment. The presence of significant natural background radiation from the Radon and Thoron progenies interfere with the Pu energy region and make the prompt detection difficult. From experience, it is understood that imported equipment in use have issues related to false alarms due to Indian environment conditions, maintenance difficulties etc. and also not sure of assured future supply. Considering DAEs closed fuel cycle policy, significant numbers of PuCAMs are essential to meet the safety requirement of FRFCF. In order to achieve self reliance and to meet native conditions, indigenous design of spectrometry based PuCAM was initiated in collaboration with BARC.

As a proof of concept, first version is designed and developed using off-the-shelf modules including multichannel analyser (MCA), single channel analyser (SCA), Panel PC and I/O module. BARC designed semiconductor based dual detector module (DDM) and associated electronics are used for detecting the alpha, beta and gamma radiations. A vacuum pump sucks the air at a constant rate through the filter paper and the detector facing the filter paper detects the activity from the particulates trapped. The Panel PC collects the data and subjects to processing algorithms such as region of interest, spectrum and dynamic compensation and displays the estimated values on the Panel PC display. The system was integrated, tested and deployed in the field. Gaining confidence from the operation experience of first version, the design of Field Programmable Gate Array (FPGA) based compact PuCAM was taken up for FRFCF.

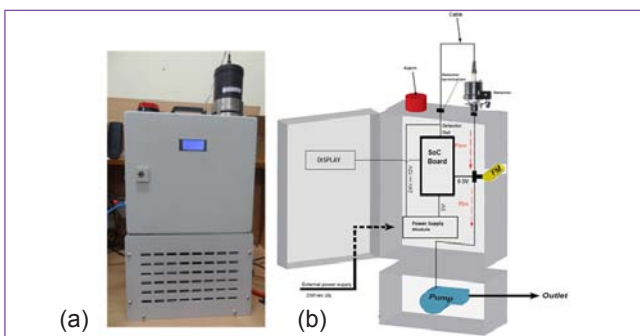


Fig. 1 PuCAM (a) Integrated unit (b) Internal view

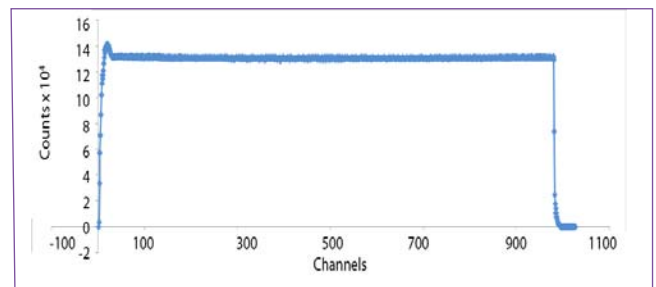


Fig. 2 Spectrum for ramp pulse

An indigenously designed FPGA based printed circuit board (PCB) replaces the functionalities of MCA, SCA, Panel PC and I/O module thus making it customized and compact. The design of PCB is carried out with a System on Chip (SoC) FPGA with a hard microcontroller core. The analog section consists of high speed ADCs which samples the pulse output from both the detectors and flowmeter interface. The digital section consists of SoC, memory interfaces, serial and parallel communication interfaces, real time clock, display interface etc. Channel energy spectrum of 1K is constructed and all the processing algorithms are executed on FPGA itself and the derived volumetric estimates of alpha, beta and gamma are displayed.

The entire system including the SoC FPGA board, DDM, power supplies, vacuum pump and front display are integrated into a compact electromagnetic compliant cabinet as shown in Figure 1. Being a mixed signal design, several challenges were faced during the design, development and testing phases. The spectrum built for a pulse ramp for 0 to 10V from a nuclear Pulser is shown in Figure 2.

Figure 3 shows the energy spectrum obtained for different radionuclides. Subsequent to post lab validations, the system will be deployed for field evaluation. The technology transfer of system to ECIL is in progress.

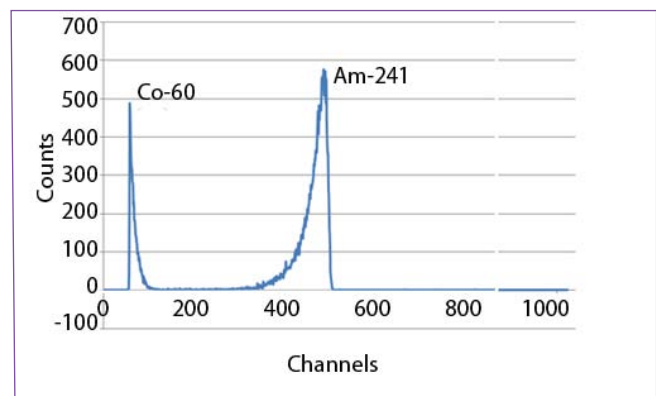


Fig. 3 Energy spectrum for radio nuclides

VII.4 Design, Fabrication and Commissioning of Automated Argon Recirculation, Re-Generation and Pressure Control System for Glove Box

Casting of metal fuel slugs and characterization pertaining to it are performed in a pressure controlled high purity argon atmosphere glove box. An automatic closed loop gas purification and pressure control system is designed to maintain purity (defined in terms of oxygen and moisture concentration) and pressure (-20 to -40 mm of WC) in a glove box of 1.6 m³ volume. System is designed to operate continuously and maintain purity levels close to that specified limits. There is also a feature for automatic regeneration of the copper catalyst and molecular sieves which are used for oxygen and moisture removal from argon. The two main problems in keeping oxygen and moisture in level are the purity of commercial argon gas and the ingress of air and moisture due to permeability of the gloves.

The system works by the principle of gas circulation, i.e. the working gas (argon) permanently circulates between glove box and purification tower. Argon is purified by recirculating it through purification tower filled-in with molecular sieve and copper catalyst. Molecular sieves & copper catalysts are interleaved in the ratio of 1:1 in the tower capacity of 30L. Dual tower concept is used in which one purifier tower can be used for removing oxygen and moisture from the argon gas, the second tower column can be regenerated by heating to 573 K. Figure 1 shows piping and instrumentation diagram of the system

The process control includes the following subsystems

1. Automatic Pressure Control System
2. Argon Purification and Recirculation System
3. Catalyst Regeneration System
4. Automatic Evacuation and Filling Cycles

Systems are controlled by Programmable Logic Controller (PLC) with feedback from differential pressure transmitter, trace oxygen sensor and dew point transmitters. Human Machine Interface (HMI) touch panel allows remote automatic operation of these sub systems and overriding it when required by the operator. Manual operation is also a viable via the control panel using pushbutton and selector switches. The indication of these process and corresponding blowers, valves, sensors in operation have been visualized in both HMI and hardware Panel. Figure 2 shows architecture of PLC-HMI control system.

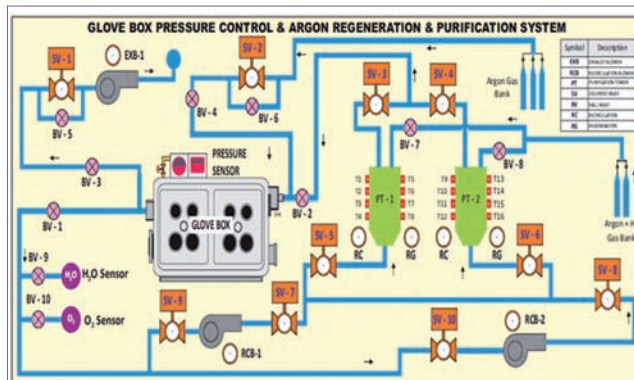


Fig. 1 Piping and Instrumentation diagram of the system

Glove box real time pressure is controlled in range with pressure sensor, corresponding feed and bleed valves. In recirculation mode, based on in-service tower and blower selections, valves are auto switched by PLC to bring the selection in operation. Once desired purity is achieved in glove box, blowers run at a speed to maintain 20 air changes in the glove box. Regeneration heaters are controlled by PLC - PID controller and thyristor control unit with feedback from temperature profile measured by thermocouple arrays located on the purification towers. Mineral insulated (MI) heaters are used in regeneration of purification towers for creating uniform hot zone and longer operating life. Auto filling and evacuation cycle dilutes initial air concentration in the glove box to bring purification tower into the system. Additionally, real time monitoring and logging of pressure, oxygen and moisture concentration, regeneration temperature, blower speed, time taken for achieving desired purity are also implemented in the system for optimizing the process.

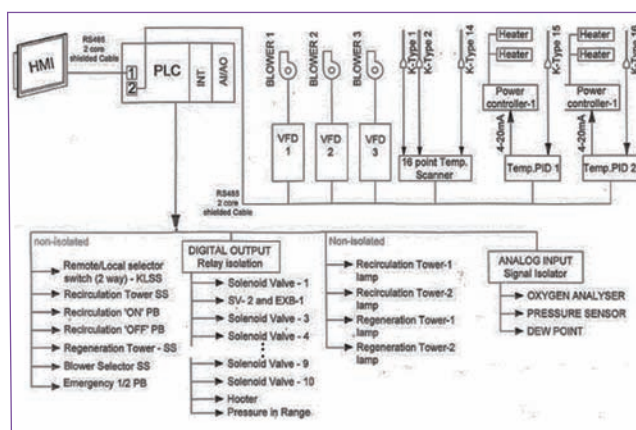


Fig. 2 Architecture of PLC- HMI control system

VII.5 Design, Fabrication and Test Bed Development for Iso-Kinetic Sampling Nozzle for Stack Sampling

Representative sampling is the biggest challenge in effluent monitoring from stacks and ducts of radioactive facilities. When multiple exhaust systems are connected to a single exhaust plenum or when multiple facilities share a common stack, sampling point shall be so chosen as to avoid drastic variations in the face velocity near the sampling point. ISO-2889 is a document that talks comprehensively about all the technicalities involved during design, construction and operation of systems that are used for sampling airborne radioactive materials from the stacks and ducts of nuclear facilities. The criterion for a successful sampling point is that it should be at least 5 hydraulic diameters from the downstream of a flow disturbance and at least 3 hydraulic diameters from the upstream of a flow disturbance. DFRP (Demonstration facility for Fast Reactor Reprocessing) shares a common stack with KARP (Kalpakkam Reprocessing Plant) and effluent monitoring is realized here by sampling from the plenum joint in the exhaust duct. Exhaust ducts from the various off gas systems, process cells, operating areas, waste vault and HEF (Head End Facility) are connected to the common exhaust plenum. In order to deal with flow disturbances expected near the sampling point due to inherent design constraint, shrouded nozzle is recommended to achieve the iso-kinetic sampling conditions. One shrouded nozzle was designed and fabricated at the central workshop, IGCAR.

The expected flow through the DFRP duct ranges from 2 to 3 lakh CMH which translates into a face velocity of 12.3 – 18.5 m/sec at the exhaust plenum. After exhaustive literature survey of various shroud designs, a model is chosen that can deliver acceptable transmission efficiency for the required range of face velocities. Accordingly, the design of the shrouded nozzle was finalised. Nozzle diameter is 26.2 mm while the shroud diameter is 78 mm with an overall length being 340.6 mm. The material

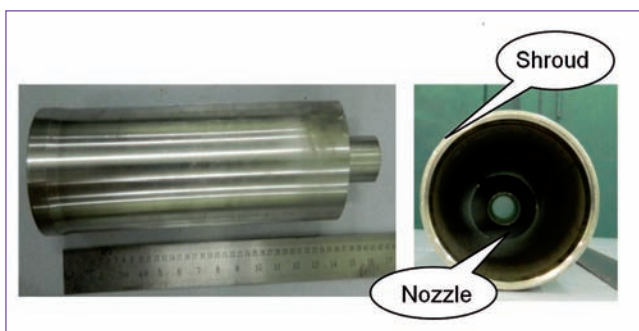


Fig. 1 Shrouded nozzle; side and cross sectional view

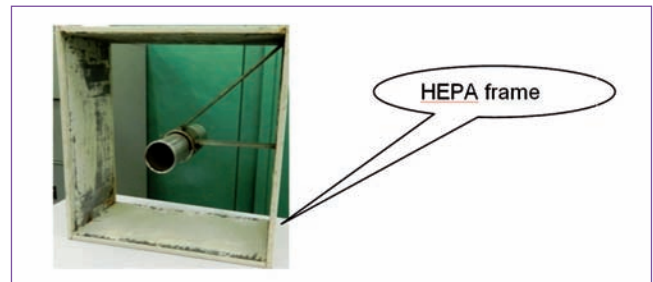


Fig. 2 Testing arrangement frame with shrouded nozzle

specifications during the fabrication of the nozzle were carefully chosen which is compatible with the chemical and physical nature of the aerosols. Nozzle is constructed using S.S 304L with an average surface roughness of the internal regions of nozzle not exceeding $0.8 \mu\text{m}$ while the average surface roughness of the external region of the sampling nozzle from the inlet plane was maintained within $1.6 \mu\text{m}$. Shroud was fabricated with an average surface roughness that does not exceed $3.2 \mu\text{m}$ as per the acceptance criteria. The shrouded sampling nozzle fabricated at central workshop is shown in Figure 1. This shrouded probe will be useful to deal with sampling circumstances in upcoming facilities which could not achieve the iso-kinetic sampling due to other design constraints.

By utilising the experimental facility at the HEPA test facility at HSEG, it is planned to test the performance of shrouded nozzle. A standard HEPA filter frame was modified to accommodate the nozzle at the centre of the frame by removing the filter elements as shown in the Figure 2. Additionally, for sampling the test aerosols, a 6.0 mm SS tube was welded in the pneumatic line which would be connected to the particle counter. Qualification of nozzle would be done by measuring the transmission ratio of aerosols up to $10 \mu\text{m}$ for different face velocities generated in the test rig. The testing arrangement in HEPA filter test facility is shown in Figure 3.

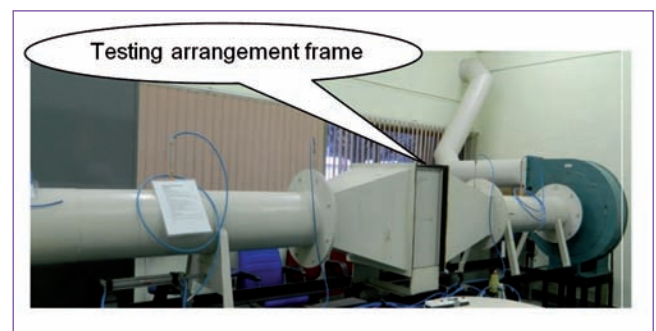


Fig. 3 HEPA filter test rig with test frame fixed

VII.6 Design and Development of Flight Controller Algorithm for Auto Stabilization of Multi-Rotor Drone

As part of sea side surveillance it is planned to have Aerial drone surveillance to assist Central Industrial Security Force in detecting encroachments along sea side which is currently unmanned. Flight controller plays crucial role in multi-rotor drone for maneuvering and operations.

Flight controller has following modules as shown in Figure 1.

- Inertial Measurement Unit
- Receiver
- Microcontroller for control

Inertial measurement unit in flight controller is an electronic device that measures and reports specific force, angular rate and the magnetic field surrounding the object of interest using combination of accelerometer, gyrometer and magnetometer sensors. Receiver module receives pilot commands (Throttle, Roll, Pitch and Yaw) from wireless 2.4 GHz transmitter in the form of pulse width modulated signals and communicates them to flight controller for control action. Control algorithm in microcontroller measures attitude of the drone in Euler (3-2-1) parameter notation using inertial measurement unit and controls the motor speeds using pilot commands and estimated attitude. To avoid singularities in attitude representation, maximum pitch and roll of drone is limited to 30°. Experimental work was carried out to characterize error from the sensors. Compensation of accelerometer bias error, turn-on to turn-on and in-run bias errors of gyroscope and soft iron error of magnetometer is done in microcontroller.

Development of Flight Controller algorithm

Flight control algorithm is coded in 'C' language and

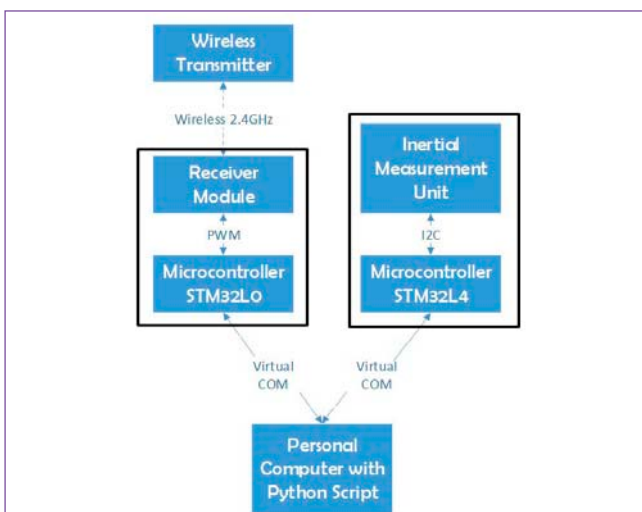


Fig. 1 Block diagram of flight controller

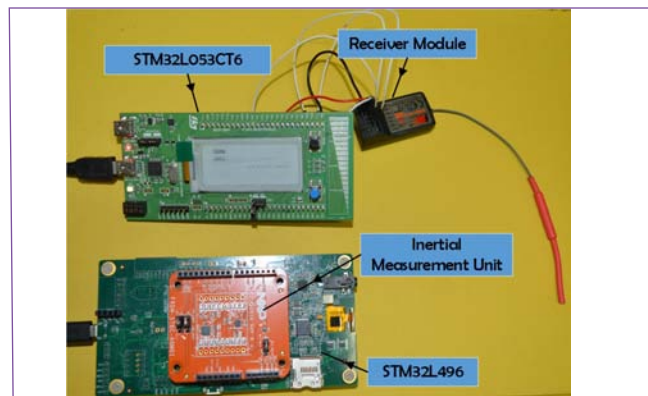


Fig. 2 Flight controller hardware setup

ported in STM32L496 microcontroller using Keil uVision. NXP based FXAS21002 gyroscope and FXOS8700 Accelerometer and Magnetometer sensors are used as part of Inertial Measurement unit. All three sensors are interfaced to microcontroller using inter integrated circuit protocol. Attitude of flight-controller is estimated using complementary filtering. Timers in STM32L053C8T6 are used to capture pulse widths signals from receiver module. Hardware setup is shown in Figure 2.

Validation

Control Algorithm developed is validated using table top assembly with flight controller and Receiver connected to Personal computer running python script. Python script is mainly used as graphical user interface. Qt is used in background and virtual COM ports are configured in Python. GUI is shown in Figure 3.

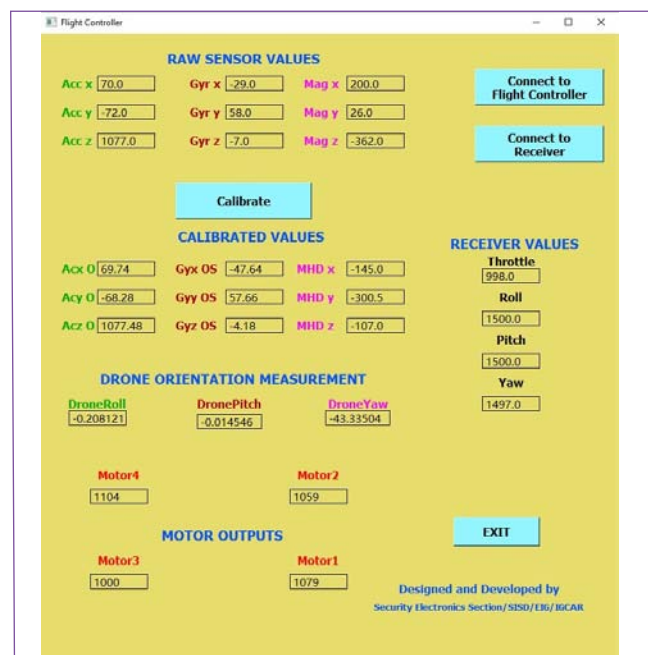


Fig. 3 Flight controller GUI

VII.7 Recommendations to Implement an Improvement in the RCC-MRx Equivalent solid plate Design Methodology for Tubesheet Analysis

Tubesheet forms a major part of a shell and tube heat exchanger from the point of view of structural analysis and economics. The most common procedure for analyzing the stresses in tubesheet is based on treating the perforated portion as an equivalent solid material with modified elastic constants. Simplified analysis with equivalent solid plate (ESP) methodology is generally carried out by considering a 2-dimensional axisymmetric model. In RCC-MRx, ESP methodology is given for carrying out the analysis of tubesheets with numerous holes. According to this methodology, the tubesheet is modeled with the dimensions similar to the actual plate but with fictitious (lower in magnitude) elastic constants (E^* and ν^*) in place of the actual material constants.

The simplified approach is applied and compared with a 3-dimensional finite element simulation carried out for typical tubesheet used in the steam generators of fast reactors. The 3-dimensional model (30° sector) with actual holes in the triangular pattern is analyzed under loading and boundary conditions similar to the ESP case. The comparison of results is carried out for (i) deflection (Figure 1), (ii) primary membrane stress intensity and (iii) primary membrane plus bending stress intensity. Stresses are linearized along the stress classification plane (SCP) to compare the results with the linearized stresses along the stress classification line (SCL) of the ESP case (Figure 2). Based on the comparison, the significance of the axial stress component and pressure inside the holes of the tubesheet is highlighted for the estimation of primary membrane plus bending stress intensities against the existing RCC-MRx design procedure.

As per the RCC-MRx procedure, the primary membrane plus bending stress intensity is calculated based on radial stress and hoop stress only. From this numerical investigation, it is noticed that the primary membrane plus

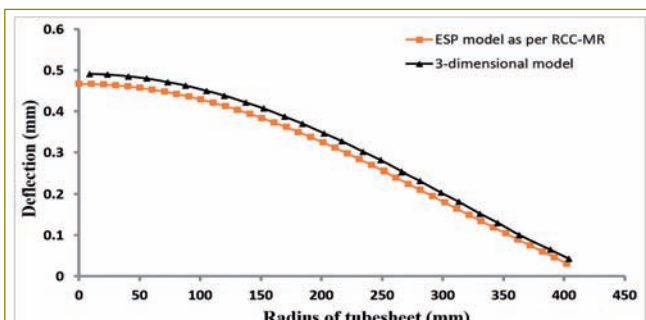


Fig. 1 Comparison between deflection of tubesheet for ESP methodology and 3-dimensional model under mechanical loading

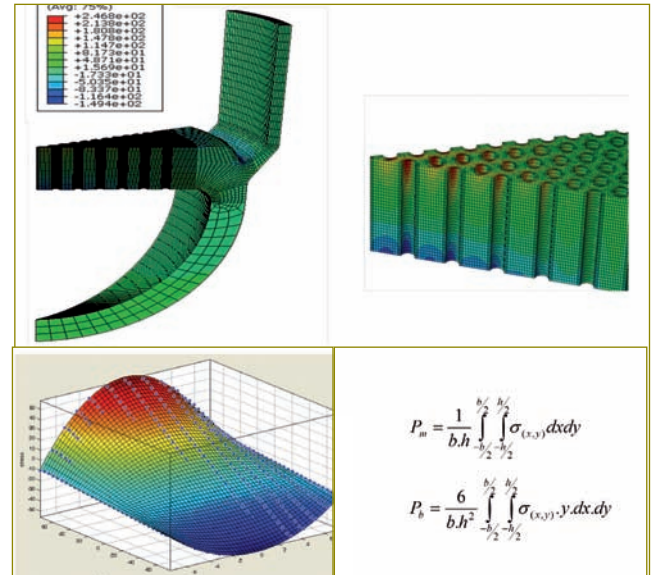


Fig. 2 (a) Stress distribution (in MPa) under pressure loading in 30° sector model. (b) Enlarged view near centre, (c) Stress distribution along SCP and (d) Expressions for stress linearization along SCP

bending stress intensity value is significantly lower in ESP methodology as compared to the 3-dimensional model results (Table 1). Due to these inconsistencies in results, the improved design procedure is recommended which accounts for the axial stress component also to estimate the primary membrane plus bending stress intensity. This stress intensity is computed using the appropriate theory of failure from all the stress components unlike by considering only radial and hoop stress values. The proposal recommending the modification in the design procedure of RCC-MRx ESP tubesheet analysis to estimate the primary membrane plus bending stress intensity was made to RCC-MRx sub-committee. The proposal was accepted and will be included in the next version of the design code.

Table 1: ESP methodology as compared to the 3-dimensional model

Stress type	R C C - MR ESP methodology	3 dimensional model	R C C - MR ESP methodology
primary membrane stress intensity	54 MPa	47 MPa	54 MPa
primary membrane plus bending stress intensity	184 MPa	212 MPa	215 MPa

VII.8 Indigenous Design & Development of Numerical Over-Current Relays for Electrical Substations

An electric power system is a network of electrical components deployed to supply, transfer, and use electric power. Primary objective of power systems is to maintain a very high level of continuity of service, when intolerable conditions occur and to minimize the extent and time of the outage. Hence suitable protection system needs to be deployed in order to isolate the faulty section from rest of the live electrical power system during the faulty condition. Protection devices detect, locate and initiate the isolation of the faulted equipment from the power network in the minimum desirable time. It is necessary that protective devices remain inoperative during short duration transient phenomena which may arise during faults, switching surges or other disturbances in the network. Numerical Protection Relays are critical elements in power distribution system. These relays employ accurate and high-speed electronics to sense over current and initiate trip to isolate the faulty electrical subsystems for avoiding catastrophic failures during abnormal conditions. Indigenous design and development of prototype protection relay is taken up owing to restrictions associated with embargo with nuclear establishments. Extensive literature survey was carried out to finalize specifications and hardware architecture. Theoretical analysis was performed using matlab/simulink to select suitable algorithm that would accurately extract fundamental component from composite signals comprised of noise, harmonics and decaying exponentials. Simulations were carried out using the three most popular and widely used Discrete Fourier Transform (DFT) based measurement algorithms, Viz. the full cycle DFT (FCDFT), half-cycle DFT (HCDFT), and the Cosine filter. The comparison

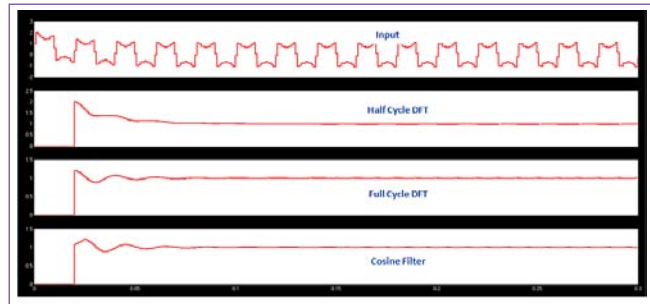


Fig. 1 Transient Response of DFT Algorithms to hostile signals

of the output transient responses among the three DFT measurement algorithms for tracking the fundamental frequency component, when the input signals are purely sinusoidal and non-sinusoidal along with decaying DC, is illustrated in Figure 1. It is found that HCDFT exhibits peak over shoot and large settling times during long exponential decays. On the other hand FCDFT exhibits medium but significant overshoot/undershoot on subjecting to decaying exponential signal. However Cosine filter responds with minimal overshoot/undershoot and least settling time when subjected to every type of hostile signals. Thereafter, fabrication of Numerical over-current relay was initiated. Three Phase and Earth fault currents are acquired through 4 separate Current Transformers (CTs) and are converted to voltage through bleed resistors. The voltage is sensed by difference amplifiers. The outputs from difference amplifiers feeds a second order low pass filters to remove noise and influence of higher order harmonics. This is followed by 1:10 gain amplifier and simultaneous sampling ADC to digitize these analog signals. The ADC outputs are read by micro-controller, which applies the cosine filter algorithm on the input signals to extract the

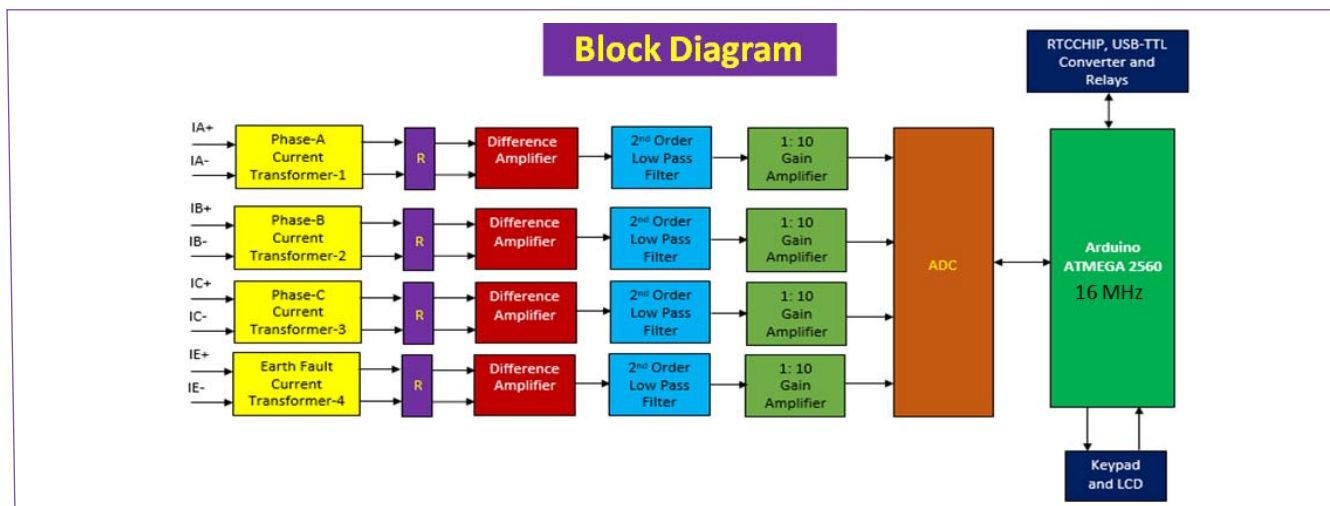


Fig. 2 Hardware architecture of Numerical Over-current Relay

magnitude of the fault current. Block diagram of the hardware architecture of relay is shown in Figure 2. The magnitude of the input is compared against the set current value and subsequent decision to initiate the trip signal time is evaluated based on IEC 60255 Inverse curve standard. User options include configurable Time Mode select, Inverse Curve selection and the pickup current. Internal storage of events with time stamping is done using EEPROM and Real Time Clock/Calendar Module. Communication modules include USB2.0 and RS485. Modbus RTU protocol is used to communicate trip values through RS485 to the external master. The



Fig. 3 Fabricated Numerical Over-current Relay Unit

fabrication and testing of the over current relay has been completed (shown in Figure 3).

VII.9 Automatic Number Plate Recognition System

In Nuclear facilities, it is necessary to maintain the record of all the vehicles entering into the DAE complex considering the security of the facility. However, manually entering the information such as vehicle registration number, entry time, exit time is quite laborious and prone to human error. Therefore, to automate this process, Automatic Number Plate Recognition system (ANPR) is designed and developed.

ANPR system is meant to automatically capture the image of the vehicle and recognize the number plate, and convert the registration number to text format using a technique called optical character recognition. The extracted vehicle registration number is stored in a database along with other necessary information such as entry date and time. ANPR system is developed in Java, making it a platform independent application. The ANPR system accepts the camera feed from any network camera identifiable by an IP address. This application consists of three major modules: Vehicle Detection module, Number Plate Recognition module and Database Storage module. Vehicle Detection module is responsible for automatically detecting the arrival of the vehicle and upon detection it captures an image from the live video stream and submits to the Number Plate Recognition module. The automatic detection of the arrival of a vehicle is achieved by means of video analytics using an open source computer vision library called Open CV.

Number Plate Recognition module, upon receiving the vehicle image from the previous module, isolates the number plate from the image to recognize the vehicle registration number and extracts it into the text format. The extracted vehicle registration number and the isolated number plate image, along with other necessary information such as entry date and time, are submitted to the Database Storage module. This module is developed using an open source library called Open ALPR.

Database Storage module stores all the data such as

extracted vehicle registration number, isolated number plate image, entry date and time etc. into a database designed using MySQL.

The ANPR system has also been integrated with IoT of Security Systems: a web based central monitoring system of all the security systems in DAE complex, Kalpakkam. This allows the security maintenance personnel, upon secure login, to monitor the information regarding ANPR system such as ongoing entries, date wise entries, ANPR live camera view etc. from any web browser within the campus network. Unlike many commercially available systems, this ANPR application is developed in such a way that it integrates with an IP camera from any manufacturer. This allows choosing a camera of user's choice (with varying resolutions and frame rates) as per the desired maximum detectable vehicle speed.

This ANPR system is capable of recognizing multiple vehicle number plates at a time, i.e., if multiple cars are present in the field of view of the camera at a time (like in case of township entries and open roads, contrary to the organized lane traffic such as in toll gates and hotel entrances), the system will still be able to recognize all the number plates and extract the numbers.



Fig. 1 Capturing the registration number of the vehicle with image of the number plate using video analytics and automatic recognition system

VII.10 Development of Servo Manipulator for Hot-cell Applications

A 15 kg Servo Manipulator (SM) is developed for the hot cell applications. The dual arm SM has a total of 15 degrees of freedom which include the shoulder rotation, shoulder elevation, elbow rotation, elbow elevation, wrist rotation and wrist elevation in each arm, and azimuth rotation, cross-travel and up-down telescopic motion. Figure 1 shows the CAD model of the slave arm of the servo manipulator. The advantage of the SM is that the master and slave arm are interconnected by communication cables instead of mechanical links, hence can be widely separated for larger distances.

The Servo Manipulator is the advanced version of the manipulators where a closed loop of position, velocity and the force is formed on real time to exactly simulate the slave side environment on the master side. This makes the operator to have a real feel of the slave environment, particularly feel of the force exerted at the end effector. Further in order to reflect the force in the master arm from the slave environment, the servo digital amplifiers are networked to read the joint motor torques and the joint motor positions. From the joint motor positions, the manipulator Jacobian is constructed in real time and from the Jacobian inverse, the joint torque is converted to the manipulator force. The methodology is programmed into the Servo Manipulator control system and tested. All joints and the gripper on slave arm are electrically driven.

In the Servo Manipulator, there is no mechanical linkage between the master arm and the slave arm and they are connected through two way communication cables through a central controller. Generally slave arm is mounted on a transporter in the hot cell, giving large effective work volume. Typically a combination of 3 revolute joints gives much articulation to the manipulator

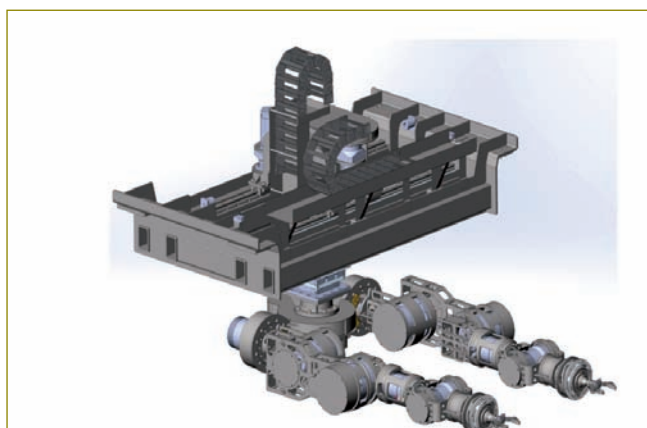


Fig. 1 CAD model of slave arm of servo manipulator

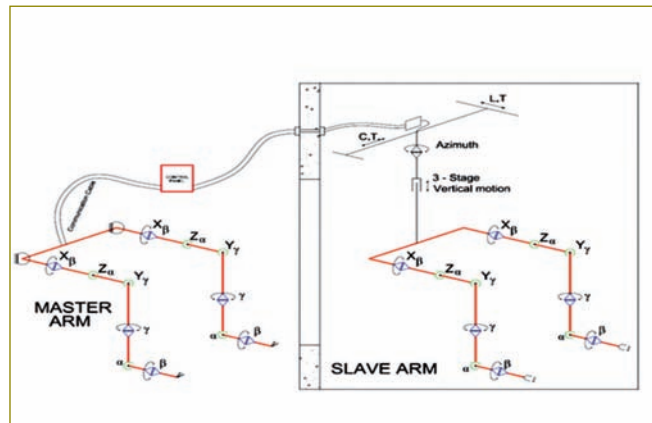


Fig. 2 Kinematic model of servo manipulator

and the wrist axes are typically for orientations. Such cases are easy to handle mathematically through a kinematic decoupling method and solve the Inverse Kinematics (IK) only for the global matrix and solve the oriental axes through a Euler rotation matrix. Figure 2 shows the kinematic model of the servo manipulator. Figure 3 shows the schematic of slave side of Servo Manipulator that clearly describes the Denavit-Hartenberg (DH) parameter which will be used for the kinematic and force synthesis. In order to have the maximum dexterity, one pair of arms is used in the construction of the servo manipulator. Table-1 shows the DH parameters for one arm of the Servo Manipulator. The same with the base orientation change is adapted for the other arm i.e the right arm.

Manipulator force estimation from the joint torques

In order to deduce the force experienced in the slave environment, the motors which are fixed in the joints for the actuation of the arms are powered with current to give the reactive force. Hence the current sensed in the joint motors when used to multiply with the torque

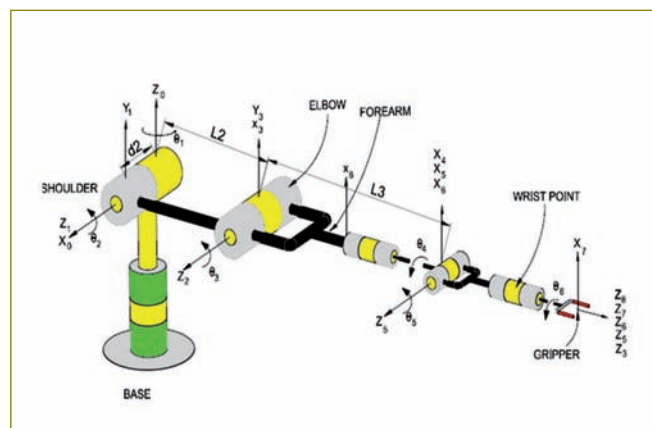


Fig. 3 Schematic of slave side of SM

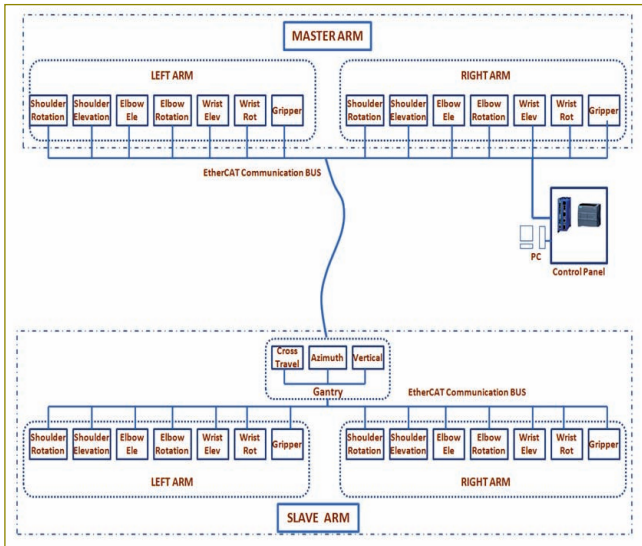


Fig. 4 Distributed Control System for Servo Manipulator

constant will give the torques.

The joint torques can be used to construct the forces in the manipulators gripper. In order to compute the force, it is easy to equate the work done at the joint space which becomes equal to the work done in the task space. The Work done by the manipulator in the task space is the total work done by the manipulator in the joint space. The Jacobian Matrix will help to move from task space to the joint space and vice versa by Jacobian inverse. The only complexity involved is the inversion of a 6X6 matrix in real time which is done through a PC. A distributed control architecture is adapted and the motor torque and position information are read through the EtherCat communication bus.

This force is computed from the variation in the motor torques and thus represents the payload acting at the



Fig. 5 Photograph of servo manipulator for hot cell applications

Table 1: DH Parameters for SM				
Link	a_i	α_i	θ_i	d_i
Link 1	0	96	θ_1	0
Link 2	400	0	θ_2	170
Link 3	0	90	θ_3	0
Link 4	0	-90	θ_4	520
Link 5	0	90	θ_5	0
Link 6	0	0	θ_6	550

end effector. This force is computed in real time by sensing the joint actuator torques from each axis of the manipulator.

Distributed Control System (DCS) for Servo Manipulator
The digital servo drives are networked through an industrial standard bus based communication protocol EtherCAT. A computing system PC is added to the network to carry out the kinematic and force synthesis in real time. A program is made in Visual Dot net C++ with the Application Program Interface drivers provided by the digital servo driver vendor. Figure 4 shows the layout of the manipulator joint axis control. The digital servo drives are networked through the EtherCAT bus and the computation PC attached to the same bus will scan the joint actuator torques. For each time step, the joint actuator encoder readings are read and the Jacobian matrix is computed in real time which is used for the force estimation. Figure 5 shows the servo-manipulator developed in IGCAR, and Figure 6 shows the delicate operations performed using SM.



Fig. 6 Delicate operations using servo manipulator

VII.11 Refurbishment and Remounting of the Oil filled Radiation Shielding Window in Hot Cell

Hot cell facility of the Radiochemistry Laboratory was commissioned in 1992 to carry out the post irradiation examination of the FBTR and MAPS fuels and reactor components. The facility consists of five hot cells in a row and each of these cells is designed to handle 370 T-Bq of ^{60}Co . Radiation shielding is provided by 1500 mm thick ordinary concrete (2.4 g/cc) in the front and the rear side and by 900 mm thick high density concrete (3.5 g/cc) in between the cells. Radiation Shielding Window (RSW) is provided in all these cells for viewing purpose. The cells were classified into two groups as air cells and inert cells. Three of these 5 cells have oil filled shielding glass windows to view and conduct various operations remotely by Master Slave Manipulators (MSM), while other two cells have solid glass windows. These oil filled windows have a series of glass slabs at the colder side with a conical reservoir for oil in the rear side at the hot end. The schematic cross sectional view of the window is shown in Figure 1. During the course of the last twenty seven years of operation, the RSW filled with oil, gradually lost its transparency and has become translucent. It was therefore difficult to perform in-cell remote operation.

Visual examination by laser flashing revealed thick deposits adhering on the both the sides of one of the middle glass slab. It was decided to retrieve the RSW, dismantle the glass slabs, execute manual cleaning of the surface by using ethanol or 1-propanol and remount it back into the liner brick wall of cell-2. Since retrieval, dismantling, cleaning and remounting of RSW involve potential breakage risk, there was a need for fabrication of special tools for each of these operations for handling fragile materials with heavy load.

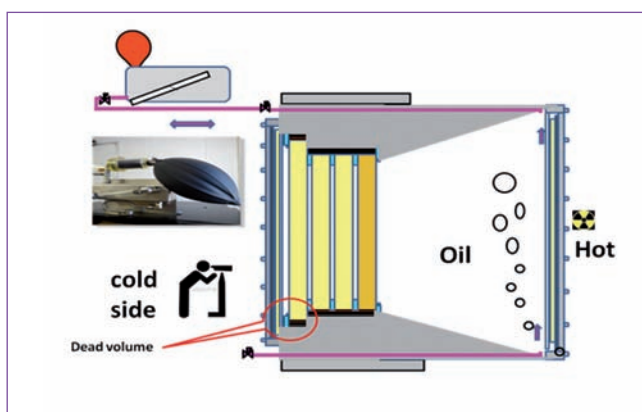


Fig. 1 Schematic cross sectional view of the radiation shielding window



Fig. 2 Translucent window

RSW was assembled with lead cerium loaded glass slabs housed in a metal frame and filled with 1200 liters of mineral oil to facilitate the optical coupling. The RSW housing has threaded holes at the bottom for handling/lifting purposes. RSW is housed in a window stepped liner brick that is a part of the cell shielding. Total weight of RSW is 8 MT, with loaded oil. Clearance between RSW and Liner brick varies from 5 to 10 mm on all sides. The partially oil filled RSW of cell-2 before retrieval is shown in Figure 2.

A heavy-duty hydraulic movable trolley of 10 tonne capacity has been fabricated especially for window retrieval purpose. It consists of roller conveyor for horizontal movement with hydraulic power pack for pulling and pushing of the window with precision forward and reverse control (12 Tonne capacity), screw jack arrangement for height adjustment and locking.

This movable trolley was aligned with the liner brick wall of the cell. During the operation of RS window retrieval and remounting, additional support structural frame, loaded with metal bars of 2 tonne capacity are provided for the support and strengthening with rear wall for

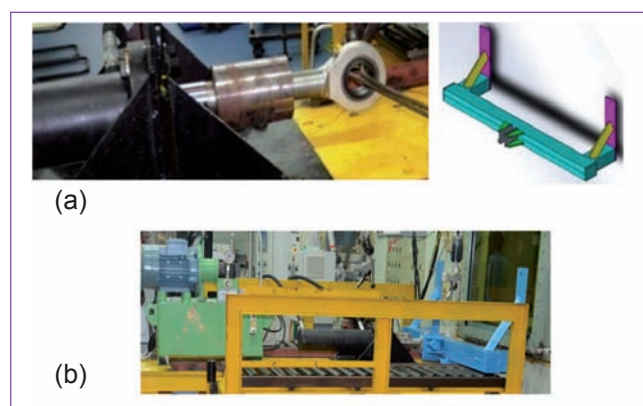


Fig. 3 (a) Flexible eye bold with connecting nut & pushing frame and (b) hydraulic piston with pushing frame



Fig. 4 (a) Structural support structure mounted with the trolley and (b) RSW retrieval from the liner brick wall

stability of the movable trolley. Flexible eye-bolt with connecting nut for hydraulic ram and suitable pushing frame for remounting were fabricated (Figure 3a and 3b). The structural frame mounted with trolley is shown in Figure 4a.

The window was fully retrieved from the liner brick wall (Figure 4b) and ventilation barrier was provided for maintaining the cell pressure. The RSW was checked for any probable contamination and was found to be clear. The entire operation was carried out with Radiation Work Permit under the supervision of the health physicist.

The hot side glass with frame was dismantled and handled using special D-Shackles & ropes. The inner glass slabs were found to have waxy thick brown deposit and the opacity was measured with standard light source and lux meter. The thick waxy brown deposit was wiped thoroughly from the surface of the inner glass slabs and was analysed using IR spectrometry. The IR spectra of the window deposit, showed characteristic peaks of the alkanes of much reduced intensity and a broad hump at 3400 and 1590 cm^{-1} region indicating the presence of H_2O in the residue (Figure 5). The small shoulder at 1703.0 cm^{-1} indicates that the brown deposit may be degraded oil and has moisture content present compared to the fresh and window oil.

The inner glass slabs were held in position by locking brackets and lead wool packing on all sides. The lead wool packing was removed using specially fabricated tools. Two glass slabs each of thickness 78 mm X 650 mm Sq and 140 mm X 650 mm Sq respectively, were removed from the window frame by using vacuum cups

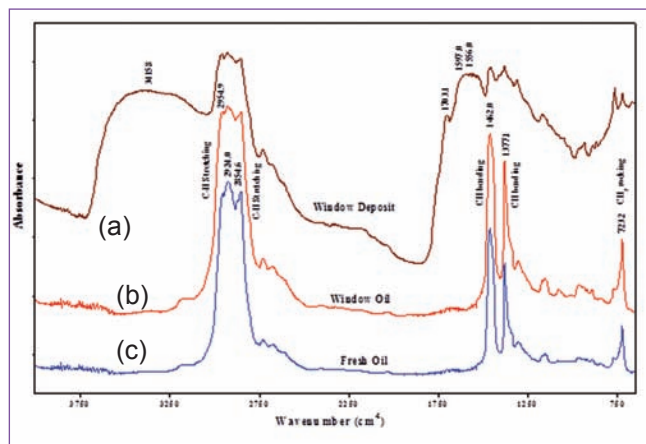


Fig. 5 IR Spectra of (a) window deposit (b) window oil and (c) fresh oil



Fig. 6 Window glass removal using vacuum cups

and specially fabricated glass holding fixtures (Figure 6 and 7). All the glass surfaces were thoroughly cleaned with hexane using lint less cloth. Transparency of the glass slabs were inspected using laser beam.

The inner glass slabs were assembled sequentially into the window frame after several mock-ups on the base plate with Teflon slides. The glasses were packed on all sides with new lead wool and ramped using special polymer ramping tools, along with lead guide plates at the top & bottom for oil flow.

The inner oil reservoir space was thoroughly cleaned with lint less cloth. The main gasket in between the outer hot side glass and the window frame was checked for any physical damage and was found to be intact. The hot side glass along with the frame was thoroughly cleaned and assembled in position with main window frame. Leak testing was carried out with Argon gas pressure for +100 mm and -100 mm of H_2O column and pressure hold-up test for one week. The RSW was maintained under Argon atmosphere and filled with the regenerated window oil. The oil filled RSW was once again tested for leak with a pressure of +100 mm of H_2O column. The transparency of the glass was checked using lux meter and the RSW was found to have regained its visibility comparable to that of a new oil window. The entire oil of 1200 litre volume was decanted in sealed containers. The RSW was then loaded back in to the liner brick wall of the hot cell using the hydraulic power RAM and the specially designed pushing fixture. The oil was refilled in to the RSW using the oil regeneration equipment. The satisfactory view of the interior of hot cell-2 after the refurbishment of the oil filled RSW is shown in Figure 8.

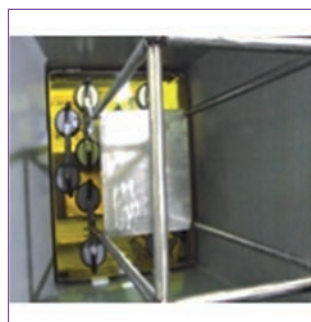


Fig. 7 Glass holding fixture

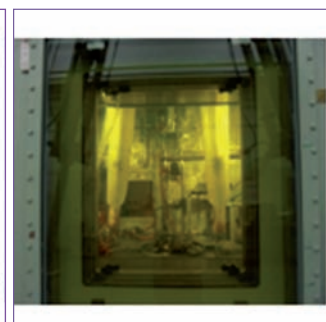


Fig. 8 Refurbished window remounted in to the cell liner brick wall with visibility

VII.12 Glove Box Adaptation of Scanning Electron Microscope for Examination of Alpha Active Samples

SEM examination and X-ray microanalysis of irradiated fuel specimens can provide valuable information on (a) irradiation induced microstructural changes (b) radial distribution of actinides and fission products and (c) chemical composition at locations of fuel clad chemical interaction (FCCI). The data regarding the irradiation behaviour is highly useful to the fuel designer for modeling the fuel performance. Examination of alpha active and irradiated samples in SEM is challenging and needs several adaptations to be made to facilitate handling and examination of such specimens. An SEM in the Radiometallurgy Laboratory has been recently adapted for examination of alpha active samples. The adaptation includes interfacing of SEM with a shielded Glove Box (GB) with a leak tight interconnection, alpha tight transfer of samples, transfer device for transferring samples from glove box to SEM and modifications in the specimen stage and vacuum system. Photograph of SEM interfaced with glove box is shown in Figure 1.

SEM which has been adapted for examination of radioactive samples has a 30 kV electron gun with LaB₆ filament having an image resolution of 2 nm. For imaging, a secondary electron detector and a motorized, retractable back scattered detector is used. X-ray microanalysis is carried out using a wavelength dispersive X-ray detector (WDS).

To handle alpha active samples and thin sections of irradiated fuel, a shielded GB of dimensions 1100 (L) x 1100 (W) x 900 mm (H) has been interfaced with SEM. GB has provisions for alpha tight transfer of samples. GB is attached to one of the spare ports of SEM through an interconnection set up consisting of hydro-formed bellow for vibration damping, pneumatically operated high vacuum gate valve and a mini-chamber extending into the glove box with a sealing door. A compact sputter coating equipment is provided inside the GB for providing a conductive coating which also serves the purpose of immobilizing the transferrable contamination. GB is provided with a once-through inert atmosphere ventilation system for handling of reactive and pyrophoric samples. Ventilation system for the laboratory is designed to provide once through ventilation meeting the requirement of controlled temperature and humidity for ensuring trouble free operation of SEM and accessories. A hood with a separate ventilation system is provided around SEM with provision for hands-on maintenance inside SEM chamber. Figure 1 shows the photograph of SEM interfaced with GB.

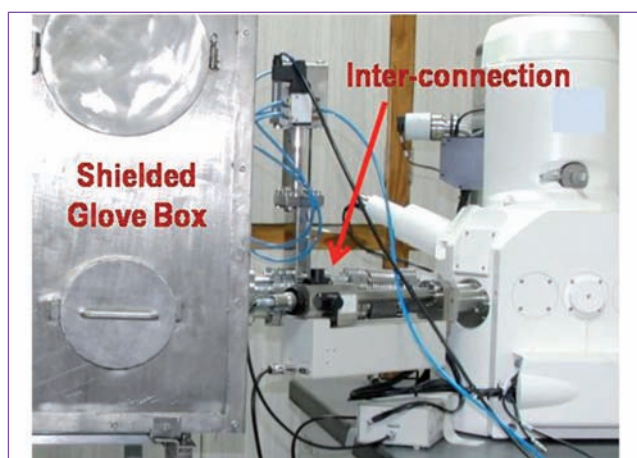


Fig. 1 Photograph of SEM interfaced with glove box

A leak tight Shielded Specimen Holder (SSH) made of tungsten alloy is used for handling prepared samples of thin sections of irradiated fuel / as-fabricated fuel mounted in 25 mm diameter stainless steel mould. Shielded specimen holder placed inside a stainless steel cassette is transferred from the hot cell through a alpha tight transfer port in the hot cell sealing door. The alpha tight container in a shielded cask interfaces with the transfer port of SEM GB for transferring the cassette, which is subsequently placed in a lead shielded pot for interim storage.

A specimen transfer device installed inside the GB enables transfer of SSH to the SEM stage. Transfer device consists of a manually operated linear stage with a screw shaft and LM guide having a travel range of 750 mm. Scissor grip mechanism of the transfer device is used to grip the SSH. The gripper with SSH moves along the LM guide driven by screw rod to travel from GB to SEM stage. Linear translation of the scissor gripper and the opening and closing of gripper jaw inside the SEM chamber is monitored using the IR chamber scope. Necessary tools and fixtures and shielding have been provided inside the GB for carrying out various operations such as opening and closing of lid of SSH, handling of SSH in sputter coater in order to minimize the radiation dose incurred to the operators.

Adaptations in the SEM include incorporation of a remotely operated flexible shaft for aperture alignment and filters/traps in the vacuum system and modifications in the SEM stage. Various safety related postulated events have been considered in the design of the system. The facility is expected to cater to the requirement of electron microscopy and microanalysis of alpha active samples.

VII.13 Wireless Power Solution using In-house Developed Rectenna Panel

The monitoring applications of Wireless Sensor Network (WSN) at hazardous zones have huge potential since they are inaccessible to humans. Life of battery powered WSN node is much limited; hence the wireless power solution is most sought. By default, wireless technology radiates energy in the form of Radio Frequency (RF) signals for establishing wireless communication. Today with the use of multiple wireless gadgets, RF energy is omnipresent. It is also feasible to intentionally transfer energy using RF waves to inaccessible areas. Hence the wireless power solutions can be designed to power the battery-free WSN nodes deployed for hazardous monitoring.

As the RF power disperses in space with inverse square law, 915MHz rectenna at the distance of 5m from the RF source of 4W is not sufficient to power the battery-free WSN node. To aggregate the dispersed RF power, rectenna panel design has been explored. Rectenna panel is the series and parallel interconnection of multiple rectenna. Apart from interconnections, the spatial arrangement of rectenna will have effect on panel aggregated power. Theoretically, it has been verified that the following rectenna panel parameters influences the performance of wireless power generation system, namely, (i) panel size (RPS), (ii) their number, (iii) spacing and (iv) panel design pattern. Maximum limit for RPS is governed by the RF beam solid angle and the distance of panel from the source. Rectenna Panel Utilization Factor (RPUF) can be increased by minimizing the rectenna aperture overlap. Elimination of the aperture overlap minimizes the Total Number of Rectenna (TNR) required for panel design. Even though optimum rectenna spacing is tightly coupled with its

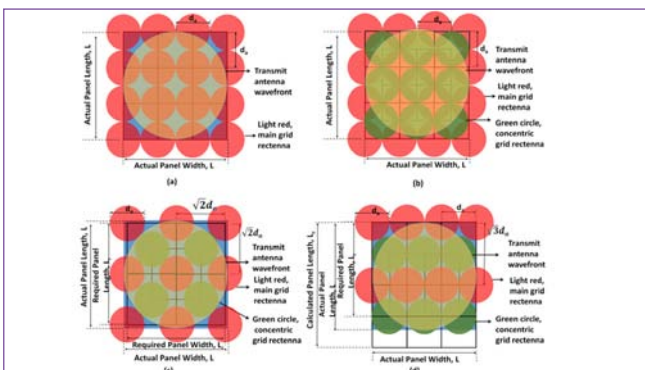


Fig. 1 Rectenna arrangement pattern comparison (a) Grid-1 (reference grid) with uniform rectenna spacing, d_a (b) Grid-2 with equal rectenna spacing, d_a (c) Grid-2_NO with equal non-overlap rectenna spacing, $\sqrt{2}d_a$ (d) Grid-2hetero with non-uniform spacing d_a & $\sqrt{3}d_a$

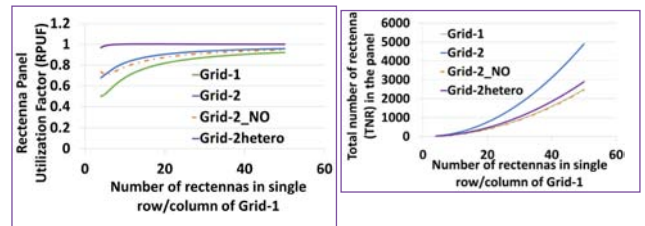


Fig. 2 RPUF and TNR plot for different rectenna arrangement shown in Fig 1.

effective aperture, their arrangement pattern (Figure 1) affects the RPUF and TNR. From Figure 2, it can be observed that Grid-2hetero results in highest RPUF.

For experimental validation, a 5x10 rectenna panel (Figure 3) was fabricated. It was observed that rectenna present at the grid corners does not contribute significantly to panel aggregated power. Further, the elimination of these rectenna demonstrates that hexagonal shape is optimum. If panel storage capacitors are not allowed to completely discharge, then the hexagonal rectenna panel with 10 number of rectenna (Figure 4) is sufficient for battery-free WSN node to transmit data at 1 sec interval when placed at 70m from the directional RF source of 4W.

This in-house development of rectenna panel demonstrates that WSN nodes deployed remotely at inaccessible zones can be powered through wireless power delivered by RF waves.

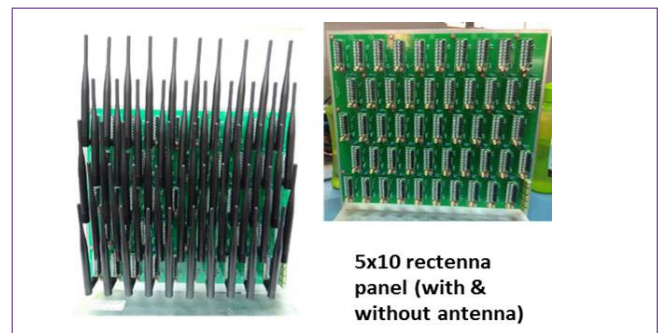


Fig. 3 Fabricated 5x10 array rectenna panel

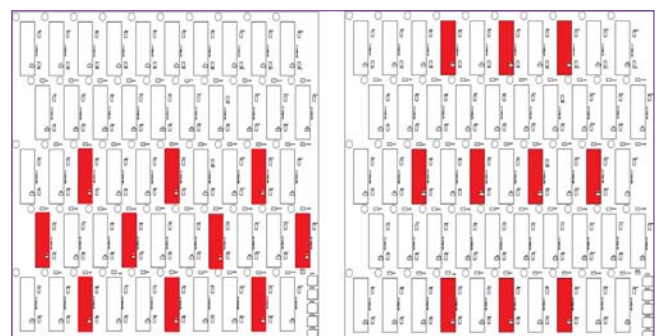


Fig. 4 Hexagonal rectenna pattern (red blocks are connected rectenna; row rectenna have parallel connection and rows output is connected in series)

VII.14 Deployment of Virtualized Graphics Workstations

Traditionally, physical workstations are used for delivering high-end graphics capabilities for 2D/ 3D modeling, simulation and analysis. They face several disadvantages in terms of investment, resource utilization and mobility. The Virtualized Graphics Workstations (VGW) provide customized workstation based on user requirement, efficient utilization of resources, ease of maintenance, reduced total cost of ownership and reduced obsolescence rate. In VGW approach, the remote server hosts Virtual Machines (VMs) that perform computation as well as graphics processing. The final displayed image is delivered through the network to the thin-clients that display those pixels and capture user I/O. A VGW setup has been configured at Computer Division by using two of the existing workstations and procuring the additional GPU card and software modules. The major steps involved in deployment are configuration & provisioning graphics enabled VMs, performance analysis and final deployment at user locations. Two virtualization servers are equipped with NVIDIA Tesla M60 GPU card and are used for hosting the vGPU enabled virtual workstations. Two management servers host the virtual machines required by the virtualization software for provisioning, authentication, monitoring, management and connection brokering. The VMware virtualization software stack and NVIDIA Virtual GPU Manager is used to achieve virtualization of graphics workstations.

Figure 1 depicts the major components of the graphics virtualization setup. Additional storage space is provided to user VMs from Network Attached Storage (NAS). The virtualization and management servers are hosted at computer Division. Users from various groups are accessing their assigned VMs through campus backbone network using thin-clients. VMware Horizon Client module is installed to access the respective users VMs. Six numbers of user VMs are provisioned on the two GPU enabled virtualization servers. The user VMs are installed with Windows 10 Operating System and loaded with high-end applications such as AutoCAD, SolidWorks, Ansys and Comsol. Three popular benchmark tools, namely, PassMark Performance Test, SPEC Workstation and SPEC Viewperf were installed and tested in virtual machines with different configurations as well as a physical workstation for comparing results. It was found that the VMs were able to run all the benchmark workloads successfully. It was concluded that a VM configured with the sufficient amount of resources can successfully run most of the workloads that typically a physical workstation is handling. Therefore, VGWs can provide high definition graphics rendering capabilities and computing power for scientific and engineering applications, with the benefits of centralized control, enhanced security and anywhere access.

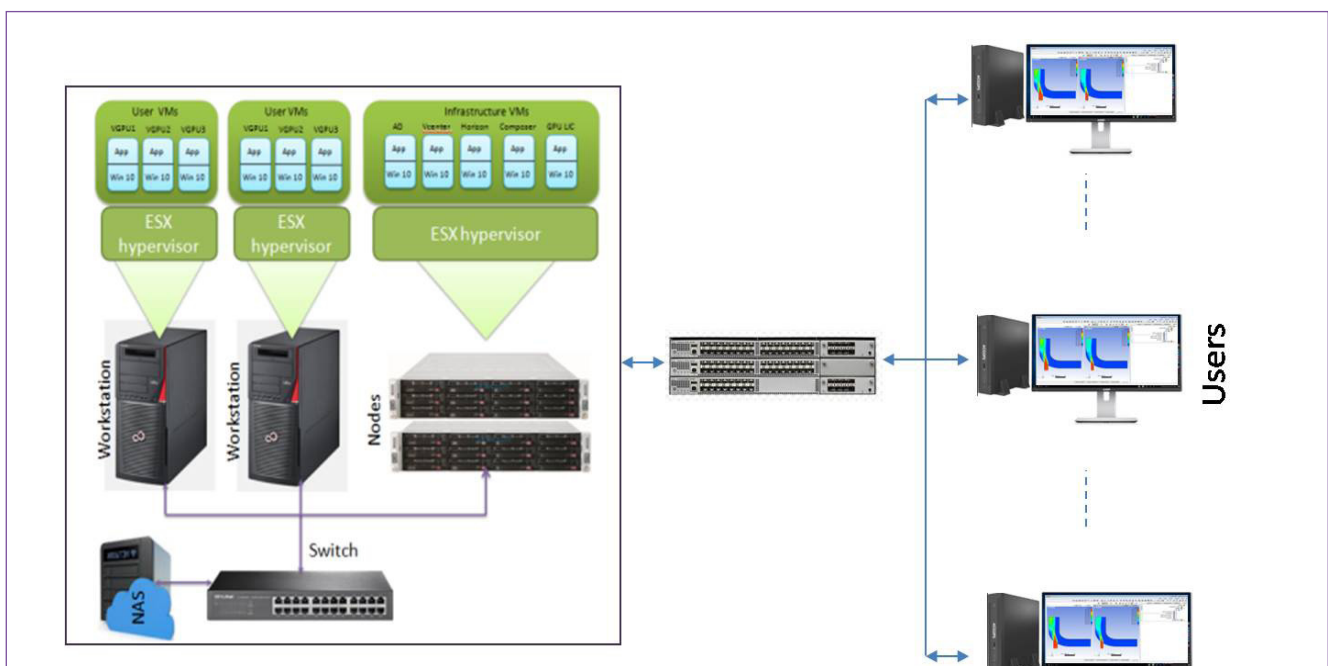


Fig. 1 Virtualized graphics workstations

VII.15 Upgradation of Sensitive Earthing System for Laboratories

Laboratories in IGCAR use many high end and sensitive equipment which are prone to power quality issues. One of the major issues observed in Labs is high neutral to earth voltage against the recommended value of < 1 Volt. Detailed study has been under taken and the major cause of this increased voltage was identified as high resistance of the neutral circuit. Triplen harmonic content was also observed to be very high. Various power quality solutions are available to correct power quality problem, including power factor correction, voltage stabilization, harmonic filtering, power conditioning and reactive power compensation. The above solutions are to be applied on case to case basis specific to the application. Procedure adopted in improving the power quality of CMPL power supply is discussed in this paper.

In CMPL building the Neutral to earth voltage of clean power system was found to be varying from 3.75 V to 4.7 V where sensitive instruments were connected. Root cause for this was examined and following issues were identified.

- Sensitive equipment for MSL & EIL are provided with dedicated isolation transformers to isolate these equipment from the disturbances in the main power system. But such a provision is not available for CMPL building. It receives power from EIL transformer that is 400 m away.
- The resistance of the neutral conductor from source end (EIL) to load end (CMPL) was relatively high.
- Neutral current was very high due to triplen harmonics generated by the EIL electronics non linear loads.

Considering all the above, following action plan was formulated.

1. Provide dedicated isolation transformer for CMPL
2. Replace cables from transformer to distribution board with cables of lower neutral impedance.
3. Replace the old fuse distribution boards (DB) and terminations with new MCB (DB) and new terminations to reduce the contact resistances.
4. Improve all the earthing connections and earth electrodes to minimize the earth resistance



Fig. 1 Clean PDP CMPL

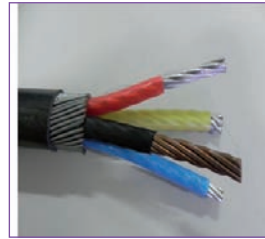


Fig. 2 4Cx35 sq.mm special cable



Fig. 3 50 kVA Dry Type isolation transformer

Based on the above, various steps were initiated.

- Replaced the existing VTPN DB with a Power Distribution Panel (PDP) (Figure 1) with neutral bus bar of copper having cross section equal to that of phase bus bar.
- Replaced existing feeder cable with special cable of neutral conductor alone made of copper with cross section of equal size to the phase conductor (Figure 2) thus reducing the resistance of the cable neutral
- Provided a 50 KVA Dry Type dedicated isolation transformer for sensitive equipment loads in CMPL (Figure 3)
- Provided a separate Neutral earth pit for Isolation transformer which is nearer to the CMPL loads.
- Treated the earth around earth electrodes to improve earth resistance and conductance.
- Replaced earth junction points with tinned copper flat supported by SMC insulator to minimise the contact resistance and isolate from other disturbances.

The following table gives the drastic improvement in power quality after completing the above steps:

Upgradation and modification of existing system for the above installation yielded positive result in overall improvement of power fed to sensitive equipment and will definitely increase the life of the electrical system.

Table 1: Improvement in power quality		
Parameter	Before up gradation	After up gradation
Feeder cable neutral Impedance.	1.624 ohm / km	0.507 ohm / km
Neutral Voltage, Vn	4.7 V	0.1 V
Neutral Current, In	6 A for 3 A Phase current.	0.5 A for 60 A Phase current
Triplen Harmonics	700 %	86.5%
Neutral Voltage Harmonics, VnTHD	740 %	120 %
Negative Sequence Voltage	0.3	0.1
Zero Sequence Voltage	0.2	0

VII.16 Development of Flowing Concrete Mixture for Construction of Congested Steel Reinforced Structures

During construction of safety critical elements having reinforcement congestion, like pin vault storage slab (Figure 1), waste tank farm floor slabs, flowing concrete is required in order to pass and fill re-entrant corners, penetrations and steel reinforcement. Although self-compacting concrete is preferable for concreting such critical elements, the associated risk of cold joint formation is managed with high production rate of concrete. At the same time, the intended shielding density at hardened state cannot be obtained. In order to meet this requirement, a flowing concrete mixture was developed at FRFCF.

A concrete mixture with Ordinary Portland Cement (OPC), flyash, Crushed Sand (CS), 12.5mm coarse aggregate, chemical admixture was developed after initial trials and tests were performed to assess its stability, uniformity of strength, density, RCPT value, spreading ability and settling time. The spreading ability measured through slump flow test of flowing concrete is 400-500 mm against 700 to 800 mm for self-compacting concrete. Typical slump flow test is shown in Figure 2.

Ultrasonic pulse velocity (UPV) and core samples were tested along the height of 750mm thick slab as depicted in Figures 3a and 3b. Flowing concrete mixture proportion and selection of admixture together altered the mixture rheology, setting time and RCPT values as shown in Table 1. The comparative gain in compressive



Fig. 2 Flow-ability using slump flow test

strength in relation to the conventional concrete is shown in Figure 3c.

The flowing concrete mixture has properties similar to that of conventional concrete but with spread limited to 400-500 mm, thus, minimizing the risk of cold joint formation when used in constructing slabs with congested steel or penetrations. This flowing concrete mixture is utilized in the construction of pin vault and waste tank farm of FRFCF having congested steel reinforcements.

Table 1: Properties of conventional and flowing concrete				
ID	Density (kg/m ³)	Setting time (hrs)		RCPT (coulombs)
		Initial	Final	
CC	2494	6	8.5	376
FC	2474	7	9.75	371



Fig. 1 View of pin vault prior to concreting

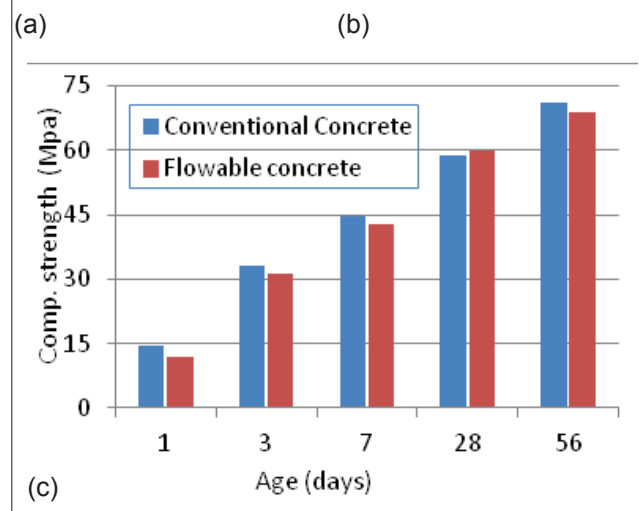


Fig. 3 (a) Core sample extraction (b) UPV testing and (c) Compressive strength of conventional and flowing concrete at different ages

VII.17 Challenges in Structural Health Assessment of Concrete Structures in Nuclear Fuel Cycle Facilities

Structural health assessment of concrete structures in the fuel cycle facility (FCF) is part of ageing management (Figures 1 to 3). The goal of ageing management is to address systematically all the time-dependent parameters that can jeopardize the FCF safety during its life. It is especially crucial for the potential life extension of the facility and for deciding its refurbishment or its shutdown and decommissioning. FCFs are characterized by their radioactive and chemical materials, in diverse physical and chemical forms, spread in interconnected vessels and equipment. The service life for most FCFs was chosen to be 30–40 years. However, due to economic benefit, utilities prefer to extend plant service life to say 60 years or more. Concrete is a durable material and its performance as any Nuclear facility has been good. However, experience shows that ageing degradation of concrete structures, often caused or accelerated by factors such as faulty design, use of unsuitable or poor quality materials, improper construction, exposure to aggressive environments, excessive structural loads and accident conditions, can impair the safety functions of concrete structures and can increase risks to public health and safety. Effective ageing management of concrete structures is required to ensure their fitness for service throughout plant service life and during decommissioning.

Generally, four stages of survey are undertaken to reach an assessment regarding the condition of a building, such as Preliminary survey, Planning, Visual inspection and Field and laboratory testing. As it is not feasible to conduct field testing on every structural member in a facility, representative structural load-bearing elements such as column, beam, wall, etc., at various elevations have to be chosen by the utility and investigating team during the walkthrough and after studying around hundreds of construction drawings for further testing. Degradation of concrete usually manifests as cracking. Cracks can be formed in concrete due to plastic settlement, early thermal contraction, long term drying shrinkage, loading or reinforcement corrosion. The cracking and permeability enhance the adverse impacts of degradation mechanisms and leads to further concrete degradation primarily involving carbonation and chloride penetration.

Nondestructive tests of rebound hammer, ultrasonic

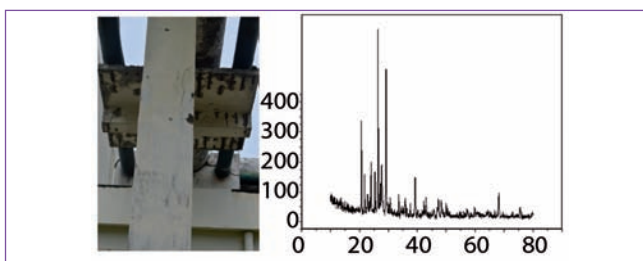


Fig. 1 Visual examination and XRD of concrete



Fig. 2 Semi destructive coring and laboratory assessment

pulse velocity (BIS), resistivity (RILEM) and Half cell potential (ASTM) were conducted in the field. Mapping in localized areas of concern is at times attempted using infrared thermography and ultrasonic impact echo methods. Tests for pH and chloride content (Table 1) (BIS) of cored samples and strength tests (BIS) are usually resorted to in the lab augmented by XRD.

Being operating plants, measures are taken for radiation safety and industrial safety of the investigating team without affecting the functions of the plant. For radiation safety, a work permit is approved only if the radiation levels are within limits in a specific facility during functioning or shutdown states. Personnel protection measures are insisted upon during testing.

At inaccessible areas such as waste vaults, in-service inspection vehicle is relied upon for visual assessment. The healthiness of the foundation and basement area generally depends upon the quality of soil and groundwater. Hence soil and water samples are collected from bores and tested. Due to limited oxygen content in groundwater, concrete elements embedded in non-aggressive soil have generally good life span. At times the foundation is bared for further investigation.

Currently, concrete structures of CORAL and DFRP are assessed to be in order, for continuing the service life and operation.

Test ID	Acid Soluble Chloride content (kg/m ³)	pH of concrete	Half cell potential values (Volts)	Resistivity (kΩcm)
1	0.306	10.86	-0.021 to -0.16	172 to 560
2	0.652	9.57	-0.003 to -0.147	395 to 678

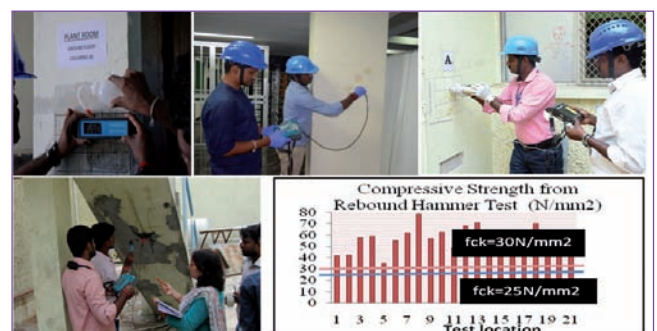


Fig. 3 Non destructive tests & results

VII.18 Seismic Response Studies on Base Isolated Multi-Storey Concrete Building

Seismic response mitigation of safety related structures and systems of nuclear power plants using various response control techniques such as base isolators and dampers are actively researched in DAE. As a part of the ongoing collaborative research activities between BARC and IGCAR, shake table experiments were performed on 100 t multi axial shake table to study the seismic response of a full scale multi-storey reinforced concrete structure to demonstrate the effectiveness of base isolators in reducing the seismic response of concrete structures.

The study aims to compare the dynamic responses of multi-storey concrete building mounted on a base isolator with that of a fixed base structure and to characterize the primary secondary structure interactions. Towards this, a three storey reinforced concrete building of dimension 4.5 m x 4.5 m x 9 m was constructed and instrumented with strain gauges, accelerometers and laser sensors. Around 50 strain gauges were pasted on the steel reinforcement rods at critical locations before pouring concrete and precautions were taken to protect the same during concreting. A lug supported steel tank was anchored at the second floor whose inlet nozzle is connected to a steel piping which penetrates both first and second floor and finally anchored at the ground floor shown in figure.1. Various tests were performed to study the responses of building-equipment systems and responses were captured using 10 tri-axial accelerometers, 50 strain gauges and 6 Laser displacement sensors mounted at critical locations. Responses of the building were measured for three cases viz. (i) structure mounted on laminated rubber bearing reinforced with steel plates; (ii) structure mounted on fiber reinforced rubber bearing and (iii) structure rigidly fixed on shake table.

For all the three cases, first the dynamic characteristics of the system such as natural frequencies, damping etc. were assessed using sweep sine tests by varying the excitation frequencies from 0.5 Hz to 50 Hz for a constant acceleration of 0.2 g and recording the responses using 128 channel data acquisition system. Experimental results indicated the reduction in fundamental natural frequency of the building from 1.8 Hz to as low as 0.7 Hz with the base isolators compared to fixed case. Subsequently to seismic zones II, III, IV and V as per



Fig. 1 Base isolated Multi storey building with equipment and piping on shake table

Indian Standard (IS-1893) by increasing the amplitude of vibrations in steps. It is observed that, the dynamic responses such as acceleration and strain values were reduced drastically (up to 40%) with base isolators and no failures were observed for the structure or equipment. As part of fragility assessment of concrete building, the earthquake excitations are increased beyond Zone-V level (more than 0.36 g) for fixed base case. Hinge formation on the base footing has been observed around 0.6 g PGA which is almost 1.6 times of Zone-V earthquake level. This series of experiments helped in demonstrating the effectiveness of base isolators in mitigating the severe seismic loading on civil structures, piping and equipment. The experiments also generated data to serve as a bench mark for the future studies in this area.

VII.19 Enhancing the Energy Efficiency of Central Water Chilling Plant at IGCAR

Central Water Chilling Plant is responsible for providing round the clock air conditioning and ventilation services to various plants, buildings & laboratories of IGCAR. The installed capacity of plant is 3100 TR. It comprises of centrifugal chillers and allied accessories like condenser water pump, chilled water pump, cooling towers and air handling units.

Average Energy consumption of Central Water Chilling Plant is 32546 kWh/day. Energy conservation measures are being implemented to reduce this energy consumption by improving the system and minimizing the wastages. The following energy conservation measures are implemented during 2019:

- 1.Revamping of old cooling towers
- 2.Revamping of 3 km long underground chilled water pipelines.

The cooling towers play a vital role in discharging heat loads removed from various buildings by means of air-water-refrigerant heat exchangers, finally to the atmosphere. The performance of the cooling towers at CWCP deteriorated over the years of continuous operation and cooling tower outlet water temperature rises thereby increasing the power consumption of chiller.

After revamping (Figure 1) it is found that the effectiveness of the cooling has improved (Cooling tower effectiveness = Range/[Range+approach) as indicated in the table and about 10-12 cells are sufficient to remove the heat load of 2000 TR against operation of 16 cells before revamping. The performance of cooling towers before and after revamping is shown in Table 1.



Fig. 1 CWCP cooling tower after revamping



Fig. 2 Erection of pre-insulated underground pipes

Chilled water from CWCP is distributed to various facilities of IGCAR through a network of underground pipelines (Figure 2). The underground pipelines are about 40 years old and leaking at different locations causing about 11 m³/h of chilled water loss.

Underground chilled water pipelines in PIF-CDO segment and HBB-MSL segment were leaking the most. Hence 3000 m of chilled water pipelines in these segments were replaced with new pre-insulated pipes and 5 m³/h chilled water leakage was reduced.

By implementation of the above measures in the Central Water Chilling Plant, about 1086 kWh/day energy was saved which is about 3.34 % of total Energy consumption of Central Water Chilling Plant per day and water saved was about 120 m³/day.

Table 1: Effectiveness before and after revamping					
Before revamping			After revamping		
Range (°C)	App. (°C)	Effective-ness	Range (°C)	App. (°C)	Effective-ness
3.1	6.4	32.6	4.8	3.8	55.81
3.5	6.5	35	4.7	3.9	54.65
2.8	6.7	29.5	4.6	4.0	53.49
3.4	6.1	35.8	4.7	3.7	55.95

VII.20 EURADOS Inter-comparison Study on the Usage of ICRP Voxel Phantoms for Occupational, Environmental and Medical Dosimetry

The European Radiation Dosimetry Group, EURADOS, is organizing an intercomparison study on the usage of the ICRP/ICRU voxel reference computational phantoms together with radiation transport codes for solving tasks of practical interest to occupational, environmental and medical dosimetry. The aim of this exercise is to investigate if the phantoms have been correctly implemented in the radiation transport codes and to give participants the opportunity to check their own calculations against quality-assured master solutions. IGCAR is participating in this exercise.

Under this exercise six tasks were provided. IGCAR has submitted the results for three cases. They are (1) estimate the organ absorbed dose for red bone marrow (RBW), colon, lungs, stomach, breast, gonads, liver, oesophagus, brain and skin for a 10 min exposure to 10GBq of ⁶⁰Co point source located at a distance of 1 m in front of the abdomen of the voxel phantoms. From these absorbed doses the participant has to estimate the sex averaged effective dose. (2) calculate organ absorbed dose rates for brain, small intestine, lungs, stomach and RBW for the voxel phantom standing at the centre of 2 m radial concrete floor having a uniform surface contamination of isotope ²⁴¹Am. From these absorbed doses as well as the absorbed doses to other organs for which tissues weighting factors are provided in ICRP 103, calculate the effective dose rate to the wholebody. (3) Estimate the absorbed fraction and specific absorbed fractions (SAF) of energy in 36 different combination of source and target organs each for 7 different mono energetic photons and electrons.

Figure 1 shows the modeling of liver as source organ and lungs as target organ. Part 2 of this task is to estimate the dose due to unit intake of ^{99m}Tc

The male and female voxel phantoms were modeled in MCNP using the square lattice structure. Heating tally (F6) was used to obtain the absorbed energy in each of the target region for all the three cases for photons and Energy deposition tally *F8 was used for electrons. Wherever multiple tissues were involved like lungs, bone marrow, colon the mass weighted dose was estimated. For bone marrow the

dose was estimated with the energy deposited in the spongiosa as there is no segmentation of bone marrow and the endosteum in ICRP voxel phantom. The dose to bone surface was calculated from the dose to spongiosa

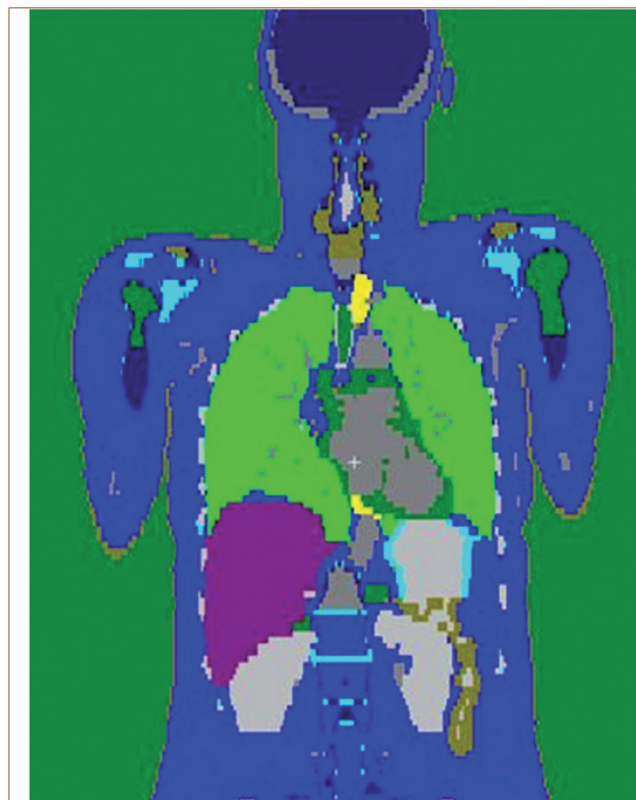


Fig. 1 Modeling of liver as source and lungs as target for SAF estimation in Task 3

and the medullary cavity. In case of ⁶⁰Co only 1173 and 1332 keV gammas photons and for ²⁴¹Am only 59.54 keV was asked to be simulated. Final compilation of the results of all participants is awaited.

(Task-1): The absorbed doses to different organs due to

Table 1 : Absorbed dose to different organs for ⁶⁰Co point source

Organ	Absorbed dose (Gy)	
	Male	female
Red bone marrow	3.21 x 10 ⁻⁴	5.16 x 10 ⁻⁴
Colon	4.02 x 10 ⁻⁴	4.07 x 10 ⁻⁴
Lungs	3.65 x 10 ⁻⁴	3.43 x 10 ⁻⁴
Stomach	4.06 x 10 ⁻⁴	3.76 x 10 ⁻⁴
Breast	1.33 x 10 ⁻³	4.81 x 10 ⁻⁴
Gonads	3.77 x 10 ⁻⁴	3.28 x 10 ⁻⁴
Liver	3.78 x 10 ⁻⁴	3.79 x 10 ⁻⁴
Oesophagus	3.52 x 10 ⁻⁴	3.66 x 10 ⁻⁴
Brain	2.82 x 10 ⁻⁴	2.93 x 10 ⁻⁴
Skin	3.15 x 10 ⁻⁴	3.15 x 10 ⁻⁴

point source are provided in Table 1. The breast of male receive more dose because of more muscle content and lesser mass compared to female breast which has more fat content. Muscle has more density and therefore attenuates the gamma photons to a greater extent. From the averaged equivalent doses of male and female organs the effective dose for human was estimated as 0.361 ± 0.036 mSv.

(Task-2): The absorbed doses to different organs due to surface source are provided in Table 2. It is observed that for both male and female the skin received higher dose because 60 keV photons being of lower energy is being cut off by the skin. It is observed that the organs in the lower half received higher dose compared to the upper half. This again is due to the attenuation of 60 keV gamma photons in the lower part of the body. The red bone marrow, bone surfaces and gonads of the male received higher dose compared to that of female. The average effective dose rate was calculated as 1.09 ± 0.05 E-07 Gy/s. The effective dose rate of male was two times higher than that of female. The IGCAR results are very close to the reference solutions.

(Task-3): Figure 2 gives the absorbed fraction of energy for liver as source organ and different target organs and different energies. From the figure it can be observed that for the same source and target organs as the energy increases the absorbed fraction decreases (liver –liver). For different source and target organs when they are close it increases upto 0.05 MeV and then decrease. (thyroid - liver and stomach wall - liver). This is due to the escaping of more fraction of energy from the target as the energy increases. In case of target organs which are far from the source organ, the absorbed fraction increases as the energy increases. This is because smaller energies get attenuated by organs present in their path. Compared to photons the electrons absorbed fraction was upto five times higher when the source and

Table 2: Absorbed dose to different organs for ^{241}Am surface source

Organ	Equivalent dose (Gy/s) ($\times 10^{-8}$)	
	Male	female
Bone marrow	10.35	7.52
Colon	7.20	7.46
Lungs	3.64	5.65
Stomach	8.97	6.02
Breast	5.85	5.86
Gonads	16.48	9.22
Oesophagus	2.55	3.43
Liver	5.03	6.39
Thyroid	3.01	4.07
Bone surface	54.2	19.50
Brain	2.61	3.36
Salivary gland	4.34	4.74
Skin	16.28	17.88
Urinary bladder	1.29	10.11
Remainder organs	5.79	7.82

target regions are same. When organs are different the values are two to four orders less. In part 2 the dose due to Auger and internal conversion electrons were significant compared to photons when the source and target organs are same. When the source and target are different the doses are more than 3 orders lower. In this task too of IGCAR results were matching within $\pm 5\%$ for 95% with the master solutions.

The participation in this intercomparison exercise gave us the confidence of usage of ICRP voxel phantoms along with transport codes for dosimetry purposes. The expertise developed in this exercise can be used to estimate the effective dose in any emergency situations or conditions in which the personal dosimeters are not available.

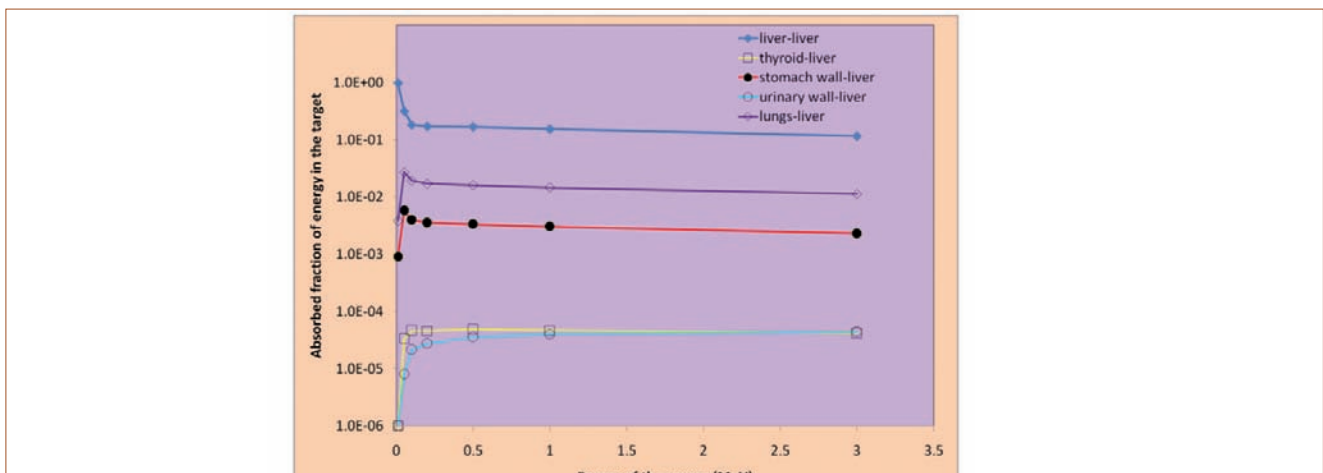


Fig. 2 Variation of absorbed fraction with energy for different target organs with liver as source

VII.21 Validation of Weather Prediction Model WRF of the Decision Support System Operational for Various NPP Sites in India

Real-time dispersion simulation of atmospheric release of radionuclides is highly essential for emergency response application in the event of accidents at nuclear facilities. The critical meteorological parameters that govern the atmospheric transport and dispersion of radionuclides are wind field, boundary layer height, turbulent fluxes, rainfall etc. These parameters widely vary across different locations due to variations in local topography. As part of Emergency Preparedness program an upgraded Decision Support System (DSS) called 'Online Nuclear Emergency Response System (ONERS-II)' has been developed in common framework for various Nuclear Power Plant (NPP) Sites of India. ONERS uses numerical weather prediction and dispersion models to project the radioactive plume and dose in the off-site ranges. The required meteorological parameters for dispersion simulations over different NPP site locations are predicted using an advanced numerical weather prediction model WRF (Figure 1). This model was configured with 40 vertical levels and eight interactive nested domains of different horizontal resolutions (outer domain with 18 km, intermediate domain with 6 km and inner fine domains over Kalpakkam, Tarapur, Rawatbhatta, Narora, Kudankulam, Kakrapara with 2 km and Kaiga with 1 km) to capture the dynamical largescale weather pattern over the Indian region and to predict the site-specific wind field precisely over each NPP site region.

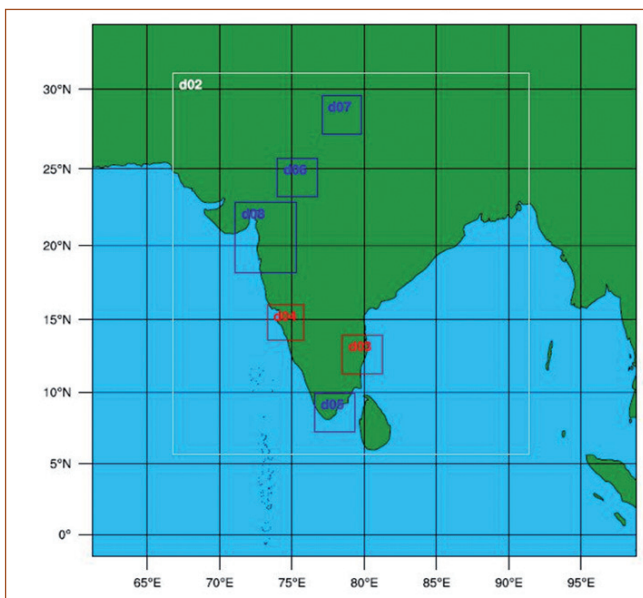


Fig. 1 WRF domain configuration

The initial and boundary conditions for operational model simulations are derived from the 0.5 x 0.5 degree resolution National Centers for Environmental Prediction (NCEP) Global Forecasting System (GFS) model analysis and 3-hourly forecasts. The archived observations over the Indian region gathered through Global Telecommunication System (GTS) from NCEP are used to enhance the initial conditions. The model is run once in a day with initialization at 06:00 IST (00:00 UTC) and is integrated for 72 hours. The finescale predictions from the inner domains are used for operational dispersion predictions in ONERS. The model is incorporated with several physics parameterizations such as simple first order K-profile based non-local eddy diffusion scheme for boundary layer turbulence, explicit land surface physics dealing with soil, vegetation, canopy and ice processes, mass-flux based convection physics for deep lagescale convection, 2nd moment 6-hydrometeor cloud microphysics, Monin-Obukhov similarity surface layer physics and Rapid-Radiative model for short and long-wave transfer. These physics parameterizations are taken into account based on past physics tests conducted for mesoscale windfield simulations using WRF.

The performance of WRF for predicting the boundary layer parameters was studied for winter (January 10-20 2017), summer (April 10-20 2017), SW monsoon (July 10-20 2017), NE monsoon (November 10-20 2017) periods by comparing with observations such as

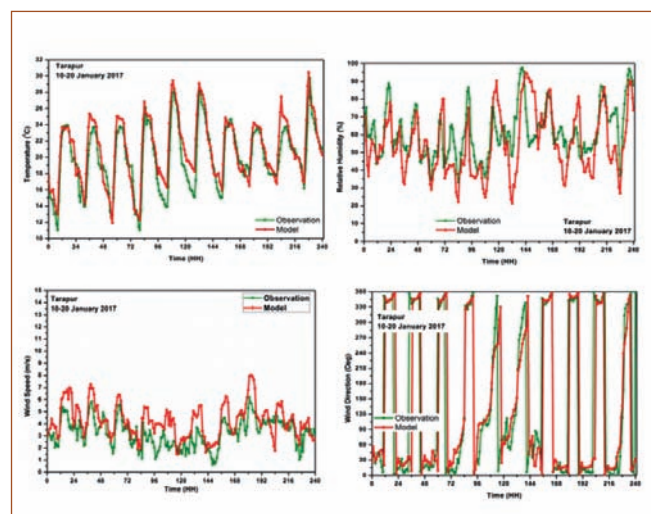


Fig. 2 Time variation of surface variables (a) temperature at 2m (b) relative humidity at 2m (c) wind speed at 10m and (d) wind direction at 10m during winter period at Tarapur

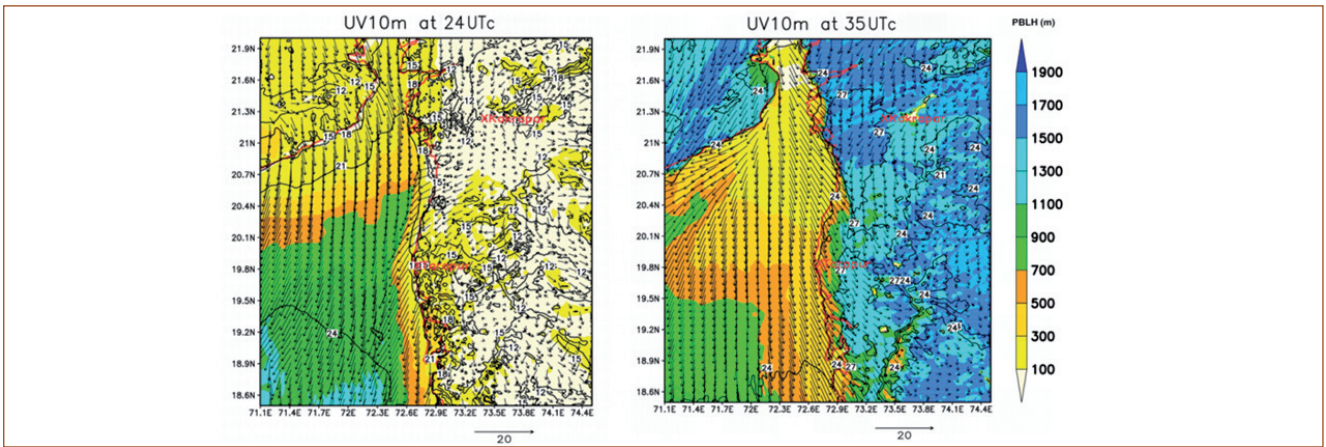


Fig. 3 Spatial distribution of temperature (contour), boundary layer height (shaded) and wind flowfield (vectors) on 11 January 2018 at 06 IST(left panel) 17 IST (right panel)

local meteorological towers at NPCIL-NPP locations, India Meteorological Department radiosonde data, and Modern-Era Retrospective analysis for research and Applications 2 (MERRA2) reanalysis datasets for all the NPP stations. As an example figure 2 shows the time evolution of temperature at 2m (T2), Relative humidity at 2m (Rh2), wind speed and wind direction at 10 m at the coastal NPP station Tarapur on the west coast during winter.

It is observed that the simulations could reproduce the diurnal variations in various surface meteorological parameters with minimum error. Also the seasonal variation of various weather parameters at all the stations could be simulated though with few differences at individual stations. The errors in winds are noted to be more at Narora where the waterbody effect could not be represented in the model. Further work to include such topographic effects is in progress.

Figure 3 shows the spatial distribution of predicted flow field, temperature and boundary layer height at 06 IST and 17 IST for 11 January 2018 during winter season. The model could reproduce the observed characteristics of shallow mixing layer during early morning hours and

deep mixed layer in the daytime. The spatial field and its diurnal variations could also be simulated well.

To validate the model vertical atmospheric structure at each NPP location radiosonde observations from nearest IMD weather observatory were used for comparison. As an example figure 4 illustrates the vertical distribution of simulated potential temperature, relative humidity, wind speed and wind direction at Mumbai (nearest IMD station to Tarapur) along with the radiosonde observation at 17.30 IST. The observations at Mumbai radiosonde station are compared with the predictions from nearest model grid. Qualitative comparison of vertical profiles indicates the model could simulate the vertical thermal and wind structure indicating the vertical variations in temperature, humidity, wind speed and wind direction in reasonable agreement with observations. Similar comparisons are done for other NPP sites as well and for all the periods.

The mean error statistics for all the simulation days indicate the surface winds are ingeneral slightly overestimated which need further investigations on the surface drag effects.

The weather prediction data for the seven NPP sites has been utilized by the NPCIL for operational dispersion analysis using Decision Support Systems. The data is also used by the Nuclear and Radiological Emergency Monitoring Centre (NREMC), AERB , Mumbai.

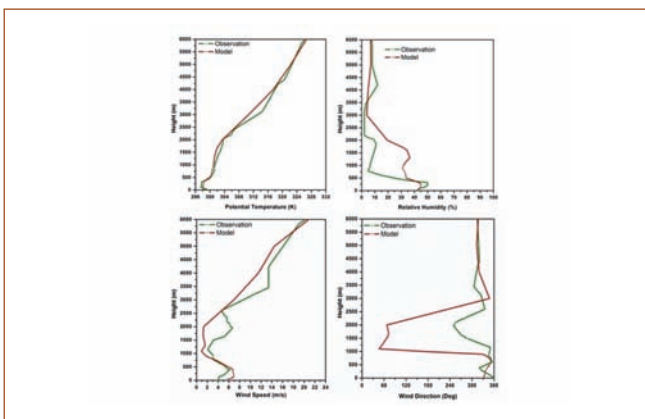


Fig. 4 Comparison of vertical profile of potential temperature, relative humidity, wind speed and wind direction with Radiosonde observations at Mumbai station during winter season

Table 1: Error analysis of the surface parameters at Tarapur station for the winter (T is the temperature, RH is the relative humidity, WS is the wind speed and U and V are the horizontal component of the wind speed)

Error	T (oC)	RH	WS	U	V
MB	0.9	-5.5	1.0	-0.10	-0.20
MAE	1.3	11.6	1.1	3.19	3.03
RMSE	1.70	14.70	1.378	3.94	3.84
CC	0.93	0.74	0.71		

VII.22 Emergency Response Actions at Site During Nuclear Emergencies / Exercise

Nuclear emergencies at nuclear installations are categorized as emergency alert, plant Emergency, site and off-site emergency. The operating organization is responsible for handling the first two types of emergencies and site emergency in a coordinated manner by Kalpakkam Emergency Committee (KEC). Off-Site Emergencies involving radiation fallout in the public domain is handled by state authorities with technical input and guidance from the operating organization. The probability of an incident to cause declaration of site/ off-site emergencies in Kalpakkam is assumed to be from MAPS and PFBR (Hazard Cat- 1). Site Emergency Exercise (SEE), a mandatory requirement of AERB to test the effectiveness of emergency plans at all levels is being conducted by KEC at Kalpakkam complex in 2019. An evaluation of the response shall be carried out at the end of each exercise to take care of any deficiency noticed and also to update the plans if required.

Site Emergency Exercise: KEC meeting conducted before exercise for various working groups to plan their activities for the smooth conduct of the exercise as per revised AERB manual EP-5. KEC decided to conduct the exercise during 21-25, October, 2019 without announcing the exact date and observe the response of different agencies involved. It was also decided to evacuate employees & contractors from work site to site boundary (Main gate & Kokiamedu gate) in first phase and from there to the respective township by separate set of buses in the second phase. A site emergency exercise coordination committee consisting of personnel from various Kalpakkam DAE facilities was constituted, to coordinate the preparations and modalities of conducting the exercise in an effective manner. Meeting of the committee was conducted to update the details of about 100 assembly area (AA) coordinators, boarding points and instructions were communicated to be followed during the emergencies and evacuation.

After declaration of plant emergency at MAPS on



Fig. 1 Contamination survey at exit gate

October 21, 2019 followed by site emergency alert, KEC assembled at Site Emergency Control Centre (SECC) at HBB, IGCAR. Site emergency has been declared and response actions were taken by KEC based on periodic injects about radiation levels received from exercise control team of AERB and NPCIL members. The sirens located at IGCAR & BARCF (K) (MSL, HBB, RDL, CWCP, Stores Building, CWMF, KARP, WIP, RCL, FBTR and DAE-UGC consortium Building) were sounded to inform site persons to assemble at designated assembly areas. All the assembly areas were contacted from KEC frequently to get the status of the assembly of personnel and the head-count for deployment of required number of buses to various boarding points for safe evacuation of site. Evacuation from the site in first phase completed in the order MAPS, BHAVINI and FRFCF through main gate. In the second phase BARCF and IGCAR were evacuated through KKM gate. About 9000 persons including contract workers were evacuated from site either by own vehicle or in departmental buses. Within 3 hours evacuation of the site was completed (Figure 1).

Decision Support System (DSS) operated at SECC to assist KEC for early response actions during emergencies. The DSS predicted cloud shine dose map using online meteorological data and using the source term (EALs) for the incident in MAPS. Evacuation routes from the site to be decided on wind direction, avoiding movement near to the affected plant. Radiation monitoring network available in the site consist of Indian Environmental Radiation Monitoring Network (IERMON), gamma dose logger, argon flounce monitor and area gamma monitors provide continuous update to DSS/ MAPS control room and SECC.

A radiation survey team went on declaration of site emergency for environmental radiation monitoring to measure (a) ambient radiation level (b) airborne radioactivity (c) ground contamination levels at various location of site and it was communicated to KEC. Contamination survey teams were deployed at the assembling areas to check the personnel contamination and for administration of prophylaxis (chocolates notionally) before evacuation. Contamination check for the vehicles leaving the site was carried at both exit points. Contaminated vehicles are being decontaminated at CWMF.

The unannounced exercise demonstrated the effectiveness of the emergency preparedness arrangements established and implemented by the Kalpakkam DAE Centre. The observations made by observers from AERB is being reviewed to initiate suitable corrective actions for enhancing the response capabilities further.

VII.23 Digitally Transformed Institutional Library with Enhanced Services

Scientific Information Resource Division (SIRD), the institutional library of IGCAR housing about 62,000 books, 48,000 back volumes, 550 e-journals, 15,000 standards, and two lakh technical reports has been catering to the research needs of scientists, engineers, technical and administrative staff of DAE campus at Kalpakkam including IGCAR, BARC(F), MAPS, PRP, GSO and Bhavini and research scholars from HBNI for now over four decades.

As part of Digital library augmentation, library information management system was streamlined by enhancing the RFID based infrastructure (Figure 1a), migrating bibliographic data to MARC format, and implementing features like virtual book racks, single window access to all holdings, user alerts, etc. Replacement of RFID Tags of 60,000 books was accomplished without affecting the regular library services.

A centralized Institutional Repository has been developed which include journal articles, theses, in-house publications (Reports, Newsletters, Annual Report etc.) and news clips using the standard D Space platform. During the year 2019, 466 scholarly articles were published by IGCAR in 220 Journals. The average Impact Factor of IGCAR for 2019 is 2.368.

SIRD provides seamless access to scientific/technical information resources (Figure 1b) and takes the responsibility to enhance the scholarly-publications of the scientific community by conducting author workshops, plagiarism checks and providing tools like endnote and grammarly.

A Materials Database has been developed for archiving and sharing the peer reviewed materials property data from IGCAR and other premier research units of India.

The centralized reprography services for IGCAR, DPS, and BARCF facilities were made cost-effective through a full-service annual maintenance contract and has been streamlined through a web portal developed by SIRD. The duplicate copies of magazines, newsletters, documents were recycled as part of the green initiative.

SIRD was awarded the “Digitally Transformed Research Library Award for 2019” by Wiley, a multinational publisher (Figure 1c). Nominations were from thirty five research institutes across South Asia. This award was due to the efforts made by SIRD in the creative and innovative use of technology and programs to excel in improving library staff productivity, increasing usage of digital library resources, and achieving high user satisfaction.

Desktop publications activities brings out annual reports, newsletters with ISSN, desktop calendars, necessary brochures, etc of the centre. The milestones and significant achievements since the inception of IGCAR were collated and the select photographs since 1971 were retrieved from the archives for the souvenir titled “Memoirs of Indira Gandhi Centre for Atomic Research” (Figure 1d) which was released during the first Foundation Day celebrations on April 30, 2019.

Also the scientific and technical events of IGCAR are regularly recorded. As part of this, 45 events were filmed, including few short films on DFRP, RML hot cell, 50th Campaign of CORAL facility, cement concrete roof slab break test, sample handling robots of DFRP, etc.

SIRD is continuously thriving to enhance its activities by promoting digital library services for achieving higher user satisfaction levels.



Fig. 1 (a) RFID hand held Reader, (b) Information Resources, (c) Wiley Library Award and (d) Memoirs of IGCAR

VII.24 Avian Fauna at DAE Campus, Kalpakkam

Scientific Information Resource Division, IGCAR has documented about 152 species of avian fauna in and around DAE Complex, Kalpakkam. Birds are sighted in large numbers in the water bodies near FBTR backwater, WIP Marsh and Mangrove vegetation behind DAE Guest House.

Few rare birds that were documented in this year in Kalpakkam are discussed very briefly. The Bar-headed goose is one of the world's highest-flying bird and travel across Himalayas during migratory period. Flock of Bar-headed geese (Figure 1) were first time sighted this year and the news was published.

Black bitterns (Figure 2) are very shy, secretive and nocturnal. They are rarely found in our campus. They were first time recorded this year in FBTR backwater.

Red-necked falcons (Figure 3) fly fast and usually hunt in pairs. Male and female look similar but the female is bigger in size. They were captured near IGCAR main gate.

White-eyed buzzard (Figure 4) is a medium sized hawk. A juvenile White-eyed buzzard was seen recently in the power lines of Kalpakkam.

According to International Union for Conservation of Nature (IUCN), Woolly-necked storks (Figure 5) are in a vulnerable status. More than seven numbers of Woolly-necked storks were spotted near IGCAR main gate.

The birds recorded were classified by Salim Ali Centre for Ornithology and Natural History, Coimbatore.



Fig. 2 Black bittern



Fig. 3 Red-necked falcon



Fig. 4 White-eyed buzzard



Fig. 1 Bar-headed geese

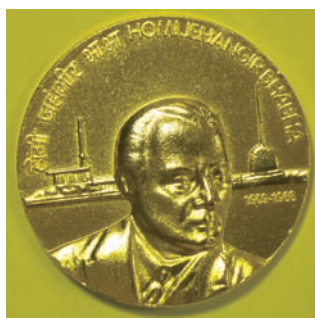


Fig. 5 Woolly-necked stork

CHAPTER
VIII

Awards/Publications/News
& Events/Organisation

DAE Awards



Department of Atomic Energy has instituted annual awards for excellence in Science, Engineering and Technology in order to identify best performers in the area of Research, Technology Development and Engineering in the constituent units (other than Public Sector Undertakings and Aided Institutions). The Young Applied Scientist, Young Engineer, Young Technologist, Homi Bhabha Science and Technology Award and Scientific and Technical Excellence Award fall under this category. Group Achievement awards for recognition of major achievements by groups have also been instituted. Life-time Achievement Award is awarded to one who has made significant impact on the DAE's programmes. They are the icons for young scientists and engineers to emulate. The awards consist of a memento, citation and cash prize.

The recipients of the Awards from IGCAR for the year 2018 were:

Homi Bhabha Science and Technology Award	: Dr. V. Jayaraman, MCD, MCMFCG
DAE Scientific and Technical Excellence Award	: Shri R. Jehadeesan, CD, EIG Dr. S. Ningshen, CSTD, MMG Shri T. V. Prabhu, CFED, MCMFCG
Young Scientist Award	: Dr. Syamala Rao Polaki, SND, MSG
Young Engineer Award	: Shri Ashok Kumar, SMD, RDTG
Young Applied Scientist/Technologist Award	: Dr. V. D. Vijayanand, MDTD, MMG
Meritorious Service Award	: Shri P. K. Samikkannan, Recruitment, Admin.
Meritorious Technical Support Award	: Shri K. Rajeev, ROD, RFG Shri R. Jayavelu, RMD, RFG

Group Achievement Awards:

Indigenous Development of Ion Mobility Spectrometer for Detection of Explosives

Dr. B. K. Panigrahi, MC&MFCG (Group Leader)

Dr. M. Joseph, **RRF, IGCAR**. Shri T. Gokulkrishnan from **EIG**, Dr. N. Sivakumar, Retired, Shri K. Vijayakumar, Dr. R. Rajaraman, and Dr. P. Manoravi from **MC&MFCG**. Shri K. Suresh from **MSG**. Shri Manojkumar and Shri S. S. Gandhi from **RC&IG-BARC**

FBTR Crossing Another Milestone-Operating at the Highest Power Level of 32 MWt

Shri A. Babu, RFG (Group Leader)

Shri S. Sathish, Ms. C. P. Deepa, Shri Devendra Kumar Sharma, Shri S. Sivakumar, Shri D. Samayaraj, Shri Liji Jacob, Shri J. Jaikhan, Shri V. Lakshmi Narayanan, Shri V. Sivakumar, Shri A. R. K. Paramaiah Krishna, Shri A. Neelamehan, Shri M. D. Vijay Kumar, Shri R. Giribabu, Shri Bishnu Nandan Madeli, Shri V. C. Rajesh, Shri Sthitapragyan Pattanayak, Shri V. Nithiyandan, Shri M. Prakash, Shri S. Mahadevan, Ms. Suceela, Shri S. Joy, Shri R. Sounder Rajan, Shri M. Karthikeyan, Shri J. Muthamizhventhan, Shri R. Jayavelu, Shri K. V. Suresh Kumar, Shri G. Shanmugam, Shri N. Manimaran, Shri M. Thangamani, Shri G. N. Chandrasekaran, Shri G. Muralitharan, Shri M. S. Koteeswaran, Shri K. Prakash, Shri D. Chandrasekaran, Shri P. V. Anil Kumar,

Shri R. Vijay Anand, Shri Ashok D. Hanimalal, Shri B. V. Chandramouli, Shri D.Visweswaran, Shri M. Neelamegam, Shri C. Mohandoss, Shri Gulam Hussain, Shri Kapil Dixit, Shri B. Balagopal, Shri A. Ravikumar, Shri K. K. Thakur, Shri S. Muthukumar, Shri M. Elumalai, Shri S. Sridhar, Shri C. Rajendran, Shri L. Anbalagan, Shri S. Anebarassane, Shri M. Vijayarman, Shri S. Haridas, Shri G. Irulandi, Shri M. Balamurugan, Shri Rajan Singh, Shri S. Dheeraj, Shri Prabhakaran, Shri P. Madan Mohan Polei, Shri S. Rajendran, Shri G. Ramalingam, Shri N. Sankaravelu, Shri C. S. Rajasekaran Nair, Shri N. Jayamoorthi, Shri S. Krishnan, Shri P. Thirumalaikumar, Shri L. Baburaj, Shri K. Rajeev, Shri M. Uthaman, Shri M. Rajendran, Shri A. Manikandan, Shri G. Thulaseedharan, Shri A. Thandavamoorthy, Shri R. Vinoth, Shri M. Mohan, Shri K. M. Mathai, Shri R. Ram Kumar, Shri D. Jayaraman, Shri G. Suresh, Shri P. Sreekumar, Shri Mohan Chowdhary, Shri V. Radhakrishnan Nair, Shri K. Ellappan, Shri P. M. Varughese, Shri K. A. Manick, Shri V. Christuraj, Shri R. Ramesh, Shri K. R. Sekaran, Shri A. Abraham John, Shri N. Anbumani, Shri S. Vijayarangan, Shri P. Murugan, Shri A. V. Mani, Shri R. Ganesan, Shri M. Karpaga Kannan, Shri S. Gunasekaran, Shri R. Balasubramaniyan, Shri P. Venkadeswaran, Shri S. Sulthan Saliheen, Shri T. Shanmugam, Shri A. Sivabalan, Shri M. Neelaikanta Pillai, Shri S. Saravanan, Shri K. G. Subramanian, Shri K. Kalyankumar, Shri R. Sekar, Shri T. Karthikeyan, Shri M. Babu, Shri S. Kanagaraju, Shri P. Samuthiram, Shri S. Gurunath, Shri P. Balamurali, Shri A. Ramamoorthy, Shri J. V. Srinivasan, Shri K. Thanigai Arasu, Shri T. Ravichandran, Shri C. Rajendran, Shri T. Arun, Shri M. Ganesan, Shri D. Vignesh Babu, Shri N. Ranjith Kumar, Shri Sonu Kumar, Shri R. Sundar, Shri I. Amir Abhas, Shri R. Vedhamanickam, Shri Suresh Mathew, Shri D. Vinoth, Shri N. Rajan, Shri R. Desingu, Shri J. Manikandan, Shri V. Sekar, Shri S. Elumalai, Shri N. Sathyanarayanan, Shri A. Nagalingam, Shri R. Sivalingam, Shri P. Sivanandham, Shri M. Jayasankar, Shri V. Velu, Shri Sakthivel, Shri G. Narayanasamy, Shri C. Kannan, Shri M. Sathish Kumar, Shri K. Gopal, Shri K. Ramesh, Shri V. Govindaraj, Shri U. Dhayalan, Shri N. Manivel, Shri M. Chitrarasu, Shri B. Y. S. Ganesh Prasad, Shri A. Udaya Sankar, Shri D. Jaisrinivasan, Shri K. Rajesh, Shri M. Soundar, Shri N. Basavaiah, Shri R. Rathinavel, Shri V. Raj Kumar, Shri Bhukya Lakma, Shri G. Kuppan, Shri P. Thyyal Nayagi, Shri R. Vasanthi, Shri K. Bhanumurthy, Shri P. Munuswamy, Shri B. Kumuda, Shri T. V. Ravindranath, Shri V. Hariharan, Shri K. Ramachandran, Shri N. Gopalakrishnan, Shri Kalyana Rao Kuchipudi, Shri M. Muthukrishnan, Shri M. Murugesan, Shri D. Loganathan, Shri A. Mani, Ms. S. Manjula, Ms. Sheela Nambiar, Shri Sushant Maruti Patil, Shri G. Raghukumar, Shri D. Gautam, Ms. E. Radha, Shri Raghav Sharma, Shri V. Sathiamoorthy, Shri N. Sanjeevan, Shri K. Rajarathinam, Ms. Neethu Hanna Stephen, Shri K. Asokan, Shri Rajesh Chandrakanth, Shri R. Sher Singh, Shri Tanmoy Biswas, Shri B. Kadhirappa, Shri K. Sasikumar, Shri T. C. Chacko, Shri S. Rama Rao, Ms. R. Premavathi, Shri M. Elango, Shri A. Lakshmanan, Shri G. Baskaran, Ms. P. Akilandeswari, Shri D. Devaraj, Shri T. Arun Kumar, Shri Dinkar Jha, Shri Abdul Mustak, Shri P. Saravanan, Shri Shobit Verma, Ms. S. Meena, Shri Satyanarayana Sahoo, Shri Immanuel Stephen, Shri B. Kumaravel, Shri Sachin Kale, Shri S. Satish Kumar, Shri R. Athisankaran, Shri K. B. Syam Kumar, Shri J. Sasikumar, Ms. T. Usha, Shri D. Ezhilan, Shri M. S. Chandrasekar, Ms. K. Vinolia, Shri S. Shanmugasundaram, Shri M. Ravi, Shri A. Murugesan, Shri Gowri Lakshmanan, Shri S. Sankilimurugan, Ms. C. Shyna, Shri A. Manjunathan, Ms. M. Devi, Shri A. Senthilkumar, Shri V. Alagudurai, Shri P. Ravi, Shri E. Ramesh, Shri P. Ragoth Kumar, Shri Ashish Jain, Shri B. Mohanarangan, Shri A. M. Kannan, Ms. Hema Ravichandran, Shri T. Kalaimagal, Ms. P. Swapna, Shri K. Dinesh, Shri Domesan, Ms. V. Jayachitra, Shri A. Arumugam, Shri Mohammed Mustafa, Shri S. A. Venkateswara Jeyaram, Shri S. Baskaran, Shri A. Suriyananarayanan, Shri S. Raja, Shri S. Sathish Kumar, Shri S. Thirunavukkarasu, Shri V. R. Naganathan, Shri G. Harish, Ms. M. Dhanya, Shri M. Muthukumarasamy from **RFG**. Shri Meikandamurthy, Shri S. Sureshkumar, Shri Sudheer Patri, Shri Mohammed Sabih, Ms. S. Narmadha from **FRTG**. Shri R. Kumar, Shri J.S. Brahmaji Rao, Shri M. Venkatesh, Shri I. Lakshmi Gandhan, Ms. S. Annapoorani from **MC&MFCG**. Shri P. Narayana Rao, Shri D. Hensonraj, Shri P. Azhagesan, Shri Navtresh Bajpai from **SQ&RMG**. Shri K. Natesan, Shri S. D. Sajish, Shri K. Devan, Shri Ram Kumar Maity, Shri S. Clement Ravichandar, Shri Ravi Prakash Pandey, Shri M. Rajendra Kumar, Shri Juby Abraham, Shri G. S. Srinivasan, Shri D. Naga Sivayya, Shri T. Rajkumar, Shri Kulbir Singh,

Shri V. L. Anuraj, Ms. Sadhna Singh, Shri P. Mohanraj, Shri Niraj Ganesh Jamdade, Shri S. Sundarlingom, Shri R. Suresh Kumar, Shri Sanjay Kumar Pandey, Shri K. Krishna Chaitanya from **RDG**. Shri Manoj Agarwal, Shri Syam Ravikumar from **BHAVINI**. Shri A. Venugopal Reddy, Shri C. Ashok Wali, Shri A. Harinarayana, Shri B. Ravinder, Shri Sanjoy Saha, Shri R. R. K. Raju, Shri Y. Ramachandra Murthy, Shri Khader Shareef, Shri G. S. N. Sastry, Shri N. Anjaiah, Shri Mohd. Yousufuddin

Indigenous Development of Indian Advanced Fast Reactor Clad (IFAC-1) for Sodium Cooled FBRs.

Dr. Shaju K. Albert, MMG (Group Leader)

Dr. Arun Kumar Bhaduri, (Member)

Dr. G. Amarendra, (Member)

Dr. Gondesh Vara Prasad Reddy, Dr. Hemant Kumar, Shri M. Arul, Dr. V. D Vijayanand ,Shri B. Aashranth, Dr. Diptimayee Samantaray, Shri Arvinth Davinci, Dr. S. Latha, Dr. G. Sasikala, Shri M. Nandagopal, Shri V. Ganesan, Dr. Kinkar Laha, Shri Utpal Borah, Dr. S. Ravi, Dr. S. Raju, Dr. V. Thomas Paul, Dr. P. Parameswaran and Dr. Harapasanna Tripathi from **MMG**. Dr. Christopher David, and Dr. S. Balaji from **MSG**. Shri V. Rajendran, Shri P. Karuppasamy, Shri A. Ramanathan, Shri S. Thiyagu, Shri V. Kodiarasan, and Dr. B. K. Panigrahi from **EIG**. Shri N. Raghu, Shri K. Krishna Chaitanya, Shri P. Azhagesan, Shri D. Hensonraj, Shri P. Narayana Rao from **SQRMG**. Dr. S. Clement Ravi Chander, Dr. S. Murugan, Shri Pramod Kumar Chaurasia, Shri M. Muthuganesh, Shri Rajesh Saxena, Shri R. Ramesh, Shri Manam Sambasiva Rao and Shri R. Ravikumar from **RDTG**. Shri Kumar Vaibhaw, Dr. Komal Kapoor, Shri K. Sunder Krishna, Dr. Pramanik, Shri J. K. Rout, Shri K. V. K. Deshpande, Shri P. K. Maity and Shri N. Harsha from **NFC**

Development of a Dual Ion Irradiation Platform for Studies of Radiation Response in Fission and Fusion Reactor Materials

Dr. G. Amarendra, (Group Leader)

Shri K. Suresh, Shri S. Chinnathambi, Dr. S. Balaji, Dr. Sachin Kumar Srivastava, Shri P. Magudapathy, Shri J. Navas, Shri A. Parthasarathi, Shri G. Natarajan, Dr. Christopher David, Dr. R. Govindaraj, Dr. M. Kamruddin from **MSG** and Dr. B. K. Panigrahi from **(EIG)**

Awards & Honours

Department of Atomic Energy had instituted “**Swachhta Pakhwada Awards**” to the constituent units of DAE for the exemplary performance during the Pakhwada. Indira Gandhi Centre for Atomic Research was awarded the Certificate of Excellence (second position among the DAE units) for its Swachhta activities (February 16-28, 2019). IGCAR has bagged this award second year in succession.

Dr. Aritra Sarkar, MMG was awarded **Alexander von Humboldt Fellowship** for Postdoctoral research by AvH foundation, Germany April - 2019

Dr. S. C. Vanithakumari, Corrosion Science & Technology Division (CSTD), MMG was awarded the **NIGIS Corrosion awareness Award 2019 for Distinction in Corrosion Science & Technology** by NACE International Gateway India

Ms. B. Madhura, Corrosion Science & Technology Division (CSTD), MMG has been selected as the recipient of **NIGIS Student Award** for M Tech for 2019 by NACE International Gateway India

The above awards were presented during **CORCON 2019** held during September 23-26, 2019 at CIDCO Convention and Exhibition Centre, Navi Mumbai

Scientific Information Resource Division, **SQRMG**, IGCAR was awarded **Digitally Transformed Research Library - 2019** by Wiley for the excellence in Digital Library Technologies and User Centric Services during Wiley Library Awards, New Delhi, December 16, 2019

N. Sreevidya, MDTD, MMG, Prize in **Metallography** contest in the category of SEM during **NMD-ATM** organized by Indian Institute of Metals, November 13-16, 2019, Thiruvananthapuram

Best Paper / Poster Awards

DST National Conference on Nanomaterials, January 24 - 25, 2019, LRG Government Arts College for Women, Tiruppur, India

Probing of Nanofiller-Polymer Matrix Interaction Using Atomic Force Microscope for the Development of X-ray opaque Fabric Material

M. Vadivel, Sangeetha Jayakumar, John Philip

5th International Conference on Nanoscience and Nanotechnology, ICONN 2019, January 28-30, 2019, SRM University, Chennai

Carbon Black and Nickel Nano Inclusions Assisted Thermal Conductivity Enhancement of an Organic Phase Change Material for Thermal Energy Storage

Amit Kumar Mishra, B. B. Lahiri, John Philip

International Conference on Computational Methods in Manufacturing, March 8-9, 2019, IIT Guwahati

Numerical Simulation and Experimental Validation of A-TIG Welding of 2.25Cr-1Mo Steel

A. R. Pavan, B. Arivazhagan, S. Arunkumar, M. Vasudevan and S. Mahadevan

International Conference on Advanced Materials (ICAM 2019), June 12-14, 2019, Nirmalagiri College, Kannur Kerala

Thermal Conductivity Enhancement of an Organic Phase Change Material using Carbon Black and Nickel Nanoinclusions for Latent Heat Thermal Energy Storage Applications

Amit Kumar Mishra, B. B. Lahiri and John Philip

International Conference on Materials and Manufacturing Methods, July 5-8, 2019, NIT, Tiruchirappalli

Numerical Simulation of Fluid Flow and Weld Penetration during A-TIG Welding of 316 LN SS

Anoop K. Unni and M. Vasudevan

International conference on Magnetic Fluids(ICMF2019), July 7-12, 2019, Paris, France

Enhancement in Field Induced Heating Efficiency in TMAOH Coated Super Paramagnetic Fe₃O₄ Nanoparticles by Texturing under a Static Magnetic Field

Surojit Ranoo, B. B. Lahiri and John Philip

National Symposium on Electrochemical Science and Technology (NSEST- 2019), July 19 -20, 2019, Indian Institute of Science, Bengaluru

Development of Silanized Graphene Oxide Based Multifunctional Hybrid Coating with Enhanced Corrosion Resistance and Antibacterial Activity in Seawater Environment

Geetisubhra Jena, Rani P. George, John Philip and G. Amarendra

7th Asian Symposium on Computational Heat Transfer and Fluid Flow - 2019, September 3-7, 2019, Tokyo, Japan

Aerosol Penetration in Submerged Gravel Bed Scrubber

Arjun Pradeep, Anil Kumar Sharma, D. Ponraju, B. K. Nashine, and P. Selvaraj

International Conference on Advanced Materials and Processes for Defence Applications, ADMAT 2019, September 23, 2019, Hyderabad

Effects of Microstructures and Cyclic Loading on Mechanical Properties of Simulated HAZS of P91 Steel Weldment

K. Mariappan

International Conference and Expo on Corrosion (CORCON 2019), September 23 - 26, 2019, CIDCO Convention and Exhibition Centre, Navi Mumbai

Porous Microcapsule Based Superhydrophobic Coating on 304L SS and Its Corrosion Properties in Chloride Medium

T. P. Rasitha, S. C. Vanithakumari, Rani P. George and John Philip

Performance Characteristics of Nanophase Modified Fly Ash Concrete for Marine Applications

Sudha Uthaman, Vinita Vishwakarma, D. Ramachandran, B. Anandkumar, Rani P. George and U. Kamachi Mudali

International Conference on Advances in Minerals, Metals, Materials, Manufacturing and Modelling (ICAM-2019), September 25 - 27, 2019, NIT, Warangal

Corrosion Kinetics Study of 316N Weldment Under Cyclic Loading in Acidified Chloride Environment

A. Poonguzhali, S. Ningshen and G. Amarendra

5th International Conference on Nanostructuring by Ion Beam (ICNIB 2019), November 6 - 8, 2019, IGCAR, Kalpakkam

Effect of Sb Ion Implantation in Bi₂Se₃ Topological Single Crystal

A. Edward Prabu, S. Abhirami, R. Rajitha, P. Magudapathy, S. Amirthapandian, C. David and Awadhesh Mani

57th National Metallurgist's Day (NMD) and 73rd Annual Technical Meeting (ATM), November 12 - 16, 2019, Thiruvananthapuram, Kovalam, Kerala

Influence of Artificial Pit on Corrosion Fatigue Behaviour of 316LN SS and its Weldment

A. Poonguzhali, S. Ningshen and G. Amarendra

Comparison of Friction Stir and A-TIG Welding Process on the Evolution of Microstructure and Mechanical Properties of 9Cr-1Mo steel to AISI 316LN Stainless Steel Weld Joint

D. Sunilkumar, S. Muthukumar, M. Vasudevan, G. Madhusudan Reddy

Characterization of Deformation and Fracture Resistance of a Reduced Activation Ferritic Steel

B. Shashank Dutt, G. Shanthi, M. Nani Babu, A. Moitra

15th International Conference on Modern Trends in Activation Analysis (MTAA-15), November 17-22, 2019 Bhabha Atomic Research Centre, Mumbai

Computer Program for Relative Method of Neutron Activation Analysis

J. S. Brahmaji Rao, R. Acharya, R. Kumar

32nd ISMAS Symposium on Mass Spectrometry (32nd ISMAS-2019), November 27-30, 2019, Bhabha Atomic Research Centre (BARC), Mumbai

A Novel Sample Loading Method for Precise Isotopic Ratio Measurement of Lanthanum using Thermal Ionisation Mass Spectrometry (TIMS)

Suranjan Bera, S. Jayalakshmi, S. Nalini, C. V. S. Brahmananda Rao, T. S. Lakshmi Narasimhan

Vaporisation Studies on LiCl(s), KCl(s) and LiCl-KCl-UCl₃ Ternary Salt System by Knudsen Effusion Mass Spectrometry

V. V. Trinadh, P. Manikandan, Suranjan Bera, C. V. S. Brahmananda Rao and T. S. Lakshmi Narasimhan

Ion Mobility and Mass Spectrometric Studies on Heroin

U. K. Maity, J. Namitha, P. Manoravi, M. Joseph

Journal of Non destructive Testing & Evaluation, Volume 17 (18), 2019, pp. 26-31. Best Technical Paper in the Industrial Application Category. Award Presented by ISNT during NDE 2019, December 5, 2019

Non-destructive Evaluation Techniques for Inspection of Components in Nuclear Applications

C. K. Mukhopadhyay and S. Thirunavukkarasu

International Conference on Recent Advances in Nanoscience and Nanotechnology, (ICRAN 2019),
 December 11 – 12, 2019, Stella Maris College, Chennai
 Synthesis of Cellulose Capped Fe₃O₄ Nanofluids Suitable for Application in Methylene Blue Dye Removal
 C. Anushree and John Philip

Springer International Conference on Communication Systems and Networks (ComNet 2019),
 December 12-13, 2019, Mar Baselios College of Engineering & Technology, Kerala
 Challenges and Impacts of RFID Technology in a Research Library
 V Sivasankar, E. Soundararajan and S. Rajeswari

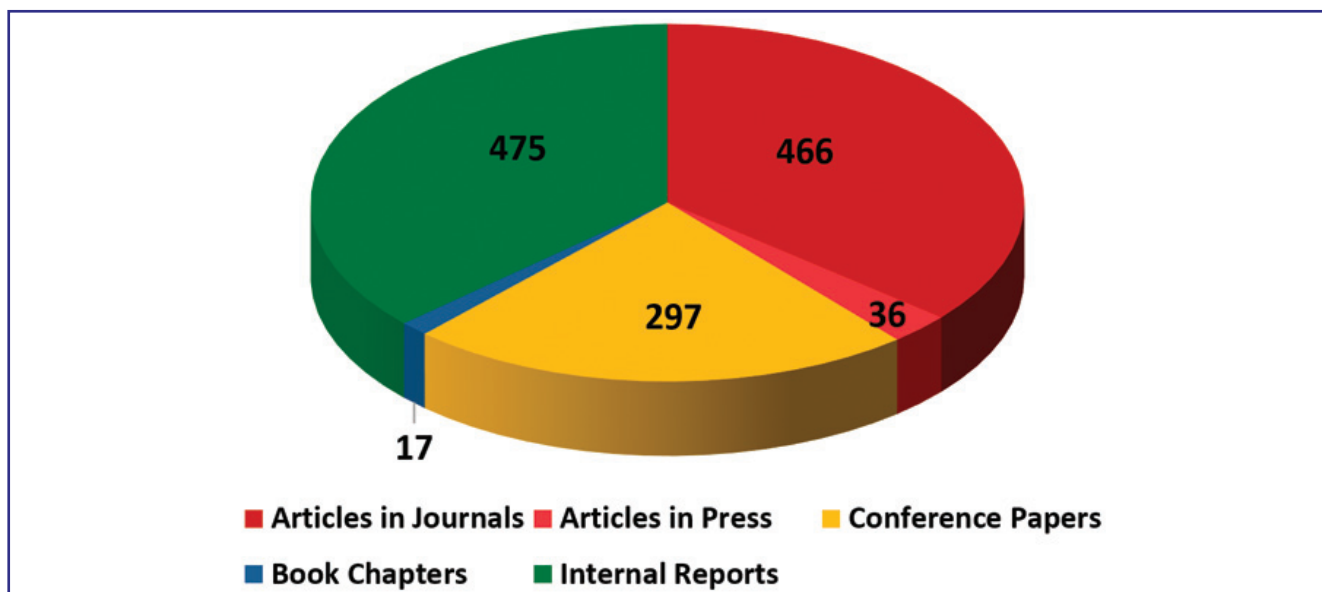
DST-SERB National Conference on “Recent Advances in Nanomaterials Chemistry for Sustainable
 Development (RANCSD), December 12 - 13, 2019, Madras Christian College, Chennai
 Tamarind Fruit Pulp Based Green Corrosion Inhibitor for Mild Steel in Acidic Environment
 Sangeetha Jayakumar, T. Nandakumar, M. Vadivel, C. Thinaharan, Rani P. George and John Philip
 Synthesis and Characterization of Phosphate Capped Magnetite Nanoparticles
 C. Anushree and John Philip

64th DAE Solid State Physics Symposium, December 18-22, 2019, IIT Jodhpur, Rajasthan,
 A Clue to the Large Magneto-resistance in the NbAs₂ Semimetal
 V. Harimohan, A. Bharathi, P. D. Babu, R. Rajaraman and C. S. Sundar

Structural Disorder and Compressibility Studies of RE₆UO₁₂ at Extreme Conditions of Pressure and
 Temperature
 Balmukund Shukla, N. R. Sanjay Kumar, N. V. Chandra Shekar, H. Jena and S. Kalavathi

2nd International Conference on Metallurgy, Materials Science and Manufacturing (IMME19),
 December 27-28, 2019, NIT, Tiruchirappalli
 Role of Tool RPM on the Evolution of Microstructure and Hardness of the Friction Stir Dissimilar Weldment of
 2.25Cr-1Mo Steel to 316LN Stainless Steel
 D. Sunilkumar, Jithin Mathew, S. Muthukumar, M. Vasudevan
 Influence of Large Strain Hot Deformation on Microstructural Evolution in Alloy D9
 M. Arvinth Davinci

IGCAR Publications during the Year 2019



Special Event

1. "Foundation Day Celebration of IGCAR", April 30, 2019

Special Lectures, Colloquia , Seminars etc.

IGC Colloquium

1. "Making Things Happen in India", by Shri. Anil Swarup, Former Secretary to Government of India, March 18, 2019
2. "Remote Sensing and its Applications for National Development" by Shri. Santanu Choudhury", April 25, 2019

Special Lectures

1. "Yoga for Harmonious Life" Sr. Prof. K. R. Munirathinam, World Community Service Centre (WCSC), Chennai, June 21, 2019
2. "Let us March for Science", Dr R. Ramanujam , Institute of Mathematical Sciences, Chennai , September 03, 2019
3. "Science Needs Funding", Dr. M. V. N. Murthy, Institute of Mathematical Sciences, Chennai, September 03, 2019

Seminars, Workshops and Meetings

1. One day Training Program on "Quality Assurance Aspects for Engineers and Supervisors", January 10, 2019
2. One-day Hindi scientific seminar, January 10, 2019
3. One day Training Programme on "Nuclear Radiation in Fuel Cycle" , May 21, 2019
4. National Conference on "Light Matter Interaction at Nanoscale (LMIN-2019)", July 15-17, 2019
5. Workshop on "Environmental Radioactivity Measurements- ERM-2019" July 25-26, 2019
6. "Graduation Function of the 13th Batch of Trainee Scientific Officers of BARC Training School at IGCAR", July 29, 2019
7. "National Technology Day Meet 2019", July 30, 2019
8. Workshop on "Current Advances in Risk Assessment for Radiological Releases during Nuclear Emergencies (CARE)", August 5-6, 2019
9. Annual Meeting of Hot Laboratories and Remote Handling (HOTLAB 2019), September 8-12, 2019
10. Theme Meeting on "Thermal Hydraulic challenges on FBR Design" , October 25, 2019
11. International Conference on "Nanostructuring by ion beams-2019", MSG, IGCAR, November 06-08, 2019
12. Awareness Programme on "Intellectual Property Rights for Scientists & Engineers", December 13, 2019
13. National Conference on "URJAVARAN-2019", ESG, IGCAR, December 20, 2019

Nurturing Activities

1. International Women's Day & The International Year of Periodic Table-2019, March 8, 2019
2. Dr. Baldev Raj Memorial Bridge Course on Non-Destructive Evaluation (NDE) and Quality Assurance (BRM-BCNQ) organised jointly by IGCAR, ISNT Kalpakkam Chapter and Society for Failure Analysis (SFA) Chennai Chapter, May 20- 24, 2019
3. "5th International Day of Yoga", June 21, 2019
4. "BITS Summer Practice School at IGCAR", May 21 - July 13, 2019
5. "Summer Training in Physics and Chemistry (STIPAC-2019)", June 3 - July 12, 2019
6. "Bridge Course on 'Welding and Fabrication'", July 22-26, 2019
7. "Eddy current Level-2 Certification Course", August 19-24, 2019
8. "Prof. Brahm Prakash Memorial Materials Quiz-2019" organized by IIM, Kalpakkam Chapter, September 20- 21, 2019

Administrative Seminars / Workshop / Events

1. "Swachhta Pakhwada", February 16-28, 2019
2. "Security Sensitisation programme", May 14, 2019
3. "Hindi Fortnight", September 16-30, 2019
4. "Vigilance Awareness week - 2019", October 30, 2019

Special Event

Foundation Day Celebration of IGCAR

April 30, 2019



From Left to right: Dr. S. A. V. Satya Murty, former Director IGCAR, Prof. P. R. Vasudeva Rao, former Director IGCAR & Vice Chancellor HBNI, Dr. Arun Kumar Bhaduri, Director IGCAR, Dr. R. Chidambaram, DAE- Homi Bhabha Chair Professor & Former Principal Scientific Advisor, Government of India, Shri K. N. Vyas, Secretary, DAE & Chairman, AEC, Shri S. K. Sharma, CMD, NPCIL, Dr. G. Amarendra, Chairman, Organising Committee and the then Director MSG & MMG, IGCAR

IGCAR celebrated its Foundation Day for the first time on April 30, 2019. It was this day in 1971 that Dr. Vikram Sarabhai, the then Chairman of the Atomic Energy Commission approved the formation of Reactor Research Centre (RRC) by an executive order, which was later renamed as Indira Gandhi Centre for Atomic Research in 1985.

The programme was conducted in a specially decorated pandal to seat about 1500 colleagues. Dr. R. Chidambaram, DAE-Homi Bhabha Chair Professor & Former Principal Scientific Advisor to Government of India was the Chief Guest of the event. Dr. Arun Kumar Bhaduri, Director, IGCAR welcomed the gathering. On this occasion, Shri K. N. Vyas, Secretary, DAE & Chairman, AEC presided over and inaugurated the 50th campaign of CORAL (COmpact Reprocessing facility for Advanced Fuels in Lead cells) facility. This has successfully demonstrated the feasibility of reprocessing high burnup mixed carbide fuel through successive campaigns over the years. A memoir cataloguing some of the major milestones of the Centre over the last forty eight years was released by the Guest of Honour, Shri S. K. Sharma, Chairman and Managing Director, NPCIL. The memoir also included rare photographs of noteworthy events of past, significant achievements in equipment design, distinguished visitors and former Directors and colleagues of the Centre, chronologically.

All former Directors and former Group Directors of the Centre were invited for the occasion. Former Directors of the Centre, Prof. P. R. Vasudeva Rao, Dr. S. A. V. Satya Murty and former Group Directors Shri G. R. Balasubramanian, Shri P. V. Kumar, Dr. R. Natarajan, Dr. D. V. Gopinath, Dr. L. V. Krishnan, Dr. A. R. Sundararajan, Shri R. D. Kale, Dr. G. Vaidyanathan, Dr. P. Kalyanasundaram, Shri M. Rajan, Dr. K. K. Rajan, Shri S. A. Weling, Shri P. Sreenivasan, Shri Y. C. Manjunatha, Shri A. Jyothish Kumar, Dr. S. L. Mannan, Dr. K. Bhanu Sankara Rao, Shri M. P. Janawadkar, Shri P. V. Ramalingam, Shri G. Srinivasan, Dr. K. Nagarajan, Dr. M. Joseph, and Dr. C. S. Sundar attended and graced the occasion. All of them were honoured by Director, IGCAR with a shawl on the occasion.

Shri K. N. Vyas, Secretary, DAE & Chairman, AEC in his presidential address mentioned that IGCAR has established a comprehensive R&D facility covering the entire spectrum of FBR technology. He appreciated the Centre's focus on cutting edge field of fast reactor technology, which is very essential to India for guaranteeing future energy independence and to raise above rest of the world. He requested the younger colleagues to raise upto the challenges and put in best efforts to make fast reactor technology as safe and economical as possible. Chief Guest, Dr. R. Chidambaram, in his special address, highlighted the uniqueness of Kalpakkam in having various reactors fuelled by all the three isotopes, (viz.) Uranium 235(MAPS-NPCIL), Plutonium 239(FBTR-IGCAR) and Uranium 233(KAMINI-IGCAR). He emphasized that nuclear energy is a near renewable source of energy because of

breeding and IGCAR plays a vital role in this mission and is hence a “Pride of the Country”.

Towards encouraging younger colleagues to pursue higher studies and update their knowledge, Homi Bhabha National Institute (HBNI) started its academic programmes in the year 2006. The strength of the research scholars in the Centre has been steadily increasing over the years from

fifteen to a present sanctioned strength of two hundred. During 2018 about 33 Scholars have completed their Ph.D. Programmes, 30 have received their M.Tech. degrees and 14 Scholars have been awarded their M.Sc. Engineering degrees. IGCAR has instituted awards for Best Thesis and Certificate of Appreciation to encourage younger colleagues and Research Scholars. A dedicated senior selection committee had looked into the research work of all the scholars, who had obtained their degrees during 2018. It identified the best performers in Physical, Chemical and Engineering Sciences streams. Totally twelve Research Scholars were selected and they received the awards during the function.

Gamma chamber facility at IGCAR is used for irradiation of seeds and plants such as Causurina, Crossandra or Kanagambaram, Guava and Chilli for enhancing their yield. It was a joyous moment when the saplings of “Kanagambaram”, which were a product of this irradiation facility, were presented to the Chief Guest, Guest-of-Honor and Chairman on this day by the Director, IGCAR. The programme concluded with a vote of thanks by Dr.G.Amarendra, Chairman Organising Committee. The dignitaries then visited various facilities in IGCAR including the construction site of FRFCF.

As a part of the foundation day celebrations, “Open House” was organized for families of employees of IGCAR. The event was conducted in two phases, on May 4 and May 11, 2019 (Saturdays) and the laboratories organizing visits were split into two groups, according to the number of employees and dependants to have roughly the same load of visitors on each day for better logistics. The visitors could see the Fast Breeder Test Reactor and also were shown a short film on its operations. The visitors were also shown various experimental facilities set up in different Groups of IGCAR, which are very unique and important. The open house was well attended and appreciated. Owing to popular demand from the employees of GSO, it was repeated on May 18, 2019 exclusively for the benefit of employees and family members of GSO. The Open House facilitating exposure to advanced experimental facilities is sure to motivate and inspire young children/students of the employees to take up scientific career in future. Totally around 1650 persons visited the Centre during this event.



Remote inauguration of 50th campaign of CORAL facility by Shri K. N. Vyas, Secretary, DAE & Chairman AEC, in the presence of Dr. R. Chidambaram, DAE- Homi Bhabha Chair Professor & Former Principal Scientific Advisor, Government of India, Dr. Arun Kumar Bhaduri, Director IGCAR and other dignitaries.



Special invitees

Open House Photo Gallery

(On the occasion of Foundation Day Celebration of IGCAR - 2019)



Shake Table Facility at Reactor Design Group



FBTR- Inside Reactor Containment Building



FBTR - Control Room



Computer Lab, Electronics & Instrumentation Group



Concrete Lab, Engineering Services Group

Conference and Meeting Highlights

A brief report on One day Training Program on Quality Assurance Aspects for Engineers and Supervisors

January 10, 2019



Dr. A. Ravisankar, the then Project Director, FRFCF delivering the Inaugural Address and Dr. B. P. C. Rao, the then CPE, FRFCF explaining the genesis & structure of the in-house Program

A one day in-house training program on Quality Assurance (QA) aspects during construction of Fast Reactor Fuel Cycle Facility (FRFCF) project was organized on January 10, 2019 for the benefit of engineers and supervisors of FRFCF. Shri D. Herbert, Additional Chief Engineer welcomed the participants and Dr. B. P. C. Rao, the then Chief Project Engineer explained the genesis & structure of this training program and its necessity in FRFCF. Dr. A. Ravisankar, the then Project Director inaugurated the program and emphasized, in his inaugural address, the importance of QA in construction & design activities and the benefits that accrue. He requested the participants to utilize this unique opportunity for enhancing their understanding and knowledge in QA in their own domain as well as in other domains.

The program consisted of lectures covering the QA basics, methods and standards followed during construction. A hand-out of important aspects of these lectures was given to all the participants. Shri M.V. Kuppusamy covered QA aspects during Mechanical Fabrication & Construction and Shri V. Venkatachalapathy gave a detailed account of QA during Civil Construction. Shri B. Sasidhar Rao delivered a lecture on QA of Electronics & Instrumentation and Equipment & Systems and Shri S. Pothiraj explained the QA aspects of Electrical Equipments and Systems during construction. The training program was attended by about 65 engineers and supervisors. A good interaction and lively discussions were observed between the speakers and the participants. In the end, feedback was solicited from the participants. Participants mentioned that the talks were informative and useful and requested the organizers for a repeat course spanning two days.

International Women's Day & The International Year of Periodic Table-2019

March 8, 2019



Presentation being made on the occasion of "International Women's day" and "International Year of Periodic Table -2019"

On March 8 of every year, UN Women, the United Nations entity is observing International Women's Day to celebrate the global push for gender equality and to make women's rights a reality. To commemorate this year's theme, "Think Equal, Build Smart, Innovate for Change" and "The International Year of Periodic Table-2019" declared by the UNESCO, a technical program covering the discovery of elements along with their applications in various fields was arranged and presentations were made by women employees and research scholars of Materials Chemistry & Metal Fuel Cycle Group.

Dr. T. Prathibha welcomed the gathering. In the inaugural address, Dr. K. Ananthasivan, the then AD, MFCG highlighted the importance and respect for women in our culture and also recalled the great contribution of the family of Nobel laureate Marie Curie.

Ms. Lithun Swain reviewed the contribution of the women to the periodic table by explaining the role of women in the discovery of elements. Ms. Beatrice Veena discussed the discovery of hydrogen and its isotopes in the chronological order and covered the application of hydrogen in various fields including her work on hydrogen sensor. Ms. J. Vithya described about the discovery of strontium, the advantage of production of radioisotopes of strontium and cobalt in the Fast Breeder Test Reactor and their medical applications especially in the treatment of cancer. Ms. S. Annapoorani described the fortuitous discovery of iodine from seaweed, the importance of iodine to health, its toxicity and the studies being carried out on trapping of iodine using Ag modified zeolite towards nuclear application. Ms. Subrame Sarkar highlighted the discovery of plutonium and described the work of extraction of actinides and other fission products carried out at MC&MFCG. The work-life balance for women was discussed by Ms. S. Nalini with the suggestions to prioritise the activities, delegation of activities, etc. A quiz program covering the 'First Woman of India' in various fields was conducted in between the sessions by Ms. Clinsha. Dr. S. Vijayalakshmi, Head, ACS, formerly at Materials Chemistry Division mentioned the need to improve the capabilities of women, the role of innovation in the employment and concluded that collective action by both men and women is required for the accelerated growth of women in employment. Dr. Kitheri Joseph, the then Head, MFC&PS, MFFD coordinated the panel discussion on leadership qualities of women. Ms. Nibedita Samanta proposed the vote of thanks

Dr. Baldev Raj Memorial Bridge Course on Non-destructive Evaluation and Quality Assurance (BRM-BCNQ)

IGCAR, Kalpakkam, May 20- 24, 2019



Inauguration of BRM-BCNQ 2019 by Dr. G. Amarendra, the then Director, MMG & MSG, IGCAR.

Dr. Baldev Raj Memorial Bridge Course on Non-Destructive Evaluation (NDE) and Quality Assurance (QA) (BRM-BCNQ 2019) was organised jointly by IGCAR, Indian Society for Nondestructive Testing (ISNT) Kalpakkam Chapter and Society for Failure Analysis (SFA) Chennai Chapter at IGCAR during May 20-24, 2019 for the benefit of students entering final year of B.E./ B.Tech/ M.E./ M.Tech (Mechanical/ Metallurgy/ Materials Science/ Industrial/ Manufacturing/ Production/ NDT/ Welding Technology) and young engineers. The objective of this unique course is to motivate young students by introducing advanced NDE science and technologies through a series of technical lectures by eminent experts and providing practical hands-on, in the state-of-the-art NDE equipments. This course was attended by 34 participants that include 18 motivated students from academic institutes and 16 engineers from IGCAR.

Dr. G. Amarendra, the then Director, MMG & MSG, IGCAR inaugurated the course on May 20, 2019. During his address, he highlighted the role of NDE and QA in nuclear industry and encouraged the students to learn as much as possible during this unique course. A special address was given by Dr. A. Ravisankar, the then Director, RpG & Project Director, Fast Reactor Fuel Cycle Facility (FRFCF), IGCAR highlighting the importance of this course and motivating the students to learn towards safe operation & effective maintenance of engineering components. Dr. B. P. C. Rao, the then Associate Director, FRFCF and Chairman, BRM-BCNQ 2019 briefed the importance of the Bridge Course and career in NDE and recalled his association with Late Padma Shri Dr. Baldev Raj, who initiated and nurtured NDE and QA fraternity in India and particularly at IGCAR.

Expert faculty from IGCAR delivered technical lectures covering various advanced NDE and QA techniques including failure analysis. The lectures were well received and the participants interacted very well with the faculty. During the afternoon sessions, participants performed mini-project to gain hands-on experience in advanced NDE equipments. The participants visited FBTR to get familiarized with the nuclear plant. A quiz competition was conducted on May 24, 2019. Dr. C. K. Mukhopadhyay, Head, NDE Division and Convener, BRM-BCNQ 2019 delivered the vote of thanks. During the feedback session on May 24, 2019, the students lauded the bridge course and mentioned that they were immensely benefitted by attending the course. They expressed that the course was well structured and executed and thanked the organisers for the rare opportunity provided to them. All the students were given participation certificates. The winner and runner teams of the quiz competition were also given certificates.

One day Training Programme on “Nuclear Radiation in Fuel Cycle”

May 21, 2019



Release of handout by Dr. A. Ravisankar, the then Project Director, FRFCF during the Inaugural Function



Presentation by one of the speakers during the programme

A one day training programme on “Nuclear Radiation in Fuel Cycle” was organised on May 21, 2019 in FRFCF. Dr. B. P. C. Rao, the then Associate Director, FRFCF welcomed the participants and briefed about the genesis and structure of the programme. He highlighted the importance of acquiring knowledge on radiation, as FRFCF will be soon taking up pre-commissioning activities after completion of construction of the 5 plants in the nuclear island. Dr. A. Ravisankar, the then Project Director, FRFCF inaugurated the programme and in his address emphasised the importance of this programme at this juncture, considering the type and nature of fuel being handled in FRFCF. He narrated his hands-on experiences on radiation during the construction and operation of CORAL and DFRP and highlighted the challenges of remotisation, shielding, and O&M. He reiterated the need for adhering to the safe practices developed over the years at IGCAR. Dr. B. Venkatraman, Director, SQRMG and ESG addressed the gathering. He stressed the need for better understanding of nuclear radiation for safe work and quality output. He advised them not to fear about the radiation, but to learn from the expert lectures being delivered by the experienced faculty in this programme, so that they can handle radiation with confidence. Dr. M. T. Jose, Convener thanked the dignitaries. The programme covered topics from basics of nuclear radiation to emergency preparedness and criticality safety.

The basics of radiation physics was explained by Dr. O. Annalakshmi. Mrs. R. Akila covered the topics on radiation monitoring in reprocessing plants. The biological effects of radiation were brought out by Dr. R. Sarangapani, SQRMG. Dr. R. V. Subba Rao, Head, PRCD, RpG delivered a talk on accounting of nuclear materials. Later, radiation safety and criticality safety aspects were covered by Shri R. Santhanam and Shri S. Chandrasekharan from SQRMG respectively. The concluding talk on emergency preparedness was given by Dr. M. T. Jose. More than 50 participants attended and interacted with the speakers. In the feedback session, they indicated that the talks and the hand-outs were very informative and useful.

Summer Training in Physics & Chemistry (STIPAC-2019)

June 03 - July 12, 2019



Chief Guests Dr. Arun Kumar Bhaduri, Director, IGCAR and Prof. P. Appa Rao, Vice Chancellor, University of Hyderabad addressing STIPAC students during inaugural and valedictory functions, respectively

Summer training in physics and chemistry (STIPAC) is a prestigious flagship programme conducted by IGCAR every year since 1995, for M.Sc. first year students. This program is intended to motivate, enthuse and encourage young students to take up scientific research as a career. STIPAC has evolved over the years to train the pre-final PG Physics & Chemistry students from across the country both in theoretical & experimental expertise available in IGCAR.

Theme chosen for this year's programme was "Physics and Chemistry of Nanomaterials" and students were asked to submit a one page write up about their perspective on the above theme. Applications were invited online and about 650 applications were received from Physics and Chemistry, representing about 100 universities across the country. Based on their academic credentials, quality of their write-up, twenty five students in each discipline were selected.

The STIPAC-19 programme was inaugurated on June 06, 2019 and Dr. Arun Kumar Bhaduri, Distinguished Scientist & Director, IGCAR graced the event and gave a special lecture on "Fast Breeder Reactor & Associated Fuel Cycle for the Second Stage of Indian Nuclear Programme".

The program was conducted for six weeks consisting of about 100 hours of lectures in theory and 50 hours of experiments. The students were encouraged to have hands-on learning experience by



Prof. P. Appa Rao, Vice Chancellor, University of Hyderabad, Dr. G. Amarendra, the then Director, MSG & MMG, Dr. B. K. Panigrahi, Director, MC&MFCG & EIG, along with senior colleagues and students of STIPAC during the valedictory function on July 12, 2019

either doing project works or carrying out experimental works on various topics. Towards the end of the course, the students gave a presentation on the project work carried out, which was evaluated by senior Scientists of the Centre. Site visits to MAPS and BHAVINI were also organized during the course of the programme. About five special lectures were delivered by renowned professors from premier institutions. In particular, the special lectures by Prof. S. Ramaprabhu, IIT-M, Chennai on “Basics and Applications of nano-materials” and Prof. D. Indumathi from IMSc, Chennai on “What is the World made of” were well received by the students.

The valedictory program was held on July 12, 2019 and the Chief Guest Prof. P. Appa Rao, Vice Chancellor, University of Hyderabad gave an inspiring speech about ethics and standards in scientific research, which was very informative and educative to the students. He gave away the participation certificates to all the students.

An online feedback form was made and students were encouraged to submit their feedback about the course. Overall feedback received from the students was positive and appreciative of the range and depth of the course content.

BITS Summer Practice School at IGCAR

May 21 - July 13, 2019



Students from BITS Practice School with Dr. B. Venkatraman, Director, SQRMG & ESG and senior colleagues of the Centre

Fifty students from BITS Pilani, Hyderabad and Goa Campuses underwent summer practice school at IGCAR during May 21 to July 13, 2019. The programme is aimed at exposing the students to industrial and research environment, how the organizations work, maintaining work ethics, and completing the projects given to them in time by effectively making use of the guidance, scientific information resources, hard work and creativity. Dr. Arun Kumar Bhaduri, Distinguished Scientist and Director, IGCAR inaugurated the practice school programme and interacted with the students. Dr. Satyapaul Singh from Hyderabad campus was the program coordinator from BITS. The students were from various disciplines like Mechanical Engineering, Chemical Engineering, Civil Engineering, Electrical and Electronics Engineering, Electronics & Instrumentation Engineering, Electronics and Communication Engineering, Computer Science and Engineering and Manufacturing Technology. They carried out challenging projects in various groups of the Centre according to their discipline under the able guidance of Scientists and Engineers at IGCAR. During the period of their stay, they visited facilities at IGCAR, BHAVINI and MAPS. As a part of the curriculum, quiz, project work presentations, group discussions, report writing and viva were conducted. The valedictory function was held on July 13, 2019. Dr. B. Venkatraman, Director, SQRMG and ESG delivered the valedictory address and gave away the certificates to the students.

National Conference on Light Matter Interaction at Nanoscale (LMIN-2019)

July 15-17, 2019



Release of Conference brochure by Prof. Chandrabhas Narayana (center), (Dean, R&D, JNCASR, Bengaluru), (L to R) Dr. G. Amarendra, Chairman, LMIN-2019, Dr. Arun Kumar Bhaduri, Director, IGCAR, Dr. Sandip Kumar Dhara and Dr. K. Prabakar

National Conference on "Light Matter Interaction at Nanoscale" (LMIN-2019) was organised at IGCAR during July, 15-17, 2019, with the support from BRNS and Kalpakkam chapter of MRSI. LMIN-2019 focused on advances in research pertaining to plasmonic, photonic nanomaterials and their applications to material science including physical, chemical and biological sciences. To deliberate on material properties of individual nanoparticles and their engineering applications was the prime objective of the conference. Dr. G. Amarendra, the then Director, MSG & MMG delivered the welcome address, highlighted the activities at Materials Science Group, IGCAR and its relevance in the National scenario. LMIN-2019 was inaugurated by Dr. Arun Kumar Bhaduri, Distinguished Scientist & Director IGCAR and in his address highlighted the importance of understanding the material performance under extreme neutron flux and the need for basic research in material science at our Centre. He also mentioned about the Centre's interest in developing new structural materials such as Oxide Dispersion Strengthened alloys (ODS) with the dispersion of oxide nanoparticles for advanced future reactors. Chief Guest Prof. Chandrabhas Narayana, Dean, R&D, JNCASR, Bengaluru delivered the plenary lecture on "Tailoring the nanostructures for trace detection and drug discovery". The talk highlighted advanced applications of physics and chemistry in biological systems. The conference was attended by about 120 scientists and students from all over India from various academic institutes like IITs, IISERs, national laboratories and DAE institutes. The scientific deliberations were conducted in nine technical sessions with invited, oral and poster presentations. The conference presented an opportunity for young researchers to interact with leading experts in the field of nanoscience and technology. More than 40% delegates were women scientists. Also, based on the assessment of a panel of judges, best poster and oral presentations were selected and the awards were presented to the winners during the valedictory function.

Bridge Course on 'Welding and Fabrication'

July 22-26, 2019



Dr. Arun Kumar Bhaduri, Director, IGCAR along with senior colleagues of the Centre and participants of the course

First Bridge Course on 'Welding and Fabrication' was organised during July 22-26, 2019 at IGCAR, Kalpakkam for the benefit of students completing first year M.E/M.Tech. This was jointly organised by the Indian Institute of Welding (IIW), Chennai branch, American Welding Society, India International Section & Indira Gandhi Centre for Atomic Research (IGCAR), Kalpakkam.

A total of 25 students from Institutes across the country such as IIT Kanpur, NIT's, PSG college of technology, MS university of Baroda, GEC Thrissur, Engineering colleges in Tamil Nadu & neighboring states participated in the course.

The course was inaugurated by Shri T. Johny, Associate Director, TSG/ESG, IGCAR, in the presence of Dr. M. V. Venkatesan, Chairman IIW-INDIA Chennai Branch and Shri Shyam Baskaran, General Secretary, AWS INDIA International Section. The valedictory function was chaired by Dr. Arun Kumar Bhaduri, Director IGCAR & President, IIW-INDIA. Prizes were given to three students who topped the evaluation conducted for them. The course convener was Dr. Shaju K Albert, the then Associate Director, MEG/MMG and was coordinated by Shri T. V. Prabhu, Shri R. Ravikumar and their colleagues.

Workshop on "Environmental Radioactivity Measurements- ERM-2019"

July 25-26, 2019



Two day workshop on "Environmental Radioactivity Measurements- ERM-2019" was held during 25-26, July 2019 at RESG in association with Indian Association for Radiation Protection (Kalpakkam chapter). Prior to workshop, a tutorial session on use of alpha, gamma and counting systems was organized for young researchers. Dr. R. Baskaran, the then Associate Director, RESG inaugurated the workshop. Experts from BARC and academic institutions delivered lectures on various topics including methodologies, issues on environmental radioactivity measurements in various matrices. The workshop was attended by 54

members from various research institutions, colleges and industries. The workshop provided a platform to unite researchers from all professional institutions, government organization and universities across the country and shared their activities and experience.

Graduation Function of the 13th Batch of Trainee Scientific Officers of BARC Training School at IGCAR

July 29, 2019



Release of souvenir at the graduation function. Dr. B. Venkatraman, Director, SQRMG & ESG, Dr. Arun Kumar Bhaduri, Director, IGCAR, Shri S. A. Bhardwaj, Former Chairman, AERB, Mumbai, Dr. Vidya Sundararajan, Head, P&HRMD and Dr. N. Madurai Meenachi, Head, OCES-Training Section, RMG

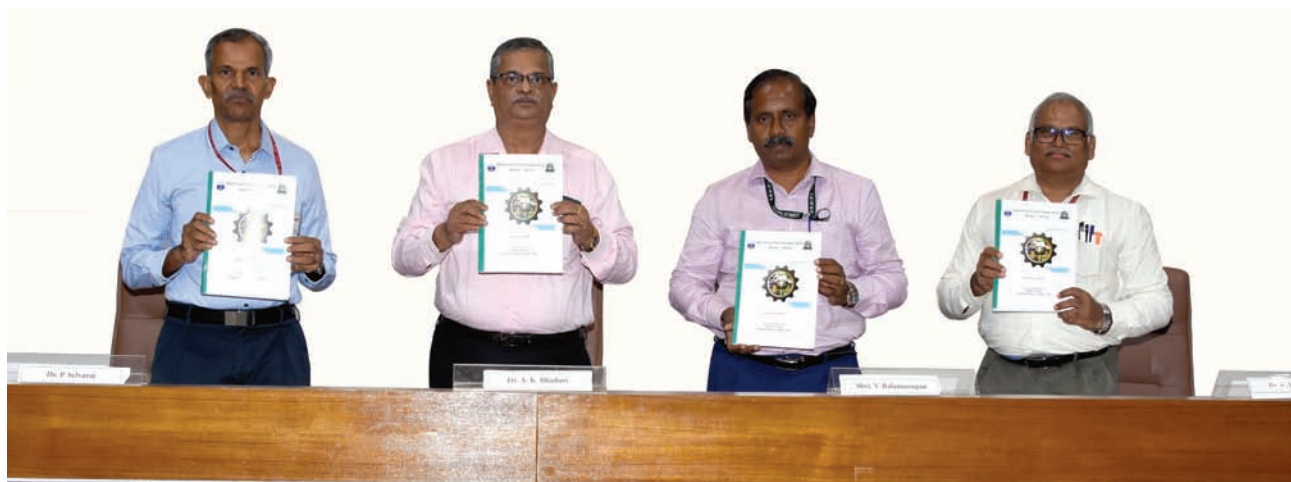
Twenty three Trainee Scientific Officers from the 13th batch of BARC Training School at IGCAR have successfully completed their training and were graduated in a special ceremony that took place on July 29, 2019. Shri S.A. Bhardwaj, Former Chairman, Atomic Energy Regulatory Board (AERB) Mumbai was the Chief Guest for the function. Dr. B. Venkatraman, Director, SQ&RMG & ESG, welcomed the gathering. Dr. Vidya Sundararajan, Head, P&HRMD briefed the audience about Orientation Course in Engineering and Sciences disciplines. Dr. Arun Kumar Bhaduri, Distinguished Scientist and Director, IGCAR delivered the presidential address. Shri S. A. Bhardwaj released the souvenir featuring the activities of the training school programme in the previous academic year. He also gave away the prestigious 'Homi Bhabha Prizes' comprising of a medallion and books worth Rs.5000 to the toppers from each discipline and addressed the gathering. He also gave away the course completion certificates to all the graduates passing out. A few of the Trainee Scientific Officers passing out shared their experience, gave feedback on the academic programme and their stay at the hostel. Shri S. A. Bhardwaj gave a very inspiring and enlightening lecture to the gathering. Dr. N. Madurai Meenachi, Head, OCES-Training Section, Resource Management Group, proposed the vote of thanks.



Graduates of BARC Training School at IGCAR with Shri S. A. Bhardwaj, Former Chairman, AERB, Mumbai, Dr. Arun Kumar Bhaduri, Director, IGCAR and senior colleagues of the Centre

National Technology Day Meet 2019

July 30, 2019



Dr. P. Selvaraj, the then Director FRTG, Dr. Arun Kumar Bhaduri, Director, IGCAR, Shri V. Balamurugan, Director, CVRDE, Dr. K. Velusamy, Convener of the meet during the release of Technology Day brochure

As a part of National Technology Day celebration, a seminar cum exhibition was conducted at IGCAR on July 30, 2019 for the non-gazetted staff (technical/administration/accounts/stores) of the DAE Units at Kalpakkam. The objective of this event was to highlight the important, innovative and novel contributions made by the staff towards the various projects and programmes of the Centre. It was conducted as a trilingual event (English, Hindi and Tamil) with the participants presenting and showcasing their works/achievements in the past two years. The seminar comprised of both oral and poster sessions. An exhibition was also arranged wherein the components / products / gadgets / devices / systems / models / concepts developed by the individuals / groups were displayed.

The meet was held in parallel sessions with wide participation of employees from IGCAR, MAPS, BHAVINI, BARC(F), SRI and GSO. Totally 167 papers were presented which included 60 oral and 94 poster presentations with remaining as exhibits. Apart from the 225 presenting authors 40 staff members who superannuated from service during July 1, 2019 to May 31, 2020 also participated in this event.

Shri V. Balamurugan, Outstanding Scientist & Director Combat Vehicles Research and Development Establishment (CVRDE) Chennai, was the Chief Guest. He made a lucid presentation on the development of Arjun Main Battle Tanks for Indian army. Panels of juries evaluated the oral, poster and exhibit presentations. Certificates for best papers / posters / exhibits were distributed by Dr. Arun Kumar Bhaduri, Distinguished Scientist & Director, IGCAR during the valedictory function.

Workshop on “Current Advances in Risk Assessment for Radiological Releases during Nuclear Emergencies (CARE)”

August 5-6, 2019



Delegates of the CARE-2019 workshop

A two-day Workshop on “Current Advances in Risk Assessment for Radiological Releases during Nuclear Emergencies (CARE)” was conducted by the Indian Nuclear Society, Kalpakkam Chapter in association with Indira Gandhi Centre for Atomic Research, during 5-6 August 2019 at IGCAR, Kalpakkam. The focal theme was to evolve Objective and Rational methodologies for radiological risk assessment for accidental releases of radionuclides during nuclear accidents involving national and international experts. About 27 Scientific Officers and Engineers from BARC, AERB, NPCIL, three Professors from U.K (Prof Philip Thomas, Prof Victor & Prof William Nuttal) and faculty from SSN College of Engineering, Chennai participated in the workshop. The lectures covered i) Judgement-value (J-value) method and its application for assessing the rationality of emergency actions implemented in public domain during big nuclear accidents Chernobyl and Fukushima highlighting life-expectancy, cost-benefit analysis parameters ii) current regulatory requirements for emergency preparedness and management in Indian scenario iii) Ensemble Kalman filters and their application in dose mapping and source term estimation during emergencies iv) consequence assessment and economic cost evaluation of counter measures during hypothetical large nuclear accidents in UK using the PACE and COCO-2 codes v) Application of Decision Support Systems for counter measure evaluation during early phase of accidents vi) Radiological Transport and Dispersion modeling for Fukushima Accident with the ONERS-DSS vii) Application of Kalman-Filters in Atmospheric Dispersion Modeling. Overall, the need of objective risk methods in realistic assessment of the radiological risk for recommendation of optimum protective actions was acknowledged by all the experts.

Eddy current Level-2 certification course

August 19-24, 2019

Level-2 certification course on Eddy Current Testing as per IS 13805 was conducted by IGCAR in association with ISNT Kalpakkam chapter during August 19-23, 2019 at IGCAR. Certification examination was conducted by National Certification Board (NCB) of ISNT on August 24, 2019. Dr. C. K. Mukhopadhyay, Head, NDE Division/MMG served as the Course Director. The course was inaugurated by Dr. Shaju K. Albert, the then Associate



Participants of the course along with senior colleagues of the Centre

Director, MEG/MMG. A special address was given by Dr. B. P. C. Rao, Project Director, FRFCF and Chairman, ISNT Kalpakkam Chapter during the inaugural session. The course was attended by nineteen participants from different organisations including IGCAR, NPCIL, BHAVINI and Heavy Water Plants. Eminent faculty like Shri Arbind Kumar, QAD, BARC, Mumbai and Shri T. S. V. R. Nageswara Rao, M-QAT, NFC, Hyderabad delivered lectures in the course. Fourteen candidates have successfully passed the examination conducted by NCB and certificates were issued to them.

Special Colloquium on 'March for Science'

September 03, 2019



Dr. Arun Kumar Bhaduri, Director, IGCAR addressing the audience

'March for Science' is a worldwide movement to spread the scientific temper and to urge greater priority for science education and research. Starting from 2017, every year science programmes and rallies are organised. Many prominent scientists have been participating in these events world over and across India. As part of this, a special Colloquium was organised by IGCAR in association with Tamil Nadu Science Forum (TNSF) on September 03, 2019 at IGCAR. Dr R. Ramanujam and Dr. M. V. N. Murthy, Institute of Mathematical Sciences, Chennai delivered lectures respectively on the topics "Let us March for Science" and "Science Needs Funding". The lectures highlighted the genesis of this global initiative and the need for such a movement. Dr. Arun Kumar Bhaduri, Distinguished Scientist & Director, IGCAR, gave a special address to the audience. At the end there was an interaction session with the speakers and the audience.

As part of this programme, a rally was organised in the Kalpakkam Township in the evening to spread the Scientific temper amongst public. Volunteers from Tamil Nadu Science Forum, Research Scholars of HBNI-IGCAR and common public participated in the rally. At the culmination point, a brief meeting was organised and Dr. B. Venkatraman, Director SQRMG and ESG gave a special address to the participants of the rally.



Participants of evening rally

Annual Meeting of Hot Laboratories and Remote Handling (HOTLAB 2019)

September 8-12, 2019



Delegates at the 56th Annual Meeting of Hot Laboratories and Remote Handling (HOTLAB 2019) at Mamallapuram

The 56th Annual Meeting of Hot Laboratories and Remote Handling (HOTLAB 2019) was organized by Indira Gandhi Centre for Atomic Research (IGCAR), Kalpakkam, in association with the International Atomic Energy Agency (IAEA) and the Indian Association for Radiation Protection (IARP), at Mamallapuram during September 8 - 12, 2019. This annual meeting was held for the first time in India. About seventy-two delegates from hot laboratories, associated institutes and companies from across the world and fifty delegates from various DAE units and supplier's representatives from India participated in the event.

The three day meeting commenced with Dr. G. Amarendra, Chairman HOTLAB 2019, welcoming delegates from India and abroad, and briefly describing structure of the technical proceedings. This was followed by the inaugural address by Dr. Arun Kumar Bhaduri, Director IGCAR, in which he highlighted the role of Post Irradiation Examination (PIE) facilities in the fast reactor programme of the Centre. The Chief Guest, Dr. Ki Seob Sim, IAEA, Chairman, International Working Group for Hot Laboratories and Remote Handling spoke on the IAEA database on PIE facilities as a resource for furthering international collaborations in the area. Dr. Ann Leenaers, SCK, Belgium spoke briefly on the activities of the Working Group. A book of abstracts HOTLAB 2019 was released on this occasion.

The technical programme distributed over three days comprised of oral and poster presentations, with over seventy papers on topics related to characterization of radioactive materials and remote handling technologies in hot cells. The presentations were distributed over ten focussed sessions covering all aspects of design, construction, operation, refurbishment, waste management and radiological monitoring at hot laboratories across the world, noted among them being from JRC at Karlsruhe, MRF of UKAEA, TRIUMF of Canada, CEA, France, apart from facilities in Argentina, Czech Republic, Japan, Norway, Romania, Sweden, Switzerland, and USA. From the Indian side, presentations covered developments in IGCAR, BARC and BRIT. Two best presentations each from oral and poster categories were selected by an international jury. Leading companies and firms associated with hot cell related technologies also participated in the annual meeting through an exhibition. The programme concluded with half a day visit to the IGCAR facilities such as FBTR, KAMINI, RML hot cell facility, and MSG Ion Irradiation Facility.

**International Conference on
Nanostructuring by Ion Beams (ICNIB-2019)
IGCAR, Kalpakkam
November 6-8, 2019**



Release of the Book of Abstracts (L to R) Dr. G. Amarendra, Chairman, ICNIB-2019, Prof. Avinash Chandra Pandey, Director, Inter-University Accelerator Centre, New Delhi, Dr. B. K. Panigrahi, Co-Chairman and Dr. C. David, Convener

The 5th International Conference on Nanostructuring by Ion Beams (ICNIB-2019) was organized by Indira Gandhi Centre for Atomic Research (IGCAR) in association with Board of Research in Nuclear Sciences (BRNS), Ion Beam Society of India (IBSI), Inter-University Accelerator Centre (IUAC) and Materials Research Society of India (MRSI) during November 6-8, 2019. This biennial international conference had participation from 10 international delegates and about 100 delegates from national research institutes and universities from various parts of India. Considering the role played by energetic ions in nanostructuring and development of nano materials, the ICNIB 2019 provided an engaging platform for scientists, engineers to discuss a host of topics involving radiation damage, ion beam induced synthesis and modification of nanostructures, ion-beam processing of novel compound phases, nanoscale precipitates and ripple formation. Preceding the conference, a two day school to expose early researchers and research scholars to ion solid interactions, defect production, defect characterization and multi-scale modelling was organized during November 4-5, 2019.

The conference was inaugurated by Prof. Avinash Chandra Pandey, Director IUAC, New Delhi. In his inaugural lecture he presented an extensive overview of accelerators in India and their applications. In his welcome address, Dr. G. Amarendra, the then Director MSG & MMG, IGCAR stressed on the accelerator based research programme of simulating radiation damage in nuclear materials, being pursued at IGCAR. Dr. B. K. Panigrahi, Director, MC&MFCG & EIG, IGCAR presented a glimpse of past and current accelerator based research activities in IGCAR using low to medium energy ion accelerators. Awards were distributed to students who made the best poster and oral presentations.

4th National Conference URJAVARAN – 2019

December 20, 2019



Shri Biswanath Sen, Convener, Dr. B. Venkatraman, Director, SQRMG & ESG, Shri M. Srinivas, Station Director, MAPS, Shri C. Subramaniam, Past President, ISHRAE HQ and Shri N. S. Gopala Krishna, Organizing secretary during release of souvenir in the inaugural function

4th National Conference URJAVARAN was organized by IGCAR in association with Indian Society of Heating Refrigerating & Air-conditioning Engineers (ISHRAE) - Kalpakkam Chapter at Sarabhai Auditorium, IGCAR on December 20, 2019. The theme of the conference was “Energy Sustainability Roadmap for Hospitality and Healthcare Facility”.

In the inaugural function, Shri Biswanath Sen, Convener, URJAVARAN – 2019 delivered welcome address, briefed about the conference and its impact on the society. He also presented a brief note about history of URJAVARAN. The inaugural function was presided over by Dr. B. Venkatraman, Distinguished Scientist and Director, SQRMG & ESG. In his address, Dr. B. Venkatraman emphasized the importance of indoor air quality in all buildings including health care facilities. He also indicated the necessity of reducing the huge energy consumption by heating, ventilation and air conditioning (HVAC) systems through innovative techniques thereby improving the efficiency. Shri M. Srinivas, Station Director, MAPS delivered the inaugural address and highlighted the significance of energy conservation for sustainable environment. He also emphasized on green and clean energy generation and role of DAE towards it. Shri C. Subramaniam, Past President, ISHRAE Headquarter delivered the keynote address on the topic “Building management systems, IoT & data analytics for MEP systems” and enlightened the audience about intelligent buildings and the role of building related data collection and its analysis towards optimizing the performance and improving sustainability. Shri N. S. Gopala Krishna, Organizing Secretary, URJAVARAN - 2019 proposed the vote of thanks. Shri A. Jyothish Kumar, Director (Operations), BHAVINI inaugurated the exhibition stalls at the venue of the conference. Various industries in the field of HVAC system and component design showcased their products.

About two hundred and sixty five delegates from DAE units at Kalpakkam, academic institutions, industries and leading consultants attended the conference. The main focus of the discussion was on products, latest technologies, and ongoing research in buildings with sustainable energy. The conference included invited talks by eminent speakers from academic institutions, industries, R&D organizations and leading consultants in the areas of air-conditioning & infection control of healthcare facilities, indoor air quality of buildings and high performance computing facility. Contributed papers from IGCAR and BARCF, covering wide spectra such as thermal energy storage by Nanotechnology, development of heat load estimation software, cooling tower performance, nuclear ventilation and energy conservation by implementing latest technology, were presented in the conference. The conference facilitated active interactions and exchange of ideas among delegates and experts in the area of HVAC.

During the valedictory function, Shri Faizan Ullah Khan, Convener, Technical Committee, URJAVARAN-2019 summed up the technical content of one-day conference. Dr. K. Ananthasivan, Director, RpG delivered the valedictory address. In his address he described how the air quality is degraded with industrial growth over time and its impact on human life. He emphasized the importance of technologies to improve air quality and sustainability. Shri Biswanath Sen, Convener, URJAVARAN – 2019 proposed the vote of thanks.

News and Events

Swachhta Pakhwada - 2019
February 16-28, 2019



Cleaning of Office premises



Visit by the members of Swachhta Cell



Shri M.S.Premnath, Superintending Engineer (Retired), Chennai Corporation during the closing ceremony

IGCAR observed “Swachhta Pakhwada” during February 16-28, 2019. Scrap, with special emphasis on e-waste, was disposed and office premises were cleaned. In order to provide a boost to the swachhta activities, members of IGCAR Swachhta Cell visited various Divisions/Groups and selected three best kept locations. Certificate of Appreciation was awarded during the closing ceremony of Swachhta Pawkhwada. A guest lecture by Shri M.S.Premnath, Superintending Engineer (Retired), Chennai Corporation on “Managing Waste” was organized on the closing day. Essay, slogan and poster competitions on the topic “Clean and Green Environment” were conducted and prizes distributed during the closing ceremony.



Shri Anil Swarup, Former Secretary to Government of India delivered IGC Colloquium on “Making Things Happen in India” on March 18, 2019



Saraansh Pustika was released by Dr. Arun Kumar Bhaduri, Director IGCAR during the inaugural function

The official language implementation committee (OLIC), IGCAR organised a one-day scientific seminar on the subject 'Clean Energy, Environment and Advance Technologies' through Hindi medium on January 10, 2019 at Sarabhai Auditorium. A summary of all the presentations in the form of a booklet, Saraansh Pustika was released by Dr. Arun Kumar Bhaduri, Director IGCAR and Chief Guest, during the inaugural function. Best paper and poster presentations were awarded cash prizes.

A one day Security Sensitisation programme for Senior Officials of DAE units was conducted at IGCAR, Kalpakkam on 14.05.2019



Security Sensitisation programme



Special lecture by Sr. Prof. K. R. Munirathinam, WCSC, Chennai. on "Yoga for Harmonious Life".

On the occasion of 5th International Day of Yoga on 21.06.2019, Sr. Prof. K. R. Munirathinam, World Community Service Centre (WCSC), Chennai delivered a lecture on "Yoga for Harmonious Life" at Sarabhai Auditorium IGCAR, Kalpakkam. This was followed by a Practical Session on Yoga.

IGC COUNCIL

Chairman

Dr. Arun Kumar Bhaduri

Distinguished Scientist & Director, IGCAR



Dr. Arun Kumar Bhaduri, a graduate and Ph.D. in Metallurgical Engineering from Indian Institute of Technology, Kharagpur, joined Department of Atomic Energy in 1983. He is with the Indira Gandhi Centre for Atomic Research, Kalpakkam since 1984, where he is presently Distinguished Scientist and Director and also a Senior Professor, Homi Bhabha National Institute. He received Research Fellowship from Alexander von Humboldt Foundation, Germany in 1994 for a 2-year post-doctoral research at University of Stuttgart, Germany. He pilots the design and technology development of sodium-cooled fast reactors and its associated fuel cycle for the second stage of India's nuclear power programme, and anchors the development of materials and their fabrication technologies for Indian programmes on sodium-cooled fast reactors, fusion reactors and advanced ultra supercritical thermal power. He specialises in the field of materials joining, and has to his credit more than 250 journal publications, 400 conference presentations and 2 international patents. He is a fellow of Indian National Academy of Engineering, Indian Institute of Metals and Fellow, Indian Institute of Welding. Some of his notable recognitions include: Doctor of Science (2017), Jadavpur University, Kolkata; Distinguished Alumnus Award (2017), IIT Kharagpur; Jaeger Lecture Award (2017), International Institute of Welding; GD Birla Gold Medal (2017), Indian Institute of Metals; Carl von Bach Commemorative Medal (2016), MPA University of Stuttgart, Germany; VASVIK Award (2005), Vividhlaxi Audyogik Samshodhan Vikas Kendra, Mumbai; DAE Group Achievement Awards (2006–2016) 11 times, including 4 times as Group Leader; National Metallurgists' Day Metallurgist of the Year Award (2003), Ministry of Steel; DAE Homi Bhabha Science & Technology Award (2002).

Members



Prof. Ajit Kumar Mohanty, a well-known nuclear physicist, completed his Bachelor's degree in 1979 from MPC College, Baripada and Master's degree in Physics in 1981 from Ravenshaw College, Cuttack which was at that time under Utkal University, Bhubaneswar. Dr. Mohanty graduated from the 26th batch of the BARC Training School and joined Nuclear Physics Division of Bhabha Atomic Research Centre in 1983 and got his PhD degree from Bombay University later on. He has taken over as Director, BARC on 12th March 2019. Before his appointment as Director BARC, Dr. Mohanty has held the position of Director of Saha Institute of Nuclear Physics, Kolkata from June 2015.

During the past 36 years, Dr. Mohanty has worked in several areas of nuclear physics covering collision energy from sub-Coulomb barrier to relativistic regime. It includes experiment using Pelletron accelerator at TIFR, PHENIX and CMS experiments at Brookhaven National Laboratory (BNL), USA and CERN, Geneva respectively. Dr. Mohanty has held several honorary positions. To name a few, he served as Secretary and Member Secretary of BRNS Basic Science Committee from 2004-2010, General Secretary of Indian Physics Association (IPA)

2012-2016 and later on President of IPA since 2018, India-CMS Spokesperson 2013-2015 and Dean, Academic, Physical & Mathematical Sciences, BARC, Homi Bhabha National Institute.

Dr. Mohanty has been recipient of several awards and recognitions during his illustrious career. Some of Dr. Mohanty's awards and recognitions are: Gold medal in Graduation, 1979, Young Scientist Award of Indian Physical Society (IPS, Kolkata, 1988), Young Physicist Award by Indian National Science Academy (INSA, New Delhi 1991) and DAE Homi Bhabha Science & Technology Award (2001) by Department of Atomic Energy, Mumbai. He was also conferred the CERN Scientific Associate position at CERN, Geneva from 2002-2004 and thereafter again from 2010-2011. Dr. Mohanty has been Director on the Board of NPCIL w.e.f. 1st April 2019.



Dr. Shaju K. Albert graduated in Metallurgy from The Indian Institute of Science in 1984 and subsequently joined Dept. of Atomic Energy. After one year of training in Nuclear Engineering at BARC, he joined Indira Gandhi Centre for Atomic Research (IGCAR) in 1985. Since then he has been working in the area of welding and joining and currently he is Director of Metallurgy & Materials Group and Material Science Group at IGCAR and Senior Professor in HBNI. He obtained his Ph.D. in 1997 from The Indian Institute of Technology, Bombay. He is responsible for research and development activities in the areas of material joining, metal forming, tribology, fracture mechanics, material characterization, corrosion, non-destructive evaluation in the Metallurgy and Materials Group and surface science, nano science, metal physics, radiation damage, theoretical physics, low temperature physics and accelerators in Material Science Group of IGCAR. He is a Fellow of the Indian Institute of Metals. He is recipient of STA and JSPS fellowships of Government of Japan and worked as Research Fellow under these fellowships in National Institute of Materials Science, Tsukuba, Japan. He has published extensively in the area of material joining and hardfacing, and is recipient of Gold Medal of Indian Nuclear Society, Science Technology Excellence Award of Dept. of Atomic Energy and many best paper awards of the Indian Institute of Welding. He is currently Chairman of the MTD-11, Welding General and Application Sectional Committee of Bureau of Indian Standards (BIS) and till recently Vice President of the Indian Institute of Welding. His research interests include welding metallurgy, consumable development, weldability testing, failure analysis, repair welding and non-destructive evaluation of welds.



Shri O.T. G. Nair joined IGCAR as Director (P & A) in June, 2018. He joined the Department of Atomic Energy in 1984. During the 35 years of his service in the Department, Shri Nair has worked in different capacities like Assistant Personnel Officer, Section Officer, Administrative Officer, Under Secretary, Deputy Secretary, Chief Administrative Officer and Director (P&A) and handled many portfolios in DAE Secretariat, BARC and IGCAR. He has received DAE Special Contributions Award - 2010



Dr. Kallol Roy, an Outstanding Scientist, is B.Tech in Electrical Engineering from NIT-Calicut; M.Tech in Electronics Design from CEDT-Indian Institute of Science; Ph.D. in Fault Diagnostics–Systems & Controls from IIT, Bombay and Post Doctorate in Computer Process Control from University of Alberta, Canada. He is from the 28th Batch of BARC Training School. Dr. Kallol Roy's field of specialisation includes Total Maintenance Management of Reactors, Upgrading and Retrofit of C&I and Computer Based Systems, EMI / EMC Studies and Modelling in Plants, Fault Diagnostics of Systems and Equipment

Reactor Safety, Surveillance & Tech-Specs, Analysis (CRP with IAEA) using Bayesian Estimation techniques and Safety and Security aspects of Computer based Systems. He was also a Professor of HBNI. Dr. Kallol Roy took charge as Chairman & Managing Director, BHAVINI on 31st March 2016.



Dr. B. Purana Chandra Rao, Outstanding Scientist, is from the 29th batch of BARC Training School, and joined the Department in 1985. As Project Director, Fast Reactor Fuel Cycle Facility (FRFCF) he is spearheading the construction, commissioning and management activities of FRFCF. Dr. Rao developed and effectively implemented innovative approaches and achieved decent physical progress with construction reaching finished floor level for 5 island FRFCF plants viz. CSP, RUP, FFP, FRP & WMP. He designed effective progress review & monitoring strategies with well-defined targets, responsibilities, timelines, micro-scheduling, snapshots etc. and ensured steady progress in Civil, Mechanical, Electrical, E&I, QA, Safety, Security and Utilities & Services works. He guided & motivated engineers and efficiently managed construction & procurement activities by paying proactive attention to critical-path aspects. Dr. BPC Rao proactively ensured procurement of IGC qualified SS plates, rounds & fittings, optical shielding slabs, lead bricks, process equipment, Material Handling Equipment, Radiation Monitoring Instruments, AC Ventilation, Low-level Liquid Waste, fire hydrant systems, storage tanks, annular tanks, radiography inspection equipment etc. He developed comprehensive QA methodologies for forged fittings, master-slave manipulators, fume-hoods and glove boxes of FRFCF. Dr. BPC Rao developed advanced NDE techniques & probes for inspection of fast reactor components and extended expertise to several organisations in solving challenging problems related to NDE, ISI, QA, Welding, Corrosion, Condition Monitoring, Structural Integrity Assessment and Failure Analysis. He has over 175 research publications to his credit. He has been conferred Homi Bhabha Science & Technology award of DAE, National NDT award & International recognition award of ISNT and Indian Nuclear Society Gold Medal and several DAE group achievement awards. He has received more than 25 best paper awards. As a Senior Professor of HBNI, Dr. BPC Rao guided several PhD, M.S and M.Tech students.



Dr. B. Venkatraman, post graduate in physics and doctorate from University of Madras is from the 27th batch of BARC Training School and joined IGCAR in 1984. He has specialized in the areas of Non-Destructive Evaluation, Radiation sciences, its applications and quality assurance. He has been primarily responsible for establishing the conventional, digital X-ray, neutron radiography and thermal imaging facilities at IGCAR. He has developed many NDE procedures and techniques such as microfocal radiography for steam generator of Fast reactor, X-ray and neutron radiography for highly irradiated fuel pins, neutron radiography of pyro-devices, NDE of tail rotor blades of defence helicopters, to name a few. All these have been successfully implemented in the Centre and in other industries. He is certified by American Society for NDT Level-III in X-ray and gamma radiography, penetrant testing, Visual testing and neutron radiography. He is a Senior Professor of Homi Bhabha National Institute. He has over 300 publications in Journals and Conferences including two articles in Encyclopedia of Material Science, two monographs, three books and is the series editor for the NDT handbooks published by National Certification Board, ISNT. He is the recipient of Homi Bhabha Science and Technology Award 2007 for Individual Excellence (highest award of the Department of Atomic Energy for individual scientific excellence). DAE Group Achievement Awards in 2008, 2010, 2011, 2012, 2015, D&H Schereon Award, 1993, ISNT-NDT Man of the Year Award (R&D) 2001, INS Gold Medal 2005, IIW-Sharp Tools Award 2011, International Recognition Award 2013, and has won more than 10 best paper awards. He is a Honorary Fellow of ISNT, Board Member, Asian Pacific Federation of NDT, President Elect, Indian Society for NDT, Vice President, Indian Association for Radiation Protection. He is presently Distinguished Scientist and Director, Safety, Quality & Resource Management Group and Engineering Service Group, IGCAR and he is also serving as Director, Medical Group, GSO.

Organisation and Activities of Various Groups

Dr. Arun Kumar Bhaduri
Director, IGCAR



Electronics and Instrumentation Group



Dr. B. K. Panigrahi
Director, EIG



Ms. T. Jayanthi
AD, RCCG



Shri R. Jehadeesan
Head, CD



Shri G. Prabhakara Rao
Head, SISD



Shri M. Sakthivel
Head, RTSD



Dr. D. Thirugnanamurthy
Head, EID



Shri A. Venkatesan
Head, ICD

Electronics and Instrumentation Group is focused on design and development of indigenous technology in the areas of Electronic Instrumentation & Control systems for fast breeder reactors and reprocessing plants that include Development of Distributed Digital Control System, Safety Critical and Safety Related Systems, Safe & Secure PLC, Virtual Control Panel based Control Room, Full-scope Operator Training Simulator, 3D modeling, animation & visualization of FBR subsystems and VR walkthrough of structures, Cyber Security Management for IT and I&C systems. Design and Development of advanced equipment and technology such as, indigenous Wireless Sensor Networks for nuclear facilities, strategic and societal applications, Time Domain Electromagnetic for Deep Seated Atomic Minerals Exploration, Plutonium Condition Air Monitoring System for reprocessing plants, Test Instrument for Steam Generator Tube Inspection, Radar Level Probe for Liquid Sodium Level Measurement, radiation resistance MEMS based sensor for nuclear applications and innovative sensors and instruments for nuclear facilities have been completed. Considerable expertise exists in designing, building and maintaining state-of-the-art high-performance supercomputing facility that continues to meet large scale compute- and data-intensive requirements in multi-disciplinary domains. Implementation of IT-enabled Nuclear Knowledge Management system for Fast Reactors and associated domains, computational intelligence systems, cryptography, cyber security solutions, knowledge management and development and deployment of modern security systems for access control and physical protection of nuclear complexes are initiated.

Engineering Services Group



Dr. B. Venkatraman
Director, ESG



Shri B. Harikrishnan
AD, CEG



Shri T. Johnny
AD, TSG & Head, CWD



Shri K. P. Kesavan Nair
Head, ESD



Shri H. R. Sridhara
Head, ASED



Shri N. Suresh
Head, CED



Shri Biswanath Sen
Head, AC&VSD



Shri Sudipta Chattopadhyaya
Head, CM&MWD

The Engineering Services Group is responsible for the development of infrastructure in line with the mandate & the vision program of the centre. It provides quality services and activities pertaining to Civil, Electrical, Mechanical engineering including Voice Communication Systems, Air-conditioning and Ventilation Systems. In the mechanical engineering domain, one key element is the manufacturing of critical components towards the development of fast reactor & reprocessing technologies. The group also coordinates with BSNL for providing data communication and for mobile communication. The group has a mandate to establish additional infrastructure requirements so as to meet Design, R&D and operational objectives of IGCAR which includes the backend fuel cycle. The group consists of expert teams with capability to design, engineer and execute systems under their jurisdiction. Aesthetically designed buildings & structures, providing reliable power supply, potable water, quality-air and other services including services from Central Workshop are being extended to other units of DAE located at Kalpakkam. The group is also involved in the horticulture development, which enhances the green cover and maintenance of roads and drainage system. The nature of work involves interaction with several State and Central Government Organisations. The group is responsible for providing reliable air-conditioning and ventilation services to various R&D facilities of the Centre. The group ensures that all infrastructural developments are carried out in harmony with environment.


Fast Reactor Fuel Cycle Facility



Dr. B. Purna Chandra Rao
Project Director



Shri B.M. Ananda Rao
AD, DFE



Shri. V. Manoharan
Chief PE



Shri K. Gopal
HEAD, B&PD



Dr. M. T. JOSE
HEAD, IFS



Shri. C. Chandran
Additional CE



Shri L. Davy Herbert
Additional CE

Fast Reactor Fuel Cycle Facility is entrusted with the work of planning, designing, constructing and commissioning the Fast Reactor Fuel Cycle Facility to close the fuel cycle of PFBR. FRFCF is a multi unit project piloted by IGCAR involving BARC, NRB and NFC and the construction is being executed by IGCAR. Detailed engineering design of the facility has been completed and regulatory clearance and financial sanction have been obtained. The Group is currently engaged in the construction and commissioning of FRFCF. Civil construction activity is under progress for all the five radiological plants in the nuclear island namely the Fuel Reprocessing Plant, Fuel Fabrication Plant, Reprocessed Uranium oxide Plant, Core Subassembly Plant and Waste Management Plant. Construction of all the infrastructure buildings such as administrative building, Training Centre, Centralized Surveillance, Safety and Health Physics Building and Utility & Service buildings such as DG building, Central chilling plant, Air compressor building etc have been completed. Concurrently the design and development of process equipment to meet the required capacities of FRFCF is also being completed and many equipments are manufactured, delivered to site and erection & installation is under progress. Successful commissioning of FRFCF is an essential step for embarking on construction of Second Stage nuclear power plants based on plutonium fuel that would pave the way for achieving energy security for the nation.


Materials Chemistry & Metal Fuel Cycle Group



Dr. B. K. Panigrahi
Director, MC&MFCG



Dr. B. Prabhakara Reddy
AD, MFRG



Dr. N. Sivaraman
AD, M&FCG & Head, FChD



Dr. V. Jayaraman
Head, MCD



Shri B. Muralidharan
Head, PPED



Dr. R. Kumar
Head, AC&SD



Shri T. V. Prabhu
Head, CF&ED



Dr Kitheri Joseph
Head, MF&PD

The mandate of Materials Chemistry and Metal Fuel Cycle Group (MC&MFCG) is to carry out broad based research and development on advanced fuel fabrication methods; advanced methods of fuel reprocessing technology & development of back-end fuel cycle technology; and sodium chemistry and novel chemical sensors; that includes chemistry of un-irradiated as well as irradiated fuels, development of alternate solvents and extractants for the separation of actinides and lanthanides and development of processes for minor actinide partitioning. Some of the current activities include fabrication of sodium bonded metal fuel pins & sub-assembly for test irradiation in FBTR, Development of process for pyro-chemical reprocessing of U-Pu-Zr alloy in 500 g batch scale, Development of radioanalytical, electron microscopy and optical methods (ICP-OES, AAS) for fresh fuel characterization, prototype development of electrochemical hydrogen burner for cold trap regeneration, development of flow sheet for minor actinide partitioning and establishing a sol-gel laboratory for incorporation of minor actinide in MOX matrices. The materials chemistry related activities include sodium chemistry, high temperature chemistry, R&D on suitable electrolyte and electrode materials for ECHM, development of novel thin film based chemical sensors, and development of molten salt electrolytic process. The group is also carrying out post irradiation studies such as dissolution of fuel, measurement of burn up, recovery of minor actinides; to provide expert analytical services to various programmes in the Centre and other DAE units and to develop new analytical techniques; to carry out basic chemical studies to fine tune the R&D capabilities and be in a state of readiness to undertake challenging investigations for furthering the Department's goal.



Materials Science Group



Dr. Shaju K. Albert
Director, MSG



Dr. M. Kamruddin
AD, A&NG



Dr. N. V. Chandra Shekar
Head, CMPD



Dr. Sandip Kumar Dhara
Head, SND



Dr. R. Govindaraj
Head, MPD

The Materials Science Group (MSG) comprising of Accelerator and Nanoscience Group (A&NG) and Condensed Matter Physics Division (CMPD) has the mandate of pursuing basic research on topical problems in Materials Science relevant to fast reactors. The Accelerator and Nanoscience Group (A&NG) consists of Materials Physics Division (MPD) and Surface and Nanoscience Division (SND). MPD focuses on the studies on defects, defect-impurity interactions in materials and supplemented by computations. Ion beam simulation of radiation damage is mainly carried out using a 1.7 MV tandem accelerator along with 400 keV in-house built linear accelerator for dual ion beam irradiation for defects studies and radiation response in materials of relevance for fusion and fission reactors. Defects in particular the open volume defects such as vacancies and their clusters are studied using positron annihilation spectroscopy. Positron beam based Doppler broadening studies have been mainly used for depth resolved defects studies in ion irradiated materials. Ion beam based characterization techniques such as high resolution RBS, channeling, focused ion beam SEM and luminescence are also being used as needed. Irradiation creep studies are being planned with proton beam of high energy and high beam current. Various experimental results related to defects and materials modeling are mainly understood based on extensive computations using a variety of simulation and ab-initio codes. High speed cluster computers at IGCAR are being extensively utilized for computation of materials properties. Besides there is also an intense effort towards nucleating quantum metrology based research studies.

The SND focuses on the study of monolithic and multilayered thin films and nanostructures using a variety of techniques such as secondary ion mass spectrometry, nanomechanical testing, FIB based nanostructuring and nanopatterning, Scanning Probe Microscopy based characterization of various electrical and mechanical properties at nanoscale, and Nanospectroscopy with tip enhance Raman spectroscopy (TERS) and Nanoscopy with near-field scanning optical microscopy (NSOM) specializing innovative methodology of imaging at sub-diffraction limit using confinement of polarized light. The division is also specialized in high temperature tribological studies for strategic materials along with carbon nanostructure and TiO₂ nanotube based research for energy harvesting. Furthermore, development of novel nanomaterials for advanced sensor applications is being carried out. Research activities relating to sensors based micromachined cantilevers and MEMS are also being pursued.

Condensed Matter Physics Division (CMPD) pursues several theme based research programs, such as investigation of structure and physical properties of materials under extreme conditions such as high pressures, low temperatures, high temperatures and high magnetic fields. Further, over the years various facilities for the synthesis of novel, superhard materials have been established including Laser Heated Diamond Anvil Cell (LHDAC) facility. The systems under investigation encompass nuclear materials, superconductors, strongly correlated systems, multiferroics, frustrated systems, f-electron based intermetallics and oxides, glasses and super hard transition metal borides. The Division also concentrates on the development of technologically important single crystals for detector applications. Dynamic light scattering and confocal microscopy are utilized for studies on soft condensed matter. SQUID based systems for Magneto-Cardiography (MCG) and Magneto-Encephalography (MEG) have been successfully designed, assembled, standardized and used for clinical studies. Further, SQUID based measuring systems such as high field SQUID magnetometer, SQUID VSM, SQUID based set-up for Non-Destructive Evaluation (NDE) have been developed.


Metallurgy and Materials Group



Dr. Shaju K. Albert
Director, MMG



Dr. S. Raju
AD, MCG



Dr. R. Divakar
AD, MEG



Dr. John Philip
Head, CSTD



Dr. P. Parameswaran
Head, PMD



Dr. C. K. Mukhopadhyay
Head, NDED



Dr. M. Vasudevan
Head, MDTD

The Metallurgy and Materials Group (MMG) of IGCAR has been actively driving the development of advanced nuclear structural materials, processes and technologies for Sodium Cooled Fast Reactors (SFR) and associated closed fuel cycle technologies through a directed metallurgy and materials research and development programme. MMG has made major strides towards the successful development of structural materials aimed at withstanding demanding operating and environmental conditions which included austenitic and ferritic steels, including ODS alloys with improved swelling resistance for reactor core applications, 316L(N) austenitic stainless steel for reactor components, modified 9Cr-1Mo steel with controlled B addition for steam generator applications. MMG is also involved in the development of an array of novel application specific functional materials such as ferroseals for sodium pumps, tungsten carbide for enhanced in-core shielding of life-determining core permanent structures, iron based soft magnetic alloy for control rod applications and corrosion resistant materials and coatings for aqueous and pyrochemical reprocessing applications. Extensive post-irradiation examination facilities have been effectively utilized for obtaining extremely valuable data on in-pile performance of indigenous fuels, structural and shielding materials to aid materials optimisation for future FBRs and life-extension of FBTR. Further, the group has immensely contributed towards developing a spectrum of Non-Destructive Evaluation (NDE) techniques for inspection, qualification and surveillance of large-sized and intricate reactor components both during their fabrication and while they are in service. The expertise developed in house on NDE is offered not only for FBRs but also for PHWRs, aerospace, defense and other industries. The group has also made immense contributions towards assessment of weldability of alloys and development of advanced welding techniques for joining special materials, with tight control over process parameters and ensuring component integrity. The extensive facilities for evaluation of mechanical properties of FBR materials include innovative small specimen testing techniques and evaluation of mechanical properties in severe environments such as dynamic sodium and steam under multi-axial loading. On the theoretical front, robust modelling protocols for predicting high temperature phase stability, thermophysical properties, deformation behavior and mechanical properties of materials under various loading conditions etc. are also being pursued. MMG houses sprawling and state-of-the-art materials characterization facilities that have been employed for catering to materials developmental issues of fission and fusion nuclear reactors. The corrosion control and prevention activities include estimation of corrosion behavior of structural materials and concrete structures for long term uninterrupted service of reactor systems and reprocessing plants. Presently, MMG is also closely working with M/s BHEL and M/s NTPC for Government of India's Mission Project on Development of Advanced Ultra Super Critical Power Plant (AUSCPP) to develop materials, fabrication and inspection technologies and to generate material data base required for design and construction of the first AUSCPP in the country. Due to its focused and balanced research and developmental efforts, the Group is able to sustain vibrant HBNI academic programmes at the Centre for students and research fellows pursuing M.Tech. and doctoral degrees. The Metallurgy and Materials Group thus maintains a seamless synergy between academic, research and technological developmental activities.

Reactor Design & Technology Group



Shri S. Raghupathy
Director, RDTG



Ms. R. Vijayashree
AD, NSDG



Shri B. K. Nashine
AD, SFG



Dr. S. Murugan
AD, CD&HG



Shri Jose Varghese
Head, CH&MD



Shri U. Parthasarathy
Head, SHTD



Shri S. Clement Ravi Chandar
Head, RC&AD



Dr. K. Devan
Head, RND



Shri N. Kasinathan
Head, THD



Dr. A. John Arul
Head, RS&DD



Shri S. Jalaldeen
Head, SMD



Shri N. Theivarajan
Head, PPCD



Shri B. Babu
Head, DD&RSD



Shri I.B. Noushad
Head, ROD



Shri V. Vinod
Head, ETHD



Shri Joseph Winston
Head, RH&IED



Shri B. K. Sreedhar
Head, SE&HD

Reactor Design & Technology Group (RDTG) is responsible for the design, structural & thermal hydraulics analysis, core safety & plant dynamics analysis, structural mechanics including seismic testing, manufacturing technology development, engineering development, testing and qualification of Fast Breeder Reactor (FBR) components/ systems. In addition, the responsibility of RDTG includes: Development of In service inspection devices & remote handling equipment for FBRs & FBR fuel reprocessing plants, Development of sensors & devices for sodium applications, Planning of irradiation experiments for testing of various fuel, structural and shielding materials in FBTR, Design, development & fabrication of various irradiation devices for experiments in FBTR, Out-of-pile testing, precision machining and welding of miniature components and planning & execution of Shielding / Foil Activation experiments in KAMINI reactor.

RDTG has expertise in design & engineering development of various systems/components of FBRs covering the Nuclear Steam Supply Systems (NSSS) and Balance of Plant (BoP) systems viz. Reactor Physics & Core

Engineering, Reactor Assembly, Absorber Rod and Component Handling Mechanisms operating in sodium, Primary & Secondary Sodium Heat Transport Systems, Decay Heat Removal systems, Tertiary Steam Water Systems, Various Plant Auxiliary Systems, Electrical Power Systems, Plant Layout, Sodium Pumps, Electromagnetic Pumps, Cold Trap and Ultrasonic devices for use in sodium.

RDTG has indigenously developed the design of Prototype Fast Breeder Reactor (PFBR) of 500 MWe capacity based on a detailed design, R&D program and Technology Development exercise and with the support from and in association with various other groups of IGCAR. The group is extending its technical support and design expertise to the PFBR project which is under commissioning by BHAVINI and is responsible for getting design safety clearances for PFBR from the Atomic Energy Regulatory Board (AERB). It also provides analytical support to other groups in the Centre. RDTG constantly provides the design and analytical expertise for the continuous enhancement of fuel & core performance of the Fast Breeder Test Reactor (FBTR) and operation at higher powers and higher operating temperatures focusing on the core engineering design, plant dynamics and core safety analysis. RDTG also plays a major role in the development of future Metallic fuel and has designed the metal fuel pins of different designs and fuel compositions for irradiation testing.

Design validation of critical components of FBRs are achieved through testing in sodium and in water using scaled down/full scale models. RDTG has acquired expertise in the development of sensors and devices for sodium applications, such as electromagnetic flow meters, level probes and leak detectors. Expertise has also been developed in handling of sodium and in the design, construction, commissioning & operation of various high temperature sodium test loops/facilities. The major sodium test facilities of RDTG include 5.5 MWt Steam Generator Test Facility (SGTF) for testing model steam generators of FBRs, SADHANA loop for experimentally demonstrating natural convection based safety grade decay heat removal system, Large Component Test Rig (LCTR) for testing critical full scale components, In Sodium Test facility (INSOT) for creep and fatigue testing of advanced materials, Sodium Water Reaction Test (SOWART) facility to study self wastage & impingement wastage of Steam Generator tubes and a state-of-art Sodium Facility for Component Testing (SFCT) for testing small and medium sized components and sensors. To meet the requirements of future FBRs, a new facility called Sodium Technology Complex is under execution.

Recent achievements of RDTG: Design studies towards raising FBTR power to 40 MWt, Analysis of on-site performance of PFBR secondary sodium pumps and EM pumps, Qualification of Transfer Arm for high temperature nitrogen environment, shielding design of additional spent subassembly storage facility, Design of a system to localise failed fuel pin at dry rupture stage itself, Steady state and transient pool hydraulics for FBR 1&2, Pressure transient analysis in secondary sodium piping, 3D CFD analysis towards enhancement of heat transfer from core debris post CDA, Development of code CRaD to estimate the metrics of primary radiation damage, Performance qualification of indigenously developed 4.6 m diameter large size bearing in a dedicated test facility, Indigenous development of 2 m diameter silicone rubber inflatable seals & backup seals for qualification, High temperature qualification of dissimilar metal weld inspection device (DISHA) in mockup facility, Development of servo manipulator for hot cell applications, Qualification of sodium aerosol detector in nitrogen environment for sodium leak detection, Testing and qualification of FBTR gripper bellows in sodium at 530°C, Development of explosive plug welding technique for plugging of degraded steam generator tubes, Development of mockup steel special subassembly for irradiation of seven numbers of test fuel pins in FBTR, Seismic testing of a multi-storey building in shake table to verify the efficiency of seismic isolators and Development of permanent magnet based magnetic particle collector for primary sodium system.

Besides providing technical support to PFBR, RDTG is currently engaged, in the development of future FBRs incorporating enhanced safety and improved economy. It has finalised the conceptual design of the future FBR and is currently undertaking the development of key systems and components and detailed engineering. Further, RDTG has evolved the preliminary conceptual design of a metal fuelled 100 MWt test reactor, planned to be launched after FBTR. These apart, it has a modern design office with many advanced modeling and analysis

softwares, experimental facility for testing major Reactor Assembly systems, Structural Mechanics Laboratory (SML) having state-of-the-art facilities for carrying out tests at component level to verify structural integrity at high temperature and a 100 t shake table with six degrees-of-freedom for seismic tests. The shake table is extensively used for the design validation of reactor systems and components of Nuclear Power Plants of NPCIL and other research projects undertaken by BARC.

RDTG plays a major role in developing highly competent human resources by undertaking academic courses for the various science and engineering disciplines through the BARC Training Schools located at Mumbai, at IGCAR, Kalpakkam and at NFC, Hyderabad and provide guidance to many employees / students / JRF & SRF in their Post graduate, Ph.D and Research Programs.

Reactor Facilities Group



Shri K. V. Suresh Kumar
Director, RFG



Shri A. Babu
AD, OMG



Shri M. S. Chandrasekar
Head, THRDD



Shri K. Dinesh
Head, TSD



Shri G. Shanmugam
Head, RMD



Shri N. Manimaran
Head, ROD

The Reactor Facilities Group (RFG) is responsible for safe operation of Fast Breeder Test Reactor (FBTR), KAMINI Reactor and Interim Fuel Storage Building (IFSB). FBTR is presently rated for operating at a power level of 32 MWt. Towards raising FBTR power level to its design power level of 40 MWt using Mark-I subassemblies and introducing poison subassemblies, a preliminary safety report is prepared and submitted to Regulatory body and it is under review. Progressive modifications are being carried out in FBTR to increase its availability and for gaining newer experience in operation. All post Fukushima & Seismic retrofitting were completed and FBTR is relicensed to operate upto June 2023. Utilizing the reactor for irradiation of advanced fuels and materials for fast reactors and conducting safety related experiments form a major part of RFG's activities. KAMINI Reactor is extensively used for neutron radiography activation studies and testing of neutron detectors. RFG is also responsible for fabrication and safe storage of fuel, blanket and control subassemblies for PFBR and required number of these subassemblies for the first core is fabricated and stored in IFSB. The Training section of the group is responsible for training the O&M staff of PFBR and future FBRs besides training of newly recruited category I & II trainees of IGCAR. The group also takes part in the operational safety review of PFBR project.



Reprocessing Group



Dr. K. Ananthasivan
Director, RpG



Shri B. M. Ananda Rao
AD, HCSPG



Shri N. K. Pandey
Head, RRDD



Shri K. Rajan
Head, RPDCD



Shri Shekhar Kumar
Head, RPOD



Dr. R. V. Subba Rao
Head, PRCD



Shri. M. Geo Mathews
Head, RpMD

Reprocessing Group of IGCAR is responsible for the various activities pertaining to fast reactor fuel reprocessing technology such as the design, construction, commissioning and operation of the fast reactor fuel reprocessing plants and associated R&D activities. CORAL (Compact facility for Reprocessing Advanced fuels in Lead cells) a pilot plant facility, commissioned in 2003, continues to operate successfully, processing the mixed carbide spent fuel from FBTR. The facility continues to serve as a test bed and has provided valuable feedback for the design and construction of future reprocessing plants. CORAL has completed its original mandate of reprocessing of FBTR fuel sub assemblies and closing the fast reactor fuel cycle and has been further relicensed for a period of five years by the regulatory body, after upgradation of the safety systems. In Demonstration fast reactor Fuel Reprocessing Plant (DFRP), stagewise regulatory clearance is being obtained from AERB for commencing regular operation, and recently consent for taking up Acid-TBP runs have been obtained. The group is also carrying out the design activities of the Fuel Reprocessing Plant of Fast Reactor Fuel Cycle Facility, which is a commercial scale reprocessing plant. In addition the group also lends its expertise in procurement of long delivery items such as the optical glass slabs for radiation shielding windows, various types of master slave manipulators, lead bricks etc. Concurrently focused R&D is being pursued in equipment development, alternate processes and aqueous processing of metallic fuel.

Safety, Quality & Resource Management Group



Dr. B. Venkatraman
Director, SQRMG



Dr. T. S. Lakshmi Narasimhan
AD, RMG



Shri S. Athmalingam
AD, HSEG & Head, QAD



Dr. D. Ponraju
Head, SED



Dr. M. T. JOSE
HEAD, HISD



Dr. R. Venkatesan
HEAD, RESD



Ms. S. Rajeswari
Head, SIRD



Dr. Vidya Sundararajan
Head, P&HRMD

The mandate of Safety, Quality & Resource Management Group (SQRMG) is to manage Health Physics, Radiation Safety and Quality Assurance services, studies on Environment Impact Assessment, Severe Accident & Sodium Fire and management of resources like Financial (Budget), Human, Scientific Information services and conduct Academic Programmes of BARC Training School at IGCAR. In order to effectively carry out the above activities the group is structured as Health, Safety & Environment Group (HSEG) and Resource Management Group (RMG).

HSEG comprises of Radiological & Environmental Safety Division (RESD), Health & Industrial Safety Division (HISD), Safety Engineering Division (SED) and Quality Assurance Division (QAD). RESD is responsible for providing radiation safety services such as TLD personal monitoring, Bio assay, Bio dosimeter and Whole body

counting services to all the occupational workers of the Centre. It also focuses on R&D activities in the areas of atmospheric dispersion and modeling, sodium aerosol science and technology, luminescence dosimetry, radiation safety through modeling & simulation and societal applications of ionizing and non ionizing radiations. HISD provides radiological protection and surveillance of all active plants and also services to meet the mandatory requirements of AERB (such as industrial and occupational health safety) to related projects of IGCAR. SED is carrying out studies on Severe Accident and Sodium Fire Safety. The major experimental facilities are THEME and SOFI for simulation of Molten Fuel Coolant Interaction, PATH facility for post accident heat removal studies, MINA and SOCA facilities for sodium fire studies and SFEF for large scale sodium fire and severe accident studies. QAD is primarily responsible for catering to the quality assurance, inspection, Non-Destructive Testing (NDT) and quality audit activities during fabrication, construction & erection of System, Structure & Equipments for various Groups of our Centre in order to establish and implement an effective quality management system. QAD also extends its expertise to other DAE units and other strategic sectors. HSEG organizes public awareness programmes on radiation safety and nuclear energy in addition to training and awareness programmes on industrial, radiation and fire safety to occupational workers.

RMG comprises of the Scientific Information Resource Division (SIRD) and Planning & Human Resource Management Division (PHRMD). The significant activities of PHRMD are planning and human resource management, conducting the academic programmes of BARC Training school at IGCAR and category I&II stipendary trainees, formulating and monitoring capital projects towards budget planning and management, facilitating induction of Research Scholars, Research Associates and Visiting Scientists, coordinating the visits of important dignitaries and delegations to the Centre, formulating and facilitating collaborations and MoU including patents and piloting the activities relating to technology transfer. The Group also coordinates the facilitation of undergraduate and post graduate projects by students from various academic institutions, summer school of BITS, and industrial visits of students from various institutions. Many of the above mentioned activities have been automated by creating user-friendly databases. Scientific Information Resource Division (SIRD) is an advanced Research library catering to the information needs of more than 5000 scientists, engineers, research scholars, faculty, and students of all DAE Units at Kalpakkam. SIRD has about 62,000 books, 48,000 back volumes, 550 e-journals, 15,000 standards, and two lakh technical reports. Library information management system is operating with RFID based digital library infrastructure, metadata in MARC format, and Webopac with advanced features like virtual book racks, single window access to all holdings etc. SIRD has developed an open access archive for the experimental data on materials property of IGCAR available in the public domain and other premier research institutes of India. SIRD maintains a pre-print server to ensure publication ethics as per the in-house guidelines. Documentation of avian fauna in and around Kalpakkam in collaboration with Salim Ali institute of Ornithology is being done regularly by SIRD. Recent Advancements in Information Technology (READIT), a biennial conference is being organised since 1995. The division also coordinates services like providing auditorium, photography and desktop design and printing of IGC Publications.

● ● ● **Madras Regional Purchase Unit** ● ● ●



Shri G. Padmakumar
RD, MRPU

Madras Regional Purchase Unit (MRPU) is one of the Regional Units of the Directorate of Purchase & Stores, Mumbai. The Material Management activities for IGCAR, GSO, BARCF, AERB southern regional units & HWP, Tuticorin are carried out by MRPU, Chennai. Procurement of goods, supplies and payment to suppliers are handled at Chennai and inventory and accounting are carried out by Central Stores at Kalpakkam and Tuticorin. The procurement activities for the major projects like FRFCF, INRPK, AUSC are being carried out by MRPU. Procurement is carried out through e-tendering system and through the Government e-market place (GeM). MRPU also enters into rate contracts for various medicine and drug purchase for the hospitals at Kalpakkam and other DAE units across the country. During the year 2019, MRPU processed about 2600 indents, released about 2100 purchase orders worth 355 crores. There are about 130 personnel from DPS employed in Purchase, Stores, Administration and Accounts. Another 15 from IGCAR, BARCF and HWPT provide technical and auxiliary support.

● ● ● **Administration & Accounts** ● ● ●



Shri O.T. G. Nair
Director (P&A)



Shri M. S. Saravanan
IFA



Shri V. Sivakumar
IFA[FRFCF]



Shri K. Sai Kannan
DCA



Smt S. Jayakumari
AO (E)



Shri Paresh Nath Mahadani
AO (R&V)



Shri R. Srinivasan
AO (L&G)

LIST OF IMPORTANT ABBREVIATIONS

AC&VSD	Air Conditioning and Ventilation System Division	MSG	Materials Science Group
AERB	Atomic Energy Regulatory Board	NDED	Non-Destructive Evaluation Division
A&SED	Architecture & Structural Engineering Division	NFC	Nuclear Fuel Complex
ANG	Accelerator & Nanoscience Group	NICB	Nuclear Island Connected Building
BARC	Bhabha Atomic Research Centre	NPCIL	Nuclear Power Corporation of India Ltd.
BARCF	Bhabha Atomic Research Centre Facilities	NSAG	Nuclear Systems Analysis Group
BHAVINI	Bharatiya Nabhikiya Vidyut Nigam Limited	NSDG	Nuclear Systems Design Group
BPD	Budget & Procurement Division	OMG	Operation & Maintenance Group
CD	Computer Division	PFBR	Prototype Fast Breeder Reactor
CED	Civil Engineering Division	P&HRMD	Planning & Human Resource Management Division
CEG	Civil Engineering Group	PHWR	Pressurized Heavy Water Reactor
CFD	Chemical Facilities Division	PIED	Post Irradiation Examination Division
CH&MD	Components Handling & Mechanism Division	PMPD	Pyro-chemical & Materials Processing Division
CMPD	Condensed Matter Physics Division	PMD	Physical Metallurgy Division
C&MWD	Contracts & Major Works Division	PPCD	Power Plant Control Division
CD&HG	Components Development & Hydraulics Group	PPED	Pyro Process Engineering Division
CORAL	Compact facility for Reprocessing Advanced fuels in Lead cell	PRCD	Process & Radio Chemistry Division
CSTD	Corrosion Science & Technology Division	QAD	Quality Assurance Division
CWD	Central Workshop Division	RCAD	Reactor Core & Assembly Division
DDRSD	Device Development and Rig Services Division	RDG	Reactor Design Group
DFE	Design & Field Engineering	R&ESD	Radiological & Environmental Safety Division
DFMFF	Demonstration Facility for Metallic Fuel Fabrication	RESG	Radiological & Environmental Safety Group
DFRP	Demonstration Fuel Reprocessing Plant	RIEMMD	Robotics, Irradiation experiments and Mechanical Maintenance Division
EID	Electronics and Instrumentation Division	RMD	Reactor Maintenance Division
EIG	Electronics and Instrumentation Group	RMG	Resource Management Group
ESD	Electrical Services Division	RND	Reactor Neutronics Division
ESG	Engineering Services Group	ROD	Reactor Operation Division
ETHD	Experimental Thermal Hydraulics Division	RFG	Reactor Facilities Group
FBR	Fast Breeder Reactor	RpMD	Reprocessing Maintenance Division
FBTR	Fast Breeder Test Reactor	RpG	Reprocessing Group
FChD	Fuel Chemistry Division	RPDCD	Reprocessing Plant Design & Commissioning Division
FRFCF	Fast Reactor Fuel Cycle Facility	RpOD	Reprocessing Operation Division
FRTG	Fast Reactor Technology Group	RRDD	Reprocessing Research and Development Division
HCSPG	Hot Cell Systems and Project Group	RSDD	Reactor Shielding and Data Division
HISD	Health & Industrial Safety Division	RTSD	Real Time Systems Division
HSEG	Health, Safety & Environment Group	RTCCG	Real-time Controls & Computer Group
GSO	General Services Organisation	SED	Safety Engineering Division
IAEA	International Atomic Energy Agency	SE&HD	Sodium Experiments & Hydraulics Division
IIT	Indian Institute of Technology	SFG	Sodium Facility Group
IMSc	Institute of Mathematical Sciences	SFR	Sodium cooled Fast Reactors
I&CD	Instrumentation & Control Division	SGTFD	Steam Generator Test Facility Division
MAPS	Madras Atomic Power Station	SHTD	Sodium Heat Transport Division
MCG	Materials Characterization Group	SIRD	Scientific Information Resource Division
MC&MFCG	Materials Chemistry & Metal Fuel Cycle Group	SISD	Security and Innovative Sensors Division
MCD	Materials Chemistry Division	SMD	Structural Mechanics Division
MDTD	Materials Development & Technology Division	SND	Surface and Nanoscience Division
MEG	Materials Engineering Group	SQRMG	Safety, Quality & Resource Management Group
MFCG	Materials & Fuel Chemistry Group	TCPAD	Technical Coordination & Public Awareness Division
MFFD	Metal Fuel Fabrication Division	THD	Thermal Hydraulics Division
MFRG	Metal Fuel Recycle Group	THRDD	Training & Human Resource Development Division
MMG	Metallurgy and Materials Group	TSD	Technical Services Division
MPD	Materials Physics Division	TSG	Technical Services Group
MRPU	Madras Regional Purchase Unit		

INDIRA GANDHI CENTRE FOR ATOMIC RESEARCH

Dr. Arun Kumar Bhaduri
Director, IGCAR

IGC Council

IGC Scientific Committee
[IGSC]

Programme Review & Monitoring
Committee [PRMC]

Dr. B. Venkatraman
Director
Engineering Services Group
and Safety, Quality &
Resource Management Group

Shri S. Raghupathy
Director
Reactor Design & Technology Group

Shri K. V. Suresh Kumar
Director
Reactor Facilities Group

Dr. B. K. Panigrahi
Director
Electronics & Instrumentation Group and
Materials Chemistry & Metal Fuel Cycle Group

Dr. K. Ananthasivan
Director
Reprocessing Group

Dr. B. Purna Chandra Rao
Director
Fast Reactor Fuel Cycle Facility

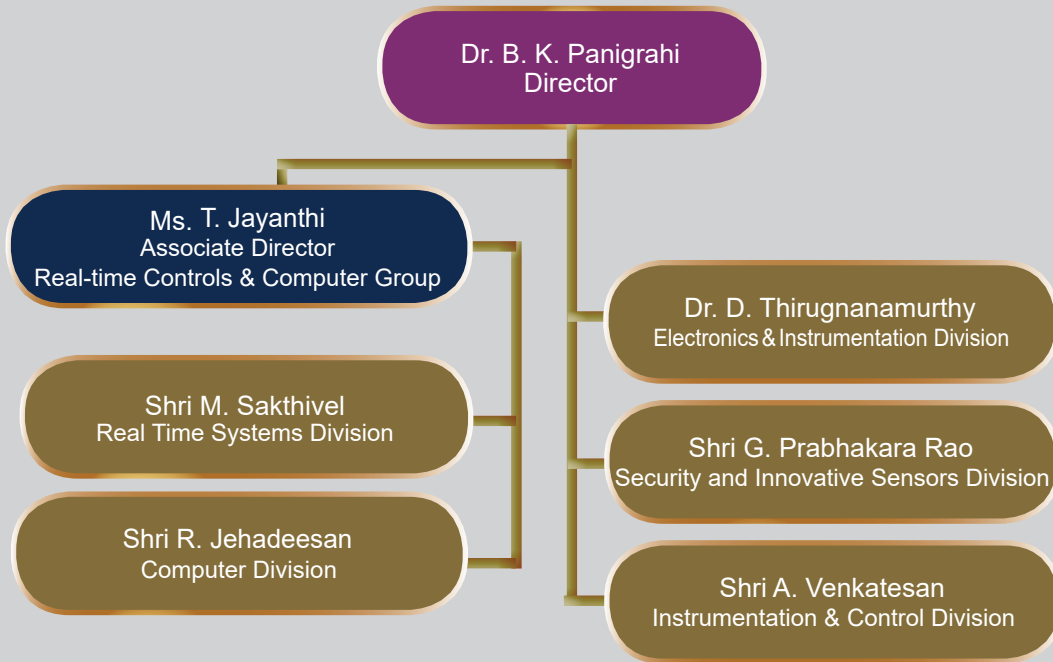
Dr. Shaju K. Albert
Director
Metallurgy & Materials Group
and Materials Science Group

Shri O.T. G. Nair
Director (P&A), Administration

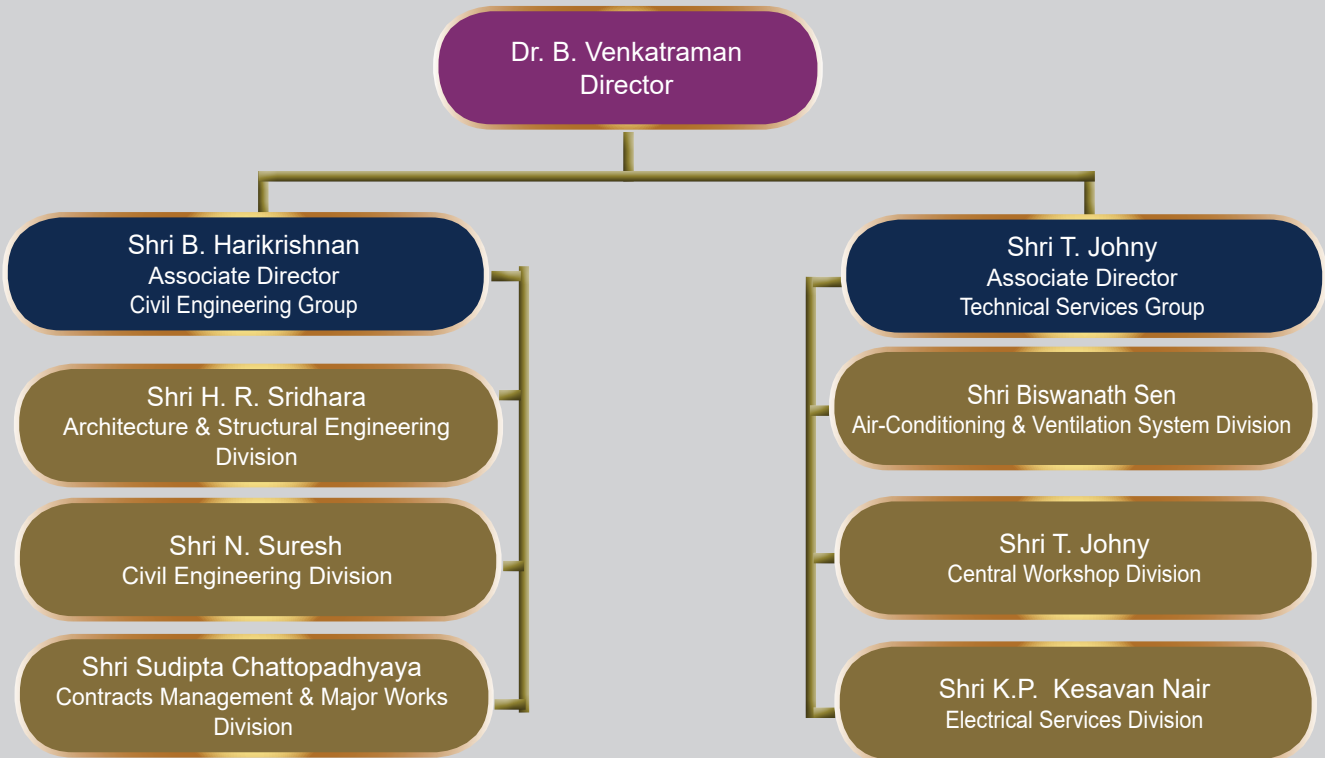
Shri M. S. Saravanan
IFA

Shri V. Sivakumar
IFA [FRFCF]

Electronics & Instrumentation Group



Engineering Services Group



FAST REACTOR FUEL CYCLE FACILITY

Dr. B. Purna Chandra Rao
Director

Shri V. Manoharan
Chief Project Engineer
Construction

Shri L. Davy Herbert
Additional CE

Shri C. Chandran
Additional CE

Shri B.M. Ananda Rao
Associate Director
Design & Field Engineering

Shri K. Gopal
Budget & Procurement Division

Dr. M. T. Jose
Industrial & Fire Safety

Materials Chemistry & Metal Fuel Cycle Group

Dr. B. K. Panigrahi
Director

Dr. B. Prabhakara Reddy
Associate Director
Metal Fuel Recycle Group

Shri T.V. Prabhu
Chemical Facilities & Engineering Division

Dr. Kitheri Joseph
Metal Fuel and Pyro-processing Division

Shri B. Muralidharan
Pyro Process Engineering Division

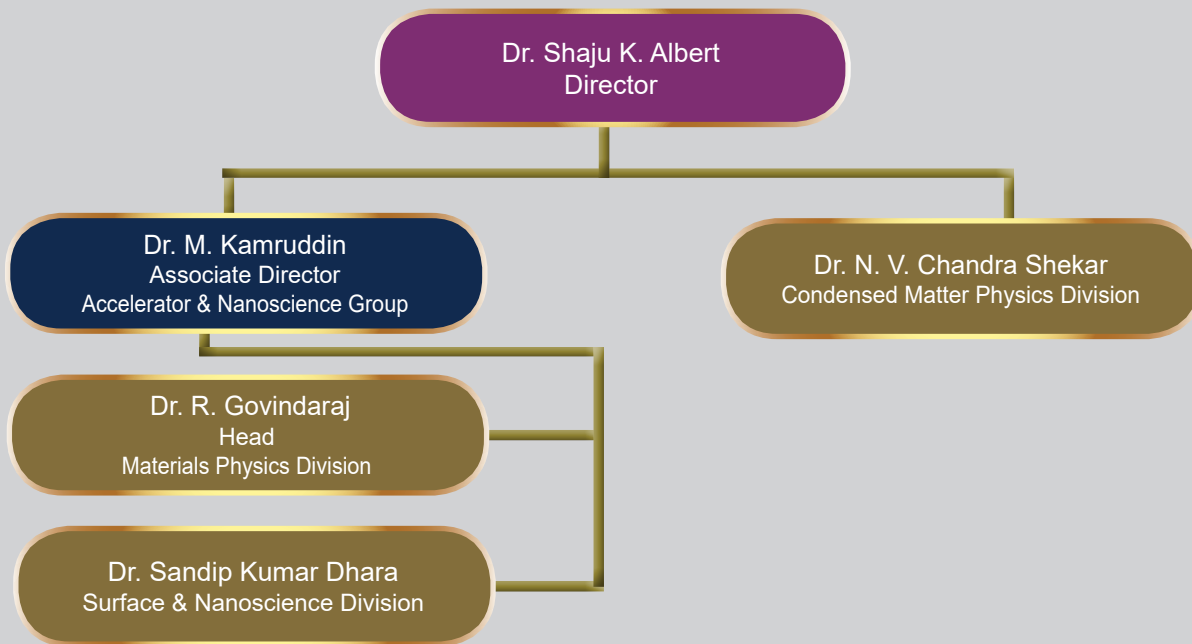
Dr. N. Sivaraman
Associate Director
Materials & Fuel Chemistry Group

Dr. R. Kumar
Analytical Chemistry & Spectroscopy Division

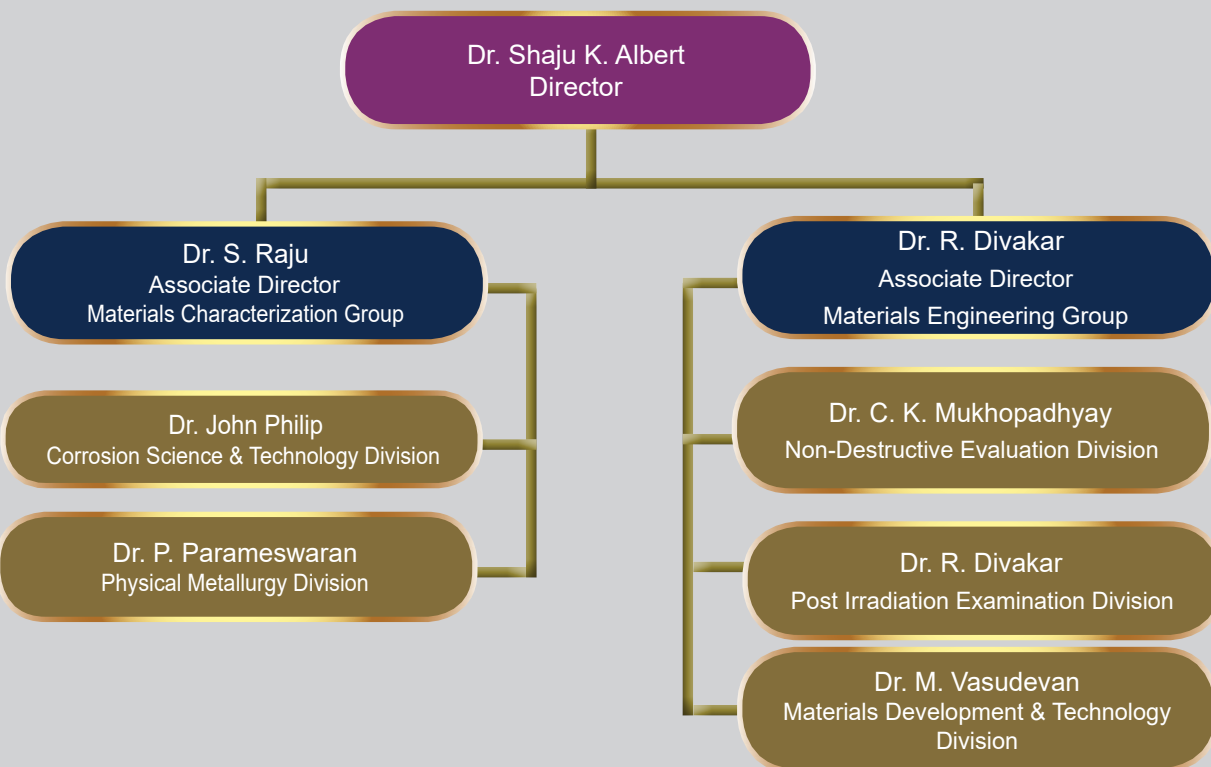
Dr. N. Sivaraman
Fuel Chemistry Division

Dr. V. Jayaraman
Materials Chemistry Division

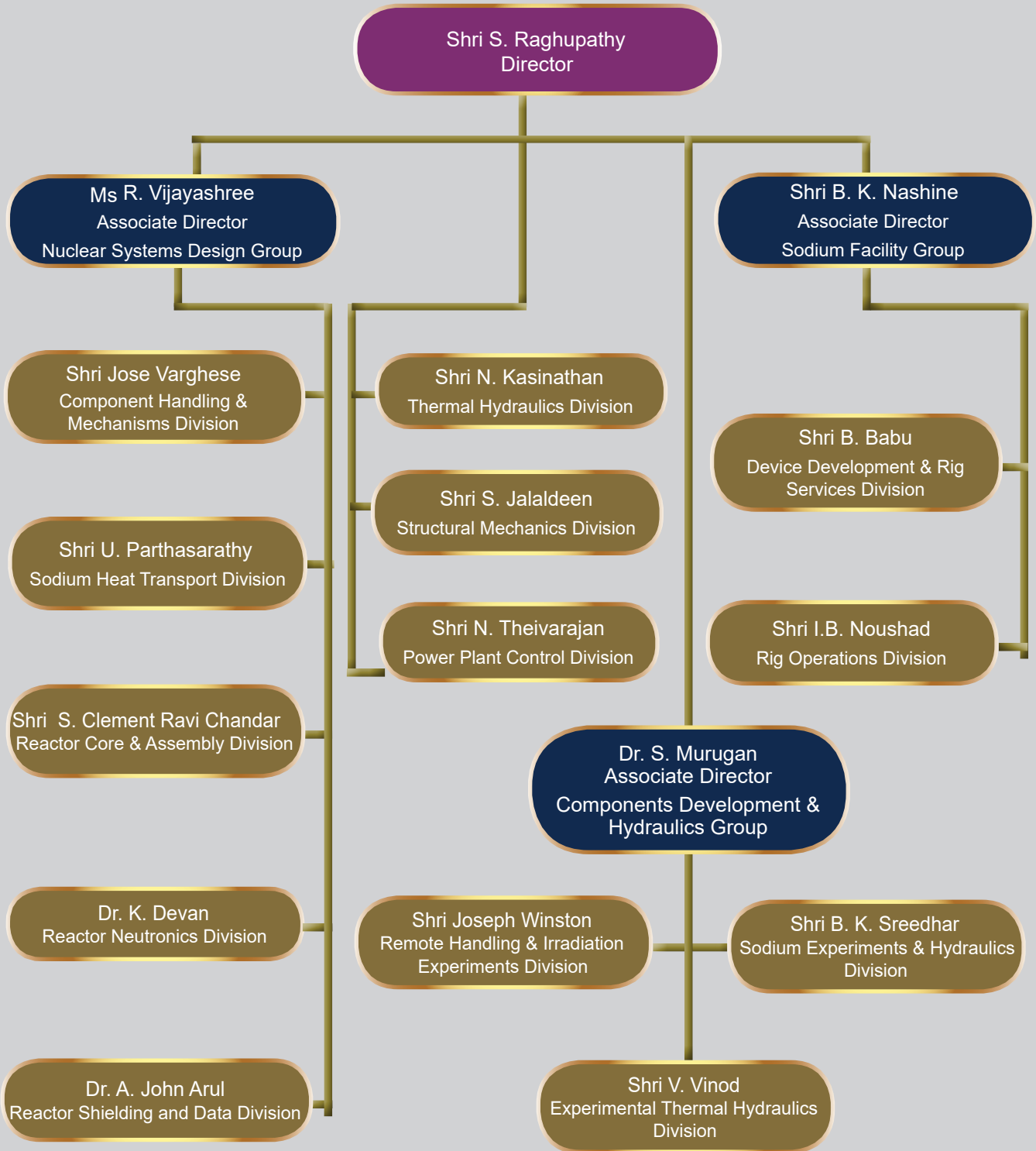
Materials Science Group



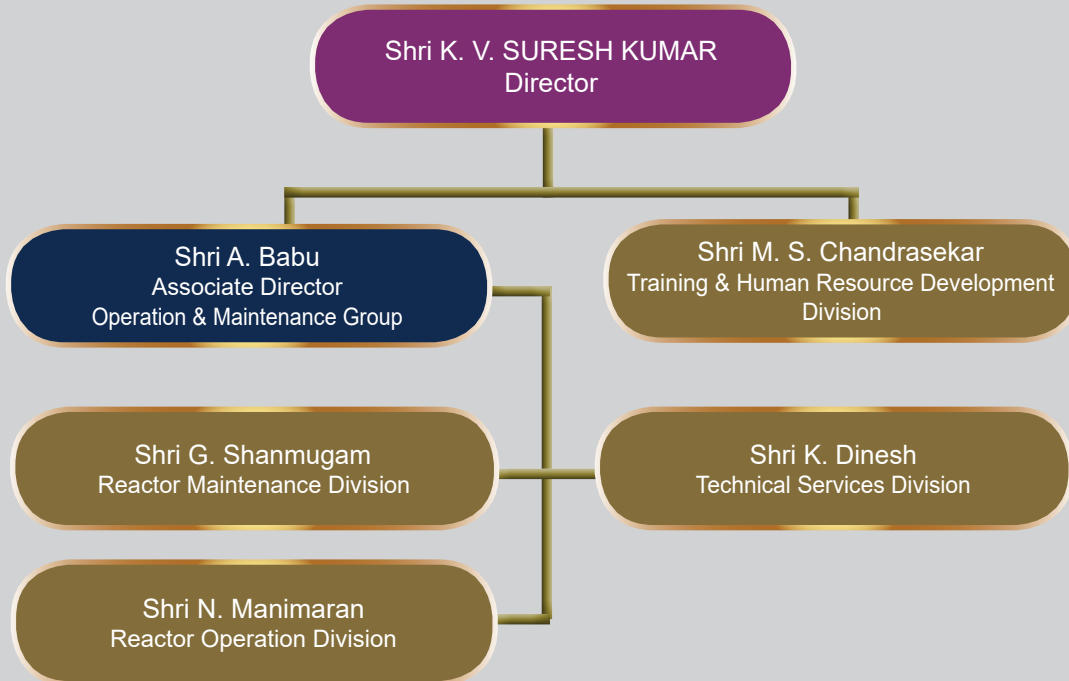
Metallurgy & Materials Group



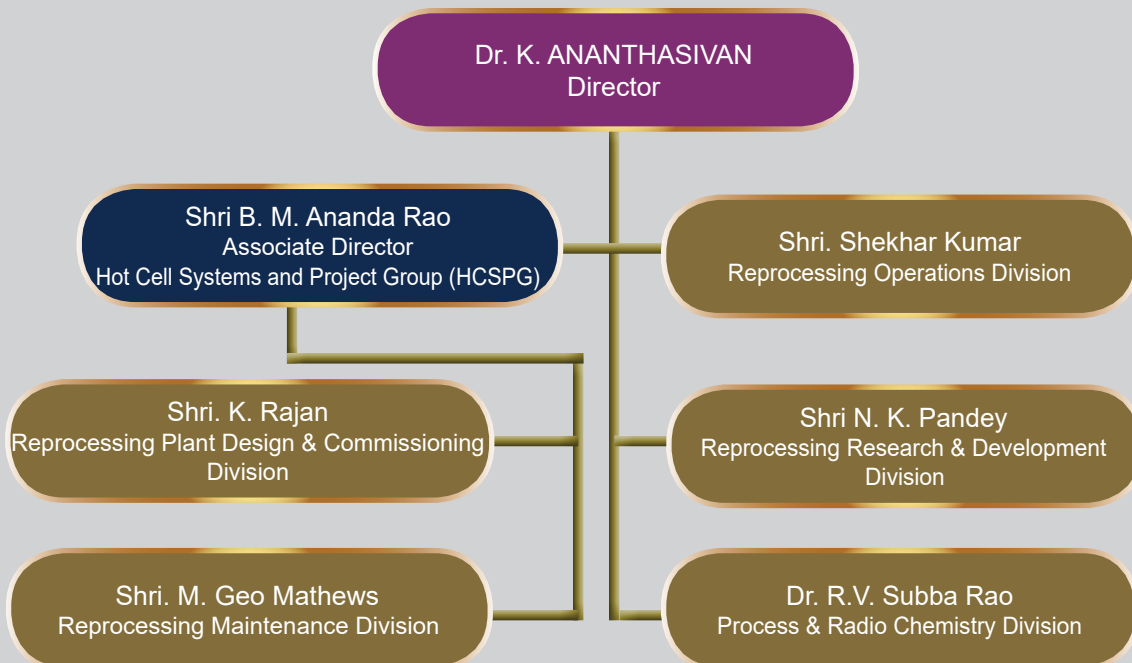
Reactor Design & Technology Group



Reactor Facilities Group



Reprocessing Group



Safety, Quality & Resource Management Group

Dr. B. Venkatraman
Director

Shri S. Athmalingam
Associate Director
Health, Safety & Environment Group

Shri S. Athmalingam
Quality Assurance Division

Dr. M.T. Jose
Health & Industrial Safety Division

Dr. R. Venkatesan
Radiological & Environmental Safety Division

Dr. D. Ponraju
Safety Engineering Division

Dr. T. S. Lakshmi Narasimhan
Associate Director
Resource Management Group

Dr. Vidya Sundararajan
Planning & Human Resource Management
Division

Smt. S. Rajeswari
Scientific Information Resource Division

Administration

Shri O.T. G. Nair
Director (P&A)

Shri R. Srinivasan
Administration (Legal & General)

Shri Paresh Nath Mahadani
Administration (Recruitment & Vigilance)

Smt. S. Jayakumari
Administration (Establishment)

Accounts

Shri M.S. Saravanan
IFA

Shri V. Sivakumar
IFA [FRFCF]

Shri K. Sai Kannan
DCA

